Imperial College London

Computational Study of Mixture Preparation in Direct-Injection Spark-Ignition Engines with Advanced Valvetrain System

Alexandros Kountouriotis

Imperial College London
Department of Mechanical Engineering

Thesis submitted for the degree of
Doctor of Philosophy and the Diploma of Imperial College London
August 2018

Abstract

Nowadays, ground transportation is a major source of air pollution with an impact on the greenhouse effect and on the public health, especially in urban areas. In this work, an investigation of the capabilities of a Continuous Variable Valve Lift system with the use of computational fluid dynamics was carried out. The aim was to understand the benefits and drawbacks of several valvelift strategies at various engine loads. This required validation of the commercial code STAR-CD and the models associated with engine simulations as well as implementation of a new flash-boiling model for fuel injection at low engine load. A generalised approach was adopted for sub-cooled and flash-boiling sprays by minimising the differences of the implementation. The Single Valve Actuation (SVA) was proved beneficial compared to the Dual Valve Actuation (DVA) because of the increase of the turbulent kinetic energy (TKE) and thus, the reduction of the combustion duration which allowed extension of the dilution limit. Moreover, it increased the mixture homogeneity because of the introduction of a strong swirl motion. However, the enhanced flow motion increased the heat transfer from the gas to the walls which offset the benefit of faster combustion. In addition, the difference in homogeneity was affecting the emissions depending on the dilution level. The benefits and drawbacks were balanced with the use of two differential intake valve lift strategies. The heat transfer could be reduced while the TKE and mixture homogeneity improved in comparison to the DVA. Lastly, the cyclic variability of the DVA and SVA were studied at high EGR levels. The lower in-cylinder velocity variability and lower variability of the laminar burning velocity due to lower residual mixing variability with the SVA denoted the lower combustion variability seen in the experiments.

Declaration of Originality

I, Alexandros Kountouriotis, declare that the work in this thesis is my own. Material taken from other sources is appropriately referenced.

Copyright Declaration

‘The copyright of this thesis rests with the author and is made available under a Creative Commons Attribution Non-Commercial No Derivatives licence. Researchers are free to copy, distribute or transmit the thesis on the condition that they attribute it, that they do not use it for commercial purposes and that they do not alter, transform or build upon it. For any reuse or redistribution, researchers must make clear to others the licence terms of this work’

Acknowledgments

First of all, I would like to thank my supervisor, Prof. Pavlos Aleiferis for giving me the opportunity to work on this exciting project. His recommendations, advice and guidance and the dedication he showed to support me and my work during the PhD are appreciated.

I would also like to thank the people at Jaguar Land Rover for sponsoring this project and contributing with their knowledge and experience. Dave Richardson was always trying to help by answering all my questions and organising meetings with people within JLR who could further assist me. I am grateful for the frequent discussions and advice from the CAE group and special thanks to Li Cao, Paul Dunkley and Giuseppe Virelli who were my first points of contact, always trying to assist me. I would particularly like to thank Phil Roberts whose initiative, constructive comments and ideas resulted in a publication. Last but not least, I would like to thank Nathan Hinton for his help and for providing me 1D simulation data for my thesis.

I wish to acknowledge the help provided by the support team of STAR-CD and STAR-CCM+ for their help and support and predominantly to Karl Bass, Rohan Wanchoo, Alexandros Panagoulias and Rickard Solsjo who were the main support for es-ice. With their help I managed to deal with numerous issues with the code.

My special thanks are extended to my PhD colleagues and more specifically, Ahmad, Arash, Calo, Chris, Jai, Kobi, Niko, Pawel, Reza and Stavro for their support and invaluable discussions about CFD and non-CFD matters.

Moreover, I would like to express my gratitude to all the people of the college for their assistance.

My deepest appreciation goes to my parents and my brother for standing always by my side and encouraging me to overcome all the difficulties I faced during this period. Finally, Laura's support and patience were invaluable.

Table of Contents

Table of Contents **5**
List of Figures **8**
List of Tables **18**
Nomenclature **19**
Introduction and Literature Review **23**
1.1. Introduction 23
1.2. Thesis outline 29
1.3. Exhaust gas recirculation 31
1.4. Valve control strategies 37
1.5. Gasoline direct injection 43
1.6. Pollutant formation 59
1.7. Synopsis and present contribution 63
Mathematical Formulation **67**
2.1. Basic flow solution 67
2.2. Turbulence modelling 68
2.3. Residuals and EGR Concentration Calculations 74
2.4. Wall heat flux 79
2.5. Spray modelling 80
2.5.1. Flash boiling modelling 82
2.5.2. Break-up modelling 83
2.5.3. Droplet-Droplet Interaction 84
2.5.4. Droplet-Wall Interaction 86
2.6. Liquid film modelling 91
2.7. Combustion and emissions modelling 94
2.8. Numerical methodology 100
Preliminary Studies and Model Validation **101**
3.1. Grid independence study 101
3.2. Initialisation study 108
3.3. Validation of pressure traces 111
3.4. Validation of flow field 123
3.5. Steady state port flow simulations 132
3.6. Evaluation of turbulence models 136
3.7. Engine heat flux 140
3.8. Validation of fuel injection 142
3.8.1. Sub-cooled fuel injection – quiescent chamber 142

3.8.2. Sub-cooled fuel injection – optical engine 153
3.8.3. Flash-boiling fuel injection – validation and development 159
3.9. Validation of fuel impingement and film formation 184
3.10. Closure 198
Effects of Valve Deactivation on In-Cylinder Flow 203
4.1. Introduction 203
4.2. Engine simulation setup 205
4.3. Engine load: 3.6 bar GMEP, 1500 RPM 207
4.3.1. Experimental results 207
4.3.2. In-cylinder flow properties 209
4.3.3. Laminar burning velocity 219
4.4. Engine load: 7.9 bar GMEP, 1500 RPM 228
4.4.1. Experimental results 228
4.4.2. In-cylinder flow properties 229
4.4.3. Laminar burning velocity 233
4.5. Engine load: 9.8 bar GMEP, 2000 RPM 234
4.5.1. Experimental results 234
4.5.2. In-cylinder flow properties 234
4.6. Heat transfer effects 237
4.7. Closure 243
Effects of Valve Deactivation on Mixture Preparation and Emissions 247
5.1. Introduction 247
5.2. Engine load: 7.9 bar GMEP, 1500 RPM 254
5.2.1. In-cylinder flow properties 254
5.2.2. Mixture preparation 257
5.2.3. Emissions 264
5.2.4. Combustion 278
5.3. Engine load: 3.6 bar GMEP, 1500 RPM 284
5.3.1. In-cylinder flow properties 284
5.3.2. Mixture preparation 285
5.3.3. Emissions 291
5.4. Closure 297
Differential Intake Valve Lift 303
6.1. Introduction 303
6.2. Experimental results 305
6.3. Late Intake Valve Opening (LIVO) 307
6.3.1. In-cylinder flow properties 307

6.3.2. Mixture preparation 316
6.3.3. Emissions 320
6.4. Early Intake Valve Closure (EIVC) 324
6.4.1. In-cylinder flow properties 325
6.4.2. Mixture preparation 333
6.4.3. Emissions 337
6.5. Closure 342
Effects of Valve Deactivation on Cyclic Variations 345
7.1. Introduction 345
7.2. Model validation 348
7.3. Averaged in-cylinder flow properties 350
7.4. Spatial distribution of in-cylinder flow properties 355
7.5. Closure 374
Conclusions and Future Work 377
8.1. Summary and conclusions 377
8.2. Future work 388
References 391

List of Figures

Figure 1.1 Historical data and proposed targets for CO2 from various countries normalised to NEDC. Source: The International Council on Clean Transportation (ICCT).....24
Figure 1.2 P-V diagrams and Schematics of the actual and ideal cycle in a spark ignition engine (Çengel and Boles, 2015).....26
Figure 1.3 Thermal Efficiency of Otto cycle versus compression ratio for three different values of γ.....26
Figure 1.4 Pollutant concentrations as a function of equivalence ratio (Φ) (Lumley, 1999).....28
Figure 1.5 The effect of EGR on NO_x emissions for various fuels (Mardi et al., 2014).....33
Figure 1.6 Two different methods for EGR stratification (Dong et al., 2002).....35
Figure 1.7 Four investigated strategies for radial EGR stratification (Sarikoc et al., 2006).....36
Figure 1.8 The effect of LIVC on tumble ratio and the flow field at 100 deg CA after BDC (Mito et al., 2012) 38
Figure 1.9 Spatial distribution of TKE for Dual and Single valve Actuation. (Jovanovic et al., 2011)...40
Figure 1.10 Various valve strategies to increase tumble and swirl motion for improved combustion (Mahrous et al., 2007).....41
Figure 1.11 Injector geometries and spray patterns for GDI engines (Baumgarten, 2006).....44
Figure 1.12 Stratified charge techniques, and injector positions. (Lee and Abraham, 2011).....45
Figure 1.13 A schematic of a full cone engine spray (Baumgarten, 2006).....45
Figure 1.14 the break up regimes on the Ohnesorge diagram and the schematic description of jet break-up regimes (Baumgarten, 2006).....46
Figure 1.15 Various mechanisms explaining the primary break up (Baumgarten, 2006).....47
Figure 1.16 Main droplet break up regimes (Otto and Kruger, 2006).....48
Figure 1.17 A schematic of the geometric collision parameters.....49
Figure 1.18 A schematic representation of the droplet collision mechanisms (Baumgarten, 2006).....50
Figure 1.19 Distillation curves of various fuels (Kountouriotis et al., 2014).....51
Figure 1.20 A schematic representation of a droplet evaporation (Baumgarten, 2006).....51
Figure 1.21 Comparison of conventional injection and flash-boiling injection in a pressure-enthalpy diagram (Baumgarten, 2006).....52
Figure 1.22 Comparison of gasoline sprays with different fuel temperatures at 0.5 bar ambient pressure (van Romunde and Aleiferis, 2009).....52
Figure 1.23 schematic of the six impingement regimes (Bai and Gosman, 1996).....54
Figure 1.24 Grid dependency of spray due to collision modelling for hollow cone and solid cone sprays (Schmidt and Rutland, 2000; Hou and Schmidt, 2006).....57

Figure 2.1 A schematic of the Exhaust Gas Recirculation (EGR).....77
Figure 2.2 Predicted droplet diameter at varying temperature at ambient pressures of $P\infty$ = 1.0 bar, $P\infty$ = 0.5 bar, and $P\infty$ = 0.3 bar.....83
Figure 2.3 Representation of the Bai-ONERA regimes.....88
Figure 2.4 Representation of the Senda regimes.....89
Figure 2.5 Representation of liquid film stripping due to wave and body-force induced instability. (Methodology, STAR-CD, 2016 CD-adapco).....91
Figure 2.6 Representation of liquid film stripping due to break-up caused by flow over a sharp edge....92
Figure 2.7 Boiling curve for water at 1 atm. (Cengel et al., 2011).....92
Figure 2.8 A graphical representation of the film boiling as it is calculated by the software (blue line) and the theoretical/experimental film boiling model (black line).....93

Figure 2.9 A graphical representation of the ECFM-3Z model in a computational cell (Colin and Benkenida, 2004)....95

Figure 3.1 CFD model of the AJ20 thermal engine....103
Figure 3.2 Number of in-cylinder cells during a cycle for four different grid size models....103
Figure 3.3 In-cylinder pressure traces for four different model sizes....104
Figure 3.4 Average in-cylinder velocity magnitude for four different model sizes....105
Figure 3.5cont. The 2D template from which the mesh is based on and a cross-sectional view of the four models at mid-valve point at BDC....107
Figure 3.6 Velocity magnitude for four model sizes at 20 deg CA before TDC....108
Figure 3.7 Comparison of the in-cylinder velocity magnitude during three consecutive cycles for two different initialised simulations....110
Figure 3.8 Comparison of the in-cylinder velocity magnitude for three consecutive cycles when initialised before EVO....110
Figure 3.9 Comparison of the velocity field at intake and exhaust valve opening....111
Figure 3.10 CFD model of the AJ133 optical engine and the AJ20 single cylinder thermal engine....112
Figure 3.11 Theoretical exhaust and intake cam profiles and derived valve profiles....115
Figure 3.12 In-cylinder pressure for four experimental and five numerical cases from the AJ133 optical engine....116
Figure 3.13 In-cylinder pressure focused around TDC for four experimental and five numerical cases from the AJ133 optical engine....117
Figure 3.14 Experimental and numerical in-cylinder pressure and valve lifts for 1 bar intake pressure. Intake cam: base position, Exhaust cam: 50 deg CA retard (AJ20)....119
Figure 3.15 Experimental and numerical in-cylinder pressure and valve lifts for 1 bar intake pressure. Intake cam: 50 deg CA advance, Exhaust cam: 50 deg CA retard (AJ20)....119
Figure 3.16 Experimental and numerical in-cylinder pressure and valve lifts for 1 bar intake pressure. Intake cam: base position, Exhaust cam: base position (AJ20)....120
Figure 3.17 Experimental and numerical in-cylinder pressure and valve lifts for 0.5 bar intake pressure. Intake cam: base position, Exhaust cam: base position (AJ20)....120
Figure 3.18 Experimental and numerical in-cylinder pressure and valve lifts for 0.5 bar intake pressure. Intake cam: 50 deg CA advance, Exhaust cam: 50 deg CA retard (AJ20)....121
Figure 3.19 Investigation into the recompression at gas exchange TDC (AJ20)....122
Figure 3.20 Experimental U velocity component at the intake runner and the region of the measurement (AJ133)....124
Figure 3.21 Numerical velocity magnitude at the intake runner and experimental and numerical U velocity component at specific crank angles (AJ133)....125
Figure 3.22 Experimental velocity profile of 200 cycles in the intake runner at five specific crank angles....125
Figure 3.23 Region of pent roof measurements....126
Figure 3.24 Experimental mean velocity of the valve jet at the mid-valve plane....127
Figure 3.25 Numerical mean velocity [m/s] of the valve jet at the mid-valve plane....127
Figure 3.26 Comparison of experimental PIV data and numerical results of the velocity field for specific crank angles....129
Figure 3.27 Velocity magnitude along x-axis at three different z-axis locations and three different crank angles. First row z=-8mm, second row z=-28mm, third row z=-48mm. Data from current study, PIV and Beavis et al. (2017)....131
Figure 3.28 Polyhedral and hexahedral grids of the port flow model....134

Figure 3.29 Grid independence study for port flow simulation and comparison with experimental data of the AJ133 engine head.....135
Figure 3.30 Experimental and numerical results of the AJ133 flow coefficient for four different turbulence models and two different types of grid.....136
Figure 3.31 In-cylinder trapped mass for the four turbulence models.....138
Figure 3.32 Velocity magnitude at the intake runner for the four different turbulence models.....138
Figure 3.33 Comparison between the PIV data and the flow field from the four turbulence models.....140
Figure 3.34 Heat flux at 0.5 bar intake pressure, 1500RPM (AJ133).....141
Figure 3.35 Heat flux at 1 bar intake pressure, 1500RPM (AJ133).....142
Figure 3.36 AJ133 six-hole injector spray pattern.....143
Figure 3.37 AJ20 detailed head geometry with zoom on the injector and how the six individual plumes were located in the grid of a constant volume domain.....144
Figure 3.38 Mass flow rate and injection velocity for the case with the Rosin-Rammler distribution...145
Figure 3.39 Spray formation and droplet diameter 0.78 ms after star of injection. Fuel: iso-octane, T=20°C, P∞=0.5bar. Experiments from Van Romunde et al. (2007).....147
Figure 3.40 Experimental and numerical spray penetration of iso-Octane at 0.5 bar ambient pressure and 293K fuel temperature.....148
Figure 3.41 Experimental and numerical spray tip velocity.....149
Figure 3.42 Numerical SMD number for the optimised blob method and the Rosin-Rammler distribution, 25 mm below the injector tip.....150
Figure 3.43 Experimental droplet size scatter plot versus time for gasoline at 20 °C and ambient pressure of 0.5 bar and 1.0 bar.....151
Figure 3.44 Numerical droplet size scatter plot versus time for iso-octane at 20 °C and ambient pressure at 0.5 bar for the optimised blob method and the Rosin-Rammler distribution, 25 mm below the injector tip.....151
Figure 3.45 Experimental and numerical D10.Numerical setup: iso-Octane at 0.5 bar ambient pressure and 293K fuel temperature. Experiment: gasoline at 20 °C and ambient pressure of 0.5 bar and 1.0 bar.....152
Figure 3.46 Numerical spray development and experimental spray development in the AJ133 optical engine, sub-cooled spray, swirl plane.....156
Figure 3.47 Numerical spray development and experimental spray development in the AJ133 optical engine, sub-cooled spray, tumble plane. Images not in scale.....157
Figure 3.48 Experimental in-cylinder equivalence ratio distribution at 60° BTDC for the three different tracers (1500 rpm and 0.521 bar intake pressure).....158
Figure 3.49 Numerical in-cylinder equivalence ratio distribution at 60° BTDC.....158
Figure 3.50 Experimental spray penetration of iso-octane at 0.5 bar ambient pressure and 293K fuel temperature and of n-pentane at 393K fuel temperature, Numerical spray penetration of iso-octane at 0.5 bar ambient pressure and 293K fuel temperature and of n-pentane at 393K fuel temperature.....160
Figure 3.51 Numerical tuning process of the flash boiling model with n-pentane in the AJ133 optical engine. Experiments from Serras-Pereira et al. (2008).....162
Figure 3.52 Comparison of spray behaviour of gasoline and n-pentane at various temperatures and 0.5 bar ambient pressure. Experiments from van Romunde et al. (2007).....163
Figure 3.53 Numerical tuning process of the flash boiling model with iso-hexane in the AJ133 optical engine. Experiments from Serras-Pereira et al. (2008).....164
Figure 3.54 Behaviour of the original flash-boiling spray with the EB2 injector location at two different positions in respect to the mesh.....166
Figure 3.55 EB2 injector location at two different positions in respect to the mesh with the plumes spaced according to the Figure 3.37.....167

Figure 3.56 Behaviour of the flash-boiling spray with the EB2 injector location at two different positions in respect to the mesh at two fuel temperatures.....169
Figure 3.57 Representation of the refined grid around the injector tip and the location of the plumes in respect to the mesh.....170
Figure 3.58 Behaviour of the spray at three fuel temperatures on the refined grid.....171
Figure 3.59 Behaviour of the spray at 90°C fuel temperatures on the refined grid for three different cone angles. Collision geometric constraints applied. Blob method applied.....172
Figure 3.60 Behaviour of the spray at 90°C fuel temperatures on the refined grid for three different cone angles. Collision geometric constraints applied. Rosin-Rammler method applied.....173
Figure 3.61 Experimental results of sub-cooled and flash-boiling sprays by Yang et al. (2013).....174
Figure 3.62 Spray structure and pressure field at the EB2 injector symmetry plane. Fuel temperature at 90°C, cone angle 17°, blob method, geometric constraints applied. (Figure 3.59, row 1).....175
Figure 3.63 Numerical spray structure of the AJ133 injector for three different plume cone angles. Fuel at 90°C, Rosin-Rammler, geometric constraints applied.....176
Figure 3.64 Experimental penetration of gasoline and n-pentane at 90°C and 120°C. Numerical penetration of n-pentane at 90°C with various cone angles at coarse and refined grid. Ambient pressure at 0.5 bar.....178
Figure 3.65 SMD number of the optimum flash-boiling case for the AJ133 injector, 25 mm below the injector tip.....179
Figure 3.66 The EB2 flash-boiling spray structure for two plume cone angles. Fuel temperature at 90°C and ambient pressure 1bar. Comparison against gasoline at 90°C and 1 bar ambient pressure.....180
Figure 3.67 Numerical spray development and experimental spray development in the AJ133 optical engine, optimised flash-boiling spray, swirl plane.....182
Figure 3.68 Numerical spray development and experimental spray development in the AJ133 optical engine, optimised flash-boiling spray, tumble plane.....183
Figure 3.69 Experimental average peak heat flux and numerical peak heat flux of Senda model with coarse and refined surface mesh, with and without the 1DCHT model, with droplet to film transition model, various wall temperatures.....186
Figure 3.70 Experimental average peak heat flux and numerical peak heat flux of Bai-ONERA model with coarse and refined surface mesh, with and without the 1DCHT model, with droplet to film transition model, various wall temperatures.....187
Figure 3.71 Experimental average peak heat flux and numerical peak heat flux of Senda model with coarse and refined surface mesh, with and without the 1DCHT model, without droplet to film transition model, various wall temperatures.....188
Figure 3.72 Experimental average peak heat flux and numerical peak heat flux of Bai-ONERA model with coarse and refined surface mesh, with and without the 1DCHT model, without droplet to film transition model, various wall temperatures.....189
Figure 3.73 Experimental mean heat flux signal and numerical heat flux signal for coarse and refined surface mesh, with and without 1DCHT model, without droplet to film transition model, various wall temperatures.....192
Figure 3.74 Experimental liquid film footprint and film thickness, numerical liquid film footprint and film thickness for Bai-ONERA and Senda models, coarse surface mesh with and without 1DCHT model and refined surface mesh.....194
Figure 3.75 Artefacts coming from the Lagrangian multi-phase treatment for both Bai-ONERA and Senda models.....195
Figure 3.76 Experimental and numerical heat flux for the motoring AJ133 engine. 0.5 bar intake pressure, 1500 RPM, 20°C wall temperature.....197

Figure 4.1 Typical valvelift strategies of the Jaguar Land Rover CVVL system (Roberts et al. 2018)..205
Figure 4.2 Comparison of the combustion stability limit for DVA and SVA. 3.6bar GMEP, 1500 RPM. (Roberts et al., 2018).....207
Figure 4.3 Comparison of the comparison of the ignition to 10% MFB duration for DVA and SVA. 3.6bar GMEP, 1500 RPM. (Roberts et al., 2018).....208
Figure 4.4 (a) normalised GSFC for DVA and SVA for a fixed combustion stability limit of 3% COV of NM EP. (b) fuel consumption (GSFC) reduction from DVA to SVA. (Roberts et al., 2018).....209
Figure 4.5 Experimental and CFD pressure traces for DVA and SVA and for λ=1.0 and λ=1.5. 3.6 bar GMEP, 1500 RPM.....210
Figure 4.6 In-cylinder Velocity for DVA and SVA at λ=1.0 and the ratio SVA/DVA. 3.6 bar GMEP, 1500 RPM. 211
Figure 4.7 Tumble and swirl for DVA and SVA at λ=. 3.6 bar GMEP, 1500 RPM.....212
Figure 4.8 Representation of the mechanism responsible for the reverse of the tumble.....212
Figure 4.9 Tumble and swirl plane positions, representation of the global coordinate system and the position of the intake and exhaust ports.....213
Figure 4.10 Velocity magnitude contour and vector plots for DVA and SVA at λ=1.0, 20 °CA before TDC.....213
Figure 4.11 TKE for intake and compression strokes and a focus on the compression stroke. 3.6 bar GMEP, 1500 RPM.....214
Figure 4.12 Spatial distribution of TKE for DVA and SVA at λ=1.0, 20 °CA before TDC. 3.6 bar GMEP, 1500 RPM.....215
Figure 4.13 In-cylinder temperature for DVA and SVA at λ=1.0. 3.6 bar GMEP, 1500 RPM.....216
Figure 4.14 Trapped mass for DVA and SVA at λ=1.0. 3.6 bar GMEP, 1500 RPM.....217
Figure 4.15 Total heat transfer from liner, piston and dome for DVA and SVA for λ=1.0. 3.6 bar GMEP, 1500 RPM.....218
Figure 4.16 Comparison of stoichiometric iso-octane burning velocity correlation of Metghalchi and Keck (1982) (solid lines) and Marshall et al. (2011) that excludes data affected by cellularity (dashed lines) with three different residual mass fractions, at 101 kPa. Taken from Marshall et al. (2011).....219
Figure 4.17 Spatial distribution of laminar burning velocity for DVA and SVA at λ=1.0, 20 °CA before TDC. 3.6 bar GMEP, 1500 RPM.....220
Figure 4.18 Laminar burning velocity for DVA and SVA at λ=1.0, 10 °CA before TDC. 3.6 bar GMEP, 1500 RPM.....220
Figure 4.19 Laminar burning velocity versus residuals mole fraction and temperature at P=7 bar and λ=1. Calculations from Marshall et al. (2011).....222
Figure 4.20 Residuals concentration and temperature for DVA and SVA at λ=1.0, 10 °CA before TDC (tumble plane), 10 °CA before TDC. 3.6 bar GMEP, 1500 RPM.....223
Figure 4.21 Residuals concentration and temperature for DVA and SVA at λ=1.0, 10 °CA before TDC (swirl plane), 10 °CA before TDC. 3.6 bar GMEP, 1500 RPM.....224
Figure 4.22 In-cylinder Velocity for DVA and SVA at λ=1.0 and λ=1.5. 3.6 bar GMEP, 1500 RPM....225
Figure 4.23 In-cylinder TKE for DVA and SVA at λ=1.0 and λ=1.5. 3.6 bar GMEP, 1500 RPM.....226
Figure 4.24 Laminar burning velocity and residuals concentration for DVA and SVA λ=1.5, 10 °CA before TDC, (tumble plane). 3.6 bar GMEP, 1500 RPM.....227
Figure 4.25 Laminar burning velocity versus residuals mole fraction and temperature at P=6 bar and P=8 bar at λ=1.5.....227
Figure 4.26 Comparison of the 10% to 90% MFB duration for DVA and SVA. 7.9bar GMEP, 1500 RPM. (Roberts et al., 2018).....228
Figure 4.27 Fuel consumption (GSFC) reduction from DVA to SVA. 7.9bar GMEP, 1500 RPM. (Roberts et al., 2018).....229

Figure 4.28 In-cylinder velocity for DVA and SVA at λ=1.0 and the ratio SVA/DVA. 7.9 bar GMEP, 1500 RPM..... 230
Figure 4.29 In-cylinder TKE for DVA and SVA at λ=1.0 and the ratio SVA/DVA. 7.9 bar GMEP, 1500 RPM..... 231
Figure 4.30 Total heat transfer from liner, piston and dome for DVA and SVA for λ=1.0. 7.9 bar GMEP, 1500 RPM.....232
Figure 4.31 Laminar burning velocity for DVA. 10 °CA before TDC λ=1.0. 7.9 bar GMEP, 1500 RPM.....233
Figure 4.32 Comparison of the combustion stability limit for DVA and SVA. 9.8 bar GMEP, 1500 RPM. (Roberts et al., 2018).....234
Figure 4.33 In-cylinder velocity for DVA and SVA at λ=1.0 and the ratio SVA/DVA. 9.8 bar GMEP, 1500 RPM..... 235
Figure 4.34 In-cylinder TKE for DVA and SVA at λ=1.0 and the ratio SVA/DVA. 7.9 bar GMEP, 1500 RPM..... 236
Figure 4.35 Total heat transfer from liner, piston and dome for DVA and SVA for λ=1.0. 9.8 bar GMEP, 1500 RPM.....237
Figure 4.36 Comparison between the actual and close cycle simulations for the in-cylinder velocity and TKE at 3.6 bar GMEP, 1500RPM.....239
Figure 4.37 Total heat transfer for the four closed cycle simulations and the two actual cycles. 3.6 bar GMEP, 1500 RPM.....241
Figure 4.38 Total heat transfer for the four closed cycle simulations and the two actual cycles. 7.9 bar GMEP, 1500 RPM.....242
Figure 4.39 Total heat transfer for the four closed cycle simulations and the two actual cycles. 9.8 bar GMEP, 2000 RPM.....243

Figure 5.1 Spray structure for DVA and SVA for two loads (3.6 bar GMEP and 7.9 bar GMEP, 1500 RPM), tumble view.....249
Figure 5.2 Spray structure for DVA and SVA for two loads (3.6 bar GMEP and 7.9 bar GMEP, 1500 RPM), swirl view.....250
Figure 5.3 Convergence of global Lambda for DVA and SVA.....250
Figure 5.4 Intake pressure trace at various intake runner locations calculated with 1D simulation....251
Figure 5.5 Original AJ20 geometry and geometry with extended intake runner.....252
Figure 5.6 Verification of the normalisation approach for Lambda. Calculations at 20 degrees before TDC.....253
Figure 5.7 In-cylinder velocity magnitude for DVA and SVA, with and without injection. 7.9 bar GMEP, 1500 RPM.....255
Figure 5.8 In-cylinder TKE magnitude for DVA and SVA, with and without injection. 7.9 bar GMEP, 1500 RPM.....255
Figure 5.9 Total heat transfer for DVA and SVA, with and without injection. 7.9 bar GMEP, 1500 RPM.....256
Figure 5.10 Spatial distribution of Lambda for DVA at various crank angles during compression, λ=1.0, 7.9 bar GMEP 1500 RPM.....258
Figure 5.11 Spatial distribution of Lambda for SVA at various crank angles during compression, λ=1.0, 7.9 bar GMEP 1500 RPM.....259
Figure 5.12 Homogeneity Index for DVA and SVA at 7.9 bar GMEP, 1500 RPM, λ=1.0.....260
Figure 5.13 Spatial distribution of Lambda for DVA and SVA 10 degrees CA before TDC, λ=1.5, 7.9 bar GMEP 1500 RPM.....261

Figure 5.14 Spatial distribution of laminar burning velocity for DVA and SVA 10 degrees CA before TDC, λ=1.0, 7.9 bar GMEP 1500 RPM.....262
Figure 5.15 Accumulated liquid film mass at the piston and liner for DVA and SVA versus time. λ=1.0. 7.9 bar GMEP, 1500 RPM.....263
Figure 5.16 Liquid film thickness at the piston for DVA and SVA at 20 degrees after SOI. λ=1.0. 7.9 bar GMEP, 1500 RPM.....264
Figure 5.17 Experimental emissions of NO_x, THC and CO. 7.9 bar GMEP, 1500 RPM.....265
Figure 5.18 The size of the smallest and biggest spheres relative to the cylinder. Tumble and swirl views.....265
Figure 5.19 Percentage of the respective spherical volumes occupied with a rich mixture (λ<1.0) for DVA. Global λ=1.0. 7.9 bar GMEP, 1500 RPM.....268
Figure 5.20 Percentage of the respective spherical volumes occupied with a rich mixture (λ<1.0) for SVA. Global λ=1.0. 7.9 bar GMEP, 1500 RPM.....268
Figure 5.21 Average lambda of the rich mixture within each spherical volume for DVA. Global λ=1.0. 7.9 bar GMEP, 1500 RPM.....269
Figure 5.22 Average lambda of the rich mixture within each spherical volume for SVA. Global λ=1.0. 7.9 bar GMEP, 1500 RPM.....269
Figure 5.23 Percentage of the respective spherical volumes occupied with a lean mixture in the range λ[1.05,1.15] for DVA. Global λ=1.0. 7.9 bar GMEP, 1500RPM.....271
Figure 5.24 Percentage of the respective spherical volumes occupied with a lean mixture in the range λ[1.05,1.15] for SVA. Global λ=1.0. 7.9 bar GMEP, 1500RPM.....271
Figure 5.25 Percentage of the respective spherical volumes occupied with a lean mixture in the range λ[1.05,1.15] for DVA. Global λ=1.1. 7.9 bar GMEP, 1500RPM.....272
Figure 5.26 Percentage of the respective spherical volumes occupied with a lean mixture in the range λ[1.05,1.15] for SVA. Global λ=1.1. 7.9 bar GMEP, 1500RPM.....273
Figure 5.27 Percentage of the respective spherical volumes occupied with a lean mixture in the range λ[1.05,1.15] for DVA. Global λ=1.2. 7.9 bar GMEP, 1500RPM.....274
Figure 5.28 Percentage of the respective spherical volumes occupied with a lean mixture in the range λ[1.05,1.15] for SVA. Global λ=1.2. 7.9 bar GMEP, 1500RPM.....275
Figure 5.29 Experimental in-cylinder temperature derived from the experimental in-cylinder pressure for DVA and SVA and for four different dilution cases.....276
Figure 5.30 Temperature term angle of eq. 5.2 versus crank for three dilution cases. 7.9 bar GMEP, 1500RPM..... 277
Figure 5.31 Validation of the in-cylinder pressure trace and accumulated heat release rate for DVA and SVA. Global λ=1.0. 7.9 bar GMEP, 1500RPM.....279
Figure 5.32 Numerical predictions of CO and NO_x for DVA and SVA. Global λ=1.0. 7.9 bar GMEP, 1500RPM..... 280
Figure 5.33 Spatial distribution of CO at the peak production (15 degrees after TDC) for DVA and SVA. Global λ=1.0. 7.9 bar GMEP, 1500RPM.....281
Figure 5.34 Spatial distribution of NO_x at the peak production (20 degrees after TDC) for DVA and SVA. Global λ=1.0. 7.9 bar GMEP, 1500RPM.....282
Figure 5.35 Spatial distribution of temperature at the peak NO_x production (20 degrees after TDC) for DVA and SVA. Global λ=1.0. 7.9 bar GMEP, 1500RPM.....282
Figure 5.36 Numerical predictions of soot for DVA and SVA. Global λ=1.0. 7.9 bar GMEP, 1500 RPM..... 283
Figure 5.37 Spatial distribution (3D) of soot at EVO for DVA and SVA. Global λ=1.0. 7.9 bar GMEP, 1500 RPM.....283

Figure 5.38 Spatial distribution of Lambda for DVA at various crank angles during compression, λ=1.0, 3.6 bar GMEP, 1500 RPM.....286
Figure 5.39 Spatial distribution of Lambda for SVA at various crank angles during compression, λ=1.0, 3.6 bar GMEP, 1500 RPM.....287
Figure 5.40 Homogeneity Index for DVA and SVA at 3.6 bar GMEP, 1500 RPM, λ=1.0.....288
Figure 5.41 Spatial distribution of laminar burning velocity for DVA and SVA 10 degrees CA before TDC, λ=1.0, 3.6 bar GMEP 1500 RPM.....289
Figure 5.42 Accumulated liquid film mass at the piston and liner for DVA and SVA versus time. λ=1.0. 3.6 bar GMEP, 1500 RPM.....290
Figure 5.43 Liquid film thickness at the piston for DVA and SVA at 20 degrees after SOI. λ=1.0. 3.6 bar GMEP, 1500 RPM..... 290
Figure 5.44 Experimental emissions of NO_x, THC and CO. 3.6 bar GMEP, 1500 RPM.....292
Figure 5.45 Percentage of the respective spherical volumes occupied with a rich mixture (λ<1.0) for DVA. Global λ=1.0. 3.6 bar GMEP, 1500RPM.....293
Figure 5.46 Percentage of the respective spherical volumes occupied with a rich mixture (λ<1.0) for SVA. Global λ=1.0. 3.6 bar GMEP, 1500RPM.....294
Figure 5.47 Average lambda of the rich mixture within each spherical volume for DVA. Global λ=1.0. 3.6 bar GMEP, 1500 RPM..... 294
Figure 5.48 Average lambda of the rich mixture within each spherical volume for SVA. Global λ=1.0. 3.6 bar GMEP, 1500 RPM..... 295
Figure 5.49 Percentage of the respective spherical volumes occupied with a lean mixture in the range λ[1.05,1.15] for DVA. Global λ=1.0. 3.6 bar GMEP, 1500 RPM..... 296
Figure 5.50 Percentage of the respective spherical volumes occupied with a lean mixture in the range λ[1.05,1.15] for SVA. Global λ=1.0. 3.6 bar GMEP, 1500 RPM.....296

Figure 6.1 The five different LIVO valve lifts and the full lift as applied in the model.....304
Figure 6.2 The five different EIVC valve lifts and the full lift as applied in the model.....305
Figure 6.3 Comparison of the experimental ignition to 10% MFB duration between LIVO and EIVC mode. DVA and SVA are included.....306
Figure 6.4 Comparison of the experimental 10% to 90% MFB duration between LIVO and EIVC mode. DVA and SVA are included.....306
Figure 6.5 Experimental in-cylinder pressure trace during combustion for the five different LIVO cases.....307
Figure 6.6 In-cylinder velocity magnitude for DVA, SVA and the five different LIVO lift cases.....309
Figure 6.7 Swirl ratio for DVA, SVA and the five different LIVO lift cases.....310
Figure 6.8 Tumble ratio for DVA, SVA and the five different LIVO lift cases.....311
Figure 6.9 Turbulent kinetic energy for DVA, SVA and the five different LIVO lift cases with a zoom on the compression stroke after IVC.....312
Figure 6.10 Spatial distribution of TKE for DVA, SVA and the five different LIVO lift cases for the tumble and swirl planes at ignition (10 degrees CA before TDCf).....314
Figure 6.11 Heat transfer from the gas to the walls for DVA, SVA and the five different LIVO lift cases.....316
Figure 6.12 Spatial distribution of Lambda for DVA, SVA and the five different LIVO lift cases for the tumble and swirl planes at ignition.....318
Figure 6.13 Homogeneity Index for DVA, SVA and the five different LIVO lift cases.....319
Figure 6.14 Total film mass on the piston versus crank angle for DVA, SVA and the five different LIVO lift cases.....320

Figure 6.15 Film thickness on the piston at maximum accumulated film mass for 1 mm and 5 mm lift LIVO cases..... 320
Figure 6.16 Experimental data of NO_x, CO and THC for DVA, SVA and the five different LIVO lift cases with various dilution.....321
Figure 6.17 Percentage of the interrogating spherical volumes occupied by a mixture with $\lambda<1.0$ and Average Lambda of the lambda zones below $\lambda=1.0$ for various interrogating spherical volumes for the five different LIVO lift cases..... 323
Figure 6.18 Percentage of different interrogating spherical volumes occupied by a mixture with λ in the region [1.05,1.15] for the five different LIVO lift cases.....324
Figure 6.19 Experimental in-cylinder pressure trace during combustion for the five different EIVC cases.....325
Figure 6.20 In-cylinder velocity magnitude for DVA, SVA and the five different EIVC lift cases.....326
Figure 6.21 Swirl ratio for DVA, SVA and the five different EIVC lift cases.....327
Figure 6.22 Tumble ratio for DVA, SVA and the five different EIVC lift cases.....328
Figure 6.23 Turbulent kinetic energy for DVA, SVA and the five different EIVC lift cases with a zoom on the compression stroke after IVC.....329
Figure 6.24 Spatial distribution of TKE for DVA, SVA and the five different EIVC lift cases for the tumble and swirl planes at ignition.....331
Figure 6.25 Heat transfer from the gas to the walls for DVA, SVA and the five different EIVC lift cases.....332
Figure 6.26 Spatial distribution of Lambda for DVA, SVA and the five different EIVC lift cases for the tumble and swirl planes at ignition.....334
Figure 6.27 Homogeneity Index for DVA, SVA and the five different EIVC lift cases.....335
Figure 6.28 Total film mass on the piston versus crank angle for DVA, SVA and the five different EIVC lift cases.....336
Figure 6.29 Film thickness on the piston at 20 degrees after SOI for the five different EIVC lift cases.....337
Figure 6.30 Experimental data of NO_x, CO and THC for DVA, SVA and the five different EIVC lift cases with various dilution.....338
Figure 6.31 Percentage of the interrogating spherical volumes occupied by a mixture with $\lambda<1.0$ and Average Lambda of the lambda zones below $\lambda=1.0$ for various interrogating spherical volumes for the five different EIVC lift cases.....340
Figure 6.32 Percentage of different interrogating spherical volumes occupied by a mixture with λ in the region [1.05,1.15] for the five different EIVC lift cases.....341

Figure 7.1 Turbulence resolution parameter for DVA and SVA at 30 and 25 degrees before TDC respectively. Cutting line at z=+5mm, x=0mm and y=0mm.....348
Figure 7.2 Experimental and average over 25 cycles LES in-cylinder pressure trace for DVA.....349
Figure 7.3 Experimental and average over 25 cycles LES in-cylinder pressure trace for SVA.....350
Figure 7.4 in-cylinder velocity magnitude of the 25 individual cycles and their mean for DVA and SVA.....353
Figure 7.5 Standard deviation of average in-cylinder velocity for 25 cycles during intake and compression strokes for DVA and SVA.....354
Figure 7.6 CoV of average in-cylinder velocity for 25 cycles during intake and compression strokes for DVA and SVA.....354
Figure 7.7 Statistical convergence of the velocity magnitude for the first 5, 10, 15, 20 and 25 cycles in the tumble and swirl planes for DVA.....356

Figure 7.8 Mean velocity magnitude along the x- and y-axis at z=+5 mm for the five different averaging groups. DVA.....357
Figure 7.9 Statistical convergence of the standard deviation of the velocity magnitude for the first 5, 10, 15, 20 and 25 cycles in the tumble and swirl planes for DVA.....358
Figure 7.10 Standard deviation of velocity magnitude along the x- and y-axis at z=+5 mm for the five different averaging groups. DVA.....359
Figure 7.11 Statistical convergence of the velocity magnitude for the first 5, 10, 15, 20 and 25 cycles in the tumble and swirl planes for SVA.....361
Figure 7.12 Mean velocity magnitude along the x- and y-axis at z=+5 mm for the five different averaging groups. SVA.....361
Figure 7.13 Statistical convergence of the standard deviation of the velocity magnitude for the first 5, 10, 15, 20 and 25 cycles in the tumble and swirl planes for SVA.....363
Figure 7.14 Standard deviation of velocity magnitude along the x- and y-axis at z=+5 mm for the five different averaging groups. SVA.....363
Figure 7.15 Spatial distribution of mean, standard deviation and coefficient of variation of DVA and SVA over 25 cycles. Tumble plane.....365
Figure 7.16 Spatial distribution of mean, standard deviation and CoV of DVA and SVA over 25 cycles. Swirl plane.....366
Figure 7.17 Spatial distribution of mean, standard deviation and CoV of laminar burning velocity of DVA and SVA over 25 cycles. Tumble plane.....367
Figure 7.18 Spatial distribution of mean, standard deviation and CoV of laminar burning velocity of DVA and SVA over 25 cycles. Swirl plane.....368
Figure 7.19 CoV of laminar burning velocity for DVA and SVA along the x- and y-axis at z=+5mm...368
Figure 7.20 Spatial distribution of mean, standard deviation and CoV of temperature for DVA and SVA over 25 cycles. Tumble plane.....370
Figure 7.21 Spatial distribution of mean, standard deviation and CoV of temperature for DVA and SVA over 25 cycles. Swirl plane.....371
Figure 7.22 CoV of temperature for DVA and SVA along the x- and y-axis at z=+5mm.....371
Figure 7.23 Spatial distribution of mean, standard deviation and CoV of residuals for DVA and SVA over 25 cycles. Tumble plane.....373
Figure 7.24 Spatial distribution of mean, standard deviation and CoV of residuals for DVA and SVA over 25 cycles. Swirl plane.....374
Figure 7.25 CoV of residuals for DVA and SVA along the x- and y-axis at z=+5mm.....374

List of Tables

Table 2.1 Mass fraction calculations of various species for initialisation before EVO.....79

Table 3.1 Characteristics of the AJ20 thermal engine for the preliminary studies.....102
Table 3.2 Initial and boundary conditions for the grid dependence study.....104
Table 3.3 Characteristics of the AJ133 single cylinder optical engine and the AJ20 single cylinder thermal engine.....113
Table 3.4 Initial and boundary conditions for the validation of the AJ133 optical engine.....114
Table 3.5 Boundary conditions for the steady state port flow simulations.....133
Table 3.6 Valve lift and L/D equivalence.....133
Table 3.7 Initial droplet size and Reitz break-up constants for the baseline and optimised cases.....146
Table 3.8 Injection parameters for the AJ133 optical engine.....154
Table 3.9 Liquid film mass for Bai-ONERA and Senda models with coarse and refined surface mesh and comparison with experiments.....195

Table 4.1 Engine test matrix.....205
Table 4.2 Polytropic indexes for DVA and SVA at λ=1.0 and λ=1.5. 3.6 bar GMEP, 1500RPM.....218
*Table 4.3 Closed cycle simulation at 3.6 bar GMEP, 1500RPM. *represents the actual cycles.....239*

Table 5.1 Experimental and numerical compression polytropic index (γ) for DVA and SVA at various lambdas. 7.9 bar GMEP, 1500 RPM.....254

Table 6.1 Velocity reduction of the five different lifts from the SVA and the ratio LIVO / DVA velocity at ignition..... 308
Table 6.2 Percentage reduction of the swirl ratio from SVA at ignition for the LIVO mode.....310
Table 6.3 TKE reduction of the five different lifts from the SVA and the ratio LIVO / DVA velocity at ignition.....312
Table 6.4 Heat transfer reduction of the five different LIVO lifts from the SVA and the relative reduction with respect to DVA and SVA.....316
Table 6.5 Velocity reduction of the five different lifts from the SVA and the ratio EIVC / DVA velocity at ignition..... 326
Table 6.6 Percentage reduction of the swirl ratio from SVA at ignition for the EIVC mode.....327
Table 6.7 TKE reduction of the five different lifts from the SVA and the ratio EIVC / DVA velocity at ignition.....329
Table 6.8 Heat transfer reduction of the five different EIVC lifts from the SVA and the relative reduction with respect to DVA and SVA.....333

Table 7.1 Statistical convergence of the mean, standard deviation and CoV average in-cylinder velocity for DVA and SVA.....351
Table 7.2 Mean, standard deviation and CoV of in-cylinder pressure over 25 cycles.....351
Table 7.3 Mean, standard deviation and CoV of in-cylinder temperature over 25 cycles.....352

Nomenclature

Abbreviations

1DCHT	1D Conjugate Heat Transfer
AIAA	American Institute of Aeronautics and Astronautics
ASOI	After Start Of Injection
BDC	Bottom Dead Centre
BMEP	Brake Mean Effective Pressure
CA	Crank Angle
CFD	Computational Fluid Dynamics
CI	Compression Ignition
CNG	Compressed Natural Gas
CO	Carbon Monoxide
CO2	Carbon dioxide
CoV	Coefficient of Variance
CR	Compression ratio
CVVL	Continuous Variable Valve Lift
DI	Direct Injection
DISI	Direct Injection Spark Ignition
DNS	Direct Numerical Simulation
DVA	Dual Valve Actuation
ECFM3Z	3-Zones Extended Coherent Flame Model
EGR	Exhaust Gas Recirculation
EIVC	Early Intake Valve Closure
EVO	Exhaust Valve Opening
GDI	Gasoline Direct Injection
GMEP	Gross Mean Effective Pressure
GSFC	Gross Specific Fuel Consumption
H	Hydrogen
H2	Hydrogen Molecule
HC	Hydrocarbons (unburnt)
HI	Homogeneity Index
IMEP	Indicated Mean Effective Pressure
ISFC	Indicated Specific Fuel Consumption
IVC	Intake Valve Closing
IVO	Intake Valve Opening
JLR	Jaguar Land Rover
KHRT	Kelvin-Helmholtz Rayleigh-Taylor instabilities
LES	Large Eddy Simulation
LIVC	Late Intake Valve Closure
LIVO	Late Intake Valve Opening
MFB	Mass Fraction Burnt
N	Nitrogen
N2	Nitrogen Molecule
NMEP	Net Mean Effective Pressure
NO	Nitric Oxide
NO_x	Oxides of Nitrogen

O	Oxygen
O2	Oxygen molecule
OH	Hydroxide
PDA	Phase Doppler Anemometry
PFI	Port Fuel Injection
PIV	Particle Image Velocimetry
PM	Particulate Matter
PN	Particulate Number
QPLIF	Quantitative Planar Laser-Induced Fluorescence Imaging
RANS	Reynolds-averaged Navier–Stokes
RNG	Re-Normalisation Group
RPM	Revolutions Per Minute
SACI	Spark-Assisted Compression-Ignition
SGS	Sub-Grid Scale
SMD	Sauter Mean Diameter
SST	Shear Stress Transport
SVA	Single Valve Actuations
TAB	Taylor Analogy Break-up
TDC	Top Dead Centre
TDCf	Firing Top Dead Centre
TDCgx	Gas Exchange Top Dead Centre
THC	Total Hydrocarbons
TKE	Turbulent Kinetic Energy
TMB	1,2,4 tri-methyl benzene
VVT	Variable ValveTrain, Variable Valve Timing
WOT	Wide Open Throttle

Latin symbols

A_d	Droplet cross-sectional are
A_s	Droplet surface area
B	Impact parameter
C_d	Drag coefficient
C_f	Flow coefficient
C_p	Specific heat capacity
$C_{\varepsilon 1}, C_{\varepsilon 2}, C_{\varepsilon 3}, C_{\varepsilon 4}, C_\mu$	Turbulence model coefficients
D, d	Diameter, Diffusivity in ECFM3Z model
D_m	Diffusivity of vapour
D_v	Diffusion coefficient of air-vapour mixture
$E_{1,2}$	Collision efficiency
e	Internal energy
h	Heat transfer coefficient
h_d	Heat of vaporisation
h_{fg}	Latent heat of phase change
j	Integer
K_g	Mass transfer coefficient
k	Turbulent kinetic energy
k_m	Thermal conductivity
La	Laplace number

M_i	Molecular weight of component i
m	Mass
Nu	Nusselt number
n	Efficiency
Oh	Ohnesorge number
Pr	Prandtl number
p	Pressure
Q, q_w	Heat transfer, Heat flux
R	Ideal gas constant
Re	Reynolds number
R_δ	Roughness parameter
r_d	Radius of droplet
r_c	Compression ratio
Sc	Schmidt number
Sh	Sherwood number
S_i	Source term, internal energy
S_{ij}	Strain rate tensor
S_l	Laminar burning velocity
S_m	Source term, momentum
S_T	Turbulent burning velocity
T	Temperature
T_L	Leidenfrost temperature
T_N	Nukiyama temperature
T_{sat} , T_s	Saturation temperature
T_W	Wall temperature
t	Time
u_d	Velocity of droplet
u_i	Velocity component
u_τ	Friction velocity
v	Kinematic viscosity, Collision frequency
v_{SGS}	SGS turbulent viscosity
V	Volume
V_d	Droplet volume
W	Work
We_l	Liquid weber number
We_g	Gas weber number
x_j	Cartesian coordinate
Y_{Fu}^b	Fuel mass fraction in the burnt gases
Y_{Fu}^u	Fuel mass fraction in the unburnt gases
Y_i	Mass fraction of a component i
y	Distance from wall

Greek symbols

γ	Specific heat ratio or polytropic exponent
Δ	Filter width
ΔT_{sh}	Degree of superheat
δ_{ij}	Kronecker's delta

ε	Turbulence dissipation rate
θ	Angle
λ	Excess air Equivalence ratio
μ	Dynamic viscosity
μ_l	Dynamic viscosity of Liquid
μ_t	Turbulent viscosity
ρ_l	Liquid density
Σ	Flame surface density
σ	Surface tension
σ_k, σ_ε	Turbulent Prandtl number
σ_ω	Empirical coefficient
$\tau_{SGS,ij}$	SGS stress tensor
$\tau_{SGS,kk}$	Isotropic part of the sub-grid scale stresses
Φ	Equivalence ratio
Ψ_ι	Mole fraction
ω	Specific dissipation rate
ω_ι	Reaction rate for species i
$\dot{\omega}_{fu}$	Burning rate

Chapter 1

Introduction and Literature Review

1.1. Introduction

Since the late 19th century, when the spark-ignition engine appeared, a lot of developments and improvements have been applied to the early designs as new technologies were available. However, the operation of an engine still relies on the understanding of basic thermodynamics and fluid mechanics. The aim of this research project is to obtain fundamental understanding of complex multiphase flow phenomena in direct-injection spark-ignition engines using Computational Fluid Dynamics.

In our days, the climate change is evident and the impact of air pollution on human health is leading governments and organisations to decrease the emissions onto the atmosphere. More specifically, in order to reduce the pollution caused by road vehicles, stricter emission limits are established (Figure 1.1), such as the Euro 6 standard in Europe. Complying with these limits is a major challenge as aiming at reducing one pollutant (CO, NO_x etc.) can increase the others. Moreover, the reduction of non-renewable energy sources (crude oil and its derivatives) demands lower fuel consumption and higher engine efficiency to decrease the rate of their usage and sustain them for longer.

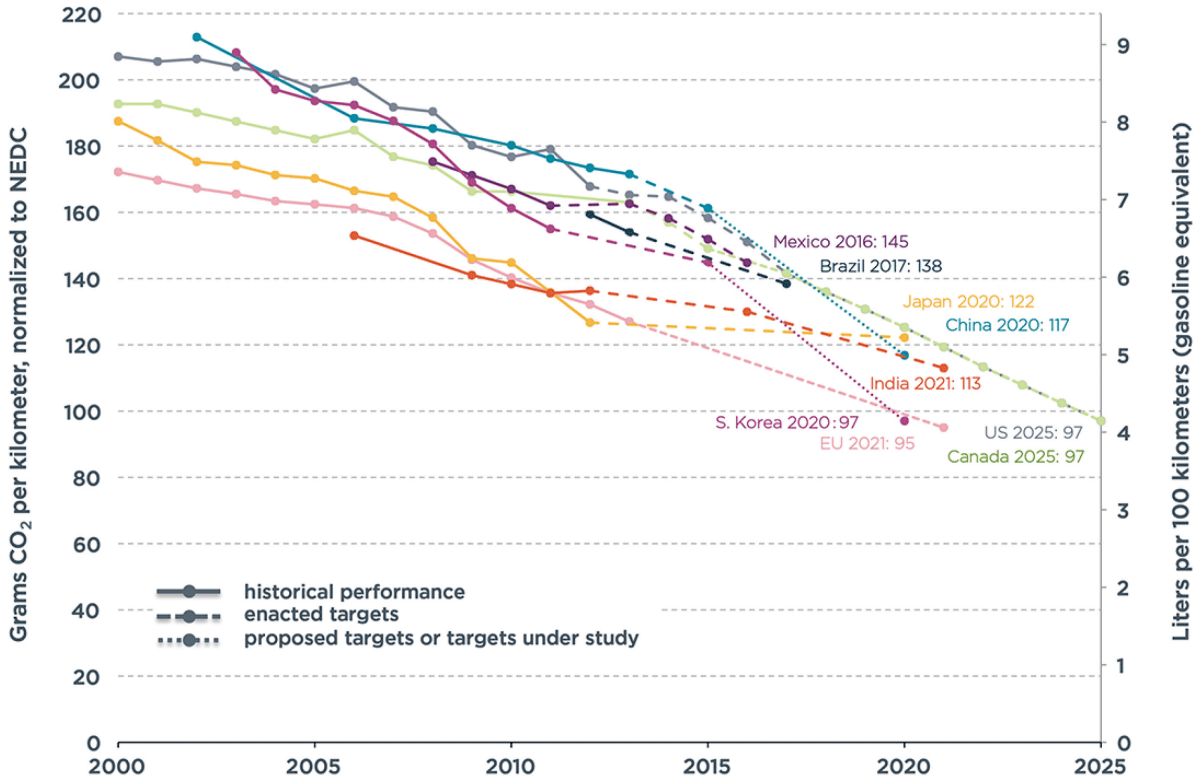


Figure 1.1 Historical data and proposed targets for CO_2 from various countries normalised to NEDC. Source: The International Council on Clean Transportation (ICCT)

To begin with, a simplified model of an actual system allows engineers to study this system and its basic parameters before any in-depth study. The idealised cycle for four-stroke spark-ignition engines is called Otto cycle and a schematic of an actual spark ignition engine cycle and Otto cycle is showed at Figure 1.2. The thermal efficiency of the Otto cycle under the air-standard assumptions (Çengel and Boles, 2015) can be written as:

$$n_{Otto} = \frac{W_{net}}{Q_{in}} = 1 - \frac{q_{out}}{q_{in}} = 1 - \frac{T_4 - T_1}{T_3 - T_2} = 1 - \frac{T_1(T_4/T_1 - 1)}{T_2(T_3/T_2 - 1)} \tag{1.1}$$

Because the processes 1-2 and 3-4 are isentropic:

$$\frac{T_1}{T_2} = \left(\frac{V_2}{V_1}\right)^{\gamma-1} = \left(\frac{V_3}{V_4}\right)^{\gamma-1} = \frac{T_4}{T_3} \tag{1.2}$$

and the compression ratio r_c is:

$$r_c = \frac{V_1}{V_2} \tag{1.3}$$

the thermal efficiency can be written as:

$$n_{Otto} = 1 - \frac{1}{r_c^{\gamma-1}} \quad (1.4)$$

This means that the efficiency of the engine depends on the compression ratio and the specific heat ratio γ. By plotting the thermal efficiency versus compression ratio (eq. 1.4) it can be seen that for a specific ratio γ the efficiency increases (Figure 1.3). Thus, higher compression ratio (CR) is a sector to which automotive industry is working on. However, by increasing the CR, the knock tendency increases, and this is of particular interest in engine studies.

Moreover, the specific heat ratio γ of the working fluid (trapped mass in an engine) is the other parameter that affects the thermal efficiency. For a specific compression ratio, efficiency decreases as γ decreases. At room temperature $\gamma = 1.4$ for air, $\gamma = 1.3$ for carbon dioxide and $\gamma \approx 1.2$ for carbon dioxide at around 700°C. In order to achieve high values of γ, which means closer to pure air, lean combustion is preferred. Lean combustion is also preferred (if the combustion efficiency is not deteriorated) because of the reduction of the incomplete combustion products such as CO and unburnt hydrocarbons as well as the NO_x emissions at very lean mixtures as it can be seen from Figure 1.4. Furthermore, with lean combustion the fuel efficiency increases and thus, the production of CO_2 decreases. However, the main disadvantage of lean burn is that the 3-way catalyst cannot work with excess oxygen to reduce the NO_x emissions and the engine has to work near the stoichiometric region.

Exhaust gas recirculation (EGR) is a technique used to dilute the intake charge and overcome the problem of lean burn with excess air. Therefore, CO_2 can be a considerable amount of the mixture composition and the specific heat ratio of this mixture can be decreased which affects the thermal efficiency of the engine. However, the use of exhaust gases can be beneficial for NO_x reduction, for reduction of heat losses to the walls and also suppression of knock as the peak in-cylinder temperature is decreased. This means that EGR can be a compromise between thermal and fuel efficiency and emissions control.

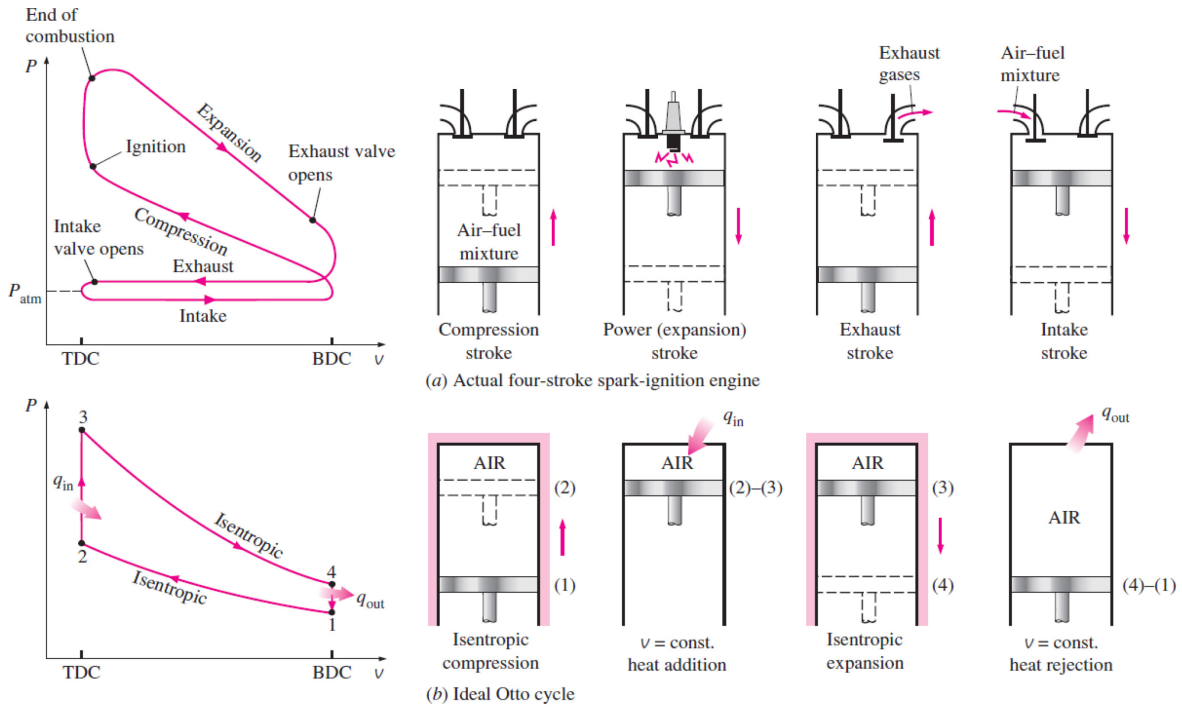


Figure 1.2 P-V diagrams and Schematics of the actual and ideal cycle in a spark ignition engine (Çengel and Boles, 2015)

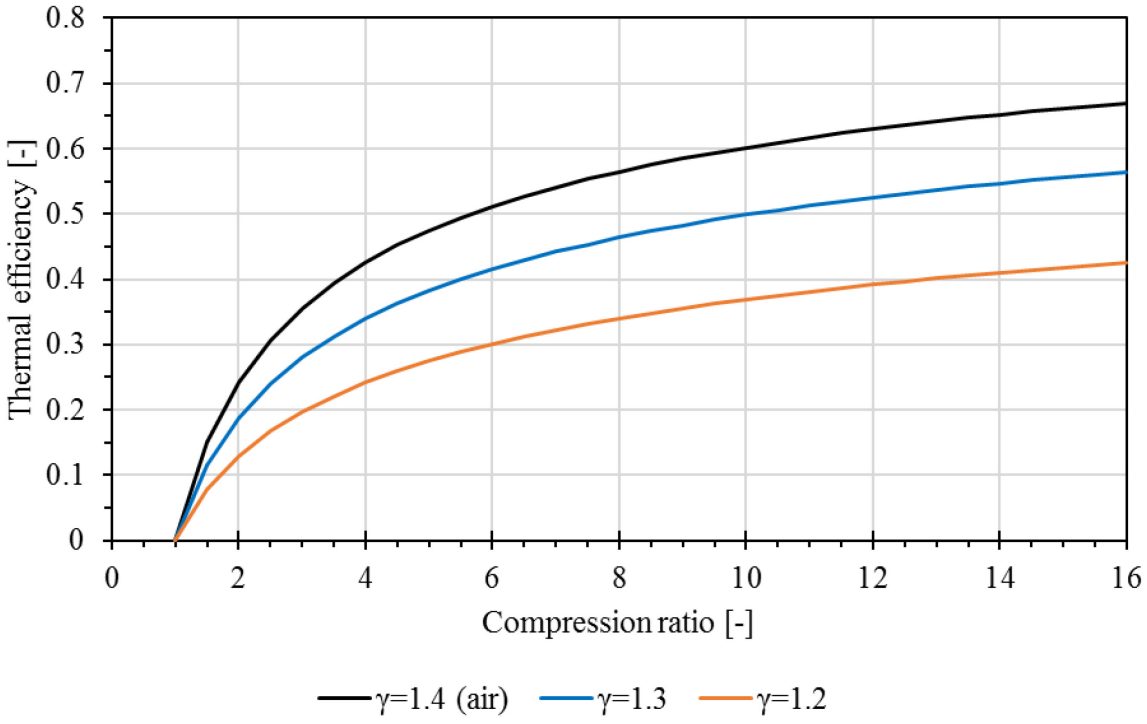


Figure 1.3 Thermal Efficiency of Otto cycle versus compression ratio for three different values of γ

In addition to the above, direct injection is another development for spark-ignition engines. This offers some advantages over earlier methods of fuel delivery in the cylinder. Alkidas and El-Tahry (2003) reported that direct injection has a 15% improvement on fuel economy over Port Fuel Injection (PFI). Most importantly, direct injection has higher resistance to knock and allows higher compression ratios due to lower in-cylinder temperatures. The evaporation of the liquid fuel reduces the temperature of the in-cylinder charge, which can also increase the volumetric efficiency by up to 10% according to Eichlseder *et al.* (2000). This is more evident when fuels with higher heat of vaporisation are used such as alcohol fuels. Another advantage is the possibility of stratified charge, which is a stoichiometric air/fuel mixture cloud near the spark plug while in the rest of the volume the mixture is very lean. With this approach, extreme lean combustion can be achieved for fuel economy. Nonetheless, direct injection can have negative effects on the emissions if it is used without deep investigation. Stratified combustion can be the cause of unburnt hydrocarbons and NO_x emissions (Baumgarten, 2006). Moreover, fuel impingement on the cylinder walls and piston can be the reason of high particulate matter during combustion. Various injection strategies such as double and triple injections as well as flash boiling are under consideration to minimise the drawbacks of direct injection.

Lastly, alternative designs of those to Otto's four stroke engine with different theoretical cycles were proposed. One example is James Atkinson who built an engine with longer expansion than compression stroke and had high efficiency for that time (Heywood, 1988). Nowadays, the idea of Atkinson cycle can be used in a conventional four stroke engine by using appropriate intake valve timing. More specifically, the valve is kept open longer on the compression stroke, late intake valve closing (LIVC), thus some of the intake charge is directed back to the intake manifold instead of being compressed. With this technique, the engine has higher efficiency because less work is needed for the compression stroke while the expansion stroke is kept the same. Nevertheless, the Atkinson cycle has less power output compared to Otto cycle for the same engine because less air and fuel mas is trapped. Therefore, Atkinson cycle is used at low load or in conjunction with hybrid systems such as electric motor when fuel efficiency is the key. An alternative to Atkinson cycle that can be applied to an engine is referred as Miller cycle (Zhao, 2010). In this case, the intake valve closes before bottom dead centre, which is called early intake valve closure (EIVC), therefore, the actual compression stroke is smaller. Again, the trapped mass is lower than a conventional valve timing due to the early closing of the valve and consequently, loss of power follows. To overcome the problem of lower power output of both cycles, the loss of air is compensated with the use of a supercharger. Depending on the

operating conditions, either Otto or Atkinson/Miller cycles can be applied on a modern internal combustion engine by a variable valve train (VVT) system.

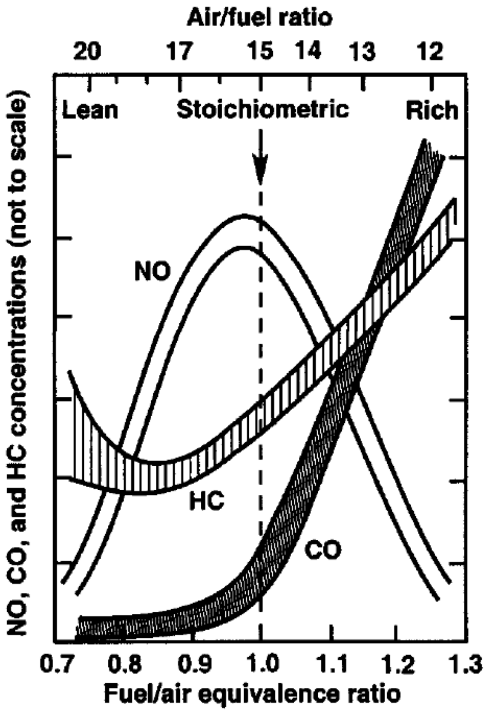


Figure 1.4 Pollutant concentrations as a function of equivalence ratio (Φ) (Lumley, 1999)

To sum up, various approaches have been proposed and are being investigated at the moment in order to meet emissions regulations and improve the efficiency of a spark ignition engine. These are:

- Increased compression ratio
- Use of EGR
- Various valve control strategies
- Various direct injection strategies

All of them have their advantages and disadvantages and with compromises, the right combination can lead to an improvement overall. This can be achieved by experimentation and the use of CFD. CFD is a useful tool for engineers to simulate and predict the behaviour of different designs of a combustion chamber without the cost of manufacture and it is essential to optimise the parameters that affect the formation of air pollutants and the efficiency of an engine.

1.2. Thesis outline

Nowadays, ground transportation is a major source of air pollution with an impact on the greenhouse effect with CO_2 emissions as well as on the public health, especially in urban areas with high concentrations of oxides of nitrogen, CO, particulate matter, and unburnt hydrocarbons. Legislations across the globe have been posed to reduce these emissions and for the automotive industry it is a challenge to meet these targets while maintaining high efficiency and low fuel consumption. In order to do so, novel strategies such as variable valvetrain systems, Exhaust Gas Recirculation (EGR) and increased compression ratio are introduced to direct injection spark ignition engines.

In Chapter 1, an introduction to the internal combustion engines and the basics of the thermodynamics is presented. In addition to this, a literature review for the advancements of gasoline direct injection, variable valvetrain systems, exhaust gas recirculation and the pollutant formation is performed. This is done with the aim of giving an insight of the benefits and drawbacks that these strategies introduce in an engine, together with revealing any contradictions that may exist between researchers. Moreover, topics and areas with limited work and information are identified. According to the findings of the literature review, the objectives of this study are defined.

In Chapter 2, the basic mathematical formulations of the flow solution and the turbulence modelling that govern computational fluid dynamics (CFD) are reported. Moreover, the calculations of the species that are present in the combustion chamber and the intake and exhaust ports before Exhaust Valve Opening (EVO) for various dilution cases with EGR, excess air or combination of both is presented. In addition, the formulations which govern the Lagrangian multi-phase treatment for spray modelling along with all the relevant sub-models of droplet break-up, droplet-droplet interactions, droplet-wall interaction and liquid film modelling are described. Lastly, the basic formulation of the combustion modelling is also described.

In Chapter 3, some preliminary studies are conducted, focused on the in-cylinder flow. More specifically, a grid dependence investigation for engine simulations is carried out to identify the grid size which can be supported by the available computational power without compromising the accuracy of the solution. Furthermore, a study for the most appropriate initialisation point is done due to various cases seen in the literature. This is important in order to minimise the effect of initial conditions to the rest of the simulation. With the findings of the

preliminary studies, validation of the commercial code STAR-CD for engine simulations is performed by comparing numerical data against experimental in-cylinder pressure traces from two different Jaguar engine families, a thermal and an optical research engine. In addition, Particle Image Velocimetry (PIV) data from the Jaguar optical research engine are compared against the flow field predicted by the CFD code. Moreover, steady state port flow simulations are conducted for the optical engine to identify the reasons behind the differences in the predicted and experimental flow field and the performance of four different turbulent models is investigated for both steady state and dynamic simulations. Further validation was carried out for the engine heat flux. The predicted heat flux from the gas to the walls of a motoring engine throughout the engine cycle is compared against experimental data. Furthermore, validation of the fuel injection and spray modelling is performed in a quiescent chamber and in the dynamic model of the optical engine. The spray structure, the penetration and the droplet sizes are matched those of the experimental data. This procedure is completed for sub-cooled fuel injection, as well as for a newly developed flash boiling model. A generalised procedure is adopted for sub-cooled and flash-boiling spray modelling by minimising the differences of the implementation. Lastly, validation is carried out for the fuel impingement on a wall and the creation of the liquid film.

In Chapter 4, the above findings are used to study the effects of valve deactivation and give an insight into the experimental results of the AJ20 thermal engine. More specifically, the enhancement and the alteration of the in-cylinder flow and turbulent kinetic energy is investigated when single valve is adopted without the fuel injection. Other in-cylinder quantities such as temperature, residuals and laminar burning velocity, as well as the heat transfer from the gas to walls are also studied. Benefits and drawbacks of the Single Valve Actuation (SVA) are identified. Due to the increased heat transfer when utilising SVA, the reasons behind the increase are investigated. All the above are done for three different engine loads at two engine speeds.

In Chapter 5, the spray modelling is introduced to study the combined effect of valve deactivation and fuel injection on the flow properties, air-fuel mixture and pollutant formation for two different engine loads at 1500 RPM. Due to the different in-cylinder conditions for the two loads, both sub-cooled and flash-boiling modelling are implemented. Combustion modelling is also introduced to test and validate suggested theories behind pollutant formation.

In Chapter 6, to utilise the benefits seen when SVA is adopted while minimising the drawbacks, an investigation of the capabilities of the CVVL system with staggered intake valve lift in order to achieve the optimal level of charge motion for reduced fuel consumption and heat transfer is carried out. Two different methods of differential valve lift are tested; Late Intake Valve Opening and Early Intake Valve Closure. The in-cylinder flow properties with and without fuel injection, the air-fuel mixture and the pollutant formation are studied at 7.9 bar GMEP and 1500 RPM.

In Chapter 7, due to the differences in the combustion stability between the Dual and Single Valve Actuation at high dilution levels, an investigation of the cycle-to-cycle variations of DVA and SVA at these conditions is performed. Firstly, an in-cylinder pressure validation is performed, and the adequacy of the grid is checked. The variations of the average in-cylinder quantities as well as the spatial distribution within the cylinder are studied at 3.6 bar GMEP and 1500 RPM.

In Chapter 8, the conclusions of the current studies and recommendations for future work have been presented.

1.3. Exhaust gas recirculation

Introducing exhaust gases into the cylinder as a charge dilution method was first applied to diesel engines in order to reduce NO_x emissions (Wei *et al.,* 2012). With the stricter emissions regulations, the necessity of reducing NO_x and CO_2 led the engineers to implement the technique of EGR in the gasoline engines as well. Generally, EGR can be beneficial for NO_x reduction, for reduction of heat losses to the walls, reduced throttling losses and suppression of knock. The EGR can be classified into two categories, internal EGR or internal residuals and external EGR. The internal EGR technique can be achieved with appropriate valve strategies in order to trap some of the combustion products into the cylinder. In the external EGR method, some of the exhaust gases are taken from the exhaust port and are fed back to the intake manifold and two categories of external EGR exist. If the exhaust gases are cooled down before directed to the intake manifold then the method is called cooled EGR, otherwise the gases are recycled directly to the intake and this is called hot EGR. Each technique has its benefits with cooled EGR being able to reduce further the NO_x emissions and it is better for knock suppression while with hot EGR faster combustion can be achieved and lower hydrocarbons are emitted (Wei *et al.,* 2012)

In the literature, a lot of studies can be found for compression ignition (CI) engines mostly experimental and some numerical, however, CFD studies about EGR in spark ignition engines are more limited. As an example, a review of EGR on gasoline engine (Wei *et al.,* 2012) only stated two numerical studies. The internal EGR distribution and scavenging process was the aim of Copeland *et al.* (2013). Two scenarios were investigated in this preliminary, part load and full load at low speed (1500 and 2000 RPM). The simulations started before exhaust valve opening (EVO) and the initial gas was assumed to be 100% burned gas. Firstly, at full load, the engine was boosted with intake pressure at around 2 bar. The results showed that the scavenging takes place rapidly because of the pressure difference between intake and exhaust manifold and the 67 deg CA valve overlap, thus, almost any exhaust gases remain. When the overlap was reduced to 27 deg CA, the amount of residuals was increased (1.7% total residual mass) but the differences were minor. This has also a minor effect on the in-cylinder temperature which indicates that low amount of EGR cannot affect the charge temperature. However, at part load in which the intake pressure was 0.5 bar absolute, the airflow from the intake to the exhaust valves was not strong enough to flush the residuals and a higher amount of exhaust gasses was trapped compared to full load. Moreover, the in-cylinder temperature was affected with almost 100K more that the full load case, due to higher residual concentration (30% total residual mass). It has to be said that in this study, the authors did not mention the properties of the residuals as this can affect the mixing process with the air and the in-cylinder pressure. Moreover, no spray was modelled which can affect the in-cylinder temperature especially with direct injection.

Pan *et al.* (2014) studied the effect of compression ratio on cyclic variations at an engine speed of 1000 RPM. In that study the authors also investigated the reasons of the variations with the presence of EGR, using CFD. More specifically, they focused on the flame speed, turbulence intensity and mean velocity at spark timing, parameters that affect combustion process. Simulations showed that EGR had a minor effect on turbulence intensity and mean velocity but had a significant impact on flame speed. Higher EGR, produced lower flame speed which effects the flame propagation, an indication of cycle to cycle variation. However, no details were given for the mixing process of EGR and the presence exhaust residuals of a previous cycle. Moreover, this study used a PFI engine therefore, a direct injection can have an effect on the turbulence intensity during air-fuel-EGR interaction.

Two numerical studies which investigated the cyclic variability due to EGR and compared to experimental results were performed by Scarcelli *et al.* (2014) and Scarcelli *et al.* (2015). The

first interesting point of this work was that while RANS modelling of the whole cycle including combustion was used, and an averaged result was expected, they were able to capture variations of consecutive cycles. The authors stated that the reason of this behaviour was the different initial conditions for each cycle that were never damped out. While these papers focus on the cyclic variability of RANS simulations, some useful conclusions can be derived about the EGR effect. The engine speed was 2000 RPM and two stoichiometric cases were compared, one without EGR and one with 18% EGR. Both the experiments and the simulations showed a much higher cycle to cycle variability on pressure traces when EGR was introduced.

Mardi *et al.* (2014) investigated the effect of EGR on emissions and performance of a supercharged direct injection spark ignition engine using CFD. Their study was focused on the closed system, from intake valve closure to exhaust valve opening at an engine speed of 2000 RPM. This means that combustion at stoichiometric ratio and NO_x formation was modelled however, the mixing process during intake was omitted. Various fuels were simulated, and the results showed that the use of EGR reduced the NO_x formation for all the fuels. Hydrogen and Methane, due to higher flame temperature produced high numbers of NO_x when no EGR was used. With increased EGR ratios, the NO_x production was reduced and but for EGR rates above 15% the changes were minor for all fuels (Figure 1.5). At constant initial pressure of 1 bar, which represents the intake pressure, the increase of EGR led to decrease of IMEP and increase of ISFC.

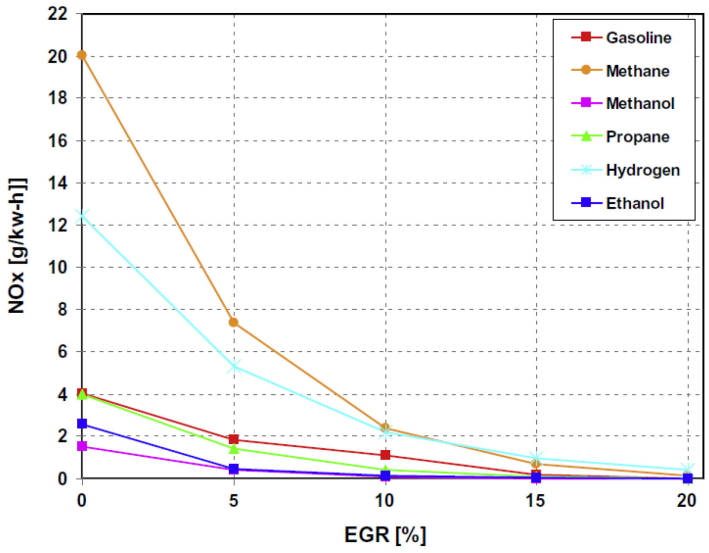


Figure 1.5 The effect of EGR on NOx emissions for various fuels (Mardi et al., 2014)

Another CFD study on the effect of EGR on the combustion process and NO_x emissions on direct injection spark ignition (DISI) engine was carried out by Polat *et al.* (2016). The analysis

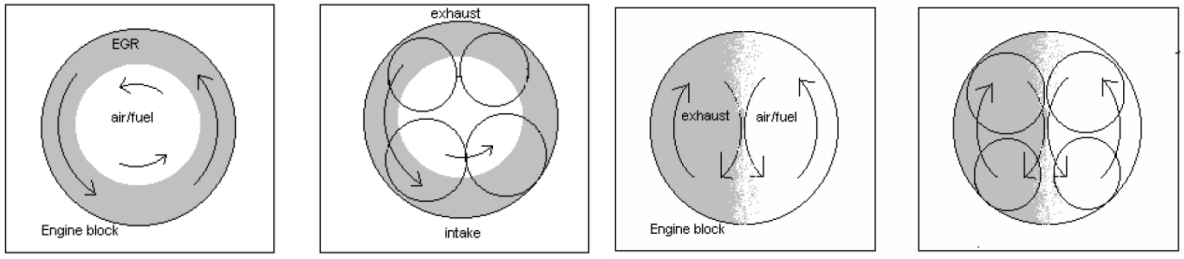
was performed at 2500 RPM with five different EGR ratios, from 0% to 20%. While fuel injection is mentioned, it is not clear if the whole cycle is simulated, or a homogenous mixture is assumed at spark timing. From the results, it can be derived that the presence of exhaust gases affects the knock tendency, heat release rate, in-cylinder pressure and temperature. An increase of EGR ratio lead to reduction of in-cylinder pressure and temperature which also benefits the knock suppression. Moreover, higher levels of EGR reduce the heat release rate and slows the combustion. Lastly, it was observed that NO_x emissions were reduced with increased EGR ratios, nonetheless, ratios above 10% did not have any significant influence, an observation that has already noted by Mardi *et al.* (2014)

Galloni *et al.* (2012) investigated the effect of EGR on flame propagation, knock and in-cylinder temperatures by means of CFD at an engine speed of 4000 RPM. Comparisons were made between a base case without exhaust gas recirculation and a case which consists of about 11% of EGR at intake valve closing (IVC). The authors mentioned that this value was taken from 1D analysis but it was not stated how this was applied on the 3D model and if it was external or internal EGR. Nevertheless, some important conclusions were derived from this work. First of all, the peak pressure and temperature were reduced with the use of EGR. Moreover, the heat release rate was reduced and the flame speed was slower. Comparing the base case with the EGR case, the use of exhaust gases allowed a 3 degree CA spark advance. Lastly the authors stated that the benefits of EGR can be exploited however, a new optimisation is needed for the performance of the engine.

An optimistic idea with potential benefits when using EGR is called stratified EGR. In this method, the stoichiometric air-fuel mixture is kept separated from EGR or the mixing between them is minimised for stable combustion. The benefits of this approach were demonstrated by Xu *et al.* (2000) with various EGR ratios and swirl ratios at 1500 RPM. The effects of temperature and density difference were also studied. The simulation only included the closed system, from IVC to EVO and the stratified EGR was initialised according to the theoretical idea. The exhaust gas occupied an outer ring of the cylinder and the mixture occupied the central volume. Moreover, simulations were run for less idealised initial conditions, again for a closed system, to investigate the effect of air-EGR mixing. For the idealised tests, EGR ratios up to 90% were tested. The simulations showed that this method could be beneficial for reduced fuel consumption and decreased in-cylinder temperature, heat losses to the walls and NO_x. Because EGR is not included in the combustible mixture, the heat release rate and the combustion are similar to cases without EGR. Although high EGR ratios were tested, values

above 50% were not suitable for stable combustion due to over-mixing. Furthermore, high swirl ratios are also a barrier as they promote the mixing process. While this method can have theoretical advantages, obstacles have to overcome for a feasible application.

The same team conducted a preliminary study of the preparation of EGR stratified distribution Dong *et al.* (2002). The aim was to prepare the charge and keep EGR and air-fuel mixture separated using two different methods namely corndog and conjugate vortex EGR (Figure 1.6). In order to achieve these two methods, various geometrical configurations of the combustion dome, intake and exhaust ports and valve masks were simulated at 1500 RPM. The results showed that during the early intake stroke, it is possible to achieve both types of EGR stratification with the correct geometry of the combustion chamber and valve timing. However, during the late intake all the compression stroke mixing of exhaust gases and fresh air takes place. The tumble due to piston movement, the turbulent intensity and the temperature and density difference are factors that affect the mixing of the two species. Furthermore, the authors stated that it is difficult to calibrate the formation of stratified EGR for various loads and speeds. Lastly, in this study fuel injection was not included which can affect the flow field and mixing process even to cases in which partial stratification can be achieved.



Corndog Concept Conjugate vortex Concept

Figure 1.6 Two different methods for EGR stratification (Dong et al., 2002)

Despite the difficulties of EGR stratification that were described above, another group (Sarikoc *et al.,* 2006) exploited the potential use of radial stratified EGR with experiments and CFD and compared to results of homogeneous EGR which was the base case. In order to achieve stratified EGR, the intake manifold had to be redesigned with special air baffles to guide the air and EGR flow. The numerical results showed a very good mixing for the case of homogeneous EGR and the experiments revealed the benefits of it (NO_x reduction of 58% compared to non EGR operation). The engine could tolerate EGR up to 16%, without misfires, a finding reported by others. Moving to the stratified EGR, four strategies were tested and showed at Figure 1.7. In all strategies, the air and EGR were fed in the chamber separately, the one after the other. The first two cases had the left port closed to achieve a swirl motion. CFD

showed that for the first strategy no stratification can be achieved, and the experimental results were similar or worse compared to the homogeneous EGR case meaning of a bad mixing process. A minute stratification with low exhaust gas concentration was achieved with the second process. This lead to a higher EGR tolerance of 24% compared to homogeneous EGR case (16%) in the experiment. Also, the reduction of NO_x was about 50% compared to homogeneous EGR. The other two strategies had both ports open for the air and one port open for the exhaust gas. The experiments showed an increase of EGR tolerance of 26% and the reduction of NO_x was about 80% compared to the base case. The reason of this behaviour was the much better stratification of the exhaust gas. Lastly, the experiments of strategy four, were further improved with EGR tolerance of 39% and an 88% reduction of NO_x compared to the base case. The CFD showed the best stratification among the four strategies, the reason of the experimental improvements. Whilst it was demonstrated that EGR stratification can be beneficial, to achieve the best outcome, a redesign of the intake manifold is needed, and more complicated systems have to be applied.

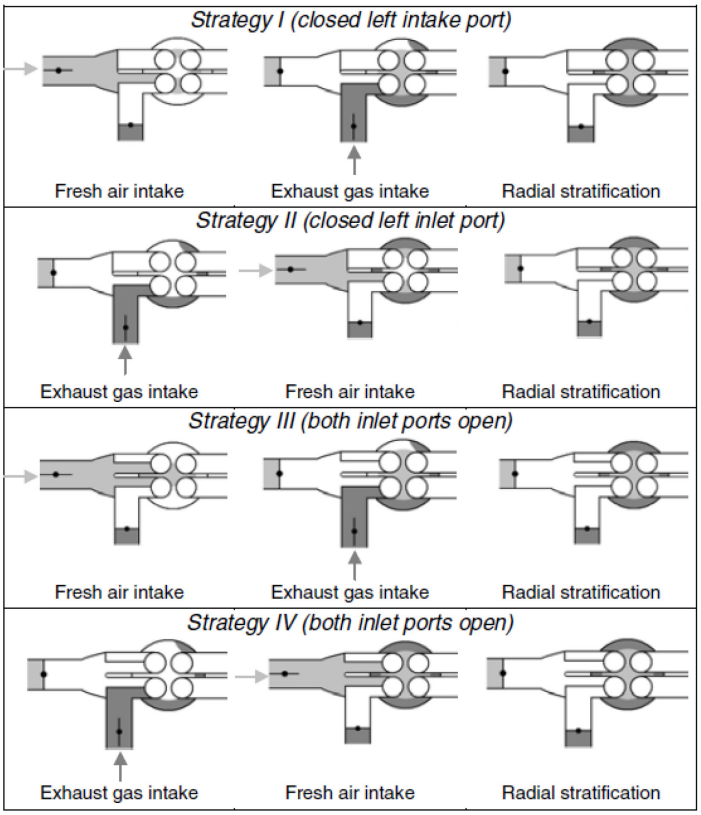


Figure 1.7 Four investigated strategies for radial EGR stratification (Sarikoc et al., 2006)

To sum up, the use of EGR on a DISI engine becomes more popular due to stricter emissions regulations. The major benefit that was reported in the aforementioned numerical studies is the

reduction of NO_x. Moreover, the presence of EGR reduced the peak pressure and temperature which helps to knock suppression and reduces the heat losses. This can be beneficial for the increase of CR. Furthermore, it was stated that the use of EGR can reduce the throttling losses. The disadvantages though are the slower combustion and the increase of cycle to cycle variability. While there are data about the positive and negative effects of EGR, there is lack of data about the mixing process of internal residuals, external EGR and fuel vapour during intake and compression stroke. Moreover, how this mixture is distributed in the cylinder and near the spark plug at spark time as well as the properties of the mixture are not showed. Studies that use closed system, assume prefect homogeneous mixture at IVC and subsequently at spark timing. Moreover, works that simulate the intake process do not specify the mixture formation and potential residuals due to previous cycle. Lastly, the effect of internal and external EGR temperature on fuel evaporation and mixture formation and distribution needs investigation.

1.4. Valve control strategies

To further increase the efficiency of an engine, Atkinson and Miller cycles were proposed to substitute Otto cycle. Both Atkinson and Miller cycles are based on the difference between geometrical and effective compression ratio while the expansion ratio is the same and can be assumed as the geometrical compression ratio. For the effective compression ratio, the total volume is calculated as the volume at IVC. It has been reported that the efficiency increases with increased expansion ratio (Heywood, 1988). These two cycles allow the increase of geometric compression and expansion ratios while having a reasonable effective compression ratio, limited due to knock Ferrey *et al.* (2014) However, the in-cylinder pressure and temperature were reduced and the knock was supressed. It has to be mentioned here that some studies refer Miller cycle as late intake valve closing. For this reason, the use of late or early closing will be used. Except from the impact on the thermodynamic cycle, the valve lift and timing have an effect on the flow field which potentially can be detrimental for air-fuel mixing and combustion efficiency thus, all the aspects have to be investigated.

The study of Ferrey *et al.* (2014) showed that Miller cycle and increased CR can improve the thermal efficiency. However, the slow combustion duration can be due to EIVC. In order to reduce the Indicated Specific Fuel Consumption (ISFC), quicker combustion is suggested. For this reason, comparison between EIVC and LIVC showed that the second strategy can increase the turbulence and thus reduce the combustion duration. Experimental comparison between

LIVC and EIVC valve strategies showed minor differences for ISFC but lower with LIVC. This was due to the combustion duration which was 20% lower in LIVC compared to EIVC a finding that was validated with the simulations. However, no results were showed of the effect of these two strategies on the flow field and turbulence.

The numerical part of Diana *et al.* (2001) investigated the effect of various EIVC strategies on tumble flow, in-cylinder TKE and air-fuel distribution and the results were compared to a base case of conventional valve timings. It was clear that these strategies produced much higher tumble and TKE values. The tumble motion peaked at the time of the maximum valve lift, but during the compression stroke was decaying. However, the higher values were kept at spark timing with EIVC. For the case of TKE, during compression the values converged to the same value. Lastly, it was evident that the air-fuel mixing was enhanced with the EIVC strategies.

Mito *et al.* (2012) have developed a new 1.2 L inline 3-cylinder supercharged gasoline engine in a LIVC in order to meet EURO 5 emission regulations and improve fuel efficiency using CFD and experiments. CFD was used to determine the best design of the fuel spray geometry, intake port geometry and the geometry of the flow control device in order to improve the flow characteristics of LIVC. CFD simulations at 2000 RPM were used to address the problem of weak in-cylinder flow related to the late intake valve closing (LIVC). The tumble ratio of a late IVC (100CA after BDC) was compared with an ordinary IVC (59 deg CA after BDC) when the intake valve opening (IVO) was the same for both cases. Results showed very similar tumble ratio during intake, however, for the LIVC cycle it was much weaker at ignition timing (Figure 1.8). This indicates that the flow has to be strengthened if this valve strategy is applied. Nevertheless, back to 1995, a numerical study from Mazda Motor Corporation (Fujimoto *et al.,* 1995) showed that the TKE can be intensified with a LIVC strategy.

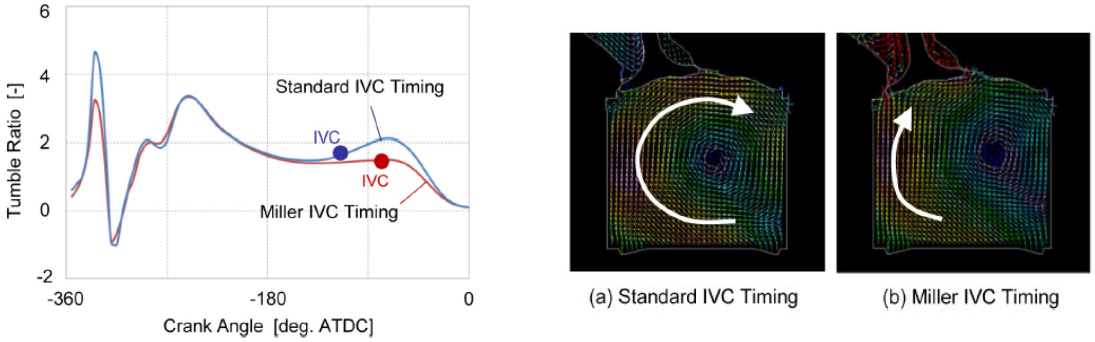


Figure 1.8 The effect of LIVC on tumble ratio and the flow field at 100 deg CA after BDC (Mito et al., 2012)

De Bellis *et al.* (2014a, 2014b) showed briefly the effect of various valve closing timings on the mean in-cylinder velocity. Four cases were presented with four different engine speeds (5100, 2500, 3000, 2000 RPM) and four different valve lifts and durations. For the two first speeds, full valve lift was applied with very similar duration and for the last two speeds, lower lift was used, again with very similar durations but smaller than the duration of the full lift. Results were presented at mid-intake stroke which corresponds to the time of the case with the earliest IVC and at compression TDC. Due to different speeds, lifts and durations, safe conclusions cannot be derived. It was shown that at mid-intake stroke the flow fields had noticeable differences however, at TDC the differences were partially damped out. It was concluded that EIVC allow longer time for turbulence decay.

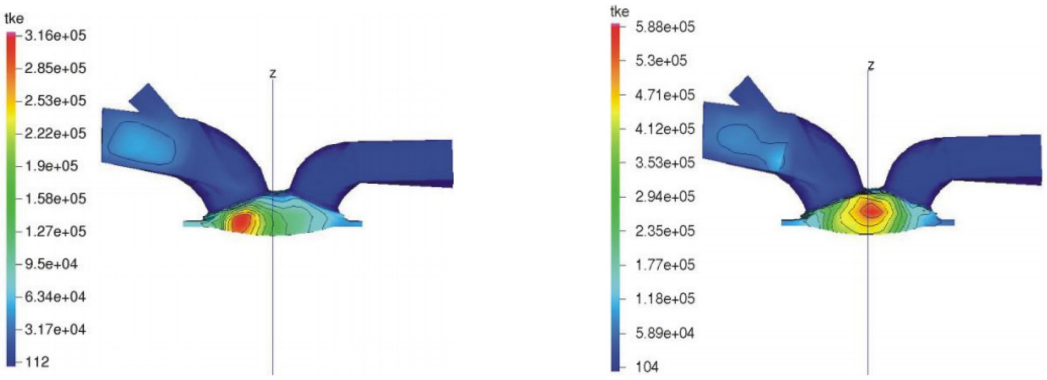
Horie *et al.* (1992) developed a lean-burn four-valve engine with the use of differential valve lift which lead to an increase in the lean operating limit and a reduction in Brake Specific Fuel Consumption (BSFC). In addition, the combustion duration as well as the cyclic variations were decreased showing improved combustion event. This was achieved by a special variable-swirl system in which one valve was completely open with the maximum lift on the second valve altered to achieve optimum levels of charge motion. The authors also suggested a change-over point from differential lift to two-valve operation at 2500 RPM for high load (1 bar intake pressure) and at 3200 RPM for lower loads (intake pressure < 0.9 bar).

Another study, by Wilson *et al.* (1993) investigated the effect of asymmetric valve strategies including valve deactivation. It was found that by increasing the swirl ratio the combustion duration was decreased with the highest swirl ratio produced by the valve deactivation. In addition, the increase of tumble ratio also decreased the combustion duration, but it was concluded that the increase of the swirl was the dominant factor of the reduction of the ignition delay (ignition to 10% MFB). Lastly, they investigated the effect of asymmetric valve strategies on the idle stability. It was found that the valve deactivation greatly improved the stability especially when compared to the dual, symmetric lift operation.

Similarly, Kreuter *et al.* (1992) studied potential improvements of a spark ignition engine with variable valve lift and valve deactivation. By operating with a single valve, and depending on the lift of the other valve, flow velocities ranging from 50 m/s up to 200 m/s could be achieved. Moreover, with the valve deactivation shorter combustion delay, improved stability and efficiency were observed.

Matsumoto *et al.* (2011) and Moore *et al.* (2011) used CFD to support experimental measurements and predict the charge motion for EIVC and LIVC strategies with either one or both intake valves in operation at 1000 RPM. When both valves were in operation, the tumble motion produced by LIVC was greater than EIVC. When only one valve was in operation, the CFD study showed an increase of charge motion with the valve deactivation by increasing the tumble motion and producing high swirl motion. Moreover, due to lower lift of EIVC the airflow was stronger and the TKE was higher in this case and this strong air flow, also benefitted the fuel vaporisation. At spark timing though, the TKE was higher with LIVC. Moreover, they found higher gas temperature and heat transfer with the single valve. For these reasons, the air-fuel distribution and homogeneity have to be investigated for the intake and compression stroke in order to assess the benefits and the drawbacks of each valvetrain strategy.

Another study of valve deactivation by Jovanovic *et al.* (2011) showed increase of TKE and generation of swirl motion. In addition, the spatial distribution of TKE was also improved by occupying the whole area from piston to cylinder head and in was centrally positioned, closer to the spark plug. From Figure 1.9 it can be seen the more favourable location of the TKE which is near the spark plug and with higher magnitude when valve deactivation was used.



Dual Valve Actuation Single valve Actuation

Figure 1.9 Spatial distribution of TKE for Dual and Single valve Actuation. (Jovanovic et al., 2011)

Other researchers (Kim *et al.,* 2008) investigated the valve deactivation and valve lift asymmetry concerning in-cylinder flow and air-fuel mixing. Their study showed that the valve deactivation improved the air-fuel homogeneity by increased swirl and tumble motion. However, their results showed no difference in in-cylinder temperature prior to combustion for the various simulated cases.

Ramasamy *et al.* (2016) studied the increase of swirl motion via dissimilar valve lift in a bi-fuel Compressed Natural Gas (CNG) engine. It was found that when the one valve was operating with lower lift that the baseline, the TKE and the swirl number was increased and as a result the flame propagation speed was increased.

In order to strengthen the swirl and tumble motion for improved combustion Mahrous *et al.* (2007) investigated unconventional intake valve strategies with different lifts (high or low lift) and durations for each valve. The simulated engine is a 4 stroke 4 valve motored at 1500 RPM and four different cases were tested (Figure 1.10). Case 1 is the base case where both intake valves have the same lift and duration. To quantify the flow field swirl and tumble motions were calculated and compared for the four cases. Swirl motion was only produced for the cases with different intake valve lifts which was increasing until the maximum lift of the high lift valve. During compression, the swirl was decreasing but comparing to other studies, the differences were noticeable at TDC for the three cases (Fontana and Galloni, 2009). Comparison of tumble ratios showed that the base case has a positive tumble (counter clockwise) and slightly different behaviour of the other three scenarios which have a negative tumble with similar trends. Moreover, all tumble ratios decayed during compression and at TDC all converged to similar values. Lastly, similar trends could be seen for the TKE, with cases 3 and 4 reached higher values but at TDC again all scenarios converged.

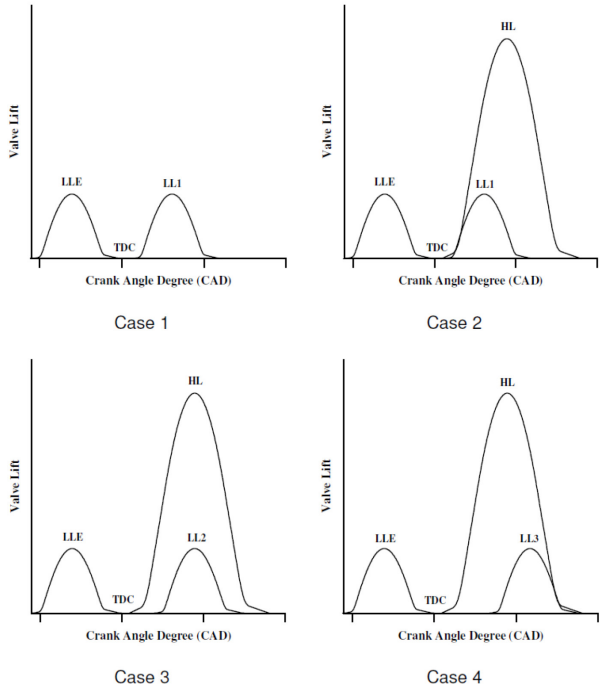


Figure 1.10 Various valve strategies to increase tumble and swirl motion for improved combustion (Mahrous et al., 2007)

In addition to the above strategies, Mahrous *et al.* (2008) investigated the effect of low lift and short duration at different timings with an aim at improved in-cylinder mixture formation. In this study, all four valves were operating with the same profile of 150 deg CA duration and maximum lift of 3 mm. Three different cases of intake valve timing were tested, the two first sets were with both valves working at either early or late timing and the third case one valve was working at the early closing and the other at the late closing profile. The parameters that were examined to evaluate the effect of valve timing on the flow field were the tumble and swirl ratios and turbulent intensity. As it was expected, when the intake valve timings were different, the swirl ratio was significantly increased. For the cases with the same valve timing for both valves, the late intake valve duration produced higher swirl motion. In these two cases, the tumble motion is characterised by a rapid increase followed by a rapid fall, with the late timing strategy to generate higher values. The non-identical intake timings had a gradual increase and decrease of the tumble motion which was better maintained until compression TDC. Lastly, the late valve timing produced the highest values of turbulent intensity and the case of the non-identical timings had similar results. The early valve timing gave significantly lower values of turbulent intensity. In this work, not only the effect of valve deactivation on the charge motion was studied, but also on the exhaust residuals and their role on combustion efficiency. It was concluded that non-identical intake valve timing can improve the mixture preparation with increased tumble and swirl ratio. When the other two cases were compared, the late valve timing gave better results of flow motion and turbulent intensity.

Clenci *et al.* (2014) studied numerically the effect of low valve lift on the in-cylinder aerodynamics of a PFI 2 valve 4 stroke engine at idle speed (800 RPM). While this type of engine has differences on the combustion chamber geometry and flow motion (designed for swirl motion) compared to a 4 valve 4 stroke engine Direct Injection (DI) with a pent-roof head. However, some interesting findings of this work can be derived. Firstly, with higher valve lift there is a backflow to the intake manifold, but at the end, higher mass is trapped at the IVC compared to the lower lift profile. Moreover, the pumping work was higher with the low lift profile. Considering the flow field, the swirl ratio decreases during compression for both cases, but the low lift case produced higher values, and these were kept for the whole cycle, which is important for the mixing process. In addition, TKE is much higher in the case of low lift, up to the end of the intake stroke, however, at spark timing the value is very similar in both cases. In other words, the valve lift strategy can be beneficial for the mixing process, but the kinetic energy of the charge has to be increased in order to improve the combustion process. The

authors also mentioned reduction of internal residual with low lift but no modelling of EGR or results with EGR are showed.

Another analysis for a 2 valve 4 stroke engine of the effect of variable valve timing on the in-cylinder phenomena including internal EGR distribution, this time with an engine speed of 2000 RPM low load, was carried out by Fontana and Galloni (2009). Three cases with both valve retards (constant overlap) of 46, 50, 54 deg CA compared to a base case. First of all, results showed that retarded valve timings, result a backflow of exhaust gases and thus residuals are trapped in the cylinder and also in the intake manifold due to the valve overlap. This results in added residuals to the next cycle, a point that needs caution when specific amount of EGR is needed. Moreover, it was observed that a delay of intake valve timing resulted in a reduction of swirl motion due to having the maximum lift at BDC and the flow is generally small. The maximum swirl ratio was observed with the base case. The same behaviour was seen with TKE, lower values were produced with retarded valve timings.

To summarise, numerical studies and theoretical analyses have pointed the benefits of altering valve lift and opening and closing timings for different loads and speeds of a 4 stroke DI gasoline engine. However, it is essential to understand the impact of variable valve lift and timing on the in-cylinder gas motions and mixing processes as well as to the efficiency of the cycle. Because of contradicted studies, the literature needs to be enriched with more data. Examples of these contradictions are the studies of Ferrey *et al.* (2014), Schernus *et al.* (2013) and Benz *et al.* (2013) who suggested LIVC over EIVC due to increased turbulence while Mito *et al.* (2012) showed a decreased tumble which had to be improved and Diana *et al.* (2001) showed improved data with EIVC. Matsumoto *et al.* (2011) agreed with Ferrey *et al.* (2014) that LIVC is a more beneficial strategy for strengthening the flow field. For the reasons mentioned above, more work has to be done on the effect of valvetrain strategies on the engine cycle and coupled with other aspects such as increased compression ratio and internal and external EGR.

1.5. Gasoline direct injection

The idea of gasoline direct injection was first applied in aircraft piston engines during the 1930 and the first automotive application was done by Goliath and Gutbrod in 1952 (Zhao, 2010). During the last 20 years, car manufacturers have put effort on exploring the benefits of gasoline direct injection with various injection systems and techniques. More specifically, three injector

types are used in GDI engines namely, multi-hole, outwardly opening and in-wardly opening pressure-swirl injector. Schematic diagrams of the three types and their spray patters are showed in Figure 1.11. Direct injection has the ability of fuel delivery during the intake or compression stroke leading to a homogeneous or stratified charge respectively, depending on the engine load. The three most common strategies to achieve a stratified charge are wall-guided, air-guided and spray-guided injection and are illustrated in Figure 1.12. In the recent years, the spray-guided strategy has been adopted by the automotive industry. In addition, split injection techniques are used to overcome problems of the GDI such as fuel impingement and as a result, soot formation and increased unburnt hydrocarbons. As it can be seen, depending on the strategy, different injector type and position (side or top mounted injector) have to be applied. From all the above, it is evident that the design choices for a GDI system are numerous, which makes CFD an important tool for design exploration. A schematic of a full cone engine spray is showed in Figure 1.13 and includes the phenomena of:

- primary and secondary break up
- droplet collision and coalescence
- sub-cooled and flash boiling evaporation
- spray-wall interaction and wall impingement.

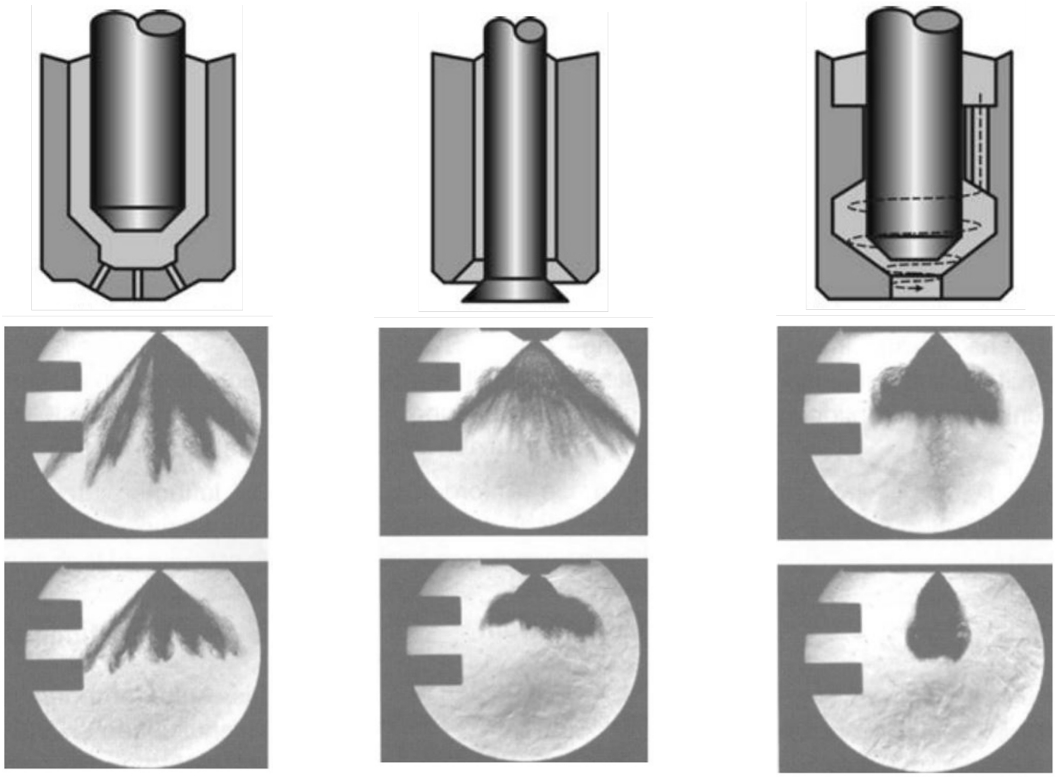
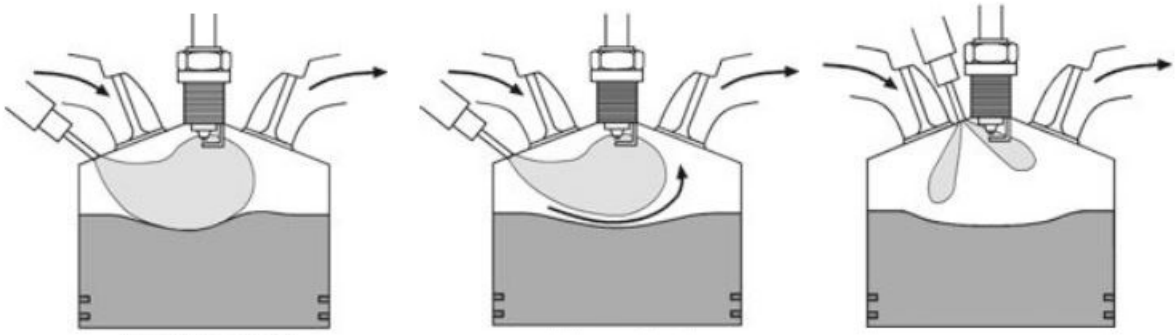


Figure 1.11 Injector geometries and spray patterns for GDI engines (Baumgarten, 2006)



Wall-guided injection Air-guided injection Spray-guided injection

Figure 1.12 Stratified charge techniques, and injector positions. (Lee and Abraham, 2011)

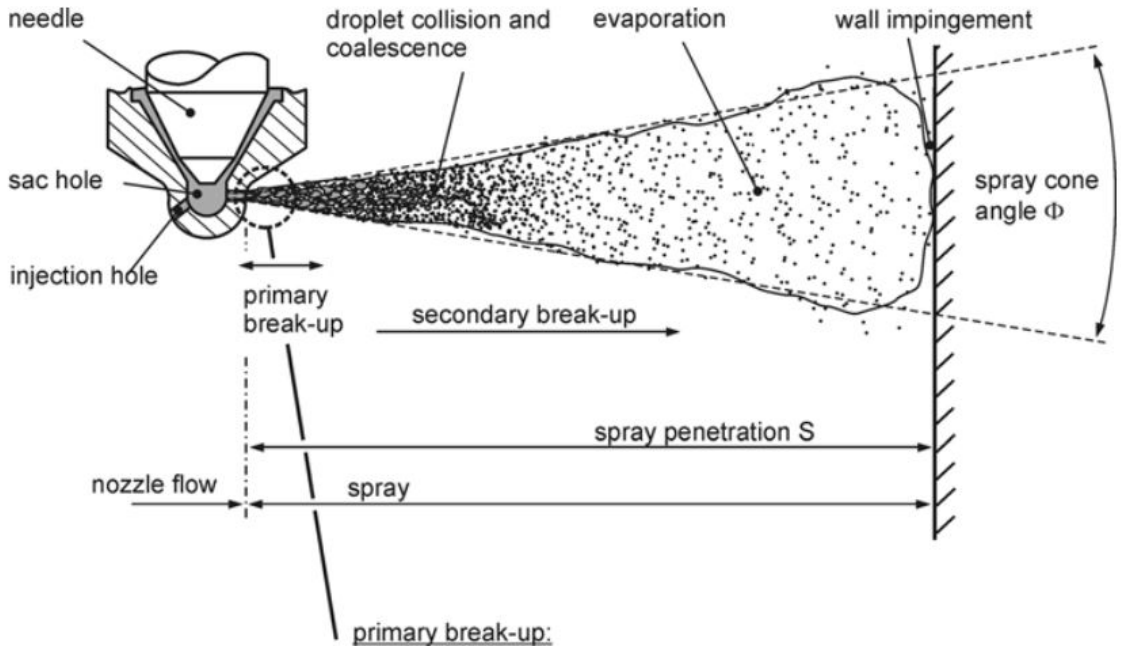


Figure 1.13 A schematic of a full cone engine spray (Baumgarten, 2006)

In order to model fuel sprays, the principals of liquid jets and spray development have to be analysed. Four forces that act on a liquid jet are important for the liquid break up. These are gravity force, inertia, surface tension and viscous force and can be related to each other with non-dimensional expressions of Reynolds number (eq. 1.5) (ratio of inertial forces to viscous forces), Weber number (eq. 1.6) (ratio of inertial forces to surface tension forces) and Ohnesorge number eq. (1.7) (ratio of viscous forces to the inertial and surface tension forces,) (Sirignano and Mehring, 2000).

$$Re = \frac{uD\rho_l}{\mu_l} \tag{1.5}$$

$$We_l = \frac{u^2 D \rho_l}{\sigma} \tag{1.6}$$

$$Oh = Z = \frac{\sqrt{We_l}}{Re} = \frac{\mu_l}{\sqrt{\sigma \rho_l D}} \tag{1.7}$$

Where ρ_l is the liquid density, u is the jet velocity, μ_l is the dynamic velocity of the liquid jet, σ is the surface tension, D is the nozzle hole diameter. Depending on the relative velocity and properties of the liquid jet and the surrounding gas, four liquid jet break up regimes (Primary break up) can be identified; the Rayleigh regime, the first and second wind-induced regime, and the atomization regime (Reitz and Bracco, 1982). Figure 1.14 shows the break up regimes on the Ohnesorge diagram and the schematic description of jet break-up regimes (Baumgarten, 2006). The atomisation regime is related to engine sprays and various theories have been proposed to explain the mechanisms of primary break up. These include growth of surface waves due to aerodynamic forces, turbulence, relaxation of the velocity profile and cavitation as showed in Figure 1.15. Reitz and Bracco (1982) by eliminating one by one the aforementioned mechanisms found that atomisation could occur in the absence of these four mechanisms. It has to be mentioned that all these regimes take place inside the nozzle, which is difficult to investigate them experimentally, especially under engine conditions. Arcoumanis *et al.* (2000), Gilles-Birth *et al.* (2005) and Serras-Pereira *et al.* (2010) are examples in the relatively limited literature of experimental investigations of the effect of cavitation in primary break up in real size transparent injectors.

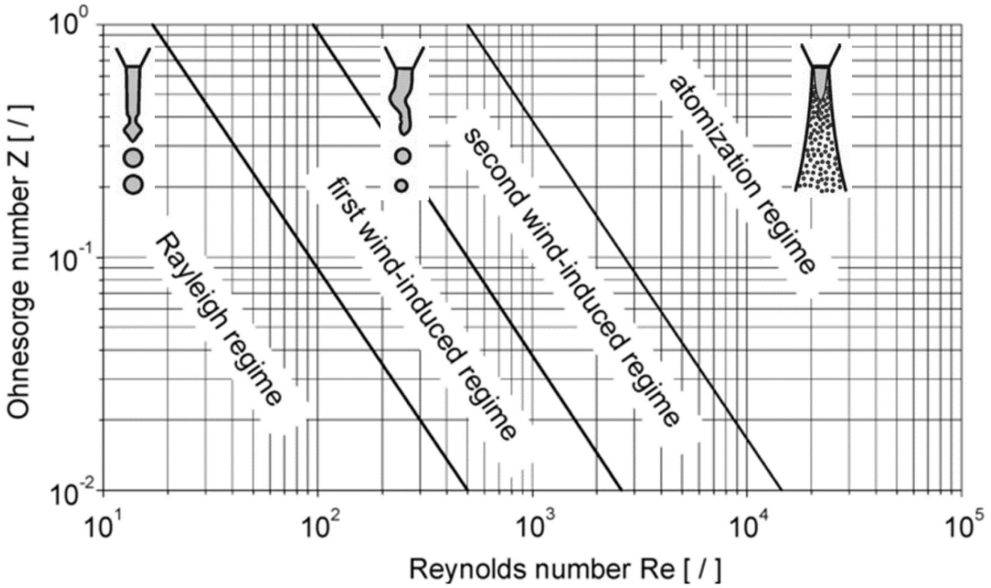


Figure 1.14 the break up regimes on the Ohnesorge diagram and the schematic description of jet break-up regimes (Baumgarten, 2006)

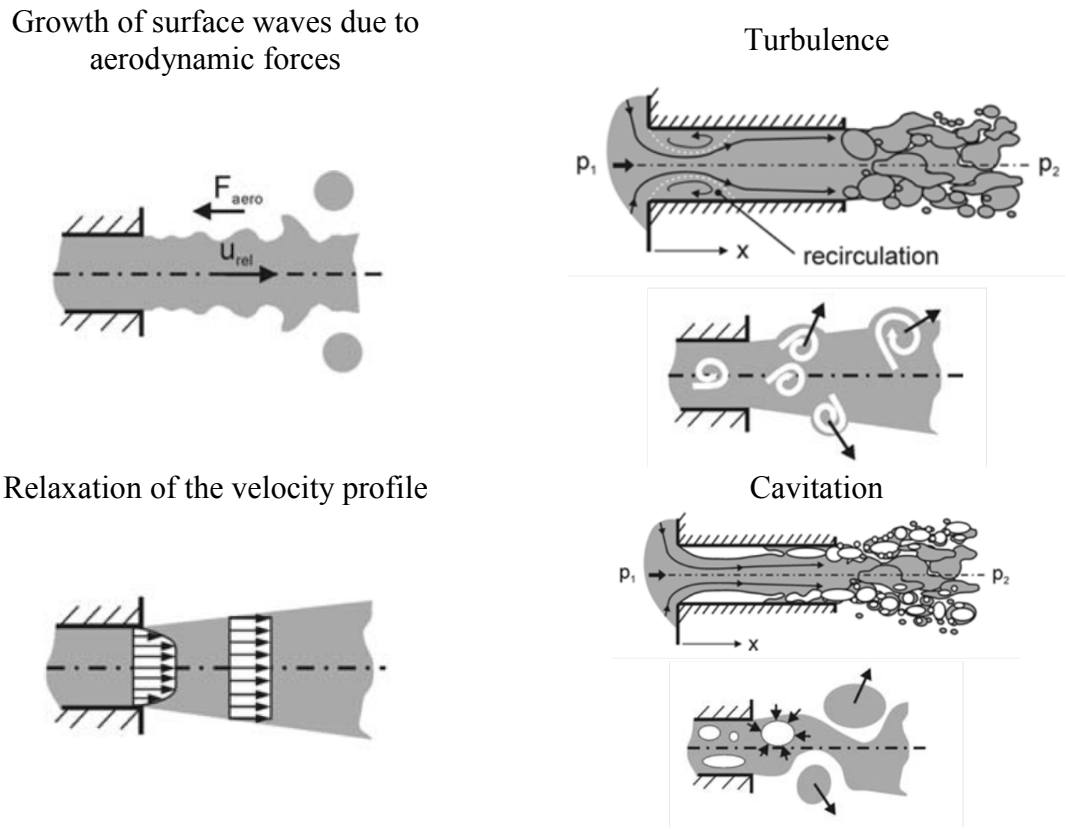


Figure 1.15 Various mechanisms explaining the primary break up (Baumgarten, 2006)

After the primary break-up of the liquid jet and the formation of droplets, further break up mechanisms (secondary break up) occur to each droplet itself due to aerodynamic forces of friction and pressure caused by the relative velocity of the droplet and the surrounding gas. This process can be expressed by the gas phase Weber number and depending on the value of this number, different droplet break-up regimes exist as shown in figure 1.16. While distinct boundaries of these droplet break up regimes do not exist, and various researchers propose different transition numbers (Krzeczkowski, 1980; Wierzba, 1990; Hwang *et al.*, 1996; Arcoumanis *et al.*, 1997), all droplet break up mechanisms occur in an engine spray.

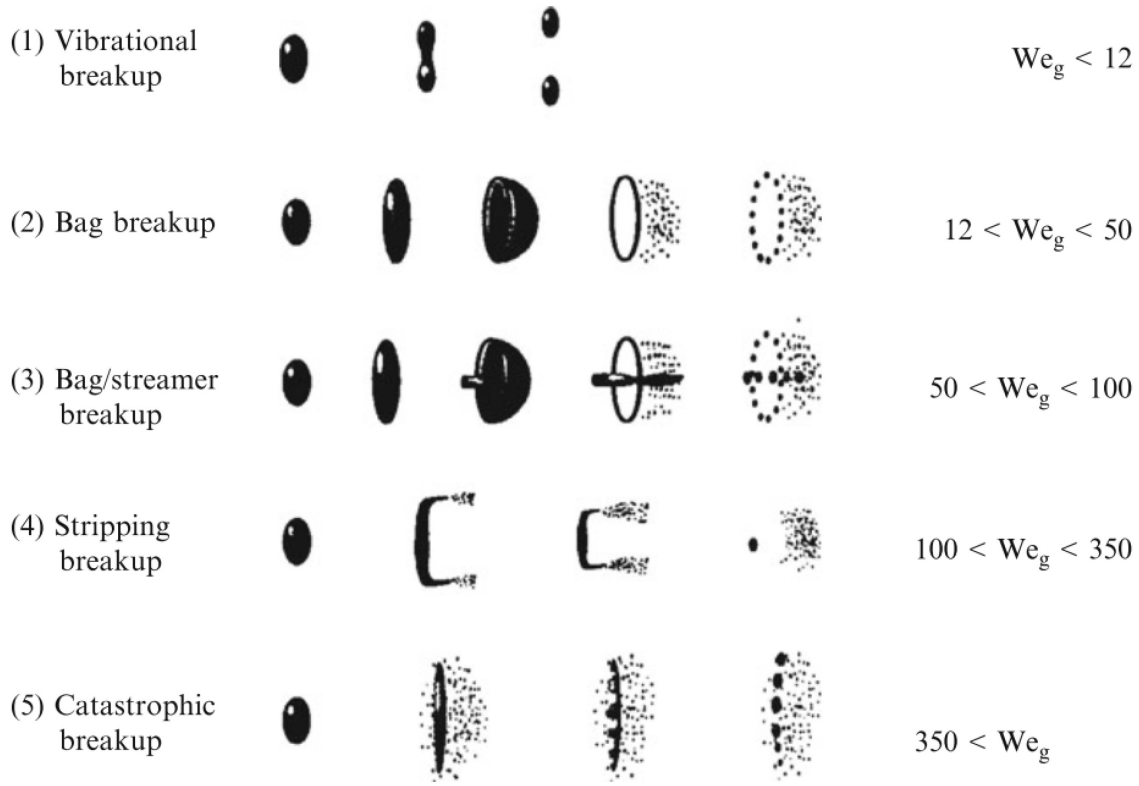


Figure 1.16 Main droplet break up regimes (Otto and Kruger, 2006)

A collision occurs when two droplets travelling towards each other and the dimensionless impact parameter B eq. 1.8 is in the range of [0,1]. When B=0 the collision is called "head-on collision" and when B=1 the collision is called "grazing collision". The distance X is the distance between the droplet centres in the direction normal to that of the relative droplet velocity U_{rel} as shown in Figure 1.17. Depending on the droplet sizes, the impact energy and the conditions surrounding the droplets, the outcome of the collision can be classified in five regimes (bouncing, coalescence, reflexive separation, stretching separation and shattering collision). During bouncing it is believed that a layer of the ambient gas is trapped between the two droplets and their surfaces are prevented from contact. As a result, the droplets deform and bounce back, having the same volume as before impact. Coalescence occurs when the two impacting droplets merge and form a new droplet with the new volume equal to the sum of the two droplets. For head-on or near head-on collisions, the phenomenon of reflexive separation occurs. The liquid system that forms upon impact, due to the high kinetic energy of the impacting droplets, breaks up and often to three droplets. If the kinetic energy of the droplets is not high enough, then coalescence will be observed. With an impact parameter greater than 0.5 (B>0.5) the stretching separation regime can be seen. During this type of collision, a smaller

area of the impacting droplets interacts and forms a common region. Due to the inertial motion, the droplets separate, and they form two or more droplets. However, if the kinetic energy of the initial droplets is not high, coalescence will occur. Lastly, when the relative velocity of the impacting droplets is very high, deformation and finally fragmentation into many smaller droplets is seen. A schematic representation of the aforementioned regimes is shown in Figure 1.18. More information about droplet collisions can be found in Baumgarten (2006) and Brenn (2011).

$$B = \frac{2X}{d_1 + d_2} \tag{1.8}$$

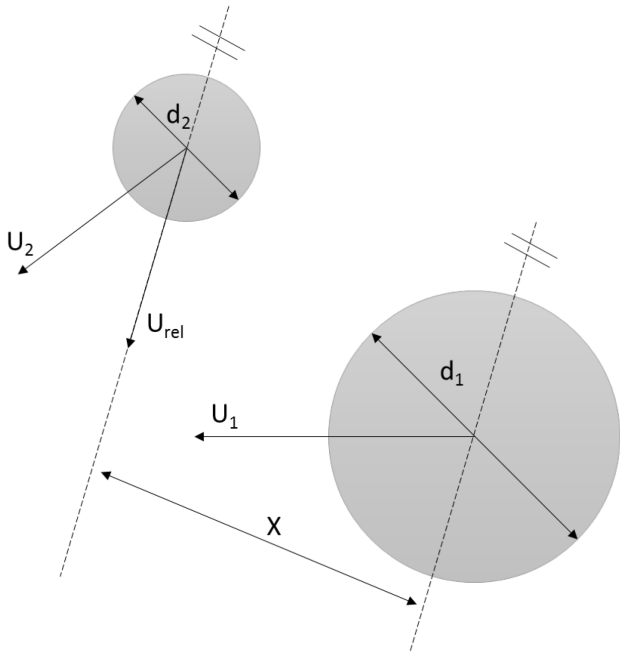


Figure 1.17 A schematic of the geometric collision parameters

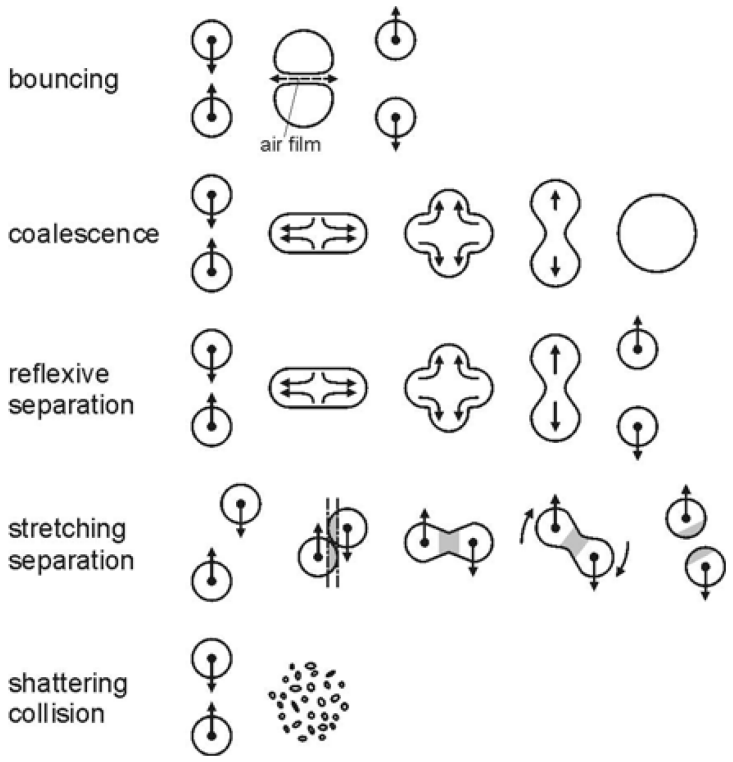


Figure 1.18 A schematic representation of the droplet collision mechanisms (Baumgarten, 2006)

Evaporation is the phase change from liquid to vapour from the liquid-gas interface when the gaseous phase is not saturated. In a single droplet basis, the evaporation process includes heat and mass transfer from and to the surrounding gas. The evaporation process can be increased by supplying heat to the liquid or reduce the ambient pressure. The energy is transferred from the in-cylinder gas to the droplet in terms of conductive, convective, and radiative heat transfer. The mass transfer is done via diffusion and convection of the fuel vapour to the surrounding gas. While typical pump-grade gasoline consists of over 150 hydrocarbon compounds, experimental data with single component fuels such as *iso*-Octane, *n*-Pentane and Ethanol (comprise about the 70% of the volume of gasoline, Kountouriotis *et al.,* 2014) are also available (Van Romunde and Aleiferis, 2009). The distillation curves of different gasoline types and various single components (Figure 1.19) show that the concentration of each compound affects the evaporation, with the more volatile components to evaporate faster while those with higher molecular weight to evaporate later. A schematic representation of a droplet evaporation is shown in Figure 1.20. The evaporation of the liquid droplets plays a significant role in the mixing process and the air-fuel distribution. In addition, the cooling effect of the fuel evaporation, especially in DI engines, reduces the temperature of the charge with the benefits that have already been discussed.

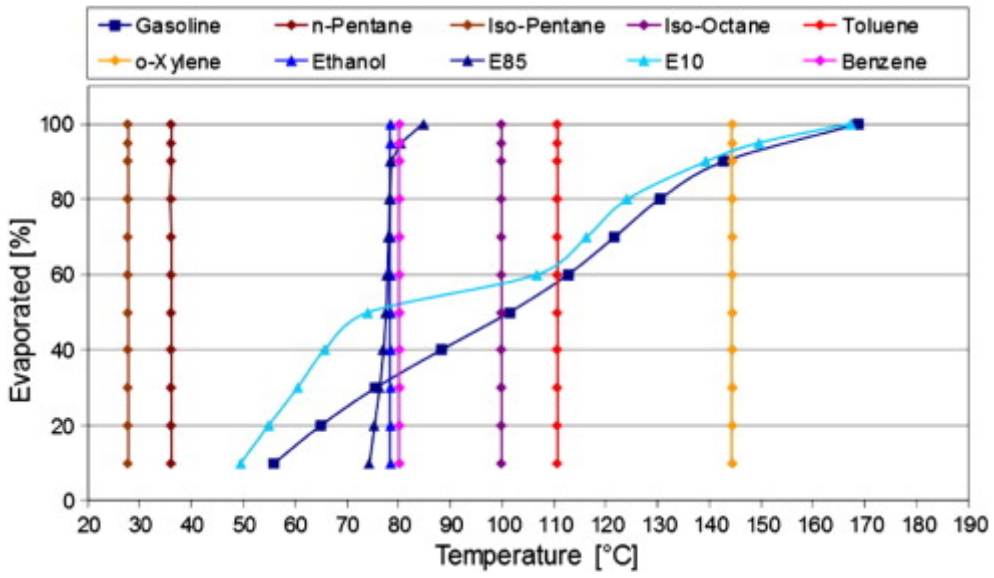


Figure 1.19 Distillation curves of various fuels (Kountouriotis et al., 2014)

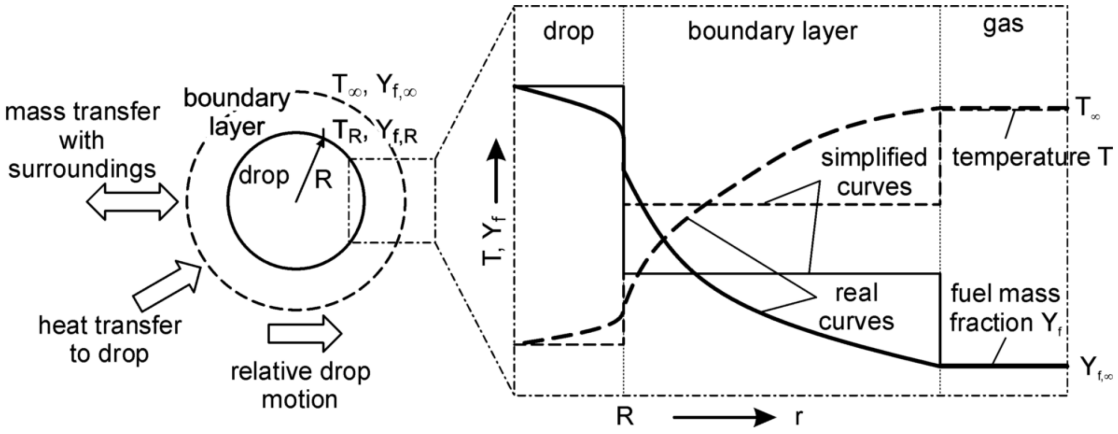


Figure 1.20 A schematic representation of a droplet evaporation (Baumgarten, 2006)

As it was said, the evaporation can be increased by reducing the ambient pressure. When the pressure is below the saturated vapour pressure of the fuel, the liquid undergoes a rapid boiling process which is called flash-boiling. During this process the liquid evaporates almost instantly, which results in the increase of the spray volume, the break-up of the droplets is accelerated and the spray pattern changes. Flash-boiling is easier to be achieved during gasoline injection at low engine loads due to the lower boiling curve and low saturated vapour pressure of some gasoline components. A comparison of a sub-cooled and a flash-boiling injection in a pressure-enthalpy diagram is shown in Figure 1.21. For the sub-cooled case the highly pressurised fuel leaves the nozzle and the pressure decreases to the ambient pressure but due to the low fuel temperature and thus low enthalpy the liquid saturation line is not crossed. In the case of flash-

boiling, the increased fuel temperature allows the fuel to cross the liquid saturation line and vapour bubbles are formed (point 2 to 3). Just under the liquid saturation line, the first nuclei (vapour bubbles) are formed at the nozzle walls due to imperfections such as roughness. As the pressure further decreases, close to point 3, the nucleation rate increases and the transition from liquid to vapour is extremely rapid. Due to the increase of the nucleation rate, bubbles grow in the liquid which result in the atomisation process through three possible mechanisms (bubble coalescence, inertial shattering and micro-explosions of droplets).

The flash-boiling injection in a direct injection gasoline engine may lead to enhanced atomisation, better air-fuel mixing and decreased penetration to avoid fuel impingement. In extreme flash-boiling conditions though, the penetration can be increased even above the penetration of the sub-cooled spray with undesired results. A comparison of a sub-cooled and a flash-boiling gasoline injection from a multi-hole injector in a quiescent chamber is shown in Figure 1.22 (van Romunde and Aleiferis, 2009).

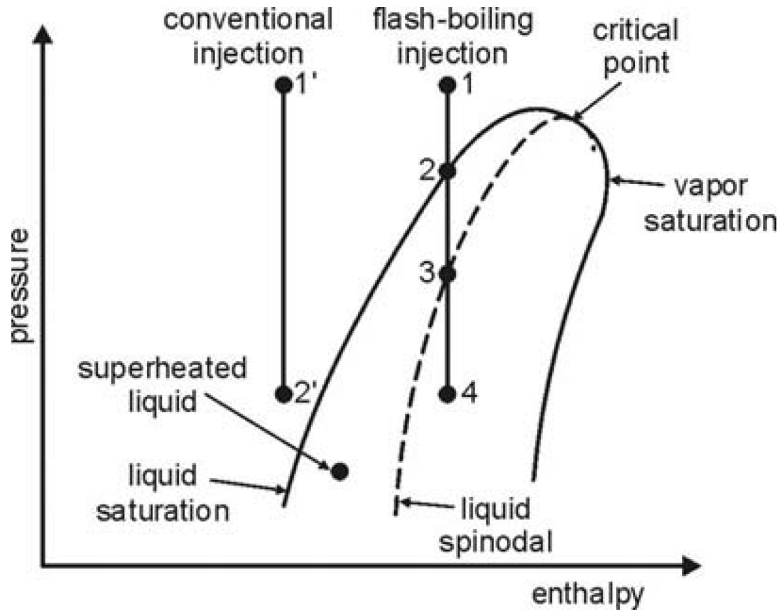


Figure 1.21 Comparison of conventional injection and flash-boiling injection in a pressure-enthalpy diagram (Baumgarten, 2006)

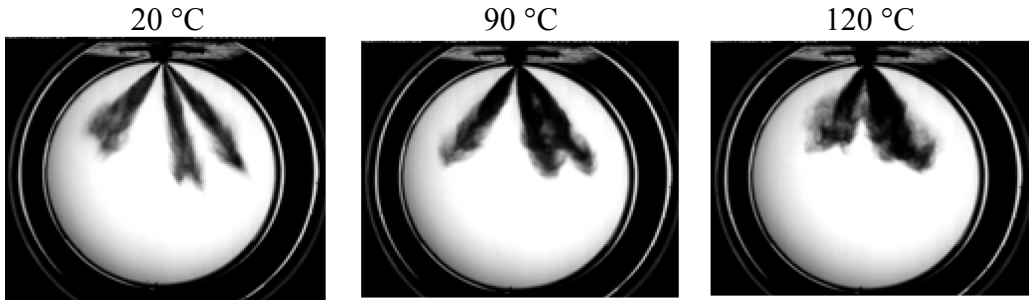


Figure 1.22 Comparison of gasoline sprays with different fuel temperatures at 0.5 bar ambient pressure (van Romunde and Aleiferis, 2009)

A penetrating spray in a direct injection gasoline engine interacts with the chamber walls and/or intake valves depending on the injection pressure, in-cylinder gas properties, injection timing, injector position, orientation and pattern. The spray-wall impingement and liquid film formation can have positive and negative effects. Droplet break up at the wall may improve the evaporation as well as the spray impingement on a hot wall can enhance the evaporation. In addition to this, intentional spray-wall interaction can be seen in wall guided stratification strategies. On the contrary, the fuel deposition on a cold wall increases the unburned hydrocarbon and soot emissions.

The impact of droplets on a solid surface may produce various impingement regimes, depending on the size, the velocity and the liquid properties of the droplets, the nature of the surface (rough or smooth, dry or wet) and the temperature of the surface. The six regimes that are mentioned in Baumgarten (2006), taken from Bai and Gosman (1996) and are also implemented in CFD codes are:

- Stick — the impinging droplet adheres to the wall in spherical form and continues to evaporate
- Spread — the droplet spreads out along the wall surface creating a wall film in case of a dry wall or mixes with the existing film in case of a wet wall.
- Rebound — the impinging droplet bounces off the wall after the impact without breaking up
- Splash — the impinging droplet breaks up into smaller droplets, some of which are reflected from the wall
- Break-up — the impinging droplet breaks up into smaller droplets and rebound from the wall.
- Boiling induced break up — The droplet disintegrates due to a rapid liquid boiling on a hot wall near the Nakayama temperature

The schematic of the six impingement regimes can be seen in Figure 1.23.

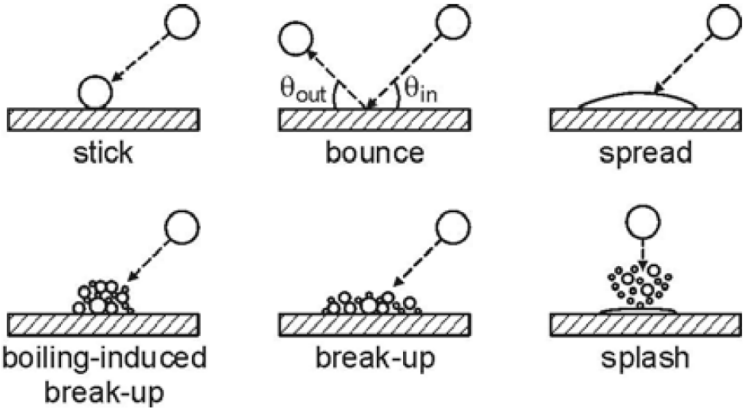


Figure 1.23 schematic of the six impingement regimes (Bai and Gosman, 1996)

The most important dimensionless numbers associated with the impacting droplet that describe the transition between these regimes are the Weber number and the Laplace number. Other dimensionless numbers related to the droplet-wall interaction can be found at Moreira *et al.* (2011). In addition, three characteristic wall temperatures that affect the impinging regimes are the liquid boiling temperature, the Nakayama temperature at which a droplet reaches its maximum evaporation rate and the Leidenfrost temperature at which a thin layer of vapour forms between the surface and the drop and evaporation is minimized

Several methods have been proposed to model the aforementioned phenomena related to engine sprays. Here, a brief description of the most common models in the literature for full cone sprays will be attempted and studies of various researchers will be discussed. In the next chapter, the methodology of the models used in this work will be further discussed. To simulate the fuel injection, the Lagrangian multi-phase treatment is used which models the liquid droplets (dispersed phase) of the fuel. The droplets are initialised at the nozzle exit of the injector which start to penetrate into the continuous phase. The role of the primary break-up is to provide the initial conditions for the droplets, mainly the velocity and the diameter. The simplest and most popular way to initialise the droplet size is the blob method suggested by Reitz and Diwakar (1987). The idea behind it is that in the domain near the nozzle exit, a liquid core exists within the dense spray which is represented by large droplets, with diameters similar to that of the nozzle. With this approach, the starting diameter of all the droplets equals to the diameter of the nozzle exit and the velocity is calculated from the conservation of mass for the flow inside the nozzle. Various researchers with different CFD codes have been using this method to initialise the droplet diameter, in both quiescent chambers and engine simulations for both gasoline and diesel fuel. (Malaguti *et al.,* 2011; Lucchini *et al.,* 2013; Pomraning *et al.,* 2014; Liu *et al.,* 1993; Lucchini *et al.,* 2014; Scarcelli *et al.,* 2015). A modified version of

the blob method which takes into account the reduction of the nozzle flow area due to cavitation has been suggested by von Kuensberg Sarre *et al.* (1999) for diesel injectors but a similar method is followed for gasoline sprays by a number of researchers such as Montanaro *et al.* (2011) and Lucchini *et al.* (2012). Due to the decrease of the effective flow area, the initial droplet diameter is smaller than the diameter of the nozzle and an increased initial velocity of the droplets is calculated. For diesel sprays, a primary break-up model was developed by Huh and Gosman (1991) in which the in-nozzle turbulence generates waves on the jet surface at the nozzle exit which grow and detach in the form of new droplets. For the initialisation of the jet however, the blob method is used. In addition, the droplet velocity and the spray cone angle are also predicted by the model. A similar approach to the Huh and Gosman atomisation was developed in the work of Malaguti *et al.* (2013) for gasoline sprays.

Another approach for the initialisation of the droplet sizes is the use of distribution functions. In this approach, it is assumed that the fuel has already been atomised at the nozzle exit and can be represented by a mathematical distribution. While the distribution of the droplet size at the nozzle exit could not be quantified experimentally until now, in this method an estimated distribution is applied so as to match the experimental data downstream the injector tip. Various distributions have been used in the literature based on the calculation of the SMD of the spray (Martinelli *et al.,* 1985), the power law (Levy *et al.,* 1998), the log-normal distribution (Costa *et al.,* 2009), the Nukiyama-Tanasawa distribution (Nukiyama, 1939; Hosaka *et al.,* 2016), the x^2-distribution (Reitz and Diwakar, 1986) and distributions that are not mentioned in the studies and were taken directly from experiments (Köpple *et al.,* 2015; Forte *et al.,* 2014b; Dahms *et al.,* 2009; Frottier *et al.,* 2014). However, the Rosin-Rammler distribution is the most widely used for initialisation of the fuel droplets (Huang and Lipatnikov, 2011; Verma *et al.,* 2016; Breda *et al.,* 2016; Chryssakis *et al.,* 2003; Fontanesi *et al.,* 2006; Huang *et al.,* 2014; Habchi *et al.,* 1999) but the two constants have to be tuned to match the experimental data downstream the injector nozzle.

Various models have been developed for the secondary break-up due to the aerodynamic forces. The Taylor Analogy Break-up (TAB) model was developed by O'Rourke and Amsden (1987) initially for diesel sprays but is known that underpredicts the penetration when it is combined with the blob-method (Liu *et al.,* 1993). Modified versions of the TAB model have also been developed however, they have lost their position with regards to break-up modelling. Another model for the secondary breakup which is widely used nowadays was proposed by Patterson and Reitz (1998) initially for diesel engine and it is named KHRT break up model.

This takes account the Kelvin-Helmholtz aerodynamic instabilities growing from the droplet surface and the Rayleigh-Taylor instabilities due to the deceleration of the droplets. An alternative secondary break up model which is popular for fuel injection was described by Reitz and Diwakar (1986) and is based on the 'bag' or 'stripping' droplet break-up due to aerodynamic forces on a diesel fuel droplet. Other break up models have been proposed such as those by Pilch and Erdman (1987) which distinguishes five regimes of break up instead of the two and by Hsiang and Faeth (1992) for diesel spray applications. Moreover, models for primary break up such as the Huh and Gosman (1991) model has been used for gasoline sprays as primary or secondary break-up in various studies. It is clear that a general, unified methodology for modelling the droplet break up during gasoline injection does not exist and various models can be used but the constants of the models have to be tuned for a specific application to match the experiments. In addition, models that were initially developed for diesel sprays are used for gasoline sprays as well with the appropriate constant tuning.

To model the inter-droplet collisions, the statistical approach proposed by O'Rourke (1981) is the most common in the literature. This model distinguishes three regimes: coalescence, separation and bouncing. However, it has been observed that the original modelling approach is sensitive to the grid size, type and orientation relative to the nozzle. This sensitivity has been observed for both hollow-cone and solid-cone sprays in various studies (Aneja and Abraham, 1998; Schmidt and Rutland, 2000; Hou and Schmidt, 2006; Li *et al.,* 2006). This dependency on the grid can be seen in Figure 1.24 for hollow-cone sprays and solid-cone sprays.

The root of the problem comes from the fact that only parcels within a computational cell can collide. Parcels which are travelling 90° apart have high relative velocity and this increases the possibility of collision. The velocities after the collision are near the mean velocity of the original velocities due to coalescence or separation. In addition, the original model calculates all possible collisions and then checks if they reside in the same cell which made it time consuming. To overcome these issues, the O'Rourke model has been extended with a speed-up algorithm suggested by Schmidt and Rutland (2000), geometrical constraints proposed by Nordin (2001) and coalescence timescale described by Aamir and Watkins (1999). Except from the speed-up algorithm, Schmidt and Rutland introduced a secondary mesh which is independent of the computational mesh and randomly rotates around the injector axis in order to supress the numerical artefacts.

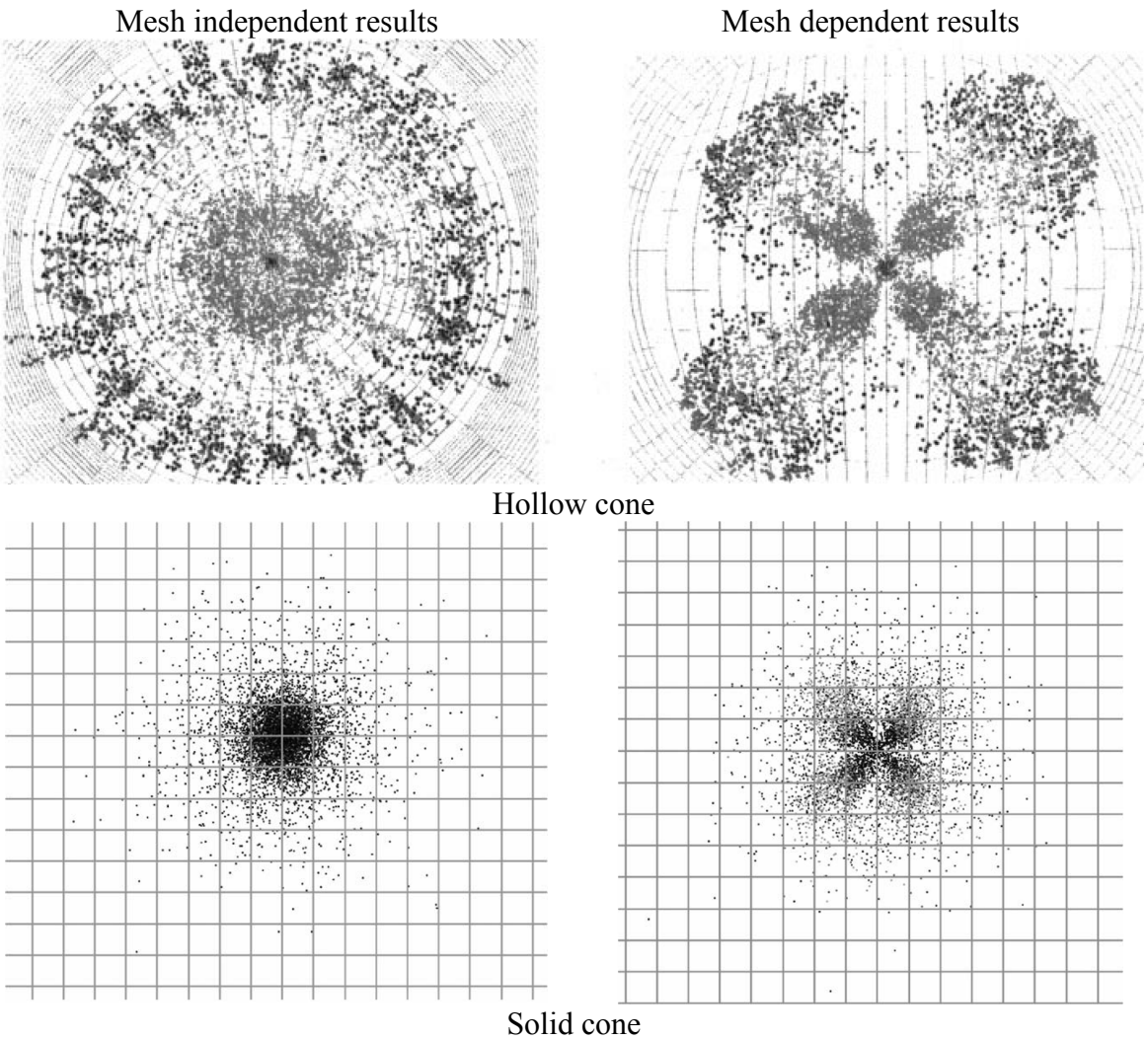


Figure 1.24 Grid dependency of spray due to collision modelling for hollow cone and solid cone sprays (Schmidt and Rutland, 2000; Hou and Schmidt, 2006)

For the mass transfer of a single component sub-cooled fuel, various models can be found in the literature such as the one described by Bird *et al.* (1966) and is implemented in STAR-CD, by Dukowicz (1979) and it has been used in the work of Costa *et al.* (2009) and Li *et al.* (2014) among the others and the model by Borman and Johnson (1962). Common ground of these models is the use of the Nusselt number for the heat transfer and the Sherwood number for the mass transfer described by Ranz and Marshall (1952).

The modelling of flash-boiling is challenging due to the complex phenomena taking place within the nozzle, the limitations of the experimental techniques and the lack of fundamental understanding of the flash-boiling which is still under investigation with new experiments. One of the earliest numerical studies for the atomisation and vaporisation of flash-boiling spray was carried out by Senda *et al.* (1994). Results of spray angle and droplet sizes were in a good

agreement with the experiments however, this was a 1D modelling approach and the spray structure was not presented. Another attempt of 1D modelling of a multi-component flash-boiling spray was carried out by Negro *et al.* (2011). Various blends of gasoline/ethanol were studied and their effect on evaporation and atomisation were analysed. Again, due to the 1D modelling, no spray structures were modelled. Attempts to model flash-boiling with the Lagrangian method using 3D CFD have been made by Zeng and Lee (2001), Zuo *et al.*, (2000), Kim and Park (2018), Huang *et al.* (2017) and Price *et al.* (2015, 2016). Zeng and Lee developed an atomisation model for flash-boiling which essential is the competition of aerodynamic break-up based on the TAB model and bubble growth.

Zuo *et al.* (2000) modified the existing LISA break-up model for hollow-cone sprays to include atomisation due to flash-boiling and superheat evaporation according to Adachi's experimental correlation (Adachi *et al.,* 1996). Kim and Park (2018) developed a break-up mechanism for flash-boiling sprays based on bubble growth dynamics which was calculated by the Rayleigh-Plesset equation. Price *et al.* (2016) and Huang *et al.* (2017) used the technique of the reduction of the initial droplet diameter in the blob concept. The reduction factor is calculated via either the Riznic heterogeneous nucleation model (Riznic and Ishii, 1989) or by the model proposed by Janet *et al.* (2015). In addition, Price *et al.* (2015) included a flash-boiling evaporation model by adding the superheated droplet evaporation term by Adachi.

One of the first attempts to model fuel impingement was done by Naber and Reitz (1988). In this model, three regimes of droplet-wall interaction were defined (stick, rebound and slide). In the stick regime, the droplets stick to the wall and continue to evaporate. In the rebound regime, a perfect reflection of the droplet occurs. In the case of the slide, the droplets follow a motion tangential to the wall, with the same velocity magnitude as before the impact. In all the regimes, the droplet sizes do not change due to the droplet-wall interaction. In addition, no liquid film formation is described in the model. A more detailed model for droplet-wall interaction was developed by Bai and Gosman (1995) based on their literature review of experimental data. The regimes for this model are the adhesion, rebound, splash, break-up or a combination of them. In addition, the model distinguishes the difference between a dry and a wetted wall and different regimes are applied to each case. The stochastic nature of wall impingement is replicated by a random procedure which allows the post-impinging droplets to have a distribution of size and velocity. Similar wall-impingement models to the Bai and Gosman (1995) have been proposed by Stanton and Rutland (1996) and O'Rourke and Amsden (2000). The main differences of these models appear on the splash regime in terms of transition

criteria, splash mass ratio and secondary droplet sizes and distribution after the impingement. Rosa *et al.* (2006) developed a model for smooth and dry wall based on experimental data. Another detailed droplet-wall interaction model was developed by professor Senda in series of publications (Senda and Fujimoto, 1999; Senda *et al.,* 1997; Ashida *et al.,* 2000; Senda *et al.,* 1996; Matsuda and Senda, 2003) based on extensive experimental data. The model has many similarities to Bai and Gosman (1995) such as the regimes distinguished by the model and the conditions of the wall (dry or wetted). More specifically, the treatment of the adhesion and rebound are identical and only the splash regime differs in terms of splash mass ratio, secondary droplet number, sizes and velocities. All the aforementioned models have been developed and validated based on specific experiments and the most popular in the literature for engine simulations is the Bai and Gosman model. However, in most cases, the model is used without being validated for the specific application (Fontanesi *et al.,* 2014; Wang *et al.,* 2015; Köpple *et al.,* 2015) due to the difficulty of in-cylinder measurements. For some studies (Malaguti *et al.,* 2011; Lucchini *et al.,* 2013), an endoscopic method has been used to identify the areas of fuel impingement and validate the numerical results qualitatively. To quantitatively assess the performance of a droplet-wall interaction model, Piazzullo *et al.* (2017) utilised experiments in a constant volume chamber in order to measure the liquid film footprint and liquid mass with the method of laser induced fluorescence (LIF).

1.6. Pollutant formation

It was mentioned in the introduction that effort is made to reduce the carbon dioxide as it is the main substance which contribute to the greenhouse effect and global warming. However, CO_2 occurs naturally in the atmosphere and it is the main product of complete combustion along with water vapour. In the exhaust gases after the combustion event of a spark ignition engine, more substances are contained such as oxides of nitrogen, carbon monoxide, unburnt hydrocarbons and particulates. These species are the major source of urban pollution and legislations have been posed for their reduction. One of the most important factors of the spark-ignition engine emissions is the air-fuel ratio and the spatial distribution of the air-fuel ratio. Figure 1.4 shows how the first three aforementioned pollutants vary with the equivalence ratio.

The oxides of nitrogen are known as NO_x and consist mostly of nitric oxide (NO) and small amounts of nitric dioxide (NO_2). The NO is mostly formed in the high temperature post flame gases where oxygen and nitrogen molecules react. Thus, high temperatures and high oxygen

concentration result in high NO production. In a spark ignition engine, the peak of the NO production is seen for mixtures slightly leaner than stoichiometric and around λ=1.1. At this dilution level, the combustion temperature is high while the availability of oxygen starts to increase. Further dilution with excess air, increases the availability of oxygen nevertheless, the temperature of combustion decreases, leading to lower NO formation. The reactions taking place during the NO production were firstly discussed by Zeldovich *et al.* (1947) who proposed:

$$O + N_2 \leftrightarrow NO + N \tag{1.9}$$

$$N + O_2 \leftrightarrow NO + O \tag{1.10}$$

Later, Lavoie *et al.* (1970) suggested a third reaction which contributed significantly on the NO production mechanism and it is given by:

$$N + OH \leftrightarrow NO + H \tag{1.11}$$

While mechanisms exist to describe the NO formation in the flame front, the reaction zone in engine combustion is thin enough with very short timescales and as a result the NO formation is dominant in post flame gases.

It was mentioned that the air-fuel mixture determines the NO formation which peaks at λ≈1.1. The combustion event itself and the spatial distribution of the air-fuel mixture also play a role on the NO formation. As an example, in the work of Zhou *et al.* (2017) the same engine for the same load which operates with a tumble flap for increased tumble motion showed different NO concentration depending on the position of the flap. With the increased tumble ratio, the NO_x production was higher than the case with the lower tumble ratio for all tested dilution levels with excess air and peaked for both tumble ratios at λ=1.1. The increase of the NO_x was believed to be due to the faster combustion which increased the in-cylinder temperature. In the work of Wilson *et al.* (1993) it was mentioned that the NO_x emissions with different valve strategies at stoichiometric air-fuel ratio were very small (less than 5%) but the trend was NO_x reduction with shorter combustion duration. As it can be seen from these two different studies, the reasons behind the increase of NO_x are contradicted. Moore *et al.* (2011) investigated among other quantities the emissions of NO_x when the engine was operated either with two or one intake valves at various engine speed and load conditions. There was not a clear trend of the differences of NO_x between single and dual valve activation for the range of the operating conditions.

Carbon monoxide is formed during combustion at zones of rich air-fuel mixture where the insufficient oxygen is partially burnt with the fuel forming CO instead of CO_2. Generally, engines operate at stoichiometric or slightly rich mixtures thus, the CO emissions are significant. For lean mixtures the CO emissions vary little and are much lower than the stoichiometric mixture. The air-fuel mixture distribution is also important for the CO production. Better air-fuel homogeneity leads to less rich zones and as a consequence reduced CO. This was demonstrated by Huang *et al.* (2016) who showed the CO spatial distribution for various injection timings. The increased CO was linked to the uneven mixture and the regions with higher CO concentration were those with rich mixture. When the CO emissions were compared for dual and single valve actuation in the study of Moore *et al.* (2011), there trend for all engine load conditions was the reduction of CO with the valve deactivation. Similarly, in the work of Zhou *et al.* (2017) the increase tumble motion with the use of the tumble flap, reduced the CO emission when compared to the low tumble case. This was again linked to the uneven air-fuel mixture.

The unburnt hydrocarbons (HC), as their name denotes, are organic compounds that emitted into the atmosphere due to the incomplete combustion of the fuel. In a spark ignition engine, various sources of HC exist. Again, the equivalence ratio is an important variable for the HC. As the mixture becomes richer, the insufficient oxygen leads to partially burnt fuel and thus increase of the unburnt hydrocarbons. In very lean mixtures where the combustion efficiency deteriorates the HC increase due to misfires or partially burnt cycles. Other mechanisms for HC emissions are the flame quenching at the combustion chamber walls, the filling of crevices with unburnt mixture, absorption and desorption of liquid or gaseous fuel into oil film (Heywood, 1988). With an aim to reduce the unburnt hydrocarbons with the use of differential valve lift, Nakayama *et al.* (1994) showed that a reduction of 45% could be achieved during cold start by optimising the air-fuel ratio (AFR=15.5) and ignition timing. However, this was achieved because the variable valve lift allowed lean burn in comparison to the rich mixture of the baseline. In addition, they showed that by reducing the combustion duration with the differential valve lift, the HC emissions were increased for stoichiometric combustion. In the work of Wilson *et al.* (1993) however, it was stated that reducing the ignition delay via changes to in-cylinder flow decreased the unburnt hydrocarbons. They also stated that asymmetric inlet valve strategies showed improvements in HC emissions over the baseline strategy because of the increased charge motion which promoted a more homogenous mixture. The same conclusion of reduced HC with the valve deactivation compared to the two-valve baseline was

reported in the work of Kreuter *et al.* (1992). Moore *et al.* (2011) also showed that the unburnt hydrocarbons could be reduced with the valve deactivation in a range of engine speeds and loads.

The particulate emissions of gasoline engines were traditionally much lower than those of diesel engines and for this reason no regulations were posed. The lower particulates were due to port fuel injection which resulted in the fuel being very well mixed with the air before the combustion. When gasoline direct injection was introduced, it was found that this approach leads to produce up to two times more Particulate Matter (PM) than the PFI (Raza *et al.,* 2018) and for this reason, legislations have been applied to limit the PM which is essentially the total mass of the particulates. However, the size of the particles has also an impact on human health, especially the ultrafine particles with sizes below 100 nm (Kampa and Castanas, 2008). Particulate mass can be misleading in measuring the health hazard, because one particle of 10 μm size has approximately the same mass as 1 million particles of 100 nm size. Thus, the latest European legislation limits both the PM (4.5 mg/km) and the particulate number (PN) (6×10^{11} #/km). The global air-fuel ratio and the air-fuel distribution play an important role in the particulate formation. Rich mixtures give an order of magnitude greater numbers of particles compered to stoichiometric combustion (Pei *et al.,* 2014) and rich pockets due to air-fuel inhomogeneity even at lean operating condition can result in an increase of particulates. In addition, pool fires which is the combustion of liquid fuel is another dominant factor for particulate emissions from GDI engines. The fuel spray impingement on the engine walls, the interaction with the lubricant and the formation of liquid film is the source of pool fires (Drake *et al.,* 2003). In the work of Moore *et al.* (2011), the valve deactivation showed a decrease of soot emissions for various engine speeds and loads and for both rich and stoichiometric combustion which was about 95% reduction when compared to the dual valve activation. This was believed to be due to reduced fuel impingement on the walls and better mixing of the fuel and air. Sukegawa *et al.* (2014) proposed a method to estimate the PM based on the fuel mass in regions of rich mixtures at the time of ignition obtained by non-combustion CFD of a gasoline direct injection engine. A correlation between the amount of PM and the amount of fuel in rich mixtures due to inadequate mixing and due to the evaporation of the liquid film was derived. After tuning the constants of this correlation with the use of experimental and CFD data, various engine running conditions with different spray patterns and strategies (start of injection and split injections) were tested and experimental measurements were reproduced using that correlation.

1.7. Synopsis and present contribution

In the last decade, effort is being made to reduce the emissions of greenhouse gas and other pollutants produced by road vehicles as well as to increase the efficiency of the engine. However, due to higher cost, lower than expected fuel economy and the need of a lean NO_x aftertreatment of a gasoline engine, nowadays, more than 50% of the passenger cars in Western Europe operate with a diesel engine (Zhao, 2010). As a result, extended research, numerical and experimental, has been done and focused on direct injection diesel engine. Nevertheless, because of the refinery of crude oil, production and usage of gasoline is inevitable and possible future stricter emissions regulations for diesel engines, it is necessary to improve the direct injection gasoline engines that can close the gap.

The two most important improvements on a gasoline engine is the increased geometrical compression ratio and the increase in the ratio of specific heats (γ) for increased thermal efficiency. The dilution tolerance of the engine can be improved by manipulating the in-cylinder charge motion to increase the turbulent kinetic energy, accelerate the combustion rate and reduce the cycle-to-cycle variations. In addition, exhaust gas recirculation is an approach for increased dilution, for reduced NO_x emissions and supress the knock limit due to lower temperatures. Experimental studies have showed the benefits of the aforementioned strategies, more limited for the extension of dilution tolerance with the use of variable valve systems. However, fundamental understanding of the processes that take place in the cylinder with these strategies and the effect on the airflow and mixture formation is needed in order to optimise the use and incorporate all of them. Optical engines, with the use of high quality images and particle image velocimetry (PIV) data can give an insight of the in-cylinder phenomena. Nevertheless, the optical access can be limited, obstructed by engine parts and/or restricted in terms of engine load.

As the computational power increases and becomes cheaper, CFD simulations can give an insight on the processes and the physical phenomena taking place within an engine cylinder and explain the benefits and drawbacks of each adopted strategy on the engine cycle. Moreover, new designs and ideas can be tested without the cost of manufacture. This can guide the optimisation for a future high efficiency gasoline engine with reduced emissions.

In the literature, extensive studies have been carried out for improving the direct injection diesel engines however, for gasoline engines the work is more limited and mostly experimental. More

work is needed to improve the accuracy of the CFD solution for better interpretation of the experimental results. Studies have showed the benefit of using variable valvetrain systems to either control the effective compression and expansion ratio or to manipulate the in-cylinder flow motion with an ultimate goal the increased thermal efficiency. However, different valve strategies have an effect on the flow field, which can reduce the in-cylinder velocity and kinetic energy with a negative effect on combustion efficiency and fuel consumption. In the literature, findings of different researchers contradict each other, and further investigation is needed to understand the reasons of these conflicts and improve these methods. To achieve the increased thermal efficiency, this has to be done within the total range of operating conditions of an engine, from low to high load. It is not clear at which engine load the benefits of each adopted strategy diminish and what are the causes behind this. Models have to be implemented and work accurately within this range. Truthful prediction of the fuel injection event is a key to achieve the increased thermal efficiency however, the behaviour of the spray alters depending on the conditions. Limited work has been done in implementing flash-boiling modelling on engine simulations which is crucial at low engine load.

The objectives of the present work based on the findings of the above literature review and the needs for an accurate CFD simulation are:

- Establish a best practice approach for setting up in-cylinder simulations with grid independent solution and without the effect of the initial conditions.
- Validate the CFD code for the in-cylinder pressure and flow field according to available experimental pressure traces of the AJ20 thermal engine equipped with a Continuous Variable Valve Lift (CVVL) system and the AJ133 optical engine as well as PIV data from the AJ133.
- Further validate the code for the flow around the valves and identify limitations of the grid resolution and the turbulence modelling.
- Establish a modelling approach for sub-cooled fuel injection with the use of the Lagrangian multi-phase treatment and validate it against detailed experimental data of spray structure, penetration and droplet sizes in a quiescence chamber and in the AJ133 optical engine. Validate all necessary sub-models within the Lagrangian framework.
- Introduce an in-house flash-boiling model to two different engine geometries and validate its behaviour against experimental data of flash-boiling spray structure in the AJ133 optical engine.

- Establish a best practice approach for implementing both sub-cooled and flash-boiling spray modelling in a quiescent chamber and in engine simulations with the least possible differences in the implementation process. This means improvement of the grid independency of the existing flash-boiling model and align it with the existing setup of a sub-cooled spray.
- Investigate the effects of valve deactivation on the in-cylinder flow and heat transfer for different engine loads. Provide interpretation of the experimental results of the valve deactivation and give an insight of the reasons behind benefits and drawbacks.
- Investigate the effects of valve deactivation on the in-cylinder air-fuel mixture at two different loads with the use of the appropriate spray modelling for each load. Understand the behaviour of the flash boiling model on real engine operating conditions. Provide interpretation of the experimental results of emissions with and without the use of combustion modelling.
- Utilise the capabilities of the CVVL system with differential intake valve strategies, understand and exploit the benefits and reduce the disadvantages of the valve deactivation. Provide interpretation of the experimental results and guide the development of valve strategies to extend the dilution tolerance of the engine and increase the thermal efficiency.
- Investigate the reasons of cyclic variability differences at high dilution levels of Dual and Single Valve Actuation.

Chapter 2

Mathematical Formulation

2.1. Basic flow solution

In this study, the commercial CFD code STAR-CD, which is based on the finite volume method, is used to calculate fluid flow, heat and mass transfer and other related phenomena by using numerical methods that solve the well-known Navier-Stokes partial differential equations which govern them. These equations are based on the conservation laws of mass and momentum and are showed below (Versteeg and Malalasekera, 2007):

$$\frac{\partial \rho}{\partial t} + \frac{\partial}{\partial x_i}(\rho u_i) = 0 \tag{2.1}$$

$$\frac{\partial (\rho u_j)}{\partial t} + \frac{\partial}{\partial x_i}(\rho u_j u_i) = -\frac{\partial p}{\partial x_j} + \frac{\partial}{\partial x_i}\left(\mu \frac{\partial u_i}{\partial x_j}\right) + S_m \tag{2.2}$$

Where, t is time, x_i the Cartesian coordinate $(i = 1, 2, 3)$ the Cartesian coordinate, u_i the absolute fluid velocity component in direction x_i, ρ the density, p the pressure, μ the dynamic viscosity and S_m is the momentum source term.

In addition, the conservation of energy is considered:

$$\frac{\partial(\rho e)}{\partial t}+\frac{\partial}{\partial x_i}(\rho e u_i)=-p\frac{\partial u_i}{\partial x_i}+\frac{\partial}{\partial x_i}\left(k\frac{\partial T}{\partial x_j}\right)+S_e \tag{2.3}$$

Where, e is the internal energy, k is the thermal conductivity, T is the temperature and S_e the energy source term.

One more equation can be added, the equation of state and it is related to the density. A common assumption in the case of liquids or incompressible gases is $\rho = costant$. Also, the ideal gas law can be used for the equation of state. In this study, the ideal gas law was used:

$$\rho=\frac{p}{RT\left(\sum_i \frac{Y_i}{M_i}\right)} \tag{2.4}$$

Where p is the pressure, R is the universal gas constant, T is the temperature, Y_i is the mass fraction of a component with molecular weight M_i.

The viscosity was calculated based on the Sutherland's law:

$$\mu=\left(\frac{T}{273.15}\right)^{1.5}\frac{273.15+C_s}{T+C_s}\mu_0 \tag{2.5}$$

Where $\mu_0 = 1.716e-05\ \frac{kg}{ms}$ and $C_s = 116\ K$.

2.2. Turbulence modelling

The air flow in an internal combustion engine is turbulent with Reynold number of the order of $5{\cdot}10^4$ - $4{\cdot}10^5$ in the manifold branch, depending on the engine speed (Heywood 1988). Turbulence affects not only the manifold flow field but also the in-cylinder flow, the mixture formation and the combustion.

In order to capture the turbulence of the flow, various methods have been proposed. The most accurate way is the Direct Numerical Simulation (DNS) which resolves all the scales of turbulence from the smallest (Kolmogorov scale) to the largest without any turbulence model. However, this method is very expensive computationally and it is not used in industrial applications. Another approach based on space-filtered equations called Large Eddy Simulation (LES) is getting more popular as the computational power is increased. In this approach, it is assumed that the large eddies of the flow are dependent on the geometry and

they are numerically solved while the sub-grid scales are modelled. It is less expensive than DNS but it provides very accurate results. Because engineers are generally interested in mean values and properties of a turbulent flow, using the two methods discussed above, are not typical in common engineering practice. For this reason, the time-averaged Reynolds-Averaged Navier-Stokes (RANS) method is used to predict the average of turbulent flows. This method is based on equations obtained by averaging the equations of motion over time to which approximations are introduced with the turbulence models. Specifically, Reynolds averaging gives rise to velocity covariances$\overline{u_i' u_j'}$ referred to as the Reynolds Stresses. Boussinesq (1877) proposed that the turbulent shear stress arising from the cross-correlation of fluctuating velocities could be determined as: $-\rho\overline{u_i' u_j'} = \rho v_t \frac{\partial U}{\partial y}$, where v_t is the Turbulent Viscosity or Eddy Viscosity that needs to be modelled. Based on the RANS equations the most popular models for turbulence, are the two-equation standard k-ε and k-ω models and their variants. In the current work, the RANS approach was used to obtain understanding of the average of the in-cylinder phenomena with the use of the k-ε RNG model which seemed to be the most appropriate for engine simulations and the LES approach was used to obtain understanding of the variability of the in-cylinder parameters. Due to modifications that the STAR-CD software applies to some formulations, the description of the models bellow, follows the notation of the STAR-CD code.

Standard k-ε model

Based on the work of Jones and Launder (1972) and Launder and Spalding (1974), the transport equations as they are solved by the software are:

Turbulence kinetic energy (k):

$$\frac{\partial}{\partial t}(\rho k) + \frac{\partial}{\partial x_j}\left[\rho u_j k - \left(\mu + \frac{\mu_t}{\sigma_k}\right)\frac{\partial k}{\partial x_j}\right] = \mu_t(P + P_B) - \rho\varepsilon - \frac{2}{3}\left(\mu_t \frac{\partial u_i}{\partial x_i} + \rho k\right)\frac{\partial u_i}{\partial x_i} \tag{2.6}$$

Where,

$$P \equiv S_{ij}\frac{\partial u_i}{\partial x_i} \tag{2.7}$$

$$P_B \equiv -\frac{g_i}{\sigma_{h,t}}\frac{1}{\rho}\frac{\partial \rho}{\partial x_i} \tag{2.8}$$

and σ_k is the turbulent Prandtl number. The first term on the right-hand side of the equation represents turbulent generation by shear and normal stresses and buoyancy forces, the second viscous dissipation, and the third amplification or attenuation due to compressibility effects. The last term accounts for the non-linear contributions.

Turbulence dissipation rate (ε):

$$\begin{aligned}\frac{\partial}{\partial t}(\rho\varepsilon) + \frac{\partial}{\partial x_j}\left[\rho u_j \varepsilon - \left(\mu + \frac{\mu_t}{\sigma_\varepsilon}\right)\frac{\partial \varepsilon}{\partial x_j}\right] \\ = C_{\varepsilon 1}\frac{\varepsilon}{k}\left[\mu_t P - \frac{2}{3}\left(\mu_t \frac{\partial u_i}{\partial x_i} + \rho k\right)\frac{\partial u_i}{\partial x_i}\right] + C_{\varepsilon 3}\frac{\varepsilon}{k}\mu_t P_B - C_{\varepsilon 2}\rho\frac{\varepsilon^2}{k} \\ + C_{\varepsilon 4}\rho\varepsilon\frac{\partial u_i}{\partial x_i}\end{aligned} \tag{2.9}$$

Where, σ_ε is the turbulent Prandtl number, $C_{\varepsilon 1}, C_{\varepsilon 2}, C_{\varepsilon 3}, C_{\varepsilon 4}$ are coefficients that were kept constant at their default values. The first term on the right-hand side represents the contribution to the production of dissipation due to linear stresses and dilatation/compression effects, the second the contribution due to buoyancy, the third term in the equation accounts for the dissipation destruction, the fourth the contribution due to temporal mean density changes and the fifth the contribution due to non-linear stresses. The turbulent viscosity is defined as:

$$\mu_t = \frac{C_\mu \rho k^2}{\varepsilon} \tag{2.10}$$

With C_μ and empirical coefficient.

RNG (Re-Normalisation Group) k-ε model

Based on the work of Yakhot and Orszag 1986 and Yakhot *et al.*, 1992 the transport equations as they are solved by the software are:

Turbulence kinetic energy (k):

$$\frac{\partial}{\partial t}(\rho k) + \frac{\partial}{\partial x_j}\left[\rho u_j k - \left(\mu + \frac{\mu_t}{\sigma_k}\right)\frac{\partial k}{\partial x_j}\right] = \mu_t(P + P_B) - \rho\varepsilon - \frac{2}{3}\left(\mu_t \frac{\partial u_i}{\partial x_i} + \rho k\right)\frac{\partial u_i}{\partial x_i} \tag{2.11}$$

Turbulence dissipation rate (ε):

$$\begin{aligned}\frac{\partial}{\partial t}(\rho\varepsilon) + \frac{\partial}{\partial x_j}\left[\rho u_j \varepsilon - \left(\mu + \frac{\mu_t}{\sigma_\varepsilon}\right)\frac{\partial \varepsilon}{\partial x_j}\right] &= C_{\varepsilon 1}\frac{\varepsilon}{k}\left[\mu_t P - \frac{2}{3}\left(\mu_t \frac{\partial u_i}{\partial x_i} + \rho k\right)\frac{\partial u_i}{\partial x_i}\right] + C_{\varepsilon 3}\frac{\varepsilon}{k}\mu_t P_B - C_{\varepsilon 2}\rho\frac{\varepsilon^2}{k} \\ &+ C_{\varepsilon 4}\rho\varepsilon\frac{\partial u_i}{\partial x_i} - \frac{C_\mu \eta^3(1-\eta/\eta_0)}{1+\beta\eta^3}\frac{\rho\varepsilon^2}{k}\end{aligned} \tag{2.12}$$

Where, $\eta \equiv S\frac{k}{\varepsilon}$ and η_0, β are empirical coefficients.

Comparison of the equations of standard k-ε and RNG k-ε shows that the only difference appears at the turbulence dissipation rate (ε) equation. In the RNG model an extra term at the end of the equation is added and represents the effect of mean flow distortion on the turbulence which was described by Rodi (1979). Moreover, minor differences exist between standard and RNG model at the values of the coefficients. Again, they were kept constant at their default values. Lastly, it has to be noted that in the original form of the RNG model, no compressibility or buoyancy effects were taken account however, in STAR-CD are modelled as in the standard k-ε model.

Standard k-ω model

Based on the work of Wilcox (1998) the transport equations as they are solved by the software are:

Turbulence kinetic energy (k):

$$\frac{\partial}{\partial t}(\rho k) + \frac{\partial}{\partial x_j}\left[\rho u_j k - \left(\mu + \frac{\mu_t}{\sigma_{k\ k}^{\omega}}\right)\frac{\partial k}{\partial x_j}\right] = \mu_t(P + P_B) - \rho\beta^* k\omega \tag{2.13}$$

Specific dissipation rate (ω):

$$\frac{\partial}{\partial t}(\rho\omega) + \frac{\partial}{\partial x_j}\left[\rho u_j \omega - \left(\mu + \frac{\mu_t}{\sigma_\omega^\omega}\right)\frac{\partial \omega}{\partial x_j}\right] = \alpha\frac{\omega}{k}\mu_t P - \rho\beta\omega^2 + C_{\varepsilon 3}\mu_t P_B C_\mu \omega \tag{2.14}$$

and by definition

$$\omega = \frac{\varepsilon}{C_\mu k} \tag{2.15}$$

Where,

$$\beta = \beta_0 f_\beta, \beta^* = \beta_0^* f_\beta^* \tag{2.16}$$

$$f_\beta = \frac{1 + 70\chi_\omega}{1 + 80\chi_\omega}, f_\beta^* = \begin{cases} 1 & \chi_k \le 0 \\ \dfrac{1 + 680\chi_k^2}{1 + 400\chi_k^2} & \chi_k > 0 \end{cases} \tag{2.17}$$

$$\chi_k = \frac{1}{\omega^3}\frac{\partial k}{\partial x_j}\frac{\partial \omega}{\partial x_j}, \chi_\omega = \left|\frac{\Omega_{ij}\Omega_{jk}S_{ki}}{(2\beta_0^*\omega)^3}\right| \tag{2.18}$$

$C_{\varepsilon 3}, C_\mu$, are empirical coefficients and the turbulent viscosity is given by:

$$\mu_t = \rho v_t = \rho\frac{k}{\omega} \tag{2.19}$$

k-ω SST (Shear Stress Transport) model

Based on the work of Menter (1993) the transport equations as they are solved by the software are:

Turbulence kinetic energy (k):

$$\frac{\partial}{\partial t}(\rho k) + \frac{\partial}{\partial x_j}\left[\rho u_j k - \left(\mu + \frac{\mu_t}{\sigma_k^\omega{}_k}\right)\frac{\partial k}{\partial x_j}\right] = \mu_t(P + P_B) - \rho\beta^* k\omega \tag{2.20}$$

Specific dissipation rate (ω):

$$\frac{\partial}{\partial t}(\rho\omega) + \frac{\partial}{\partial x_j}\left[\rho u_j \omega - \left(\mu + \frac{\mu_t}{\sigma_\omega^\omega}\right)\frac{\partial \omega}{\partial x_j}\right] = \alpha\frac{\omega}{k}\mu_t P - \rho\beta\omega^2 + C_{\varepsilon 3}\mu_t P_B C_\mu \omega + 2(1-F_1)\rho\frac{1}{\sigma_{\omega 2}^\omega}\frac{1}{\omega}\frac{\partial \omega}{\partial x_j}\frac{\partial k}{\partial x_j} \quad (2.21)$$

Where the blending function F_1 is:

$$F_1 = \tanh(arg_1^4) \quad (2.22)$$

$$arg_1 = \min\left[\max\left(\frac{\sqrt{k}}{0.09\omega y}, \frac{500v}{y^2\omega}\right), \frac{4\rho k}{\sigma_{\omega 2}^\omega CD_{k\omega} y^2}\right] \quad (2.23)$$

$$CD_{k\omega} = \max\left(\frac{2\rho}{\omega\sigma_{\omega 2}^\omega}\frac{\partial k}{\partial x_j}\frac{\partial \omega}{\partial x_j}, 10^{-20}\right) \quad (2.24)$$

The turbulent viscosity is:

$$\mu_t = \rho\frac{\alpha_1 k}{\max(\alpha_1\omega, \Omega^* F_2)} \quad (2.25)$$

Where $\alpha_1 = 0.31$ and the blending function F_2 is:

$$F_2 = \tanh(arg_2^2) \quad (2.26)$$

$$arg_2 = \max\left(2\frac{\sqrt{k}}{0.09\omega y}, \frac{500v}{y^2\omega}\right) \quad (2.27)$$

Comparison of the equations of the standard k-ω model and the k-ω SST model shows difference only on the specific dissipation rate (ω) equation. For the k-ω SST model an extra term is added at the end of the equation. The two equations of k and ω of the SST model are a blend of the standard k-ω model and the k-ε model in order to incorporate the advantages of both models. With this, standard k-ω is used near the boundary layer (wall) and it gradually changes to k-ε for the rest of the flow.

The constants φ of the model are functions of the blending function F_1 and are expressed in the general form:

$$\varphi = F_1\varphi_1 + (1-F_1)\varphi_2 \quad (2.28)$$

Where φ_1, φ_2 represent the constants of the k-ω and k-ε models respectively and are given by two separate sets of constants. The first set corresponds to the standard k-ω model and the second corresponds to the k-ε model.

However, deeper investigation of the turbulence models was out of the scope of this study, thus, detailed information about the aforementioned models and their mathematical formulations can be found elsewhere (Blazek 2015), (Ferziger and Peric 2012), (Versteeg and Malalasekera 2007) and (Wilcox 1998).

LES – Smagorinsky sub-grid scale model

As discussed before, the concept of the LES is to solve explicitly the large-scale eddies which are dependent on the flow geometry, while the eddies smaller than the computational grid (sub-grid scale or SGS) are modelled. The LES approach does not use an averaging procedure but applies a spatial filter to the Navier-Stokes equations and for a flow variable $\varphi(x,t)$ the filtered variable is defined as:

$$\bar{\bar{\varphi}}(x,t) = \iiint_{-\infty}^{+\infty} G(x-x',\Delta)\varphi(x',t)\,dx' \tag{2.29}$$

Where G is the filter function with filter width of $\Delta = \sqrt[3]{V_{vell}}$.

When the LES filtering is applied to the Navier-Stokes equations, it results in the SGS stress tensor $\tau_{SGS,ij} = \bar{\bar{\rho}}\left(\langle u_i u_j\rangle - \langle u_i\rangle\langle u_j\rangle\right)$ which requires modelling.

The simplest way to model this SGS stress tensor is by using a Boussinesq assumption and takes the form:

$$\tau_{SGS,ij} = -2\bar{\bar{\rho}}\nu_{SGS}S_{ij} + \frac{1}{3}\tau_{SGS,kk}\delta_{ij} \tag{2.30}$$

Where $\bar{\bar{\rho}}$ denotes filtered density, S_{ij} is the strain rate tensor and $\tau_{SGS,kk}$ is the isotropic part of the sub-grid scale stresses which is not modelled, but added to the filtered pressure equation.

The sub-grid scale turbulent viscosity equation was suggested by Smagorinsky (1963) and is given by:

$$\nu_{SGS} = (C_s\Delta)^2\sqrt{2S_{ij}S_{ij}} \tag{2.31}$$

The constant C_s is the Smagorinsky constant and typically is in the range of 0.1 – 0.2. In this work $(C_s)^2 = 0.02$.

2.3. Residuals and EGR Concentration Calculations

The residuals (combustion products) and EGR concentration before Exhaust Valve Opening (EVO) in the cylinder and the intake and exhaust ports were calculated based on the complete stoichiometric (Φ=λ=1) or lean (Φ<1 or λ>1) combustion reaction. To begin with, the stoichiometric combustion equation of a hydrocarbon in oxygen is:

$$\mathrm{C_\alpha H_\beta O_\gamma} + \left(\alpha + \frac{\beta}{4} - \frac{\gamma}{2}\right)\mathrm{O_2} \rightarrow \alpha CO_2 + \frac{\beta}{2}\mathrm{H_2O} \tag{2.32}$$

In an IC engine, air is used as a source of oxygen and nitrogen can be added to the equation. While nitrogen can be oxidized to NOx due to the high combustion temperature, the amount of NOx is significantly less compared to the other products. For this reason, nitrogen was added to the equation, but it was assumed that it does not take place to the chemical reaction. The approximate air composition in mole basis is 21% oxygen (O2) and 79% nitrogen (N2). Thus, the stoichiometric combustion equation of a hydrocarbon in air can be written as:

$$\mathrm{C_\alpha H_\beta O_\gamma} + \underbrace{\left(\alpha + \frac{\beta}{4} - \frac{\gamma}{2}\right)\left(\mathrm{O_2} + \frac{79}{21}\mathrm{N_2}\right)}_{\mathrm{AIR}} \rightarrow \alpha CO_2 + \frac{\beta}{2}\mathrm{H_2O} + \left(a + \frac{\beta}{4} - \frac{\gamma}{2}\right)\frac{79}{21}\mathrm{N_2} \tag{2.33}$$

For lean combustion, the chemical reaction can be written as:

$$\begin{aligned}\frac{1}{\lambda}\mathrm{C_\alpha H_\beta O_\gamma} + \underbrace{\left(\alpha + \frac{\beta}{4} - \frac{\gamma}{2}\right)\left(\mathrm{O_2} + \frac{79}{21}\mathrm{N_2}\right)}_{\mathrm{AIR}} \\ \rightarrow \frac{1}{\lambda}\alpha CO_2 + \frac{1}{\lambda}\frac{\beta}{2}\mathrm{H_2O} + \left(a + \frac{\beta}{4} - \frac{\gamma}{2}\right)\frac{79}{21}\mathrm{N_2} \\ + \left(1 - \frac{1}{\lambda}\right)\left(\alpha + \frac{\beta}{4} - \frac{\gamma}{2}\right)\mathrm{O_2}\end{aligned} \tag{2.34}$$

When EGR is used, an X (mass fraction) amount of combustion products remains in the chamber and the combustion equation with EGR can be written as:

$$\begin{aligned}&\frac{1}{\lambda}\mathrm{C}_{\alpha}\mathrm{H}_{\beta}\mathrm{O}_{\gamma}+\underbrace{\left(\alpha+\frac{\beta}{4}-\frac{\gamma}{2}\right)\left(\mathrm{O}_2+\frac{79}{21}\mathrm{N}_2\right)}_{\mathrm{AIR}}\\&+\underbrace{X\left(\frac{1}{\lambda}\alpha CO_2+\frac{1}{\lambda}\frac{\beta}{2}H_2O+\left(a+\frac{\beta}{4}-\frac{\gamma}{2}\right)\frac{79}{21}N_2+\left(1-\frac{1}{\lambda}\right)\left(\alpha+\frac{\beta}{4}-\frac{\gamma}{2}\right)\mathrm{O}_2\right)}_{EGR}\\&\rightarrow(1+X)\frac{1}{\lambda}\alpha CO_2+(1+X)\frac{1}{\lambda}\frac{\beta}{2}\mathrm{H}_2\mathrm{O}+(1+X)\left(a+\frac{\beta}{4}-\frac{\gamma}{2}\right)\frac{79}{21}\mathrm{N}_2\\&+(1+X)\left(1-\frac{1}{\lambda}\right)\left(\alpha+\frac{\beta}{4}-\frac{\gamma}{2}\right)\mathrm{O}_2\end{aligned}\tag{2.35}$$

Therefore, the relative mass of exhaust gases is given by:

$$\begin{aligned}M_{eg}=(1+X)\frac{1}{\lambda}\alpha W_{CO_2}+(1+X)\frac{1}{\lambda}\frac{\beta}{2}W_{\mathrm{H_2O}}+(1+X)\left(a+\frac{\beta}{4}-\frac{\gamma}{2}\right)\frac{79}{21}W_{\mathrm{N_2}}\\+(1+X)\left(1-\frac{1}{\lambda}\right)\left(\alpha+\frac{\beta}{4}-\frac{\gamma}{2}\right)W_{\mathrm{O_2}}\end{aligned}\tag{2.36}$$

Experimentally, engine out emissions, EGR and Air Fuel Ratio (AFR) were measured using a Horiba Mexa One emissions analyser. EGR was measured in volume fraction (or mole fraction for ideal gas) which was based on the equation:

$$EGR\%(vol)=\frac{\left(\Psi_{CO2_int}-\Psi_{CO2_air}\right)}{\left(\Psi_{CO2_exh}-\Psi_{CO2_int}\right)}100\%\tag{2.37}$$

Where Ψ_{CO2_x} is the mole fraction of CO2 at an x location which is the intake, exhaust or ambient air. All the data except from Ψ_{CO2_int} where recorded by the analyser, thus Ψ_{CO2_int} could be calculated.

For the Horiba Mexa One analyser the EGR is defined as $EGR=\frac{EGR\ volume\ flow\ rate}{Fresh\ Air\ volume\ flow\ rate}$

However, STAR-CD is working with mass fractions and all the volume fractions had to be converted. Thus, the EGR mass fraction was calculated from:

$$EGR(mass)=\frac{\left(Y_{CO2_int}-Y_{CO2_air}\right)}{\left(Y_{CO2_exh}-Y_{CO2_int}\right)}\tag{2.38}$$

$$EGR(mass)=\frac{\left(\Psi_{CO2_int}\frac{M_{CO2}}{M_{int}}-\Psi_{CO2_air}\frac{M_{CO2}}{M_{air}}\right)}{\left(\Psi_{CO2_exh}\frac{M_{CO2}}{M_{exh}}-\Psi_{CO2_int}\frac{M_{CO2}}{M_{int}}\right)}\tag{2.39}$$

Where M_x is the molecular weight of CO2, the intake mass, exhaust mass and the ambient air.

The molecular weights of intake mass and exhaust mass where calculated from:

$$M_{exh} = \Psi_{CO2_exh} \cdot M_{CO2} + \Psi_{CO_{exh}} \cdot M_{CO} + \Psi_{O2_{exh}} \cdot M_{O2} + \Psi_{HC_{exh}} \cdot M_{HC} + \Psi_{NOx_{exh}} \cdot M_{NOx} + \left(1 - \Psi_{CO2_exh} - \Psi_{CO_exh} - \Psi_{HC_exh} - \Psi_{NOx_exh}\right) \cdot M_{N2} \quad (2.40)$$

$$M_{int} = M_{air} + (M_{exh} - M_{air}) * \frac{\left(\Psi_{CO2_int} - \Psi_{CO2_air}\right)}{\left(\Psi_{CO2_exh} - \Psi_{CO2_air}\right)} \quad (2.41)$$

M_{i_exh} is the molar mass of its substance at the exhaust. Again, all the concentrations for the above calculations were taken from the analyser.

The mass fraction of the EGR in the intake port is:

$$Y_{EGR}^{in} = \frac{EGR\ mass\ flow\ rate}{Total\ mass\ flow\ rate} = \frac{EGR(mass)}{1 + EGR(mass)} \quad (2.42)$$

Finally, the calculation of the exhaust and intake gas mass fraction are calculated from the Table 2.1. Because the simulation started before EVO, the cylinder was initialised with exhaust gases.

It can be seen that the $(1 + X)$ term is cancelled out for the mass fraction calculations, meaning that the EGR is not taking part in the combustion formula and it can be omitted.

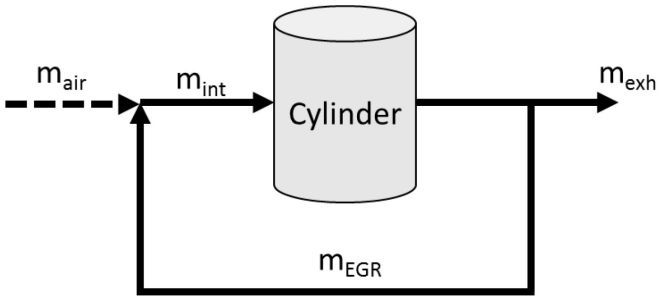


Figure 2.1 A schematic of the Exhaust Gas Recirculation (EGR)

To calculate the EGR mass fraction of equation 2.35 we have:

At the intake port the mass of CO2 can be written as $m_{CO2_int} = m_{CO2_air} + m_{CO2_EGR}$

The mass fraction of CO2 in each location (intake, EGR and ambient air) can be written as:

$$Y_{CO2_air} = \frac{m_{CO2_air}}{m_{air}} \quad (2.43)$$

$$Y_{CO2_EGR} = \frac{m_{CO2_EGR}}{m_{EGR}} \tag{2.44}$$

$$Y_{CO2_int} = \frac{m_{CO2_int}}{m_{int}} \tag{2.45}$$

With $Y_{CO2_EGR} = Y_{CO2_exh}$

Thus,

$$Y_{CO2_int} \cdot m_{int} = Y_{CO2_air} \cdot m_{air} + Y_{CO2_exh} \cdot m_{EGR} \tag{2.46}$$

With

$$m_{int} = m_{air} + m_{EGR} \tag{2.47}$$

And rearranging:

$$\frac{m_{EGR}}{m_{air}} = \frac{\left(Y_{CO2_int} - Y_{CO2_air}\right)}{\left(Y_{CO2_exh} - Y_{CO2_int}\right)} = EGR(mass) \tag{2.48}$$

The same procedure can be followed for the calculation of the $EGR(vol)$.

At the intake port the mole of CO2 can be written as:

$$n_{CO2_int} = n_{CO2_air} + n_{CO2_EGR} \tag{2.49}$$

The mole fraction of CO2 in each location (intake, EGR and ambient air) can be written as:

$$\Psi_{CO2_air} = \frac{m_{CO2_air}}{m_{air}} \tag{2.50}$$

$$\Psi_{CO2_EGR} = \frac{m_{CO2_EGR}}{m_{EGR}} \tag{2.51}$$

$$\Psi_{CO2_int} = \frac{m_{CO2_int}}{m_{int}} \tag{2.52}$$

And thus:

$$EGR(vol) = \frac{\left(\Psi_{CO2_int} - \Psi_{CO2_air}\right)}{\left(\Psi_{CO2_exh} - \Psi_{CO2_int}\right)} \tag{2.53}$$

Species	In-cylinder and Exhaust Gas Mass Fractions	Intake Gas Mass Fractions
CO2	$Y_{CO_2}^{exh} = \frac{1}{\lambda}.\frac{\alpha.W_{CO_2}}{M_e}(1+X)$	$Y_{EGR}^{in} \cdot Y_{CO_2}^{exh}$
H2O	$Y_{H_2O}^{exh} = \frac{1}{\lambda}.\frac{\frac{\beta}{2}.W_{H_2O}}{M_e}(1+X)$	$Y_{EGR}^{in} \cdot Y_{H_2O}^{exh}$
N2	$Y_{N_2}^{exh} = \frac{\frac{79}{21}.\left(\alpha+\frac{\beta}{4}-\frac{\gamma}{2}\right).W_{N_2}}{M_e}(1+X)$	$0.767.\left(1-Y_{EGR}^{in}\right)+Y_{EGR}^{in} \cdot Y_{N_2}^{exh}$
O2	$Y_{O_2}^{exh} = \left(1-\frac{1}{\lambda}\right).\frac{\left(\alpha+\frac{\beta}{4}-\frac{\gamma}{2}\right).W_{O_2}}{M_e}(1+X)$	$0.233.\left(1-Y_{EGR}^{in}\right)+Y_{EGR}^{in} \cdot Y_{O_2}^{exh}$
$M_{eg} = \left(\frac{1}{\lambda}.\alpha.W_{\mathbf{CO_2}} + \frac{1}{\lambda}.\frac{\beta}{2}.W_{\mathbf{H_2O}} + \left(a+\frac{\beta}{4}-\frac{\gamma}{2}\right).\frac{79}{21}.W_{\mathbf{N_2}} + \left(1-\frac{1}{\lambda}\right)\left(\alpha+\frac{\beta}{4}-\frac{\gamma}{2}\right).W_{\mathbf{O_2}}\right)(1+X)$		

Table 2.1 Mass fraction calculations of various species for initialisation before EVO

2.4. Wall heat flux

The wall heat transfer was dealt with by the Angelberger model (Angelberger *et al.* 1997), which is given by Equation 1. q_w is heat transfer that is calculated according to equation 2.51, density ρ, specific heat capacity at a constant pressure c_p, friction velocity u_τ, and temperature T with subscript w referring to wall values:

$$q_w = -\frac{\rho_w c_p u_\tau T_w}{\theta^+}\ln\left(\frac{T}{T_w}\right) \tag{2.54}$$

$$\theta^+ = \begin{cases} Pr\, y^+, & y^+ \le 13.2 \\ 2.075\, \ln(y^+) + 3.9, & y^+ > 13.2 \end{cases} \tag{2.55}$$

The friction velocity is calculated from:

$$u_\tau = \frac{u - u_w}{u^+} \tag{2.56}$$

with $u^+ = \begin{cases} y^+, & y^+ \le y_m^+ \\ \frac{1}{\kappa}\ln(Ey^+), & y^+ > y_m^+ \end{cases}$

The y_m^+ satisfies the equation $y_m^+ = \frac{1}{\kappa}\ln(E\ y_m^+)$, κ is the von Karman constant ($\kappa = 0.4$) and E is an empirical coefficient which depends on the turbulence model which is $E = 9$ for k-ε RNG.

Pr is the Prandtl number, u is the tangential fluid velocity and u_w is the tangential wall velocity. For the k-ε model the y^+ is given by: $y^+ = \rho {C_\mu}^{1/4} k^{1/2}\, y/\mu$ with $C_\mu = 0.085$ for k-ε RNG model.

2.5. Spray modelling

The Lagrangian multi-phase modelling was adopted to simulate the fuel injection. In this framework, the dispersed phase consists of liquid droplets which interact with the continuous phase, with each other and with solid boundaries. The interaction with the continuous phase can lead to change of the trajectory of the droplet, heat and mass transfer, and break up of the element due to aerodynamic forces. The interaction of each other can lead to further break up, coalescence etc. Finally, the interaction with boundaries may result to liquid film formation depending on the impact conditions.

The momentum equation for a droplet of mass m_d travelling with a velocity u_d is:

$$m_d \frac{du_d}{dt} = F_{dr} + F_p + F_{am} + F_b \tag{2.57}$$

Where:

- F_{dr} is the drag force of a spherical droplet:

$$F_{dr} = \frac{1}{2} C_d \rho A_d (u - u_d)^2 \tag{2.58}$$

where C_d is the drag coefficient, ρ is the density of the continuous phase, A_d the droplet cross-sectional area and $(u - u_d)$ is the relative velocity between the droplet and the continuous phase.

The drag coefficient is based on a sphere:

$$C_d = \begin{cases} 24\left(1 + 0.15 {Re_d}^{0.687}\right)/Re_d, & Re_d \le 1000 \\ 0.44, & Re_d > 1000 \end{cases} \tag{2.59}$$

$$Re_d = \frac{\rho|u - u_d|D_d}{\mu} \tag{2.60}$$

- F_p is the pressure force:

$$F_p = -V_d \nabla p \tag{2.61}$$

where V_d is the droplet volume and ∇p is the pressure gradient in the carrier fluid.

- F_{am} is called virtual mass and it is given by the formula:

$$F_{am} = -0.5\rho V_d \frac{d(u_d - u)}{dt} \tag{2.62}$$

- F_b represents the gravitational force.

The rate of change of mass for a single component droplet according to Bird *et al.* (1966) is:

$$\frac{dm_d}{dt} = -A_s K_g p_t \ln\left(\frac{p_t - p_{v,\infty}}{p_t - p_{v,s}}\right) \tag{2.63}$$

Where A_s is the droplet surface area, K_g is the mass transfer coefficient, p_t, $p_{v,\infty}$,and $p_{v,s}$ are the gas pressure and partial pressures of the vapour in the droplet surroundings and at its surface, respectively. The surface vapour pressure is assumed to be equal to the saturation pressure at the droplet temperature. The mass transfer coefficient is taken from Ranz and Marshall (1952):

$$K_g = \frac{Sh\ D_m}{R_m\ T_m\ D_d} \tag{2.64}$$

Where R_m is the mixture gas constant, T_m is the mean (film) temperature and D_m is the vapour diffusivity. The Sherwood number Sh is given by:

$$Sh = 2\left(1 + 0.3{Re_d}^{0.5} Sc^{1/3}\right) \tag{2.65}$$

And the Sc is the Schmidt number: $Sc = \frac{\mu_m}{\rho D_v}$, μ_m is the average viscosity of air-vapour mixture in the film and D_v is the diffusion coefficient of air-vapour mixture.

The conservation of energy of a droplet is:

$$m_d c_{p,d} \frac{dT_d}{dt} = -A_s \dot{q}_d'' + h_{fg} \frac{dm_d}{dt} \tag{2.66}$$

Where $c_{p,d}$ is the droplet specific heat, h_{fg} is the latent heat of phase change and $\dot{q}''_d$ is the surface heat transfer rate given by:

$$\dot{q}''_d = h(T_d - T) \tag{2.67}$$

And h is the heat transfer coefficient taken from El Wakil *et al.* (1954):

$$h = \frac{k_m \, Nu \, Z}{(e^Z - 1)D_d} \tag{2.68}$$

where k_m is the average thermal conductivity of air-vapour mixture in film, Z is a correction factor and Nu is the Nusselt number according to Ranz, and Marshall (1952):

$$Nu = 2\left(1 + 0.3{Re_d}^{0.5} Pr^{1/3}\right) \tag{2.69}$$

in which Pr is the Prandtl number: $Pr = \frac{c_{p,m}\,\mu_m}{k_m}$ and $c_{p,m}$ is the average specific heat of air-vapour mixture in film at constant pressure.

The correction factor is given by:

$$Z = \frac{c_{p,m}\,(dm_d/dt)}{\pi \, D_d \, k_m \, Nu} \tag{2.70}$$

2.5.1. Flash boiling modelling

The flash boiling modelling was based on the work of Price *et al.* (2015, 2016). A brief description of the models follows. More information can be found in the aforementioned publications.

During flash boiling cases, an empirical equation of superheated droplet evaporation proposed by Adachi *et al.* (1996) based on experiments of *n*-Pentane was added to the subcooled rate of change of mass. This equation is:

$$\frac{dm_{d,sh}}{dt} = \frac{A_s \alpha \Delta T_{sh}}{h_d} \tag{2.71}$$

where α is a heat transfer coefficient, ΔT_{sh} is the degree of superheat, and h_d is the heat of vaporisation. Depending on the superheat degree, the heat transfer coefficient α is:

$$\alpha = \begin{cases} 760\Delta T_{sh}{}^{0.26}, & \Delta T_{sh} \leq 5 \\ 27\Delta T_{sh}{}^{2,33}, & 5 < \Delta T_{sh} \leq 25 \\ 13800\Delta T_{sh}{}^{0,39}, & \Delta T_{sh} \geq 25 \end{cases} \quad (2.72)$$

Where $\Delta T_{sh} = T_d - T_{sat}$

A flash boiling boundary condition model documented in Price *et al.* (2016) in order to estimate the initial droplet diameter was applied. With this, the initial droplet diameter is smaller than the nozzle diameter by a reduction factor which depends on in nozzle cavitation and vapour generation through wall nucleation. This model is based on the work of Riznic and Ishii (1989). In Figure 2.2 the diameter reduction factor is displayed for *n*-Pentane and *iso*-Octane versus fuel temperature at three different ambient pressures. It is evident that the rate of reduction increases as the fuel temperature is increased. A limit of 14 μm has been applied to the model as the minimum droplet diameter

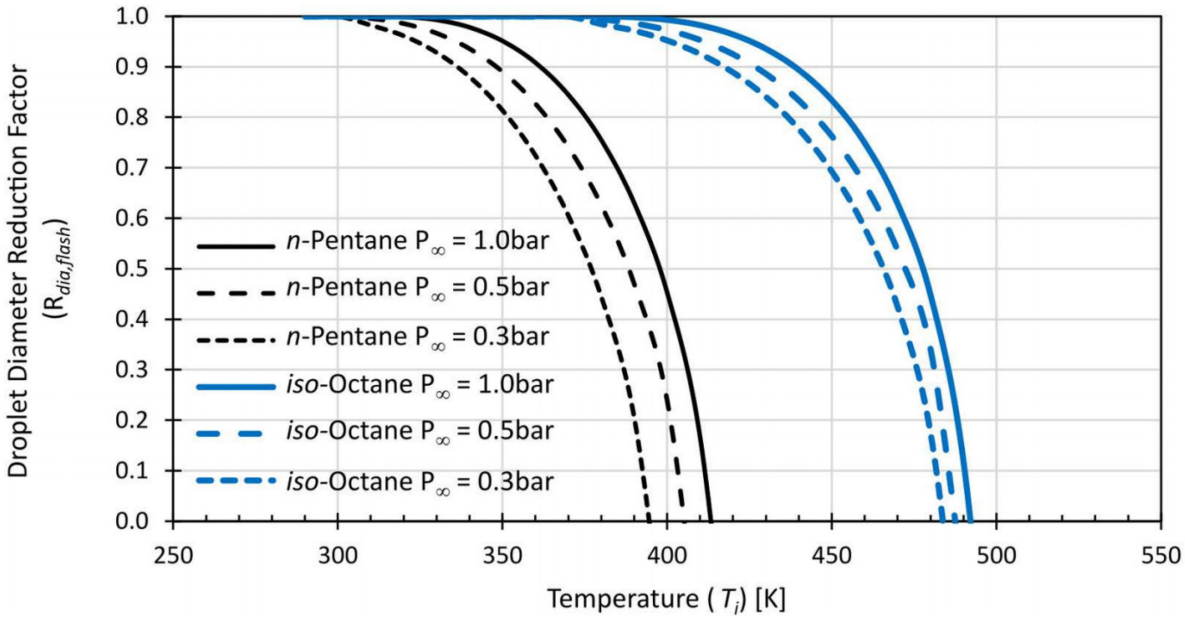


Figure 2.2 Predicted droplet diameter at varying temperature at ambient pressures of P∞ = 1.0 bar, P∞ = 0.5 bar, and P∞ = 0.3 bar. Price et al. (2016)

2.5.2. Break-up modelling

The Reitz-Diwakar model based on the work of Reitz and Diwakar (1986) was chosen in this study which takes into account the aerodynamic forces in the break-up mechanism. Two regimes of the break-up process are modelled, named 'Bag' and 'Stripping'. During the bag break-up, the droplet expands in the low pressure wake region and collapses when the surface

tension is overcome. In the stripping mechanism liquid fragments are stripped from the droplet surface. The break-up rate (rate of reduction of droplet diameter) is calculated from:

$$\frac{dD_d}{dt} = -\frac{\left(D_d - D_{d,stable}\right)}{\tau_d} \tag{2.73}$$

Where D_d is the instantaneous droplet diameter, $D_{d,stable}$ is the stable droplet diameter and τ_d is the characteristic time scale of the break-up process.

The instability criterion for the bag break-up is determined by the critical value of the Weber number:

$$We = \frac{\rho(u - u_d)^2 D_d}{2\sigma_d} \geq C_{b1} \tag{2.74}$$

The stable diameter is calculated when the equality is satisfied. Here, σ_d is the surface tension of the droplet, and C_{b1} is an empirical constant and the default value is 6.

The time scale of the bag break-up is calculated by:

$$\tau_d = \frac{C_{b2}\,{\rho_d}^{0.5}\,{D_d}^{1.5}}{4{\sigma_d}^{0.5}} \tag{2.75}$$

The default value of the constant C_{b2} is 3.1416.

The instability criterion for the stripping break-up is determined by:

$$\frac{We}{\sqrt{Re_d}} \geq C_{s1} \tag{2.76}$$

The default value of the C_{s1} constant is 0.5.

The time scale of the stripping break-up is calculated by:

$$\tau_d = \frac{1}{2} C_{s2} \frac{D_d}{|u - u_d|} \sqrt{\frac{\rho_d}{\rho}} \tag{2.77}$$

The default value of the C_{s2} constant is 20.

These four constants can be altered in order to increase or reduce the severity of the break-up mechanisms and ultimately determine the penetration and droplet size of a spray.

2.5.3. Droplet-Droplet Interaction

The inter-droplet collisions are modelled according to the work of O'Rourke (1981). Which distinguishes three regimes (coalescence, separation and bouncing) and it is based on a statistical approach. For the separation and bouncing regimes, only momentum is exchanged between droplets and in coalescence mass and energy are also exchanged. In addition, in the O'Rourke model, neither shattering of the droplets nor formation of satellite droplets due to the collision are considered.

In the model, all droplets are considered to be uniformly distributed in each computational cell. A collision frequency is calculated from:

$$v = \frac{\pi}{4}(D_{d1} + D_{d2})^2 |u_{d1} - u_{d2}| E_{1,2} \frac{N_{d2}}{V} \tag{2.78}$$

In this equation the subscript 1 denotes the parcel with the larger diameter (collector) and the subscript 2 denotes the parcel with the smaller diameter (donor). N_{d2} is the number of the droplets in the donor and V is the cell volume. The parameter $E_{1,2}$ is called collision efficiency and it is given by:

$$E_{1,2} = \begin{cases} \left(1 + \dfrac{0.75 \ln(2\,W)}{W - 1.214}\right)^{-2}, & W > 1.214 \\ 0, & W \leq 1.214 \end{cases} \tag{2.79}$$

The parameter W is given by:

$$W = \frac{\rho_{d2}\,|u_{d1} - u_{d2}|\,D_{d2}^2}{9\,\mu\,D_{d1}} \tag{2.80}$$

The probability of n collisions follows a Poisson distribution:

$$P_n = \frac{(n')^n}{n!} e^{-n'} \tag{2.81}$$

Where n' is the mean value of the distribution: $n' = v\,\delta t$, and δt is the time interval.

After that, a random number N_{r1} from the interval (0 – 1) is chosen and if $N_{r1} < P_n$ then no collision occurs.

As soon as a collision is detected, the type of collision is calculated based on the droplet Weber number We_L and the probability of coalescence E_{coal}.

$$We_L = \frac{\rho_d (u - u_d)^2 D_d}{2\sigma_d} \tag{2.82}$$

$$E_{coal} = \min\left[\frac{2.4\, f(\gamma)}{We_L}, 1\right] \tag{2.83}$$

Where $f(\gamma) = \gamma^3 - 2.4\gamma^2 + 2.7\gamma$ with $\gamma = D_{d1}/D_{d2}$

A second random number N_{r2} is generated and if $N_{r1} < E_{coal}$ then coalescence or bouncing occurs. For the bouncing regime the criterion of $We_L < We_{bou}$ has to be met as well. The We_{bou} is given by $We_{bou} = 2.4\, f(\gamma)\, {N_{r2}}^3$.

From the above description it can be seen that O'Rourke did not propose a trajectory model, with associated grid dependence effects as reported in Hou and Schmidt (2006). For this reason, a geometric constrain proposed by Nordin (2001) was also applied. In this, the droplets have to travel towards each other meaning that:

$$U_{12} = (u_{d1} - u_{d2}) \frac{x_{d2} - x_{d1}}{|x_{d2} - x_{d1}|} > 0 \tag{2.84}$$

Where u_d are the droplet velocities and x_d are the parcel position vectors.

Furthermore, the relative displacement between the parcels must be larger than the distance between them:

$$U_{12}\, \Delta t > |x_{d2} - x_{d1}| - (r_{d1} + r_{d2}) \tag{2.85}$$

Where Δt is the timestep and r_{d1} the droplet radius.

2.5.4. Droplet-Wall Interaction

For the droplet - wall interaction, various theories have been proposed depending on various experimental data with different liquids, however, a generalised theory does not exist. Some of the theories or combination of them are implemented in STAR-CD. Two of the most detailed, with different sub-models depending on the wall conditions, the dynamic characteristics of the impacting droplets and the physical properties of the droplets are the Bai-ONERA and Senda models. The first model is a combination of the work of Bai and Gosman (1995) and Rosa *et al.* (2006) along with modifications made for STAR-CD to incorporate non-smooth and wetted walls. The Senda model is based on a series of publications of Prof. Senda and his co-workers but some of the droplet - wall interaction regimes (deposition and rebound) described in Senda

model are identical to these of Bai and Gosman. In addition, some features of the Bai-ONERA have been introduced to the Senda model by the STAR-CD software. These two models were used in the validation of the liquid film generation and a brief description of them will follow.

Both of the models are based on the dimensionless parameters:

- Droplet Weber number We
- Reynold number Re
- Ohnesorge number $Oh = \frac{\mu_d}{(\rho_d D_d \sigma_d)^{0.5}}$
- Laplace number La, where $Oh = La^{-0.5}$
- Dimensionless temperature T^*: $T^* = \frac{T_W - T_N}{T_L - T_N}$

Where T_W is the wall temperature, T_N is the Nukiyama temperature and T_L is the Leidenfrost temperature.

The Nukiyama temperature is given by $T_N = B_S T_{boiling}$ where B_S is a constant and for *iso*-Octane $B_S = 1.062$.

The Leidenfrost temperature is given by the Habchi model (Habchi 2010):

$$T_L = T_s + \Delta T, \Delta T = \begin{cases} T_{L1} - T_{boiling}, \ P \leq 1 \ bar \\ \frac{T_{L1} - T_{boiling} - A}{T_c - T_b}(T_c - T_S) + A, \ P > 1 \ abr \end{cases} \quad (2.86)$$

Where T_c is the critical temperature and T_S the saturation temperature. $A = \max|1, T_{L1} - T_C|$ and T_{L1} is calculated based on the Speigler *et al.* (1963) model: $T_{L1} = \frac{27}{32} T_C$.

In addition, both models distinguish three regimes depending on the value of T^*. These regimes are:

1. Natural convection and nucleate boiling regimes, $T^* \leq 0.0$
2. Transition boiling regime, $0.0 < T^* \leq 1.0$
3. Film boiling regime, $T^* > 1.0$

Bai-ONERA model

The three regimes of the model, along with the various impingement outcomes are shown in Figure 2.3.

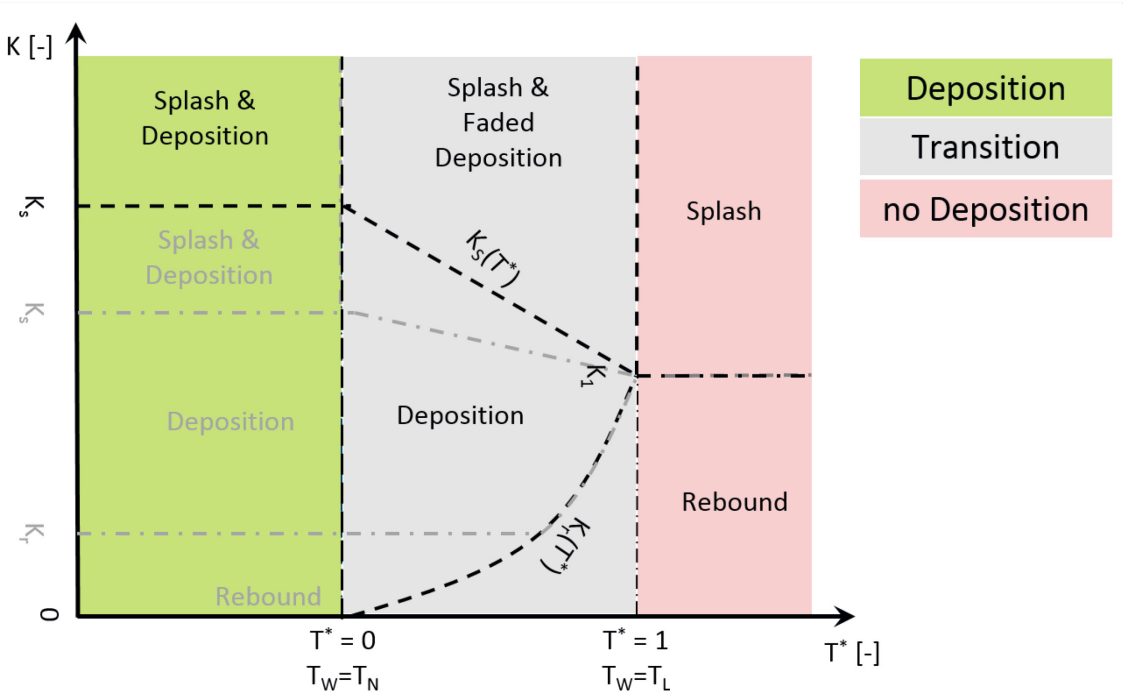


Figure 2.3 Representation of the Bai-ONERA regimes. (Solsjo, personal communications)

The dimensionless number K of the y-axis is given by $K = We\ Oh^{-0.4}$. Depending on the K number of the droplet and the T^*, the outcome of the impact may be deposition, rebound or splash or a combination. In the deposition outcome, liquid film is created. In the rebound, the impacting droplet bounces off the wall. During splash, the impinging droplet breaks-up into many secondary droplets. These outcomes were firstly discussed in the work of Bai and Gosman (1995).

The K_s value defines the transition between deposition and splashing and the K_r value defines the transition between deposition and rebound. The grey lines of K_s and K_r denote alternative critical values which depend on the roughness of a dry wall in the case of K_s and the Laplace number of the droplet in the case of a wet wall. The equations which govern these transitions are:

$$K_s = \begin{cases} K_0, & T^* \leq 0.0 \\ K_0 + T^*(450 - K_0), & 0.0 < T^* \leq 1.0 \\ 450, & x \geq 0 \end{cases} \tag{2.87}$$

$$K_r = \begin{cases} 0.0, & T^* \leq 0.0 \\ 450 + (T^*)^3, & 0.0 < T^* \leq 1.0 \\ 450, & x \geq 0 \end{cases} \quad (2.88)$$

Where $K_0 = 3000$ for a smooth and dry wall. For a non-smooth and dry wall the K_0 is given by: $K_0 = \begin{cases} 180\ {R_\delta}^{-0.35}, & R_\delta < 0.03 \\ 600, & R_\delta \geq 0.03 \end{cases}$

Where, R_δ is the roughness parameter

For a wetted wall the rebound to deposition transition is affected (grey line of K_r) by $K_r \leq 5\ La^{0.2}$

Senda model

The three regimes as in the Bai-ONERA model, depending on the value of $T^*$are shown in Figure 2.4 together with the outcome of the impact.

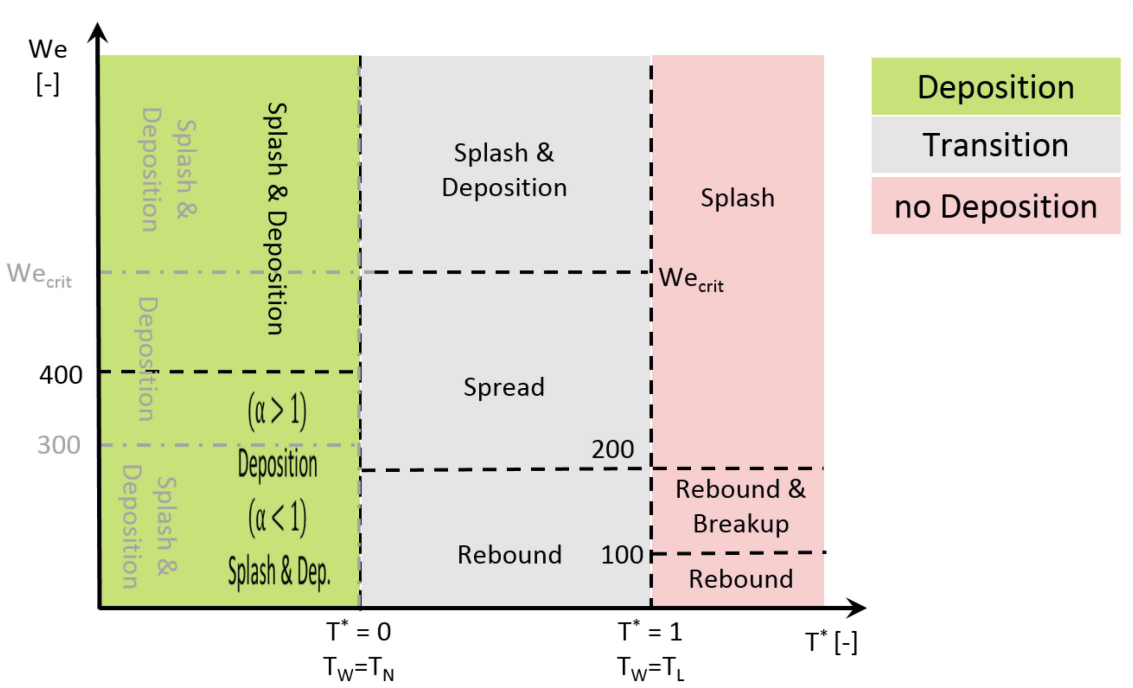


Figure 2.4 Representation of the Senda regimes (Solsjo, personal communications)

Here, the outcome of the impact which can be deposition, rebound or splash or a combination depends on the Weber number of the droplet and the condition of the wall (dry or wet).

1. Natural convection and nucleate boiling regimes, $T^* \leq 0.0$

For a dry wall and $We \leq 400$ the outcome of the impact can be either deposition or deposition and splash. This depends on a time scale parameter a. For Weber number greater than 400 ($We > 400$) the outcome is deposition and splash. After the impingement outcome, splash mass ratios, the diameters and the reflection angles of the secondary droplets are calculated.

For a wetted wall, Weber numbers smaller than 300 and also depending on the thickness of the existing film the splashing mechanism is classified into three types (rim-type, cluster-type, and column-type). Depending on the splashing type, which is the interaction between droplet and existing film, various numbers of secondary droplets are generated. For $300 < We < We_{cr}$ the outcome is deposition of the droplet into the existing film. For Weber numbers greater than the critical, the impacting outcome is splash. The critical Weber number is given by:

$We_{cr} = (2164 + 7560\delta^{1.78})La^{-0.2}$. δ is called dimensionless film thickness which depends on the Weber number of the impacting droplet.

2. Transition boiling regime, $0.0 < T^* \leq 1.0$

In this temperature region the original Senda model does not allow deposition however, in STAR-CD, features of the Bai-ONERA were applied for partial deposition. The distinction between the three outcomes is again the Weber number. For $We \leq 200$ the outcome is rebound, for $200 < We \leq We_{cr}$ the outcome is deposition/spread and for $We > We_{cr}$ the outcome is splash. The critical Weber number is calculated with the same equation as the first regime. The post-impingement behaviour for rebound and spread is identical to that used in the Bai and Gosman (1995) model.

3. Film boiling regime, $T^* > 1.0$

For this regime, there is no deposition due to the high temperature of the wall. As a result of a vapour layer between the surface and the droplet, the possible impacting outcomes are rebound, splash or combination which depends on the Weber number of the impacting droplet. If $We < 100$ then the outcome is rebound, for $100 \leq We < 200$ the outcome is rebound and break up and if $We \geq 200$ the outcome is splash. For different Weber numbers the secondary droplets will have different diameters and reflecting numbers.

2.6. Liquid film modelling

The result of the deposition from a droplet - wall interaction is the formation of liquid film. In STAR-CD, the work of Bai and Gosman (1996) has been implemented to solve the liquid film conservation equations and it is based on an Eulerian model within the boundary-layer framework. These take into account phenomena such as the change of mass due to droplet impingement, film separation, and/or evaporation, exchange of momentum with the gas or impacting droplets, heat transfer from/to the wall (conduction) and air (convection).

Depending on the geometry of the wall where the film resides and the flow condition, film stripping may occur. During the film separation or film stripping, an amount of liquid is detached from the film and takes the form of droplets into the Eulerian phase. Three mechanisms are responsible for the stripping:

- Stripping due to wave instability generated by an adjacent gas flow
- Stripping due to body-force induced instability (gravity, piston acceleration)
- Break-up caused by flow over a sharp edge

The two first mechanisms are modelled in STAR-CD based on the work of Foucart (1998). Due to external forces, waves are generated on the liquid surface and as these waves grow, they become unstable and are separated from the liquid film, generating droplets. These instabilities are based on the Kelvin-Helmotz model and the detach is based on the Rayleigh-Taylor model. An illustration of the first two processes is displayed in Figure 2.5

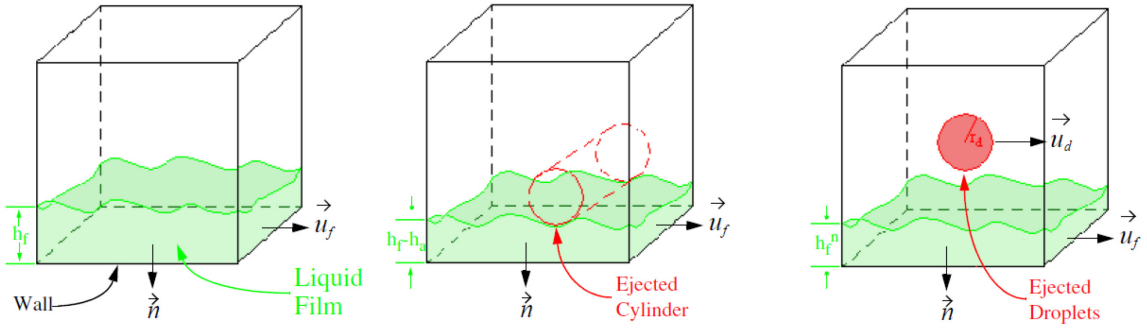


Figure 2.5 Representation of liquid film stripping due to wave and body-force induced instability. (Methodology, STAR-CD, 2016 CD-adapco)

The third mechanism is modelled according to the work of Friedrich *et al.* (2008) which is based on a force balance and the generated droplets follow a distribution proposed by Maroteaux *et al.* (2002). The representation of the film stripping is showed in Figure 2.6. The model is activated only when θ is smaller than a critical value with a default value of 45°.

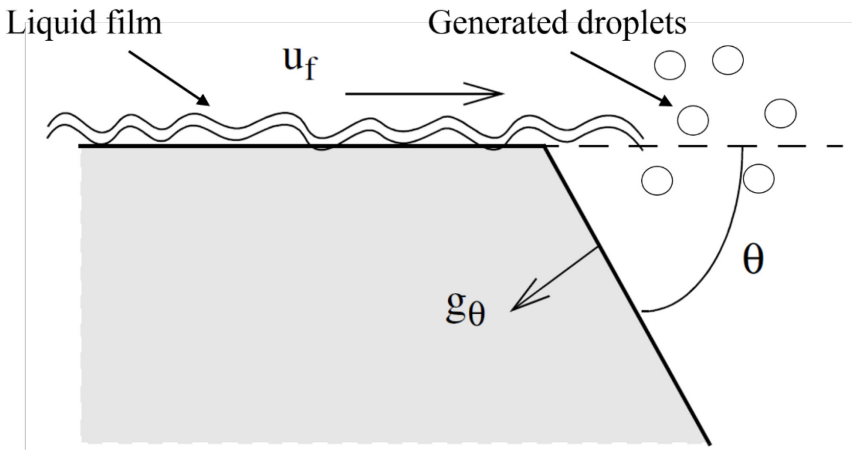


Figure 2.6 Representation of liquid film stripping due to break-up caused by flow over a sharp edge. Based on Methodology, STAR-CD, 2016 CD-adapco

Lastly, the evaporation of the liquid film is based on the wall temperature and the characteristic liquid temperatures (saturation, Nukiyama and Leidenfrost temperatures).

For $T_w < T_{sat}$ the evaporation is slow and depends on the turbulence level in the ambient gas (Habchi 2010). The evaporation is modelled based on Torres *et al.* 2003.

When the wall temperature exceeds the saturation temperature of the liquid, then the so-called pool boiling model is applied (White 1988). A graphical representation of pool boiling for water at atmospheric pressure taken form (Cengel *et al.* 2011) is shown in Figure 2.7.

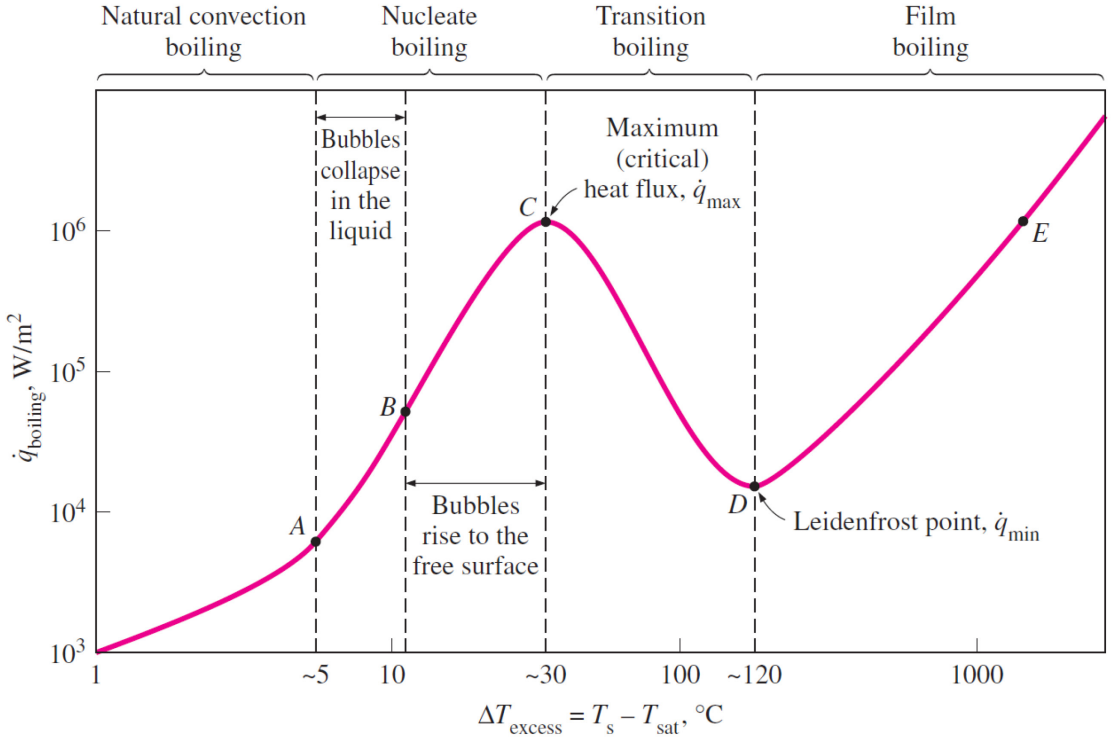


Figure 2.7 Boiling curve for water at 1 atm. (Cengel et al. 2011)

For $T_{sat} < T_w < T_N$ the film starts to boil and the heat flux q_b from the wall to the liquid is proportional to the cubic power of $T_w - T_{sat}$. In addition, it is related to the liquid properties and the wall surface as well as empirical coefficients which depend on the liquid and wall properties. The increase of heat flux reaches a maximum value q_{max} near the Nukiyama temperature, which is called T_S in the code. At this point the code is keeping the q_{max} for a small range of wall temperatures above T_S. The maximum of the range is specified by an empirical constant $C_s$based on the liquid properties.

Above this temperature and $T_w < T_L$, the heat flux is reduced to a minimum value q_{min} at $T_w = T_L$ (Leindfrost temperature).

For wall temperatures above the Leindfrost temperature, the heat flux increases linearly in the code.

A graphical representation of the film boiling as it is calculated by the software (blue line) and the theoretical/experimental film boiling model (black line) is shown in Figure 2.8. For each quantity, the parameters that affect the calculations are in the parenthesis. These are the viscosity μ_f, Prandtl number Pr_f, specific heat c_{pf}, the density ρ_f, surface tension σ_f and the heat of vaporization $h_f$of the liquid and the density ρ_g of the gas phase.

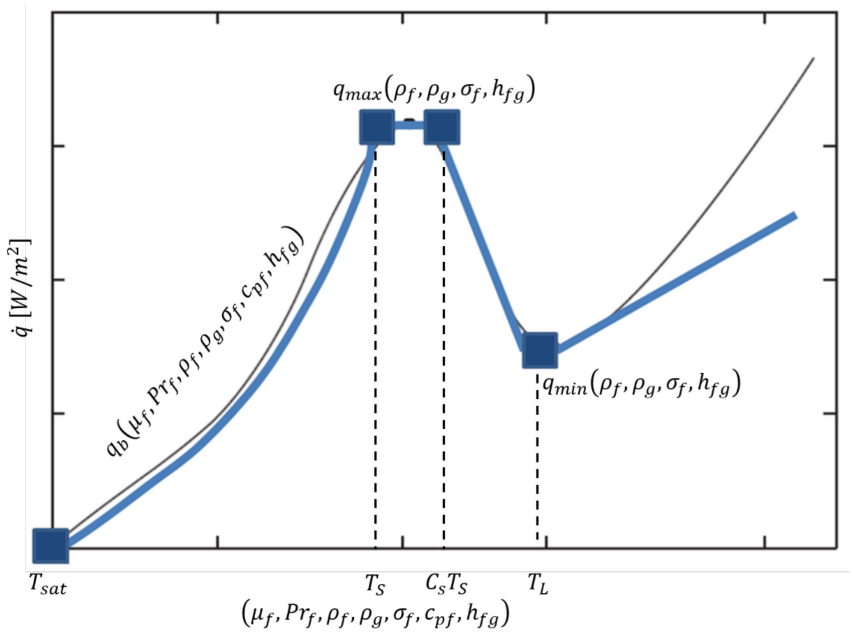


Figure 2.8 A graphical representation of the film boiling as it is calculated by the software (blue line) and the theoretical/experimental film boiling model (black line). Based on (Solsjo, personal communications)

For this research, the liquid properties for both droplets and film are applied through user defined temperature dependent polynomials. These properties are:

- Density [kg/m3]
- Surface tension [N/m]
- Viscosity [kg/(m s)]
- Thermal conductivity [W/(m K)]
- Specific heat [J/(kg K)]
- Heat of vaporisation [J/kg]
- Saturation pressure [Pa]

and were taken from Yaws and Gabbula (2003).

2.7. Combustion and emissions modelling

In this study, to model the combustion process and subsequently the emissions in a direct injection spark ignition engine, the 3-Zones Extended Coherent Flame Model (ECFM3Z) model based on the work of Colin and Benkenida (2004) was used. This model is the development of the Extended Coherent Flame Model (Colin *et al.* 2003) which was developed for simulating the combustion in a direct injection spark ignition engine and introduced a description of the mixing state of the gases. The ECFM3Z model is based on four components:

- Mixing model (3-Zones)
- Flame propagation model (ECFM)
- Post-flame and emissions model
- Spark ignition and auto-ignition/knock model

The mixing model represent three mixing zones, a pure fuel zone, a pure air plus residual gases zone and a mixed air and fuel zone in which the ECFM combustion model is applied. A schematic representation of the ECFM3Z model in a computational cell is represented in Figure 2.9. The mass fractions of species in the computational cell can be defined:

$$\frac{\partial \rho\, Y_i}{\partial t} + \nabla \cdot (\rho\, \boldsymbol{u}\, Y_i) - \nabla \cdot \left[\left(D + \frac{\mu_t}{Sc_t}\right) \nabla Y_i\right] = \dot{\omega}_\iota \qquad (2.89)$$

where Y_i is the mass fraction of the species i and $\dot{\omega}_i$ is the reaction rate for species i. All species in ECFM-3Z are present in the mixed zone. These species are: fuel, O_2, N_2, NO, CO_2, CO, H_2, H_2O, O, H, N, OH, and soot.

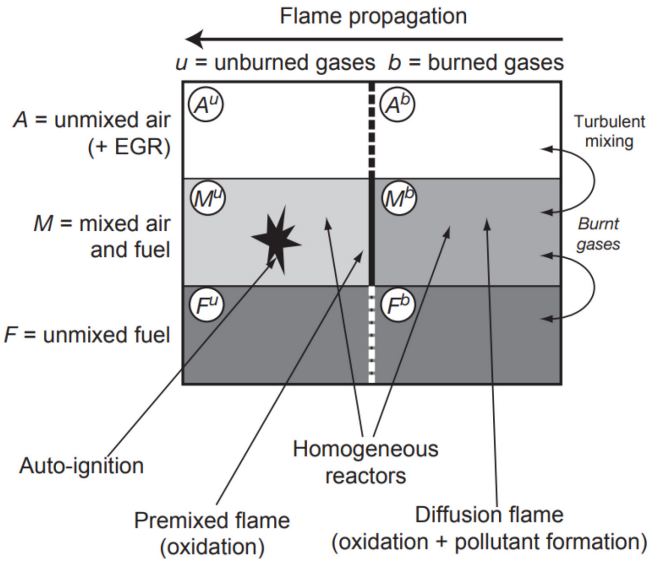


Figure 2.9 A graphical representation of the ECFM-3Z model in a computational cell (Colin and Benkenida 2004)

The equation (2.89) for the fuel mass fraction in the unburnt gases (Y_{Fu}^u) and the burnt gases (Y_{Fu}^b) becomes:

$$\frac{\partial \rho\, Y_{Fu}^u}{\partial t} + \nabla \cdot (\rho\, \boldsymbol{u}\, Y_{Fu}^u) - \nabla \cdot \left[\left(D + \frac{\mu_t}{Sc_t}\right) \nabla Y_{Fu}^u\right] = \dot{\omega}_{Fu}^u + \dot{\omega}_{Fu,evap}^u \tag{2.90}$$

$$\frac{\partial \rho\, Y_{Fu}^b}{\partial t} + \nabla \cdot (\rho\, \boldsymbol{u}\, Y_{Fu}^b) - \nabla \cdot \left[\left(D + \frac{\mu_t}{Sc_t}\right) \nabla Y_{Fu}^b\right] = \dot{\omega}_{Fu}^b + \dot{\omega}_{Fu,evap}^b \tag{2.91}$$

Where $\dot{\omega}_{Fu,evap}^u$ and $\dot{\omega}_{Fu,evap}^b$ is the fuel evaporation in the unburnt and burnt gases respectively, $\dot{\omega}_{Fu}^b$ is the fuel post-oxidation in the burnt gases (eq. 2.103) and $\dot{\omega}_{Fu}^u$ is the reaction rate which represents the oxidation of the unburnt fuel by auto-ignition or premixed flame and it is given by:

$$\dot{\omega}_{Fu}^u = -\rho_u U_l Y_{Tf}^m \Sigma \tag{2.92}$$

In the above reaction rate (eq. 2.92) Σ is flame surface density function which is determined by the equation (2.97). To describe the three mixing zones, the unmixed fuel and the unmixed oxygen are introduced to the mixing model. The equations governing the mass fractions of the unmixed fuel (Y_{fum}) and unmixed oxygen (Y_{O2um}) are:

$$\frac{\partial \rho\, Y_{fum}}{\partial t} + \nabla \cdot \left(\rho\, \boldsymbol{u}\, Y_{fum}\right) - \nabla \cdot \left[\left(D + \frac{\mu_t}{Sc_t}\right) \nabla Y_{fum}\right] = -\frac{\beta}{\tau_m} Y_{fum} \left(1 - Y_{fum} \frac{\rho}{\rho_u} \frac{W_m}{W_f}\right) + \dot{\omega}_{evap} \tag{2.93}$$

$$\frac{\partial \rho\, Y_{O2um}}{\partial t} + \nabla \cdot \left(\rho\, \boldsymbol{u}\, Y_{O2um}\right) - \nabla \cdot \left[\left(D + \frac{\mu_t}{Sc_t}\right) \nabla Y_{O2um}\right] = -\frac{\beta}{\tau_m} Y_{O2um} \left(1 - \frac{Y_{O2um}}{Y_{O2inf}} \frac{\rho}{\rho_u} \frac{W_m}{W_{O2}}\right) \tag{2.94}$$

where W_m, W_f and W_{O2} are the molecular mass of the mean gases, fuel and oxygen, respectively, β is a tuning coefficient (with a default value of 1.0), and τ_m is the mixing timescale calculated as: $\tau_m = k/\varepsilon.\ Y_{O2inf}$. The oxygen concentration in the unmixed air is computed as: $Y_{O2inf} = Y_{TO2}/\left(1 - Y_{Tf}\right)$

Species in the mean space are transformed to the corresponding species in the mixed zone. The mass fraction of the species *i* is then given by:

$$Y^m_{(T)i} = \left(Y_{(T)i} - Y_{Ti}\, C_x\right) \frac{\rho}{\rho - \rho^{UM}} \tag{2.95}$$

Where the suffix T denotes the tracer species, brackets "()" denote either tracer (T) or non-tracer species and ρ^{UM} is the mass of the unmixed zone per unit of gas volume given by:

$$\rho^{UM} = \rho\left[C_x(Y_{TO2} + Y_{TH2} + Y_{TCO} + Y_{TNO} + Y_{Tsoot} + \cdots) + Y_{fum}\right] \tag{2.96}$$

And the C_x is a coefficient ratio of the unmixed to mean masses and it is given by: $C_x = Y_{O2um}/Y_{TO2} = Y_{i,um}/Y_{T,i}$, where $Y_{i,um}$ is the mass fraction of species i in the unmixed zone.

The flame propagation is modelled by the flame surface density Σ function which is determined by the transport equation:

$$\frac{\partial \Sigma}{\partial t} + \nabla \cdot (\boldsymbol{u}\Sigma) - \nabla \cdot \left[\left(D + \frac{\mu_t}{Sc_t}\right) \nabla \left(\frac{\Sigma}{\rho}\right)\right] = \Sigma \left[C_{divu} \frac{2}{3} \nabla \cdot \boldsymbol{u} + C\alpha\Gamma \frac{\varepsilon}{k} + C \frac{2}{3} \frac{\rho_u}{\rho_b} U_l \Sigma \frac{1 - c}{c} - \beta U_l \Sigma \frac{1}{1 - \bar{c}} - \frac{2}{3} \frac{1}{\gamma p} \frac{\partial p}{\partial t}\right] + S_{conv} \tag{2.97}$$

Where D is the molecular diffusivity, $C_{divu} = 1$ an empirical parameter, Γ the ITNFS (Net Flame Stretch) function, ρ_u and ρ_b are the density of the unburnt and burnt gases respectively,

$U_l = S_l Q_l$ is the effective laminar flame speed, where S_l is the theoretical laminar flame speed and Q_l a heat-loss effect correction factor, γ is the isentropic coefficient, S_{conv} is an additional contribution to the flame surface density from convection at the spark plug, $\alpha = 1.6$ and $\beta = 1.0$, μ_t is the turbulent viscosity, $c = 1 - Y_f/Y_{Tf}$ is the progress variable, $\bar{c} = 1 - \rho\, Y_f/\rho_u Y_{Tf}$ is the Reynolds-averaged progress variable.

The theoretical laminar flame speed is based on the correlations of Metghalchi & Keck (1982) and Gülder (1991) and it is given by:

$$S_l = S_{l0}\left(\frac{T_u}{T_0}\right)^a \left(\frac{p}{P_0}\right)^b \max[1 - U_{lam1}X_r, \exp(U_{lam2}X_r)] \tag{2.98}$$

With $b = b_0 - 0.08(p/U_{lam3})$, S_{l0}, a and b are functions of the fuel used and the equivalence ratio, T_0 and p_0 is the reference temperature and pressure and X_r is the mole fraction of the residual gases. The parameters $U_{lam1} = 2.1$, $U_{lam2} = -3.0$, $U_{lam3} = 40.0$. The correction factor C is given by:

$$C = q_w/\left\{1 + \left[\frac{\alpha\Gamma\varepsilon}{k} + \frac{2}{3}\frac{\rho_u}{\rho_b}U_l\frac{1-c}{c}\Sigma\right]\tau_c\right\} \tag{2.99}$$

Where $\tau_c = \delta_l/(U_l Ze)$ is the chemical time scale, $\delta_l = 2\mu_b/(\rho_u U_l Pr)$ is the laminar flame thickness and Ze is the Zeldovich number. The factor q_w is the flame quenching factor given by:

$$q_w = \begin{cases} 1, & y^+/11.5 < 5 \\ 0, & y^+/11.5 \geq 5 \end{cases} \tag{2.100}$$

The source term S_{conv} is coming from the convection at the spark plug and is given by:

$$\int_V S_{conv}dV = C_{conv}2\pi R_k \frac{\rho}{\rho_u}U \tag{2.101}$$

where V is the total volume, U the fluid velocity at the spark plug, R_k the flame laminar kernel radius and $C_{conv} = 1.0$. The contribution is added only during a time interval of 2 ms.

The burning rate due to flame propagation is added to equation 2.91 to represent the transport equation of fuel in the mixed zone.

The reaction mechanism of the premixed combustion for a fuel $C_nH_m$is:

$$C_nH_m + F\left(n+\frac{m}{4}\right)O_2 + (1-F)\left(\frac{n}{2}\right)O_2 \rightarrow FnCO_2 + (1-F)nCO + F\left(\frac{m}{2}\right)H_2O + (1-F)(\frac{m}{2})H_2 \quad (2.102)$$

Where $F = \begin{cases} 1, & \Phi < 1 \\ 1\left[\frac{4\left(n+\frac{m}{4}\right)}{\Phi} - 2n\right]/(2n+m), & 1 < \Phi < (2+\frac{m}{2n}) \\ 0, & \Phi \geq (2+\frac{m}{2n}) \end{cases}$

Any species in the burnt gases can undergo a series of reactions such as fuel post-oxidation chemistry, dissociation and radical formation chemistry, $CO \leftrightarrow CO_2$ kinetics chemistry, NO chemistry and soot chemistry. Firstly, the composition of the fuel in the burnt gases in the mixed zone is given by: $Y_b^m = \frac{Y^m-(1-c)Y_u^m}{c}$

When fuel evaporates into burnt gases or when there is insufficient oxygen to burn the existing fuel partially into CO, an additional fuel species is created. This will be burnt behind the flame (diffusion-mode combustion). The oxidation reaction is: $Fuel + O_2 \rightarrow CO_2 + H_2O$ and the burning rate is:

$$\dot{\omega}_{Fu}^b = C\frac{\varepsilon}{k}\min\left[Y_{fb}^m, Y_{O2}^m/S_{O2}\right] \quad (2.103)$$

S_{O2} is the stoichiometric coefficient (number of moles) for O_2 for the oxidation reaction.

The model takes account the dissociation effects in the post-flame gas and assume that the species are in equilibrium.

The reactions are:

$$N_2 \leftrightarrow 2N \qquad 2OH \leftrightarrow O_2 + H_2$$
$$H_2 \leftrightarrow 2H \qquad 2H_2O \leftrightarrow 2H_2 + O_2$$
$$O_2 \leftrightarrow 2O$$

In addition, a simple reaction for the $CO \rightarrow CO_2$ is used: $CO + OH \leftrightarrow CO_2 + H$.

The soot chemistry is based on the competing processes of soot formation and soot oxidation (Das *et al.* 1999). The model works by consuming fuel in order to produce soot. The total amount of soot is:

$$\frac{d[soot]}{dt} = \frac{d[soot]_{form}}{dt} - \frac{d[soot]_{ox}}{dt} \tag{2.104}$$

Where:

$\frac{d[soot]_{form}}{dt} = A_{sferc}[F_b]p^{0.5}e^{-T_{sferc}/T}$ and $\frac{d[soot]_{ox}}{dt} = \frac{12}{\rho_{soot}D_{soot}}[soot]R_t$

with $A_{sferc} = 450$ and $T_{sferc} = 1000K$. The symbol [] denotes molar concentration, ρ_{soot} is the soot particle density, D_{soot} the diameter, F_b is the fuel in the burnt gases and R_t the net reaction rate of the intermediate reactive site.

Lastly, for the NO predictions the 3-step Zeldovich mechanism is used and the three reactions are:

$$O + N_2 \leftrightarrow N + NO$$

$$N + O_2 \leftrightarrow O + NO$$

$$N + OH \leftrightarrow H + NO$$

The rate coefficients for the above reactions are given by:

$$K_1 = 1.8 \cdot 10^{11} \exp\left(\frac{-38370}{T}\right) \qquad K_{-1} = 3.8 \cdot 10^{10} \exp\left(\frac{-425}{T}\right)$$

$$K_2 = 1.8 \cdot 10^{7} T \exp\left(\frac{-4680}{T}\right) \qquad K_{-2} = 3.8 \cdot 10^{6} T \exp\left(\frac{-20820}{T}\right)$$

$$K_3 = 7.1 \cdot 10^{10} \exp\left(\frac{-450}{T}\right) \qquad K_{-3} = 1.7 \cdot 10^{11} \exp\left(\frac{-24560}{T}\right)$$

The positive numbering of the rate coefficients represents the forward reaction and the negative numbering represent the backward reaction. The instantaneous rate of NO formation is given by:

$$\frac{dNO}{dt} = \frac{\rho^2}{1 + K_{-1}\frac{Y_{NO}}{M_{NO}} / \left(K_2\frac{Y_{O2}}{M_{O2}} + K_3\frac{Y_{OH}}{M_{OH}}\right)} \left[2K_1 \frac{Y_O}{M_O}\frac{Y_{N2}}{M_{N2}} - \frac{2K_{-1}\frac{Y_{NO}}{M_{NO}}}{K_2\frac{Y_{O2}}{M_{O2}} + K_3\frac{Y_{OH}}{M_{OH}}} \left(K_{-2}\frac{Y_O}{M_O}\frac{Y_{NO}}{M_{NO}} + K_{-3}\frac{Y_H}{M_H}\frac{Y_{NO}}{M_{NO}}\right) \right] \tag{2.105}$$

Lastly, for the spark ignition, the model comprises two stages. The first stage is the time delay between the spark and the appearance of the flame surface. The second stage takes care of the actual deployment of the flame surface.

The first stage is modelled using a function I that starts from zero and reaches the value of 1. This function is given by:

$$\frac{dI}{dx} = A1_{ign} \frac{(\rho^*)^{A2_{ign}}}{\tau_f} \tag{2.106}$$

Where ρ^* is the ratio between the current gas density and the air density at 1 bar and 300K, τ_f is given by $\tau_f = \delta_l / U_l$ and $A1_{ign} = 1.0$ and $A2_{ign} = 3.0$

When the function I reaches the value of 1, a spherical flame surface is generated with radius:

$R_k = \min\left(15 F_{actker} \delta_l \frac{T_b}{T_u}, R_{klimit}\right)$ with $F_{actker} = 1.0$ and $R_{klimit} = 10^{20}$

2.8. Numerical methodology

In STAR-CD only implicit schemes are used for the time and more specifically, in this work the Pressure Implicit with Splitting of Operator (PISO) algorithm was used for the temporal discretisation based on the fully-implicit Euler scheme. This results in an accuracy between first and second order. The spatial discretisation was implemented using second-order schemes depending of variable. For the density, the only option allowed was the central differencing scheme. For the rest of the variables, the Monotone advection and reconstruction scheme (MARS) was used. The benefit of this scheme is that can support all mesh types and flows, and it is the least sensitive of solution accuracy to the mesh structure and skewness. This is particularly important for engine simulations with geometries which by nature promote mesh skewness due to sharp edges and irregular shapes.

Chapter 3

Preliminary Studies and Model Validation

3.1. Grid independence study

Firstly, in order to reduce the computational cost without compromising on the accuracy of the solution, a grid independence study was conducted using an early stage AJ20 geometry (Figure 3.1). The characteristics of the engine are showed at Table 3.1. In this process, an initial coarse grid is gradually refined until some certain key values do not change. In this case, the key values are the in-cylinder average velocity and the velocity vectors on the tumble plane and their magnitude.

Grids ranging from 1.36 million to 4 million cells at BDC were investigated. The maximum cell height was 3mm for the case of the 1.36 million cell grid and 0.8mm height for the case of the 4 million cell grid. The number of the in-cylinder cells during a cycle for four different sizes of the model are showed at Figure 3.2. Initial and boundary conditions as well as valve timings for all the simulations were kept the same and are showed at Table 3.2. These conditions are typical Wide-Open Throttle (WOT) motoring conditions and the walls were set to adiabatic in order not to increase the complexity of the problem with wall heat transfer.

Bore	83 mm
Stroke	92.3 mm
Connection rod	152.72 mm
Pin offset	11.5 mm
Compression ratio	9.5:1
Intake valve opening (0.1mm)	296 deg CA
Intake max lift	9.44 mm at 416 deg CA
Intake valve closing (0.1mm)	492 deg CA
Exhaust valve opening (0.1mm)	125 deg CA
Exhaust max lift	9.9 mm at 239 deg CA
Exhaust valve closing (0.1mm)	365 deg CA

Table 3.1 Characteristics of the AJ20 thermal engine for the preliminary studies

Results showed that quantities such as in-cylinder pressure, temperature and trapped mass were not affected by the size of the model as it can be seen from Figure 3.3, however, the flow field was highly dependent on the resolution of the mesh. Figure 3.4 shows the averaged in-cylinder velocity for four different sizes of the model. Differences in the velocity field start to appear after the mid intake stroke (450 deg CA) and continue up to compression TDC. This is due to the differences in mesh resolution at these crank angles and can be seen at Figure 3.5. The flow field has to be accurately predicted at this period of time as it affects the air-fuel mixing and combustion.

The maximum difference of the velocity magnitude between 1.36 million and 4 million cells was about 12% while between 2.2 and 4 million cells was 2% at 20 deg CA before TDC (spark timing). Visualisation of these differences on the flow field at 700 deg CA can be seen at Figures 3.6. To conclude, the mesh of 2.2 million cells at BDC was chosen in a compromise between quality of the mesh, grid independence and available computational power. Other researchers also stated that 2 million cell grid is the preferred benchmark for engine simulations (Beavis *et al.* 2015). Due to the fact that the cell count is the double in the cylinder throughout the cycle, the grid independence is evident. It is apparent that the differences at the velocities are much higher in the coarser mesh during the intake and compression strokes. It has to be noted that grid independence was observed in the transition from 1.9 million to 2.2 million cells and with the choice of the finer mesh the initialisation study was carried out. For

completeness, the 4 million cell grid was run using the findings of the initialisation study, which will be described in the next chapter.



Figure 3.1 CFD model of the AJ20 thermal engine

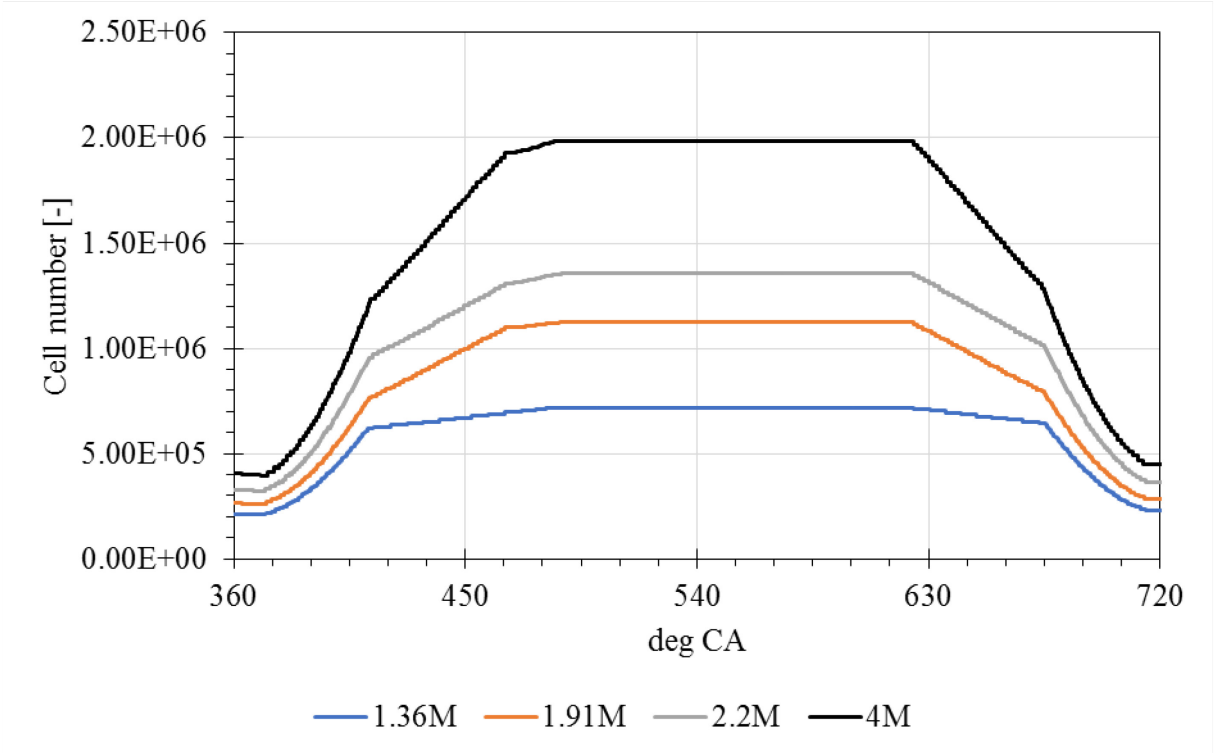


Figure 3.2 Number of in-cylinder cells during a cycle for four different grid size models

Initial Conditions	Boundary Conditions
Cylinder Pressure: 1.05 bar	Intake port Pressure: 0.98bar
Cylinder Temperature: 293K	Intake port Temperature: 293K
Intake port Pressure: 0.98bar	Exhaust port Pressure: 1.03bar
Intake port Temperature: 293K	Exhaust port Temperature: 293K
Exhaust port Pressure: 1.03bar	Walls: Adiabatic
Exhaust port Temperature: 293K	

Table 3.2 Initial and boundary conditions for the grid dependence study

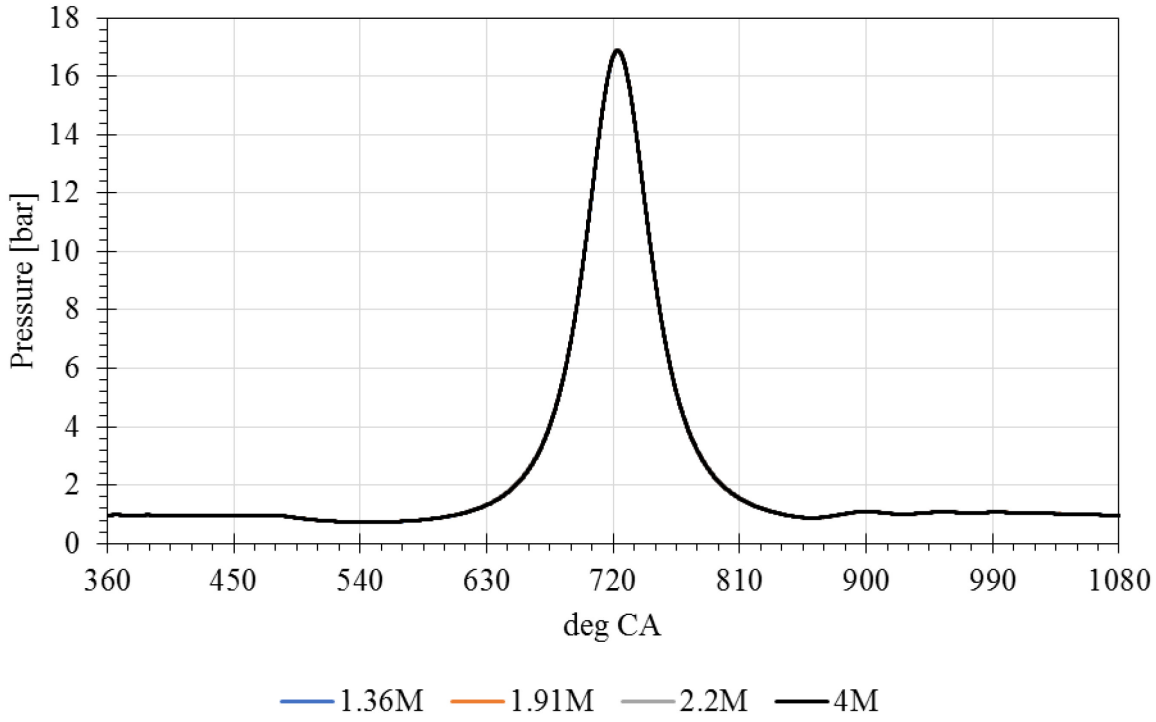


Figure 3.3 In-cylinder pressure traces for four different model sizes

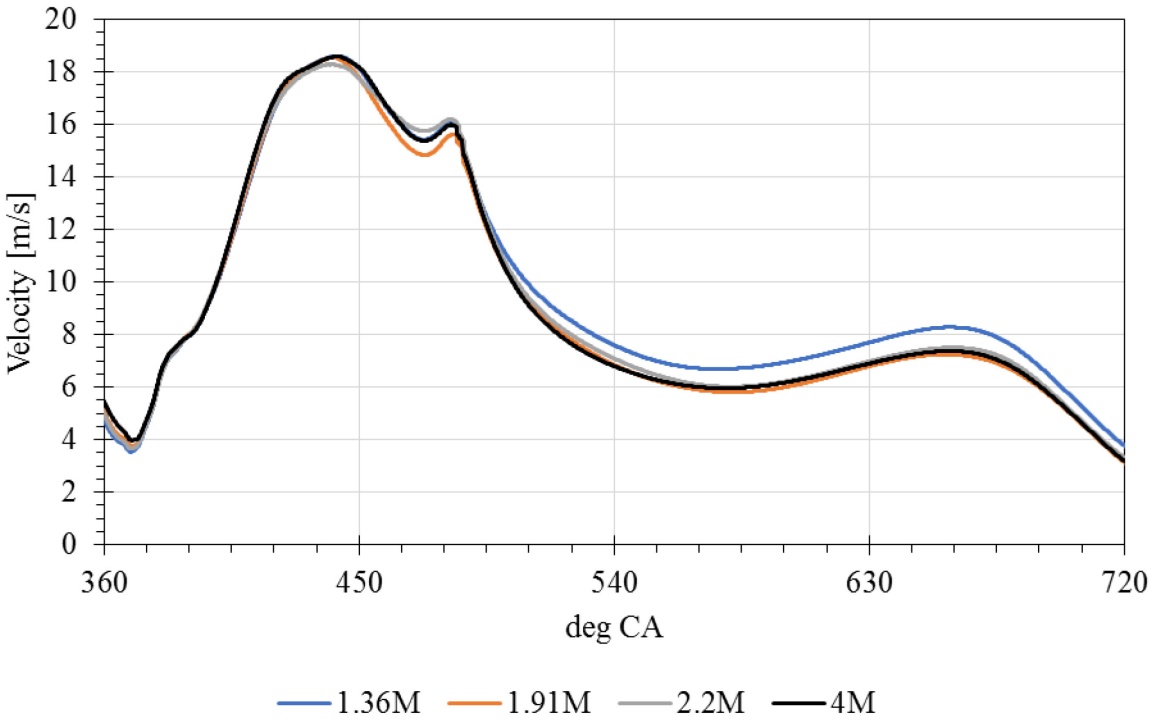


Figure 3.4 Average in-cylinder velocity magnitude for four different model sizes

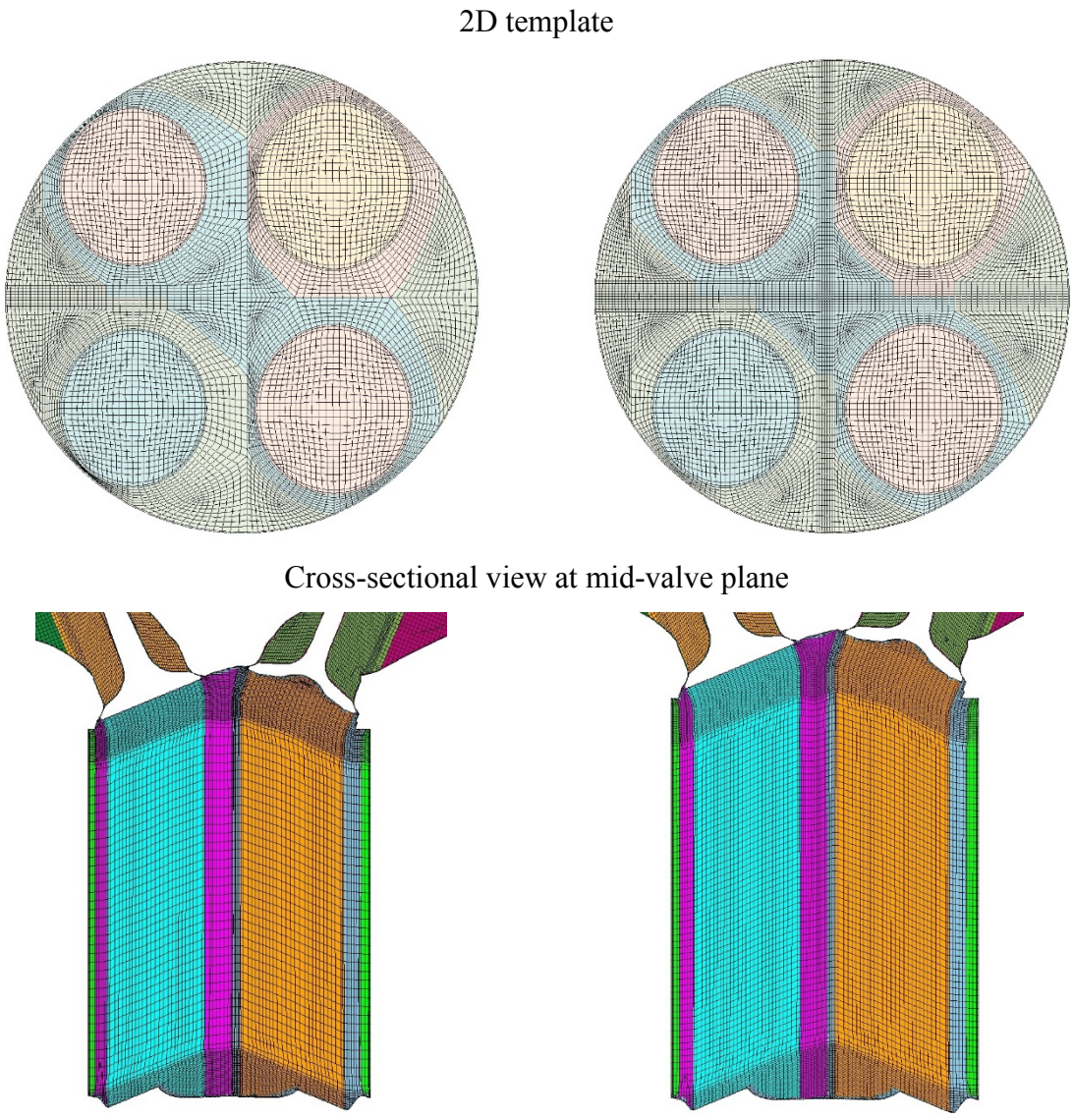
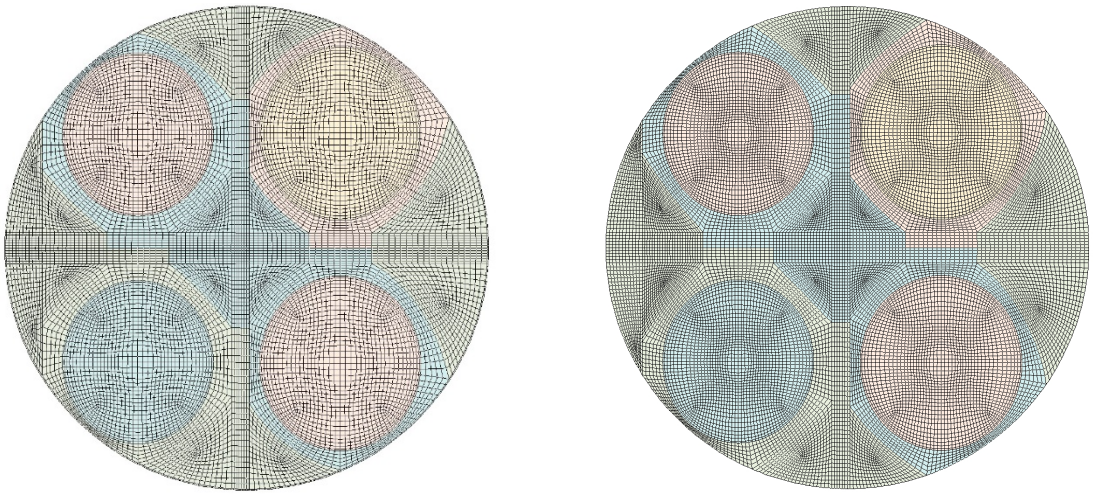
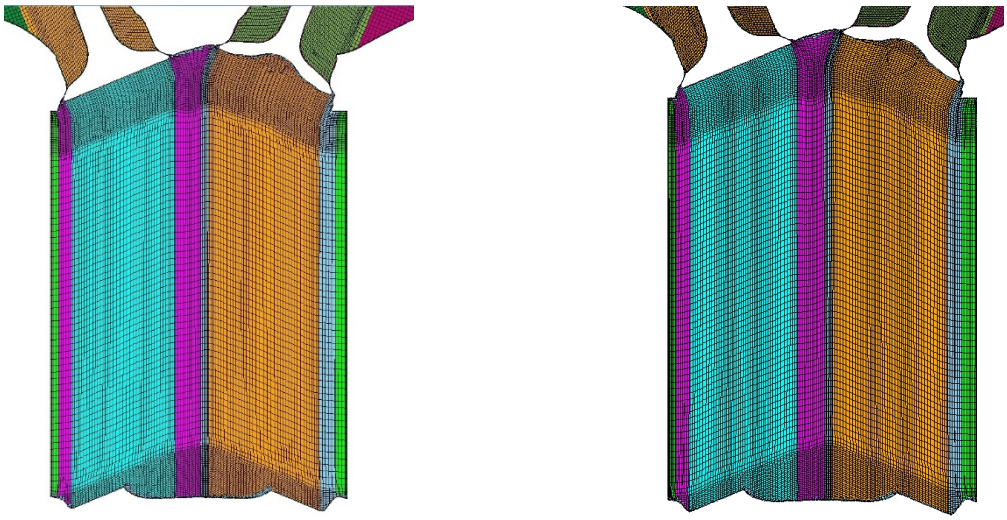


Figure 3.5 The 2D template from which the mesh is based on and a cross-sectional view of the four models at mid-valve point at BDC

2D template



Cross-sectional view at mid-valve plane



2.2 million cells 4 million cells

Figure 3.5cont. The 2D template from which the mesh is based on and a cross-sectional view of the four models at mid-valve point at BDC

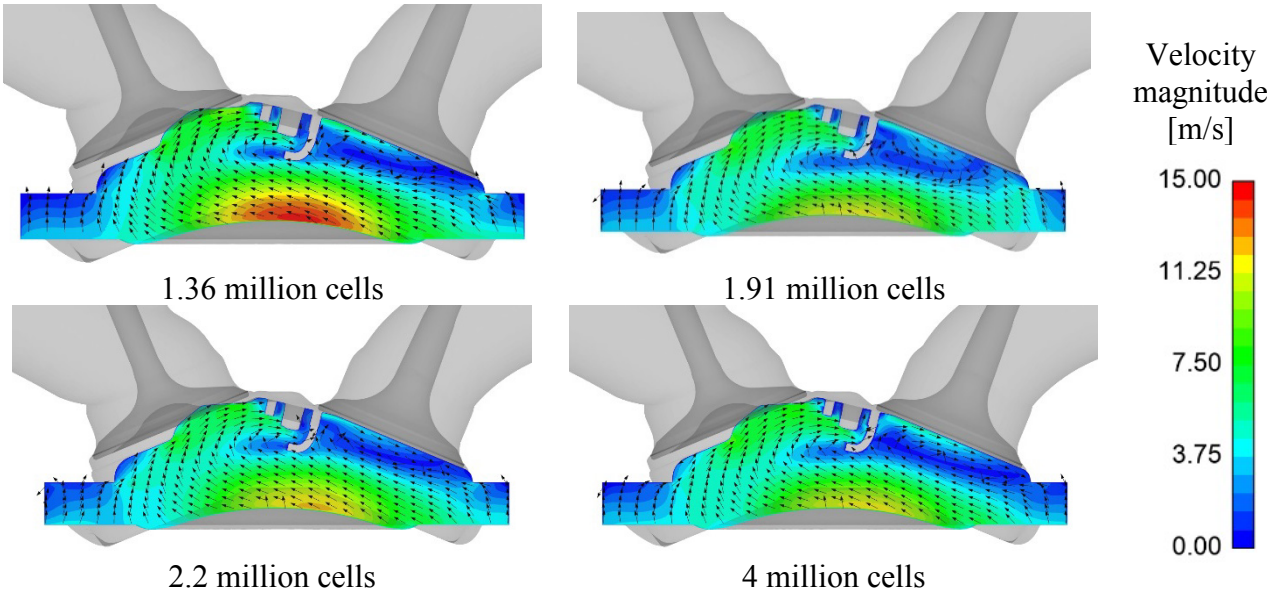


Figure 3.6 Velocity magnitude for four model sizes at 20 deg CA before TDCf

3.2. Initialisation study

Ideally, in engine simulations, multiple cycles are needed to eliminate the effect of initial conditions and obtain an independent solution. However, this procedure demands high computational power and it is very time consuming especially if grids with high resolution are used, combined with complex phenomena such as spray injection and combustion. Various researchers are using different conditions and initial crank angle for their model. Therefore, accurate initialisation of the simulation is needed to minimise the necessity of running multiple cycles and to improve the stability of the solver. Generally, it is expected that after two or three cycles, the final result shouldn't have difference from the previous cycle.

Two cases were investigated, either to start the simulation before IVO (260 deg CA) or EVO (110 deg CA) which are the recommended settings for the CFD code or seen in literature such as Devassy *et al.* (2014), Copeland *et al.* (2013), Costa *et al.* (2014) and Kurniawan *et al.* (2007). The boundary conditions and the rest of the setup were kept the same as the grid dependence study and the model was the 2.2 million cell. Both of the cases were run for three consecutive cycles and the results showed that while the initialisation did not have an impact on the in-cylinder pressure, the average in-cylinder velocity was affected by the initialisation. More specifically, the average velocity had maximum discrepancies of about 30% over the three simulated cycles when the start of the simulation was before IVO (Figure 3.7, orange line). When the simulation started before EVO, cycle 2 and 3 had minor differences in the in-cylinder velocity of 2.5%. This can be seen at Figure 3.7 (blue line). During the intake and

compression strokes for the initialisation before EVO, the maximum difference between cycles 1 and 3 was about 8% and occurred 15 degrees CA before BDC. This was the maximum difference throughout the intake and compression strokes as it can be seen in Figure 3.8.

When starting before the EVO, the in-cylinder velocity is very low with a uniform vertical direction and in a closed system without interacting with the intake and exhaust ports, thus, it can be either applied an initial vertical velocity or assumed that the initial velocity is zero with some accuracy if the exact value is not known. Also, the velocity at both intake and exhaust ports are approaching to zero in the model, so the zero initial condition can be a good assumption for the ports. Moreover, at this stage of the engine cycle (before EVO), it can be assumed that the cylinder is composed of exhaust gases as opposed to an unknown mixture of exhaust and intake gases during the intake process. This makes easier the initialisation when combustion is simulated or the combustion products have to be simulated. However, this cannot be applied for a crank angle before IVO as the valve timing indicates that the exhaust valve is open and there is a flow between exhaust port and the cylinder which is more difficult to predict and apply specific initial conditions and as well, more cycles will be needed in order to damp out the assumed initial conditions. These differences are showed at Figure 3.9. For the above reasons, and especially if the processing time is limited to a single cycle, it was concluded that the initial crank angle should be before EVO, around 10-15 deg CA.

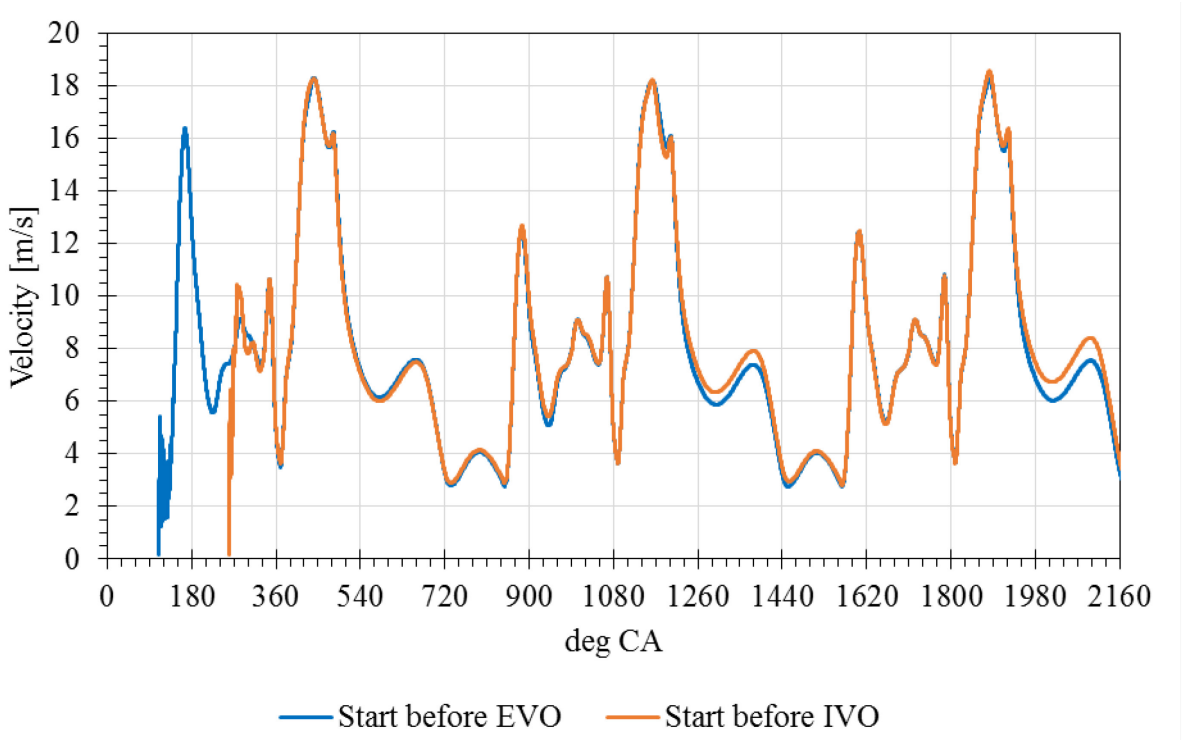


Figure 3.7 Comparison of the in-cylinder velocity magnitude during three consecutive cycles for two different initialised simulations

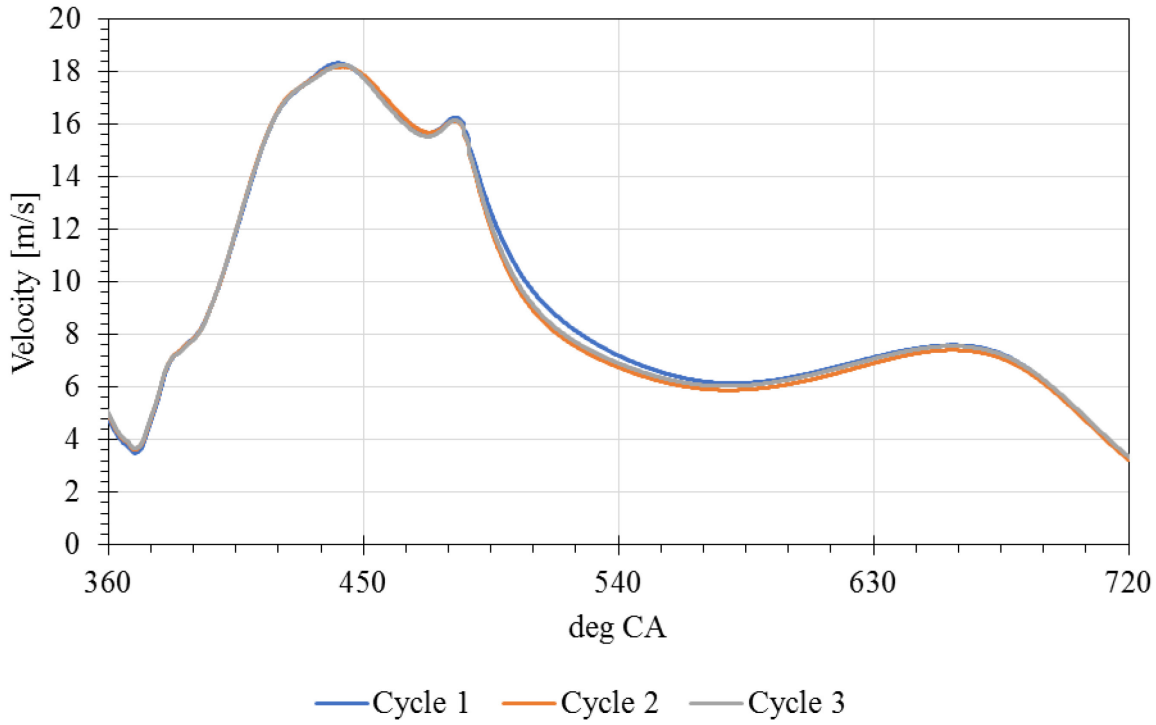
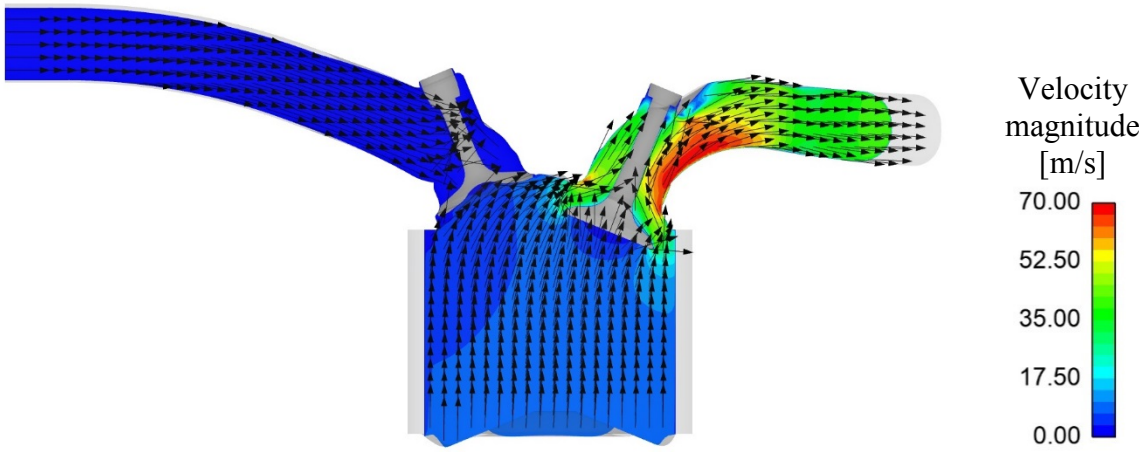
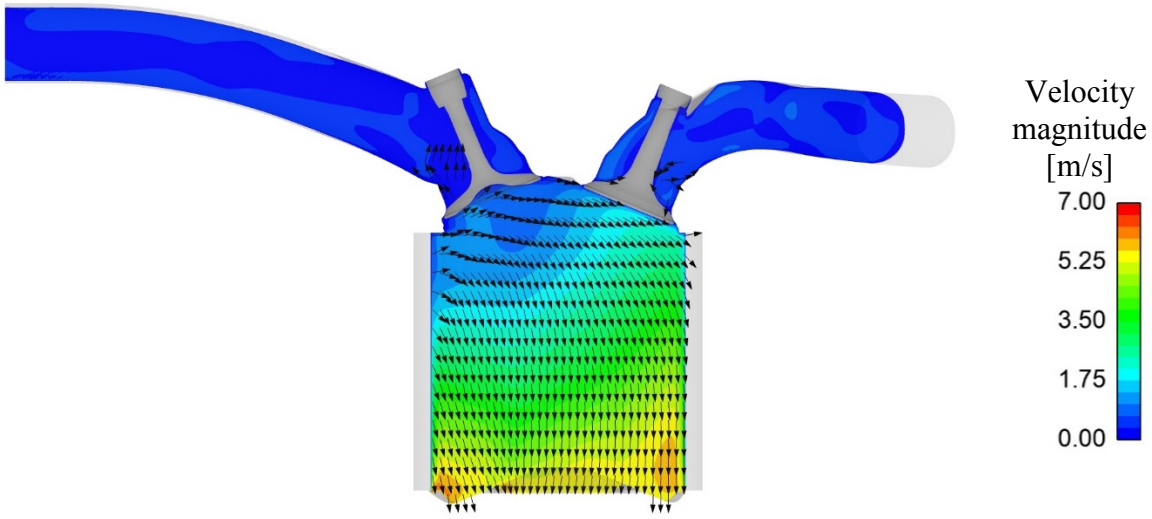


Figure 3.8 Comparison of the in-cylinder velocity magnitude for three consecutive cycles when initialised before EVO



Intake valve opening 271°CA



Exhaust valve opening 847°CA

Figure 3.9 Comparison of the velocity field at intake and exhaust valve opening

3.3. Validation of pressure traces

"The process of determining the degree to which a model is an accurate representation of the real world from the perspective of the intended uses of the model" (AIAA Standards Committee, 1998), simply referred as validation, is essential for a CFD study. Validation involves detailed experimental data and information about boundary conditions for the model. Most often in the literature, validation of a CFD engine model is done by comparing experimental and CFD in-cylinder pressure traces (Fontanesi *et al.* 2014, Bonatesta *et al.* 2014, Forte *et al.* 2014, Lucchini *et al.* 2013). Seldom, PIV data from an optical SI engine are

available and further validation analysis of the velocity flow field can be carried out (Malcolm *et al.* 2011, Beavis *et al.* 2015).

In this study, two different Jaguar Land Rover engine families were used for validation. Firstly, a CFD model of an old optical, single-cylinder engine (AJ133) was used to establish best practice approach by comparison with extensive database of Particle Image Velocimetry (PIV) (Justham 2010) and in-cylinder pressure traces of the AJ133. The design of the engine gave full optical access to the combustion chamber with a full-length quartz cylinder liner allowing full-stroke and 360° optical access, a triangular pent-roof window at the engine head and an optical piston with a circular quartz window. However, the optical liner could be replaced by a steel liner that allowed cooling or heating it via a water jacket. Moreover, optical access to the intake flow was possible with an intake runner made by clear resin. Uncertainties related to boundary conditions, valve profiles, heat transfer and blow-by were studied. Furthermore, the numerical results of the AJ133 engine were compared against CFD results of other researchers (Beavis *et al.* 2015) who simulated the same type of engine.

Secondly, detailed experimental data of intake and exhaust manifold pressures and valve profiles were obtained from the new thermal, single cylinder engine (AJ20) with a Continuous Variable Valve Lift (CVVL) system for the intake valves and the in-cylinder pressure was compared to CFD results. The geometric characteristics of the two aforementioned engines can be found in table 3.3 and the CFD models are showed at Figure 3.10.

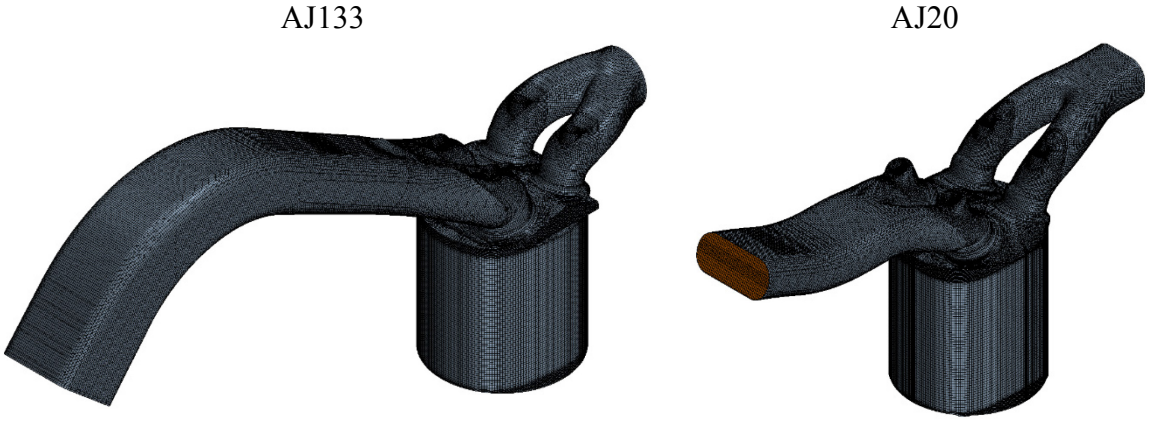


Figure 3.10 CFD model of the AJ133 optical engine and the AJ20 single cylinder thermal engine

	AJ133	**AJ20**
Bore	89 mm	83 mm
Stroke	90.3 mm	92.3 mm
Connection rod	148.97 mm	152.72 mm
Compression ratio	10.5:1	11:1
Pin offset	0	11.5 mm
Intake valve opening (0.1 mm)	389 deg CA	269 deg CA
Intake max lift	10.5 mm at 509 deg CA	9.45 mm VVT
Intake valve closing (0.1 mm)	639 deg CA	492 deg CA
Exhaust valve opening (0.1 mm)	112 deg CA	126 deg CA
Exhaust max lift	9.5 mm at 234 deg CA	9.9 mm VVT
Exhaust valve closing (0.1 mm)	369 deg CA	365 deg CA

Table 3.3 Characteristics of the AJ133 single cylinder optical engine and the AJ20 single cylinder thermal engine

To begin with, four experimental in-cylinder pressure traces of the AJ133 during motoring, with engine wall temperature at 20°C and 90°C, pre-fire and post fire condition, were compared with CFD results. Initially, the engine was conditioned to the specified wall temperature and then motored, to acquire the in-cylinder pressure before any combustion event (pre-fire data). After that, the engine run with combustion for several minutes. Lastly, the combustion was stopped, and new motoring in-cylinder pressure traces were acquired (post-fire). The nominal experimental intake pressure was 0.5 bar absolute pressure and the engine speed was 1500 RPM.

From the conclusions of the previous chapter, the CFD model of the AJ133 engine consisted of 2.2 million hexahedra cells at BDC and the simulation was initialised before EVO. Due to the lack of time dependent data and detailed measurements, assumed constant pressure and temperature boundary conditions were applied at the intake and exhaust ports. Simulations were run for both adiabatic walls and walls with fixed temperature. A summarised table of the boundary conditions is shown at Table 3.4. Firstly, the k-ε RNG turbulence model was used as is widely accepted in the literature. Later on, a comparison of k-ε RNG with other three well known turbulence models will be discussed. Due to the uncertainties of the intake boundary conditions and blow-by of the optical engine, a reduction of 10% of the nominal intake pressure (0.5 bar) was made, in order to match the numerical and the experimental in-cylinder pressure

traces as well as taking account the loss of mass due to blow-by. Further adjustments to the intake pressure were made, with the aim of matching the in-cylinder pick pressure for the warm condition of the engine. Also, the intake and exhaust temperatures were assumed to be at room temperature supposing that the optical engine was not running for long periods.

Initial Conditions	Boundary Conditions
Cylinder Pressure: 0.55 bar	Intake port Pressure: 0.5/0.45bar
Cylinder Temperature: 293K	Intake port Temperature: 293K
Intake port Pressure: 0.5/0.45bar	Exhaust port Pressure: 1.023bar
Intake port Temperature: 293K	Exhaust port Temperature: 293K
Exhaust port Pressure: 1.023bar	Walls: Adiabatic/ 293K
Exhaust port Temperature: 293K	

Table 3.4 Initial and boundary conditions for the validation of the AJ133 optical engine

In addition, small adjustments were made to the valve profiles that were derived from the theoretical cam profiles in order to take account the valve lash and accommodate any uncertainties of the engine setup such as discrepancies at the cam timing, thermal expansion of the valves and/or valve train system and manufacturing tolerances. Firstly, the theoretical valve motions are given versus camshaft degrees and this had to be converted to crankshaft degrees. Because the crankshaft is rotating with the double of the speed of the camshaft, the theoretical duration of the valve opening has to be multiplied by two. Moreover, in the theoretical cam profile, a ramp with approximately 0.3mm height is included, named as cam quieting ramp. The ramp is designed to take up the follower near half way of the ramp with a very low speed and minimum shock before and after the fast rise flank (Heisler 1999). This means that most if not all of this ramp has to be removed for CFD simulations as it doesn't take part in the valve opening period. This is an iterative, try and error, process which can be very time consuming for 3D simulations. Thus, some trade-offs on the accuracy have to be accepted. The same approach was followed by Beavis (2017) who simulated the same engine. The theoretical cam profiles along with the valve profiles applied to the CFD model can be seen in Figure 3.11.

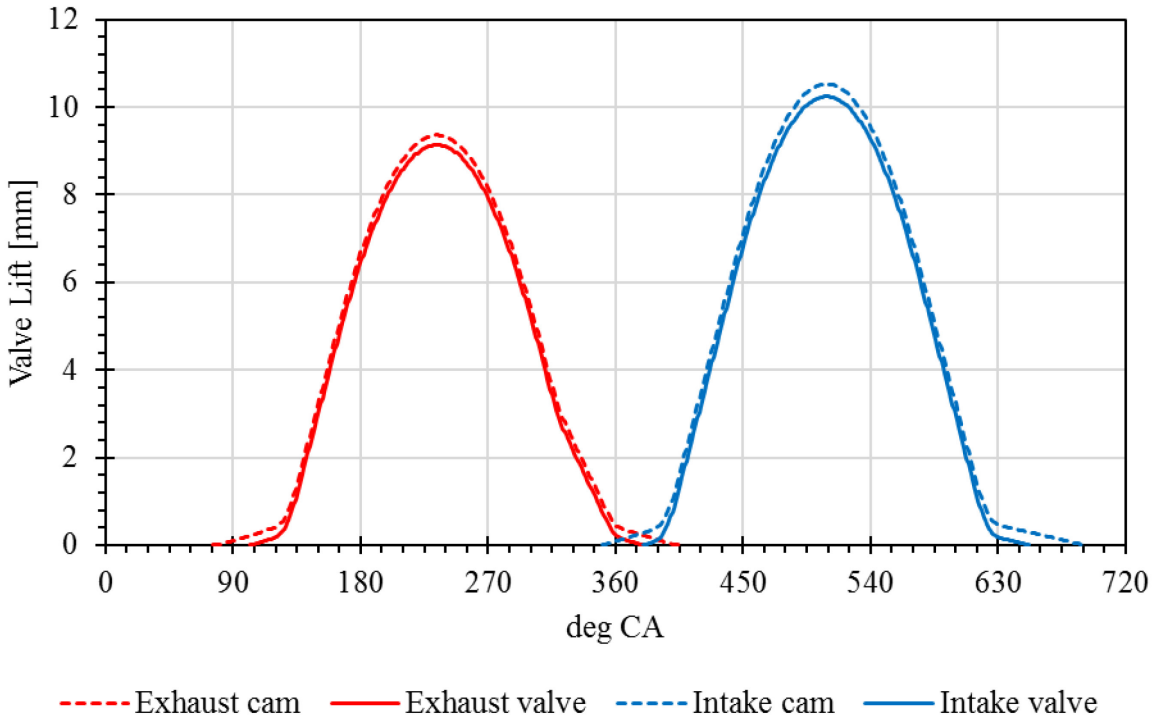


Figure 3.11 Theoretical exhaust and intake cam profiles and derived valve profiles

It can be seen from Figures 3.12 and 3.13 that a discrepancy of 0.8 bar at TDC exists between the four experimental peak pressures. The simulation with 0.5bar intake pressure and adiabatic walls over-predicted the peak pressure by 0.5bar and 1.1bar when comparing it against the maximum and minimum peak pressures of the experiments. For the same intake pressure and fixed wall temperatures at 20°C, the peak pressure matched the highest experimental peak pressure (post fire case with 90°C wall temperature), but it was higher than the pre and post fire cases with 20°C wall temperature. This behaviour can be explained by the loss of mass during compression, which is lower for post fire cases as the engine expands and the crevices are reduced and by the reduced heat loss with higher wall temperatures. When the intake pressure was reduced by 10% (at 0.45 bar), the peak pressure with adiabatic walls was reduced and it was in the range of the experimental values. The same intake pressure with fixed wall temperature at 20°C resulted a peak pressure of 0.1bar lower than the lowest experimental value. Finally, a fine tuning of the intake pressure was carried out to match the peak pressure of the experimental pre-fire condition with 90 °C wall temperature. This resulted in an intake pressure of 0.47 bar.

Because of the uncertainties and the lack of accurate experimental data of the intake pressure, it was decided to continue the validation study of the flow field using intake pressure of 0.45bar,

which produced peak pressures similar to the corresponding experiment and took account the blow-by phenomenon with reduced trapped mass. This boundary condition was also used for the validation of the sub-cooled fuel injection. For the validation of the flash-boiling spray, the 0.47 bar intake pressure was used, as it was matching the peak pressure of the experiment with 90 °C wall temperature.

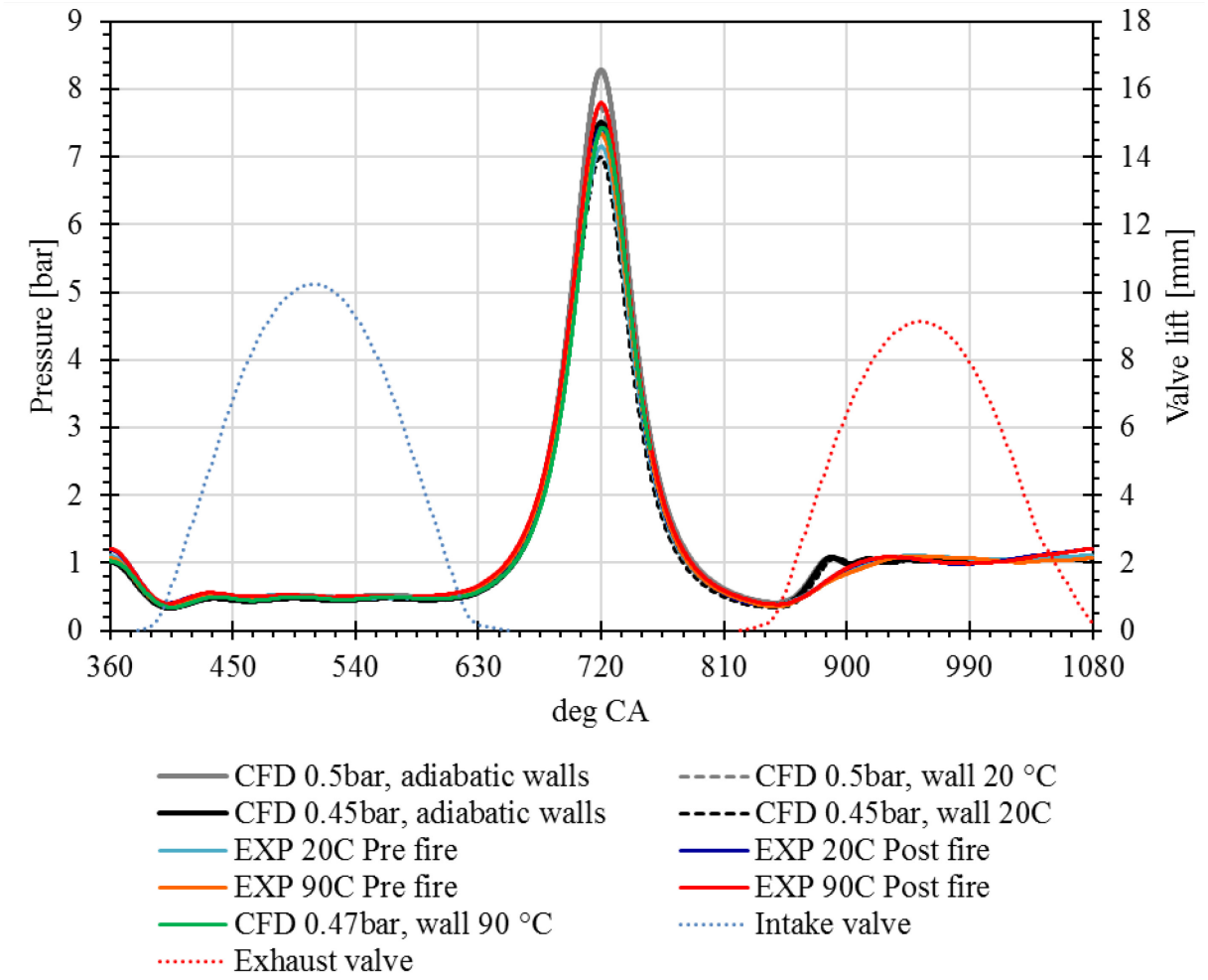


Figure 3.12 In-cylinder pressure for four experimental and five numerical cases from the AJ133 optical engine

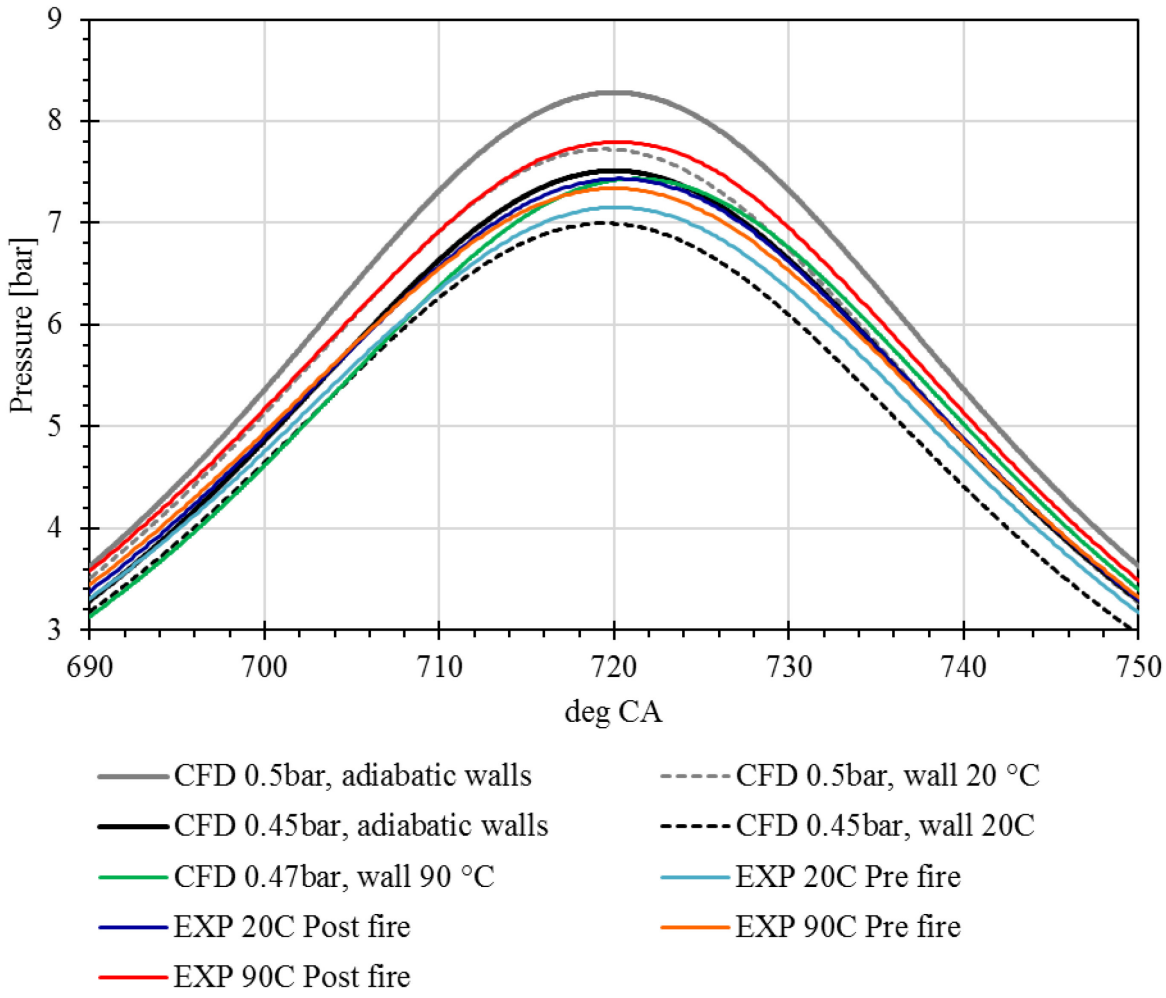


Figure 3.13 In-cylinder pressure focused around TDC for four experimental and five numerical cases from the AJ133 optical engine

Due to the uncertainties mentioned above, detailed experimental data from the new thermal, single cylinder engine (AJ20) were acquired and used for pressure trace validation of the CFD code. Five different motored conditions at 1500 RPM were run, with the use of the CVVL system. First of all, a test point as close to the AJ133 case as possible was run. This was a throttled case, at 0.5bar intake pressure, with both cams at the base positions (zero valve overlap). For this case, a pre-fired and a post-fired motoring pressure case was acquired, in the same way as for the AJ133. In addition, for the same CVVL setup and at 1 bar intake pressure, a post fire motoring pressure trace was acquired. Another two experimental pre-fire and post-fire cases at 0.5 bar and 1 bar intake pressure were run, with the intake cam at its maximum advance (50 deg CA) and the exhaust cam at its maximum retard (50 deg CA). One last pre-fire case at 1 bar intake pressure with the intake cam at the base position and the exhaust cam at its maximum retard position was acquired. The intake valve profiles were taken from the

engine's sensor with no further adjustments. The exhaust valve profile was derived from the theoretical cam profile and lash similar to the previous model (AJ133) was applied.

The model of this engine consisted of 2.1 million cells at BDC and the simulation was initialised before EVO according to the above findings. Detailed time dependent pressure trace of the intake and exhaust runner and constant temperature were applied for intake and exhaust boundary conditions which were taken from the experiment. Simulations were run for both adiabatic walls and walls with fixed temperature at 90°C as the engine's cooling system was at this temperature. The k-ε RNG turbulence model was used.

Figures 3.14 to 3.18 show the experimental and numerical in-cylinder pressures for the five motored conditions that were described above. First of all, as it was expected, the in-cylinder peak pressure was over-predicted with adiabatic walls in all cases as no losses were modelled. The results were improved and were in a very good agreement with the experiment with the use of walls with constant temperature. For all cases the maximum over-prediction was about 9% compared to the experimental peak pressure however, this difference was only seen for one case (0.5 bar intake pressure and valve overlap at 50/50). For the rest of the cases, the maximum difference between numerical and experimental pre-fire pressure traces was 3.7%. In addition, the numerical peak pressures were closer to the post-fire experimental cases, with 1%-2% difference. This supports the theory of reduced blow-by with a warm engine. A good agreement between CFD and experimental results can be seen also for the intake, compression and expansion strokes.

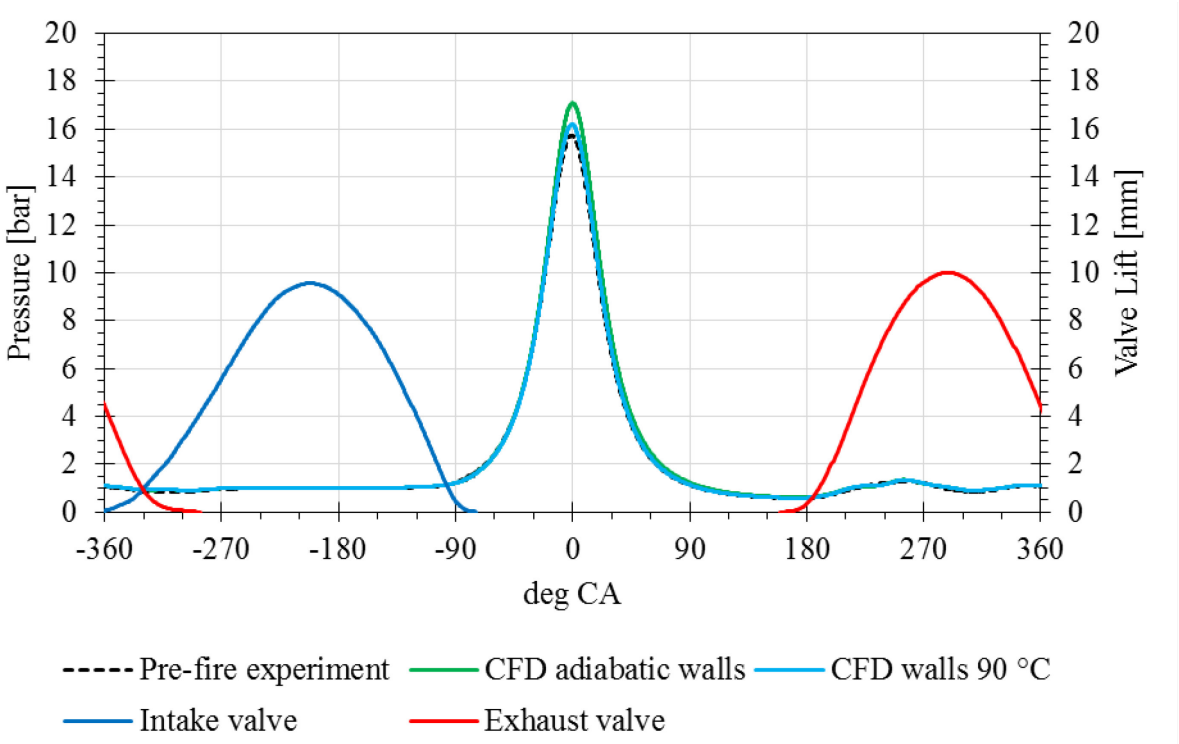


Figure 3.14 Experimental and numerical in-cylinder pressure and valve lifts for 1 bar intake pressure. Intake cam: base position, Exhaust cam: 50 deg CA retard (AJ20)

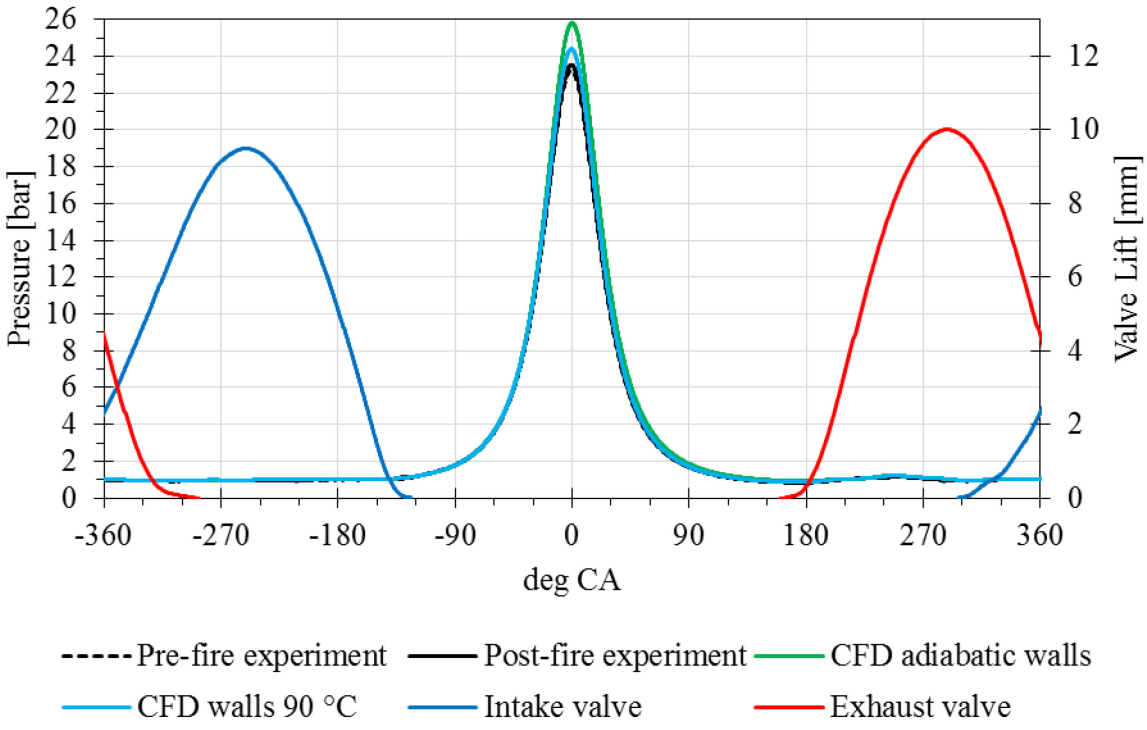


Figure 3.15 Experimental and numerical in-cylinder pressure and valve lifts for 1 bar intake pressure. Intake cam: 50 deg CA advance, Exhaust cam: 50 deg CA retard (AJ20)

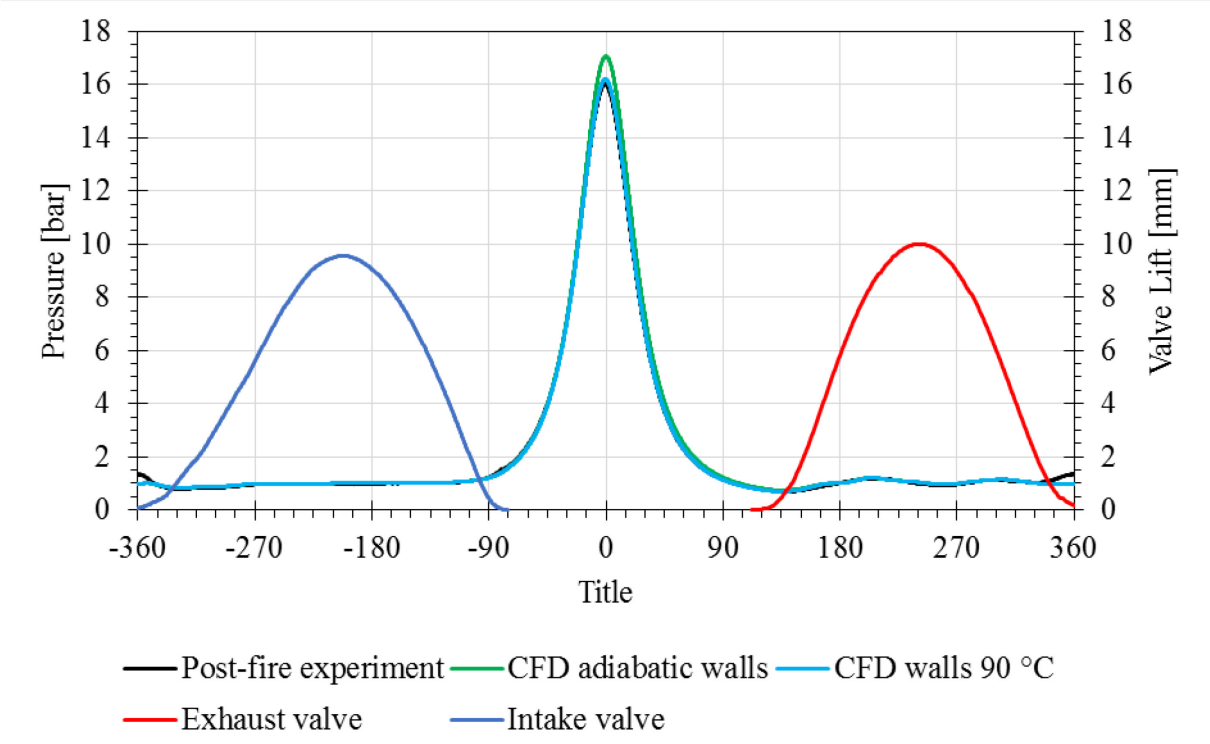


Figure 3.16 Experimental and numerical in-cylinder pressure and valve lifts for 1 bar intake pressure. Intake cam: base position, Exhaust cam: base position (AJ20)

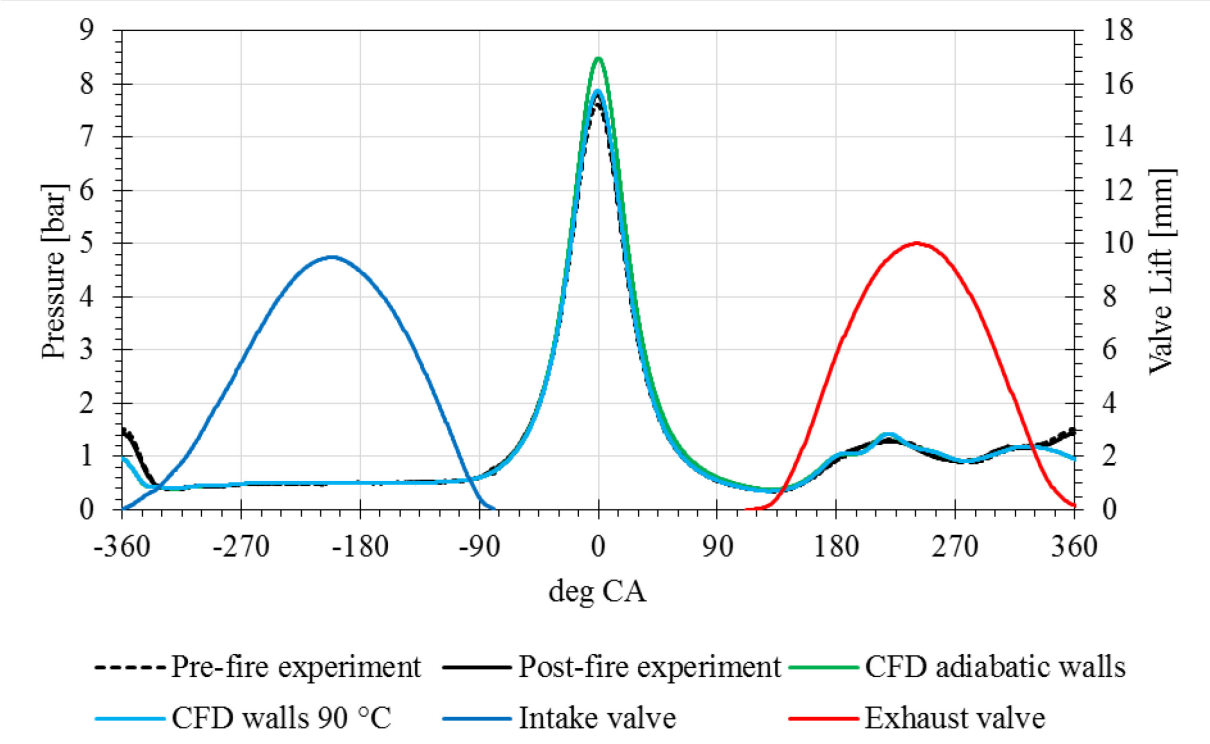


Figure 3.17 Experimental and numerical in-cylinder pressure and valve lifts for 0.5 bar intake pressure. Intake cam: base position, Exhaust cam: base position (AJ20)

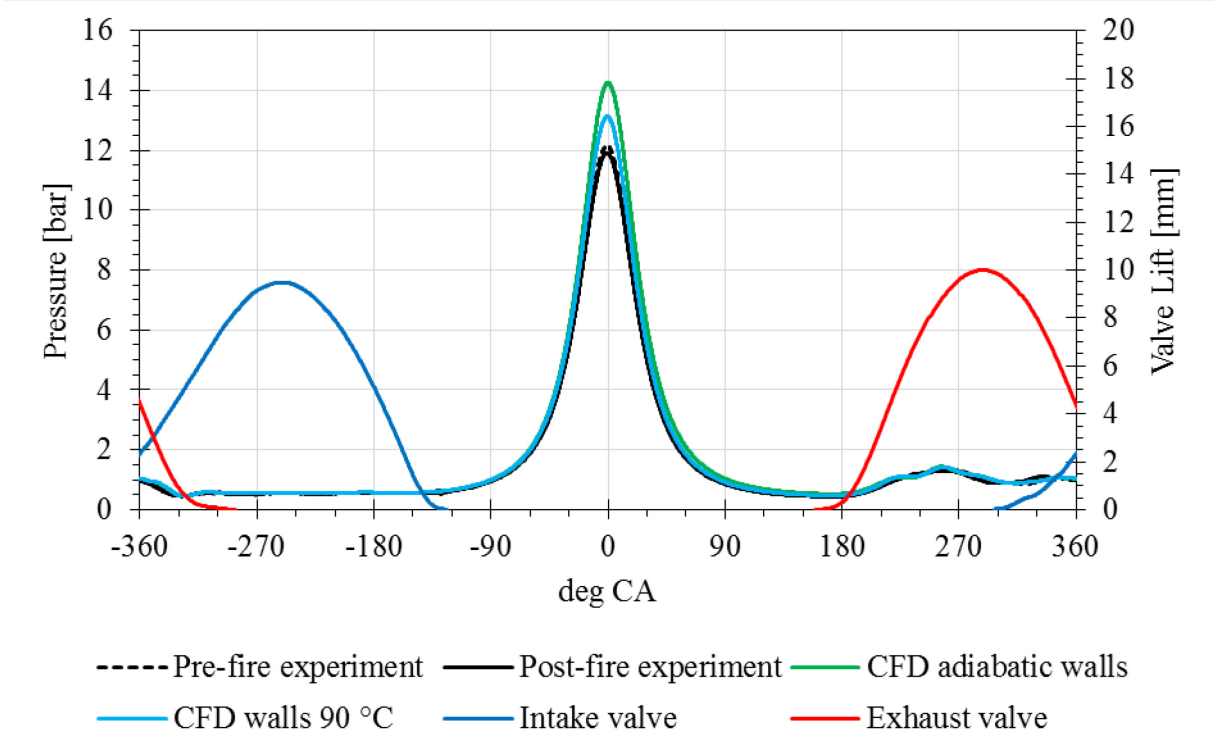


Figure 3.18 Experimental and numerical in-cylinder pressure and valve lifts for 0.5 bar intake pressure. Intake cam: 50 deg CA advance, Exhaust cam: 50 deg CA retard (AJ20)

In all cases, a small discrepancy is noticeable during the end of the exhaust stroke, near EVC. This is more evident in the cases with no valve overlap where a small re-compression can be observed in the experimental in-cylinder pressure but not in the numerical predictions. This behaviour was investigated for the throttled test point (0.5 bar intake pressure), with both cams at the base position. It is apparent that the numerical in-cylinder pressure trace follows the exhaust pressure trace during the expansion stroke while in the experiment the pressure increases after 328 deg CA (Figure 3.19).

To force the code to capture the re-compression and study the exhaust valve timing which is needed for that, the exhaust valve closure was advanced by some degrees in an iterative process. This was done by reducing the time in which the valve is open from the maximum lift until the EVC. The duration from EVO until maximum lift was not modified. This was done in order to keep the behaviour of the in-cylinder pressure trace the same during the opening of the valve. The pressure traces with two modified exhaust valve lift curves as well as the pressure with the default valve lift can be seen in Figure 3.19. This figure is colour coded meaning that each pressure trace corresponds to the valve lift with the same colour.

The two modified valve lifts had closure times 5 and 8 degrees CA before TDC. By advancing the EVC by 8 degrees the code could capture the recompression, but the pressure trace behaviour was not realistic, as it was creating a step at EVC. One cause of the absence of the re-compression could be the miss-predicted discharge coefficient during the flow from the cylinder to the exhaust port at low valve lifts. Other possible causes of this behaviour could be the lash of the cam or other faults during the machining of the cam which can lead to valve profiles somewhat different from the theoretical profiles which were applied in the model. The fact that the intake and compression strokes were in a very good agreement with the experiment which were under the influence of the actual intake valve lift as this was recorded by the CVVL system, points that the theoretical and actual exhaust lifts may have slight differences. Because it was not possible to investigate the problem further and identify the reason of the miss-prediction, the original valve profiles as they were provided by JLR were used.

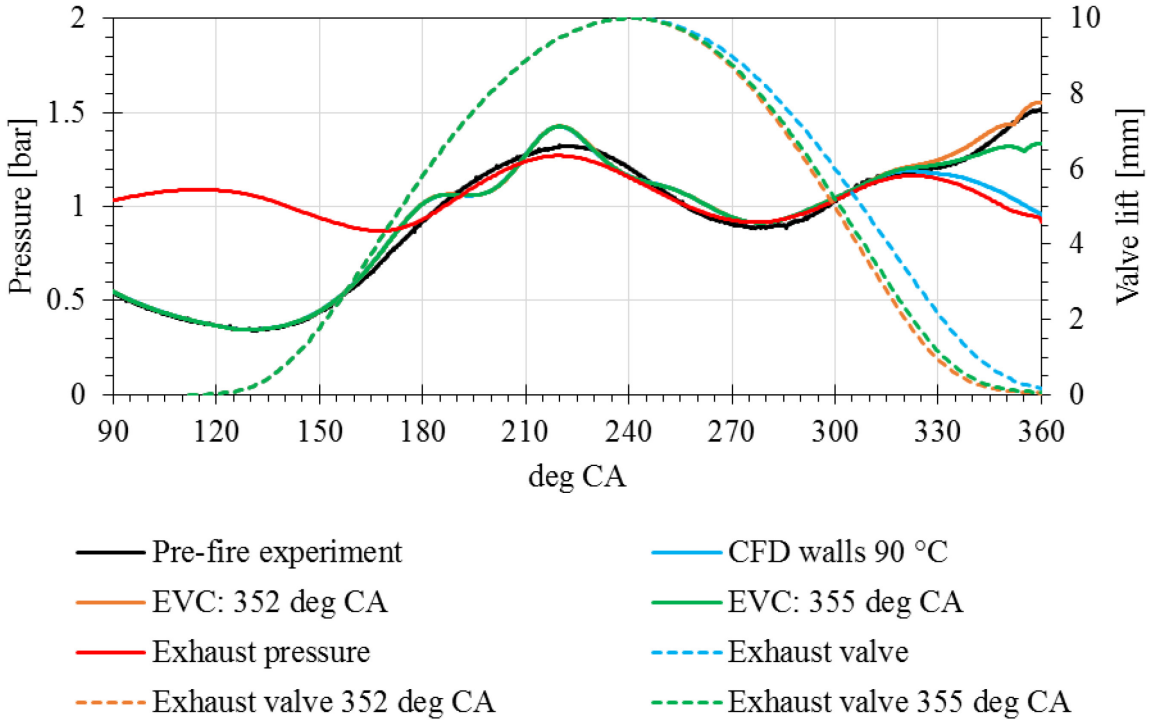


Figure 3.19 Investigation into the recompression at gas exchange TDC (AJ20)

To conclude, data from two different single cylinder engines were used for pressure trace validation. Firstly, four experimental in-cylinder pressure traces of the AJ133, with engine wall temperature at 20°C and 90°C, pre-fire and post fire condition, at 0.5bar intake pressure were compared with CFD results. However, no other data such as intake and exhaust pressure and temperature were available from these tests in order to be used as boundary conditions for the

model. For this reason, constant intake and exhaust pressure and temperature was assumed. Moreover, the four experimental in-cylinder pressures had different peak pressures with a maximum deviation of 0.8 bar. For this reason, a slight reduction of the intake pressure was needed to bring the peak pressure closer to the experiments and also to take account the effect of blow-by. Due to all the uncertainties with the previous engine, detailed data from the new CVVL AJ20 engine were acquired. Five tests were run, with two different intake pressures and different cam phases. In all these cases, the experimental and numerical in-cylinder pressures were in a good agreement. Some miss-predictions of the in-cylinder pressure during the exhaust stroke and near EVC was investigated. This part of the study shows the importance of accurate boundary conditions and detailed valve profiles that have to be applied on a model.

3.4. Validation of flow field

Following the in-cylinder pressure validation, the velocity filed and flow structure of the CFD was compared against PIV data of the intake runner, the intake valve jet and the cylinder of the AJ133 optical engine motored at 1500 RPM. The necessary information was acquired from relevant publications and PhD theses.

Firstly, the prediction of the velocity at the intake runner was investigated. The experimental graph (Figure 3.20) taken from Justham (2010) shows the U component of the velocity in the intake runner. The results of Figure 3.21 show the numerical averaged velocity magnitude for the same time domain as the experiment. In the same graph, the absolute value of the experimental and numerical U velocity component at various crank angles are showed. First of all, a qualitative comparison of the experimental U velocity component and the numerical averaged velocity magnitude, especially during the timeframe of 40 deg CA to 160 deg CA, when the flow is directed into the cylinder, showed that the model is predicting the dynamics of the flow motion (sinusoidal profile of the velocity). At 190 deg CA, the numerical velocity magnitude approached to zero and after that increased again. At the point of minimum velocity, the flow was reversed and directed out of the cylinder and the same behaviour was also seen in the experiments.

At 62 deg CA the experimental U component is 38.3 m/s and the numerical velocity is in the range of 44.3 m/s which shows that the model is over-predicting the velocity. The two maxima at 60 and 115 deg CA and two minima at 90 and 155 deg CA are predicted with some hysteresis on the wave. In addition, during intake, the maximum difference between experiments and

numerical results is 5 m/s. An important fact about the experimental intake velocity is the cycle to cycle variability which makes the comparison with the CFD more difficult. From Figure 3.22, it is evident that during the early intake process the experimental velocity discrepancies are about 4 m/s - 5 m/s which reach 8 m/s later in the cycle. Despite the experimental variations and the lack of data, comparison of the experimental u velocity component with the CFD plots of the intake runner at the specific crank angles support the conclusion of good agreement in prediction of the intake runner flow field especially during the intake process with some discrepancies on the velocity magnitude.

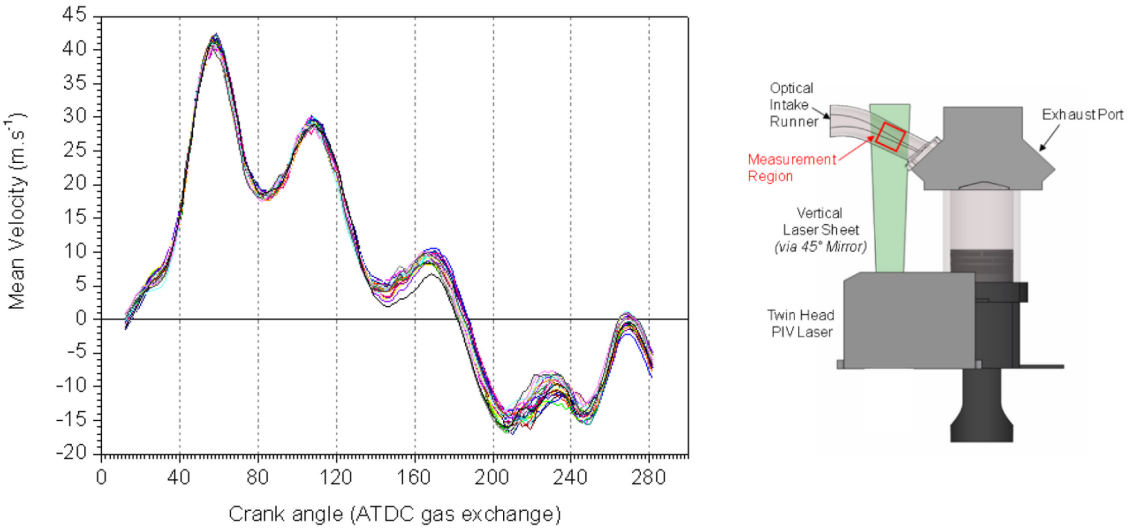


Figure 3.20 Experimental U velocity component at the intake runner and the region of the measurement (AJ133)

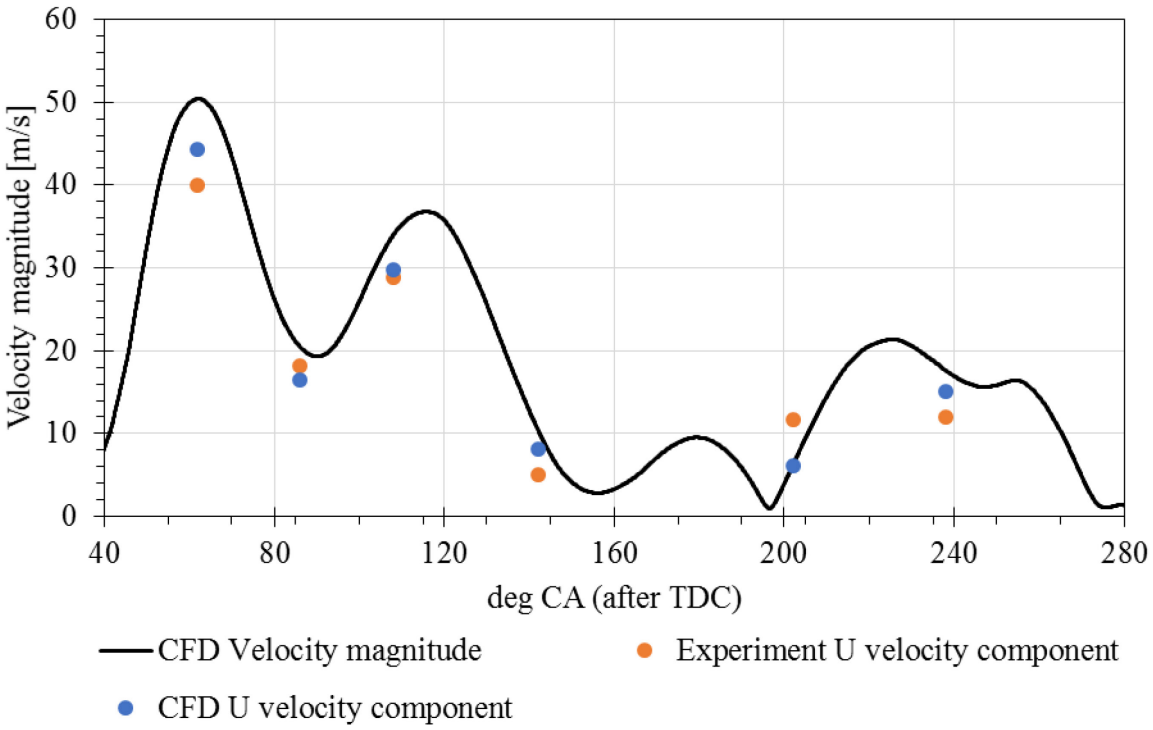


Figure 3.21 Numerical velocity magnitude at the intake runner and experimental and numerical U velocity component at specific crank angles (AJ133)

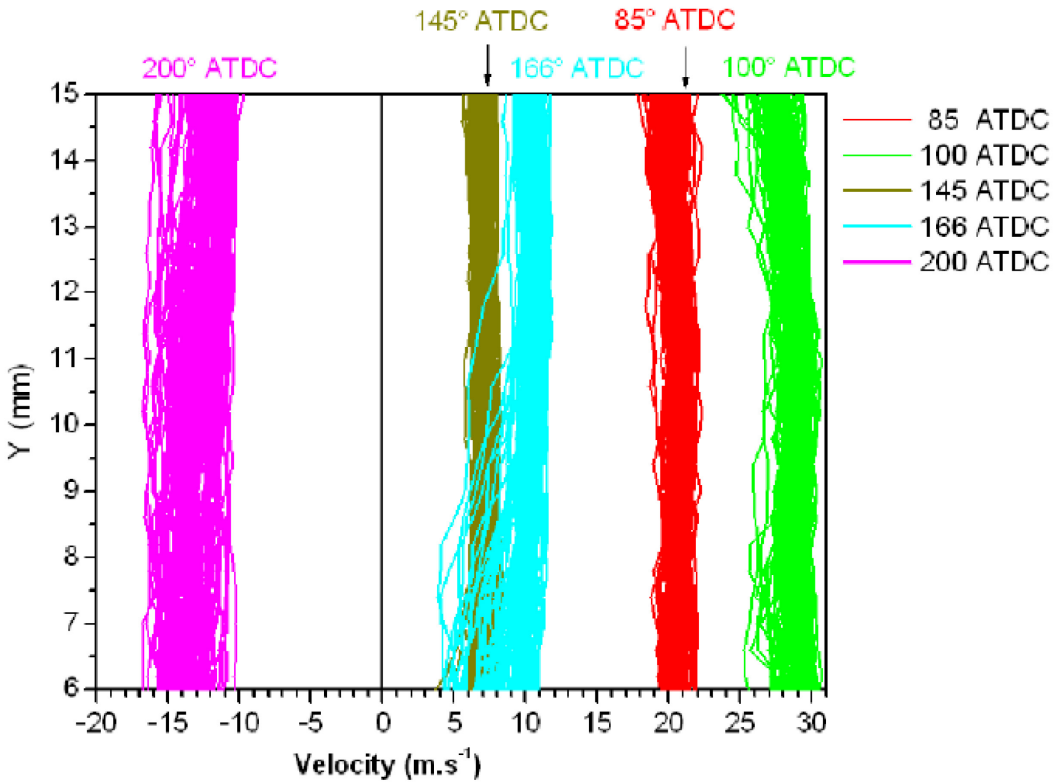


Figure 3.22 Experimental velocity profile of 200 cycles in the intake runner at five specific crank angles

Secondly, the valve jet on a mid-valve plane was studied. The PIV data were taken at the area of the pent roof window as shown at Figure 3.23. During the period 90 to 100 deg CA it was observed that there is no significant variation at the experimental valve jet with the velocity magnitude to be around 40 m/s, however variations can be seen at the CFD predictions. At 92 deg CA the velocity of the jet is under-predicted (30-35 m/s) but later on the cycle, at 100 deg CA, it is better predicted (41-45 m/s). These differences can be seen at Figure 3.24 which shows the experimental PIV data and Figure 3.25 of the predicted valve jet. The flow structure of the jet as well as the recirculation zone under the valve are well predicted.

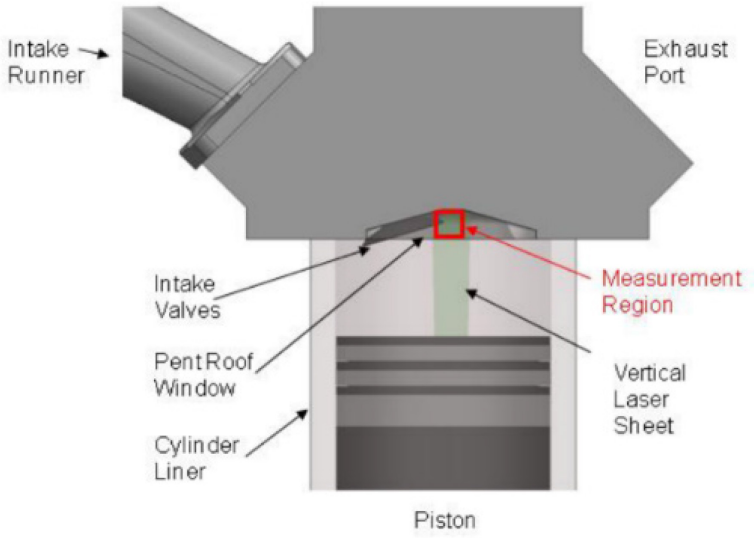


Figure 3.23 Region of pent roof measurements

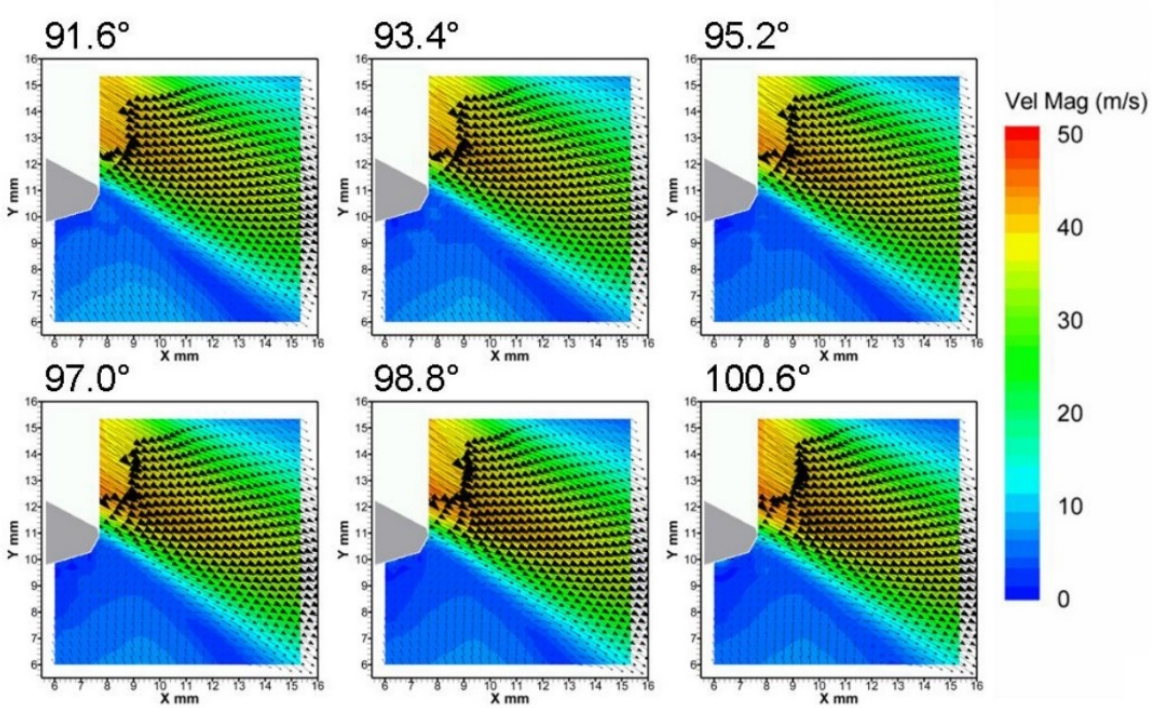


Figure 3.24 Experimental mean velocity of the valve jet at the mid-valve plane

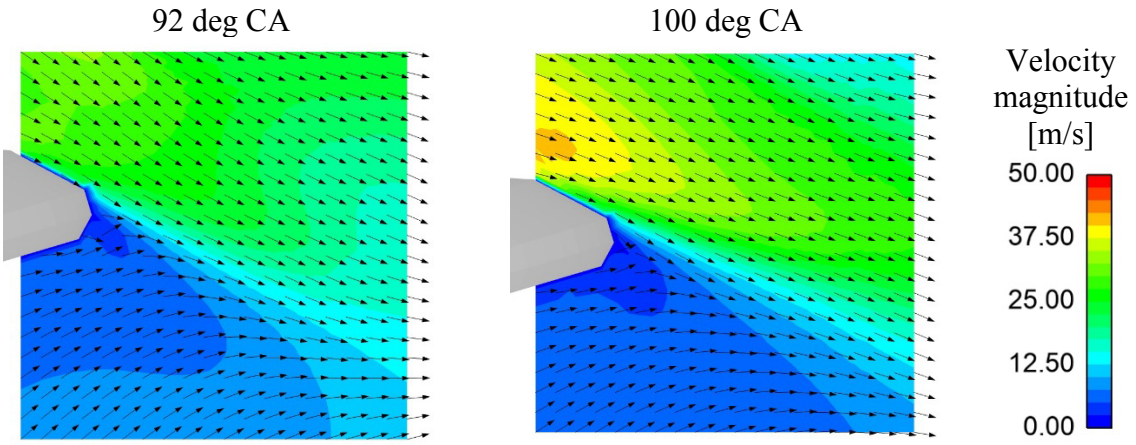
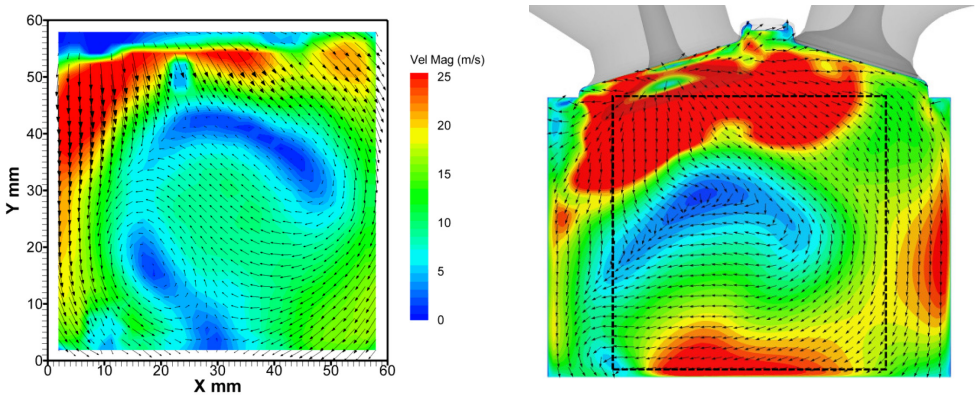


Figure 3.25 Numerical mean velocity of the valve jet at the mid-valve plane

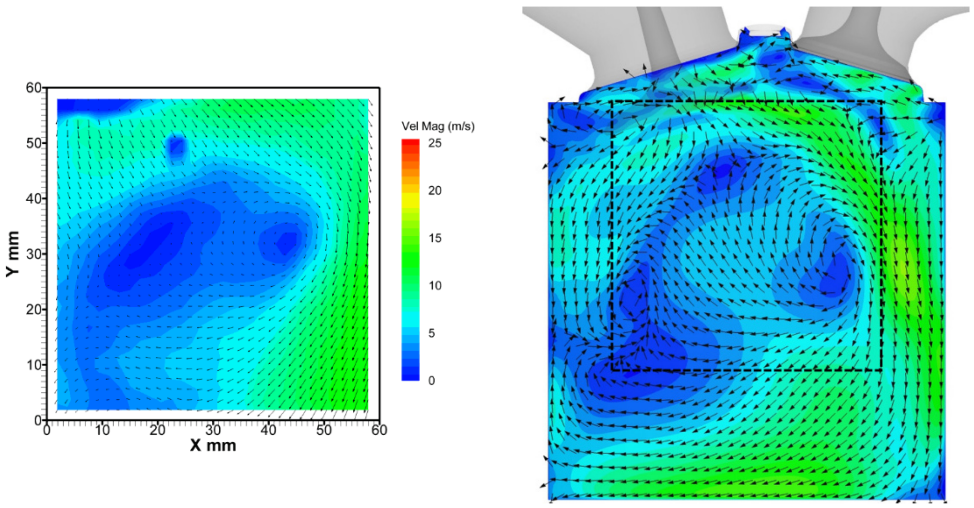
Moreover, at this stage of the cycle, available in-cylinder PIV data at a plane cutting through the bore centreline were compared against CFD data. More specifically, Figure 3.26 shows the numerical and measured velocity fields at three specific crank angles. It has to be noted here that for the PIV plot at 100 deg CA after TDC the velocities are capped at 25 m/s and it is difficult to estimate the maximum velocity near the intake valve at the top left of the figure. Nevertheless, it is evident that whilst the bulk air motion is qualitatively predicted with a weak clockwise tumble, the velocity magnitude is over-predicted. This is most probably due to the miss-prediction of the wave of the velocity magnitude in the intake runner. In addition, this

over-prediction may be due to the high cycle to cycle variation of the intake runner, valve jet and in-cylinder flow of the engine which makes the numerical prediction more difficult with RANS models. At mid-intake stroke when the valve jet is weaker, the velocity magnitude as well as the flow structure is better predicted. The tumble motion as seen in the PIV measurements is also predicted by the model, however some details of the flow such as the recirculation zones are not at the exact location of the experiment. During the compression stroke there is no influence of the valve jet on the in-cylinder air motion and the flow field is accurately captured and the velocity magnitude is well predicted. The flow motion with the upward direction towards the intake valve is well predicted. A difference was seen near the piston crown where the velocities are around 8-9 m/s while the in the PIV data the velocity is about 5 m/s. At this crank angle and at 1500 RPM, the piston velocity is about 7 m/s indicating that the experimental data may under-predict the velocity at that region. This gives confidence on the predicted in-cylinder conditions later on at the compression stroke, when the combustion is taking place.

100 deg CA



154 deg CA



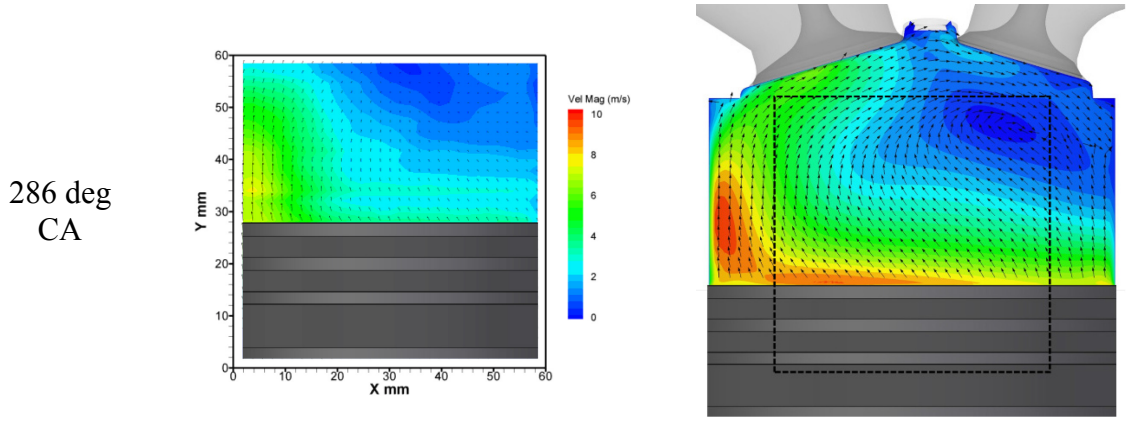
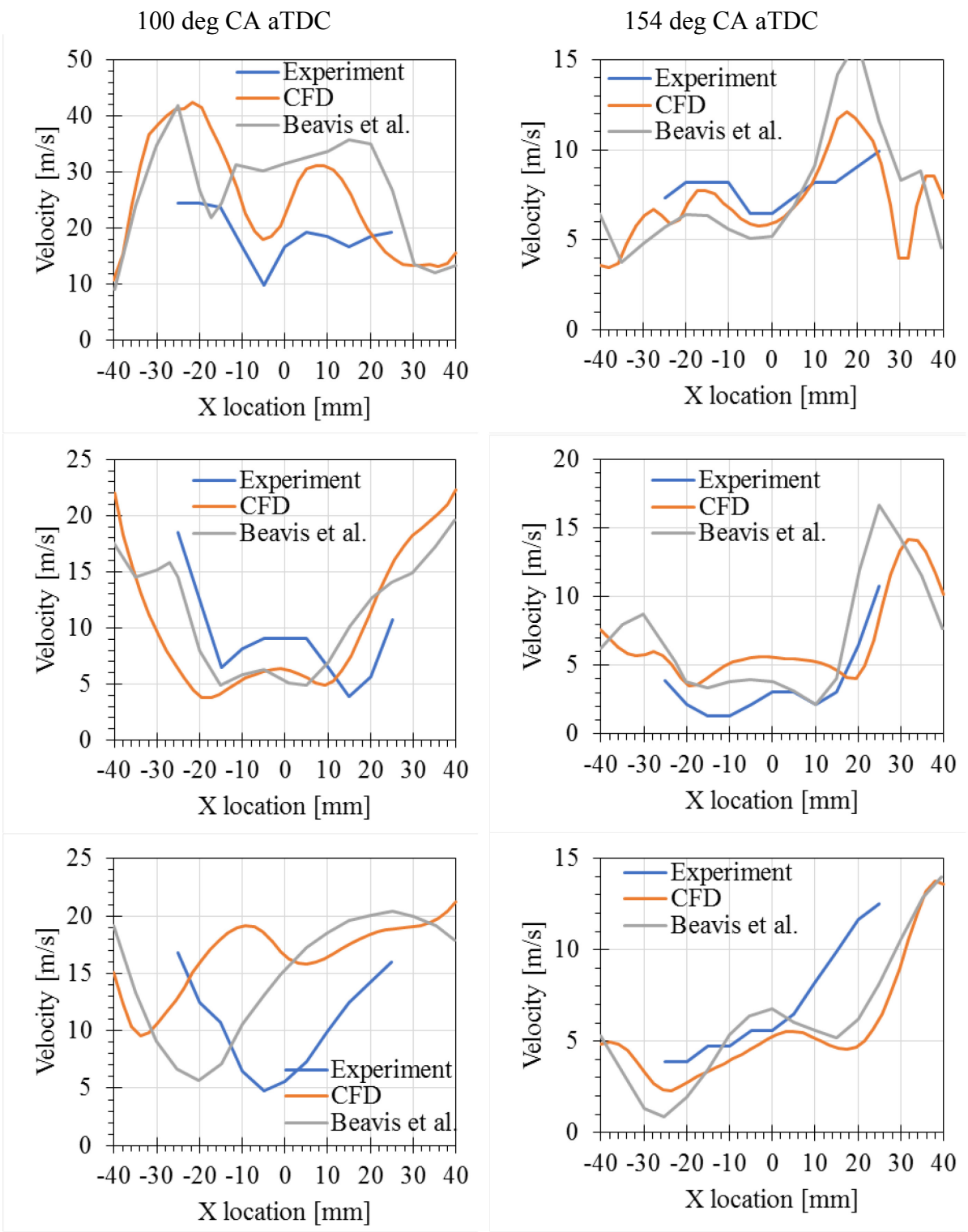


Figure 3.26 Comparison of experimental PIV data and numerical results of the velocity field for specific crank angles

To quantitatively compare the CFD velocity magnitude against the experimental measurements, the PIV maps from Figure 3.26 were imported into MATLAB and the pixels' RGB values were extracted for specific locations and translated into velocity magnitude by comparing them with the velocity legend of each map. The locations in the Y direction were 8 mm, 28 mm and 48 mm below the head gasket which translated to 50 mm, 30 mm and 10 mm in the PIV map. In the x direction, the location x=0 mm denotes the bore centreline which is the 30 mm point in the PIV maps. Similar approach was followed by Beavis *et al.* (2017). As it can be seen in Figure 3.27, at 100 deg CA a TDC and y=48 mm, the velocity magnitude is over-predicted by the CFD, however, the PIV map is capped at 25 m/s which did not allow to estimate the maximum velocity magnitude. Nevertheless, the trend of the experiment where the velocity drops near the centreline and increases in both negative and positive x location is also captured by the CFD. Similarly, at y=28 mm the "W" behaviour of the velocity in the experiment is as well predicted by the model. The biggest difference at this crank angle was seen at the location y=8 mm where the strong tumble of the CFD is dominating the flow structure and over-predicts the velocity. At mid-intake stroke (154 deg CA aTDC), the simulation was in a better agreement qualitatively and quantitatively with the PIV data. The velocity magnitude and the trend were close to the experiments for the location y=48 mm. For y=28 mm, the trend is the same but the velocity is over predicted. At the location y=8 mm the trend is similar and also the velocity magnitude is in a good agreement, especially for the negative x locations. Lastly, during compression at 286 deg CA aTDC, the CFD velocity magnitude as well as the trend is in a very good agreement with the PIV data. Similar over-predictions were seen in the study of Beavis *et al.* (2017). There are some differences between

the two studies such as the plenum which was included in that work, the valve profile tuning process, the boundary conditions and the grid of the model.



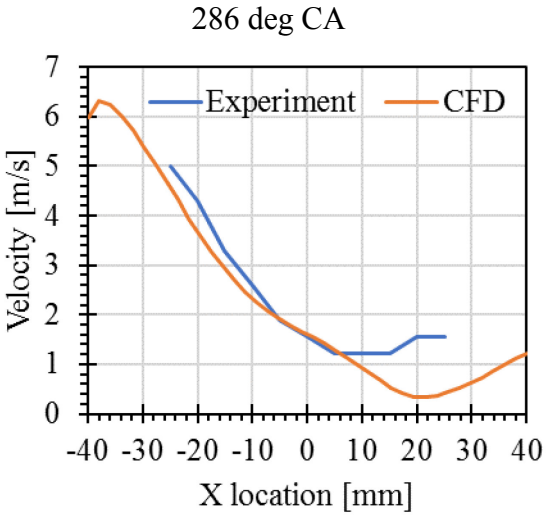


Figure 3.27 Velocity magnitude along x-axis at three different z-axis locations and three different crank angles. First row z=-8 mm, second row z=-28 mm, third row z=-48 mm. Data from current study, PIV and Beavis et al. (2017)

To conclude, the numerical results were compared against PIV data of the intake runner, the valve jet at the pent roof window and the in-cylinder flow. At the intake runner, the flow field dynamics with two maxima and two minima were predicted quantitatively but with some hysteresis. This can be an effect of the constant pressure boundary condition as opposed to a real engine's intake pressure which is a time dependent oscillation. Moreover, the valve timing of the real engine could be offset by some degrees which could affect the hysteresis observed at the intake runner. A finer tuning in the model's valve timings may be needed, however, this should had to be done in conjunction with accurate boundary conditions and high computational power. Moving to the valve jet, the recirculation zone under the valve is well predicted, and the fast decay of the velocity is well predicted, nevertheless, the velocities are either slightly over or under-predicted due to the hysteresis that was discussed before. The simulation showed a variation from 30 to 42 m/s in a window of 8 deg CA whilst the experiment did not show variations, with the velocity to be around 40 m/s. For this reason, the in-cylinder velocity field was over-predicted during the early intake process but the bulk air motion is in agreement with the tumble observed with the PIV method. At mid-intake, the velocity magnitude and the flow structures were better predicted. During the compression, when the in-cylinder flow is not affected by the valve jet, the velocity field and the air motion is in a good agreement with the optical data and this gives confidence on predicting the conditions at the moment of combustion. It has to be mentioned that this validation study was conducted with the absence of detailed data that could be used as boundary conditions and the valve profiles had to be derived from theoretical cam profiles and adjusted according to the literature and the

experimental results. Moreover, the results of the experiment showed high cycle to cycle variability, which may have affected the average of PIV data. Thus, the CFD code could predict the intake and compression strokes of a direct injection, spark engine, with all the limitations that were discussed above.

3.5. Steady state port flow simulations

In order to investigate further the reasons of the in-cylinder and intake runner velocity over-prediction, steady state port flow simulations of the AJ133 engine head were run. Available experimental data of the flow coefficient (C_f) were compared with the numerical results. It has to be mentioned here that the only available data was a graph of the flow coefficient for three manufactured engine heads named head 1, head 3 and head 5. For the study, the heads with the minimum (head 3) and maximum (head 5) flow coefficients were used. Due to the absence of the rest of the required information, the boundary conditions for the simulations had to be assumed according to similar experiments. These conditions are summarised in Table 3.5. The calculation for the C_f were based on the equation 3.1:

$$C_f = \frac{\dot{m}}{Area \cdot V_0 \cdot \rho} \tag{3.1}$$

Where,

$$Area = \pi \frac{d^2}{4} \tag{3.2}$$

$$V_0 = \sqrt{\frac{2(P_{in} - P_{out})}{\rho}} \tag{3.3}$$

$$\rho = \frac{P_{in}}{R \cdot T_{in}} \tag{3.4}$$

and d is the diameter of the valve head. The graphs of the flow bench simulations follow the industry standard in which at the x-axis the ratio $Lift/Valve\ diameter$ is plotted. To facilitate the reader the conversion from Lift to L/D is shown in Table 3.6.

P_{in} (gauge)	5000 Pa
T_{in}	288K
P_{out} (gauge)	0 Pa
R	287 J/(kg K)

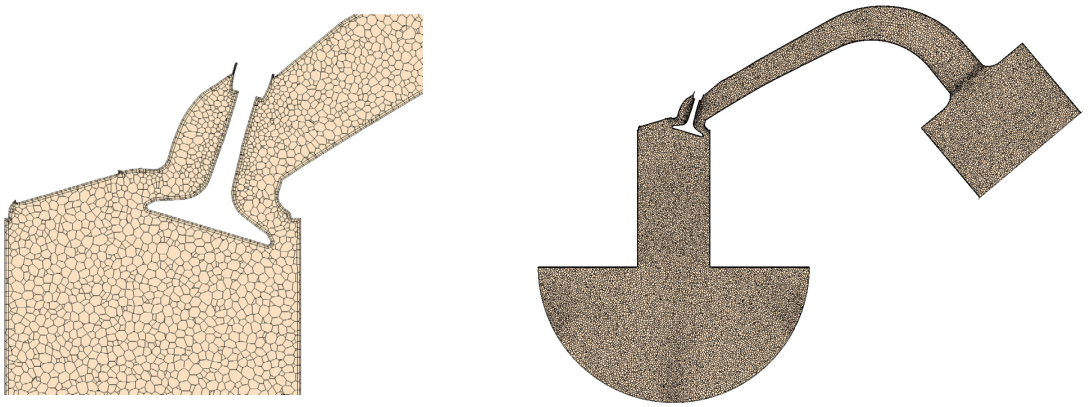
Table 3.5 Boundary conditions for the steady state port flow simulations

Lift [mm]	1.75	3.5	5.25	7	8.75	10
L/D	0.0515	0.103	0.1545	0.206	0.2575	0.2943

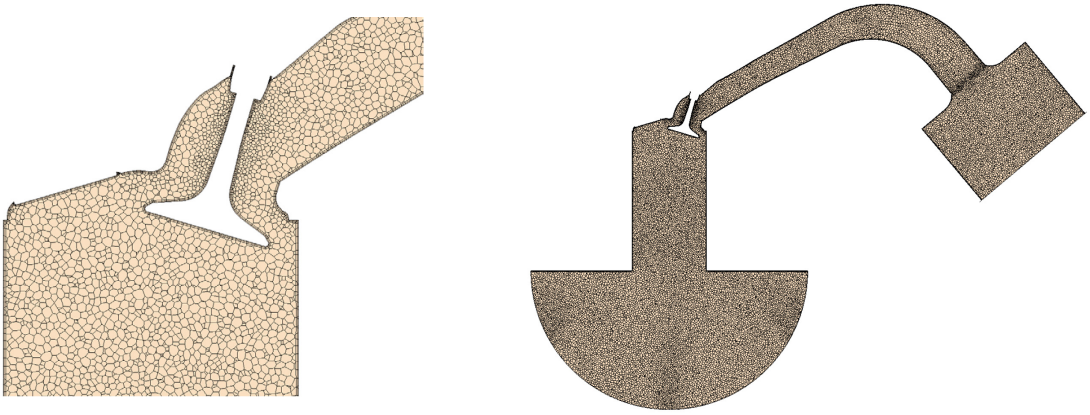
Table 3.6 Valve lift and L/D equivalence

Various researchers have suggested different approaches for these simulations. Most commonly, the choice of turbulence model and cell type is among them (Godrie and Zellat 1994, Algieri *et al.* 2007, Ramajo and Nigro 2010, Binjuwair and Ibrahim 2013, Masi *et al.* 2015). Firstly, according to the literature, polyhedral is a cell type that can substitute tetrahedral grids and their disadvantage of decreasing the accuracy of numerical schemes (Masi *et al.* 2015). A grid dependence study was conducted for three polyhedral meshes (Figure 3.28) ranging from 850 thousand cells to 3 million cells using the k-ε RNG turbulence model. The boundary conditions were the same as described above. The results in Figure 3.29 showed that around 1.6 million cells independence can be reached, which is in an agreement with other studies (Ramajo and Nigro 2010, Binjuwair and Ibrahim 2013).

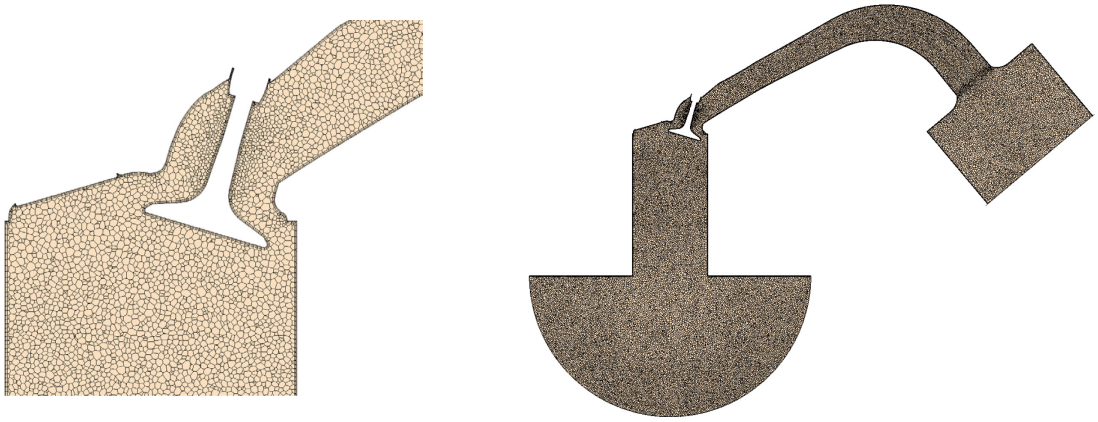
Secondly, a mesh was created using hexahedral cells (Figure 3.28) in order to replicate the mesh of the dynamic model created by es-ice. The base size of the cell was 2mm and was applied to the areas of the inlet and outlet boundaries. Closer to the area of interest (part of the intake runner and cylinder) was reduced to 1mm and around the valve was further reduced at 0.5mm as it is in the dynamic model of the engine that was presented earlier. The total number of cells was around 2.6 million which was acceptable for grid independence. The k-ε RNG model was used, as it was used for the validation of the in-cylinder flow in the dynamic model and the results of this mesh were the same as the results of the polyhedral mesh when the same turbulence model was used. Thus, it can be said that the results of the polyhedral mesh can be useful for the hexahedral mesh as well.



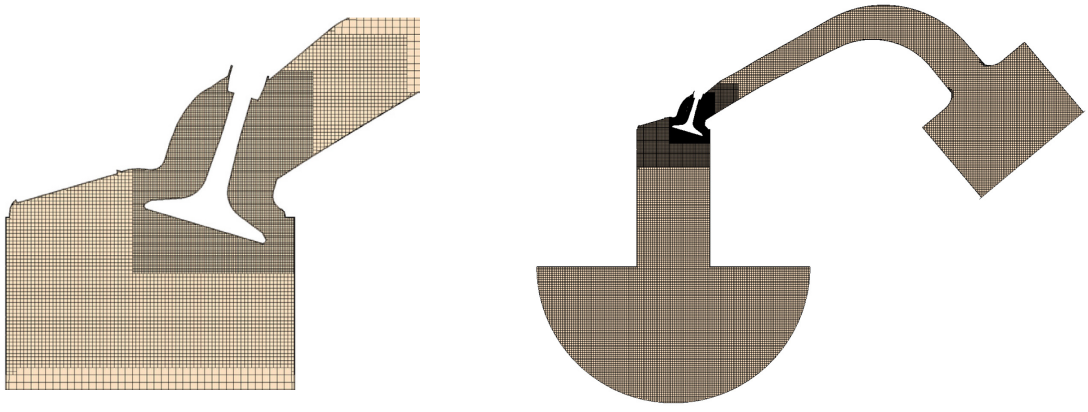
850 thousand cells



1.6 million cells



3 million cells



2.6 million cells

Figure 3.28 Polyhedral and hexahedral grids of the port flow model

With this mesh, four different turbulence models (standard k-ε, k-ε RNG, standard k-ω and k-ω SST) that were used in the literature for port flow simulations were tested. It was observed (Figure 3.30) that at very low valve lift, all the models predicted very similar flow coefficients. At lifts around 3-5mm, k-ε RNG over-predicted the C_f with a maximum difference of 14% at 3.5mm, whilst the rest of the models gave results closer to the experiment. This can be a reason of the over-prediction of the velocity at these lifts. At higher lifts, the k-ε RNG model is in a very good agreement with the experiments but the rest of the models under-predict the flow coefficient with a maximum difference of 19% given by the standard k-ω. A pattern from the literature was identified for intake port flow simulations, which was the over-prediction of the flow coefficient at medium valve lifts (~3 mm - 5 mm). However, this needs attention because of the different port geometries that may make one turbulence model more suitable due to the flow behaviour in the valve region.

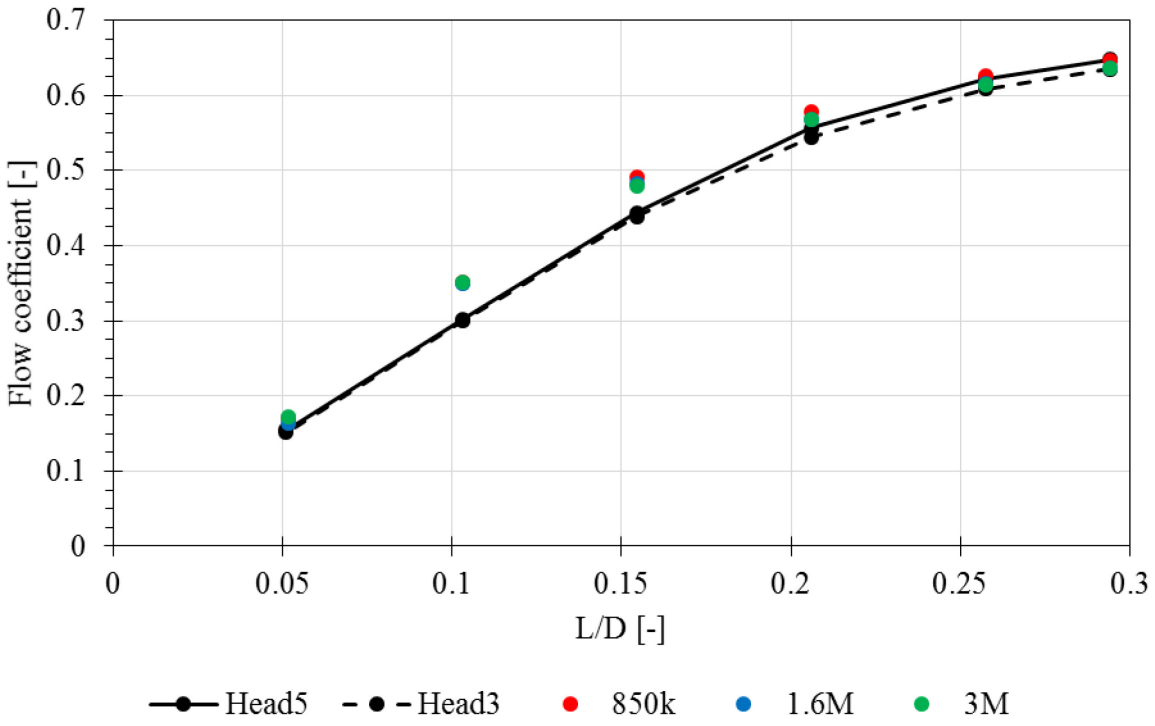


Figure 3.29 Grid independence study for port flow simulation and comparison with experimental data of the AJ133 engine head

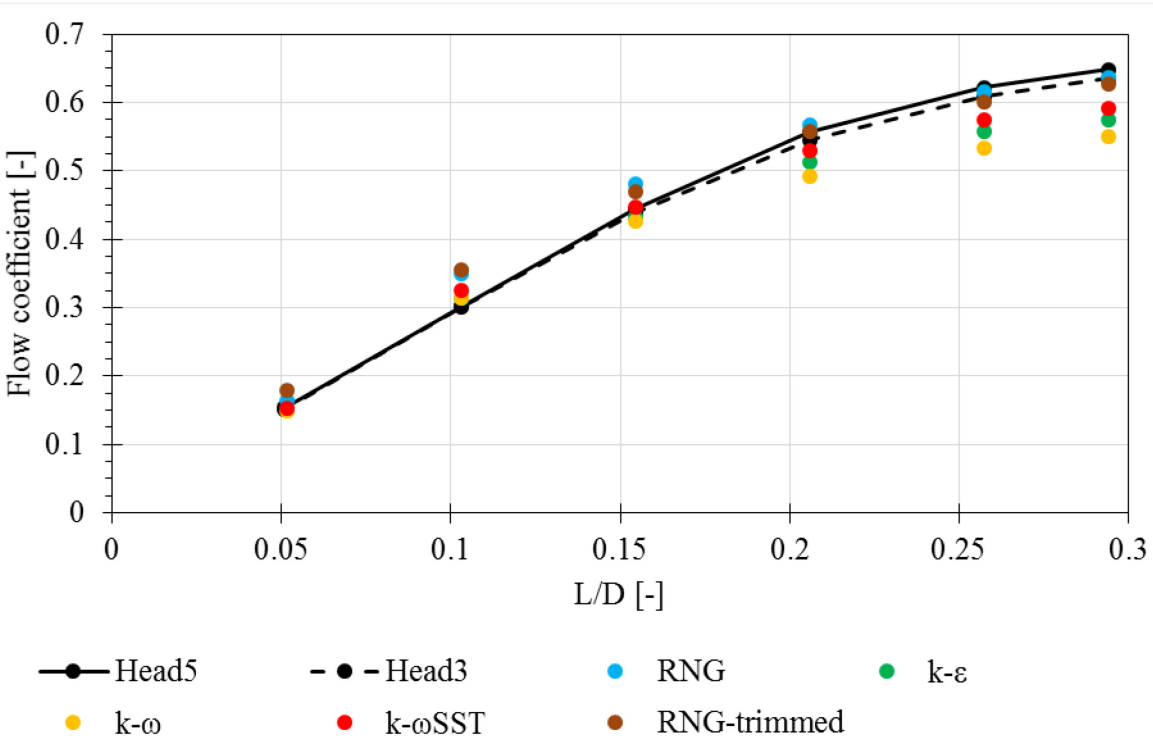


Figure 3.30 Experimental and numerical results of the AJ133 flow coefficient for four different turbulence models and two different types of grid

3.6. Evaluation of turbulence models

The standard k-ε model and its versions are widely used and validated for a range of industrial applications. For engine simulations, either standard k-ε or k-ε RNG model is used in the literature. In this study, the performance on engine simulations of these two models was investigated by comparing them against the data of the optical engine (AJ133). Another two commonly used models for CFD simulations, the standard k-ω and its derivative, k-ω SST were also tested for in-cylinder flows. The last two models were tested for completeness as they were used for the port flow simulations.

Firstly, it was observed that all four models did not have any impact on general quantities such as in-cylinder pressure and trapped mass. This can be seen on Figure 3.31 which shows the time dependent in-cylinder trapped mass. Although it was expected that the models would have an effect on the flow field this was not the case for the intake runner. As it can be seen at Figure 3.32, the velocity is the same for all four models during the intake stroke. There are some small discrepancies from 20 degrees before IVC until IVC due to the flow from the cylinder to the port at low valve lifts. However, the in-cylinder air motion was highly affected as it can be seen at Figure 3.33. because of the different predictions on the valve jet, the flow separation from

the valve and the valve seat as well as the bulk tumble motion. At 100 deg CA, standard k-ε and k-ε RNG produced similar flow fields and closer to the PIV data compared to the k-ω models. Moreover, k-ε RNG produced higher velocities with the zone of the high velocities to be wider near the valve and the recirculation zone in the middle of the cylinder is bigger. The k-ω models produced lower velocities in the zone near and below the valves compared to the k-ε models and the flow field in this area is very similar in both of the k-ω models. This behaviour can be explained from the results of the port flow simulations where RNG was predicting higher flow coefficient than the other models. The air motion in the rest of the cylinder is noticably different, especially for standard k-ω which can be described as chaotic, closer to a single cycle rather than time-averaged. k-ω SST somehow, reproduces the in-cylinder flow motion with the recirculation zone in the middle of the plot but not as close to the PIV as the k-ε. This behaviour can be explained based on the theoretical background of the SST model which is a blend of standard k-ε and k-ω.

During compression, the main vortical structure moves towards the exhaust valves and a uniform clockwise motion is observed for all four models, however, both k-ω models produce higher velocities. In addition to this, for the two aformentioned models the vortical region is smaller and differences on its structure can be observed. Again, the k-ε RNG produced a flow field closer to those of the PIV.

To sum up, during the intake stroke, standard k-ε and k-ε RNG produced very similar flow fields and closer to the experiment. The standard k-ω model predicted different flow filed from the PIV and the k-ω SST, which is a blend of standard k-ε and k-ω, produced results that can be described as in between the two models. During compression, standard k-ε and k-ε RNG were closer to the experiment but the differences between them and the k-ω models were smaller, yet noticeable. A reason for this behaviour is the difference between the valve flows and the flow separation that each model predicts. When the in-cylinder flow was not affected by the valve jet, the difference in the flow field was decreased. The conclusion of this study was that k-e RNG was more appropriate for this engine's simulations as it was producing results closer to the experiment for both intake and compression stroke and this model was used for the rest of this work.

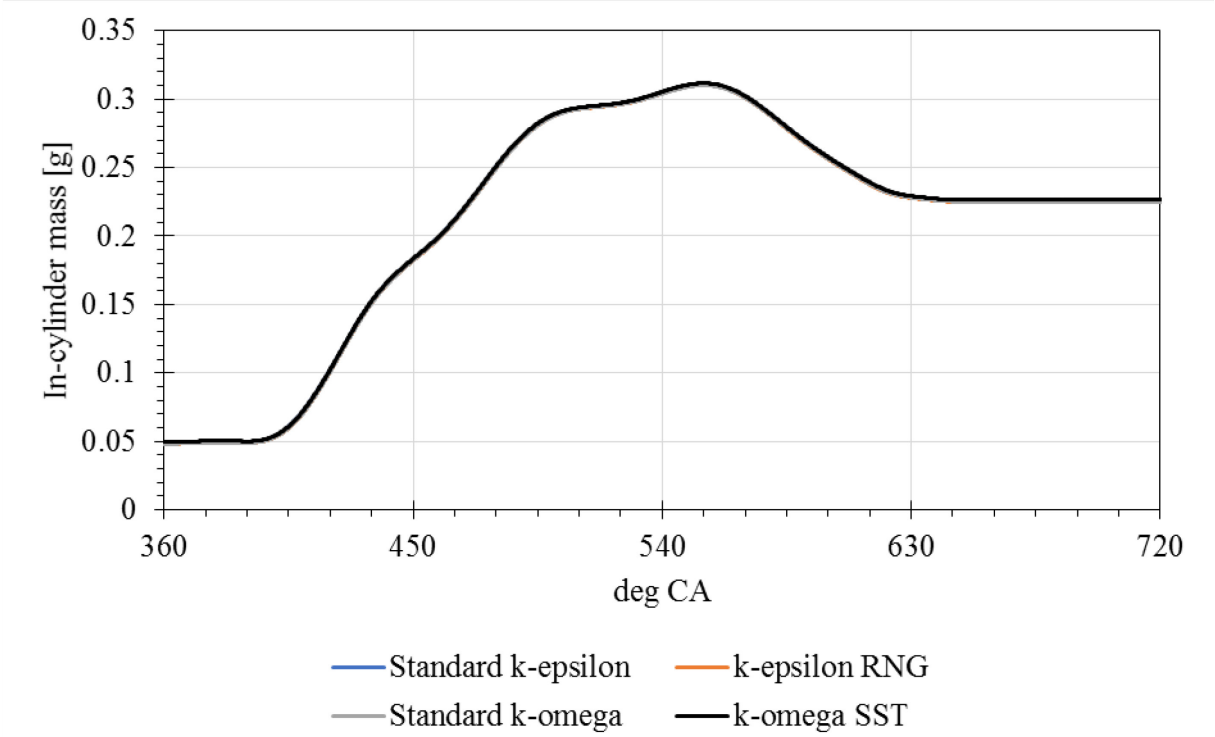


Figure 3.31 In-cylinder trapped mass for the four turbulence models

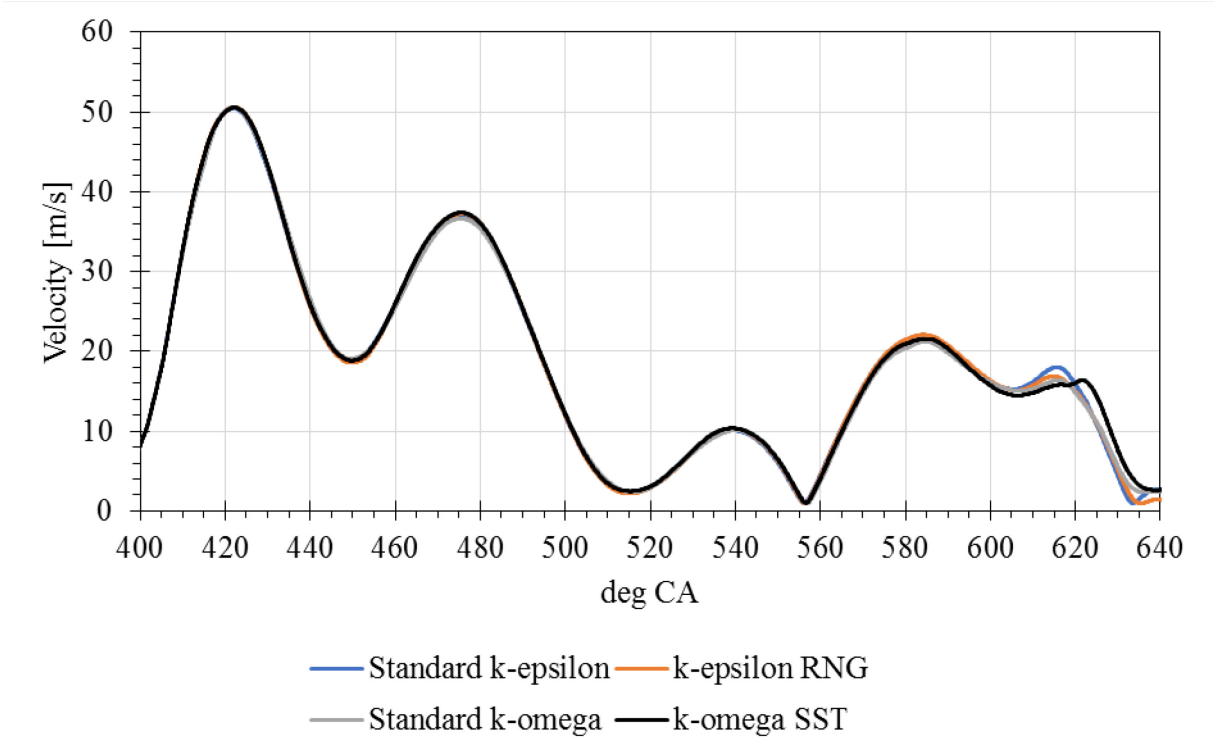
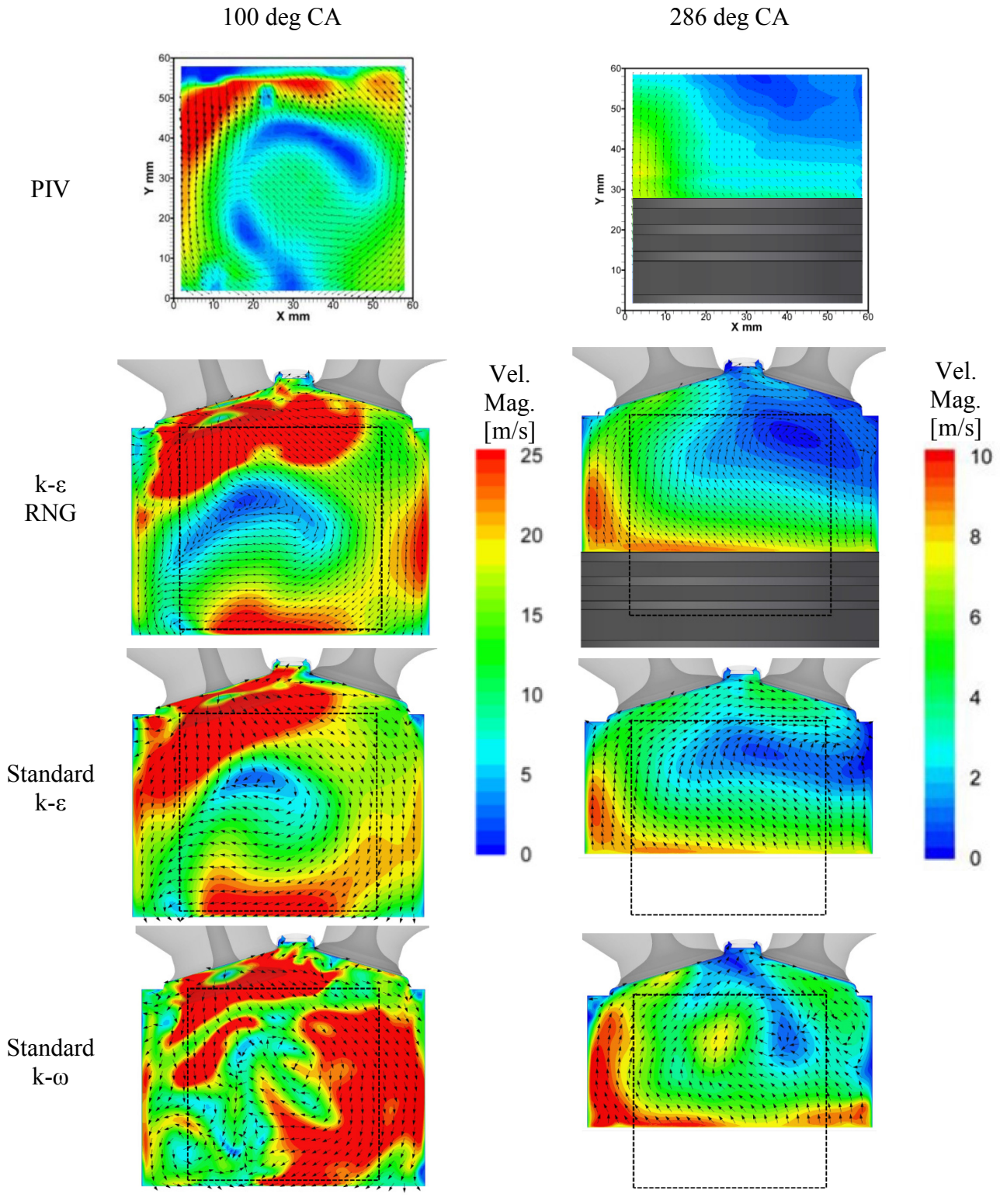


Figure 3.32 Velocity magnitude at the intake runner for the four different turbulence models


100 deg CA
286 deg CA
PIV
k-ε RNG
Standard k-ε
Standard k-ω
Y mm
X mm
Vel. Mag. [m/s]
25
20
15
10
5
0
10
8
6
4
2
0

k-ω SST

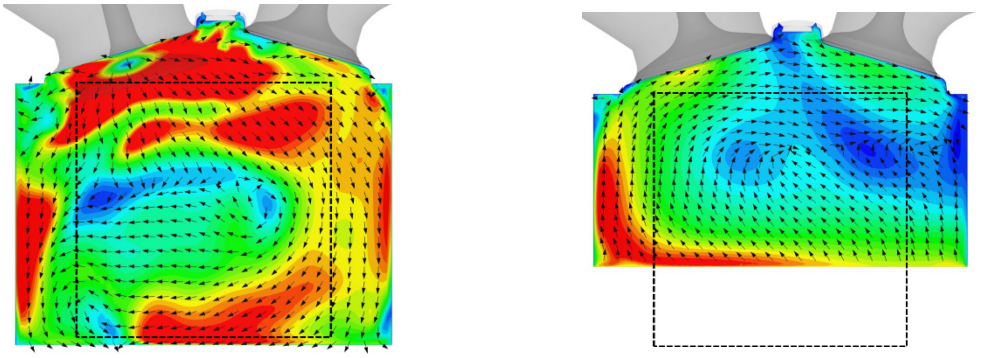


Figure 3.33 Comparison between the PIV data and the flow field from the four turbulence models

3.7. Engine Heat flux

Heat transfer affects the efficiency of the engine with higher heat fluxes to the walls will result in lower work transferred to the piston. Moreover, heat transfer is related to thermal stresses and fatigue cracking. Thus, it is important to accurately predict the heat flux during the full cycle as this is linked to engine performance.

The heat transfer from the gas to the engine walls was validated against experimental measurements (Serras-Pereira *et al.* 2012) of heat flux. The wall heat transfer was dealt with the Angelberger model (Angelberger *et al.* 1997) using the equation 2.51. The AJ133 engine was motored at 1500 RPM at two loads (0.5 bar and 1.0 bar intake pressure). The intake air and wall temperatures were 20°C for both loads as reported in the experimental study. Due to the lack of information, the exhaust temperature was assumed to be slightly higher, at 28°C and the exhaust pressure at 1 bar again for both cases.

For the CFD results shown in Figures 3.34 and 3.35, the heat flux was averaged over the liner (black line) and from a circular area of 6.4 mm diameter (heat flux sensor face) at the position of the heat flux sensor (17 mm below the head gasket) (orange line). Note that between 310°CA and 410°CA, simulated heat flux at the sensor location is not shown because the upward and downward motion of the piston leads to the sensor face not being exposed to the in-cylinder gas. In the same context, the measurements have also been affected by the piston's motion as the sensor's face resides within the crevice volume within this crank angle window.

The CFD results were in a good agreement quantitatively and qualitatively with the experiment for the whole cycle and some detailed experimental behaviour could also be captured. First of all, the small drop in the heat flux signal at the beginning of the intake cycle was predicted, due to the negative valve overlap which resulted in a small vacuum before IVO. After that, for both CFD and experiments, the heat flux was almost zero due to the marginal temperature difference

between gas and liner. During compression, the gas temperature raised which resulted in increased heat flux which was well predicted for both loads. During expansion and before EVO, the heat flux dropped slightly below zero for both loads. At EVO, the simulations predicted an increase in heat flux, higher in magnitude for the 0.5bar load. This is because just before EVO, the in-cylinder pressure is below the exhaust pressure and after the opening of the valve due to the rapid increase in pressure, the temperature also rises, well above the liner's temperature, which in turn results in increased heat flux. The pressure difference at EVO between the cylinder and the exhaust is smaller for the higher load and thus the increase in temperature is smaller.

Some minor differences can be seen between the heat flux averaged over the liner and over the sensor face. This is because the local flow at the area of the sensor face resulted in convective heat transfer slightly different than the averaged heat flux over the liner. However, the trends of heat flux for both the sensor area and the liner were the same.

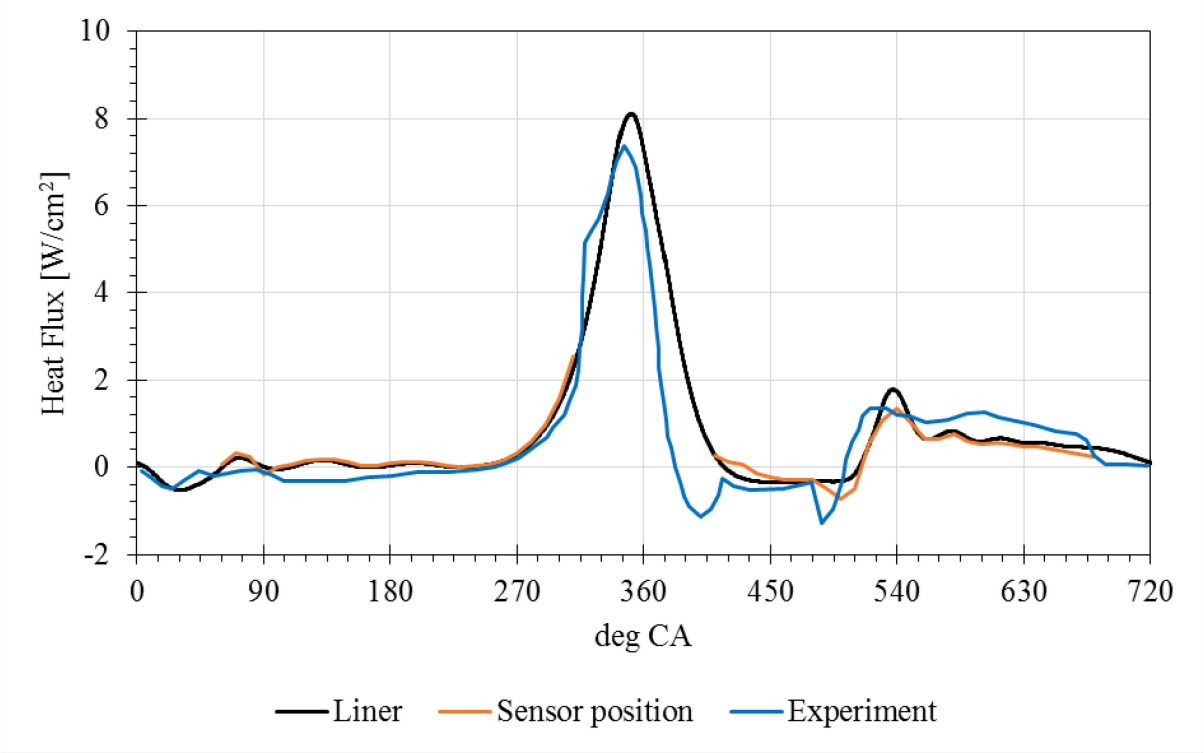


Figure 3.34 Heat flux at 0.5 bar intake pressure, 1500 RPM (AJ133)

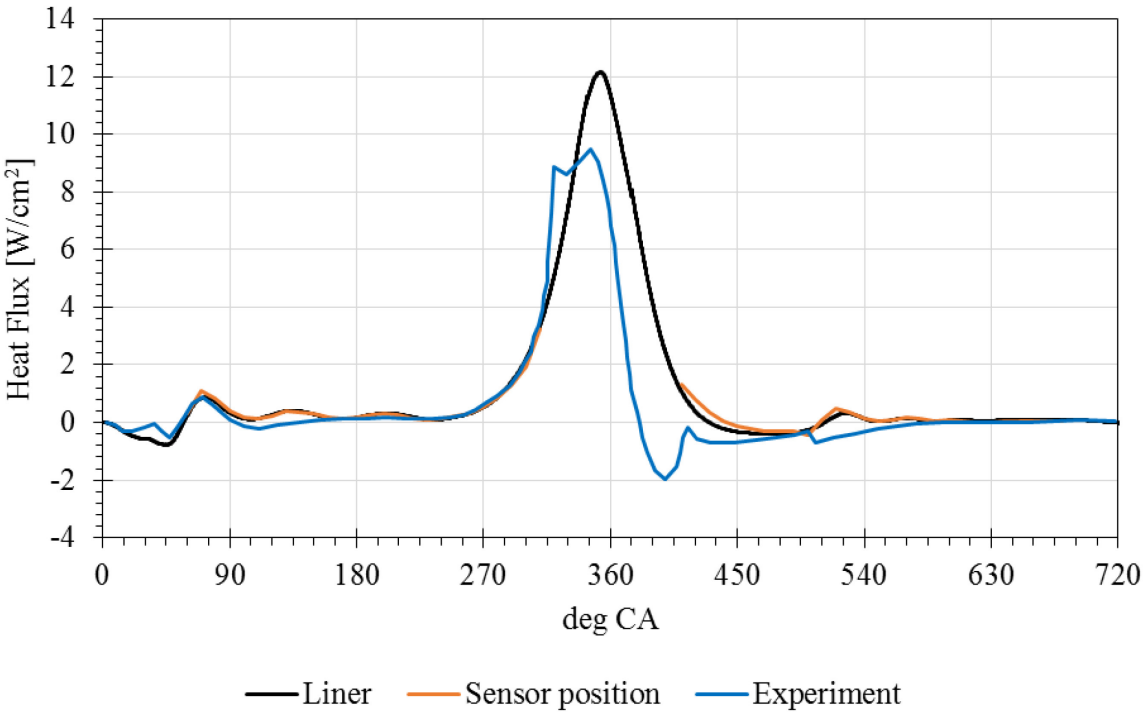


Figure 3.35 Heat flux at 1 bar intake pressure, 1500 RPM (AJ133)

3.8. Validation of fuel injection

3.8.1. Sub-cooled fuel injection – quiescent chamber

A validation study of the sub-cooled spray modelling with the Lagrangian multi-phase treatment was carried out in a quiescent environment and in the dynamic model of the AJ133 optical engine. Firstly, experimental measurements of spray tip penetration, droplet size and SMD at a location 25 mm below the injector and spray formation in a quiescent chamber were compared to numerical results. A six-hole injector designed for the AJ133 engine was used for the experiments and the orientation and geometrical characteristics were applied to the CFD model.

The inner hole diameter of the injector was 0.2 mm (Butcher *et al.* 2015), the nominal spray plume cone angle was 15° and the spray pattern is showed at Figure 3.36. In the case of the static chamber, the injector was mounted at 19° to the vertical for optimised optical access (Aleiferis and van Romunde 2013). Detailed information of the injector can be found elsewhere (Serras-Pereira *et al.* 2007 and Serras-Pereira 2010). The simulated fuel was *iso*-Octane at 293K for 0.5 bar and 293K ambient pressure and temperature. At these conditions the fuel is considered to be out of the flash boiling region and thus, no flashing spray formulation was applied. For the simulations, the mean mass flow rate for 1 ms injection pulse was 2.3 g/s per

hole and it was taken from Butcher *et al.* (2015). The injection pressure for these experiments was 150 bar.

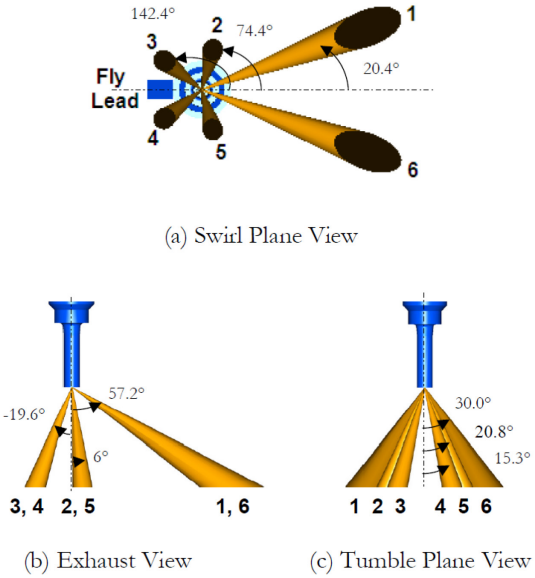


Figure 3.36 AJ133 six-hole injector spray pattern

Most of the work was carried out in a cubic domain of 80 mm each side and it was discretised using a Cartesian mesh of 1 mm size. The boundary conditions were an adiabatic wall on the top, where the injector is mounted, and the rest of the cube's sides were pressure boundaries. The location of each plume where the droplets were introduced in the domain was 1 mm downstream from the point in which all the six plumes cross each other. Figure 3.37 shows how this was applied on the injector of the AJ20 head, but this approach can be generalised for all the injectors in constant volume chamber and engine simulations. For the case of the constant volume chamber the locations of the six plumes in the domain can be seen in Figure 3.37, second row. The direction of each plume is the positive z-axis of each coordinate system. Due to the grid dependency of the collision model, the majority of the work was carried out using the geometric constrain proposed by Nordin (2001) and has been discussed in a previous chapter.

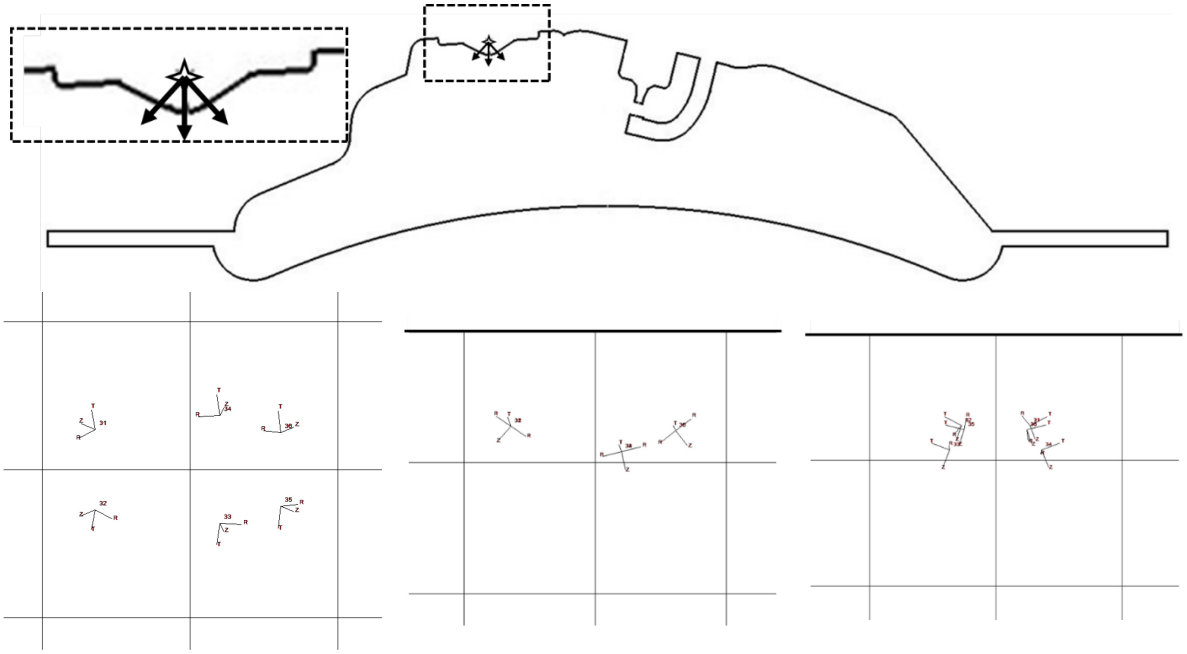


Figure 3.37 AJ20 detailed head geometry with zoom on the injector and how the six individual plumes were located in the grid of a constant volume domain.

As a base case, the blob method (Baumgarten 2006) was used to initialise the droplet size (primary break-up) at the nozzle exit. With this method, the initial diameter of each droplet is the same as the nozzle diameter, in this case 0.2 mm. To model the secondary droplet break-up, the Reitz-Diwakar model (Reitz and Diwakar 1986) was used which was the most common in the literature. For the base case the default values of the code were used. The mass flow rate for the blob method was constant at the nominal value of 2.3 g/s per plume. No time varying mass flow rate was applied because any transient phases would highly affect the Reitz-Diwakar droplet break-up model without being able to control it through time.

Following another method, the droplet size was initialised using the Rosin-Rammler distribution in order to take account any break up that may occur inside the nozzle due to cavitation or turbulence break up as described in the literature. The Reitz-Diwakar model was used again for secondary droplet break-up. For the Rosin-Rammler distribution two constants had to be defined, the q (shape parameter) and X (scale parameter). According to Lefebvre (2017) the q value lies between 1.5 and 4, thus it was set to 2.75. This also agrees with the work of S. Moon *et al.* (2007), Keller *et al.* (2015) Li *et al.* (2014). The X value was set to 22*10-6 after an iterative process which gave the best match against the experimental data (spray formation, penetration droplet size and SMD). In the work of Beavis *et al.* (2015) and

Banaeizadeh *et al.* (2013) the X value was in the range of 14 µm to 30 µm. In addition, the Rosin-Rammler distribution allowed to apply a time varying mass flow rate and injection velocity profile. While the time varying mass flow rate for this injector was not available, data of similar injectors at 100 bar and up to 200 bar injection pressure were analysed (Costa, M., *et al.* 2009; Postrioti *et al.* 2015; Gandhi and Meinhart 2009). First of all, it was observed that an initial ramp of increasing flow rate from zero up to the maximum flow rate exists. This ramp for all the injectors, irrespective of injection pressure, had a duration of about 0.11 ms. Secondly, different injectors had different behaviour at the end of this ramp. From the work of Postrioti *et al.* it was seen that for both injection pressures (100 bar and 200 bar) there was an overshoot of the mass flow rate which was about 1.6 times greater than the steady flow rate of the injection. From the work of Costa *et al.* it was seen that there was no overshoot for the 50 bar and 100 bar injection pressure and there was an overshoot of 1.25 times greater than the steady flow rate at 150 bar. The flow rate in the work of Gandhi and Meinhart 2009 did not show any overshoot at 100 bar which was the highest tested pressure. From all these, it was decided to apply an overshoot of about 1.35 times of the steady mass flow rate. Furthermore, the time from the overshoot to the steady mass flow rate was again about 0.11 ms and it was taken from the experiments. Lastly, this initial ramp and overshoot was observed with the same magnitude and duration irrespective of the duration of the total injection pulse. The mass flow rate per hole and the droplet velocity at the nozzle exit are shown in Figure 3.38.

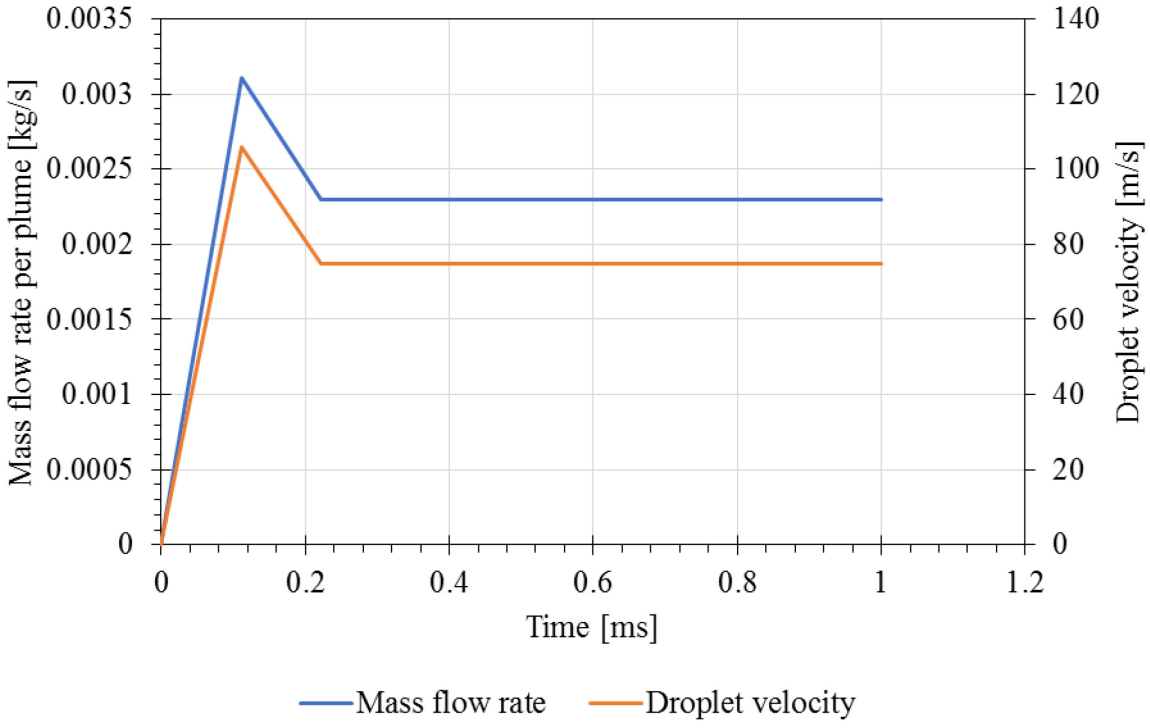


Figure 3.38 Mass flow rate and injection velocity for the case with the Rosin-Rammler distribution

Firstly, the spray shape of the simulations was compared against the experiments (Figure 3.39). The spray tip of the simulation with the default blob method was flat while in the experiment had a sharper end. The base case over-predicted the penetration 400 μs After Start Of Injection (ASOI) with an increasing rate as the time evolved. Moreover, the droplet sizes (minimum droplet diameter of 50 μm and SMD of 100 μm) was over-predicted due to low break up rate imposed by the default parameters of the model. The experiments reported droplet diameters of about 10-12 μm and SMD at the range of 11-15μm (Aleiferis and Van Romunde 2013 and Butcher *et al.* 2015). Because of the above reasons, the four constants of the break up model were reduced in order to achieve spray penetration and droplet sizes close to the experiment. After an iterative process, the final values of the constants for the optimised case which had an acceptable spray shape, penetration and droplet size can be seen in Table 3.7. A spray plume with a sharper tip was generated with both the optimised blob method and the Rosin-Rammler distribution. Also, the fishbone type core with smaller droplets at the edges of the plume was also predicted.

	Initial droplet diameter	**We (bag)**	**We (Strip)**	**Te (Bag)**	**Te (Strip)**
Base	200 μm	6	0.5	3.1415	20
Optimised	200 μm	1.8	0.1	1.5	6

Table 3.7 Initial droplet size and Reitz break-up constants for the baseline and optimised cases

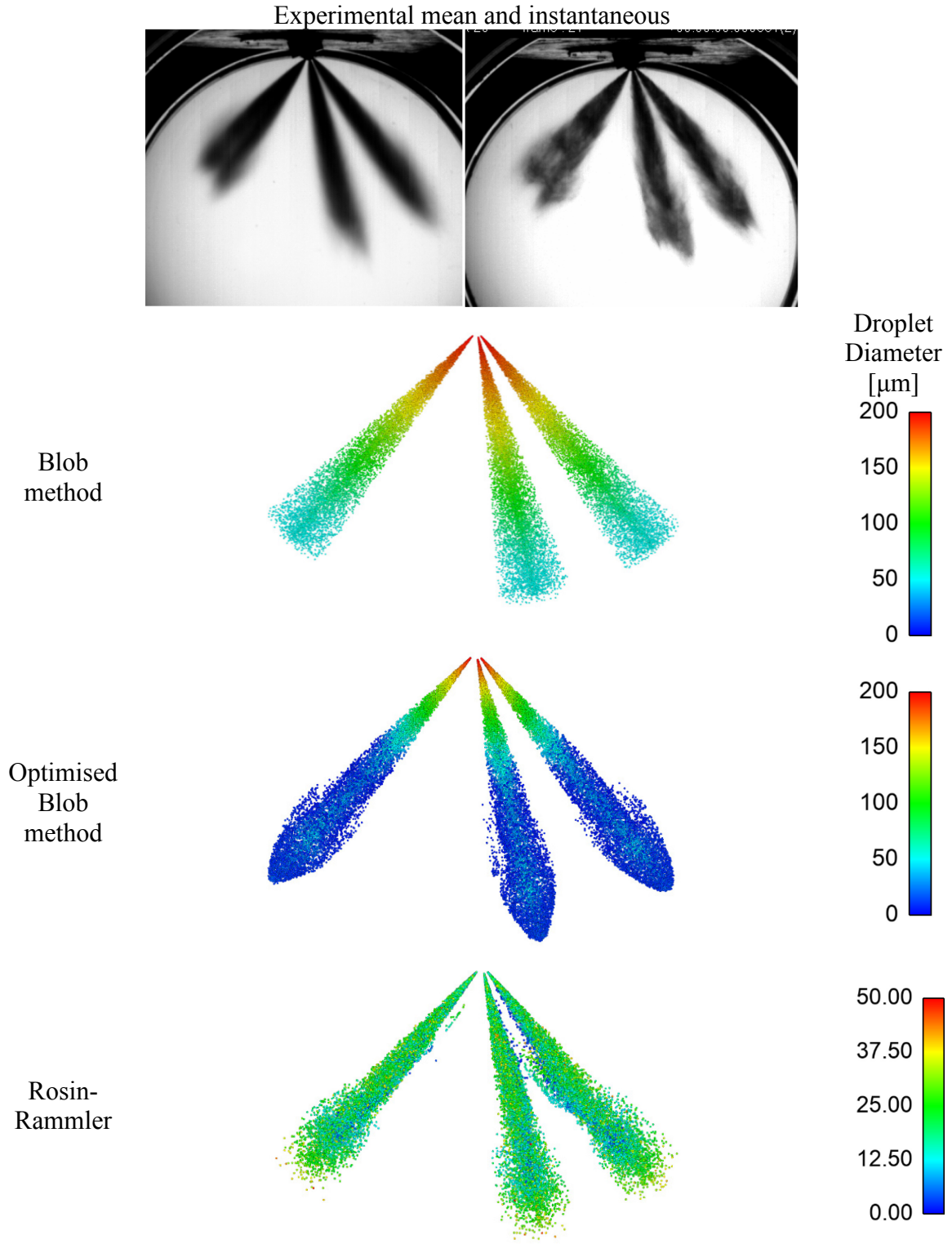


Figure 3.39 Spray formation and droplet diameter 0.78 ms after star of injection. Fuel: iso-Octane, T=20°C, P∞=0.5bar. Experiments from Van Romunde et al. (2007)

The penetration of the optimised blob method and of the case with Rosin-Rammler distribution can be seen in Figure 3.40. Overall, both of the cases are in a good agreement with the experiment and are following the trend of the increasing penetration as the time evolves. The

maximum difference between numerical and experimental penetration was about 10% at the period of 555 μs to 666 μs which was observed with the blob method. For the rest of the spray event, the penetration of the blob method was within the standard deviation of the experiment. The penetration of the spray with the Rosin-Rammler distribution was always within the standard deviation and the maximum difference from the mean experimental value was 4% showing a better agreement than the blob method.

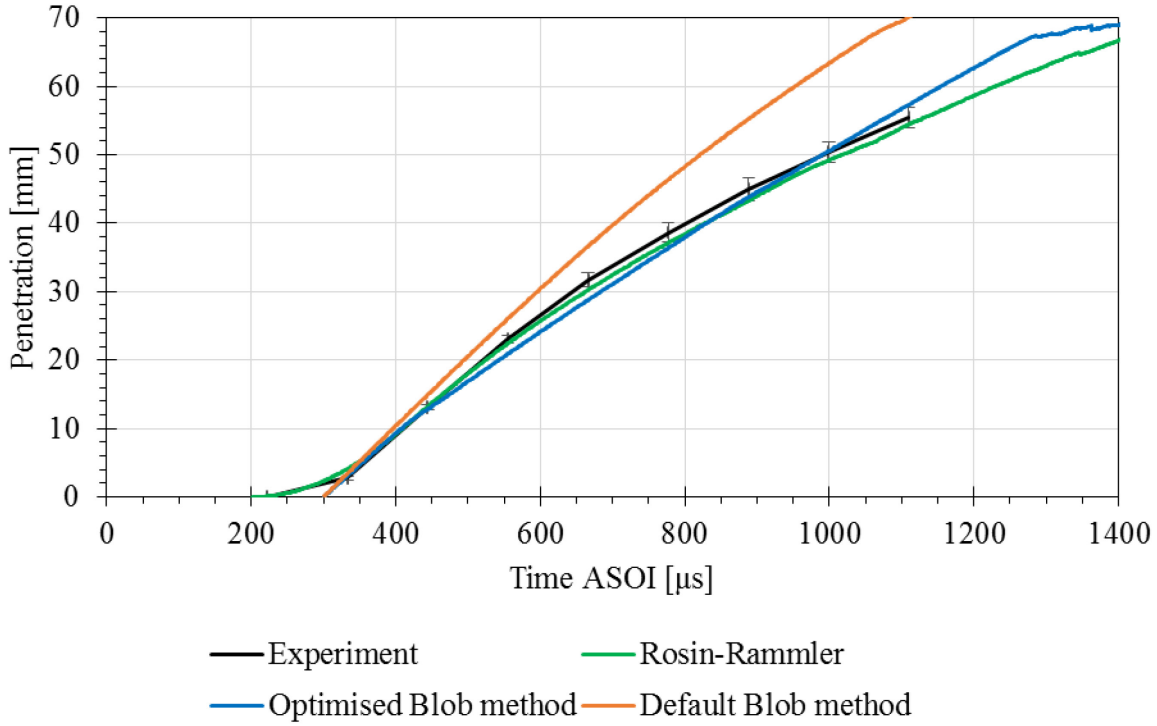


Figure 3.40 Experimental and numerical spray penetration of iso-Octane at 0.5 bar ambient pressure and 293K fuel temperature

The spray plume tip velocity was also calculated (Figure 3.41), using a central-differencing scheme and compared against the experimental data calculated in the same way Aleiferis and van Romunde (2013). The simulations of both methods are in a good agreement with the experiment and they predict accurately the initial acceleration of the spray up to 444 μs ASOI. After that, the spray tip is decelerated but the rate of deceleration of the spray with the blob method is lower while the spray with the Rosin-Rammler distribution is closer to the experimental values. This indicates better predictions of spray velocity and spray penetration for injection duration greater than 1 ms when using this method. This is very important in engine simulations of high load where the injection duration is greater than 1 ms.

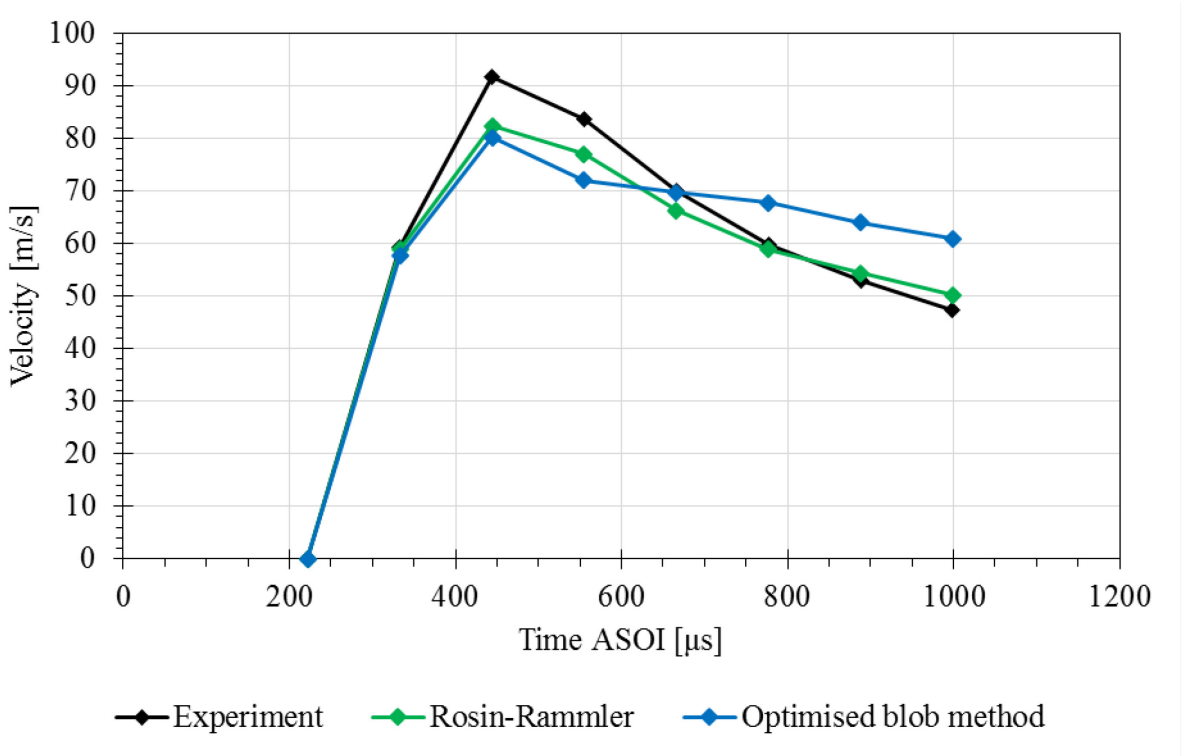


Figure 3.41 Experimental and numerical spray tip velocity

In addition, the droplet sizes predicted by the simulations were compared against Phase Doppler Anemometry (PDA) measurements (Aleiferis and Van Romunde 2013 and Butcher *et al.* 2015) which includes Arithmetic Mean Diameter (D10), SMD (D32) and spray droplet count, 25 mm below the injector tip. The calculations of these two numbers are given by equations 3.5.

$$D10 = \frac{\sum_1^n D_i^1}{\sum_1^n D_i^0} \qquad D32 = \frac{\sum_1^n D_i^3}{\sum_1^n D_i^2} \tag{3.5}$$

As it was mentioned before, the experiments reported droplet diameters of about 10-12 μm and SMD at the range of 11-15μm. Both of the methods had a converged SMD number at about 15 μm, 1.5 ms ASOI as it shown in Figure 3.42. However, the way of this convergence was occurred was different for the two cases. With the Rosin-Rammler distribution, the initial SMD number was 32 μm which dropped to the target of 15 μm as the time evolved. The opposite trend was seen when the blob method was used. The initial SMD number was 11.7 μm which was increased to 15 μm. This behaviour was further investigated and compared against experimental data of droplet size scatter plot and droplet mean diameter versus time.

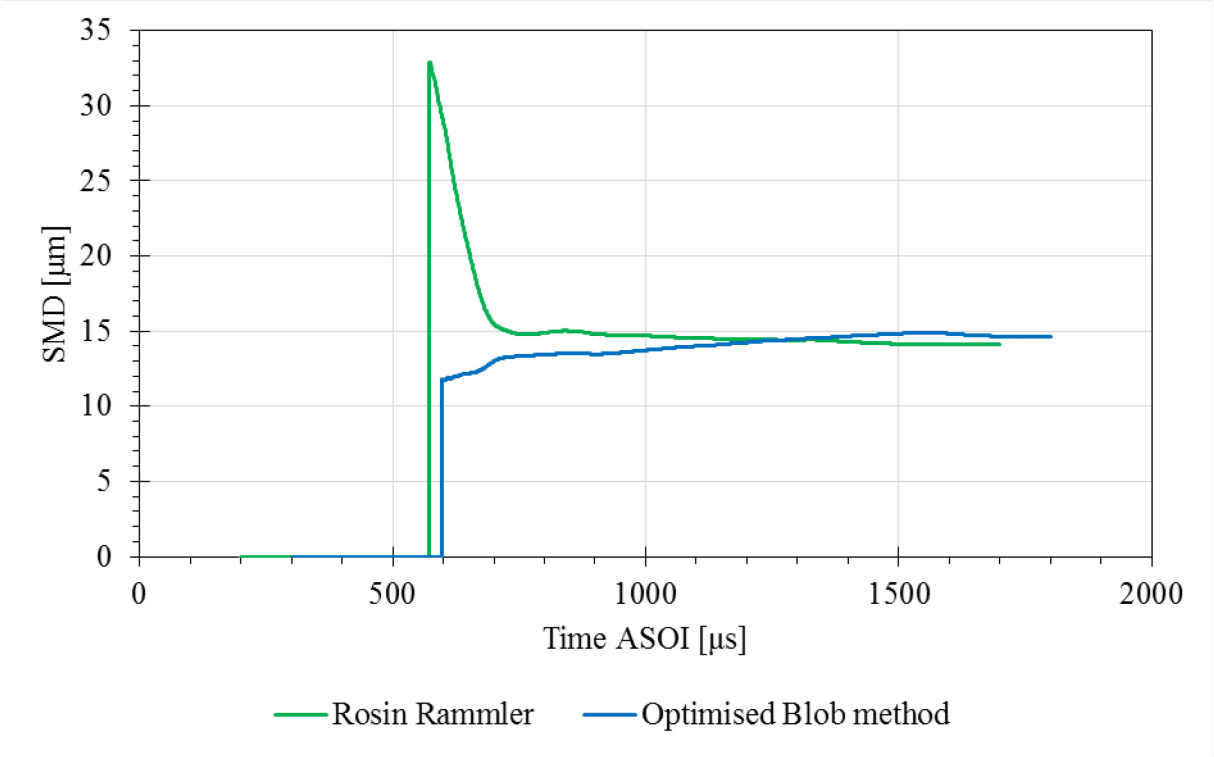
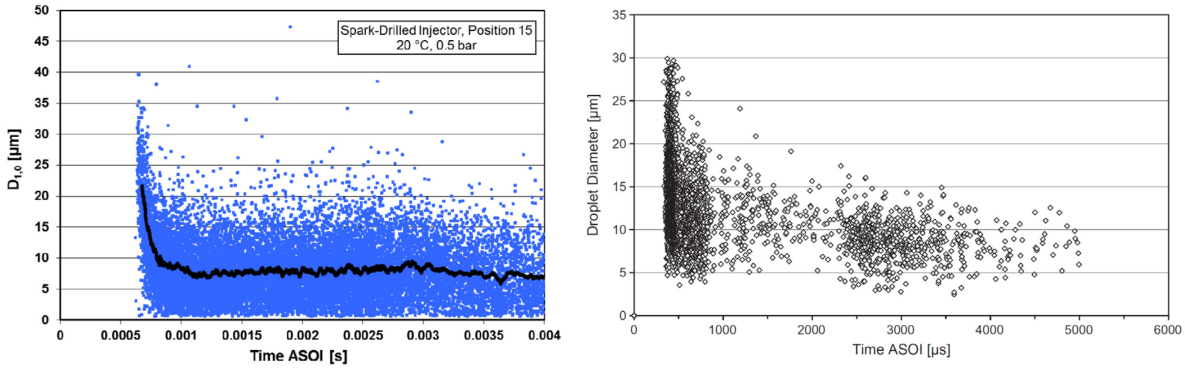


Figure 3.42 Numerical SMD number for the optimised blob method and the Rosin-Rammler distribution, 25 mm below the injector tip

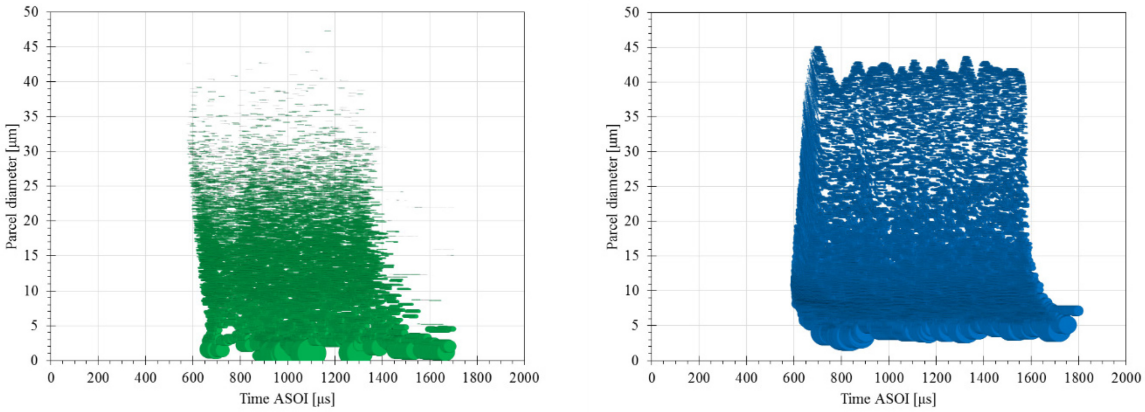
From the experimental scatter plot of Butcher *et al.* (2015) it is clear that the first droplets which arrive at the interrogation area were droplets with diameter of about 25 µm to 35 µm. After that, the majority of the droplets which arrive at that location had diameter in the range of 2 µm to 15 µm and a small number of droplets were above this range. While in the other experimental scatter plot the ambient pressure was 1 bar, the trend holds and the droplets with bigger diameter (20 to 25 µm) arrive first, and after that, smaller droplets in the range of 5 to 12 arrive. A comparison between the scatter plots produced by the Rosin-Rammler distribution and the optimised blob method (Figure 3.44) reveals that parcels (with a number of droplets within a parcel) of higher diameter in the range of 25 µm to 40 µm arrive first at the interrogation area when the Rosin-Rammler distribution was used. After that, smaller droplets in the range of 2 µm to 10 µm arrived. However, with the blob method, the first droplets to arrive at the interrogation area where in the range of 10 µm to 15 µm and after that, droplets with larger diameters were captured (up to 45 µm). This explains why the SMD number with the Rosin-Rammler distribution starts at higher values (32 µm) and converges to 15 µm as smaller droplets are added, while with the blob method the smaller droplets at the beginning give smaller SMD. In addition, the scatter plot of the simulations shows the number of the droplets in each parcel. This is shown by the size of each circle (which represents a parcel of

specific diameter) on the plot. Larger circles mean more droplets within the parcel. Both methods of droplet initialisation show a larger portion of small droplets up to 15 μm nevertheless, there are considerably more droplets of large diameters (above 25 μm) with the blob method something that was not observed in the experiments.



Gasoline, 20 °C, 0.5 bar Gasoline, 20 °C, 1.0 bar

Figure 3.43 Experimental droplet size scatter plot versus time for gasoline at 20 °C and ambient pressure of 0.5 bar and 1.0 bar. Butcher et al. (2015) and Aleiferis and Van Romunde (2013)



Rosin-Rammler distribution Optimised blob method

Figure 3.44 Numerical droplet size scatter plot versus time for iso-Octane at 20 °C and ambient pressure at 0.5 bar for the optimised blob method and the Rosin-Rammler distribution, 25 mm below the injector tip

Finally, in Figure 3.44, the moving average of D10 for the two initialisation cases was compared against the moving average of the two experimental scatter plots. It has to be mentioned here that the numerical moving average is calculated for each timestep and for this reason the lines are not smooth. The moving average of the blob method is smoother because all the droplets start with the same initial diameter and the minimum diameter is limited to 4-5 μm due to the settings of break up model which control the severity of the break up. With the Rosin-Rammler distribution though, smaller diameters in the order of 0.5 μm were allowed to

be generated which in turn, affected the D10 calculation at specific timesteps which show D10 values lower than the experiment. Despite these differences, the numerical results were in a good agreement with the experimental results.

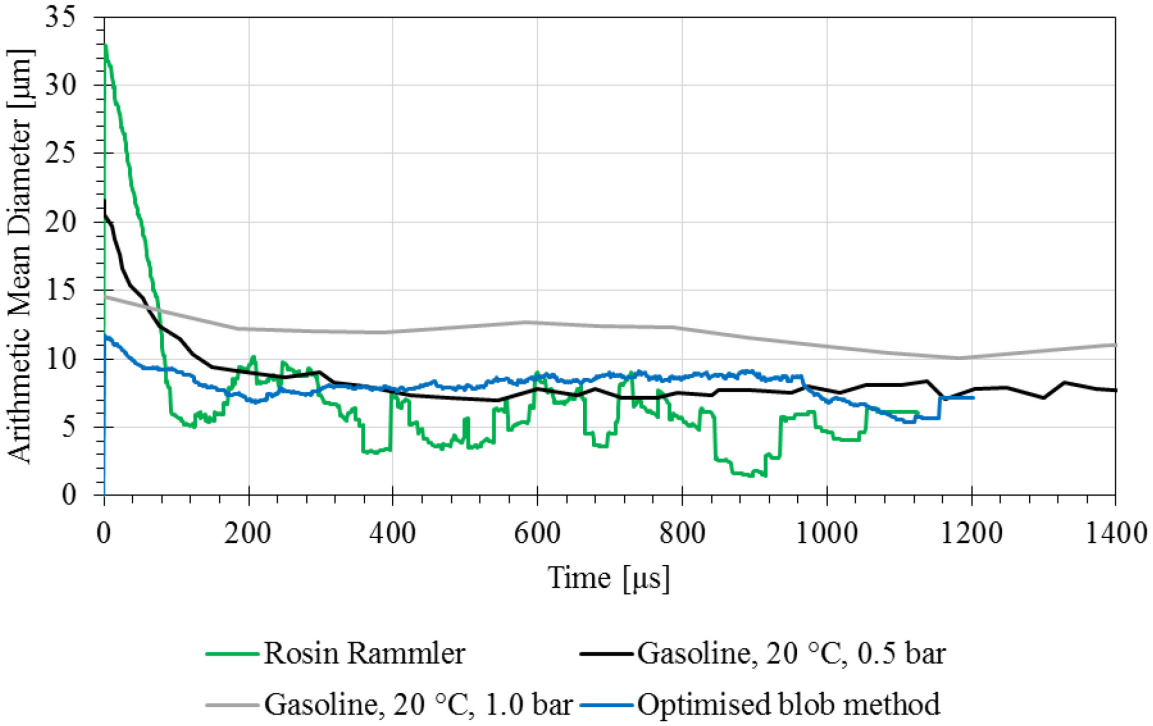


Figure 3.45 Experimental and numerical D10.Numerical setup: iso-Octane at 0.5 bar ambient pressure and 293K fuel temperature. Experiment: gasoline at 20 °C and ambient pressure of 0.5 bar and 1.0 bar

In general, both methods of initialising the droplet diameter were acceptable and agreed quantitatively and qualitatively with the experimental results, however an optimisation process was needed to represent experimental measurements. It was found that:

- The predicted penetration for both cases was close to the experiment with the Rosin-Rammler distribution showing slightly better agreement than the blob method (4% and 10% maximum difference, respectively).
- The spray tip velocity was as well in agreement with the experimental measurement at the initial acceleration, however, the blob method had greater velocities at later stages of the injection. This leads to over prediction of the penetration at long injection durations.
- The SMD number at 25 mm below the injector tip was in a good agreement with the experiments for both methods, however the behaviour differed.

- With the Rosin-Rammler distribution, larger droplets arrived first at the interrogation area, similar to the experiment. However, small droplets arrived first at the same location with the blob method.
- Droplet mean diameters similar to the experiment were recorded at the interrogation area for both cases during the steady state duration.
- The Rosin-Rammler method allowed better representation of the injection event. The initial increase and overshoot of the mass flow rate and velocity was allowed to be modelled. This was not possible with the blob method as the transient phases highly affect the Reitz-Diwakar droplet break-up model without being able to control it through time.

From all the above, it was decided for the rest of the work of sub-cooled fuel injection to use the setup with the Rosin-Rammler distribution which produced results closer to the experiments and more realistic behaviour.

3.8.2. Sub-cooled fuel injection – optical engine

The model of the AJ133 optical engine which was used for the validation of the in-cylinder pressure trace and the flow field with the same boundary conditions was used to include spray modelling in the motoring case. The injection parameters for the engine are showed at Table 3.8. It has to be noted that the triggering of the injector was 80 deg CA after TDC but there was a delay of about 0.3 ms (2.7 deg CA for the engine speed of 1500 RPM) before the spray comes out of the injector, thus the spray in the model was initiated at 82.7 deg CA after TDC. Moreover, after the 0.8 ms (7.2 deg CA) of injection the injector receives the falling edge of the trigger at 89.9 deg CA after TDC. Again, there is a small delay and the droplets leave the nozzle around 10 deg CA after the start of injection. As a result, the total injection period for the simulation was 10 deg CA. The setup of the injection was kept the same as the case with the Rosin-Rammler distribution described above and the injector was mounted vertically on the engine.

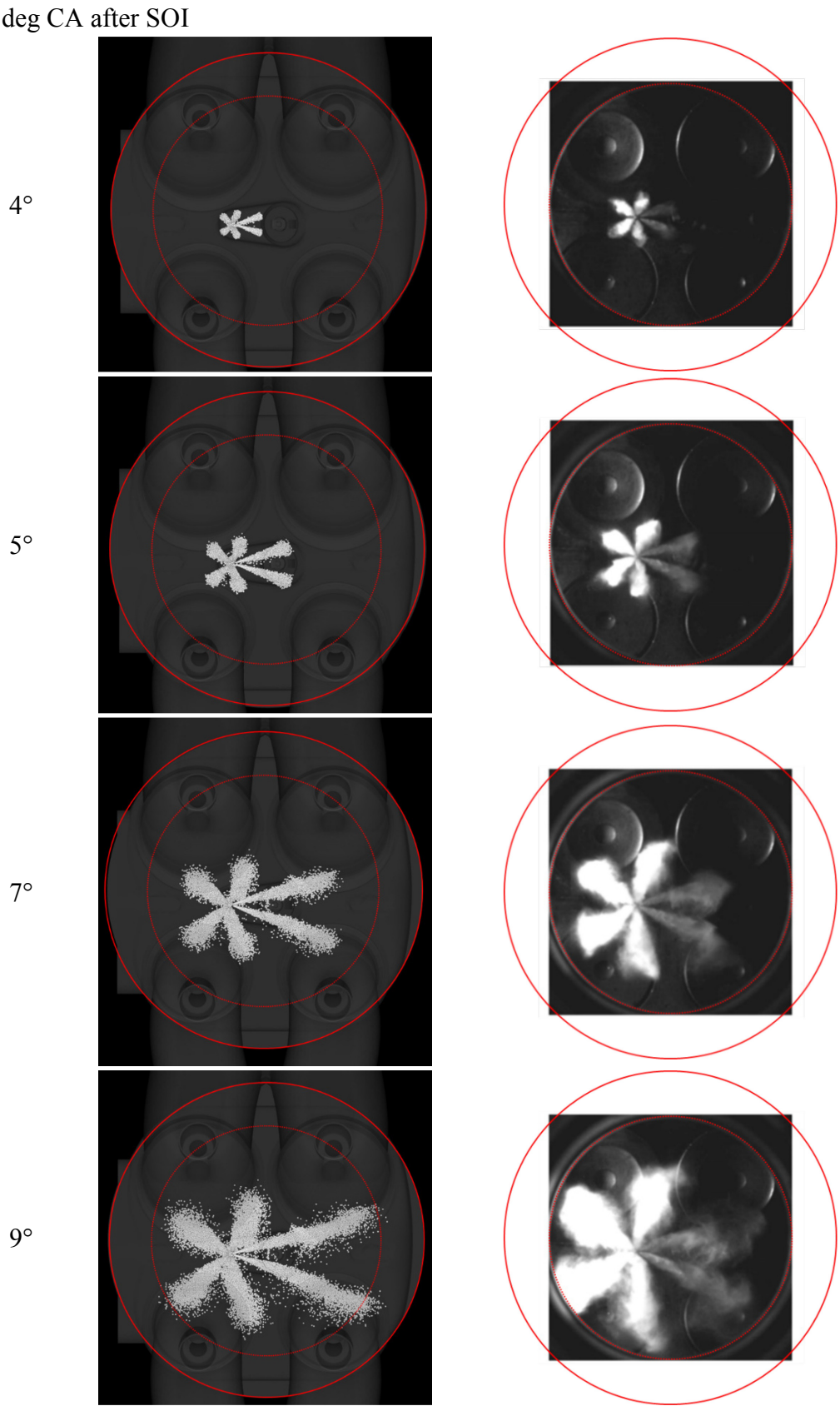
Figures 3.46 and 3.47 show the numerical and experimental mean spray development of *iso*-Octane (simulation) and gasoline (experiment) at a swirl and tumble plane respectively. The continuous red circle represents the liner of the engine and the red dotted circle represents the optical window of the piston. The results showed that qualitatively the spray penetration is well

predicted at the initial stage, but it is slightly over-predicted 9 deg CA after SOI. This is more evident for the plumes 1 and 6 that are away from the window. In the simulation, the plume 6 has passed the optical window of the piston (red dotted line) while in the experiment the whole plume can be seen within the optical window. The penetration of the plumes 3 and 4 in the swirl plane however were better predicted as they arrive at the edge of the optical access at the same time (9 degrees CA ASOI). The first droplets arrived at the piston liner 11 deg CA after SOI and the core of the plume 12 deg CA after SOI however, it was reported that the spray tip had contact with the liner 13 deg CA after SOI (Serras Pereira *et al.* 2012). However, the penetration of the vertical plumes was predicted more accurately when compared to the experimental images in the tumble plane and the spray tip reached the piston surface at the same time as the experiment.

Moreover, other qualitative aspects of the experimental images were captured with the simulation. In the experiment (swirl plane at Figure 3.46) the plumes 1 and 6 were transported by the incoming flow and especially plume 6 did not penetrate in a straight line and the spray was curved due to the intake valve jet. This bended plume was captured by the CFD model, when the spray was observed from the optical window of the piston (swirl plane at Figure 3.47). The tip of the plume 1 was also affected by the valve jet, in a smaller degree. Droplets from the spray tip were transported towards the exhaust side similar to the experiment. The velocity was higher in the pent roof and the flow was directed to the exhaust side and thus the plumes 1 and 6 were affected as they were penetrating in the domain through this high velocity flow. For the other four plumes, higher concentration could be seen between plumes 4 and 5 as these plumes were more affected by the incoming flow. Similar behaviour was observed in the experimental images of the swirl plane (Figure 3.46).

Fuel	*iso*-Octane
Fuel temperature	293 K
SOI	80 deg CA after TDC
Injection period	0.8 ms, 7.2 deg CA

Table 3.8 Injection parameters for the AJ133 optical engine


deg CA after SOI
4°
5°
7°
9°

11°

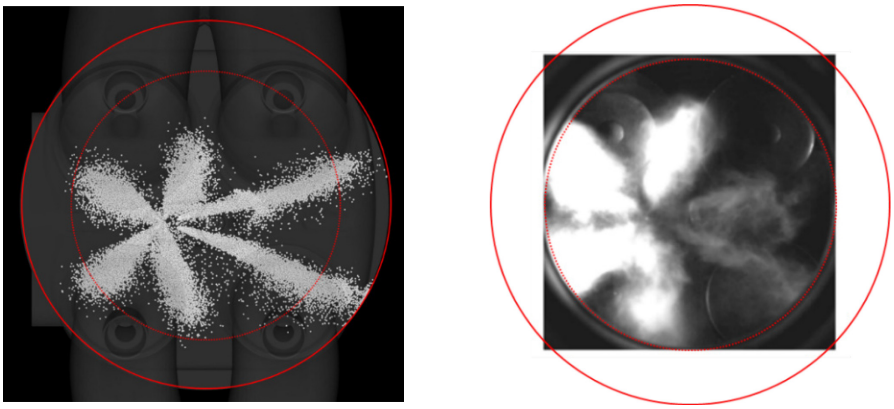
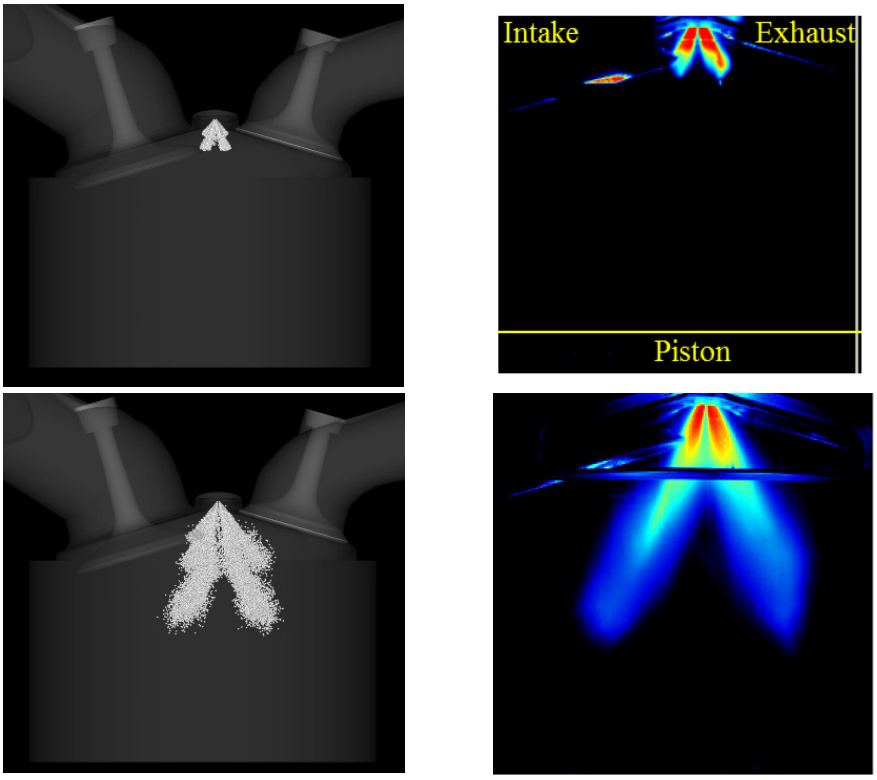


Figure 3.46 Numerical spray development and experimental spray development in the AJ133 optical engine, sub-cooled spray, swirl plane

deg CA
after SOI

4°

7°



11°

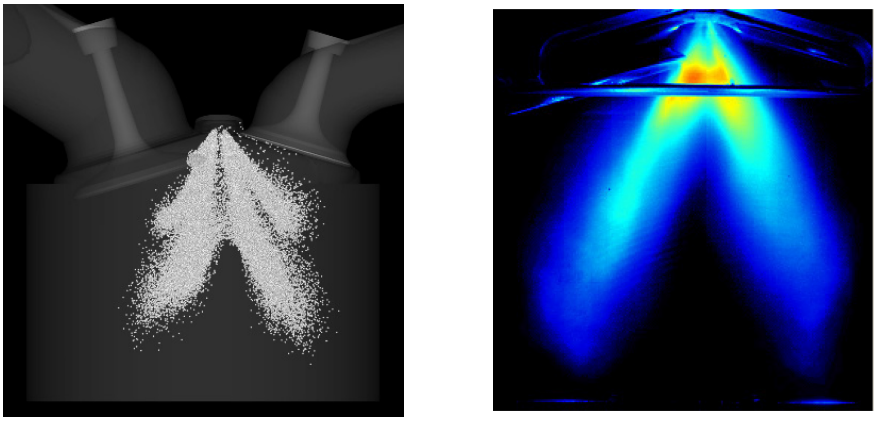


Figure 3.47 Numerical spray development and experimental spray development in the AJ133 optical engine, sub-cooled spray, tumble plane. Images not in scale

The last step of validation was the investigation of the air-fuel mixture. The experimental equivalence ratio of QPLIF data from Williams *et al.* (2010) in Figure 3.48 was compared against the numerical equivalence ratio (Figure 3.49) during the compression stroke. In this experimental work, the images were acquired in a firing engine before ignition. Because of this, the boundary and initial conditions had to be modified to represent firing conditions. The initial in-cylinder temperature and pressure were increased as well as the initial and boundary condition of the exhaust port. This was done because the residual hot gases can promote fuel evaporation. In the absence of data from the experiment, the values were taken from the experimental data of the AJ20 running at 0.5 bar intake pressure and zero valve overlap.

Three different tracers were used in this study to quantify the light, medium and heavy components of gasoline. These were acetone for the light components, toluene for the medium components and 1,2,4 tri-methyl benzene (TMB) for the heavy components. It can be seen that different behaviour and thus contours exist for the three tracers. The acetone is in higher concentrations near the piston. Toluene is in higher concentration at the exhaust side and the TMB is in higher concentrations under both intake and exhaust side.

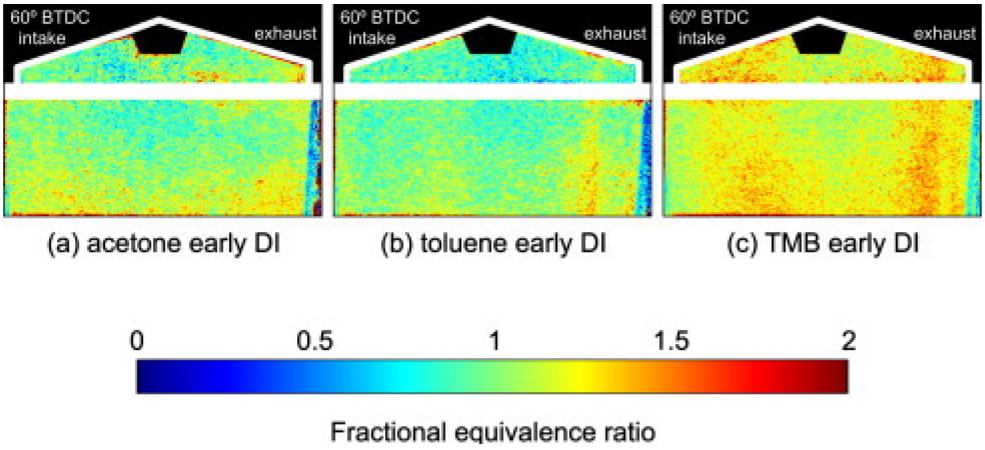


Figure 3.48 Experimental in-cylinder equivalence ratio distribution at 60° BTDC for the three different tracers (1500 RPM and 0.521 bar intake pressure)

The simulation showed that there is a rich mixture under the intake port while at the exhaust side the mixture is lean. This behaviour is due to the strong tumble motion, as it is represented by the vector arrows, which transports the fuel vapour. Similar behaviour was also found by Beavis (2017). The rich zones near the piston are due to the evaporation of the previously formed liquid film which can also be seen in the experiments.

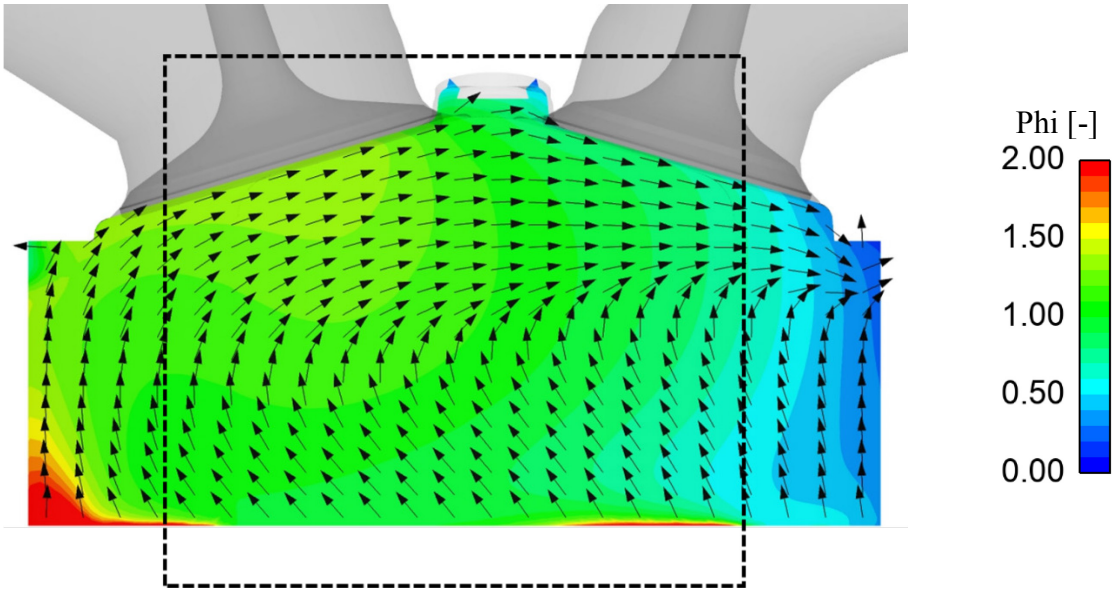


Figure 3.49 Numerical in-cylinder equivalence ratio distribution at 60° BTDC

3.8.3. Flash-boiling fuel injection – validation and development

For a fully warm engine and especially when running at low loads (wall temperature at 90 °C and ~0.5 bar at the intake runner), the fuel condition during injection initiate the phenomenon of flash-boiling. A so-called flash boiling boundary condition model and a superheat evaporation model developed by Price *et al.* (2015, 2016) and described in the mathematical formulation was used for these conditions. The development and validation in a quiescent chamber with STAR-CD, has already been published in various publications of the aforementioned authors. A comparison of the spray formation and penetration for a sub-cooled and a flash-boiling case from that work is shown in Figure 3.50. The sub-cooled case is the validated case of *iso*-Octane which was described above with the fuel temperature at 20 °C and ambient pressure at 0.5 bar. For the flash-boiling case, the fuel was *n*-Pentane at 120 °C and the ambient pressure at 0.5 bar. The components with lower boiling points such as *n*-Pentane and *iso*-Hexane are the ones which drive the flash boiling of gasoline and for this reason were used as single component fuels in the simulations. It has to be mentioned here that the development of the flash boiling model was done with a slightly different approach than the one described above for the sub-cooled spray. Firstly, the droplets of all the plumes were introduced in the domain from a single point which was the centroid of a cell, using the blob method even if a reduction of the initial droplet size was applied. In addition, the standard collision model of O'Rourke was used without the geometrical constraints of Nordin (2001).

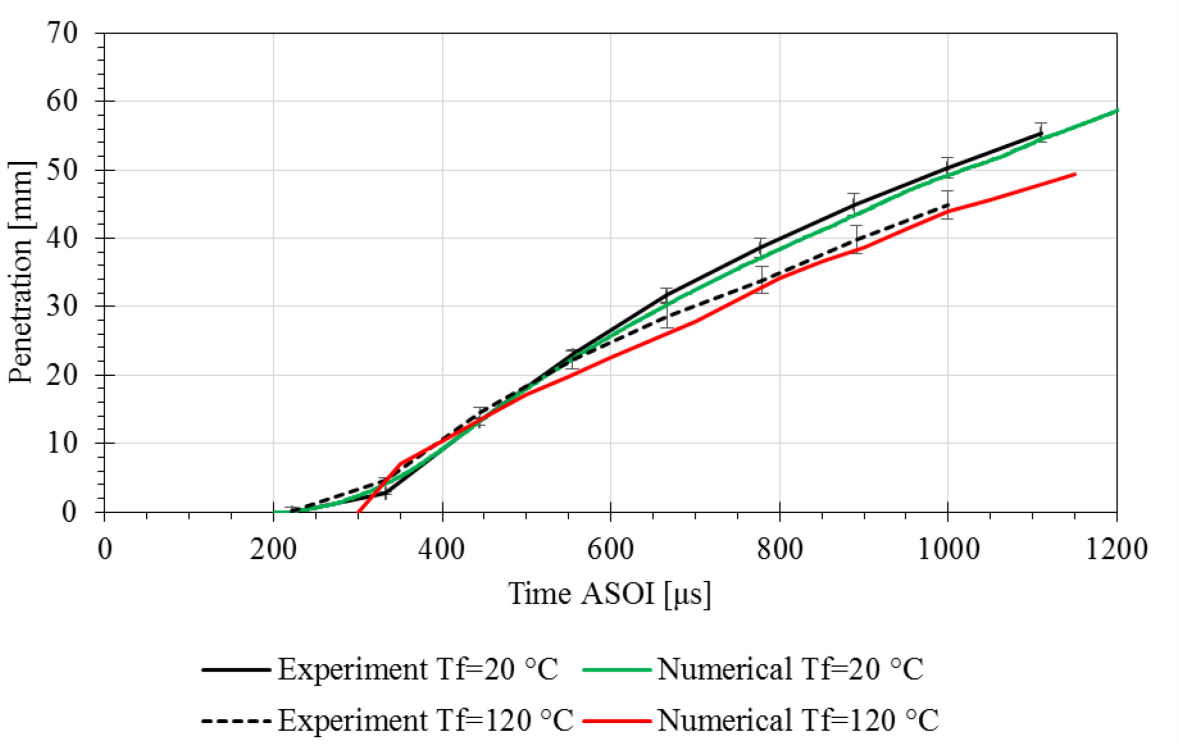
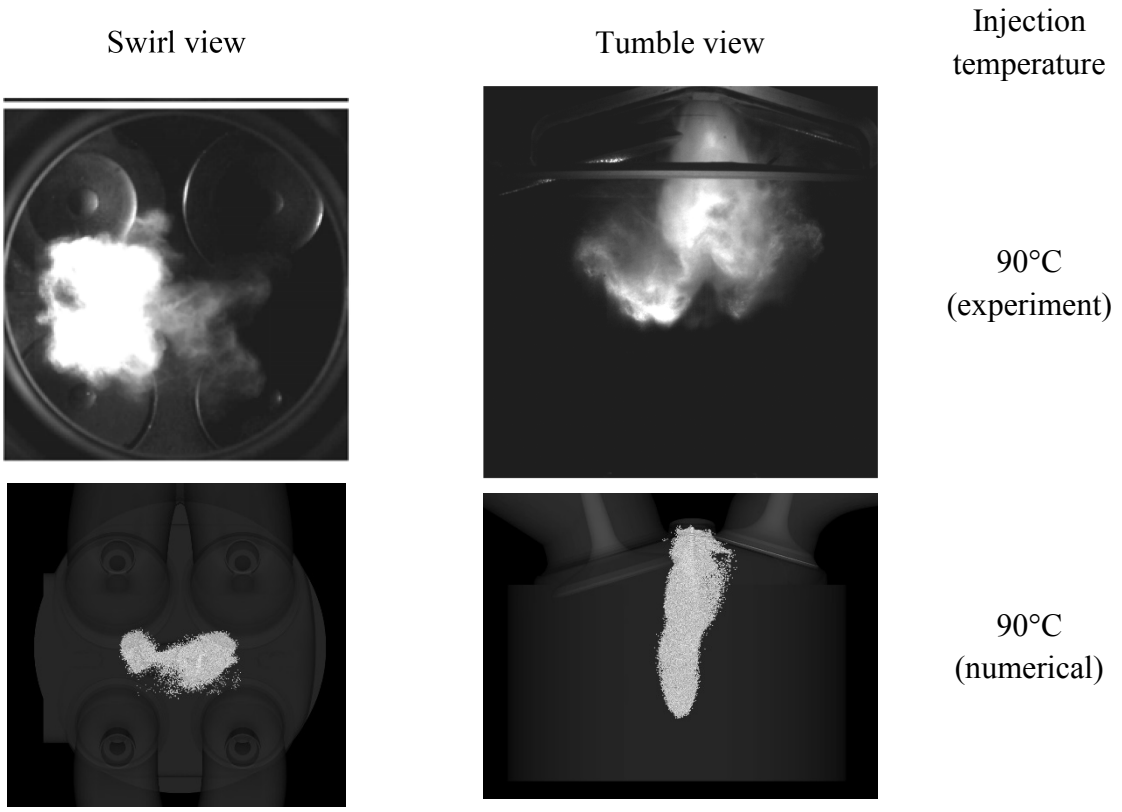


Figure 3.50 Experimental spray penetration of iso-Octane at 0.5 bar ambient pressure and 293K fuel temperature and of n-Pentane at 393K fuel temperature, Numerical spray penetration of iso-Octane at 0.5 bar ambient pressure and 293K fuel temperature and of n-Pentane at 393K fuel temperature

The performance of the model was tested, and the validation was carried out in the AJ133 optical engine while motoring with the nominal intake pressure at 0.5 bar. The engine head was warmed before the experiments at 90 °C (coolant temperature) in order to warm the injector and consequently the fuel. Thus, the nominal fuel temperature in the experiments of Serras-Pereira *et al.* (2008) was 90 °C, which represented fully warm engine conditions. For the simulations, two light components (*n*-Pentane and *iso*-Hexane) of the gasoline where used to represent the flash boiling of gasoline. The cone angle of each plume was kept at 15° as it was described in the publication of Price *et al.* (2016). According to the findings of the in-cylinder pressure trace validation, for the conditions of the motoring engine with flash-boiling (walls at 90 °C), the intake pressure was 0.47 bar.

Firstly, the model was tested with *n*-Pentane and the nominal temperature of the head was applied as the injection temperature of the fuel. The numerical results (Figure 3.51) showed that for 90 °C fuel temperature, the collapsing mechanism of *n*-Pentane is severe resulting in a narrow cone angle and greater spray penetration when compared to the experimental data of gasoline for the same conditions. The experimental data (van Romunde *et al.* 2007) which compared gasoline and *n*-Pentane flash-boiling in a quiescent chamber (Figure 3.52) also

showed that for the same conditions, the *n*-Pentane collapsing mechanism was more severe than that of gasoline due to heavier components in gasoline with higher boiling points. In order to reduce the severity of the *n*-Pentane collapsing mechanism and replicate the gasoline flash-boiling in the engine, a sensitivity study was carried out and the injection temperature was reduced from 90 °C up to 60 °C with 5 degrees increment. As it was expected, with the reduction of the injection temperature, the severity of the collapsing mechanism was reduced and the spray characteristics for injection temperatures in the range of 80 °C to 70 °C approached those of the experimental gasoline injection. In the tumble plane, the outer cone angle was increased, and the penetration was decreased while keeping a degree of merging between the four plume targeting towards the piston. In the swirl plane, the two plumes targeting the spark plug also show a degree of merging similar to the experiment especially closer to the injector. In addition, droplets from the tip of these two plumes were carried by the flow towards the exhaust ports, a behaviour also seen in the experiments. For injection temperatures lower than 70 °C, the spray formation was closer to the sub-cooled cases.



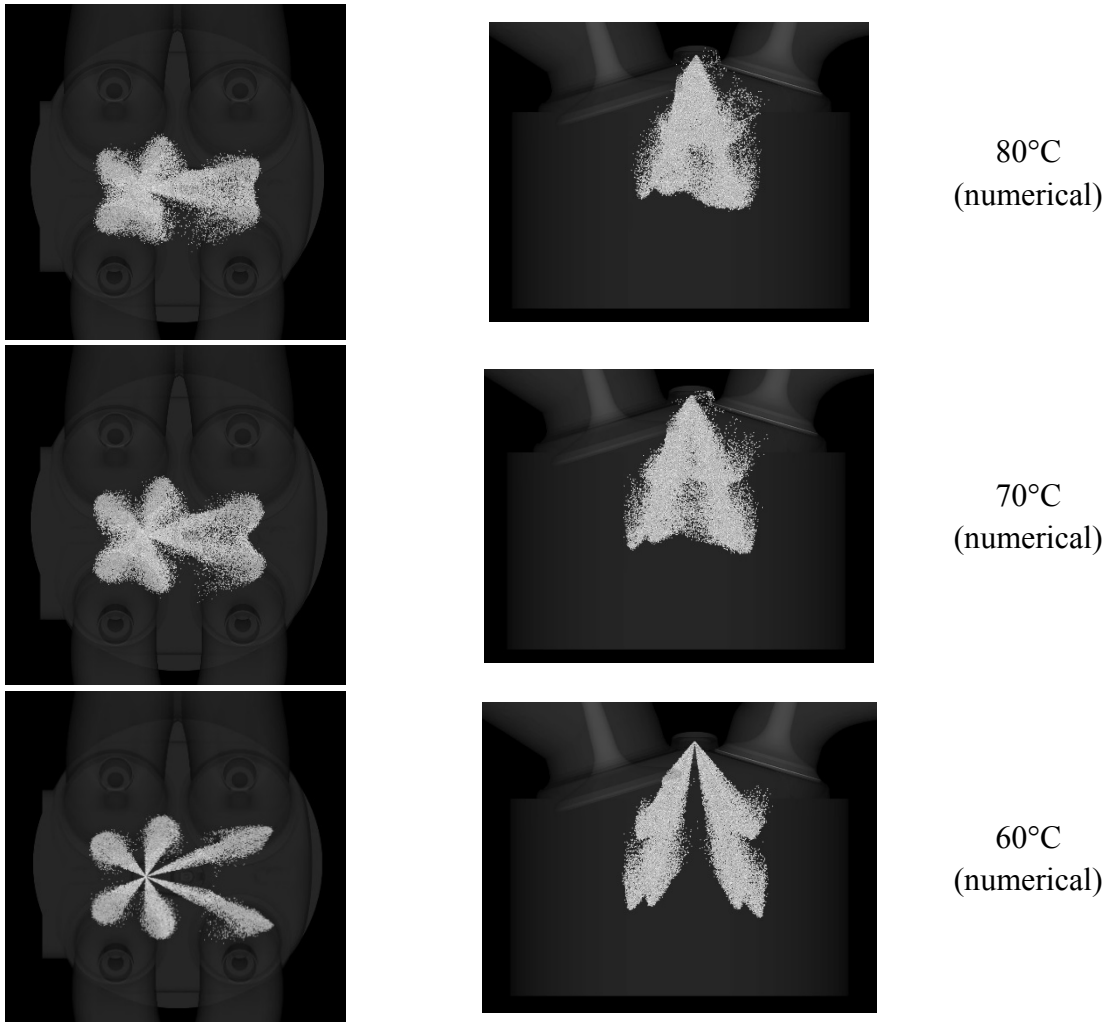
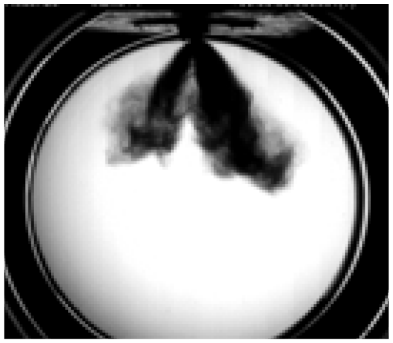


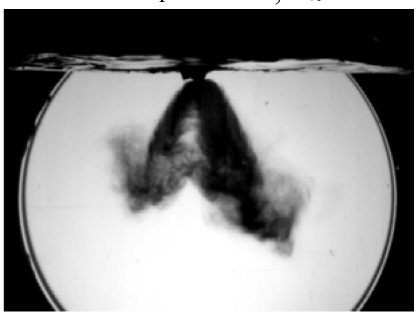
Figure 3.51 Numerical tuning process of the flash boiling model with n-Pentane in the AJ133 optical engine. Experiments from Serras-Pereira et al. (2008)



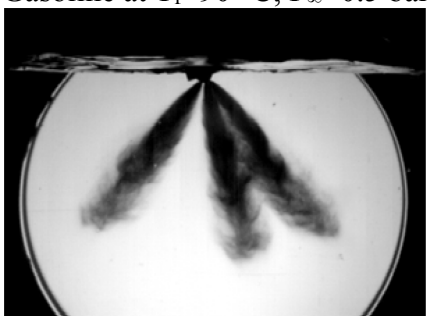
Gasoline at T_f=120 °C, P_∞=0.5 bar



Gasoline at T_f=90 °C, P_∞=0.5 bar



n-Pentane at T_f=90 °C, P_∞=0.5 bar



n-Pentane at T_f=50 °C, P_∞=0.5 bar

Figure 3.52 Comparison of spray behaviour of gasoline and n-Pentane at various temperatures and 0.5 bar ambient pressure. Experiments from van Romunde et al. (2007)

When *iso*-Hexane was used to replicate gasoline in the AJ133 engine, the results showed that for the nominal injection temperature of 90 °C, the spray formation was closer to sub-cooled cases with very small flashing behaviour (Figure 3.53). Due to the higher saturation temperature at the same pressure of *iso*-Hexane when compared to *n*-Pentane the degree of superheat is lower and thus, the flashing is lower. To replicate the experimental flash-boiling of gasoline with the single component fuel of *iso*-Hexane the injection temperature had to be increased. A sensitivity study was carried out and the injection temperature was increased from 90 °C up to 120 °C with 5 °C increment. For injection temperatures up to 105 °C the collapsing of the spray was minor, and all six plumes were distinguishable, very similar to a sub-cooled spray. When the injection temperature was further increased to 110 °C, the spray formation showed a collapsing mechanism close to the experiment, with plume to plume interaction and merging and the penetration was decreased. However, the plume merging is more severe than the *n*-Pentane with the cases which agreed with the experiments. A further increase of the injection temperature by 5 °C resulted in unrealistic results with a severe collapsing of the spray, a very narrow cone angle and an increase of penetration, greater that the sub-cooled case. The same severe collapsing mechanism was seen for higher injection temperatures. At high temperatures, a small increase in temperature results in higher droplet diameter reduction factors and in turn, the severity of the collapsing mechanism increases with high rate. However,

for the *n*-Pentane the reverse path is followed so at lower temperatures the reduction factor is decreased in a lower rate as the temperature is decreased and as a result the collapsing mechanism is less intense.

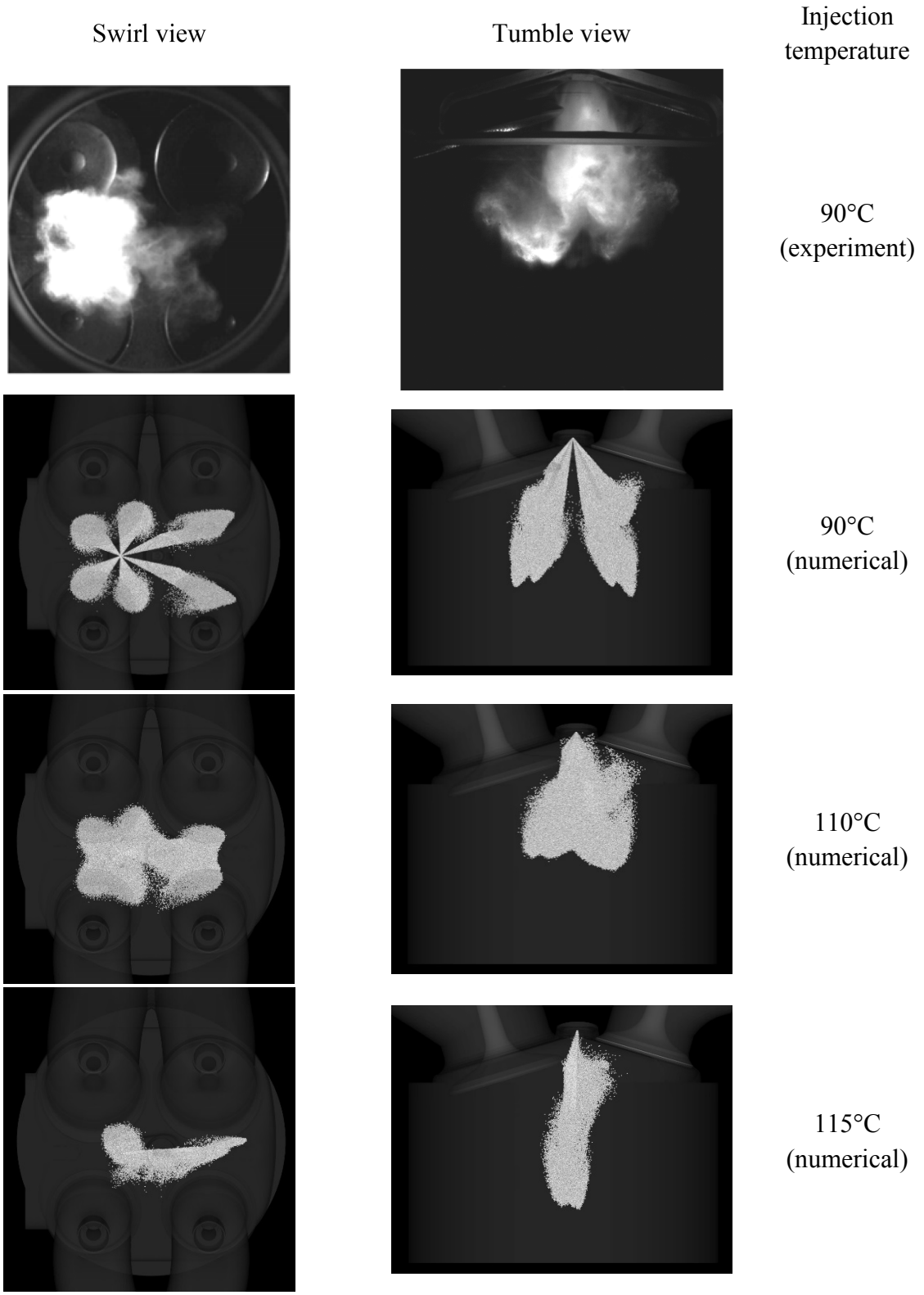


Figure 3.53 Numerical tuning process of the flash boiling model with iso-Hexane in the AJ133 optical engine. Experiments from Serras-Pereira et al. (2008)

From the above analysis it was seen that the flash-boiling mechanism of gasoline in an engine can be replicated by single component surrogates of high volatility that exist in gasoline. However, a tuning of the injection temperature is needed in order to match the single component behaviour to that of the multi-component gasoline. Both *n*-Pentane and *iso*-Hexane could predict the gasoline flash boiling when the injection temperatures were tuned. Nevertheless, the *iso*-Hexane was more sensitive to the increase of temperature due to the high increase of the droplet diameter reduction factor when going to higher superheat. On the other hand, the *n*-Pentane allowed a larger window of injection temperatures to replicate the gasoline flash boiling. It was concluded that the *n*-Pentane is more appropriate when the flash-boiling model was necessary as it was easier to be tuned.

Lastly, the air-fuel mixture of *n*-Pentane was compared against the experimental QPLIF data of from Williams, Ewart, Wang, *et al.* (2010) during the compression stroke. The same procedure as for the sub-cooled spray was followed by increasing the initial in-cylinder temperature and pressure and the initial and boundary condition of the exhaust port to replicate the conditions of the firing engine.

The validation of the flash boiling model in the AJ133 optical engine was done in order to use the same setup, due to the absence of data of the EB2 injector in flashing conditions, in the AJ20 thermal engine for further investigations. This, however, revealed problems with the way in which the injector had to be positioned and possible effects of this. First of all, in the AJ20 head, the geometry of the tip of the injector was included and ideally the approach of the sub-cooled cases had to be followed by having each plume coordinate system on a different point, around the injector tip and according to the spray pattern. However, due to the methodology of the flash-boiling model, the centroid of a cell had to be chosen in order to introduce the coordinates of the plumes. As the engine geometry was symmetric and the injector was located on the symmetry plane, the point had to be on the symmetry plane and thus, not on a cell face. For this reason, the EB2 injector was tested in a constant volume chamber and the plumes' coordinate systems were either on the centroid of a cell or a cell face in order to investigate possible differences in the spray formation. The setup was the same as the validated case of the AJ133 optical engine meaning that the fuel was *n*-Pentane, the injection temperature was 70°C and the ambient pressure and temperature were 0.5 bar and 293K respectively. The cone angle of each plume was 17°. The computational domain was as well the same; a cube of 80 mm edge discretised with a Cartesian mesh on 1 mm edge. It can be seen from Figure 3.54 that the location of the injection point has a major impact on the spray formation. When the injection

point was located on the centroid cell, a collapsing mechanism and merging of the six plumes was observed, the same as the AJ133 injector approach. When the injection point was located on the cell face, then only plumes that were travelling at the same side were interacting with each other and there was a distinguishable area in which no plume interaction was observed, which was at the symmetry plane defined by the cell face. In general, the cell face acted as a barrier in which droplets of the one side could not interact with droplets on the other side of the cell face.

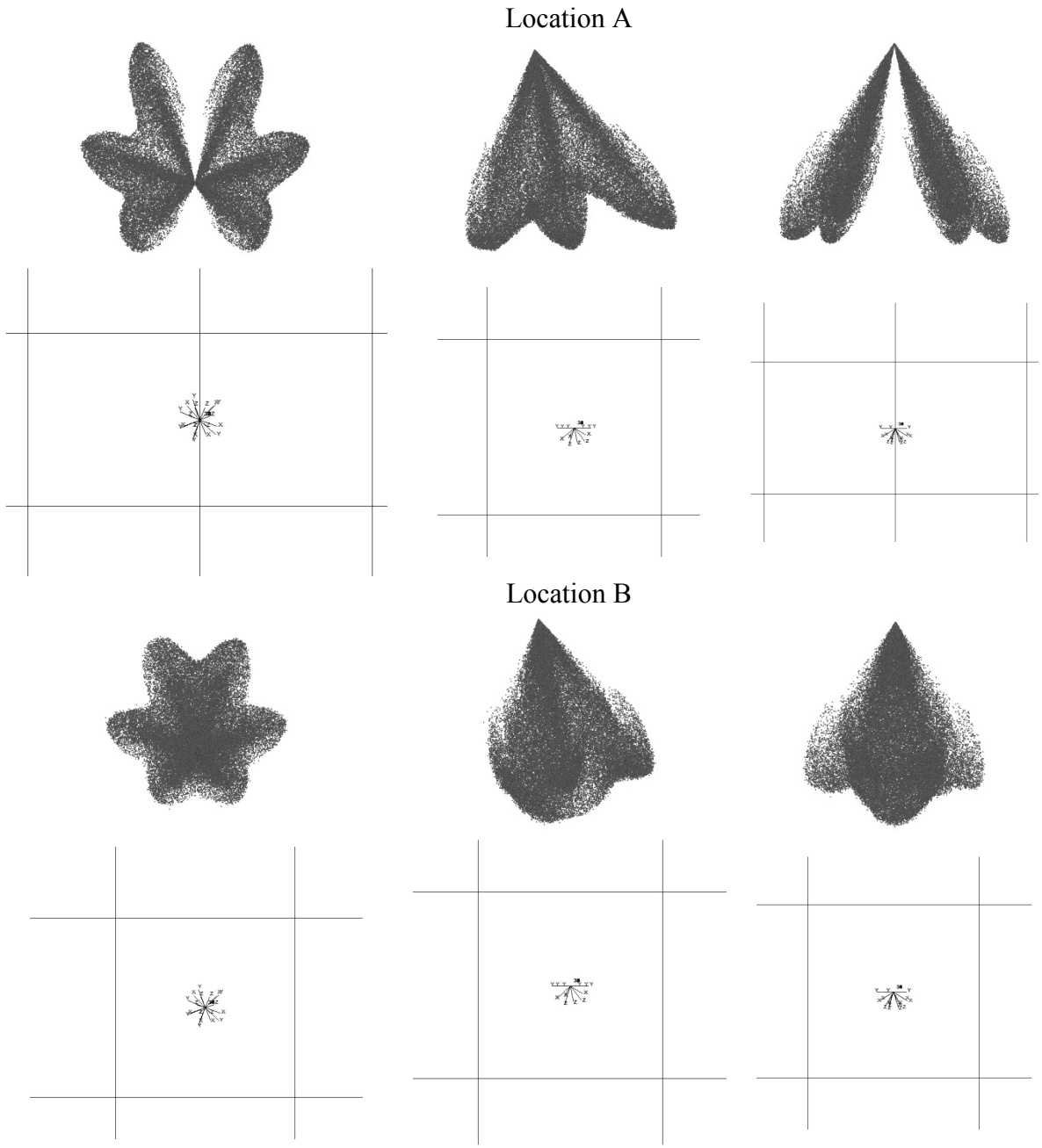


Figure 3.54 Behaviour of the original flash-boiling spray with the EB2 injector location at two different positions in respect to the mesh

For these reasons, a general approach had to be established in order to address the problem of selecting a specific point and thus a cell centroid and use the ideal approach of having each plume's coordinate system spaced according to the spray pattern. The first step was to position the coordinate system of each plume 1mm away from the common point and in the direction of each plume. This was done for the location B described above and the location A was moved to a cell vertex in order to create more barriers from all possible cell faces. After moving the coordinate system of each plume by 1mm, the modified, spaced plume locations A and B looked as in Figure 3.55.

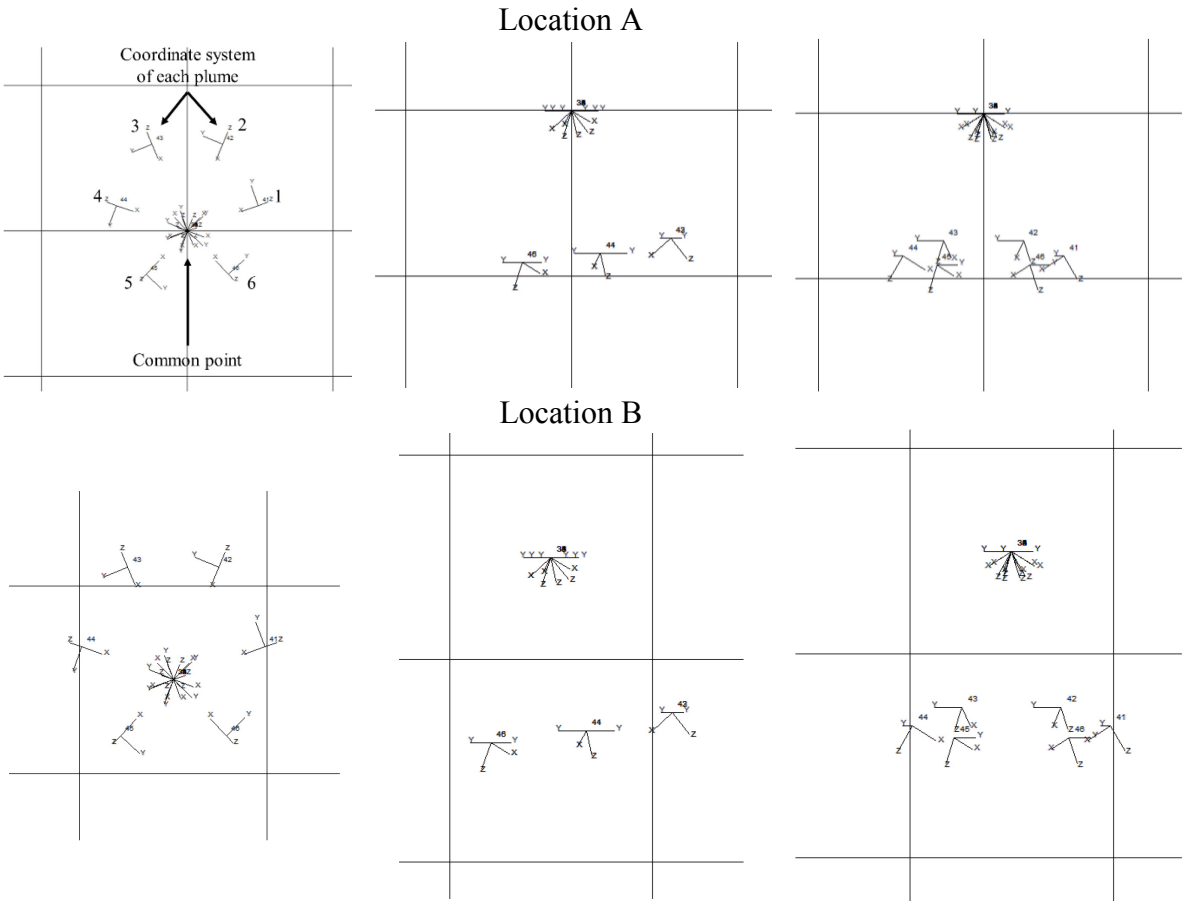


Figure 3.55 EB2 injector location at two different positions in respect to the mesh with the plumes spaced according to the Figure 3.37

The droplets of each plume were introduced at the (0,0,0) of their respective local coordinate system and their direction was the positive z-axis. The rest of the simulation setup was kept the same as the two cases described above. First of all, the results showed that when the six plumes were not initialised from the same point, the interaction of the plumes was significantly reduced, appearing more as a sub-cooled spray rather than a collapsing flashing spray. This was observed for both locations A and B. Another patter which was observed, was the way that

the plumes interacted with each other. For both locations, only the plumes which were initialised from the same cell interacted. It can be seen that for the location A, the two plumes on the left (3 and 4) and the two on the right side (1 and 2) interacted and droplets started to merge. The same behaviour was seen for the location B but this time plumes 2 and 3 and plumes 5 and 6 interacted. Because of the fact that the spray formation was closer to the sub-cooled case, the injection temperature was increased to 90°C for both locations while the rest of the setup was kept the same. The results showed a highly collapsed spray with unrealistic plume merging which is evident especially on the swirl plane. In addition to this, the behaviour of plume to plume interaction dependent on the location of the injector was as well evident. For the location A, the plumes 1 and 2 (and equally plumes 3 and 4) are collapsed and drawn together almost in a single plume and their direction was the sum of the two vectors starting for the local coordinate systems and the direction of the plume. It has to be re-iterated that for these two pairs of plumes their starting points fell into the same cell. The same behaviour was observed for the spray at the location B but this time plumes 2 and 3 (and equally plumes 5 and 6) were collapsed almost in a single plume. Moreover, the cone angle of all plumes was narrowed while a 17° cone angle was specified, and this was regardless of the location of the injector in respect to the grid. These results with the high grid dependency were pointing towards the artefacts caused by the collision model. When the number of collisions was investigated for each case it was found that for the 70°C injection temperature the average number of collisions was ~31 and with the increased temperature the number was increased to ~261 collisions per timestep with most of them separation, thus only momentum was exchanged. The reason behind this increase was the formulation of the collision model and the reduction of the initial droplet sizes due to the flash-boiling boundary condition model. The calculated initial droplet size for the 70°C injection temperature was around 160μm and for 90°C was 14μm. The mass flow rate was kept the same for all cases which means that more small droplets had to be injected when the initial diameter was reduced with increased temperature. This in turn increased the collision frequency in the collision model and the increase of the collisions and especially those of separation lead to the unrealistic plume merging. Despite these unrealistic predictions, when the spray was observed from the y-tumble plane, characteristics seen in experimental flash boiling sprays were also evident here. These were the curvature of the plumes which were drawn into the centre of the spray and the droplet recirculation at the tip of the plumes.

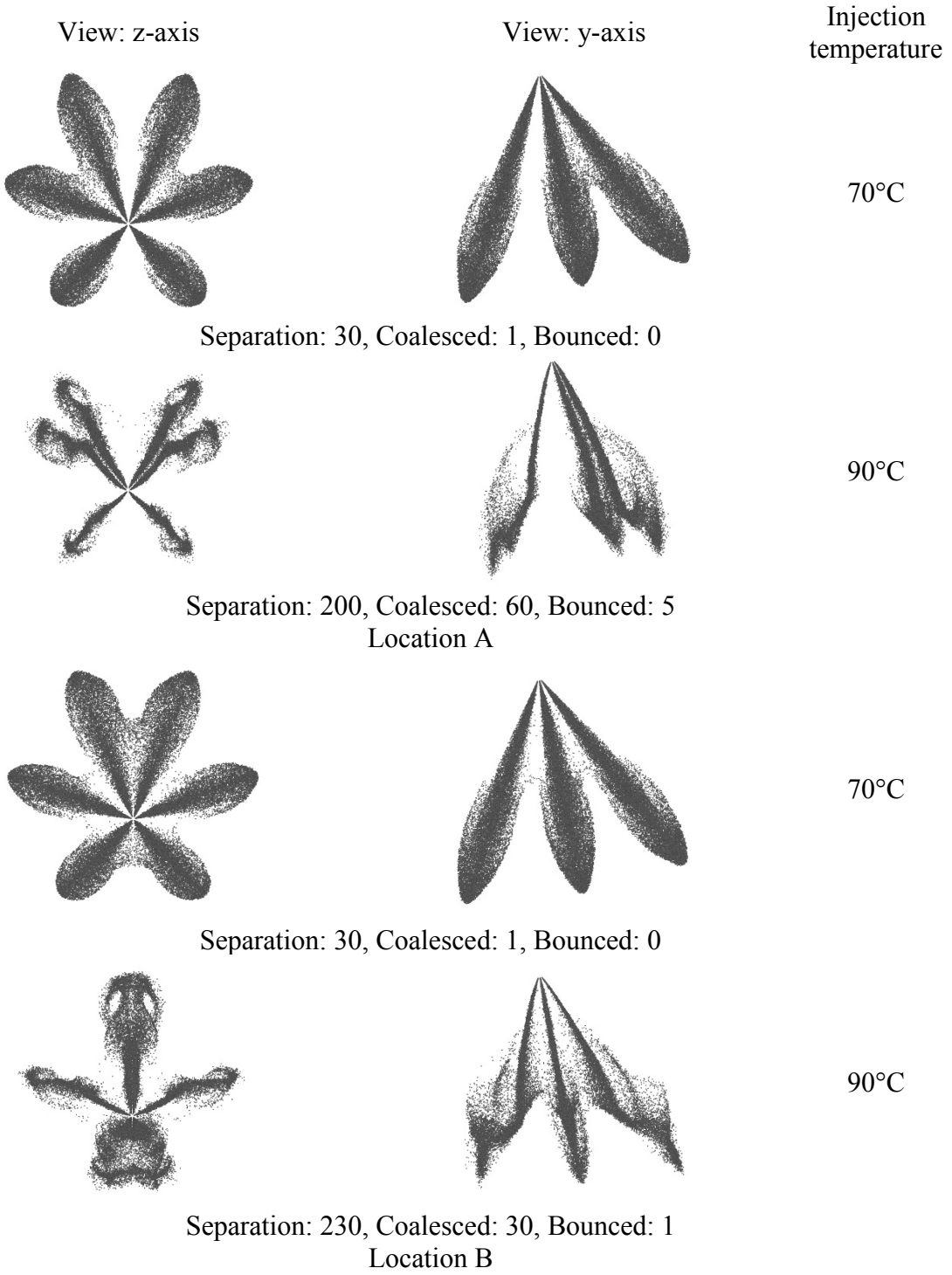


Figure 3.56 Behaviour of the flash-boiling spray with the EB2 injector location at two different positions in respect to the mesh at two fuel temperatures

In order to avoid the plume merging which was the result of two plumes starting from the same cell, the area around the injector (cube of 10 mm each side) was refined and the cell size was 0.5 mm in size. This approach assured that each plume's starting point was on a different cell. Because of this, only the location A was used. The coordinate systems of the plumes on the new mesh is shown in Figure 3.57. Two simulations were run for this grid at two different

injection temperatures (70°C and 90°C) while the rest of the setup was kept the same as the previous cases. The two results can be seen in Figure 3.58. For the 70°C injection temperature the spray formation appeared as a sub-cooled spray using the blob method for the initialisation of the droplets. There was no interaction between the plumes with no merging. When the temperature was increased to 90°C, again there was no interaction between the plumes but as seen above the cone angle of the plumes was significantly reduced despite the fact that a 17° angle was specified. Once more, the thinning of the plumes was due to the increased collisions which brought the droplets close to the nominal direction of the plume. Although there was this unrealistic prediction, for the 90°C case, the plumes had the characteristic curvature of the flash boiling and the droplet recirculation when observed from the tumble plane. In order to confirm that this behaviour of the curved plumes was coming from the superheat degree of the fuel, a case was run with initial droplet diameter at 14μm (as predicted for the flash boiling case) but the fuel temperature was 20°C. This case was run with the grid with the refined area around the injector. The results showed that the thinning of the plumes was still present which was due to the collision model. The collisions per timestep were lower than that of the case with 90°C injection temperature but significantly higher than the case with 70°C injection temperature.

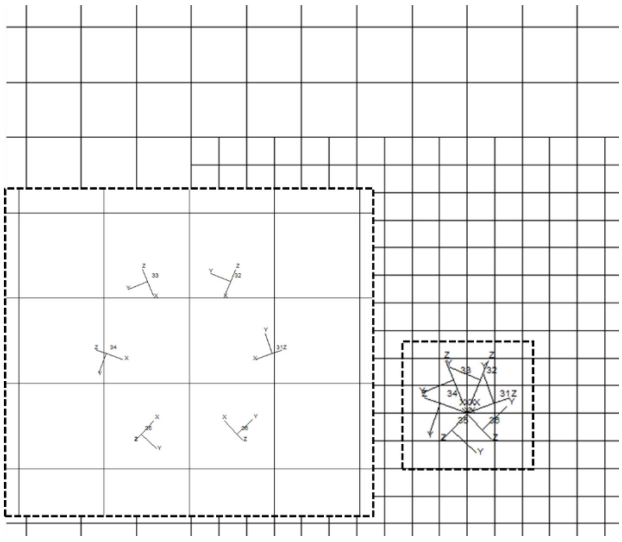


Figure 3.57 Representation of the refined grid around the injector tip and the location of the plumes in respect to the mesh

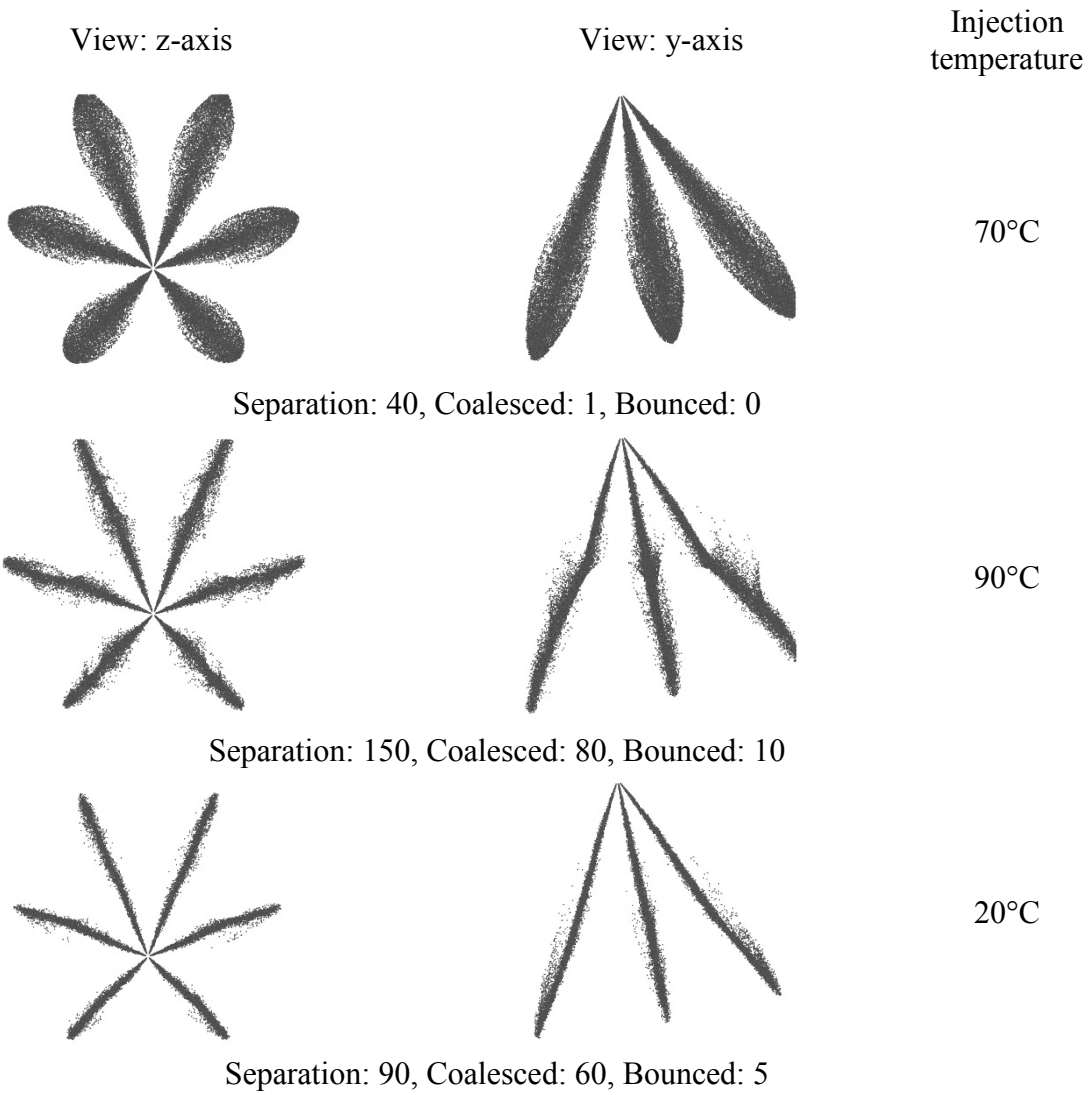


Figure 3.58 Behaviour of the spray at three fuel temperatures on the refined grid

From all the above steps, it was concluded that the standard collision model can produce unrealistic results depending on the injection temperature, superheat degree of the fuel, the grid resolution and the location of the injector in respect to the grid. For these reasons the geometric constraints proposed by Nordin and were already used for the sub-cooled sprays were applied. Now, only the 90°C injection temperature was considered as it was predicting some of the characteristics of the flash boiling observed in the experiments. The grid was kept the same as before, with the refined area around the injector. For the initial test, the plume's cone angle was kept at 17°. The results showed a major improvement especially in terms of the cone angle which was 17° as specified. In addition, as the collision model was not altering the direction of the spray, the curvature of the plume and the mechanism of the collapsing into the centre as well as the droplet recirculation at the tip of the plume was predicted. One more time, to verify that this behaviour was due to the superheat evaporation, the evaporation was turned off. The

results showed no plume curvature, no merging towards the centre and only the fishbone like behaviour of the spray due to break-up was evident. This confirms that the evaporation affects the flash-boiling behaviour. After that, the increase of the plume's cone angle as seen in experiments of flashing sprays was investigated. The individual plume cone angle was increased to 30° and 45° while the rest of the setup was kept the same. As it was expected, the cone angle of each plume was increased due to the suppressed behaviour of the collision model. The plumes were again drawn into the centre, the curvature of the plumes was apparent as well as the recirculation of the droplets at the tip of the plume. With further increase of the cone angle, there was a greater plume merging. The above process is illustrated in Figure 3.59.

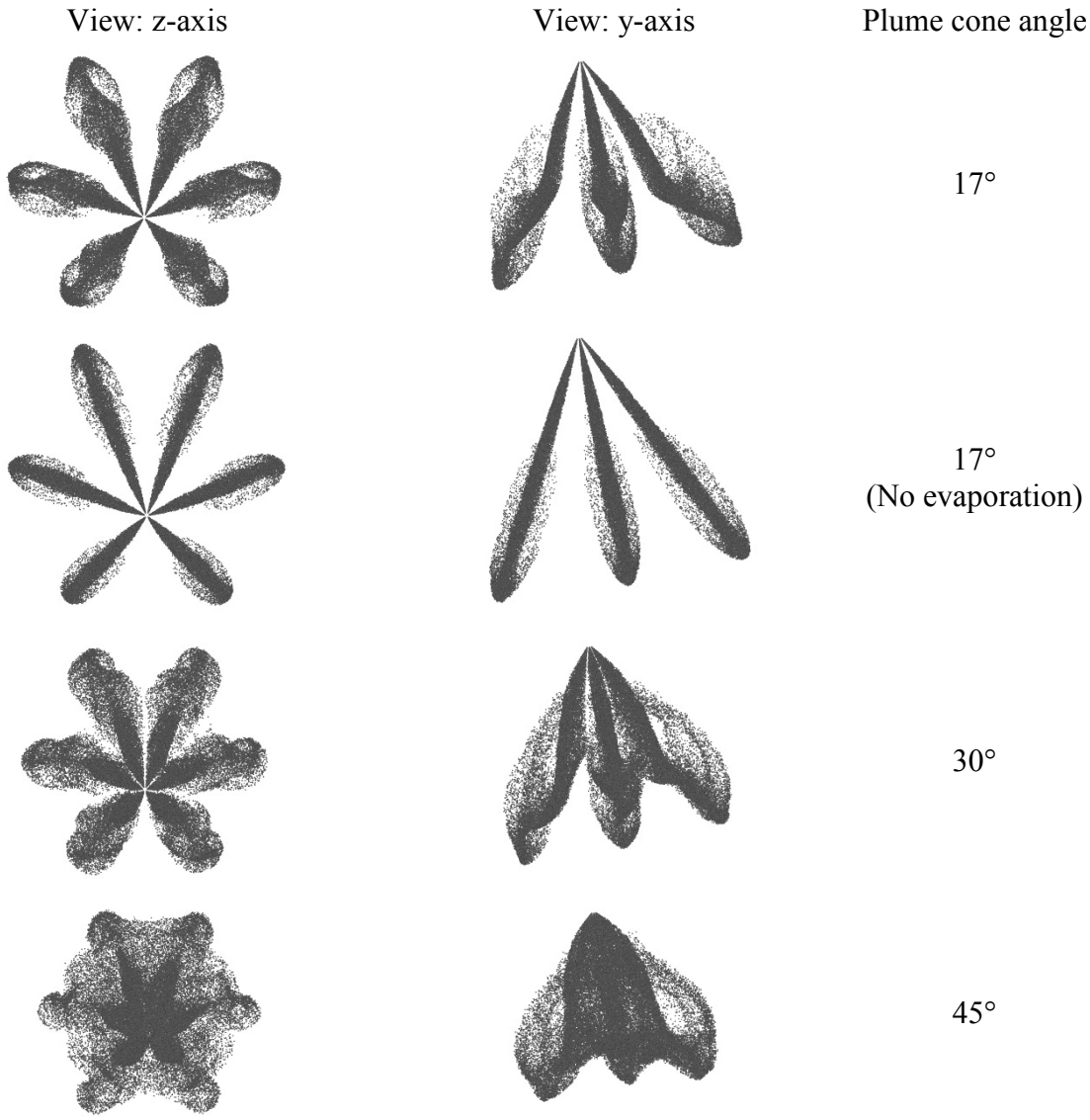


Figure 3.59 Behaviour of the spray at 90°C fuel temperatures on the refined grid for three different cone angles. Collision geometric constraints applied. Blob method applied

Until now, the initial droplet diameter was calculated from the flash-boiling boundary condition model which predicted 14μm for the 90°C *n*-Pentane. The droplets were introduced with the blob method meaning that the initial diameter of all droplets was 14μm. As it was seen for the sub-cooled spray, the use of the Rosin-Rammler distribution to initialise droplet sizes produced more realistic results and closer to experimental data. For this reason, the three cases described above for Figure 3.59 were run with the use of the Rosin-Rammler distribution. Due to the fact that these cases represent flashing sprays the distribution was different from the sub cooled spray. The shape parameter q was kept the same as before (2.75) and the scale parameter X was reduced to 16μm. With this setup the range of diameter was reduced with the maximum value being 25μm and it is according to data of flashing sprays at these conditions. In addition, the peak of the probability density function is 14μm which matched the calculations of the flash-boiling boundary condition model. The results of these simulations are shown in Figure 3.60. The results of the spray formation look more realistic as the larger droplets are less affected by the recirculation of the tip and give a randomness while for the blob method all the droplets had similar behaviour due to the same initialisation.

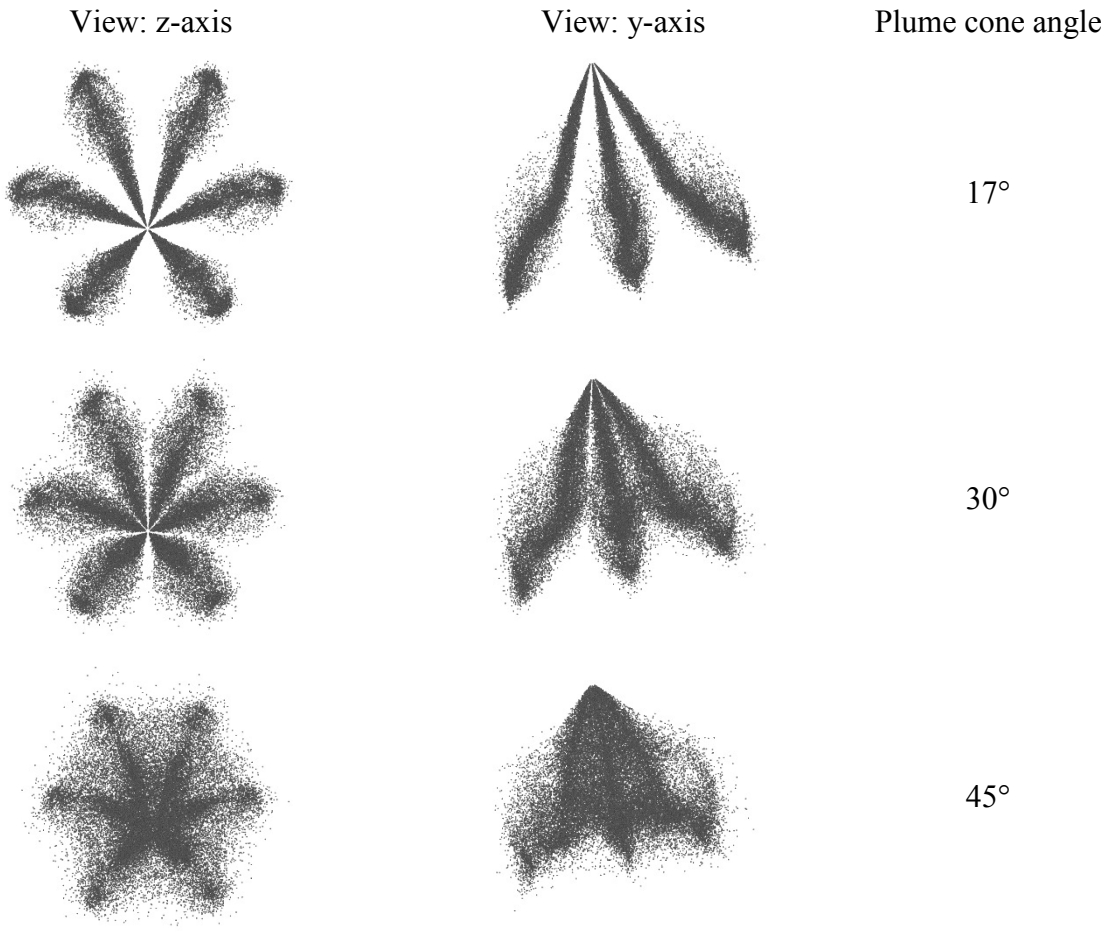


Figure 3.60 Behaviour of the spray at 90°C fuel temperatures on the refined grid for three different cone angles. Collision geometric constraints applied. Rosin-Rammler method applied

The above results from the AJ20 injector were qualitatively compared against experimental data carried out by Yang *et al.* 2013 (Figure 3.61). This study used a 6-hole Bosch injector with a similar pattern to the AJ20 injector which allowed to investigate the general behaviour of the spray in terms of shape and collapsing mechanism. The numerical predictions are very similar to the experiments of the transitional flash boiling regime (0.4 bar – 1 bar ambient, 80°C fuel temperature.)

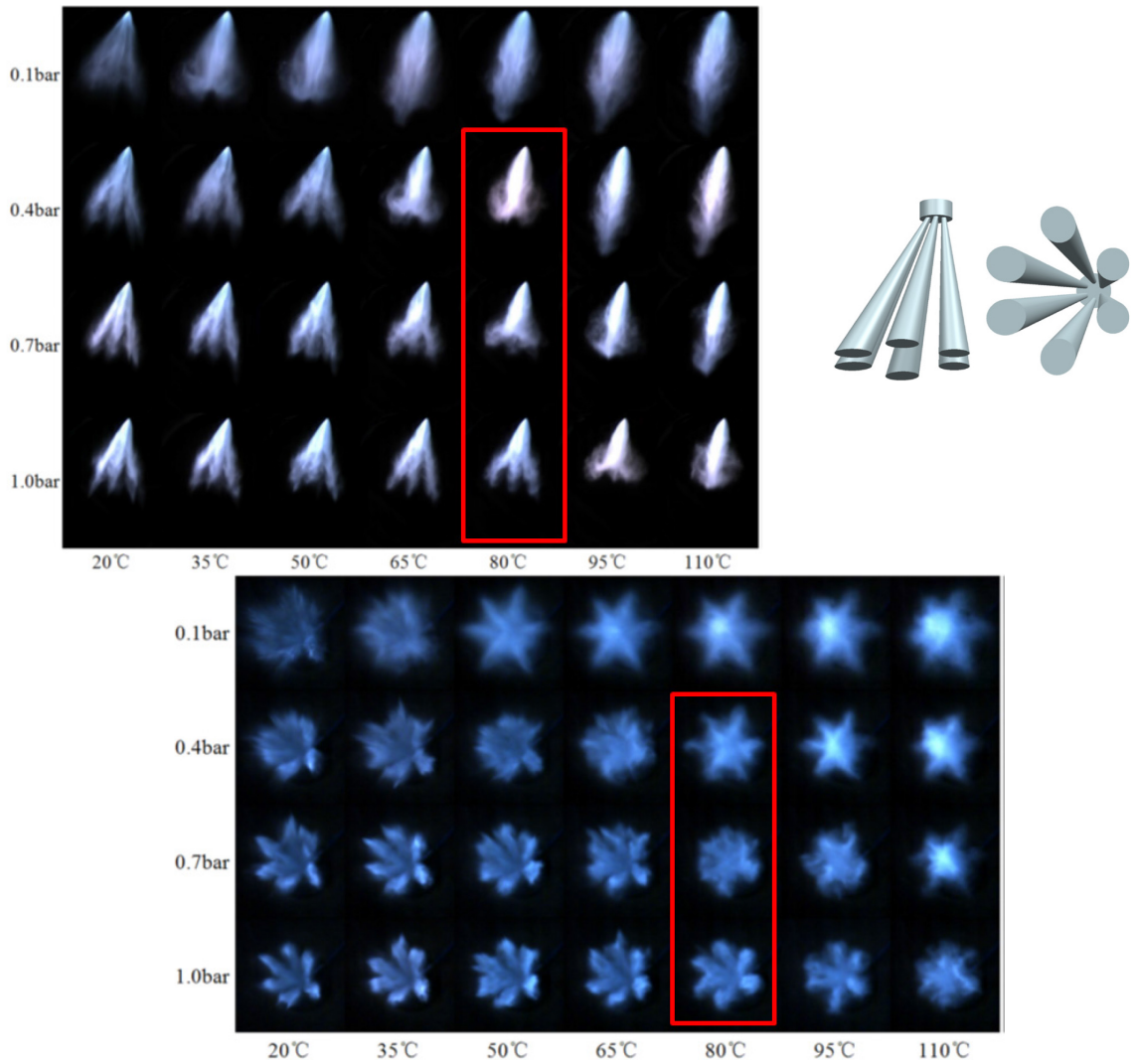


Figure 3.61 Experimental results of sub-cooled and flash-boiling sprays by Yang et al. (2013)

The behaviour of the spray structure was also investigated. More specifically, the bending of the plumes towards the centre of the injector and the bending near the plume tip was studied. The case with the fuel at 90°C and cone angle of 17° from Figure 3.59 was used (first row). In the literature it is said that a low pressure region is the cause of the plume merging and collapsing. The pressure field at the symmetry plane of the injector was plotted with the maximum value showed in red indicating the ambient pressure (0.5 bar) and the blue colour

indicated 0.48 bar. It is evident that there is a low pressure region in the injector which draws the plume into the zone. The low pressure zone is produced due to the increased evaporation of the fuel which replaced the existing air near the injector tip with fuel vapour. The molecular weight of *n*-Pentane is almost 2.5 times greater than that of air which resulted the pressure drop. Similarly, the vortex created due to the interaction of the plume with the ambient, also produced another region of low pressure which affected the propagation of the plumes.

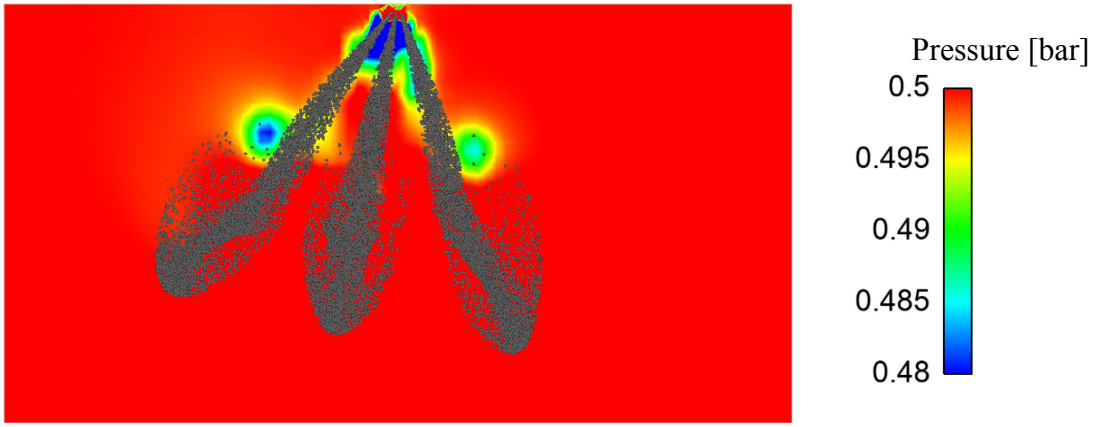


Figure 3.62 Spray structure and pressure field at the EB2 injector symmetry plane. Fuel temperature at 90°C, cone angle 17°, blob method, geometric constraints applied. (Figure 3.59, row 1)

Due to the absence of experimental data of the AJ20 injector at the conditions studied above to validatate the new approach (90°C injection temperature at 0.5 bar ambient pressure), the experiments of van Romunde and Aleiferis (2007) with the AJ133 injector were compared against numerical simulations with the improved setup (Figure 3.63). The grid initially was the one with the refined area around the injector tip. For the simulations *n*-Pentane was used, the injection temperature was 90°C and the ambient pressure 0.5 bar. The collision model with the geometric constraint activated was used and the droplet size initialisation was carried out with the Rosin-Rammler distribution. The mass flow rate was constant 2.3 g/s per hole and no further optimisation was carried out. Three different cone angles for the plumes were tested, the same as for the cases described above (15°, 30°, 45°). For the narrower angle, the curvature of the plumes and the recirculation of the droplets at the tip of the plume was evident however, the cone angle was narrow when compared against experimental images. When the cone angle was increased to 30°, the spray formation was in a good agreement to the experimental images of gasoline at 90°C temperature. A further increase of the cone angle to 45° agreed with the experimental images of gasoline at 120°C and *n*-Pentane at 90°C.

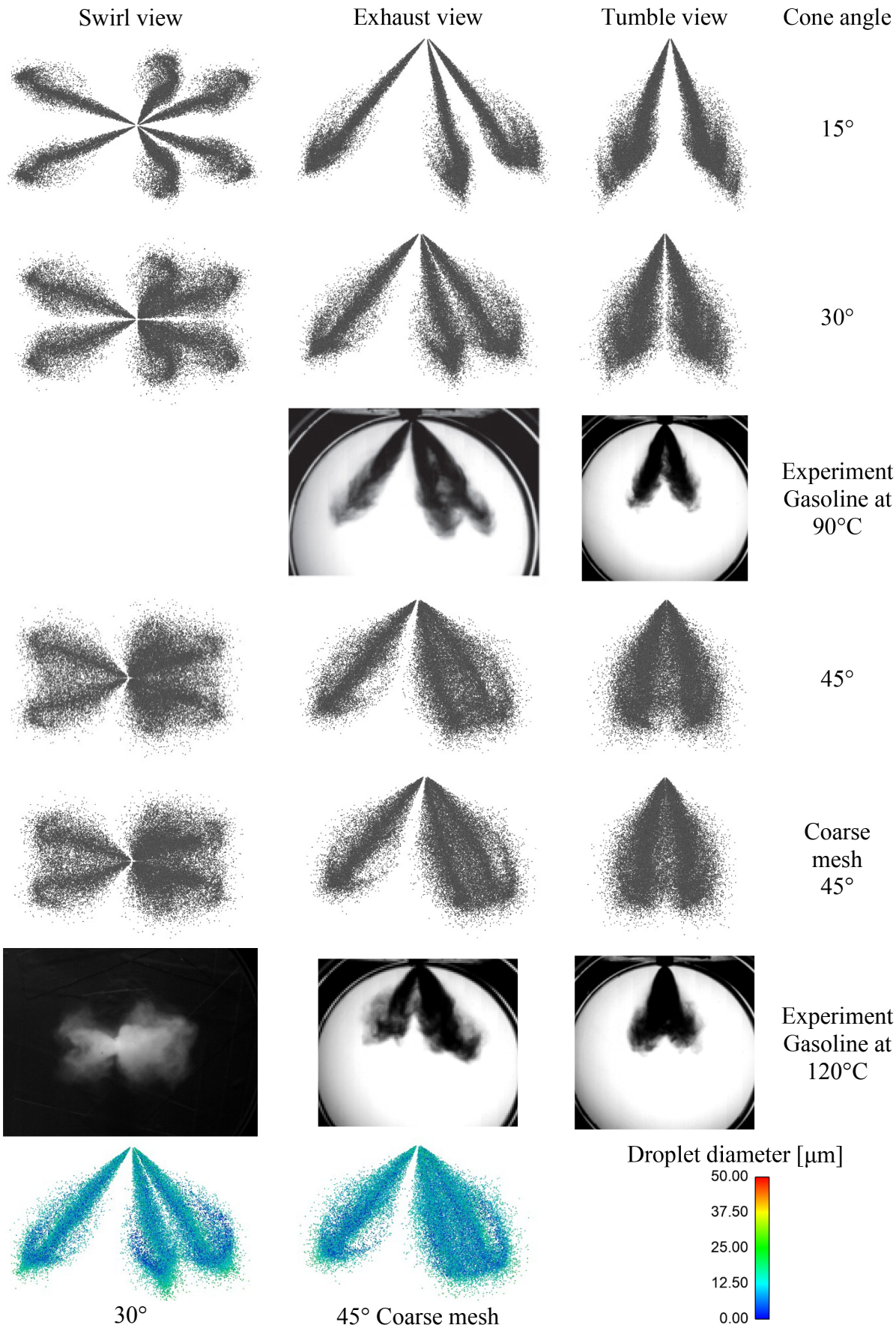


Figure 3.63 Numerical spray structure of the AJ133 injector for three different plume cone angles. Fuel at 90°C, Rosin-Rammler, geometric constraints applied

Except from the spray structure, the penetration of the plume 6 for the three cone angles was compared against experimental data (Figure 3.64). The penetration with the narrowest cone angle was predicting the penetration of gasoline at 90°C due to the high axial momentum. When the cone angle was increased and thus, the axial momentum was decreased the penetration was reduced and the results were closer to the experimental data of the fully flashing *n*-Pentane and gasoline. When 30° were used for the cone angle, the penetration was 4.5-7% above the mean penetration of *n*-Pentane at 120°C which gave the greatest penetration of all the fully collapsing sprays. However, it was very close to the upper limit of the error bars of this experimental condition. When this penetration was compared against the other experimental penetrations, the differences were greater (anywhere between 8% and 13%). For the widest cone angle, there was a very good agreement against the experimental penetrations of *n*-Pentane and gasoline at 120°C.

The last three simulations were also run for the grid without the refinement around the injector tip in order to validate the fact that these runs were independent of the cell size and the location of the initial location of each plume. In terms of spray structure, the results were almost identical and only the penetration changed of about 0.8mm. More specifically, for all three cases, the penetration was reduced when the grid without the refinement was used. The increase of the cell size caused a greater dissipation of momentum in the continuous phase and thus the gaseous velocity was reduced. As a result, the relative velocity of the droplet was higher which in turn increased the drag force on the droplet. Another case to validate the grid independency was the rotation of the injector z-axis by 35°. Again, there was no change on the structure or the penetration. In order to avoid to over-populate the graphs with lines that they fall on top of each other only cases that differed from each other were plotted. Lastly, with this setup and with the cone angle of 45° the numerical SMD number was compared against the experiments (Figure 3.65). The experiments of gasoline and *n*-Pentane for the fully flashing sprays produced SMD values of 8μm to 11μm. The converged value of the simulation was 9.5μm, which is in a good agreement with the experiments.

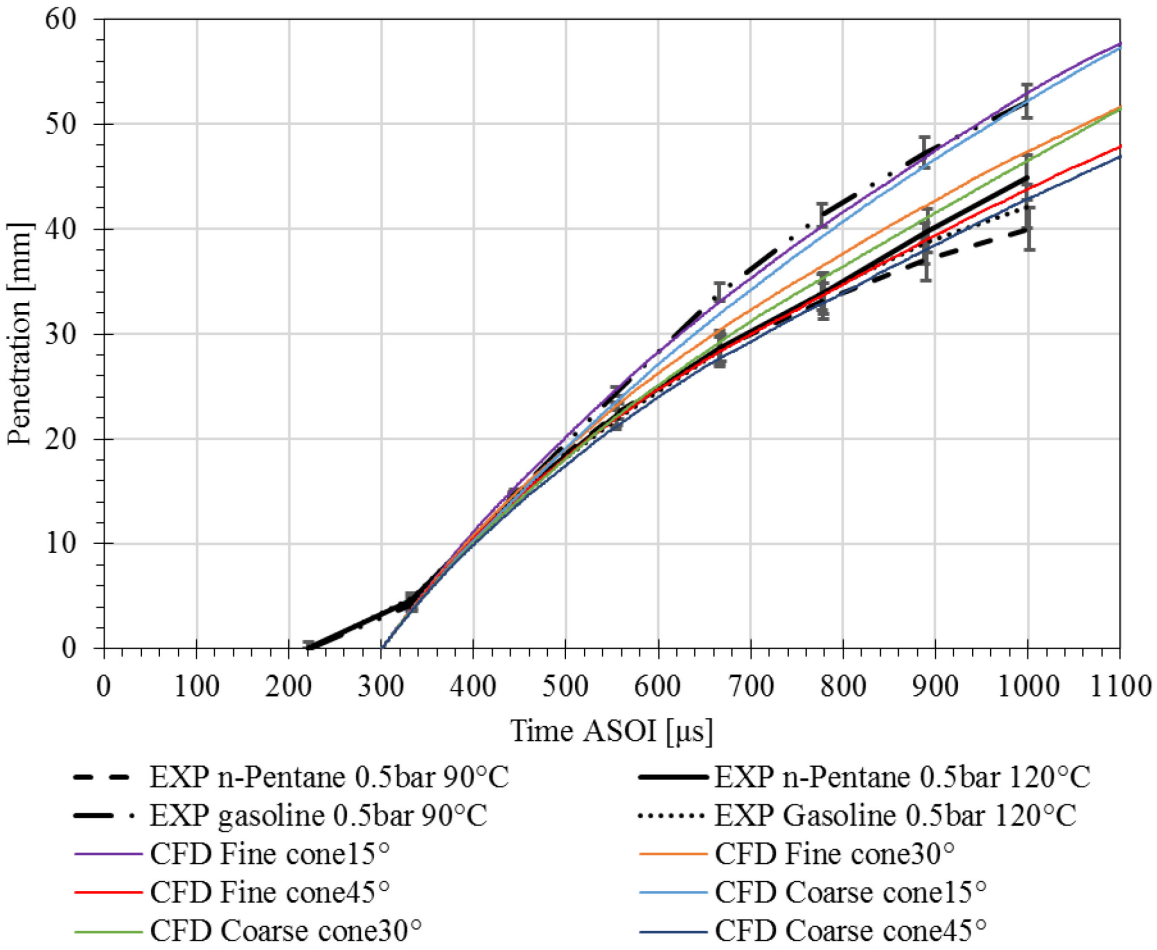


Figure 3.64 Experimental penetration of gasoline and n-Pentane at 90°C and 120°C. Numerical penetration of n-Pentane at 90°C with various cone angles at coarse and refined grid. Ambient pressure at 0.5 bar

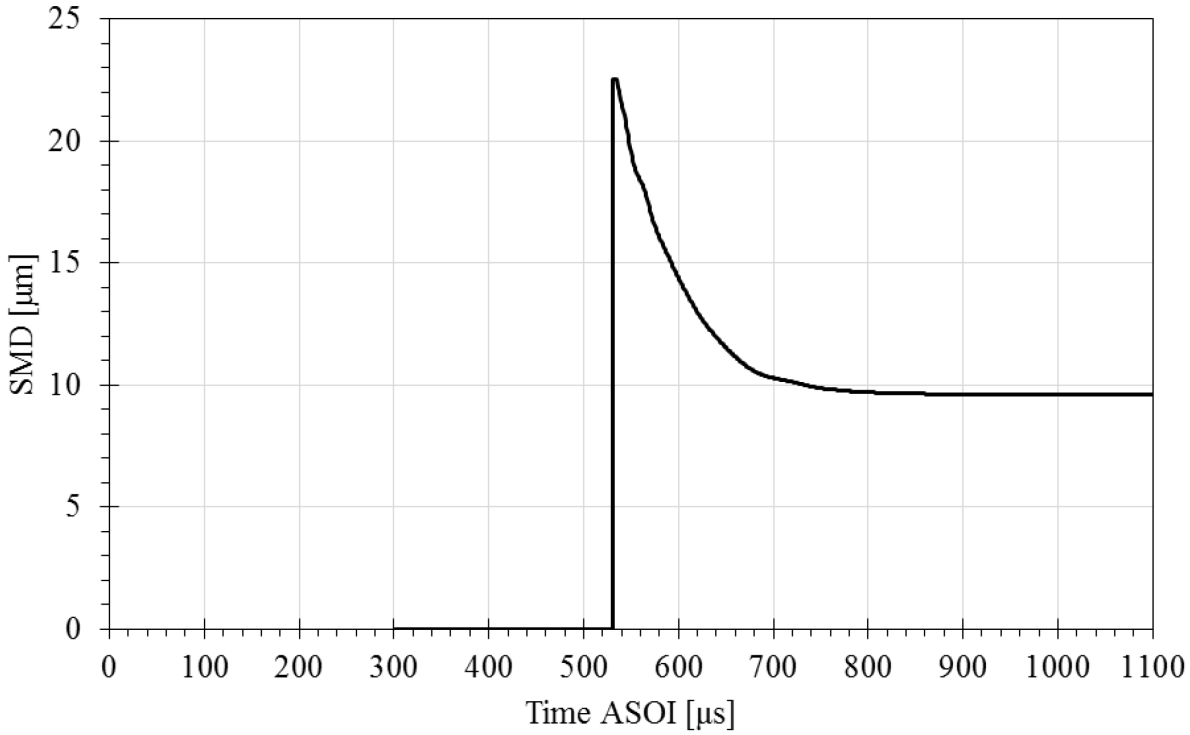


Figure 3.65 SMD number of the optimum flash-boiling case for the AJ133 injector, 25 mm below the injector tip

Lastly, a simulation was run to model an experimental case of the EB2 injector, injecting 90°C E10 gasoline at 1 bar ambient pressure (static engine). From the above findings, the simulation setup used 90°C *n*-Pentane, the droplet diameter was initialised with the sub-cooled parameters of the Rosin-Rammler distribution and the geometric constraints of the collision model were activated. From the experiments of Butcher *et al.* (2015) it was observed a small difference in droplet sizes for 20°C and 90°C gasoline injected at 1 bar ambient pressure and for that reason the sub-cooled parameters of the Rosin-Rammler distribution was used. Two plume cone angles were tested, the nominal 17° of the sub-cooled spray and 25° due to the small superheat degree of the gasoline. For this case experimental data only of spray structure were available. The comparison is shown in Figure 3.66 however, the experimental and numerical vies are not in the same scale. The spray structure with the 25° cone angle showed a good agreement with the experimental images of the swirl and tumble plane.

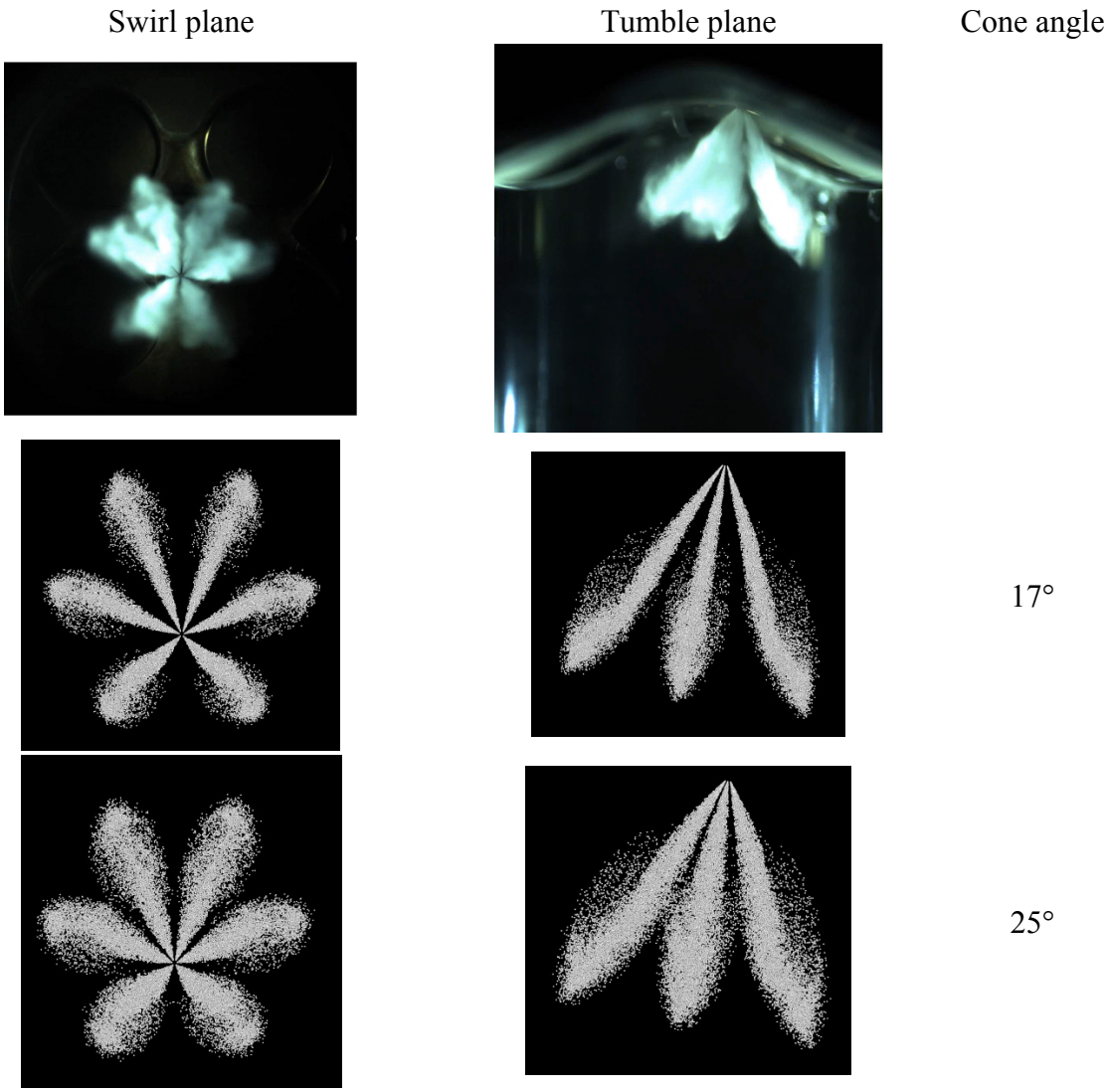


Figure 3.66 The EB2 flash-boiling spray structure for two plume cone angles. Fuel temperature at 90°C and ambient pressure 1bar. Comparison against gasoline at 90°C and 1 bar ambient pressure

From all the above tests it was concluded that the general approach should follow the steps:

- Each plume should be initialised from a different point in the domain by finding firstly the common point where all plumes cross each other
- The initial point of each plume should be ~1mm away from the common point and in the direction of the plume
- The geometric constrain of the collision model has to be activated to avoid unrealistic results due to the standard collision model.
- Preferably, the Rosin-Rammler distribution has to be applied for droplet size initialisation.

- For fully flashing gasoline sprays (90°C-120°C injection temperature at 0.5 bar ambient pressure) a cone angle in the range on 30°-45° is advisable.
- For transitional sprays a cone angle around 25° is advisable.

After the above conclusions, the flash boiling case in the AJ133 optical engine was run again with the generalised approach. This included a Rosin-Rammler distribution with 45° cone angle. At the swirl plane (Figure 3.67), the numerical predictions are in an agreement with the experimental snapshots of the spray propagation. At 4 degrees CA after SOI, the plumes 1 and 6 which are directed away from the optical window are under the spark plug, the same as in the experiments. Due to the fact that the light in the experiments is coming from the window (left side) and it is scattered by the four plumes targeting the piston, the plumes 1 and 6 are less visible. At 6 and 8 degrees after SOI, the centre of the four merging plumes is brighter due to the higher concentration of droplets and a similar behaviour can be seen in the predictions. In the tumble plane (Figure 3.68), at the 3.6 degrees after SOI, the plumes that are merging (2,3,4,5) have the same penetration as the experiment which can be identified by using the intake valve as a reference. There is small difference between experiment and CFD because of the 0.4 deg CA difference of the two images. At 9 degrees after SOI the recirculation of the droplets and the increased penetration at the intake side which was seen in the experiment was also seen in the numerical predictions.

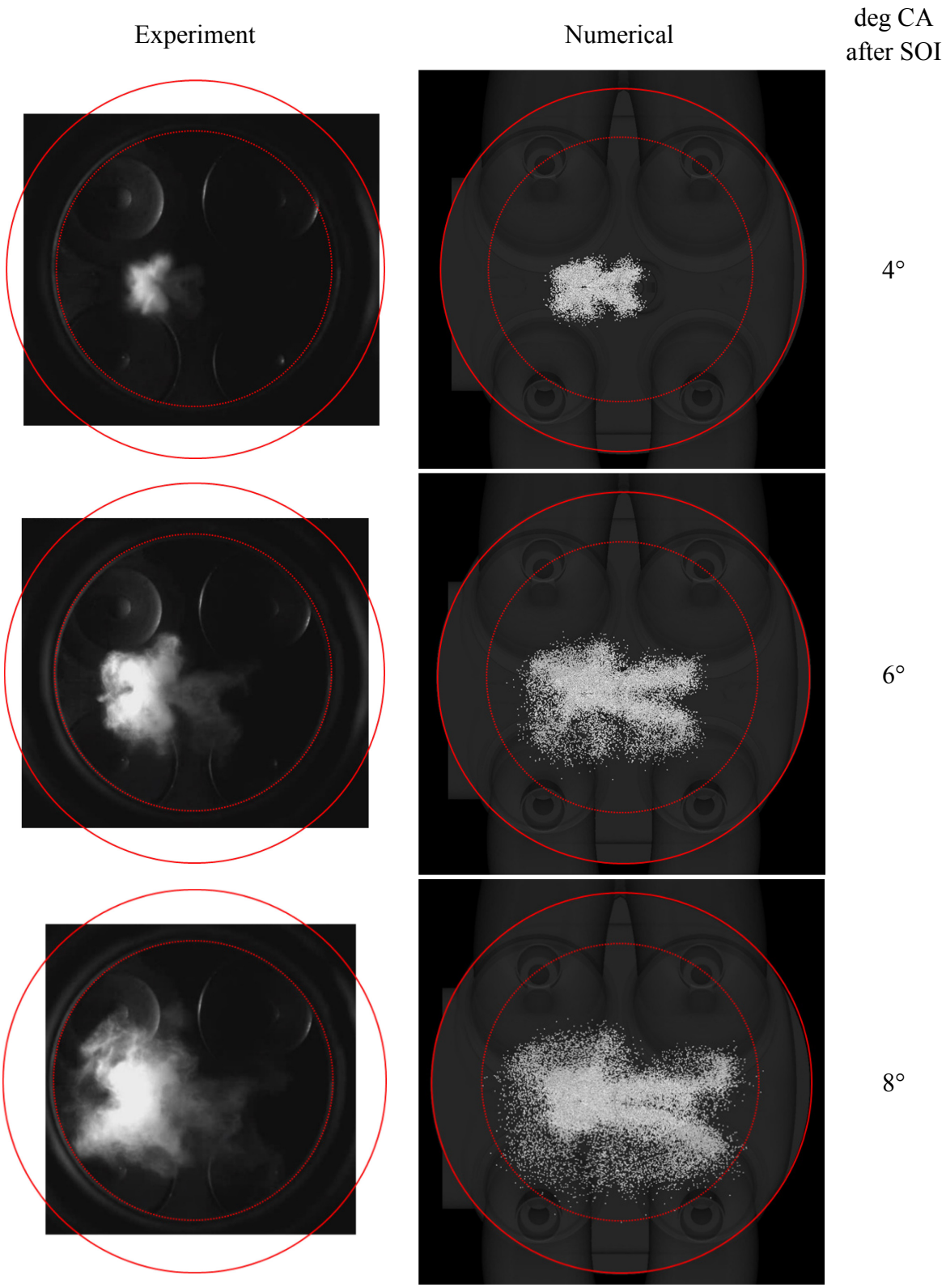


Figure 3.67 Numerical spray development and experimental spray development in the AJ133 optical engine, optimised flash-boiling spray, swirl plane

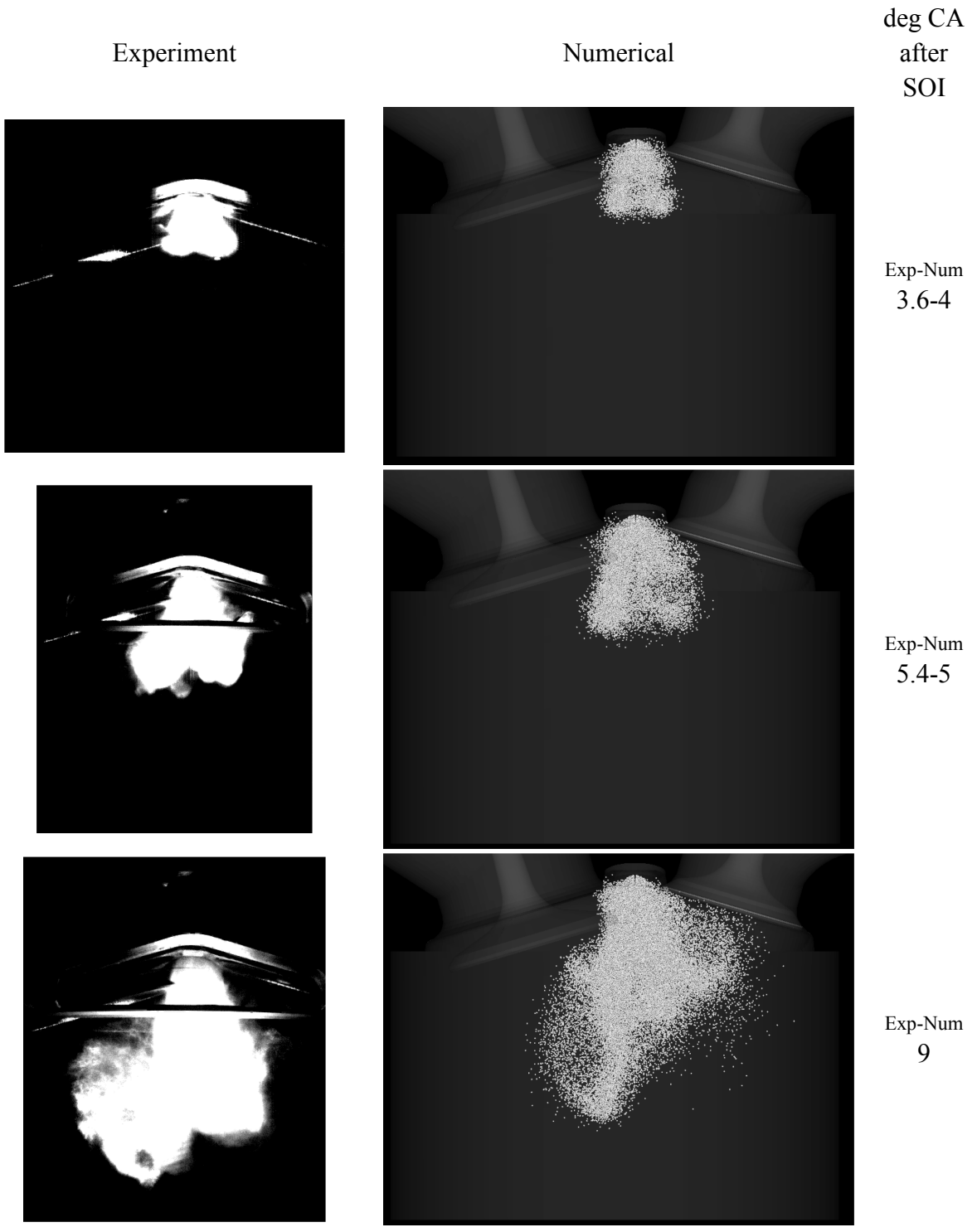


Figure 3.68 Numerical spray development and experimental spray development in the AJ133 optical engine, optimised flash-boiling spray, tumble plane

To sum up, the spray modelling was validated against experimental data of spray shape, penetration, droplet sizes and spray tip velocity. The spray tuning was done with the appropriate initial droplet size and break up parameters. When the model was introduced in an engine, the penetration of plumes 1 and 6 was slightly over-predicted and the spray reached the cylinder liner 1 degree CA earlier than the experiment but the penetration of the other plumes was closer to the experiment and reached the piston surface at the same time. Moreover, the curved behaviour of plume 6 and the transportation of the droplets from plume 1 due to the intake valve jet was accurately predicted. Furthermore, the air-fuel mixture before ignition was compared against QPLIF data which showed differences between the experiment and the predictions possibly due to the stronger tumble flow of the CFD.

A fuel spray validation and development for flash-boiling conditions was carried out in a quiescence chamber testing two approaches of droplet initialisation. Improvement of the existing model with grid independence was achieved. In addition, the conclusions of the quiescence chamber were transferred to a dynamic model of the AJ133 optical engine for further validation of the spray behaviour during motoring.

3.9. Validation of fuel impingement and film formation

Fuel-wall interaction and film formation are two factors that affect hydrocarbon and particulate emissions. Accurate prediction of these two phenomena can lead to interpretation of experimental measurements and prediction of new designs and strategies.

Validation of the predicted heat flux of an impinging spray onto the liner of the AJ133 static engine (1 bar ambient pressure) was performed and compared to measurements by a heat flux sensor (Serras-Pereira *et al.* 2013). Two droplet-wall interaction models were considered, namely Bai-ONERA and Senda which predict the outcome (adhere, bounce or shatter) of droplet impacting on a wall. For the adhesion regime, a droplet to film transition model offered by the software and was the suggested option was also considered. In addition, the area where the spray was impacting was discretised with two different cell sizes (1 mm and 0.5 mm). These sizes are typical in engine modelling for grids consisted of about 1 and 2 million cells respectively. Lastly, a 1D conjugate heat transfer model which calculates the heat conduction in the solid and the interaction of the solid-fluid interface was tested. Five different cases were tested with the fuel temperature at 20°C and the wall temperature at 10°C, 20°C, 34°C, 48°C and 66°C. The simulated fuel was *iso*-Octane with the injection duration of 0.8 ms, the same

as in the experiment. The rest of the spray setup (spray velocity, mass flow rate, initial droplet size etc.) was the same as for the validation of the AJ133 injector. The heat flux was averaged from a circular area of 6.4 mm diameter (heat flux sensor face) at the position of the heat flux sensor (17 mm below the head gasket). The sensor position around the bore is at the maximum heat flux of plume 6. In the simulations, the cell faces which had their centroid within the circle of 6.4 mm diameter were considered.

The numerical peak heat fluxes were compared against the experimental averaged peak heat fluxes. Firstly, the two droplet-wall interaction models were tested for the two surface cell sizes with and without the 1DCHT model, having activated the droplet to film transition model and the results are shown in Figures 3.69 and 3.70. Form Figure 3.69, the peak heat flux predicted by the Senda model for both cell sizes, with and without the 1DCHT model at different wall temperatures can be seen. The results for all cases, except the one with the coldest wall (10 °C) in which the peak heat flux was under-predicted (1/3 of the experimental value), are within the standard deviation of the experiment. The peak heat fluxes predicted by the smaller cell size were closer to the mean experimental values and were following the trend of increased heat flux as the wall temperature was increased with and without the 1DCHT model. However, for the coarser grid, higher discrepancies were seen as the wall temperature was increased. With the use of the 1DCHT model, the trend of high discrepancies was preserved with the coarser surface mesh. With the finer grid, the results were within the experimental range and close to the mean values (less than 10% for all temperatures) without the 1DCHT model and a difference of up to 25% with the use of the 1DCHT model.

When the Bai-ONERA model was used (Figure 3.70), the predicted peak heat fluxes were either lower than the experimental results or there was no heat flux. More specifically, the trend of the simulations with the 0.5mm cell resolution produced peak heat flux which follow the experimental trend however, they were three times lower than the experimental values and outside the standard deviation. When a coarser surface mesh was used, no heat flux signal was recorded irrespective of wall temperatures. The use of the 1DCHT model had the same results for the coarse and fine mesh. An inspection of the impingement area showed that no liquid film was formed, and the impinging droplets adhere to the wall in spherical or cylindrical form which were treated individually thereafter. The high dependence of the liquid film formation itself on the size of the surface cell lead to the investigation of this behaviour. The area of the cell face is only used in the droplet to film transition model and it is inversely proportional to the transition criterion meaning that for larger cells, more droplets have to be adhered in order

to have liquid film formation. In these cases, the number of droplets which adhered on the wall was larger with the Senda model, which lead to satisfying the droplet to film transition model. With the Bai-ONERA model, the smaller number of adhered droplets did not satisfy the criterion for the coarse grid, while for the finer grid, this process was slower resulting on fewer mass and lower heat transfer. The differences seen between the Senda and the Bai-ONERA models are due to the different criteria applied for the distinction of the droplet-wall interaction regimes.

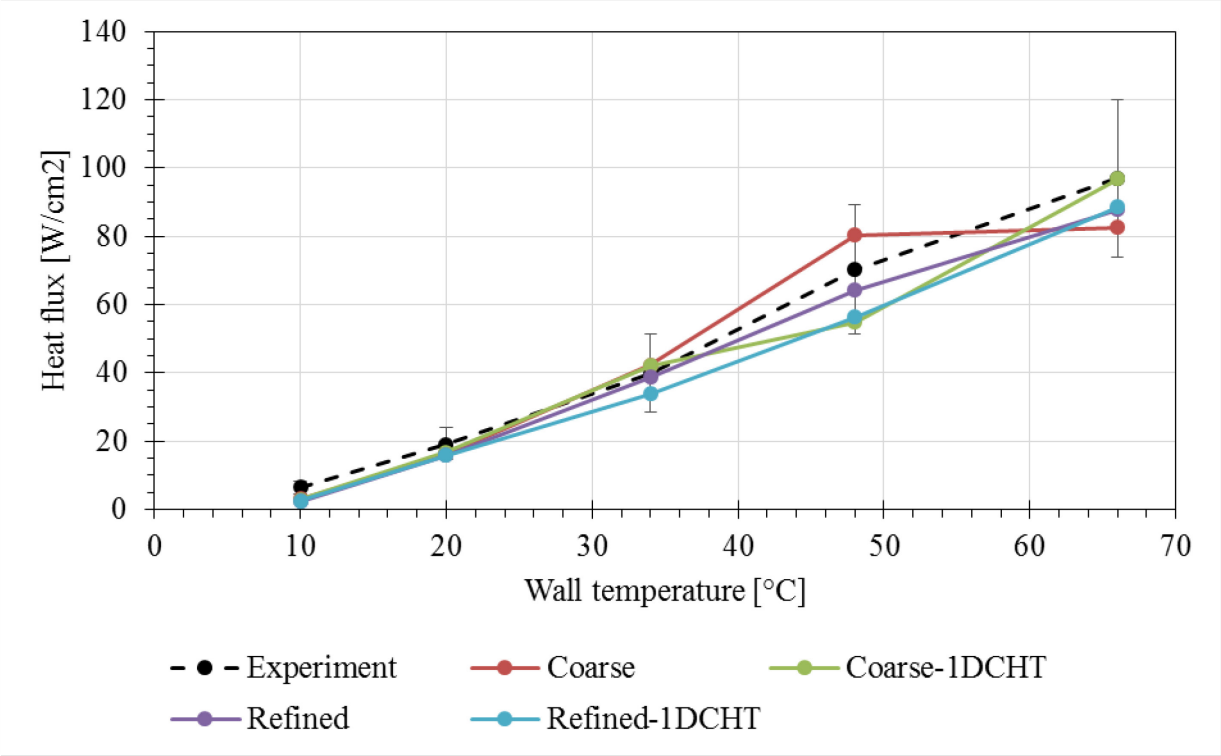


Figure 3.69 Experimental average peak heat flux and numerical peak heat flux of Senda model with coarse and refined surface mesh, with and without the 1DCHT model, with droplet to film transition model, various wall temperatures

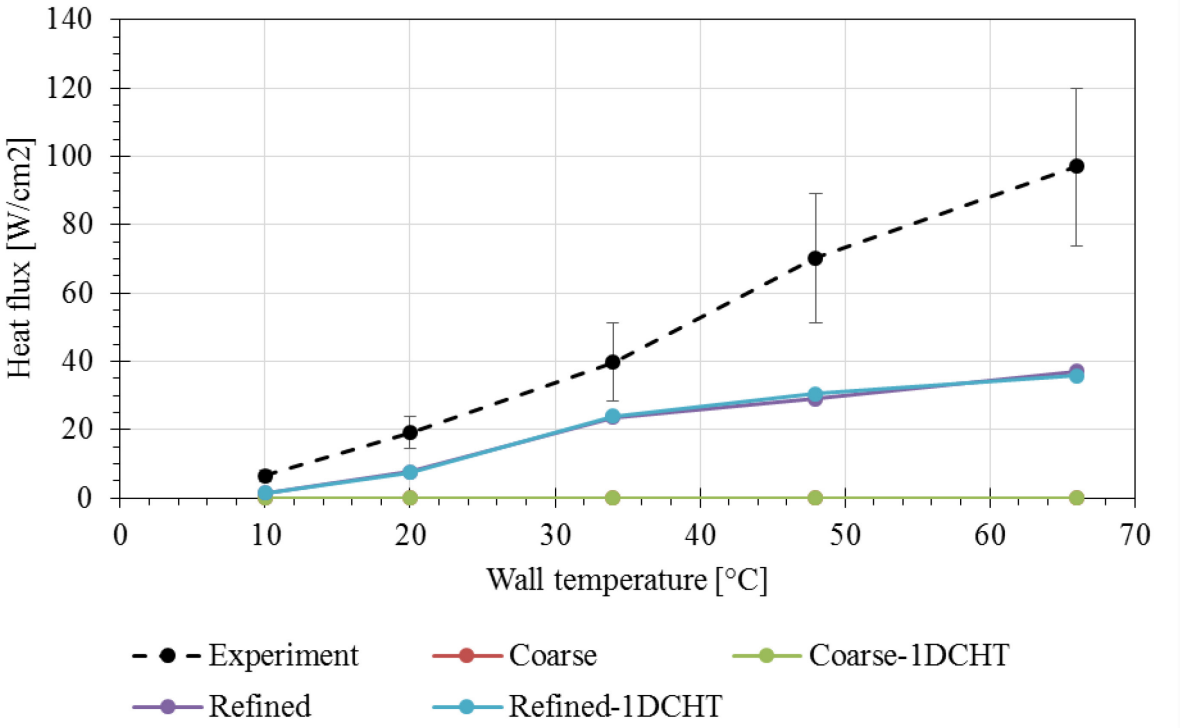


Figure 3.70 Experimental average peak heat flux and numerical peak heat flux of Bai-ONERA model with coarse and refined surface mesh, with and without the 1DCHT model, with droplet to film transition model, various wall temperatures

For the reasons mentioned above, the same simulations were run without the droplet to film transition model. The results can be seen in Figures 3.71 for Senda model and 3.72 for Bai-ONERA. The peak heat flux predicted by the Senda model were improved further, especially for the finer surface mesh which had a difference of 13% when the wall temperature was 66 °C and less for lower temperatures. However, the heat flux for case with the coldest wall (10 °C) was again below the mean experimental value. This can be explained by the fact that the injected fuel in the experiment may be slightly hotter than the nominal 20 °C (Serras-Pereira *et al.* 2013) while for the simulations the nominal value was used. Moreover, these variations have a stronger effect when the fuel-wall temperature difference is smaller. The peak heat fluxes with the 1DCHT model was very close to the simulations without the model and the differences were about 1% or less. With the coarser surface mesh, the discrepancies of the predicted peak heat fluxes continued and a maximum difference from the experiment of 30% was observed.

In addition, the deactivation of the droplet to film transition model drastically improved the peak heat flux predicted by the Bai-ONERA model. Both coarse and fine surface meshes produced liquid film and thus, the peak heat fluxes were close to the experimental averaged

peak heat fluxes and within the standard deviation. Again, the heat flux for the cases with the coldest wall was below the experimental value. The repeatability of this behaviour can support the argument of slightly hotter that the nominal injected fuel in the experiment. The use of the 1DCHT model produced again discrepancies for the coarser grid but for the finer mesh, the difference from the simulations without the model was minor (less than 1%). In addition, the finer mesh had a maximum difference of 10% observed at 66 °C wall temperature and the coarser mesh had a maximum difference of 30% at 66 °C wall temperature with the 1DCHT model and 35% difference without the 1DCHT which was seen at 34 °C wall temperature. Because of these results, it was decided to deactivate the droplet to film transition model for the rest of the studies.

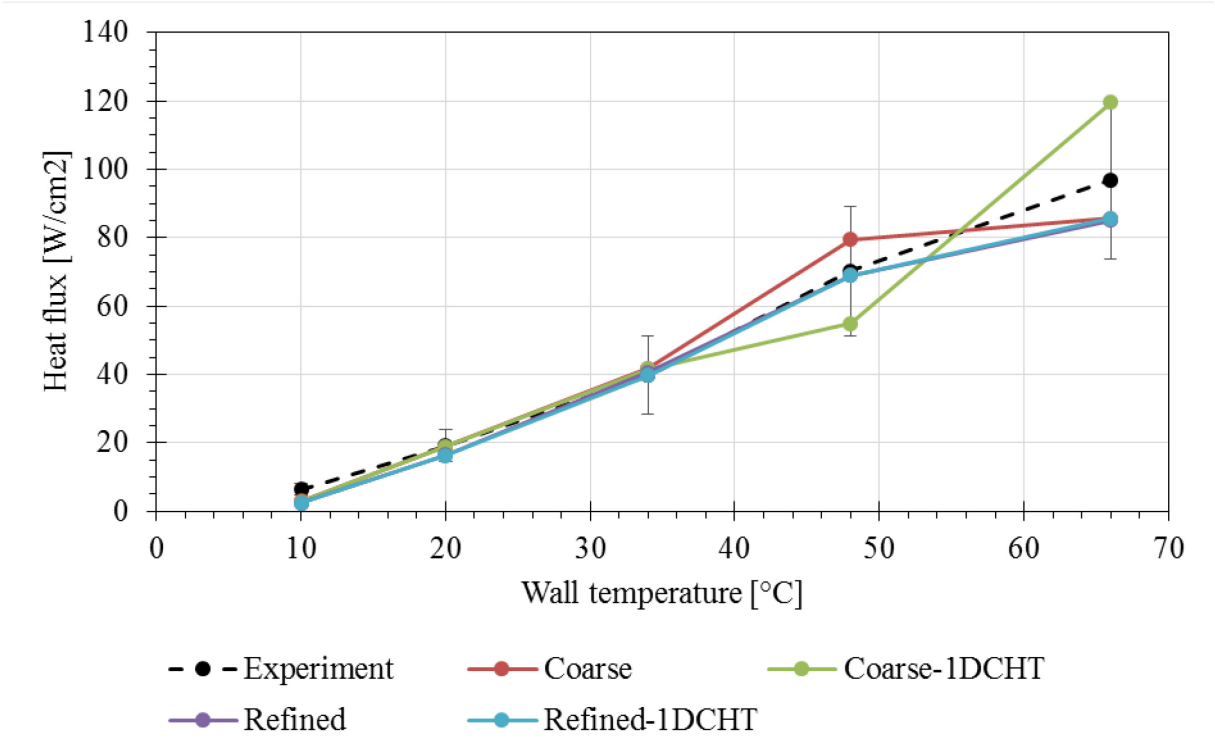


Figure 3.71 Experimental average peak heat flux and numerical peak heat flux of Senda model with coarse and refined surface mesh, with and without the 1DCHT model, without droplet to film transition model, various wall temperatures

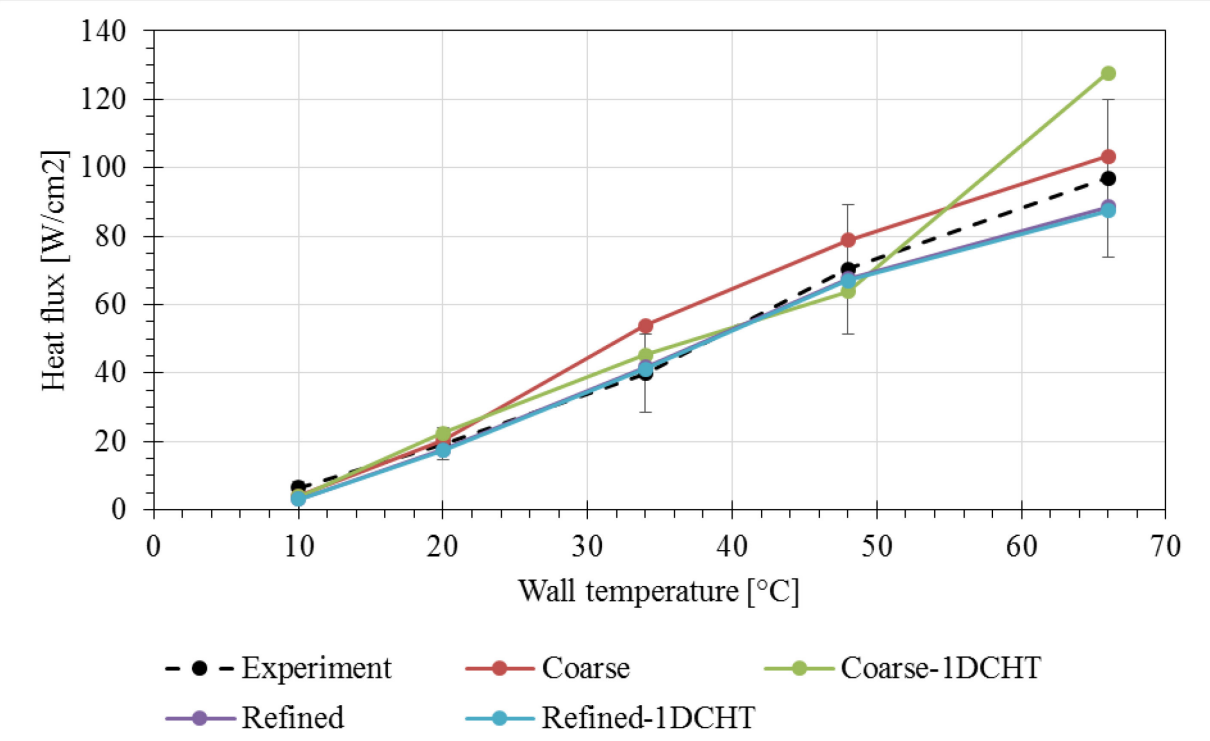
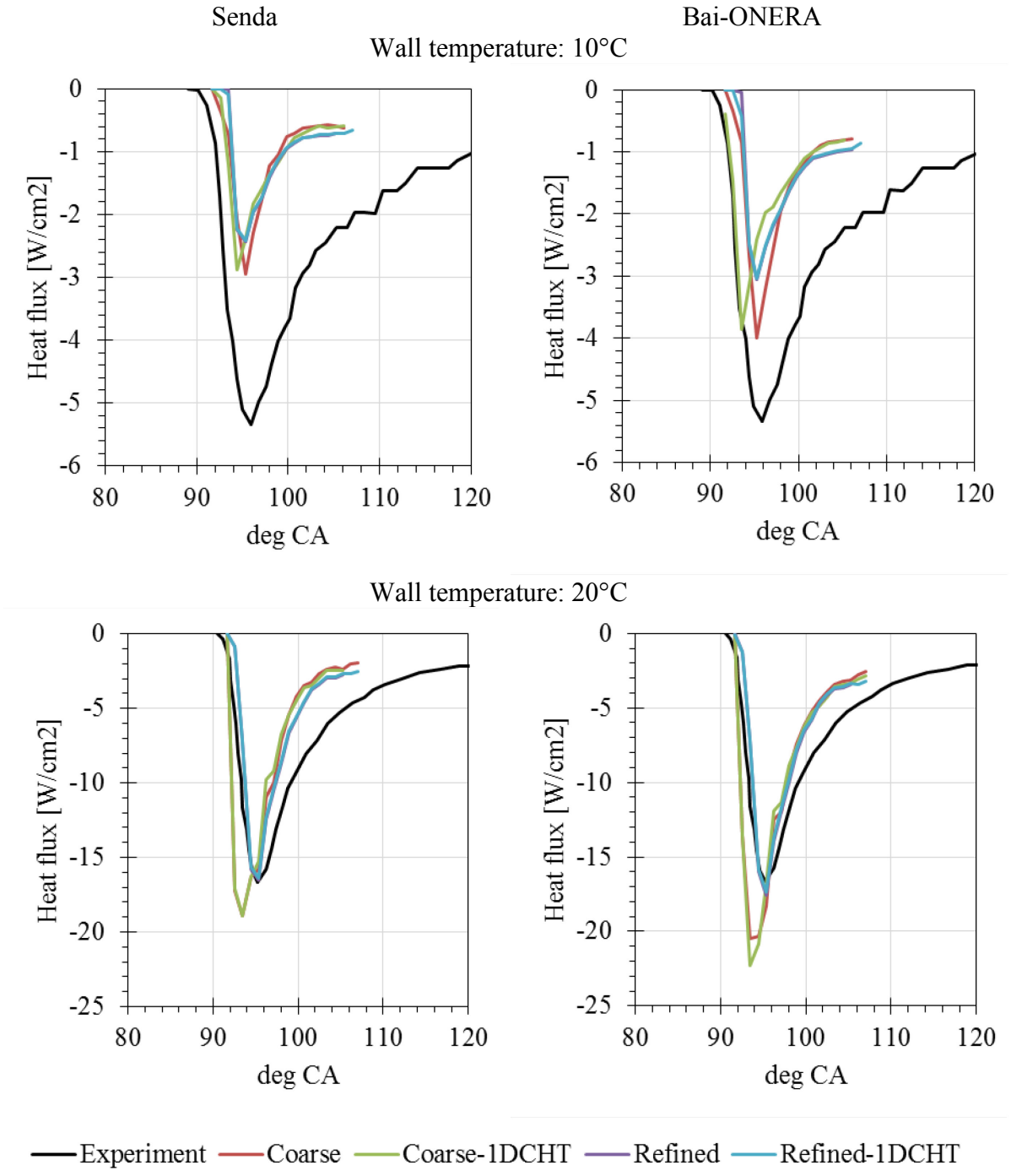
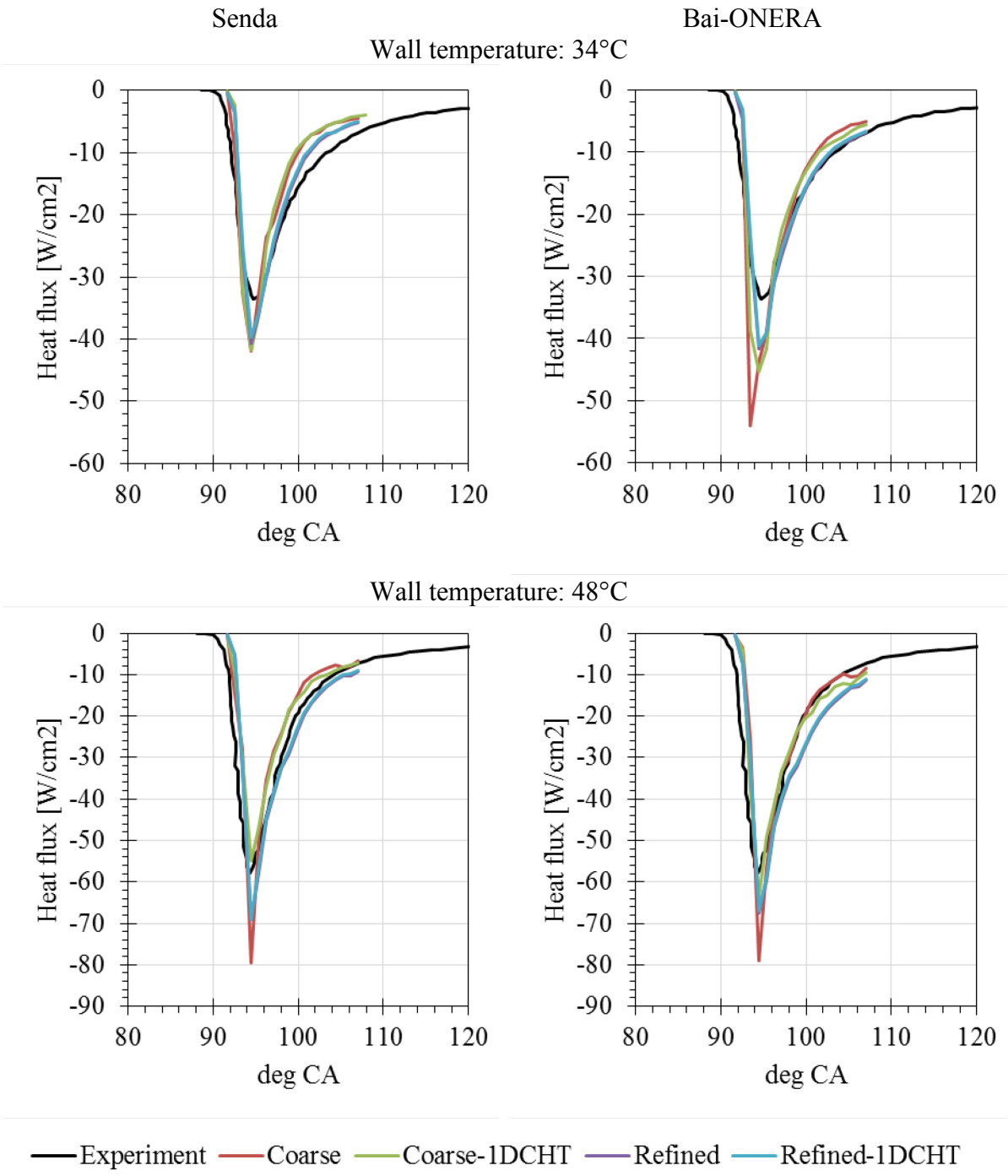


Figure 3.72 Experimental average peak heat flux and numerical peak heat flux of Bai-ONERA model with coarse and refined surface mesh, with and without the 1DCHT model, without droplet to film transition model, various wall temperatures

After the comparison between the numerical peak heat flux and the experimental averaged peak heat flux, the whole numerical heat flux signal of the above cases was compared against the experimental mean signals (Figure 3.73). Both Senda and Bai-ONERA models with and without the 1DCHT model were tested, for a coarse and refined surface mesh and without the droplet to film transition model. First of all, the initial rise of the heat flux in the simulation for all cases occurred at the same time as the experimental heat flux, meaning that the fuel spray setup and thus the validation of penetration can be supported by this study as well. Secondly, as it was seen before, the biggest differences between the numerical and experimental heat flux signals occurred for the cases with the coldest wall. As the wall temperature was increased the numerical results were closer to experimental signal and were in a good agreement. This behaviour can be seen for either of the two droplet-wall interaction models. An explanation is again the difference of the injected fuel temperature from the nominal temperature which is more profound when the fuel-wall temperature difference is lower. For a specific wall temperature and for both droplet-wall interaction models, the finer mesh produced higher (absolute number) heat fluxes than the coarse mesh of about 20% depending on the case (wall temperature) and time. This is due to the surface area that was considered within the 6.4 mm diameter of the heat flux sensor face. With the finer mesh, more cell faces with liquid film and

thus high heat flux were included within the circle which increased the average value. The differences between the use of the 1DCHT model and the constant wall temperature were minor for both coarse and fine surface mesh. The ONERA model predicted a signal closer to the experimental mean signal in the cases were the wall temperature was up to 34 °C. Above this temperature, the Senda model was closer to experiment.




Senda
Bai-ONERA
Wall temperature: 34°C
Heat flux [W/cm2]
deg CA
Wall temperature: 48°C
Heat flux [W/cm2]
deg CA
Experiment
Coarse
Coarse-1DCHT
Refined
Refined-1DCHT

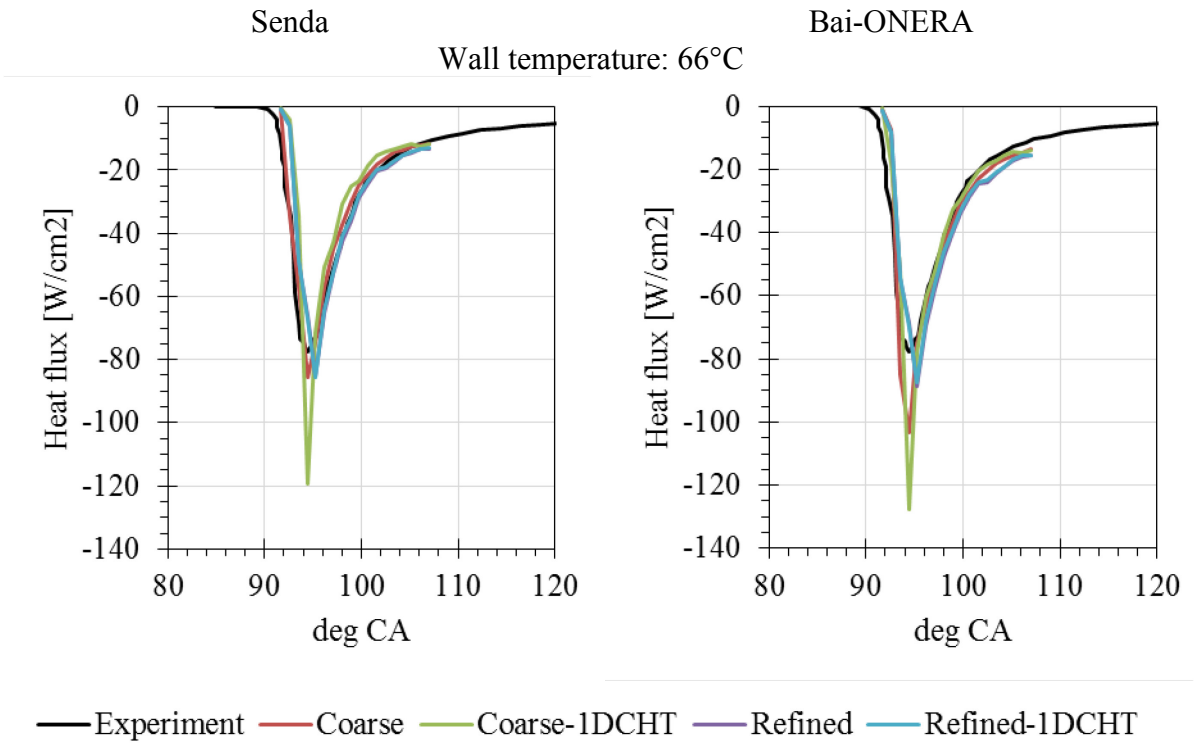


Figure 3.73 Experimental mean heat flux signal and numerical heat flux signal for coarse and refined surface mesh, with and without 1DCHT model, without droplet to film transition model, various wall temperatures

Due to the fact that both Senda and Bai-ONERA models gave results close to the experimental heat fluxes without major differences, the liquid film thickness, film mass and footprint were compared against LIF fuel wall film experimental data (Schulz *et al.* 2016). The simulated fuel was *iso*-Octane at 30 °C, at 1 bar ambient pressure and 80 °C ambient and wall temperature and each hole injected 3.63 mg of fuel. The two aforementioned droplet-wall interaction models were considered without the droplet to film transition model. In addition, the 1DCHT model was used to investigate the effect on liquid film formation, because the results of the heat fluxes did not have any improvement.

The injector used in the experiments was a symmetrical 6-hole Bosch HDEV5 with 180-210 μm hole diameter as it was mentioned in a set of publications (Schulz *et al.* 2014, 2015, 2016). The chosen rail pressure was 150 bar to match the injection pressure of the AJ133 engine. The development of the penetration of this injector was not known but at 500μs ASOI it was mentioned that it was 30mm at 1 bar ambient pressure (Schulz *et al.* 2014). The tuned setup of the AJ133 injector was used because of the similarity of the conditions of the two injectors. Furthermore, at 1 bar ambient pressure, this setup gave 30 mm spray penetration at 500μs ASOI. Due to the symmetry of the injector, only one plume was simulated to reduce the

computational domain and decrease the running time. The distance of the injector from the wall was 35 mm, the injection duration was 1.5 ms and all the data were acquired 5 ms ASOI which is according to the experimental study. This experimental configuration was chosen as the most similar to the AJ133 hardware, running conditions and validated cases.

Figure 3.74 shows the comparison of *iso*-Octane liquid film footprint size and film thickness with experimental data for the two droplet-wall interaction models. The thick lines of the grid in the figures of the simulations have 5 mm distance, the same as the dotted lines in the experimental figure. The dotted lines in the figures of the simulation have 1 mm distance. Here, the differences between the models are more profound. The width of the footprint is slightly bigger for Senda model and closer to the experiment. The biggest difference however is evident at the direction of the jet. The footprint predicted by the Senda model is 40% longer than the one by Bai-ONERA and it is also in a good agreement with the experiment. In addition, the film thickness is better predicted by Senda model. The film thickness at the location of the spray impact is similar for both models and close to the experimental footprint. However, the accumulated liquid fuel at the tip of the film is predicted only by the Senda model and it is in a good agreement with the experiment. The small ligaments of higher film thickness were not able to be predicted due to their small size which was not resolved. Their thickness though was around 24-40 μm which was predicted by the Senda model at the tip of the film. The similar numerical results of the liquid film at the impact region explains the similarity of the heat flux results. Due to the size of the sensor, only the heat flux at the area of the impact was captured and not the heat flux of the total liquid film area. Because of the similar liquid film formation at the area of the spray impact for both models the heat fluxes were very similar as well. There was no difference on the size of the footprint between the constant temperature of the wall and the 1DCHT model for both Bai-ONERA and Senda model. The liquid film predictions of the two models were also tested with a refined surface mesh (0.5 mm cell size). The size of the footprint in terms of length and width did not have significant changes when going from coarse to fine surface mesh for both models as it can be seen from Figure 3.74. The length of the footprint predicted by the Bai-ONERA model is about 1 mm shorter with the finer mesh. For the finer mesh and with the use of the Senda model, the length of the film is about 2mm shorter than with the coarse surface mesh. Again, even with these small differences, the Senda model is in a good agreement with the experiment. For these calculations of the length, the thin film traces represented by the lightest colour of the legend were not taken into account as these details can be distinguished numerically but not represented in the experimental plots.

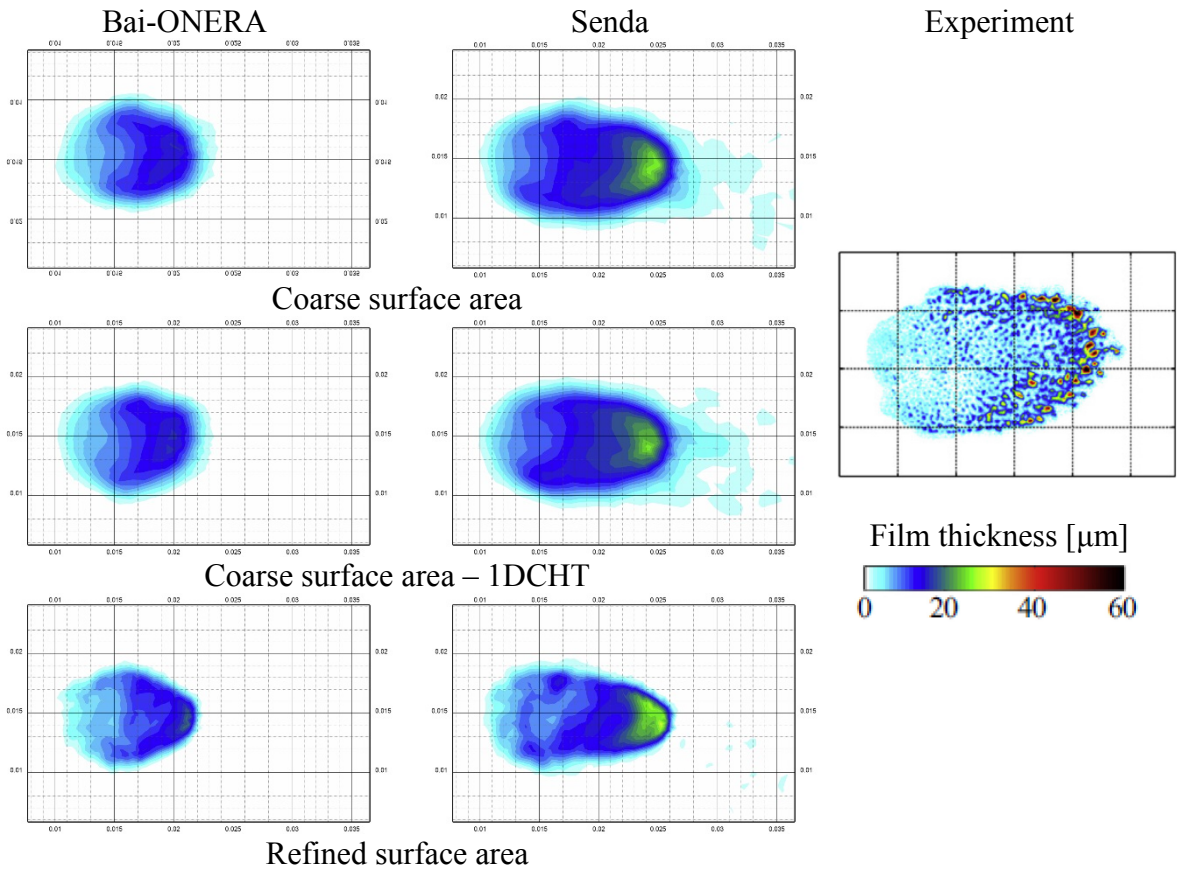


Figure 3.74 Experimental liquid film footprint and film thickness, numerical liquid film footprint and film thickness for Bai-ONERA and Senda models, coarse surface mesh with and without 1DCHT model and refined surface mesh

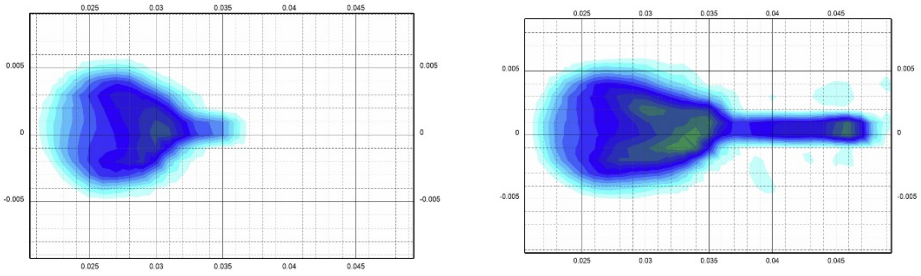
Moreover, the mass of the liquid film was calculated and compared to the experimental film mass as shown in Table 3.9. As it was expected due to the bigger footprint, the Senda model predicted 50% more liquid film mass than the Bai-ONERA model and it was also in a good agreement with the experimental film mass (8% difference from the mean value). The difference between the constant temperature wall and the 1DCHT model on the liquid film mass was minor (less than 1%) for both droplet-wall interaction models. When the surface area was refined, the liquid film mass predicted by the Bai-ONERA model increased by 3% due to the higher accumulated liquid at the tip of the footprint. However, this increase was again less than the half of the mean experimental value. With the Senda model and the refined surface mesh, the predicted liquid film mass was reduced by 20%. This reduction was due to the reduced film length and the prediction of the film thickness, especially at the area of the spray impact. While at the tip of the film the accumulated liquid gave a slight increase on the thickness but in a smaller area, the thickness at the impact area was lower. These two changes competed each other which resulted in the reduction of the total mass which however was close to the lower limit of the experimental values.

It has to be noted that in the experiment there was an 8% difference in film mass between the six plumes of the injector and ±0.15 mg deviation over a series of injections for a specific plume which can give a total difference of about ±0.2 mg. This shows that the predicted mass is within or close to the experimental variations when the Senda model is used. Another factor that may affect the differences between simulations and experiments is the surface of the experiment. The quartz glass due to the very smooth surface can affect the outcome of the droplet-wall interaction in a different way than a metallic surface with which the models and the model constants have been developed.

	Bai-ONERA	**Senda**	**Experiment**
Coarse	0.604	1.232	1.34 ±0.2 mg
Coarse - 1DCHT	0.598	1.235	
Refined	0.624	0.992	

Table 3.9 Liquid film mass for Bai-ONERA and Senda models with coarse and refined surface mesh and comparison with experiments.

It has to be mentioned that artefacts regarding the Lagrangian multiphase had to be addressed. An over-prediction of droplet penetration was observed when the axis of the spray jet was parallel to the hexahedral mesh. This also produced unrealistic liquid film irrespective of the droplet-wall interaction model, as shown in Figure 3.75. In order to resolve this, the vertical axis of the injector was rotated by 35 degrees. All the results described above were done after resolving this issue. For the AJ133 injector, there was no problem with this artefact because the injector pattern is not symmetric and thus, the orientation of the plumes was not parallel to the mesh orientation.



Bai-ONERA Senda

Figure 3.75 Artefacts coming from the Lagrangian multi-phase treatment for both Bai-ONERA and Senda models.

For the last part of the impingement validation, the heat flux signal in the motoring AJ133 engine (Serras-Pereira *et al.* 2012) with fuel injection was investigated. The findings from the

above studies were implemented, using the Senda droplet-wall interaction model. Again, the heat flux sensor was positioned 17 mm below the head gasket and at 35° in respect to the bore location and where the maximum heat flux was recorded. There is a small difference between this location and the experimental (40°-45°) probably because the plume 6 in the CFD was not diverted as much as in the experiments. Also, possible small misalignments of the injector in the engine compared to the optimum alignment in the model can have an effect. The motoring conditions were at 0.5 bar intake pressure, 1500 RPM and the wall and fuel temperatures were at 20°C. The fuel in the experiments and simulations was *iso*-Octane. The experimental and numerical heat fluxes are shown in Figure 3.76. It is evident that in both experiments and CFD, an initial drop of the heat flux due to the arrival of the spray occurred at 11 degrees ASOI (91 degrees on the graph). In addition, the peak heat flux was also recorded at the same time (15 degrees ASOI). After the peak both signals drop in magnitude. However, some differences exist between the predictions. First of all, the difference of the peak heat flux is about 40% with the numerical predictions being higher. It was stated by the same authors in a publication where the engine was static (Serras-Pereira *et al.* 2013) when heat fluxes were recorded, the mean peak heat flux values differed from the peak value showed in the mean signal due to the shot-to-shot variability. Here, with the cyclic variability also included, differences in the peak values were expected. In addition, during the reduction of the heat flux, the experimental curve is smaller (absolute numbers) than the numerical predictions. This can also be due to the averaging of the individual cycles. Moreover, at this low load, cold condition, the effect of the previous cycle was seen and reported in the experiments can have an effect on the average heat flux signal when compared to the dry wall of constant temperature of the simulation.

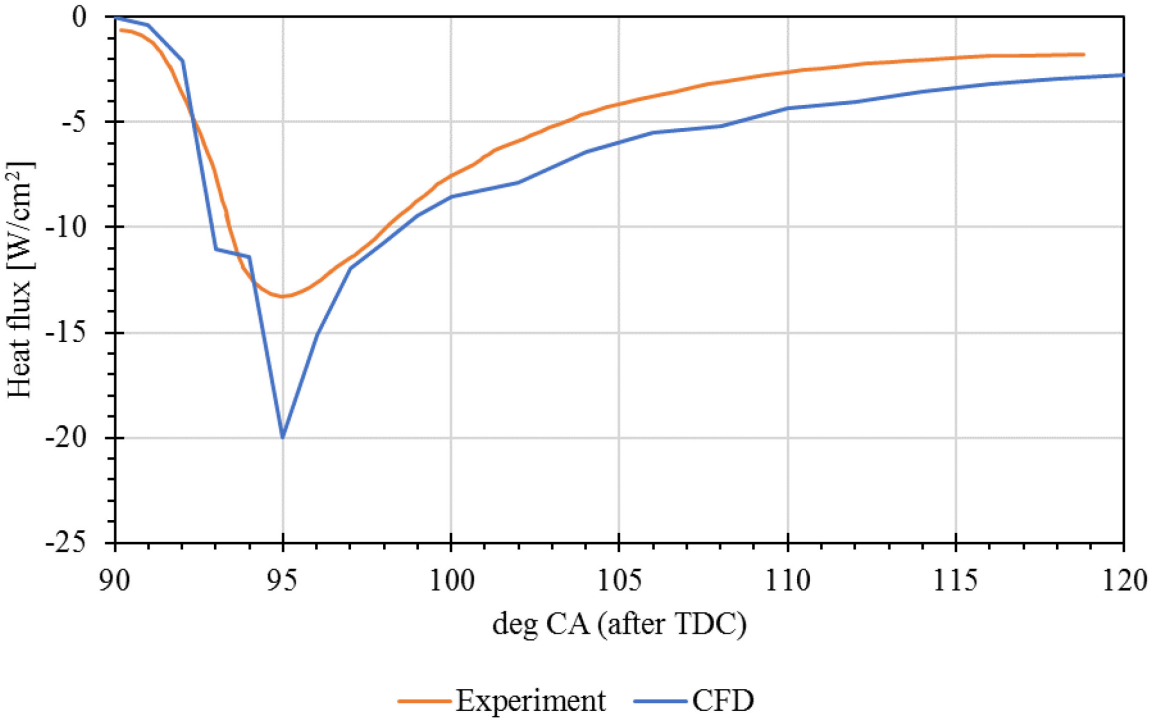


Figure 3.76 Experimental and numerical heat flux for the motoring AJ133 engine. 0.5 bar intake pressure, 1500 RPM, 20°C wall temperature

From the above studies of fuel-wall interaction and liquid film formation it was concluded that the overall predictions of Senda model were in a good agreement with the experimental heat fluxes, liquid film thickness, film mass and footprint. The Bai-ONERA model was in a good agreement with the heat fluxes but there was a 55% lower liquid film mass prediction and the film footprint was also smaller than the experiment. The results for both droplet-wall interaction models did not have significant changes when the surface mesh was refined. The cell sizes used in engine simulations (~1 mm - 0.5 mm) are sufficient for accurately predicting the liquid film. In addition, the droplet to film transition was sensitive to the cell face size which was affecting the performance of the droplet-wall interaction and liquid film formation with unrealistic results and for this reason it was deactivated. Lastly, the 1DCHT model did not have a significant effect neither on the heat flux signals especially with refined surface meshes nor on the liquid film formation. Moreover, the estimation of the thermal penetration in the metal was difficult to be established and validated for each case and the computational cost was also increased. Because of these reasons, the 1DCHT model was not used further. From all these, the final heat flux signal on the running engine was seen to be in a good agreement with the experimental data, within some errors because of the differences between experiments and CFD.

3.10. Closure

This chapter documented the preliminary studies and the validation of the CFD code along with all required sub-models to perform accurately, yet efficiently and within the computational limitations, in-cylinder flow and fuel injection simulations of a direct-injection spark-ignition engine. The main conclusions of the preliminary studies were:

- For the grid independence study, four different grids were tested with total the total number of cells ranging from 1.36 million to 4 million cells at BDC. A grid independent solution in respect to both the average in-cylinder velocity and the spatial distribution of the velocity field could be achieved with the use of a grid with 2.2 million cells. This model consisted of cells ranging from 0.5 mm to 0.8mm in the cylinder. In-cylinder quantities such as pressure were not sensitive to mesh refinement.
- The initialisation study showed that the conditions before the exhaust valve opening were easier to predict and apply (uniform vertical velocity). The velocity field had maximum discrepancies of about 30% over the three simulated cycles when the start of the simulation was before IVO. When the simulation started before EVO, cycle 2 and 3 had minor differences in the in-cylinder velocity of 2.5%. As a result, an initial crank angle should be before EVO.

After the choice of the size of the model and the initialisation strategy, the validation of the CFD code and the necessary sub-models for the in-cylinder simulations was conducted. The main findings of the pressure validation of the pressure trace were:

- From the in-cylinder pressure validation study of the AJ133 optical engine, it was showed that when the model had no losses with adiabatic walls and blow-by, the in-cylinder pressure was over-predicted. While blow-by was not modelled, it was taken into account by reducing the intake pressure by 10%, in conjunction with wall heat fluxes to match the experimental pressure trace.
- The validation of the in-cylinder pressure traces for the AJ20 thermal engine showed a very good agreement between experiments and CFD for all tested conditions. The importance of time dependent pressure and averaged temperature boundaries from the engine was demonstrated.
- In addition, accurate valve lift profiles are important for better in-cylinder pressure predictions while derivation of the valve lift from the theoretical cam profiles can lead to errors.

PIV data were analysed and compared against the numerical predictions of the flow structure and velocity magnitude. In addition, the CFD results were compared against Beavis *et al.* who used the same engine geometry.

- For the velocity in the intake runner of the AJ133, the model was predicting the dynamics of the flow motion with some hysteresis, and the predicted magnitude was higher than the experiment during early intake stroke however, high variation were seen for the experiment. Later in the stroke, the maximum difference between experiments and CFD was 2 m/s at 86deg CA after intake TDC.
- The velocity of the in-cylinder flow was higher than the PIV data during the first half of the intake stroke, however the bulk motion was well predicted. The simulations at 100 deg CA after intake TDC gave maximum velocity of 40 m/s while the PIV plots were saturated at 25 m/s. Because of this, the maximum velocity of the PIV could not be accurately estimated and compared to the CFD results. However, due to the higher velocities in the intake manifold the in-cylinder flow velocities may be higher than the experiment. During the second half of the intake stroke, the velocity field was at the same range (up to 16 m/s) as the experiments and the air motion was qualitatively well predicted. During the compression stroke, again the velocity and the flow field were well predicted with velocities at the same range (up to 10 m/s).
- The flow coefficient of the intake manifold of the optical engine was investigated numerically and compared to experimental data. k-ε and k-ω turbulent models were used, as they were seen in the literature. At low and medium valve lifts (up to 5 mm or L/D ≈ 0.15), the flow coefficient was over-predicted especially when k-ε RNG was used (maximum difference of 14% at 3.5mm) while the other models gave better predictions. At higher lifts (up to 10 mm or L/D ≈ 0.3), k-ε RNG well predicted the flow coefficient but the other models under-predicted it (maximum difference of 19% at 10 mm given by the standard k-ω). The areas around and near the valves were refined for more accurate predictions however, the results were not improved. Possible further refinements were needed for a more detailed study.
- The turbulence models from the flow coefficient study, were also tested on the dynamic model of the optical engine and compared to PIV data. All four models had the same behaviour in the intake runner and had no effect on the in-cylinder quantities such as pressure and trapped mass.

- Differences in the in-cylinder flow field were captured for the four tested turbulence models. k-ε RNG model produced wider area of high velocities below the valve than the rest of the models at the first half of the intake stroke, however, the bulk air motion was closer to the experiment. The resulted flow field of standard k-ε was also close to the experiment, however, k-ε RNG was qualitatively better when compared to PIV data. Standard k-ω, gave results that could be compared to an arbitrary cycle rather than the mean flow field. k-ω SST model, produced results that are between the solutions of standard k-ε and k-ω, as it is a blend of these two models, but not comparable to PIV.
- During compression, all four models, gave qualitatively and quantitatively better results, closer to the experimental flow field and velocity magnitude. In general, k-ε RNG was the only one which could predict more accurately the flow motion throughout intake and compression stroke considering both the velocity magnitude and the bulk flow motion. It can be said that k-ε RNG is preferred for engine simulations.
- The numerical predictions were in an agreement in terms of velocity magnitude with the work of Beavis *et al.* (2017) Differences seen between the two works were due to the valve profile tuning process, the boundary conditions and the geometry and the grid of the two models.

The heat fluxes from the gas to the walls of a motored engine without fuel injection were also validated against experimental data of two different engine loads. The results showed:

- The numerical heat fluxes were in a good agreement with the experimental data for both investigated cases. Specific behaviour, especially during the expansion which was unique for each case was also predicted. Small discrepancies were seen during the intake and expansion strokes due to the temperature differences of the boundary conditions.

The conclusions of the fuel injection validation in the quiescent chamber and the optical engine for sub-cooled and flash-boiling fuels were:

- Two different methods to initialise the droplets were tested (Blob method and Rosin-Rammler) and tuned to match the experimental data of spray structure, plume penetration, plume velocity and droplet diameter. For the blob method, a significant reduction of the break-up constants was needed to achieve satisfactory results. More realistic behaviour and results closer to the experimental data were achieved with the Rosin-Rammler distribution.

- The spray setup was implemented into the motoring AJ133 optical engine. The spray structure and the behaviour of the spray in the simulation was similar to the experimental data of the motoring engine during different instants of the injection.
- A newly developed flash-boiling spray model was successfully implemented into the motoring AJ133 optical engine. Two different single component fuels were tested (*n*-Pentane and *iso*-Hexane) for their suitability to replicate gasoline flashing sprays. The *n*-Pentane was found to be more suitable due to the better tuning process.
- The flash-boiling model was further improved by introducing a generalised approach for implementing it in quiescent chambers and dynamic models without the effects of the grid dependence seen in the original model.

Lastly, the validation of the droplet-wall interaction modelling included a study of two different models namely Bai-ONERA and Senda according to the STAR-CD code as well as droplet to film transition model and a 1D conjugate heat transfer model. Comparisons against experimental data of avegare peak heat flux, average heat flux signal and liquid film footprint, thickness and mass were carried out. The conclusions were:

- The use of the droplet to film transition model affected the results of heat flux especially those of the Bai-ONERA model. The combination of the two resulted in very grid dependent solutions. Less severe were the effects on the Senda model.
- By deactivating the droplet to film transition model, the peak heat fluxes of the simulations were in a good agreement with the average peak heat fluxes of the experimental data for both droplet-wall interaction models. Some differences were seen with low wall temperature which were due to the difference of the experimental fuel temperature from the nominal temperature. Both coarse and refined surface meshes produced results within the experimental error but with the refined mesh, the results were improved.
- The study of the heat flux signal showed that both models produced results close to the experiments, which were improved with increased wall temperature.
- The 1DCHT model did not have any effect on the heat fluxes when the surface area was refined while for the coarse surface the results were altered but within the experimental error.
- When the liquid film footprint was compared against experimental data, the prediction of the Senda model was closer to the experiments, especially the length and the tip of

the footprint. Because of the better prediction of the footprint, the accumulated mass was also better predicted by the Senda model. The 1DCHT model did not have any significant effect on the liquid film formation.

- From all the above, the Senda model was chosen as the most appropriate for the droplet-wall interaction modelling without the use of the droplet to film transition model and the 1D conjugate heat transfer model.

Chapter 4

Effects of Valve Deactivation on In-Cylinder Flow

4.1. Introduction

As it has been discussed, from a thermodynamics perspective, the two most important factors for increased thermal efficiency in spark ignition engines is the increased compression ratio and the increase of the ratio of specific heats or polytropic index (gamma – γ). The ratio of specific heats can be increased by diluting the combustible mixture with either external Exhaust Gas Residuals (EGR), excess air (lean combustion) or trapped internal EGR (or a combination of all three). As a result, the thermal efficiency is increased Caton (2013). The increased dilution however, results in reduced possibility of a strong flame kernel being established with possible misfires or partially burnt mixtures and slower flame propagation. One way to extend the dilution tolerance in a SI engine is the use of high energy ignition systems (Alger *et al.* 2011,2013; Nakata *et al.* 2015). Another way, which was investigated in this study, is the manipulation of the in-cylinder flow motion for significantly increased turbulence intensity, faster combustion and reduced cyclic variation with the use of valve deactivation.

In the literature, this method has been proven beneficial and associated with enhanced combined tumble and swirl motion and improved combustion stability at low loads. However,

there are some uncertainties with respect to in-cylinder temperature and associated heat transfer effects when adopting valve deactivation. In addition, it is not clear at which engine loads the effects of valve deactivation stop being beneficial and what are the reasons behind this limit. The aims of this chapter were to acquire fundamental understanding of the in-cylinder flow motion and to decouple the benefits and shortfalls of adopting valve deactivation across three engine running conditions (3.6 bar GMEP at 1500 RPM, 7.9 bar GMEP at 1500 RPM and 9.8 bar GMEP at 2000 RPM).

The CFD work was carried out concurrently with experiments and results of this study can be found elsewhere (Roberts et al., 2018; Okroj 2018). Briefly, the Jaguar Land Rover Single Cylinder Research Engine (SCRE) with a fully flexible valvetrain was used to investigate the extension of the dilution limit and any fuel consumption improvements of the engine. The valvetrain consisting of a CVVL electro-hydraulic system with dual independent cam phasing on both intake and exhaust camshafts. Typical valvelift strategies that can be achieved with the Jaguar Land Rover CVVL system are shown in Figure 4.1. In this study the full lift (black colour) was used. The engine was operated at three engine speeds and loads with the valvelift strategy (Dual Valve Actuation - DVA and Single Valve Actuation - SVA), Lambda and external EGR altered accordingly with EGR fractions up to 20% with the excess air dilution (Lambda) increased (to approximately 1.8) until combustion stability was deteriorated. The test matrix is shown in Table 4.1. In these cases, the engine load was set to achieve a target GMEP ±0.02 bar; thus, decoupling the combustion effects from those associated with pumping. For this SCRE, a good correlation of engine performance such as air flow, fuel flow, combustion metrics etc. exists with an equivalent Jaguar Land Rover multi-cylinder engine. Therefore, the results obtained are transferrable and scalable to multi-cylinder engine performance. More details about the experimental engine can be found at Okroj (2018).

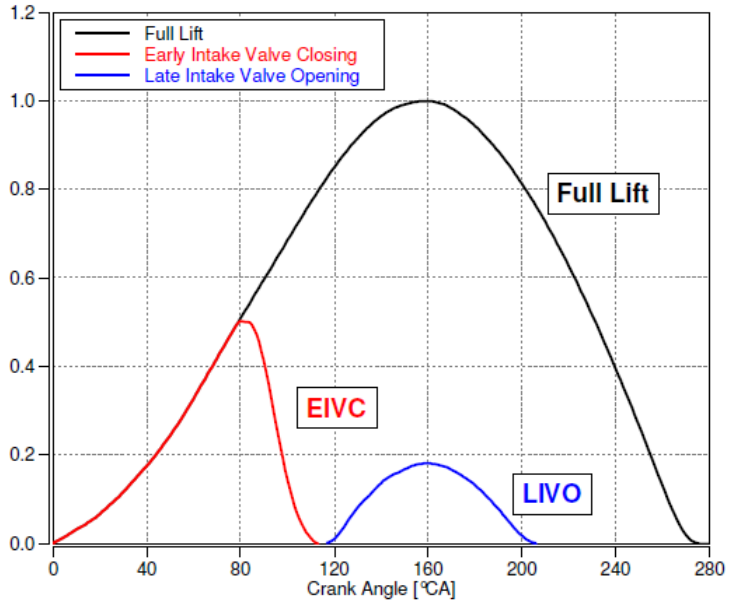


Figure 4.1 Typical valvelift strategies of the Jaguar Land Rover CVVL system (Roberts et al., 2018)

Engine Spreed	RPM	**1500**	**1500**	**2000**
Engine Load (GMEP)	bar	**3.6**	**7.9**	**9.8**
Lambda (λ)	-	1.0 - 1.8		
EGR	%	0 - 20		
Intake phasing	deg CA	Parked at 0 deg CA		
Exhaust phasing	deg CA	Parked at 0 deg CA		
MFB50	deg CA aTDCf	8		
Start of Fuel Injection	deg CA bTDCf	300		
Fuel Pressure	bar	200		
Fuel injector	-	Central Bosch DI (EB2)		

Table 4.1 Engine test matrix

4.2. Engine simulation setup

In order to investigate the reasons of the differences between DVA and SVA that were seen in the experiments and discussed briefly later on, CFD simulations of the Jaguar Land Rover (JLR) Single Cylinder Research Engine (SCRE) were run. The computational model used to simulate gas exchange, in-cylinder flow activity and in-cylinder residual concentration and distribution. It is known that the fuel injection event can influence flow patterns prior to

ignition, thus, simulations were carried out without fuel injection. This allowed to make a first comparison of the heat transfer, the flow field and residuals concentration during the cycle and at ignition timing without the effect of the spray. Following the established approach described on the validation chapter, the computational grid consisted of about 2.2 million cells at Bottom Dead Centre (BDC) including the intake and exhaust port with a cell size of 0.4 to 0.8 mm.

In the model, the k-Epsilon/RNG turbulence model with the Angelberger (1997) wall function was used. The base timestep used for the analysis was 0.05 °CA and it was reduced by half during the opening and closing of the valves. The valves were assumed to be closed when the lift was 0.1mm. This value was chosen in order not to create cells with high aspect ratios during opening and closing at the valve curtain.

The boundaries of the CFD model were equal to the position of the pressure sensors located in the intake and exhaust runners. Time dependent pressure and constant temperature were applied at the intake and exhaust boundaries of the model. In addition, appropriate mass fractions of species (N2, O2, H2O and CO2) as a function of Lambda ($\lambda \geq 1$) and EGR percentage were also applied at the boundaries. The calculations of the mass fraction of the species before EVO, assuming complete combustion followed the formulation described in Chapter 2, Table 2.1. At the piston, dome and liner wall boundaries, constant temperature of 90°C (coolant temperature) was applied. The walls of the inlet and exhaust ports were assumed to be adiabatic.

The simulations were initialised 40 °CA before Exhaust Valve Opening (EVO) and ended at firing TDC. This setup allowed to initialise each of the three sub-domains of the engine (intake, exhaust and cylinder) independently and to simulate the flow between the cylinder and exhaust port in order to capture the internal residuals later in the cycle. In addition, as it was showed before, when the simulations started before EVO, the effect of initial conditions on the flow field of the first cycle at the intake and compression strokes were minimised. The initial conditions of pressure and temperature at the intake and exhaust ports were the same as the boundary conditions at the specific initial °CA. The initial in-cylinder pressure was acquired from the testbed and the initial in-cylinder temperature of the burnt gases was calculated from the ideal gas law. The initial mass fractions of the chemical species presented in the intake and exhaust port and in the cylinder were calculated according to Residuals and EGR calculations described in the Mathematical formulation (Chapter 2).

4.3. Engine load: 3.6 bar GMEP, 1500 RPM

4.3.1. Experimental results

For the first and lowest load, Figure 4.2 shows the combustion stability in a Lambda vs. EGR rate sweep diagram for both DVA and SVA valve lift strategies. The black thick line represents a 3% Coefficient of Variance (COV) of Net Mean Effective Pressure (NMEP) combustion stability limit. It is clear that the dilution tolerance of the engine was significantly extended by utilising SVA over DVA with Lambda increased from 1.15 to 1.50 and 1.00 to 1.16 for EGR rates of 0% and 17.7% respectively for the combustion stability limit.

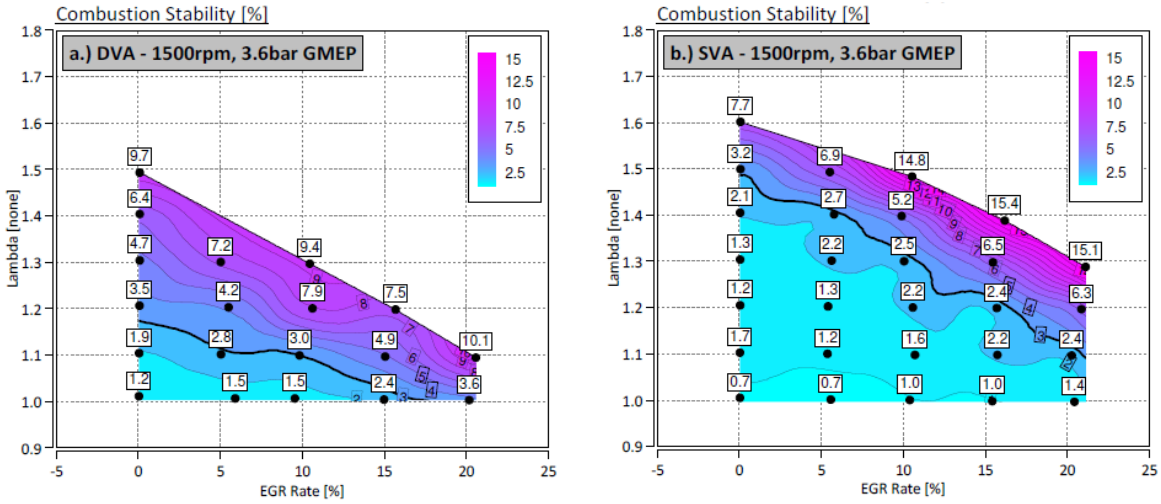


Figure 4.2 Comparison of the combustion stability limit for DVA and SVA. 3.6bar GMEP, 1500 RPM. (Roberts et al., 2018)

In addition to the extension of dilution with the use of SVA, significantly reduced ignition to 10% MFB (Figure 4.3) and 10-90% MFB durations for SVA compared to DVA were seen for equivalent levels of dilution. For the same combustion stability limit (adopting the thick black lines from DVA and SVA of Figure 4.2) and therefore increased tolerable levels of dilution for SVA compared to DVA, the ignition to 10% MFB and 10-90% MFB durations for DVA and SVA were comparable, indicating that adopting SVA with higher dilution resulted in burn durations that were similar to adopting DVA with smaller dilution quantities.

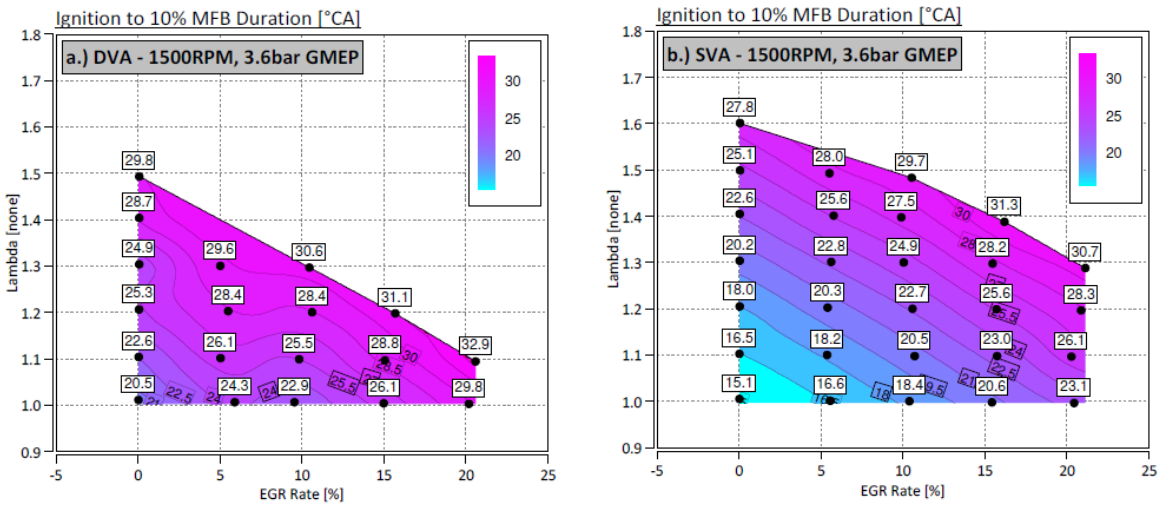
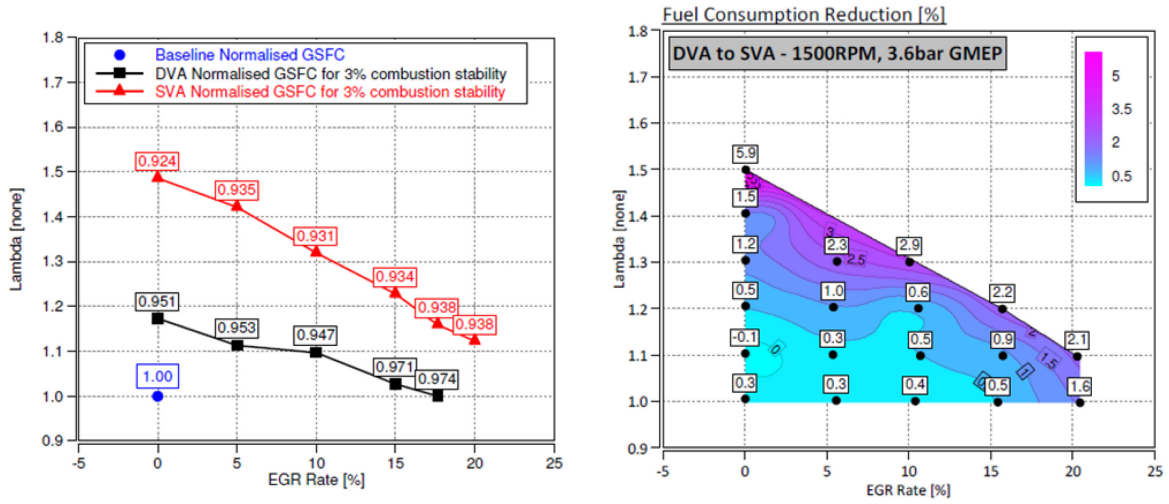


Figure 4.3 Comparison of the comparison of the ignition to 10% MFB duration for DVA and SVA. 3.6bar GMEP, 1500 RPM. (Roberts et al., 2018)

Lastly, for a given combustion stability limit of 3% COV of NMEP (adopting the thick back lines in Figure 4.2 for DVA and SVA) the increase of the dilution tolerance resulted in fuel consumption reductions of 1.7% to 3.8% (depending on EGR) when adopting SVA over DVA as a result of being able to operate the engine with more thermodynamically attractive lean mixtures. This can be seen in Figure 4.4a which displays the normalised Gross Specific Fuel Consumption (GSFC) for DVA and SVA cases. These have been normalised against the fuel consumption under DVA conditions at Lambda 1 without any dilution. However, for equivalent levels of dilution, there was little, if any reduction in fuel consumption when adopting SVA over DVA even though ignition to 10% MFB and 10-90% MFB durations were significantly shorter when adopting SVA over DVA. This was more evident at low dilution levels of Lambda 1-1.2 and EGR rates of 0-15%. These results are shown in Figure 4.4b where the percentage difference in GSFC from DVA to SVA is shown and the positive numbers indicate reduction in fuel consumption. More detailed information about the experimental data can be found in Roberts *et al.* (2018).

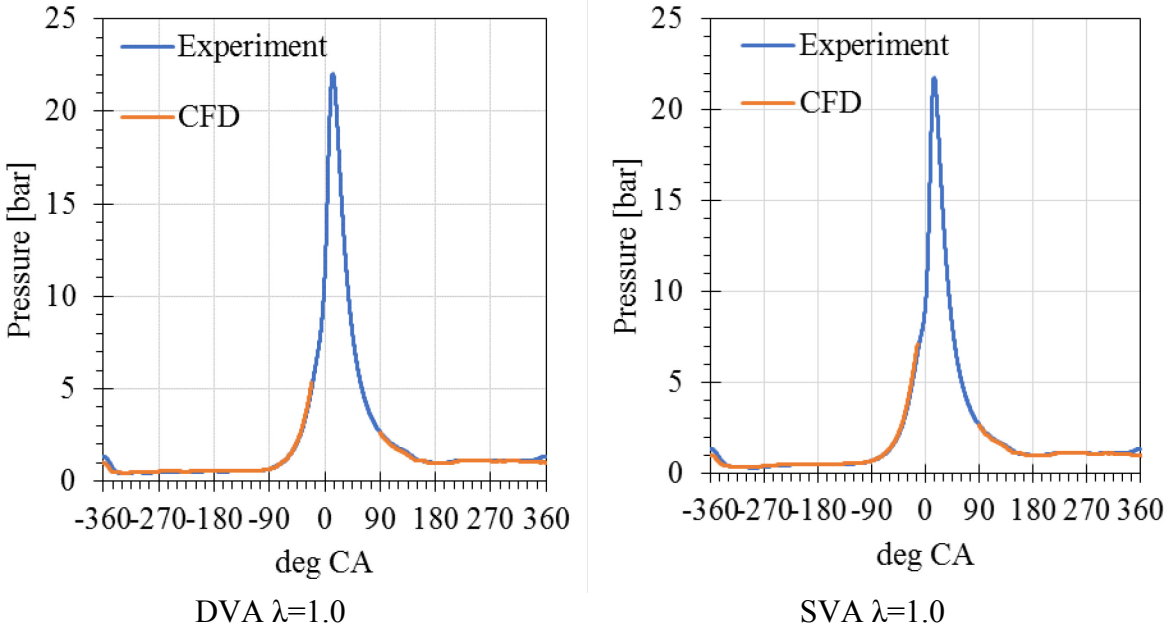


(a) (b)

Figure 4.4 (a) normalised GSFC for DVA and SVA for a fixed combustion stability limit of 3% COV of NM EP. (b) fuel consumption (GSFC) reduction from DVA to SVA. (Roberts et al., 2018)

4.3.2. In-cylinder Flow properties

First of all, as a validation of the code, the experimental in-cylinder pressure trace of each case was compared to the respective CFD pressure up to ignition. In all cases, there is a good agreement between experiment and CFD. Examples of the validation is shown in Figure 4.5.



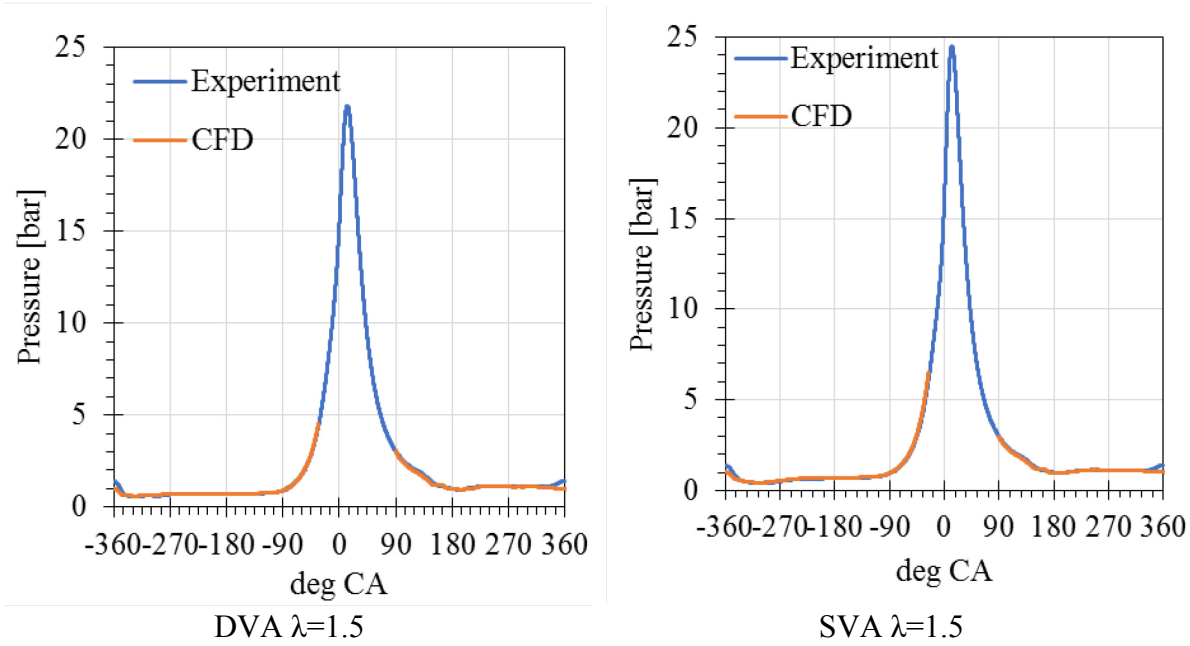


Figure 4.5 Experimental and CFD pressure traces for DVA and SVA and for λ=1.0 and λ=1.5. 3.6 bar GMEP, 1500 RPM

For all the cases, the analysis of the in-cylinder quantities which follows, was focused from the IVO until firing TDC. The increased activity with SVA compared to DVA can be seen from the in-cylinder averaged quantities of velocity, tumble, swirl and turbulent kinetic energy (TKE) plotted for λ=1. During the intake stroke, the valve jet velocity of the SVA configuration is always higher than the DVA due to the restriction of the flow area and this resulted in the increase of the in-cylinder velocity (Figure 4.6). The stronger valve jet of the SVA, has the momentum to increase the in-cylinder velocity until the mid-intake stroke where it reaches the maximum value, just above 65 m/s. However, the in-cylinder velocity with DVA reaches its maximum earlier, 40 °CA after TDC, with a magnitude of 50 m/s. After the peak, the velocity starts to decrease throughout the cycle for both DVA and SVA but the SVA maintains higher magnitude. To quantify this difference, the ratio of the in-cylinder velocity magnitude ratio SVA/DVA is plotted in the same graph. It can be seen that the velocity of the SVA is up to 2.5 times higher than the DVA for the intake and compression stroke until IVC. At that point, for both DVA and SVA the velocity is reduced but with higher rate for DVA and thus, the SVA/DVA ratio increases up to 3.2 times higher for SVA.

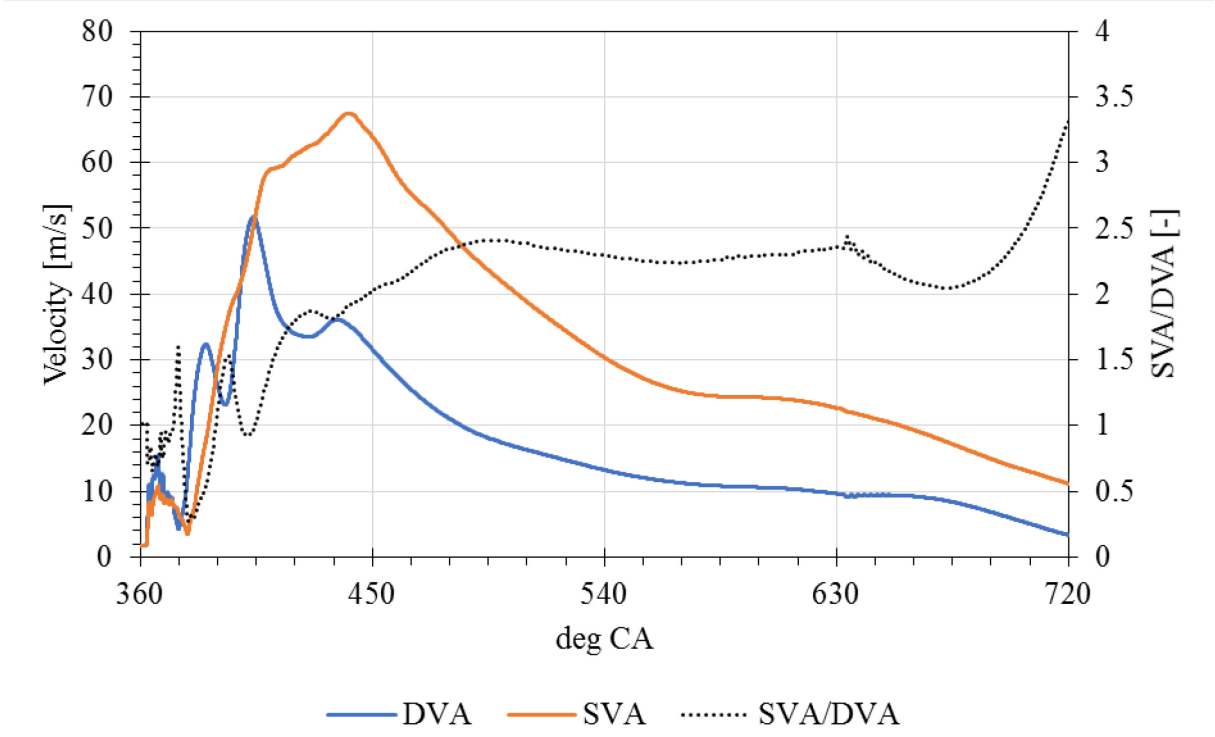


Figure 4.6 In-cylinder Velocity for DVA and SVA at λ=1.0 and the ratio SVA/DVA. 3.6 bar GMEP, 1500 RPM

The intake ports were designed to produce a high tumble motion when both valves were in operation. This can be noted from the CFD tumble and swirl calculations on Figure 4.7 for DVA. There is a clear tumble motion which is developed during the first half of intake stroke when the valve jet is stronger (with a maximum value of 29) and it is preserved with lower magnitude until firing TDC. This reduction is believed to happen due to the fact that the tumble motion is "squeezed" by the piston and weakens significantly (value of 1 at firing TDC). Due to the symmetry of the intake port, no swirl motion is produced. When one valve is deactivated, this symmetry no longer exists, which leads to the production of swirl motion. The increased valve jet velocity of the SVA has a result of a strong swirl (maximum value is 50) which, despite the fact that it is reduced after mid-intake stroke, is maintained at high levels of around 10 at firing TDC. This is due to the fact that the swirl motion is not affected as much as the tumble motion by the compression. In addition, because of the geometry of the intake ports, a tumble motion is also generated which is comparable in magnitude to the dual valve actuation. The inversion from tumble to reverse-tumble (from negative to positive values of tumble) is the effect of a non-zero swirl on tumble. If it is assumed that the two vortices (swirl and tumble) are two independent rigid motions, the stronger swirl is transporting the tumble and, therefore, rotating it during the cycle as it is represented in Figure 4.8.

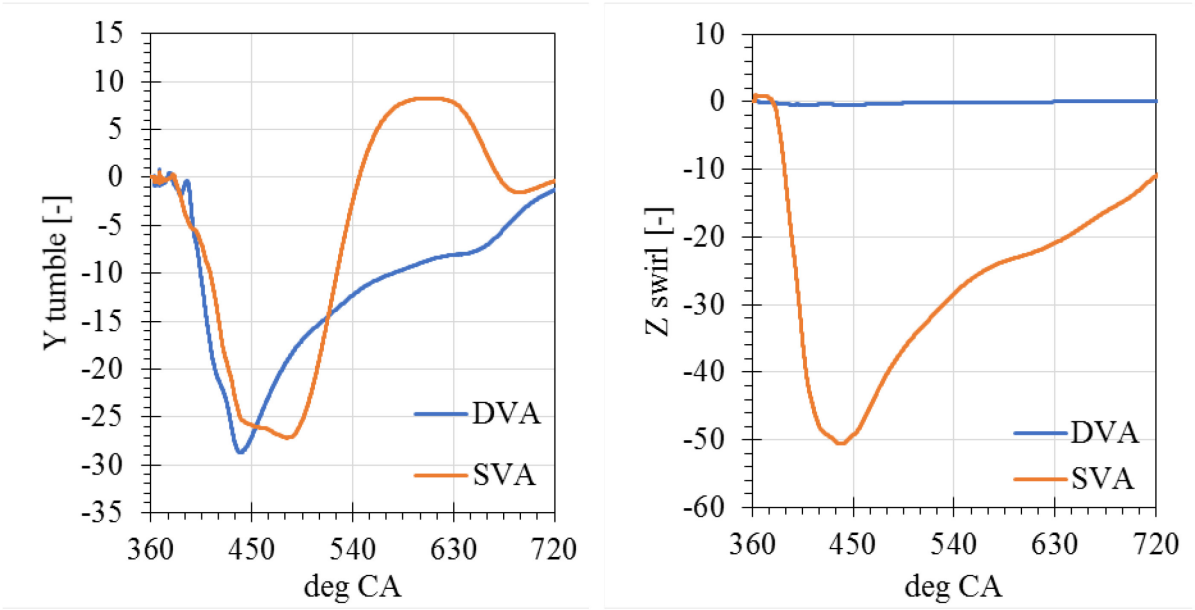


Figure 4.7 Tumble and swirl for DVA and SVA at λ=. 3.6 bar GMEP, 1500 RPM

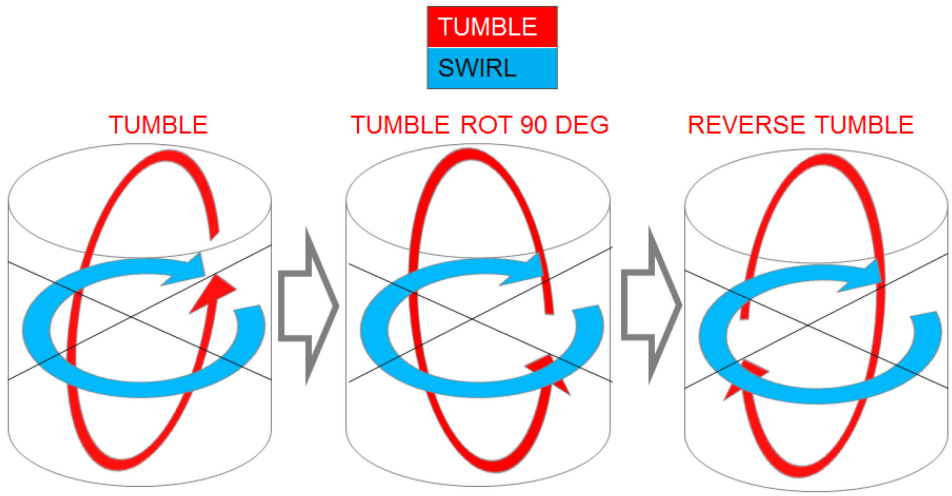


Figure 4.8 Representation of the mechanism responsible for the reverse of the tumble

In order to visualise the differences shown by the in-cylinder quantities (such as velocity, TKE, temperature) and give an insight of the spatial distribution of these quantities for DVA and SVA, contour plots are plotted in the tumble plane (Y-axis = 0 mm) through the spark plug and swirl plane (Z-axis = +5 mm) under the spark plug as shown by the dashed lines in the first row of Figure 4.9. In addition, Z = 0 mm is the head fire face. In this figure, the orientation of the engine is also displayed with respect to X-, Y- and Z-axis. When SVA was adopted, the intake valve on the +Y axis was deactivated.

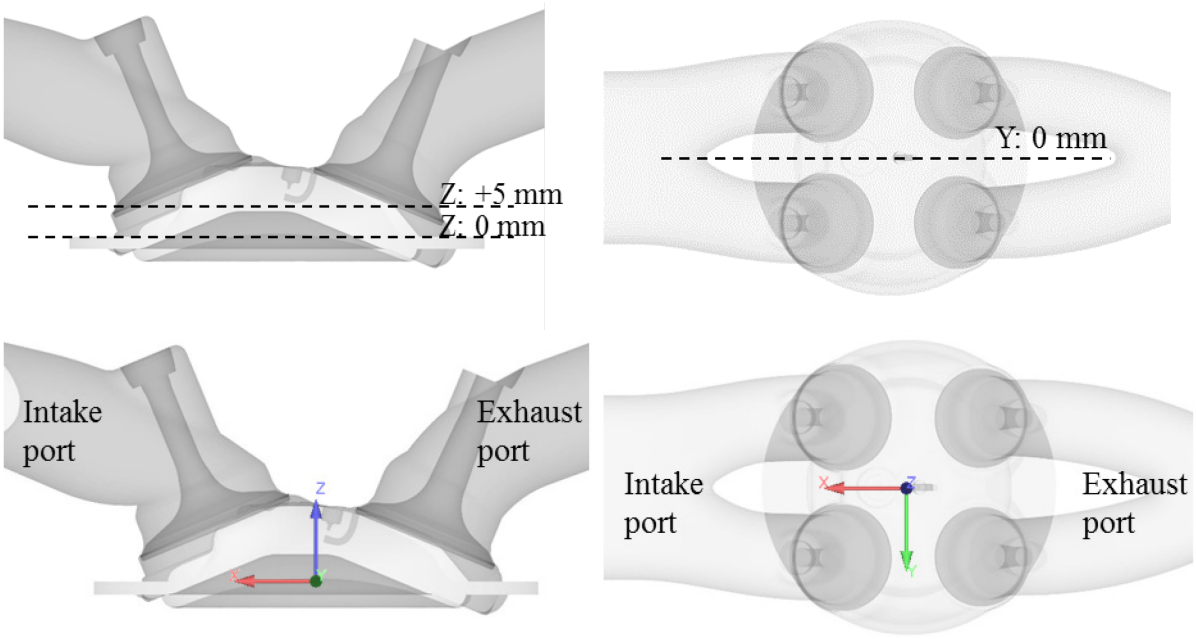


Figure 4.9 Tumble and swirl plane positions, representation of the global coordinate system and the position of the intake and exhaust ports

From Figure 4.10, the different flow fields between DVA and SVA can be seen at ignition timing. The velocity magnitude in the planes shown here is lower for DVA than SVA. Moreover, the tumble motion for DVA and the swirl for SVA are preserved and are clearly shown in the tumble and swirl planes respectively. In addition, the vortex of the tumble motion is below the spark plug, however, the vortex core of the swirl covers the spark plug with very low velocities at this area but higher near the liner walls.

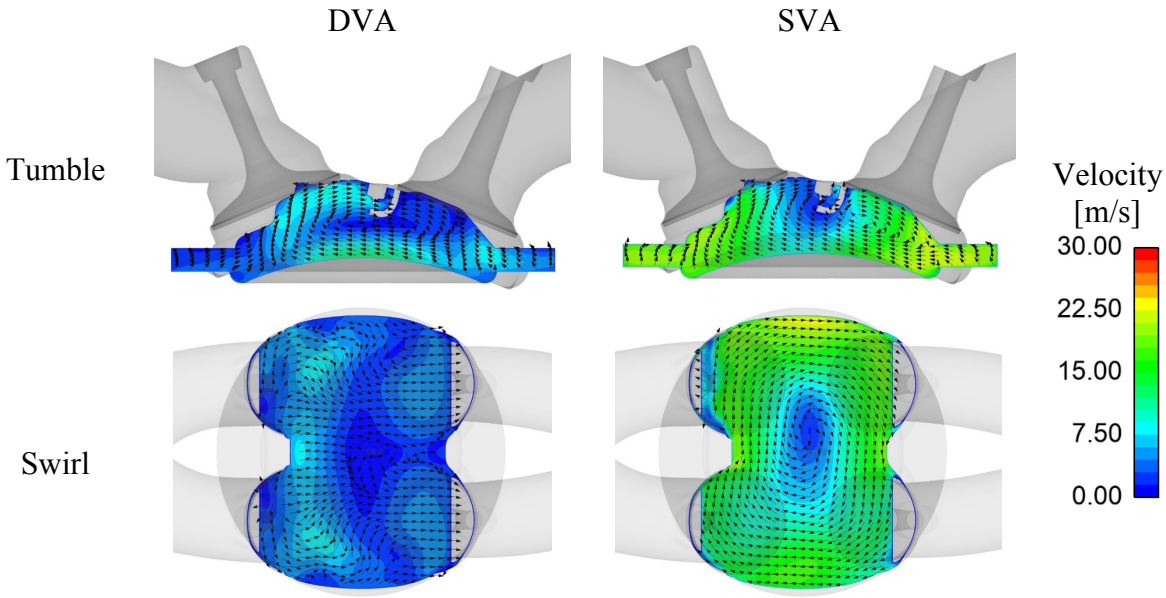


Figure 4.10 Velocity magnitude contour and vector plots for DVA and SVA at λ=1.0, 20 °CA before TDC

Adopting SVA also resulted in increased in-cylinder TKE (Figure 4.11). The behaviour is similar to the in-cylinder velocity for DVA and SVA. The TKE reaches the maximum value of 535 m^2/s^2, 40 °CA after TDC for DVA and it is reduced after that throughout the cycle. For SVA, the maximum value of TKE (700 m^2/s^2) is reached 40 °CA after TDC and it maintains these high values for another 45 °CA (around mid-intake) where it starts to rapidly decrease until firing TDC while always having higher values than DVA. A closer look to the in-cylinder TKE during the compression stroke and especially near ignition timing, which is around 30 to 10 °CA before TDC depending on the dilution, reveals that the TKE is 55% and 27% higher with SVA compared to DVA in respect to the °CA mentioned before.

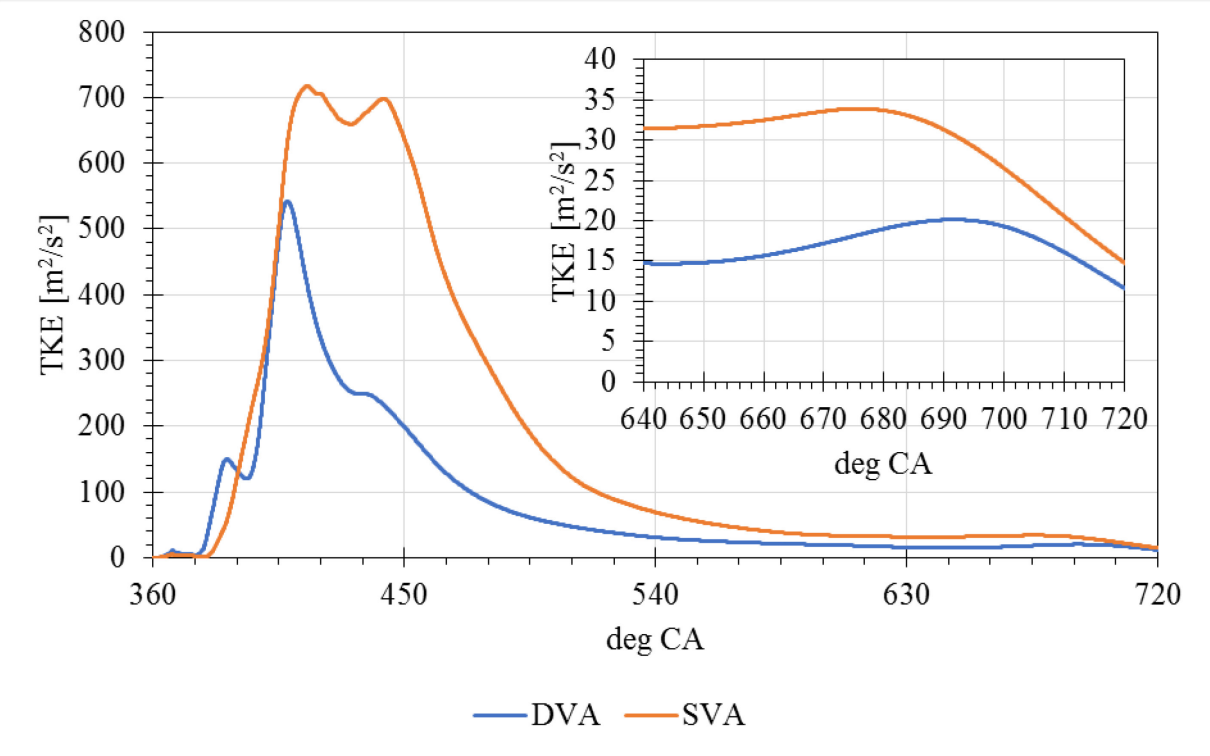


Figure 4.11 TKE for intake and compression strokes and a focus on the compression stroke. 3.6 bar GMEP, 1500 RPM

The increased TKE shown for SVA (compared to DVA) validates the reduced ignition to 10% MFB and 10-90% MFB durations and thus faster burning velocities, since the turbulent burning velocity is proportional to the root–mean–square velocity fluctuation (u') and laminar burning velocity S_L (Gülder 1991):

$$S_T \propto u' S_L \tag{4.1}$$

where $u' = \sqrt{\frac{2k}{3}}$ and k is the turbulent kinetic energy.

For the planes of Figure 4.9, contour maps of TKE at ignition timing were plotted (Figure 4.12). It has been discussed earlier that the averaged in-cylinder TKE is higher for SVA. In the maps of the TKE is evident that the area of higher TKE in near and around the spark plug for both DVA and SVA however, the SVA shows a clear benefit. The magnitude of TKE is higher, it is around the spark plug and it is spread in a wider area of the cylinder which can assist the flame propagation. For DVA, the magnitude is lower and the area of the highest TKE is below the spark plug which is not beneficial for establishing the flame kernel.

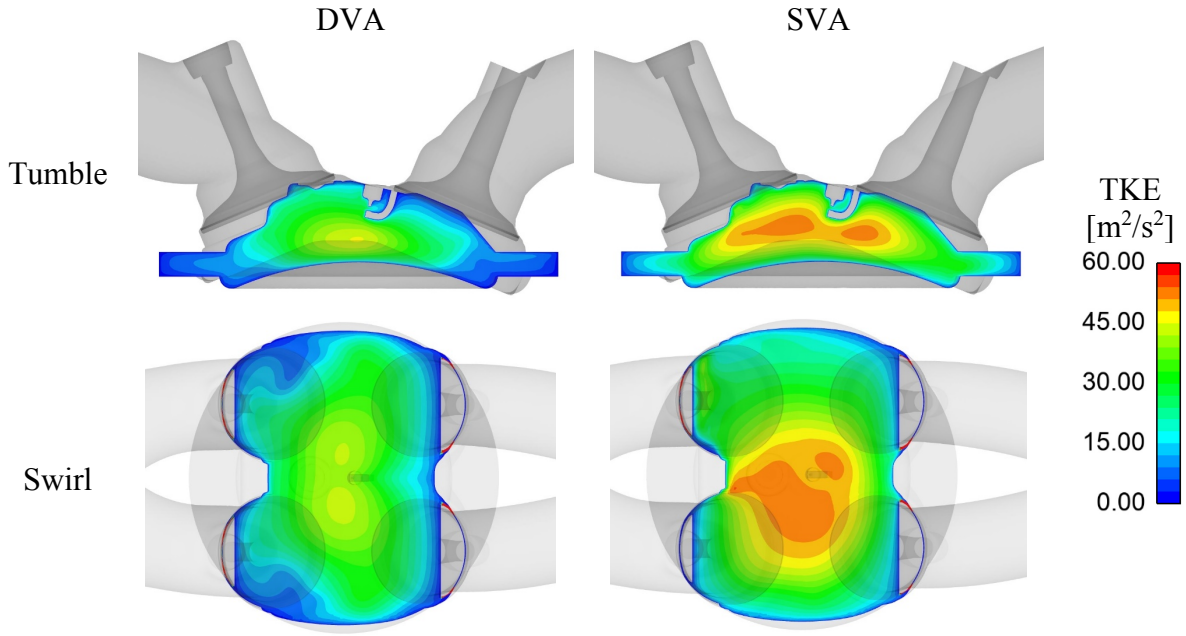


Figure 4.12 Spatial distribution of TKE for DVA and SVA at λ=1.0, 20 °CA before TDC. 3.6 bar GMEP, 1500 RPM

Another difference between DVA and SVA that the simulations revealed is the in-cylinder temperature. At the beginning of the intake stroke and for about 80 °CA, the temperature drops faster with the DVA than SVA and it continues to drop until BDC for both cases. After BDC, during compression, the in-cylinder temperature raises again until TDC. It can be seen from Figure 4.13 that the temperature of the DVA case is always lower than the SVA. This can be explained with the amount of trapped mass during the intake and compression stroke while the intake valve is open (Figure 4.14). During intake and up to BDC, the amount of trapped mass is always higher for DVA, meaning that a higher amount of fresh air is induced to the cylinder which cools the mixture, and this is reflected on the lower in-cylinder temperature. On the other

hand, with the SVA, a higher amount of residuals is retained in the cylinder. There is a point during intake (~80 °CA after TDC) where the in-cylinder temperature of DVA and SVA is the same (about 2°C difference). For the SVA, this is the result of the pressure drop in the cylinder which cools down the trapped mass. When the in-cylinder pressure and the intake pressure are balanced, the temperature increases again. During compression and while the intake valve is still open a higher amount of mass is expelled from the cylinder when both valves are in operation compared to the single valve. Finally, at IVC, a higher amount of residuals is trapped for SVA (8.1%) compared to DVA (7.0%) which are in higher temperature with the use of SVA.

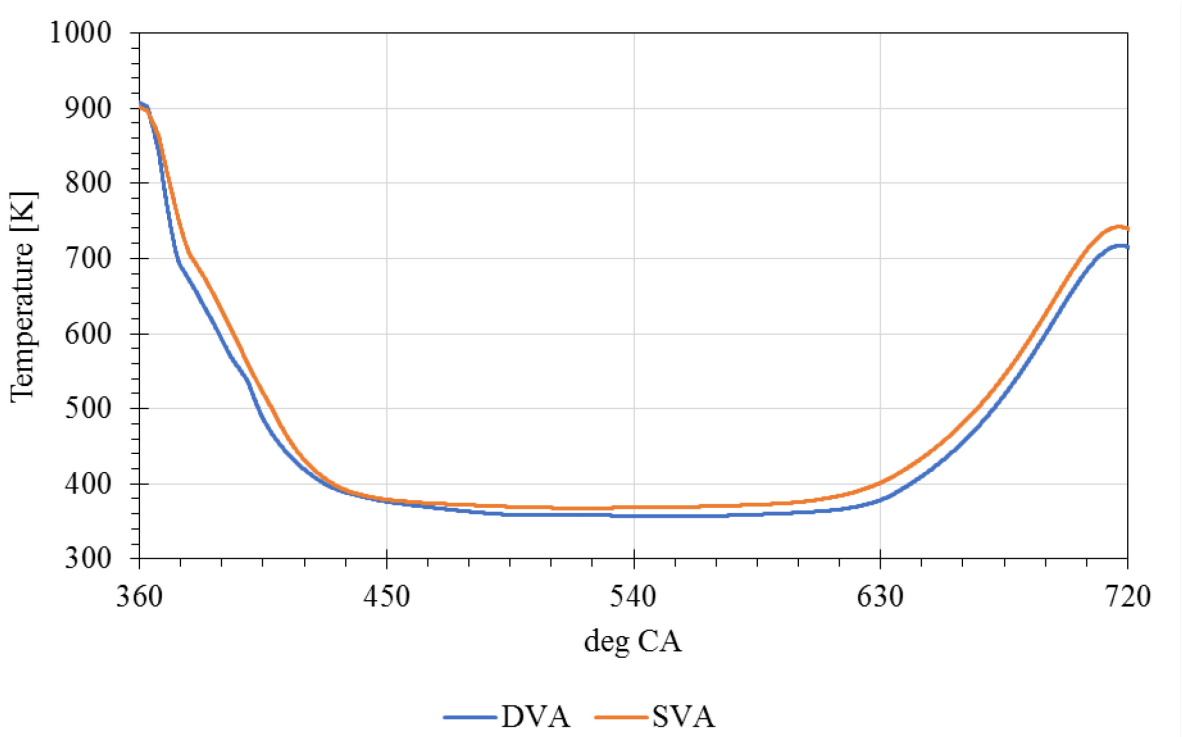


Figure 4.13 In-cylinder temperature for DVA and SVA at λ=1.0. 3.6 bar GMEP, 1500 RPM

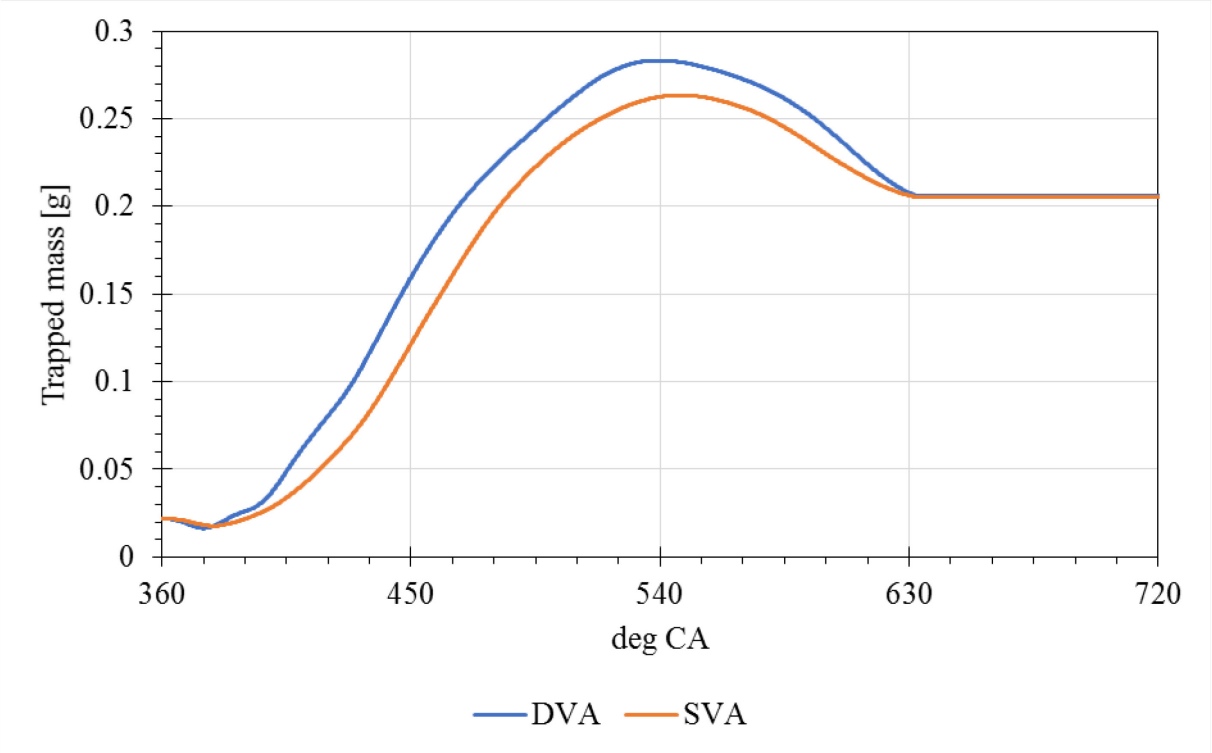


Figure 4.14 Trapped mass for DVA and SVA at λ=1. 3.6 bar GMEP, 1500 RPM

The experimental results showed a decrease of the polytropic index (γ) of the SVA when compared to the DVA, for both the compression and expansion strokes and this is believed to happen due to the increased heat losses with the SVA. For the CFD, only the polytropic index of the compression stroke was calculated and compared to the experiments as no combustion was modelled. From Table 4.2 it can be seen that the experimental trend is repeated with the numerical simulations. More specifically, for both lambdas, the polytropic index is higher for DVA than SVA. In addition, the percentage decrease of gamma from DVA to SVA matches the experimental percentage drop. There is a difference between experimental and numerical gamma (γ) values in the order of 4-5% which can be due to losses such as blow-by and losses from the crevices that are not modelled. Moreover, there is no presence of fuel vapour in these simulations which can significantly affect the polytropic index. Generally, the polytropic coefficient can be affected by heat transfer and trapped mass. Thus, for the same trapped mass at IVC, derived from CFD and shown above, the heat transfer must be affected and therefore has to be different for DVA and SVA valvelift strategies. The nature of the in-cylinder fluid flow which influences convection and the temperature difference between the engine walls and the trapped mass are two key factors that affect the heat transfer from and to (heat losses) the engine block.

		DVA	SVA	$\frac{\gamma_{SVA}}{\gamma_{DVA}}$
λ=1.0	**CFD**	1.335	1.317	0.9865
	Experiment	1.285	1.269	0.9875
λ=1.5	**CFD**	1.355	1.338	0.9875
	Experiment	1.313	1.298	0.9886

Table 4.2 Polytropic indexes for DVA and SVA at λ=1.0 and λ=1.5. 3.6 bar GMEP, 1500RPM

From the simulations, the total heat transfer from and to the liner, piston and dome were calculated. Figure 4.15 shows the crank angle resolved heat losses of the DVA and SVA strategies throughout the intake and compression strokes. Here, heat transfer from the gases to the walls (defined as negative) is greater for SVA than DVA up to a maximum of approximately 500 W - an equivalent increase of 23.6%. The focus of the heat transfer study is from the start of heat transfer from the gases to the walls for both cases which is around the IVC. For the SVA, this point is earlier in the cycle than the DVA, due to the increased gas temperature. In addition, from IVC to TDC, the amount of heat losses is considerably higher than before IVC. The increased heat losses seen with the CFD supports the fact that the polytropic index reduces with SVA.

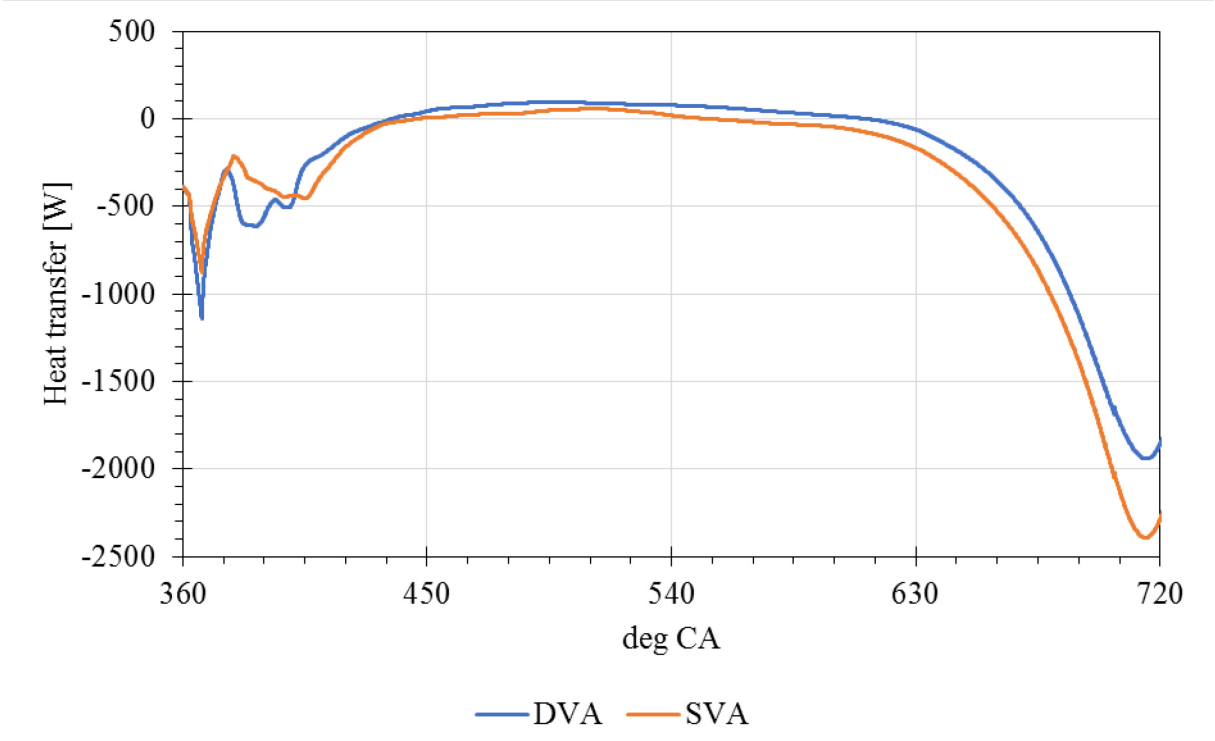


Figure 4.15 Total heat transfer from liner, piston and dome for DVA and SVA for λ=1.0. 3.6 bar GMEP, 1500 RPM

4.3.3. Laminar burning velocity

The increase of the turbulent kinetic energy is one of the contributors of the reduced combustion duration during single valve operation. Another factor that influences the turbulent burning velocity is the laminar burning velocity (eq 4.1). Analytical correlations have been derived for the laminar burning velocity such as these by Metghalchi and Keck (1980,1982) and Marshall *et al.* (2011). In these expressions, the laminar burning velocity depends on the equivalence ratio (Φ or 1/λ), temperature, pressure and residuals concentration. In this study, the correlation of Marshall *et al.* (2011) was used because it was stated by the authors that data affected by cellularity have to be excluded from the calculations of the laminar burning velocity. With this approach, the estimated laminar burning velocity is more accurate, and it resulted in lower values than those of Metghalchi and Keck (1982) but with the same trends. These differences can be seen in Figure 4.16. For the simulations without fuel injection, the maps of laminar burning velocity were plotted assuming that the equivalence ratio in the equation equals to the global ratio at which the engine was running at each case. For the rest of the terms, the value of each cell was used to calculate the laminar burning velocity maps which were plotted (Figures 4.17 and 4.18) in the same tumble and swirl planes as before at 20 °CA and 10 °CA before TDC for DVA and SVA respectively.

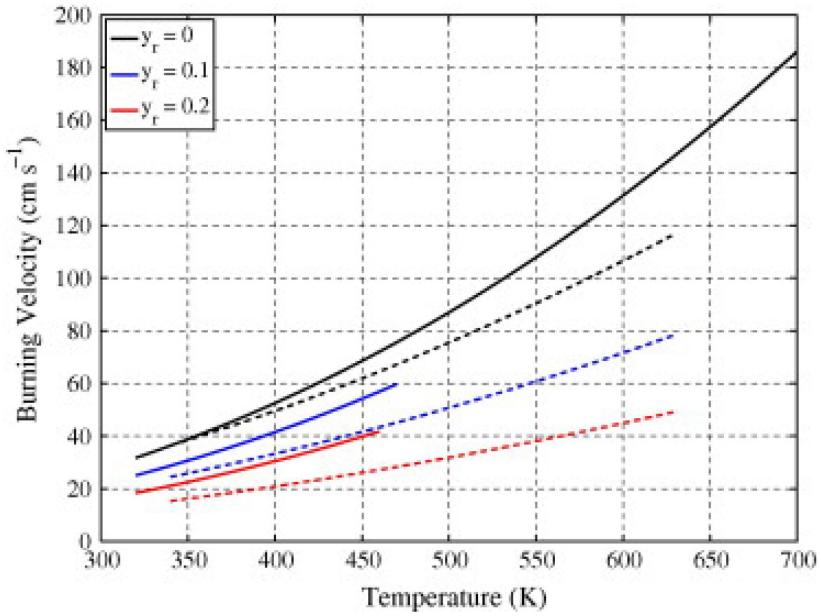


Figure 4.16 Comparison of stoichiometric iso-Octane burning velocity correlation of Metghalchi and Keck (1982) (solid lines) and Marshall et al. (2011)that excludes data affected by cellularity (dashed lines) with three different residual mass fractions, at 101 kPa. Taken from Marshall et al. (2011)

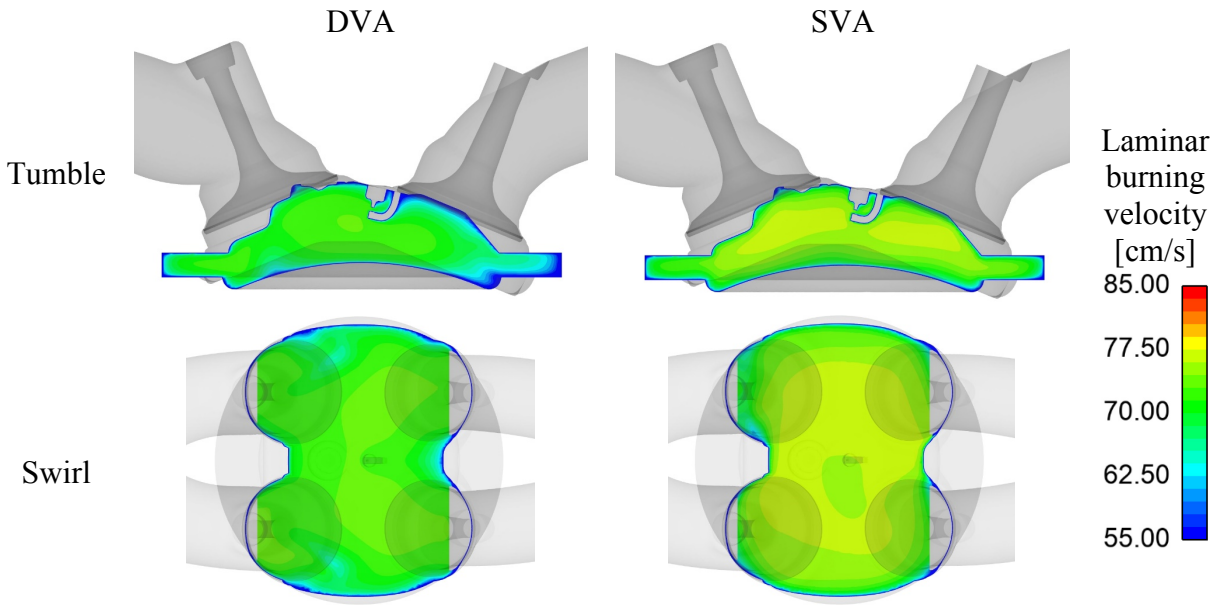


Figure 4.17 Spatial distribution of laminar burning velocity for DVA and SVA at λ=1.0, 20 °CA before TDC. 3.6 bar GMEP, 1500 RPM

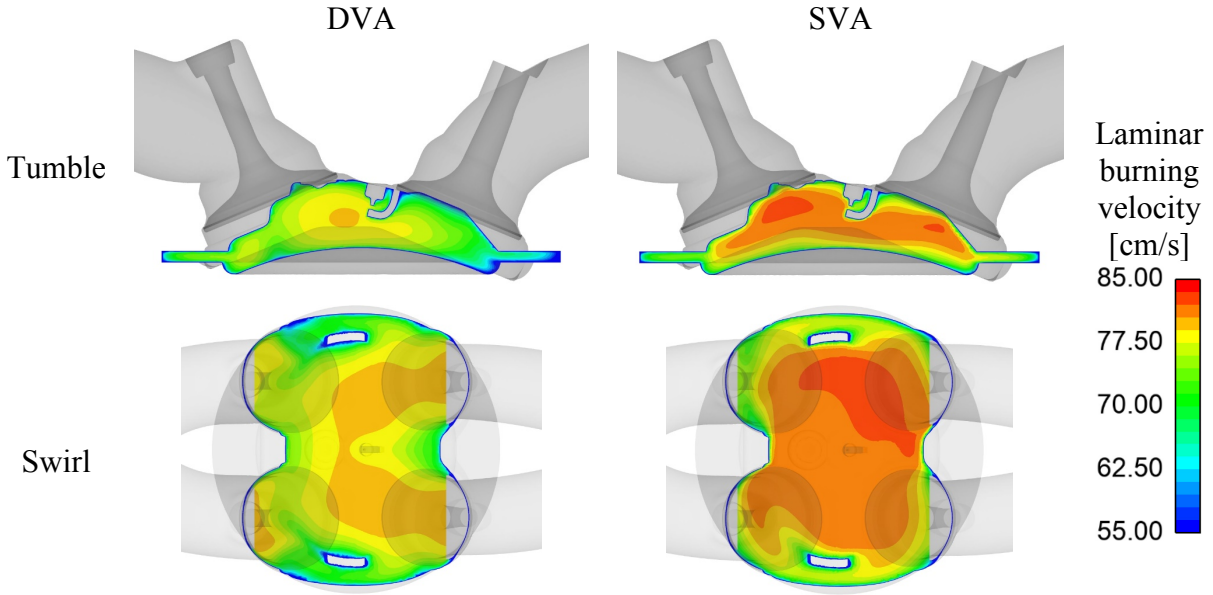


Figure 4.18 Laminar burning velocity for DVA and SVA at λ=1.0, 10 °CA before TDC. 3.6 bar GMEP, 1500 RPM

The maps show that in both crank angles, the laminar burning velocity is lower for DVA than SVA. This is the second evidence which explains the faster combustion with SVA. The average laminar burning velocity was 73.5 cm/s for DVA and 75.5 cm/s for SVA, an increase of 2.9%. In a spherical volume of 15 mm diameter round the spark plug the increase in laminar burning velocity is 3.5% at 20 °CA. Moreover, it can be seen for DVA for both time intervals that the

area below and to the sides of the spark plug closer to the exhaust port, the calculated burning velocity is the highest (74 cm/s at 20 °CA and 80 cm/s at 10 °CA) and it is reduced away from the spark plug (70 cm/s at 20 °CA and 75 cm/s at 10 °CA). For SVA, the highest value is 78 cm/s at 20 °CA and 84 cm/s at 10 °CA. The contour maps reveal that higher values are conserved in a wider area of the cylinder when adopting SVA.

In order to further understand the reasons behind the behaviour described above, the factors that affect the laminar burning velocity (pressure, temperature, and residuals concentration) for λ=1.0 at 20 °CA and 10 °CA before TDC were analysed. At these time intervals the in-cylinder pressure difference is about 0.3 bar between DVA and SVA with an average of 5.7bar at 20 °CA and 7.8 bar at 10 °CA respectively. At these pressures, a 0.3bar change in pressure has a minimal effect on the laminar burning velocity. As an example, for λ=1.0, 700K temperature and no residuals, the laminar burning velocity is 99.94 cm/s at 6 bar and 101 cm/s at 5.7 bar pressure (1% increase). Thus, the main contributors of the differences were the temperature and the residuals concentration. These two quantities have the opposite effect on the burning velocity. An increase of the temperature increases the burning velocity but an increase in residuals decreases the burning velocity. This can be seen in Figure 4.19 where the laminar burning velocity is plotted versus temperature and residuals concentration for P=7 bar and λ=1. Another information that can be extracted from this graph is that the effect of temperature is reduced with increased residuals.

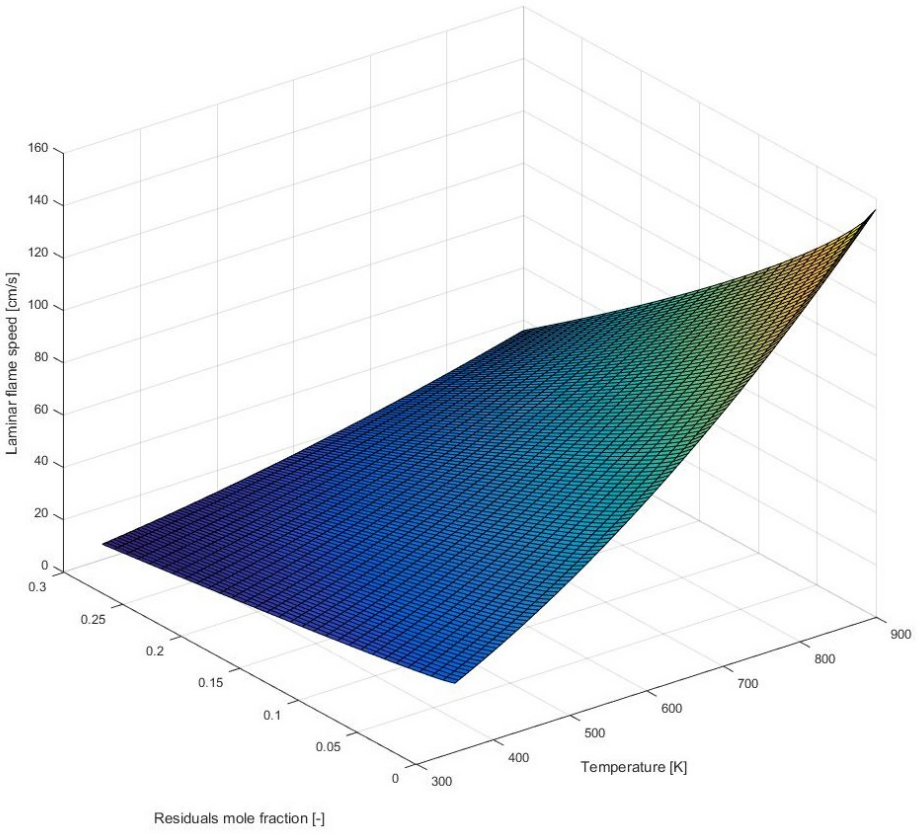


Figure 4.19 Laminar burning velocity versus residuals mole fraction and temperature at P=7 bar and λ=1. Calculations from Marshall et al. (2011)

From the averaged in-cylinder quantities discussed previously, it was concluded that for the SVA, a higher amount of residuals is trapped which preserve high in-cylinder temperatures. In order to confirm this, contour maps of the mass fraction of the in-cylinder residuals CO2 and temperature were produced. As it was expected, the mass fraction of CO2 is higher for the SVA. The maximum concentration of CO2 corresponds to 0.07 residuals mole fraction for DVA and 0.08 for SVA. At these low values of residuals, the effect of the temperature on laminar burning velocity is more profound. Consequently, this slight increase of residuals, increases the temperature by 25° in a way that the final result is the increase of laminar burning velocity. From Figure 4.20 and 4.21 the effect of the flow field can be seen. For DVA, the higher concentration of CO2 is under the spark plug and closer to the intake port, where the vortex core of the tumble is. The area of increased temperature is under the spark plug and closer to the exhaust ports, which is transported by the tumble flow. The combination of lower residuals and higher temperature under the exhaust and at the sides of the spark plug seen at the swirl plane, results in higher burning velocity. For the SVA, the residuals are pushed towards the liner leaving the centre of the cylinder with lower concentration. At the side of

higher residuals, there is an area of high temperature which produces the highest burning velocity. To conclude, there is a 'battle' between residuals and temperature which dictate the laminar burning velocity. In this case the driving force for the increased burning velocity is the temperature followed by the residuals concentration. However, the increase of the laminar burning velocity (~3% to 6%) is relatively minor when compared to the much higher increase of TKE (27% to 55%).

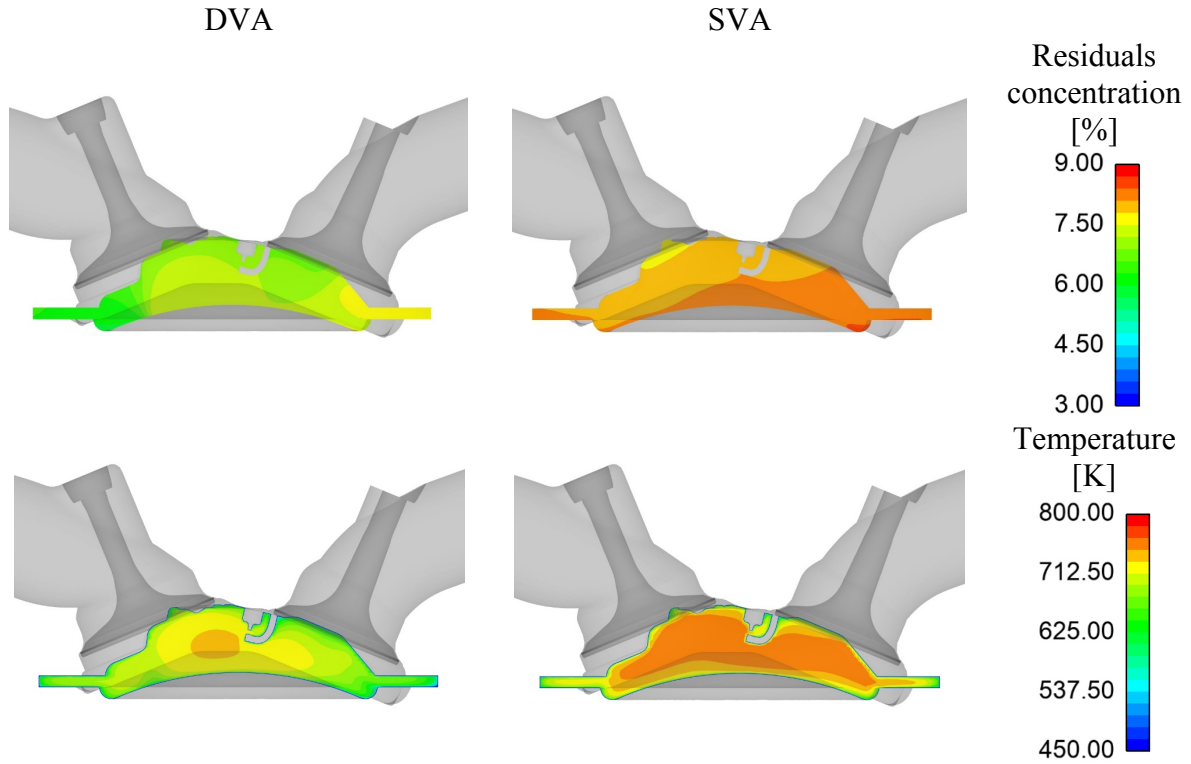


Figure 4.20 Residuals concentration and temperature for DVA and SVA at λ=1.0, 10 °CA before TDC (tumble plane), 10 °CA before TDC. 3.6 bar GMEP, 1500 RPM

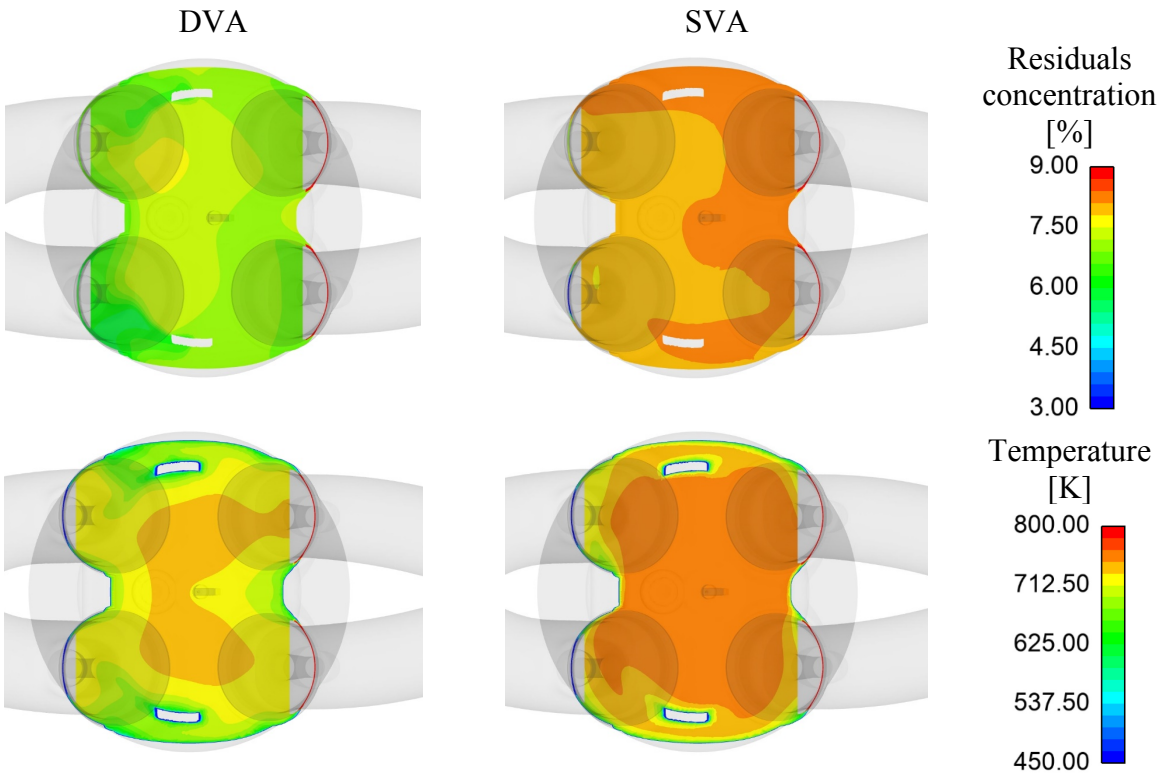


Figure 4.21 Residuals concentration and temperature for DVA and SVA at λ=1.0, 10 °CA before TDC (swirl plane), 10 °CA before TDC. 3.6 bar GMEP, 1500 RPM

Difference between Lambda cases at the same speed and load

For λ=1.5, the average in-cylinder flow quantities of velocity, tumble, swirl and turbulent kinetic energy (TKE) differed only slightly from those of λ=1.0 which was due to the increased intake pressure at λ=1.5 as it can be seen from the Figures 4.22 and 4.23 but the behaviour and the trends are the same for both lambdas. For the DVA cases, the quantities mentioned before have minor differences between lambdas but for the SVA, the differences are more noticeable. First of all, the velocity difference between λ=1.0 and λ=1.5 for DVA is less than 5% (~3.5% at 20 °CA before TDC) which resulted in the two DVA curves (blue-λ=1.0 and yellow-λ=1.5) to fall on each other especially after mid-intake stroke. For SVA, especially after the mid-intake and compression strokes, the differences are about 3% to 7% near ignition timing. For both DVA and SVA, the velocities are higher with higher lambda due to the higher pressure difference between intake and the cylinder. Because of this slight increase of velocity when running at λ=1.5, the magnitude of tumble for DVA and SVA and swirl for SVA are increased as well. Lastly, the same trend was seen for the turbulent kinetic energy which increased with increased lambda. For the DVA cases the increase during compression is about 5% and for the SVA, the maximum increase is 14% at mid-compression and the differences are reduced to

about 10% higher TKE with λ=1.5 at ignition. The in-cylinder temperature difference at ignition timing between λ=1.0 and λ=1.5 is very similar (~2° difference) for both DVA and SVA. During intake, a higher amount of fresh mass is induced to the cylinder because of the increased intake pressure when λ=1.5, which reduces the trapped mass temperature more than the λ=1.0 case. During the compression however, a higher amount of trapped mass is compressed which leads to a slightly higher temperature increase (~2°) than with λ=1.0 for both valve strategies.

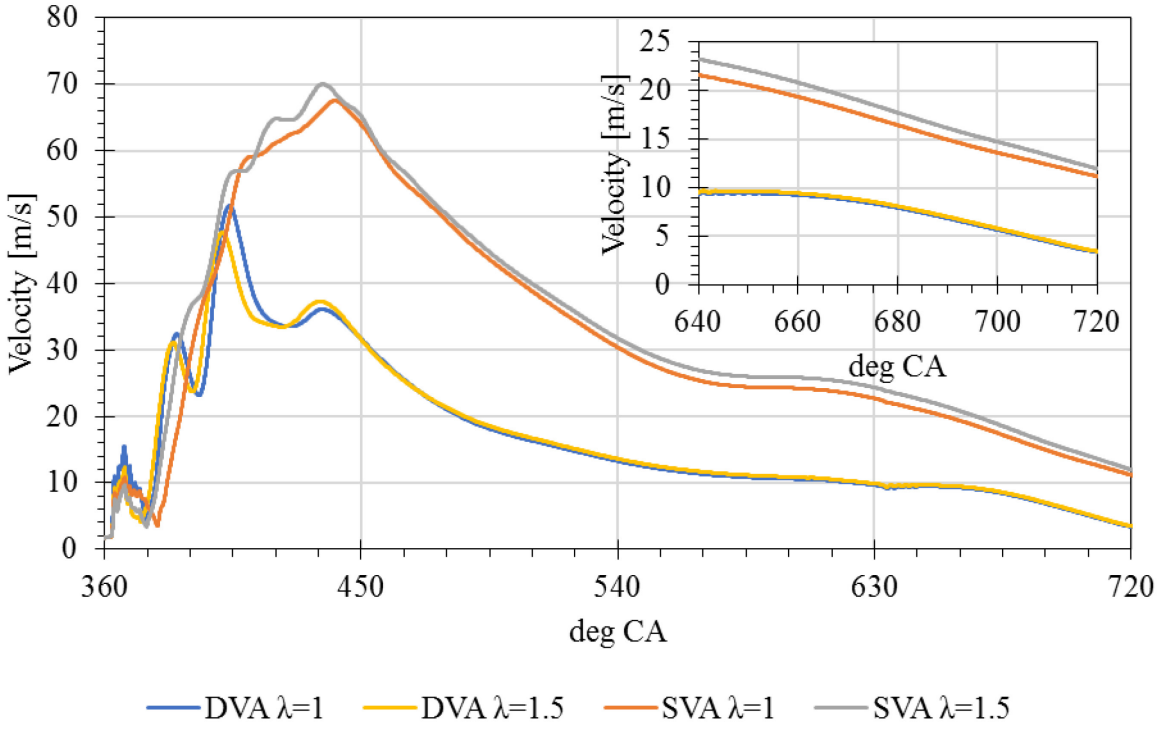


Figure 4.22 In-cylinder Velocity for DVA and SVA at λ=1.0 and λ=1.5. 3.6 bar GMEP, 1500 RPM

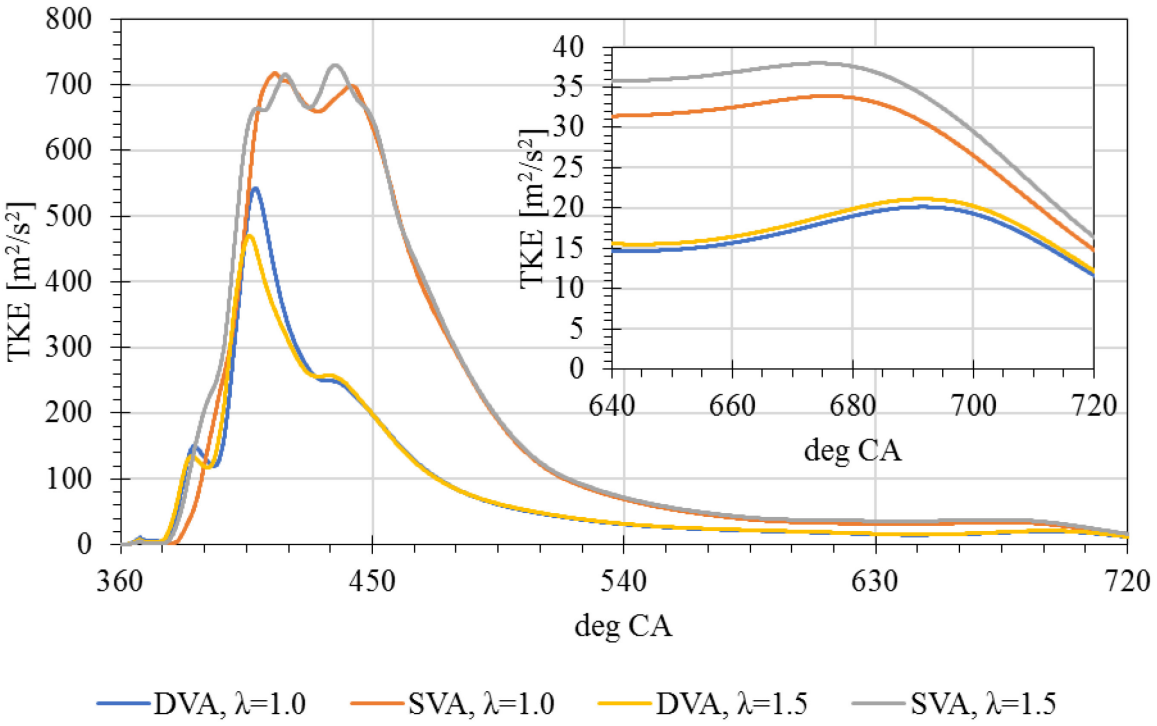


Figure 4.23 In-cylinder TKE for DVA and SVA at λ=1.0 and λ=1.5. 3.6 bar GMEP, 1500 RPM

The major difference between λ=1.0 and λ=1.5 for DVA and SVA is the reduction of laminar burning velocity as it can be seen in Figure 4.24 but again, with the SVA the S_L is higher. It has been stated that the aspects that affect the burning velocity are: equivalence ratio, temperature, pressure and residuals concentration. For a specific crank angle, the temperature difference between λ=1.0 and λ=1.5 is very small thus, the effect is minor. Due to higher induced mass, the residuals fraction is reduced as shown in Figure 4.24 which should increase the burning velocity. The residuals at the λ=1.5 case were ~3.7% for DVA and 4.1% for SVA. Consequently, the pressure and the equivalence ratio are the two contributors in the reduction of S_L. From Figure 4.25, the difference in laminar burning velocity for two pressures (6 bar and 8 bar) and λ=1.5 can be evaluated. At 6 bar, 700K temperature and o% residuals the laminar burning velocity is 46.63 cm/s and at 8 bar is 43.58 cm/s which is 6.5%reduction. That leads to the conclusion that the higher dilution (excess air and thus increased λ) is the reason for the ~50% reduction of laminar burning velocity between λ=1.0 and λ=1.5. This trend was also seen in the experimental data where the burn duration is increased with higher dilution. It has to be mentioned that while there are quantitative differences between the two Lambda cases, qualitatively, they are very similar in terms of patterns. This is very clear when the residuals

concentration for the two cases for both DVA and SVA is compared against each other, The legends of Figures 4.20 and 4.24 are different but the contour plots are very similar.

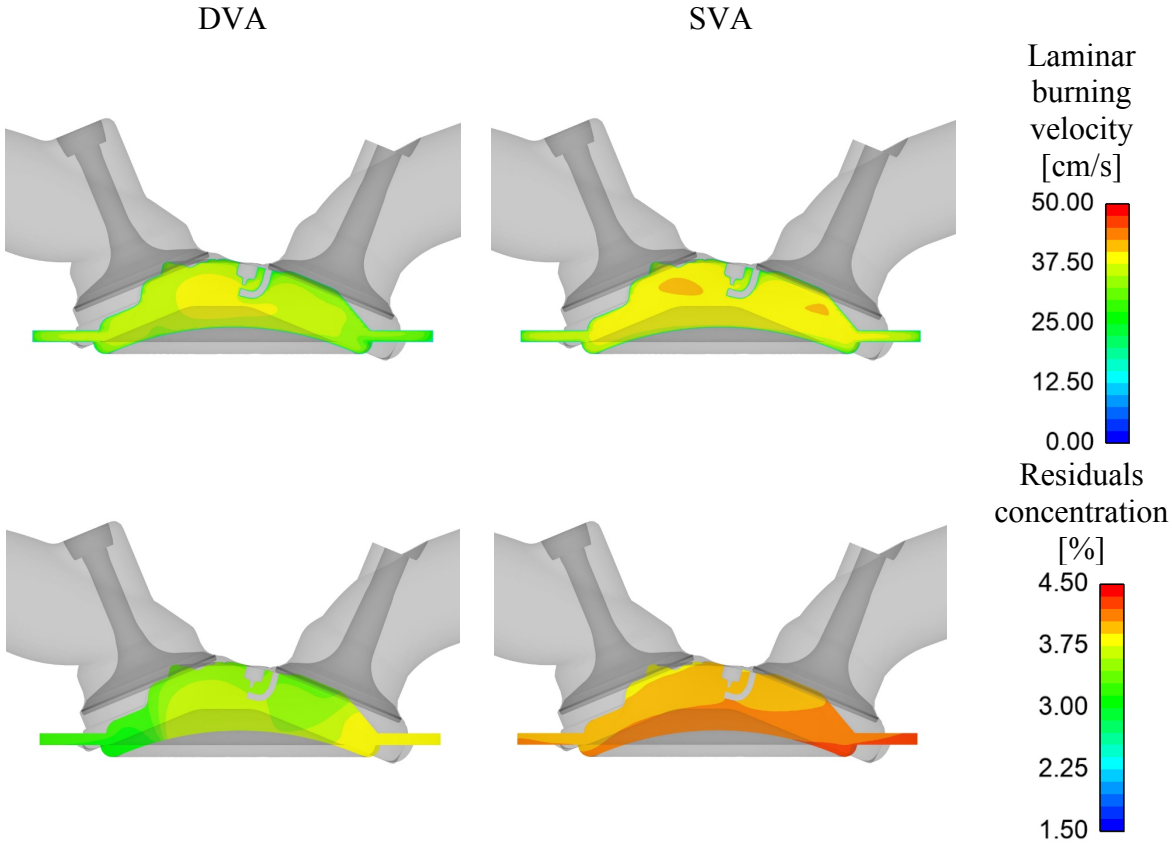
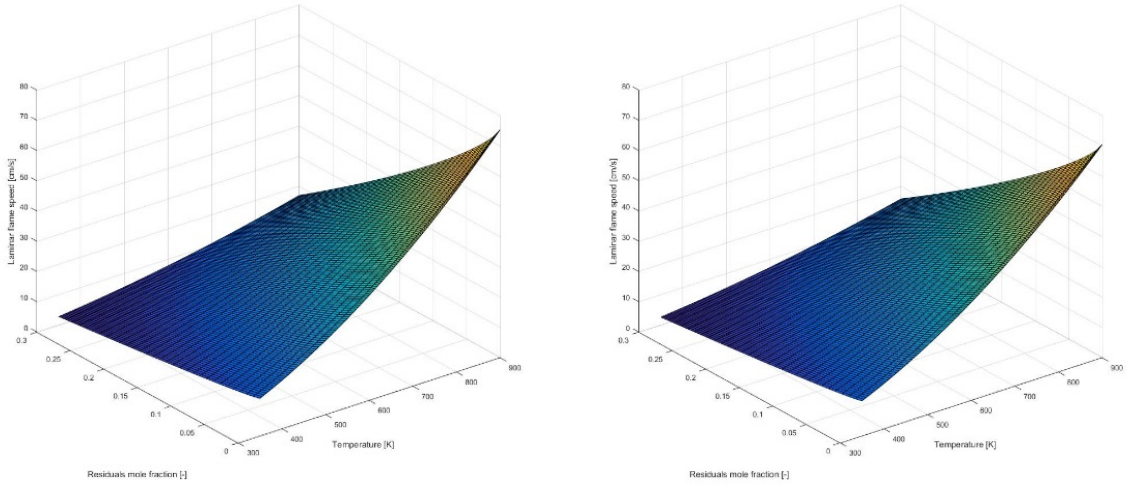


Figure 4.24 Laminar burning velocity and residuals concentration for DVA and SVA λ=1.5, 10 °CA before TDC, tumble plane. 3.6 bar GMEP, 1500 RPM



P=6 bar P=8 bar

Figure 4.25 Laminar burning velocity versus residuals mole fraction and temperature at P=6 bar and P=8 bar at λ=1.5

4.4. Engine load: 7.9bar GMEP, 1500 RPM

4.4.1. Experimental results

For this load, the use of SVA resulted in the increase of the dilution tolerance of the engine similar to the lower load. More specifically, the tolerance in Lambda was increased from 1.40 to 1.75 and Lambda 1.10 to 1.35 at 0% EGR and 20% EGR respectively for the combustion stability limit of 3% COV of NMEP. This extension of the dilution tolerance when adopting SVA resulted in a reduction in fuel consumption (GSFC) of up to 3.1%. The ignition to 10% MFB and 10-90% MFB durations for each dilution test point were significantly shorter for SVA compared to DVA for equivalent levels of dilution. This can be seen in Figure 4.26. For equivalent levels of dilution however, there was a limited reduction in fuel consumption when adopting SVA and for some dilution test points, fuel consumption actually increased with SVA shown with negative values in Figure 4.27.

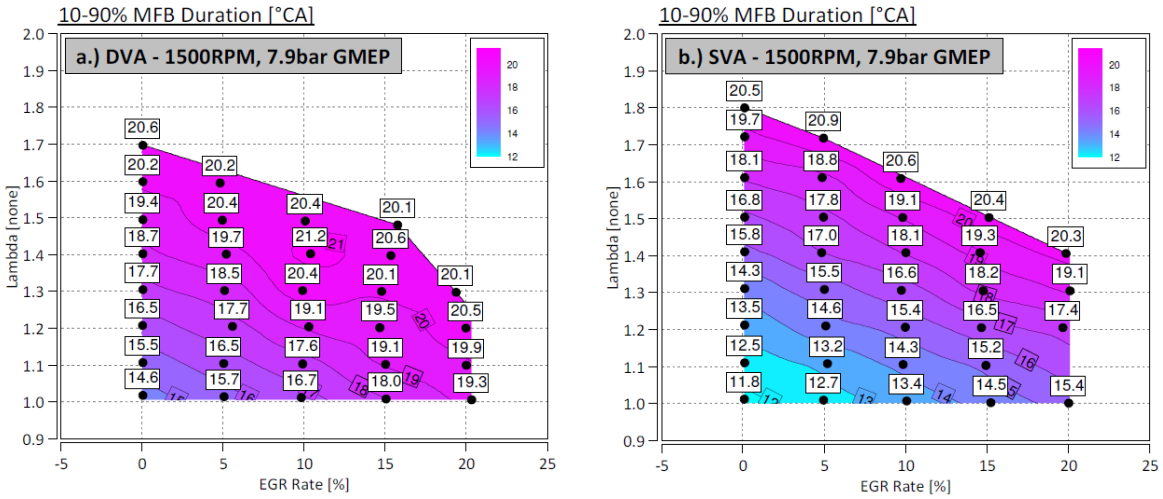


Figure 4.26 Comparison of the 10% to 90% MFB duration for DVA and SVA. 7.9bar GMEP, 1500 RPM. (Roberts et al., 2018)

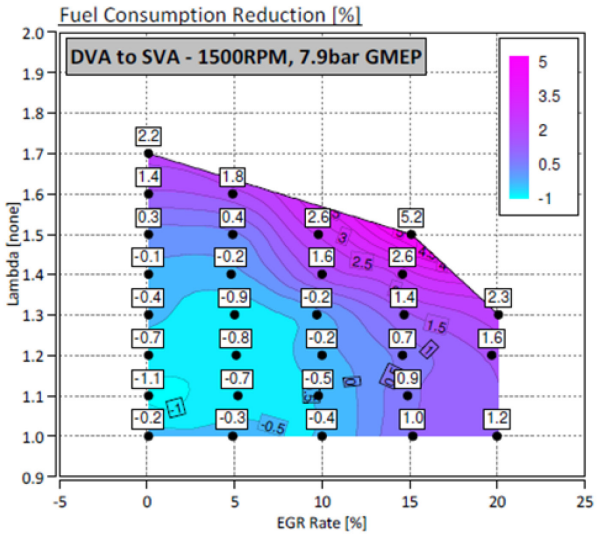


Figure 4.27 Fuel consumption (GSFC) reduction from DVA to SVA. 7.9bar GMEP, 1500 RPM (Roberts et al., 2018)

4.4.2. In-cylinder flow properties

By using the CFD methodology described in the previous case with the lowest load (3.6 bar GMEP), the in-cylinder flow field characteristics of DVA and SVA documented for this engine load (7.9 bar GMEP) were generated assuming Lambda 1 with no dilution. This action was taken after reviewing the CFD flow field data for a number of conditions with and without dilution. In these cases, there were no qualitative differences in flow field structure for the number of dilution fractions tested including the Lambda 1 condition. Hence for simplicity, all flow field characterisation data and thus differences between DVA and SVA reported hereafter assumed Lambda 1 without dilution. Some comparisons between the loads will be included.

For this higher load and for a specific dilution, the in-cylinder averaged quantities for DVA and SVA cases have no qualitative differences when compared to the respective quantities of the 3.6 bar GMEP load case. The trends for the in-cylinder velocity, tumble, swirl, turbulent kinetic energy, temperature and trapped mass are the same as for the lower load. The peak in-cylinder velocity is higher for the SVA case than the DVA and higher average velocity is maintained throughout the cycle. In addition, only tumble motion is seen for the DVA while for the SVA, strong swirl motion is seen as well as the trend of the reverse of the tumble. Furthermore, the averaged TKE is higher for the SVA and it is kept higher in the compression stroke in the same way as described for the lower load. Lastly, the temperature of the trapped mass is lower for the DVA case due to the higher amount of hot residuals trapped when a single valve is in operation as discussed for the lower load. In addition to the in-cylinder quantities,

the same trends between the two loads were seen for the total heat transfer, which was higher for the SVA.

Quantitatively, the differences between the two loads are more profound for the SVA than DVA. For the DVA, during the intake and compression strokes until firing TDC, the averaged in-cylinder velocity difference between the two loads are around ~3% but higher at higher load. For the SVA cases, after mid-intake stroke, the averaged in-cylinder velocity was higher for the higher load, and it was maintained in the compression stroke. The increased velocity at higher load was about 12% higher than the lower load at spark timing.

For the same load (7.9 bar GMEP), over a significant proportion of the cycle, the in-cylinder averaged velocity for SVA is significantly higher compared to the DVA case; with the average velocity of the SVA case being almost 2.5 times the magnitude of the equivalent DVA case across much of the cycle. This increase was caused by the restriction in the intake throat area when adopting SVA as well as the increase of the intake pressure due to the higher load. A comparison between the DVA and SVA in-cylinder average velocity for this higher load at λ=1.0 is shown in Figure 4.28. This can be compared against Figure 4.22 for the lower load (3.6 bar GMEP).

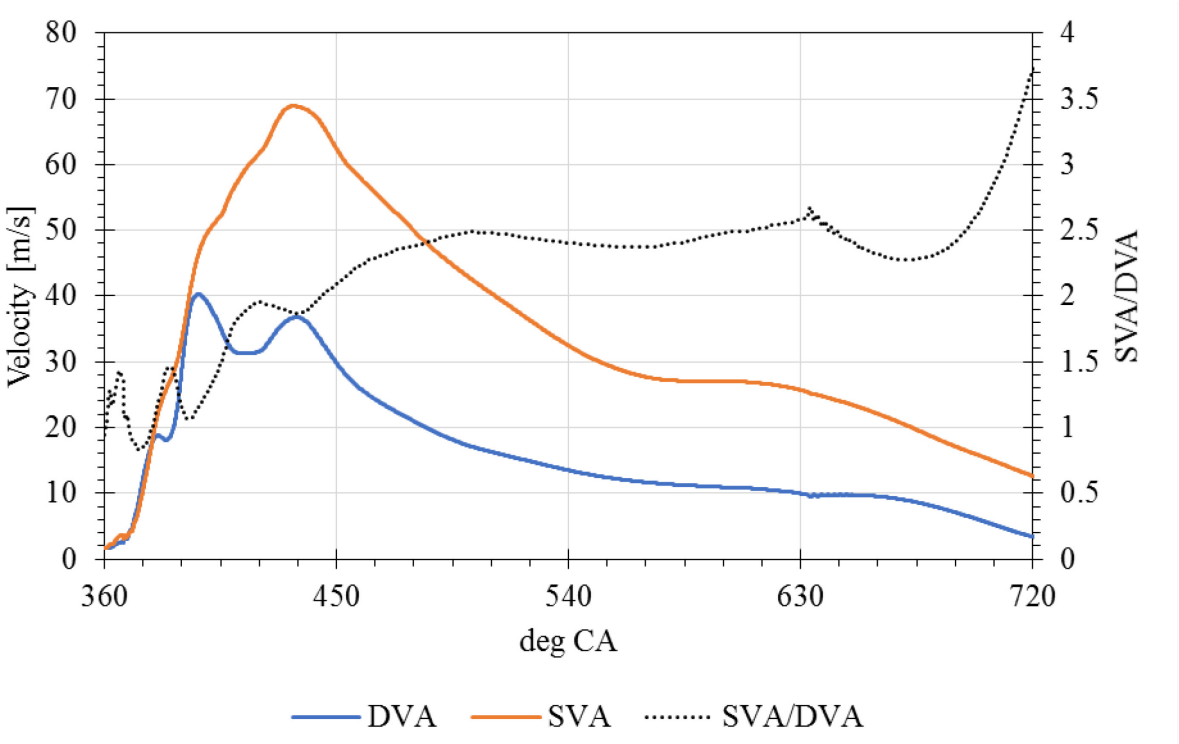


Figure 4.28 In-cylinder velocity for DVA and SVA at λ=1.0 and the ratio SVA/DVA. 7.9 bar GMEP, 1500 RPM

The behaviour of the in-cylinder velocity was reflected to the TKE where, higher energy can be seen at higher load with a more significant difference in the SVA cases. 20 degrees before firing TDC the TKE is 7.5% higher at higher load with DVA and 19.5% higher at higher load with SVA. As it was expected, for this higher load, the TKE when SVA was adopted, was almost 50% higher than the DVA 20° CA before TDC. The difference between DVA and SVA average TKE for this load (7.9 bar GMEP) can be seen in Figure 4.29. This graph can be compared against Figure 4.11 which showed the in-cylinder TKE for the lower load (3.6 bar GMEP). Contour plots of the TKE for this load are not presented here for brevity due to the very similar patterns with respect to the lower load (3.6bar GMEP). The increase of the TKE for this load validated again the increased burning rates that were seen in the experiments.

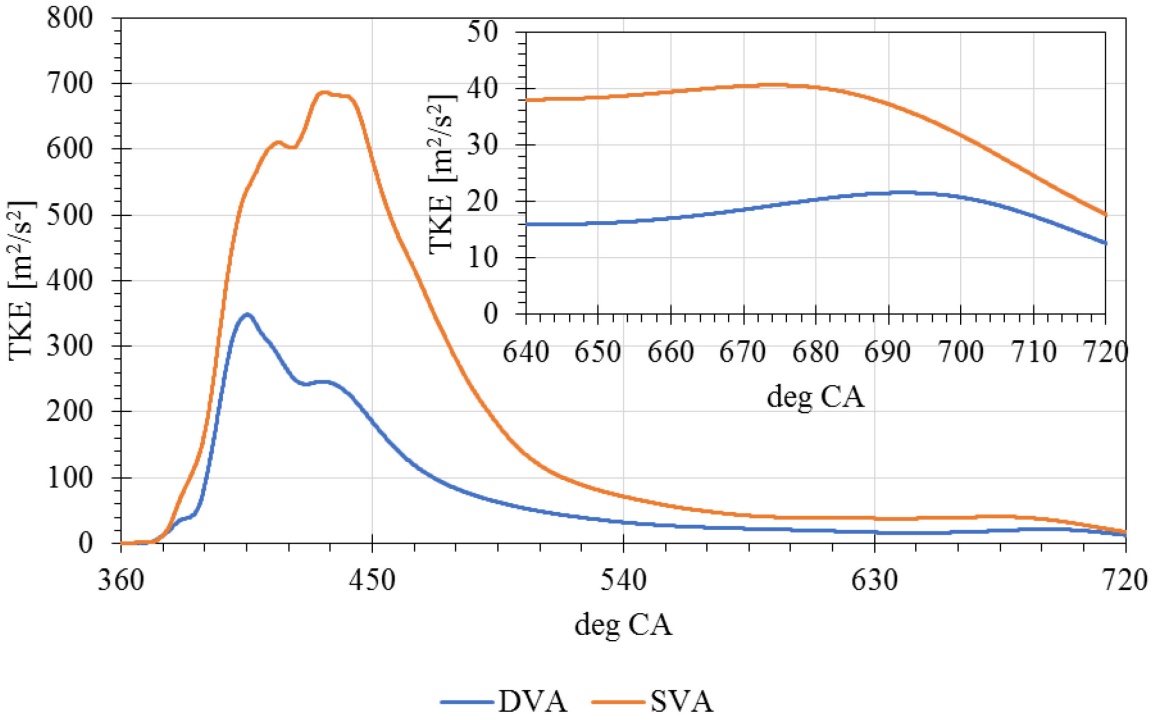


Figure 4.29 In-cylinder TKE for DVA and SVA at λ=1.0 and the ratio SVA/DVA. 7.9 bar GMEP, 1500 RPM

In terms of in-cylinder temperature, the trapped mass is cooler by 10K during intake at the higher load for both DVA and SVA because a higher amount of fresh air is induced. However, due to the compression of this higher amount of mass, the temperatures at spark timing are the same (about 2K difference) for both loads for DVA and SVA, thus the temperature difference between DVA and SVA at this load was 25K. At this test point, the major difference when compared to the lower load is the total heat transfer which was increased because of the higher density of the trapped gas. In addition, the increased flow activity of the SVA at higher load

compared to the lower load, affected further the increase of heat transfer. The peak absolute heat transfer delta between DVA and SVA from the gases to the walls was approximately 1500 W – an increase of approximately 50% as seen in Figure 4.30. Because of this great increase in heat transfer when adopting SVA at a higher load for a specific dilution, the specific fuel consumption was marginally increased with the use of SVA as the experiments showed.

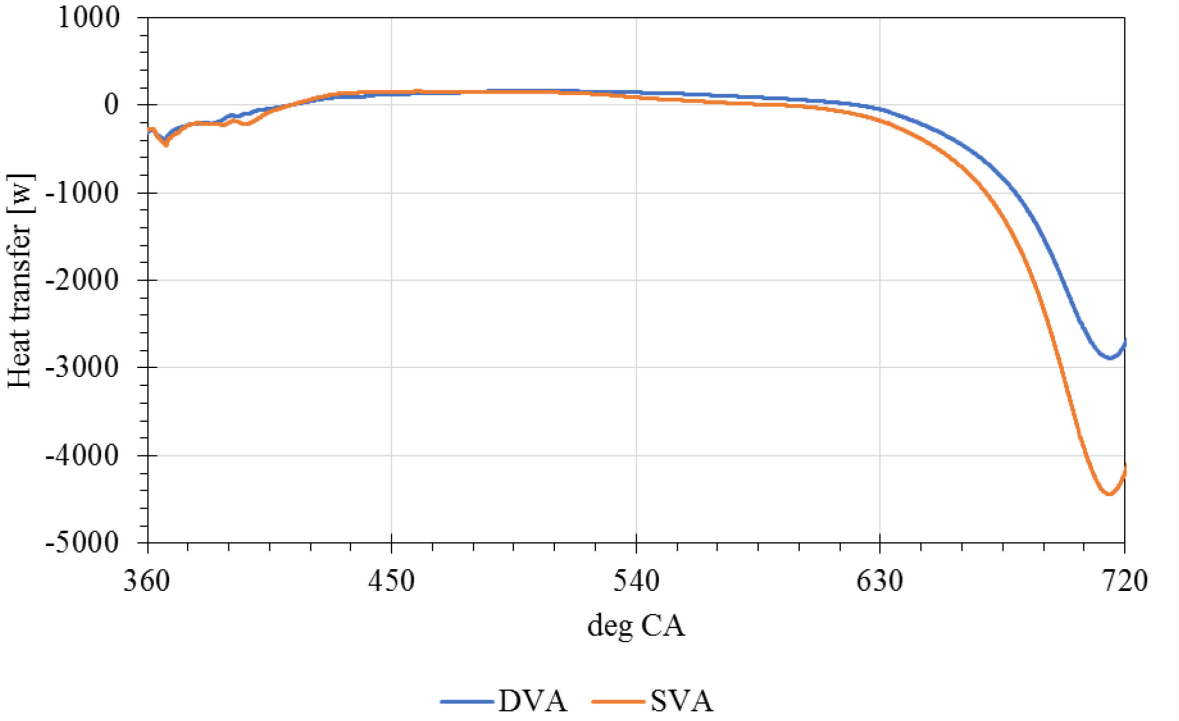


Figure 4.30 Total heat transfer from liner, piston and dome for DVA and SVA for λ=1.0. 7.9 bar GMEP, 1500 RPM

When the lambda was increased, the same trends as the lower load can be seen with a small increase in the flow activity. The averaged velocity increase from λ=1.0 to λ=1.5 is about 4% for both DVA and SVA which is similar to the lower load. This increase is reflected to the magnitudes of tumble and swirl motion which are also higher for λ=1.5. In addition, the increase in the TKE was also seen with higher lambda which was around 8% at 20 degrees before firing TDC. The in-cylinder temperature follows the same trend as for the lower load. The higher amount of the intake mass reduces the in-cylinder temperature more than in the case of λ=1.0 but during compression the higher trapped mass leads to an increase of the temperature at the same level as for λ=1.0 for both DVA and SVA (7° or 1% difference for DVA and 17° or 2.5% difference for SVA). Consequently, the increased heat transfer when adopting SVA

offset the favourably shorter burn durations resulting in a small benefit in fuel consumption (for equivalent dilution) as seen in the experiments.

4.4.3. Laminar burning velocity

Lastly, the laminar burning velocity was calculated for both DVA and SVA near ignition. The results showed the same trends as the lower load and the burning velocity was higher for SVA due to the higher in-cylinder temperature compared to DVA. In addition, the contour patterns were also similar to the lower load because only the intake boundary condition was increased which in turn increased the in-cylinder velocity, but the flow behaviour was the same as the lower load as described above. To visualise the similarities of the laminar burning velocity patterns between the two loads, the laminar burning velocity at 10 degrees before firing TDC was plotted for DVA, with slightly different legend in order to bring the contour plots at a similar colour level. This can be seen in Figure 4.31 and compared against the Figure 4.20 and 4.21 for the DVA case. Quantitatively though the burning velocity was reduced compared to the lower load which was the result of the increased in-cylinder pressure. The same patterns in laminar burning velocity between the two loads was also seen for the SVA but not showed for brevity. While the higher amount of fresh intake air was able to reduce the residual gases to about 4.5% for DVA and 5% for SVA, the in-cylinder pressure was more than the double of that of the lower load. Thus, the laminar burning velocity was decreased. The maximum value for DVA was 74 cm/s and for SVA 78 cm/s, 10 degrees before TDC. This shows again that both laminar burning velocity and turbulent kinetic energy are factors for increased burning velocity with TKE to be more significant.

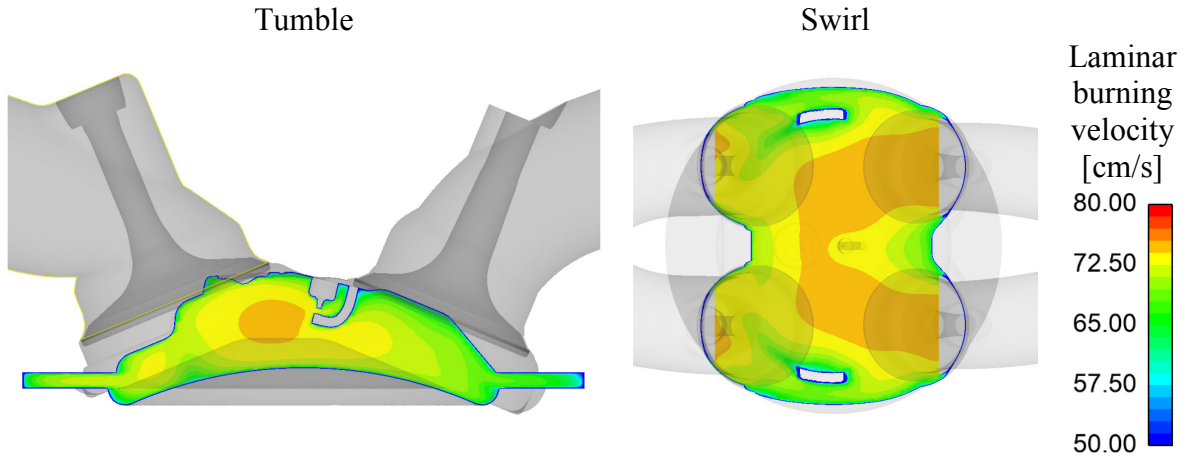


Figure 4.31 Laminar burning velocity for DVA. 10 °CA before TDC λ=1.0. 7.9 bar GMEP, 1500 RPM

4.5. Engine load: 9.8bar GMEP, 2000 RPM

4.5.1. Experimental results

At 9.8bar GMEP, 2000 RPM, adopting SVA over DVA resulted in a marginal increase in the dilution tolerance of the engine for a combustion stability limit of 3% COV of NMEP as seen in Figure 4.32. At the dilution limit of DVA and SVA strategies, fuel consumption was reduced by up to 1.3% and the ignition to 10% MFB of SVA was significantly improved over DVA with little difference in the 10-90% MFB duration between the two valvelift strategies. Furthermore, for equivalent levels of dilution the detrimental increase in heat transfer resulted in increased fuel consumption for a significant number of dilution fractions when adopting SVA over DVA. Due to these marginal benefits at the highest load, the CFD results will be briefly discussed.

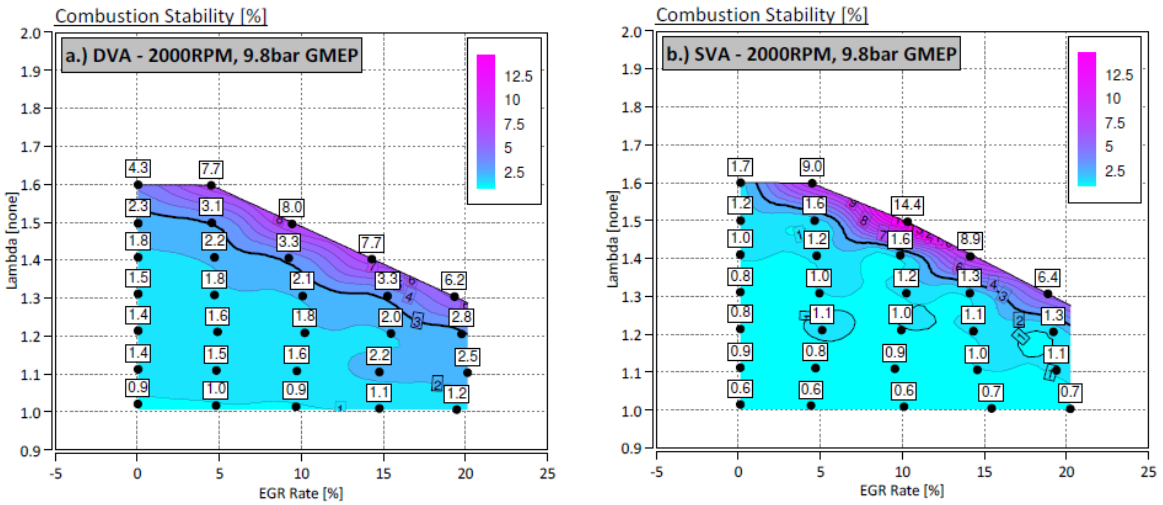


Figure 4.32 Comparison of the combustion stability limit for DVA and SVA. 9.8 bar GMEP, 1500 RPM.(Roberts et al., 2018)

4.5.2. In-cylinder flow properties

For this last operating point, the in-cylinder averaged quantities as well as the heat transfer for DVA and SVA cases have no qualitative differences and follow the same trends when compared to the other two operating points. However, the magnitude of the in-cylinder flow quantities is much higher than the other two operating points which was mainly because of the increased engine speed and to a smaller degree by the increased intake pressure. The in-cylinder flow velocity is much higher for both DVA and SVA cases which is influenced by the faster piston motion. At mid-intake stroke the velocity due to the higher engine speed is 33% higher

for both DVA and SVA cases when compared to the 7.9 bar GMEP load and this difference increases until BDC where it reaches ~55% and it is maintained until spark timing. The in-cylinder velocity for the 9.8 bar GMEP load is displayed in Figure 4.33 and can be compared against Figures 4.6 and 4.28 from the two previous loads.

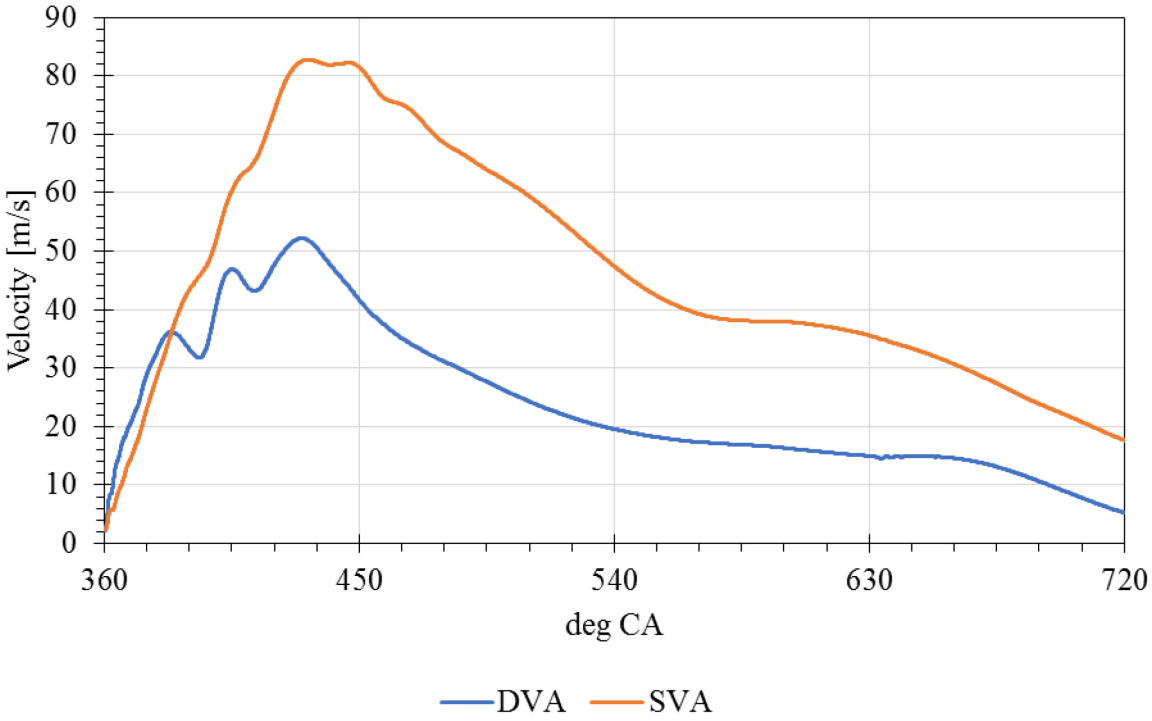


Figure 4.33 In-cylinder velocity for DVA and SVA at λ=1.0 and the ratio SVA/DVA. 9.8 bar GMEP, 1500 RPM

Because of the higher in-cylinder velocity, the magnitude of the tumble and swirl are also increased as they are directly linked to the velocity. In addition, the turbulent kinetic energy, is also increased as shown in Figure 4.34 and it is maintained higher during the intake and compression strokes. More specifically, during the intake stroke at higher engine speed the TKE is 85% higher than the TKE at lower speed with the difference to be increased and at spark timing, the TKE at 2000 RPM is the double of the TKE at 1500 RPM (the difference between the other two loads were minor compared to the highest load). While the TKE was further increased as discussed, the dilution limit was marginally extended when adopting SVA. This is due to the very strong in-cylinder flow which in combination with the high dilution did not allow a strong flame kernel to be developed which resulted in misfires or partially burnt events.

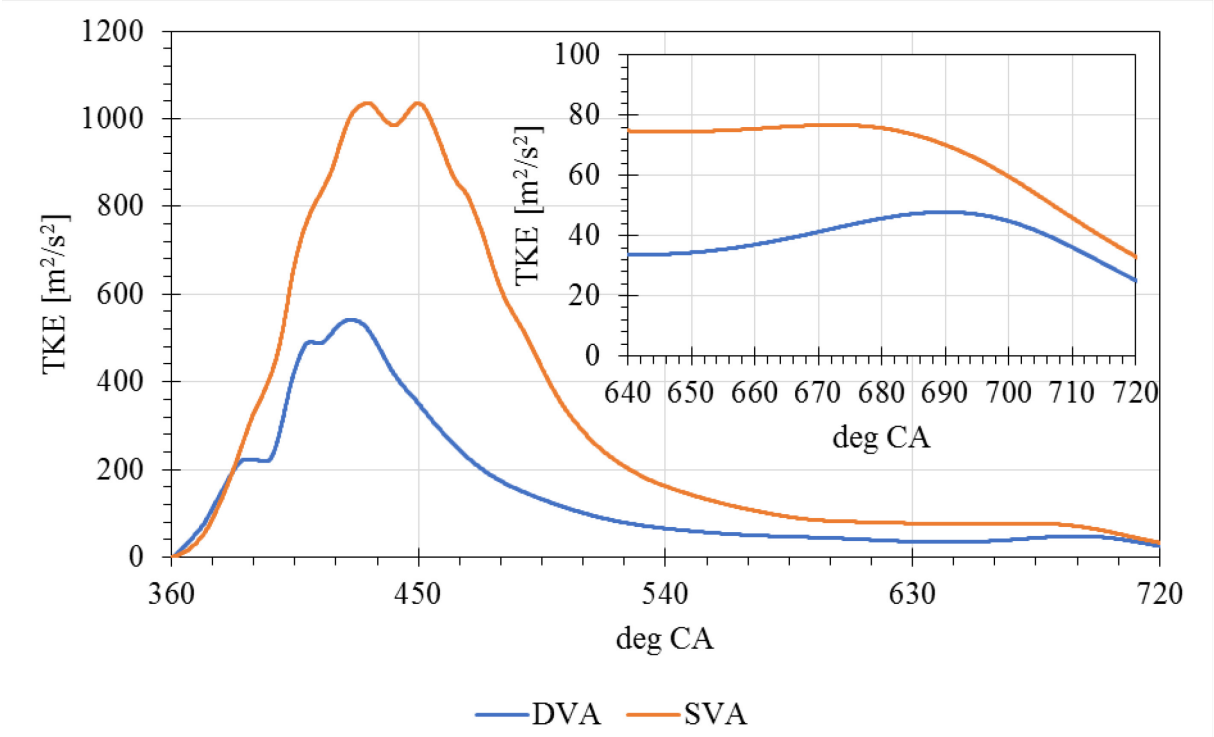


Figure 4.34 In-cylinder TKE for DVA and SVA at λ=1.0 and the ratio SVA/DVA. 7.9 bar GMEP, 1500 RPM

The high initial temperature and the higher trapped mass resulted in an increase of the in-cylinder temperature during compression. This lead to an increase of about 12K for the DVA case and 22K for the SVA at spark timing when compared to the other two loads and thus, the difference between DVA and SVA was about 30K. As a result of the significantly increased in-cylinder charge motion, temperature and gas density, the heat transfer from the gases to the cylinder walls was further increased for both DVA and SVA. The heat transfer from the gases to the cylinder walls was up to 3000 W higher (increased by 56%) for SVA compared to DVA (Figure 4.35). As such, increased heat transfer offset the shorter burn metrics resulting in little if any benefit in adopting SVA over DVA at this particular operating point as seen in the experiments.

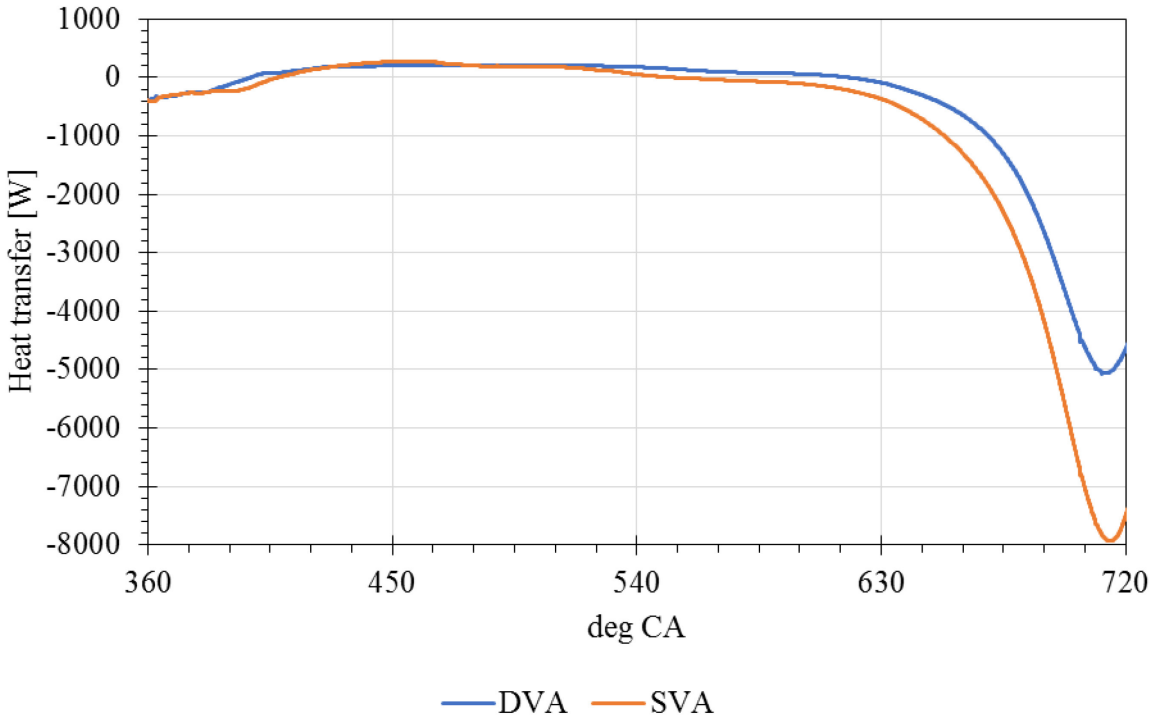


Figure 4.35 Total heat transfer from liner, piston and dome for DVA and SVA for λ=1.0. 9.8 bar GMEP, 1500 RPM

4.6. Heat transfer effects

It was mentioned that due to the increased heat transfer for equivalent levels of dilution at 3.6 bar load the benefit of fuel consumption was fractional with SVA and there was no difference at higher loads. In addition, the polytropic index (γ) for all cases utilising SVA was lower than the DVA cases pointing at the fact of the increased heat transfer associated with SVA. This was particularly pertinent at 2000 RPM, 9.8 bar GMEP where the significantly increased heat transfer resulted in an increase in fuel consumption for SVA. The calculation for heat transfer takes into account a number of parameters (density, specific heat capacity at a constant pressure, friction velocity, wall temperature and gas temperature), hence discussed in the current section are the results from an investigation into the contributory effects of each parameter to the increased heat transfer when utilising SVA.

First of all, for a given engine speed and load test point, the trapped mass and therefore density at IVC was the same for DVA and SVA. At higher loads, the trapped mass and thus the density increases which leads to increased heat transfer (eq. 2.51). From the crank resolved trapped mass diagram (Figure 4.14) it can be seen that the in-cylinder mass during intake and compression until IVC is lower for SVA than DVA which means that the induced fresh air is

smaller. As a result, the residual gas is higher for SVA (DVA: 7%, SVA: 8.1% for the 1500 RPM, 3.6 bar GMEP). Higher trapped residual therefore resulted in a higher in-cylinder gas temperature for SVA compared to DVA. More specifically, the temperature difference at IVC between DVA and SVA for the 3.6 bar and 7.9 bar loads is 25K and 30K for the 9.8 bar load.

Because of the higher concentration of residuals with SVA, the c_p is also increased however the difference is less than 1% in all cases. Note that for an extreme case of 40% trapped residuals, c_p was found to have increased by only 3% compared to the $c_p$calculated for 5% trapped residuals (at 700K). This therefore shows the relative insensitivity of c_p with respect to trapped residuals and therefore the minimal contribution to heat transfer.

Friction velocity within the heat transfer equation (u_τ) also affects the calculation of heat transfer. This term is directly linked to $u - u_w$where u is the tangential gas velocity next to the wall and u_w is the tangential wall velocity. Here, u_w is zero for the liner, dome and the flat surfaces of the piston with only a small contribution from the curved surfaces. Thus, the increased flow velocity next to the walls is another contributor to heat transfer, especially when operating with SVA. From all the above, it can be said that the increased flow activity and temperature of the SVA are the contributing factors for the heat transfer.

In an attempt to decouple the temperature difference and flow field effects on heat transfer for the DVA and SVA cases, simulations were undertaken for the compression stroke from IVC to TDCf, referred to "closed cycle" simulations. At IVC for all the closed cycle simulations the averaged trapped mass and composition of the gas were kept the same and were equal to the DVA original case at IVC. This was done to eliminate any effect of density and c_p (which is minor as discussed above). Firstly, in order to replicate the actual DVA and SVA simulations and validate the approach, using the closed cycle setup, the flow field, the average pressure and average temperature were kept the same as the original DVA and SVA cases. However, the composition of the gas and the temperature were applied homogeneously within the cylinder and were equal to the average values. This allowed to erase the mixing "history" of each case during the intake and compression which affected the temperature and concentration fields. In addition, two more closed cycle simulations were run in which the flow fields and temperatures of the DVA and SVA were swapped. In the DVA flow field, the homogeneous temperature of the SVA was applied and vice versa while keeping the trapped mass and the composition of the gas the same as the original case. Hence the only difference between the simulations was either the flow field or the temperature. All the initial conditions for the closed cycle

simulations for the 3.6 bar GMEP load can be found in Table 4.3. The average temperatures at IVC for the original DVA and SVA cases were 387K and 412K respectively. These types of simulation were also undertaken for the other speed/load test points with the relevant temperature and flow field applied.

	DVA*	**DVA**	**SVA***	**SVA**
P [bar]	0.71	~0.75	~0.75	0.71
T [K]	387	412	412	387
Cp [J/(kg K)]	DVA	DVA	DVA	DVA
Flow field	DVA	DVA	SVA	SVA

*Table 4.3 Closed cycle simulation initial in-cylinder conditions at 3.6 bar GMEP, 1500 RPM. *represents the actual cycles*

For the validation of the closed cycle simulations, the flow data of the closed cycle cases, were compared against the crank angle resolved in cylinder data (average velocity, tumble and swirl ratio and TKE) of the full cycle simulations for all test points. For the cases that were initialised with either DVA or SVA flow fields, the development of the in-cylinder flow data matched the original data as shown Figure 4.36 for the 3.6 bar GMEP case. The solid lines represent the closed cycle and the dashed lines represents the actual full cycle cases. The same trends of the validation were also observed for the other two loads.

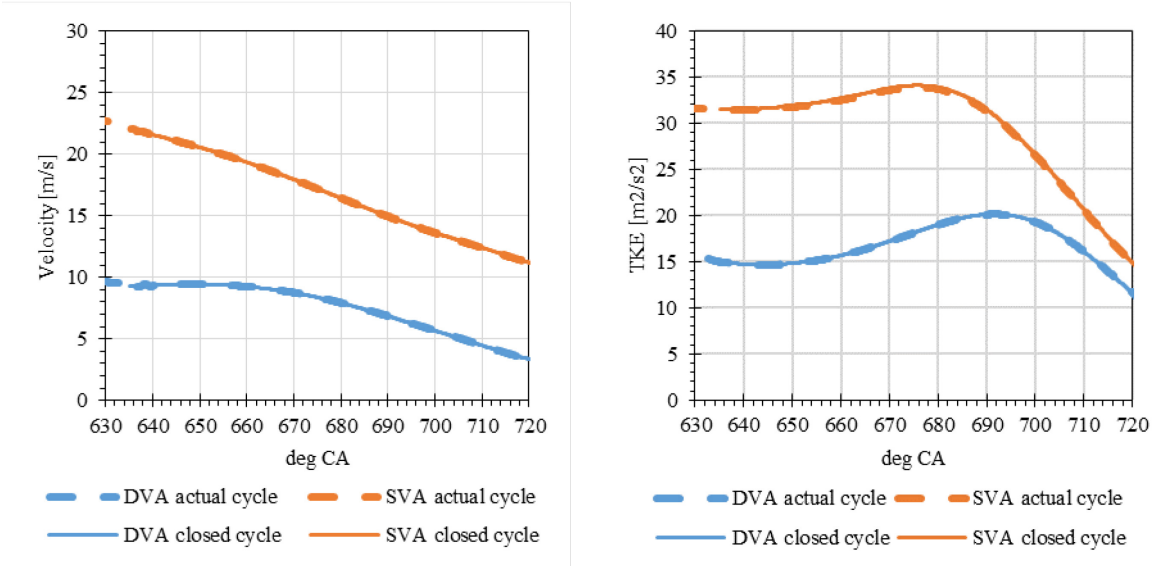


Figure 4.36 Comparison between the actual and close cycle simulations for the in-cylinder velocity and TKE at 3.6 bar GMEP, 1500RPM

In addition, the predicted heat transfer from the closed cycle simulations which replicated the actual cycles for both DVA and SVA was compared against the actual heat transfer for further validation purposes. This comparison showed that at 25 °CA after IVC, the difference between actual and replicated case was ~3% and 45 °CA after IVC, the difference between actual and replicated case was ~0.9% and this difference was dropping further as the cycle progressed. This shows that the flow field established a temperature field the same as the actual cases near the engine walls. This is showed in Figures 4.37 to 4.39 for the solid and dashed lines of the same colours.

In Figure 4.37 the heat transfer from the gas to the engine walls for the four closed cycle simulations at 3.6 bar GMEP is showed with solid lines. In addition, the heat transfer of the two original DVA and SVA cases are included and represented by the dashed lines. From the simulations of the actual DVA and SVA cases and the closed cycles which replicated them it was seen that there was an increase of 23.6% in heat transfer from DVA to SVA at the peak of the heat transfer (approximately 500 W). For a constant temperature (for both 387K and 412K), the increased activity from the DVA flow field to the SVA showed an increase of 10.5% in heat transfer. When the flow field was kept constant (DVA or SVA) and the initial temperature was increased from 387K to 412K, the increase in heat transfer was about 12.5%. As such, the dominating effect for the increased heat transfer at this engine speed and load was the higher in-cylinder temperature at IVC, caused by higher levels of trapped internal residuals. Note that the decrease in heat transfer as the piston approaches TDC is related mainly to flow field effects as density and temperature remain approximately constant close to TDC.

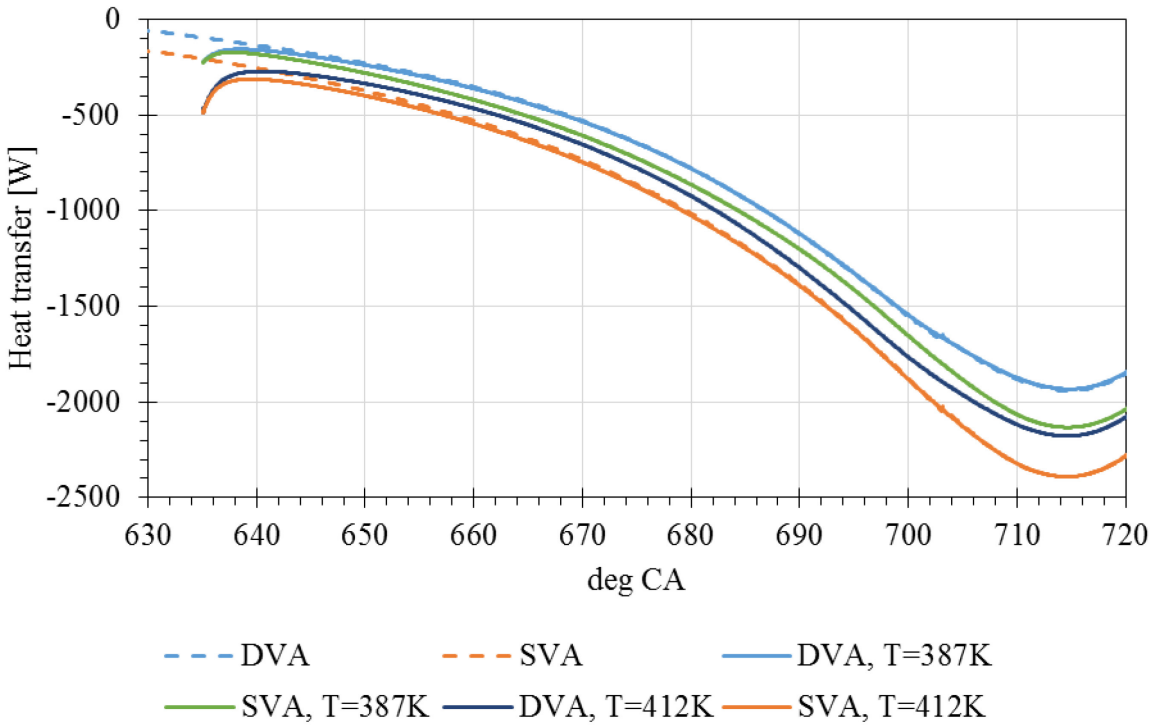


Figure 4.37 Total heat transfer for the four closed cycle simulations and the two actual cycles. 3.6 bar GMEP, 1500 RPM

The same methodology was performed for the other two loads (7.9 bar GMEP, 1500 RPM and 9.8 bar GMEP, 2000 RPM). Again, for both loads, the closed cycle cases which had the same flow field and averaged temperature as the original cases give the same heat transfer as the original simulations especially 45 °CA after IVC, however, there is a minor difference between the actual SVA cycle and the closed SVA cycle at the peak of the heat transfer which was about 1.4%-1.7%. For the 7.9 bar GMEP load (Figure 4.38), the total increase in heat transfer from the DVA to SVA is 50% (1500 W), at the peak of the heat transfer. The temperature difference at IVC was again 25 K (379 K for DVA and 404 K for SVA). For a constant flow field (DVA or SVA) and an increase of the initial temperature by 25 K, the increase of heat transfer is about 13-13.5%. When the initial temperature was kept the same for DVA and SVA (379 K or 404 K) the increase in heat transfer is about 34%. For this load, the effect of the flow field is the dominant factor for the increased heat transfer.

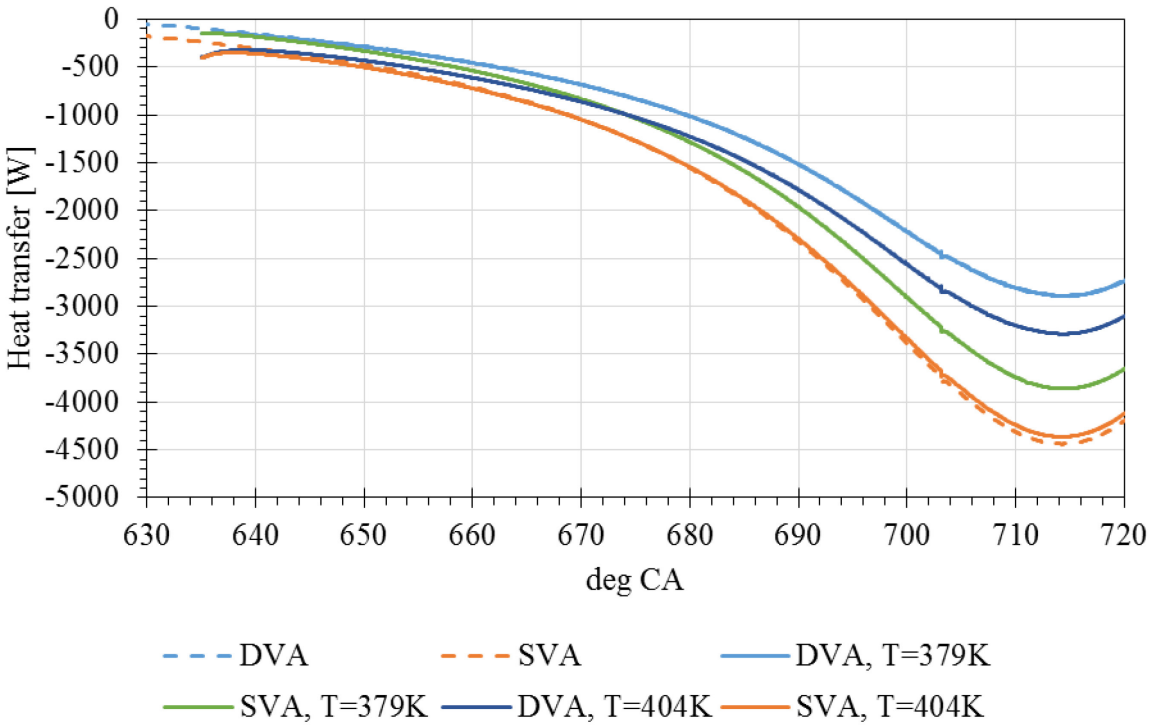


Figure 4.38 Total heat transfer for the four closed cycle simulations and the two actual cycles. 7.9 bar GMEP, 1500 RPM

For the 9.8 bar GMEP, 2000 RPM case, the increase in heat transfer from the actual DVA to SVA cycle was 56%, almost 3000W at the peak of the heat transfer as shown in Figure 4.39. In this case, the temperature difference between DVA and SVA was 30 K (384 K for DVA and 414 K SVA). For equivalent flow fields the increase of heat transfer due to the increase of temperature was about 16%. For equivalent temperatures, the increase of heat transfer because of the increased activity was 36%. Again, at this engine speed and load, the majority of the increased heat transfer when adopting SVA over DVA was attributed to the significantly enhanced charge motion of SVA. It has to be reiterated that in this case, the temperature difference was 30 K while for the lower loads was 25K. It can be concluded that for the lower loads, the dominant factor for the additional heat transfer for SVA is the increase in in-cylinder temperature, while for the higher loads, the dominant factor is the increased flow activity close to the wall. Lastly, the increase in heat transfer due to the increased temperature was very similar for all three loads (13-16%). Especially for the 3.6 bar and 7.9 bar loads which had the same temperature difference, the increase was around 13% for both.

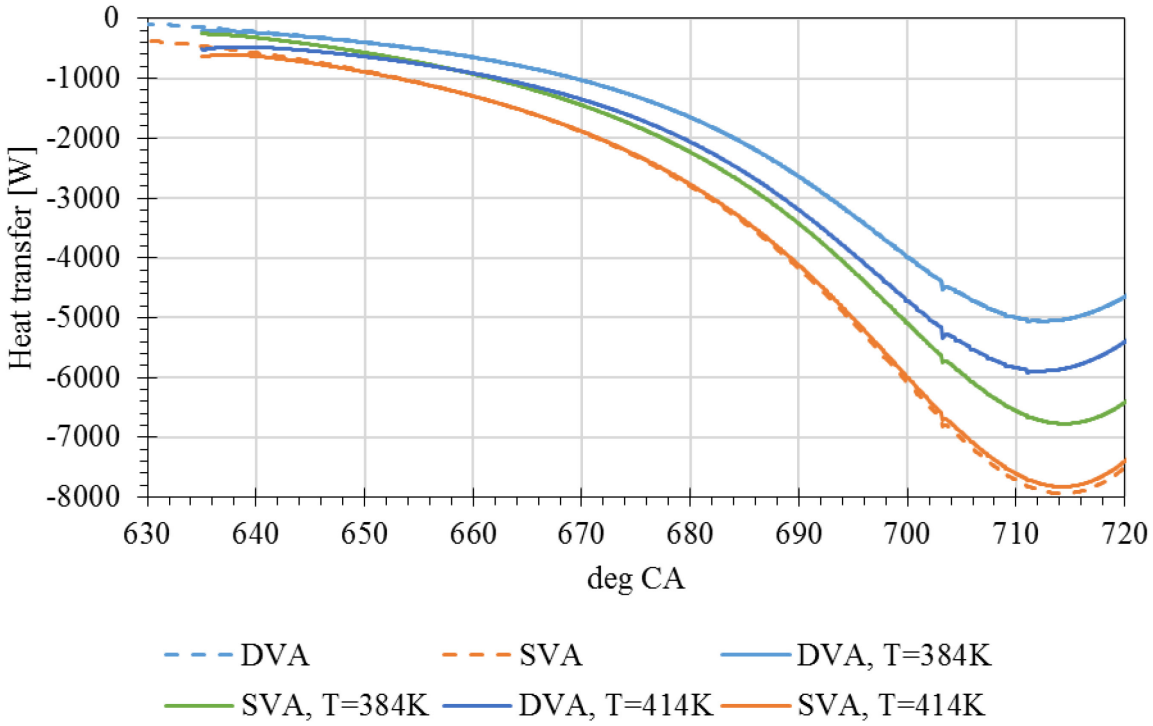


Figure 4.39 Total heat transfer for the four closed cycle simulations and the two actual cycles. 9.8 bar GMEP, 2000 RPM

4.7. Closure

The differences between the Dual and Single Valve Actuation on the in-cylinder flow field and velocity magnitude, turbulent kinetic energy, temperature and trapped mass and residuals was investigated. In addition, the spatial distribution of some of these quantities as well as the laminar burning velocity was also studied due to their importance in combustion. Moreover, the heat transfer differences and the reasons behind them for the two valve strategies were also studied. The conclusions that are irrespective of engine load were:

- There is an increased in-cylinder activity by adopting SVA due to higher valve jet which increases the in-cylinder velocity
- Due to the asymmetry created by SVA, a strong swirl motion is generated while maintaining the magnitude of the tumble at the same level as with the DVA due to the geometry of the port.
- With the use of SVA, the turbulent kinetic energy is increased at spark timing when compared to DVA. Also, the area of high TKE within the cylinder is increased by adopting SVA and also the location is more favourable for the combustion as it encloses

the spark plug. This is a factor that denotes faster combustion as seen in the experiments.

- With SVA, the trapped residuals are increased which in turn, increase the in-cylinder temperature.
- Due to the increased in-cylinder temperature, the laminar burning velocity is also increased. This is another factor for the faster combustion with SVA. With the level of residuals trapped in these cases, the dominant factor for the laminar burning velocity behaviour is the temperature.
- When the stoichiometric and lean cases were compared, there was a small increase on the in-cylinder flow quantities (velocity, tumble and swirl, TKE). This increase was due to the increased intake pressure of the lean cases. As a consequence of the increased TKE, the engine could tolerate more dilution without detrimental increases in the ignition to 10% MFB and 10-90% MFB durations. As a result of the extension of dilution, a fuel consumption reduction of up to 3.8% (at 3.6 bar GMEP, 1500 RPM) could be achieved, as seen in the experiments.
- For the lean cases (λ=1.5), the laminar burning velocity is reduced because of the high dilution. This suppresses the burning velocity even with lower residuals and high temperatures.
- The increased activity with the SVA and the higher in-cylinder temperature have a result of increased heat transfer from the gas to the engine walls. This explains the reduction of the polytropic index with SVA for both experiments and numerical predictions. For all test points, this increased heat transfer resulted in fractional improvements in fuel consumption for equivalent levels of dilution.

Some conclusions however, were dependent on the engine load and speed. Those were:

- With the increase in engine load, the heat transfer from the gas to the walls was increased mainly because of the increase of the density of the working fluid for both DVA and SVA. Moreover, the maximum heat transfer difference between DVA and SVA was increased at higher loads. The significant increase of heat transfer with SVA at higher loads, offset the favourably shorter burn durations resulting in a negligible benefit in fuel consumption for equivalent dilution, but some benefit could be gained through the extension of dilution (3.1% at 7.9 bar GMEP, 1500 RPM and 1.3% at 9.8 bar GMEP, 2000 RPM).

- The two main contributors for the increased heat transfer when adopting SVA is the enhanced flow motion and the increased in-cylinder temperature for equivalent dilutions.
- At low loads (3.6 bar GMEP, 1500 RPM), the dominant factor for the additional heat transfer for SVA is the increase in in-cylinder temperature which increased the heat transfer by 12.5%. The enhanced charge motion increased the heat transfer by 10.5%.
- At higher loads, (7.9 bar GMEP, 1500 RPM and 9.8 bar GMEP, 2000 RPM) the dominant factor is the increased flow velocity close to the walls. The increase of heat transfer due to the higher temperature was 13.5% at 7.9 bar GMEP and 16% ta 9.8 bar GMEP. Due to the enhanced charge motion the increase was 34% and 36% respectively.
- It appears that an optimum level of enhanced in-cylinder charge motion attributed to SVA exists whereby the benefits of reduced burn duration and increased dilution tolerance can be realised without the shortfalls of invoking significantly increased heat transfer

Chapter 5

Effects of Valve Deactivation on Mixture Preparation and Emissions

5.1. Introduction

This chapter presents the analysis carried out to investigate the effect of Dual and Single Valve Actuation on mixture preparation and emissions at two engine running points, (3.6 bar GMEP and 7.9 bar GMEP at 1500 RPM). The air-fuel mixture is important for the flame propagation, as it affects the laminar burning velocity which can cause combustion stability issues and misfires especially if the mixture is diluted with either fresh or exhaust gases. In addition, poor air-fuel mixture can lead to pollutant formation such as nitrogen oxides, carbon monoxide, unburnt hydrocarbons and particulate matter.

The Lagrangian multi-phase treatment was used to model the fuel injection and the approach from the validation chapter was followed. The flash boiling model was implemented at 1500rpm, 3.6bar GMEP due to the low in-cylinder pressure (~0.5 bar) during injection and the high temperature of the fuel (~90°C) in which gasoline is prone to flash boiling. For the flashing cases, *n*-Pentane was used as a single component fuel. Details of the flash boiling model have been discussed and the generalised approach was used. For the rest of the cases, a sub-cooled spray model was adopted, and *iso*-Octane was used. Briefly, the physical models of the

Lagrangian approach included turbulent dispersion, gravity effects and inter-droplet collisions based on the O'Rourke (1981) model and the Reitz and Diwakar (1986) model was used for the droplet break-up. In this study, the Rosin-Rammler distribution was used to initialise the droplet size. The rest of the boundary conditions and the initialisation procedure was the same as the previous chapter. The start of injection was 60 degrees after gas exchange TDC (420 degrees CA on the graphs) for all cases and the duration was taken from the experiments as it varied for different dilutions and loads. The spray formation for the DVA and SVA cases for both loads at λ=1.0, 7 degrees CA after start of injection is shown in Figure 5.1 for the tumble view and Figure 5.2 for the swirl view. The differences between the flash boiling and the sub-cooled modelling is evident for the two loads. In addition, the tumble motion for DVA and the strong swirl motion for the SVA as described in the previous chapter, affects the spray in different ways. For the DVA at high load, when looking the tumble view, the initial part of the plume near the engine head is directed towards the exhaust port due to the valve jet but the tip is directed towards the intake port because of the tumble flow. For the lower load of the DVA, droplets are directed towards the exhaust side, but the penetration of the spray is lower and thus at this crank angle it was not affected by the tumble flow near the piston. When the swirl plane was investigated, a symmetric spray formation was seen for DVA. When SVA was adopted, the strong valve jet and swirl motion mostly affects the plumes of the side of the open valve.

The geometry of the computational model at the intake port had to be modified in order to improve the accuracy of the simulations. Due to the Late Intake Valve Closure which was about 100 degrees after Bottom Dead Centre, an amount of trapped mass escapes from the cylinder to the intake port. When the fuel injection was introduced, a portion of the evaporated fuel escaped to the intake port, which resulted in very lean air-fuel mixture within the cylinder during the first cycle. In order to acquire the desired air-fuel ratio, the fuel vapour in the intake had to be introduced to the following cycle. After 4-5 consecutive cycles depending on the valve actuation (DVA or SVA), the in-cylinder air-fuel ratio was converged to the desired lambda. The process of the convergence of the in-cylinder lambda can be seen in Figure 5.3. For the DVA, due to the higher amount of mass escaping the cylinder, an extra cycle was needed for convergence. The simulation started at the expansion stroke, 270 degrees before gas exchange TDC and it is before EVO. This is the same procedure as the previous chapter and the gas composition of each domain (cylinder, intake port and exhaust port) was following the calculations of Table 2.1 and the initial pressure was taken from the experiments. The simulation was let to run for a whole cycle (720 degrees CA) and at the end of the cycle, the

solution of the last timestep was acquired. Following, the solution was modified for the in-cylinder and exhaust domains by imposing the same initial conditions as at the beginning of the first cycle. The intake port domain however, was not modified in order to maintain the trapped fuel and introduce it to the next cycle. This process was applied until the convergence of the air-fuel ratio.

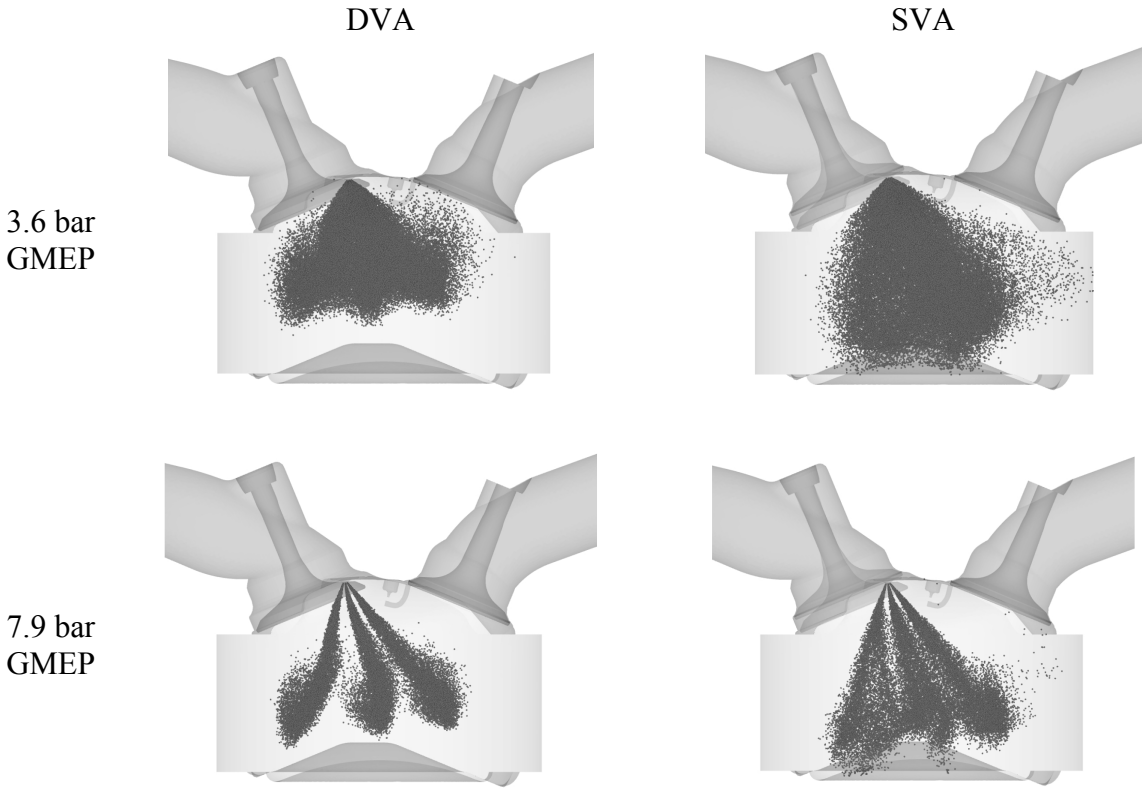


Figure 5.1 Spray structure for DVA and SVA for two loads (3.6 bar GMEP and 7.9 bar GMEP, 1500 RPM), tumble view

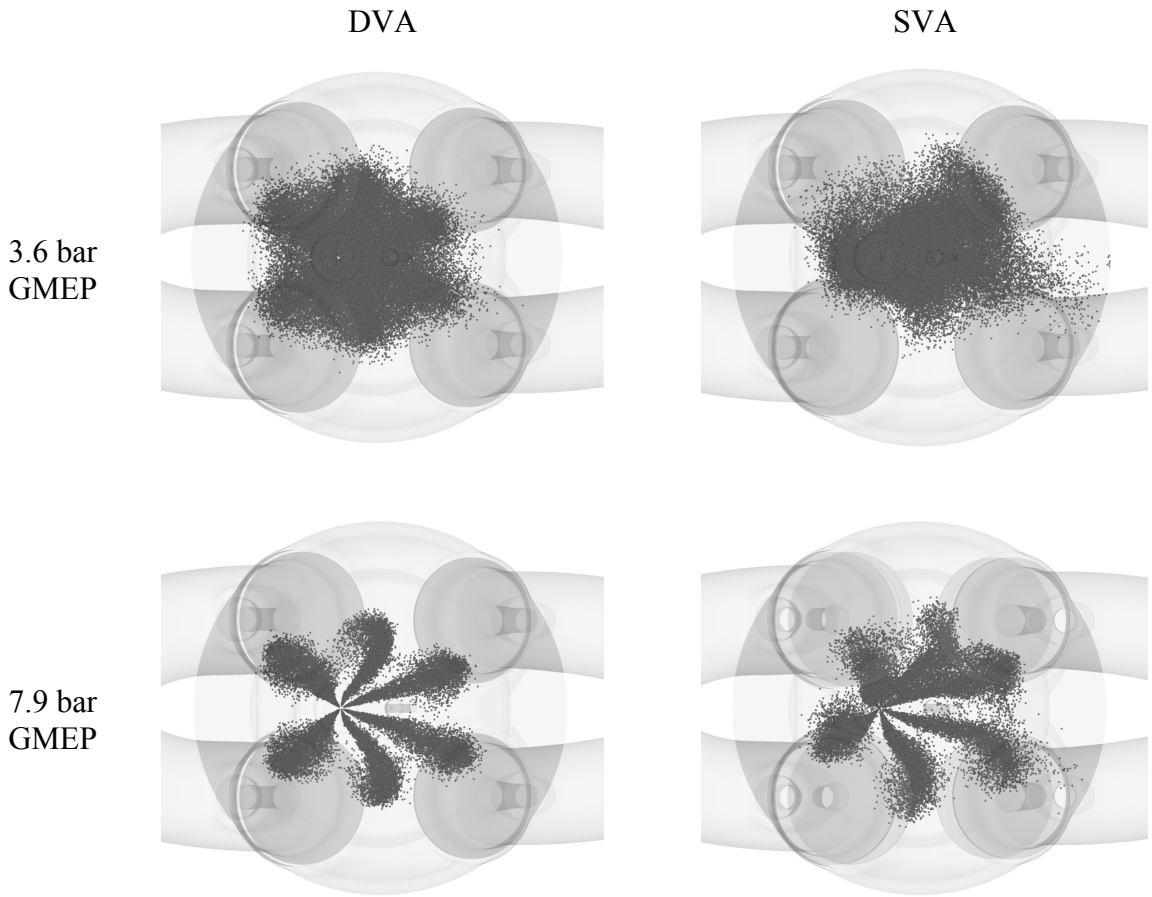


Figure 5.2 Spray structure for DVA and SVA for two loads (3.6 bar GMEP and 7.9 bar GMEP, 1500 RPM), swirl view

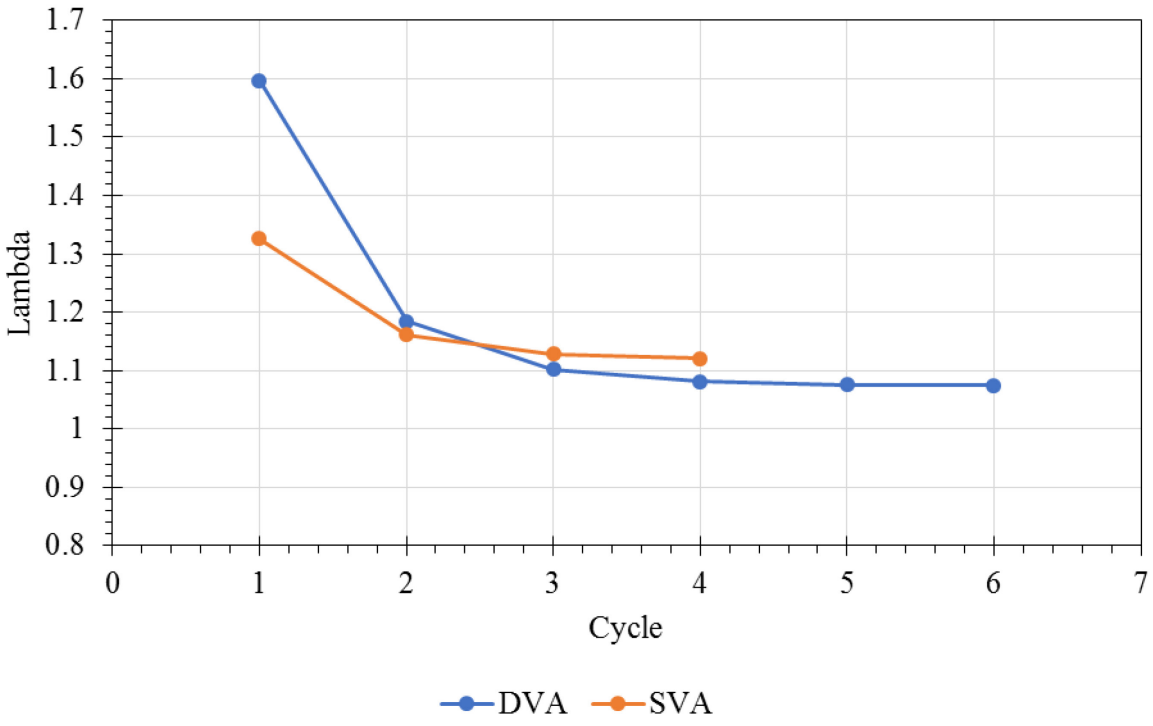


Figure 5.3 Convergence of global Lambda for DVA and SVA

To accurately capture the fuel vapour in the intake runner, the runner was extended by 140mm, which was length of the runner upstream the pressure sensor (pressure boundary of the model) and before the plenum. Without this extension, the fuel vapour was escaping and essentially lost from the pressure boundary. With the extension however, the total amount of fuel vapour was remaining in the intake which was the most accurate procedure. For the pressure boundary, the time dependent pressure from the experimental measurements was used without any modifications. A test was carried out with 1D simulation to identify possible inaccuracies when the pressure boundary was applied 140 mm upstream the actual pressure transducer position. The results presented in Figure 5.4 shown that the pressure wave frequency did not change but the magnitude was slightly reduced. The reduction was less than 1% (~200Pa). In order to do this test however, the 1D model had to be tuned for the specific test case in order to get correct in-cylinder pressure and the correct intake pressure trace at the location of the pressure sensor. Because of these small differences and the difficulty to acquire the pressure trace for the new boundary location with the 1D modelling, the original pressure was used. The differences of the intake runner geometry can be seen in Figure 5.5.

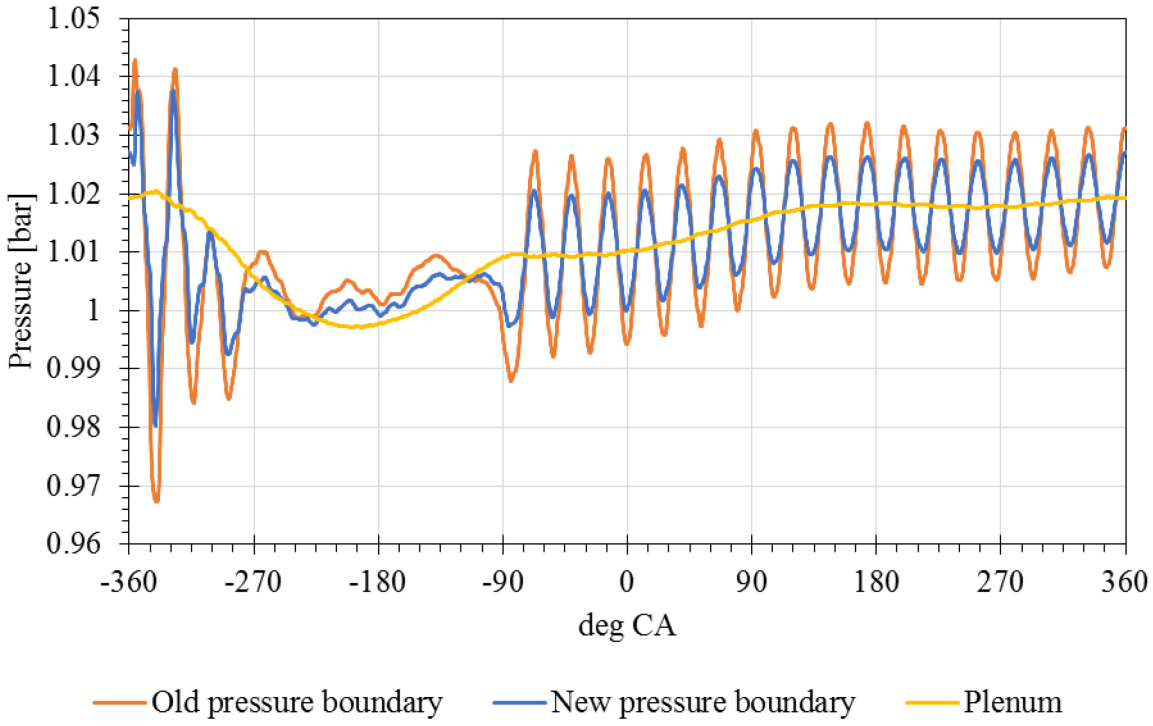
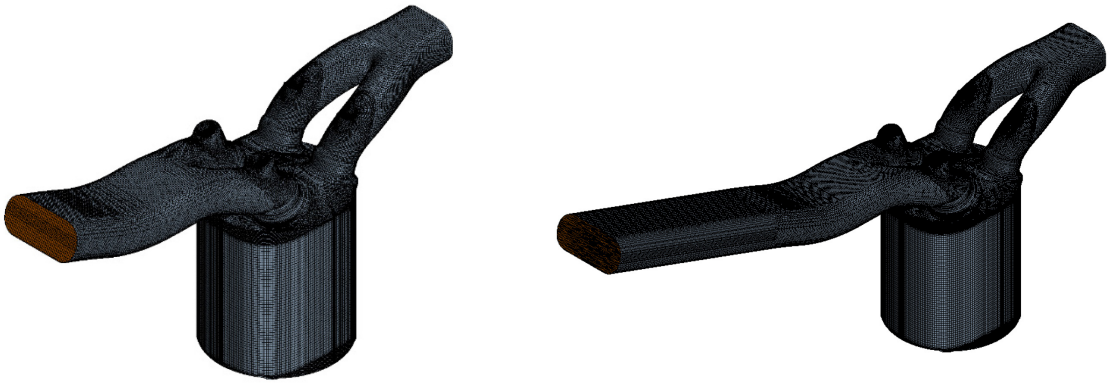


Figure 5.4 Intake pressure trace at various intake runner locations calculated with 1D simulation



Original geometry Geometry with extended intake runner

Figure 5.5 Original AJ20 geometry and geometry with extended intake runner

In order to speed up the process time and reduce the number of simulations, a normalised approach was tested. With this approach, the global air-fuel ratio of the second cycle was normalised to the desired global air-fuel ratio, such as lambda=1. In the same way, the global air-fuel ratio of the converged cycle was normalised to the desired lambda. These two normalised cases were compared to each other to identify possible patterns because of the principles of RANS simulations. Four different locations above the head gasket along the bore centreline at two different timesteps around ignition timing were tested. The results showed that the maximum difference between the normalised second and normalised sixth cycle was 0.7% and the average difference of all investigated points was less than 0.1%. An example of this comparison is displayed in Figure 5.6 which shows the Lambda versus the location of the bore centreline along the x-axis, 20 degrees before firing TDC.

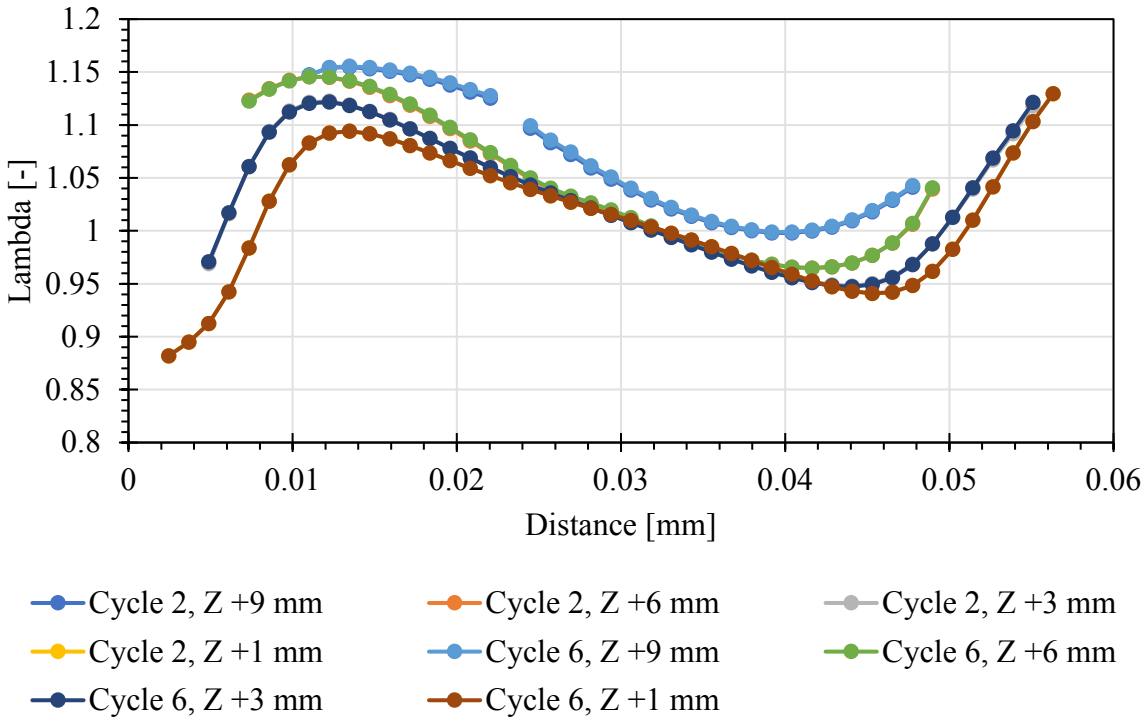


Figure 5.6 Verification of the normalisation approach for Lambda. Calculations at 20 degrees before TDC

As a form of validation, the experimental in-cylinder pressure up to ignition was compared against the numerical in-cylinder pressure with the presence of fuel. The results were in a better agreement which was also reflected on the compression polytropic index. As it can be seen in Table 5.1, for three different dilution cases at 7.9 bar GMEP, 1500 RPM, the experimental and numerical gamma values are in a very good agreement. This showed that the differences reported in the previous chapter were improved with the presence of fuel, something that existed but not simulated previously. In addition, the trends seen in the experiments were also predicted by the CFD such as the increase of gamma with increased dilution and lower gamma for SVA than DVA, as explained in the previous chapter.

		DVA	SVA
λ=1.0	**CFD**	1.294	1.274
	Experiment	1.298	1.279
λ=1.1	**CFD**	1.302	1.281
	Experiment	1.302	1.281
λ=1.2	**CFD**	1.306	1.286
	Experiment	1.306	1.286

Table 5.1 Experimental and numerical compression polytropic index (γ) for DVA and SVA at various lambdas. 7.9 bar GMEP, 1500 RPM

5.2. Engine load: 7.9 bar GMEP, 1500 RPM

5.2.1. In-cylinder flow properties

Firstly, the in-cylinder flow properties for the cases with the fuel injection were investigated and compared against the same cases without spray to study the effect of the direct injection on the in-cylinder quantities. The start of the injection is shown with the vertical black dashed line. As it was expected, during the fuel injection the in-cylinder average velocity is affected by the spray for both DVA and SVA as it can be seen in Figure 5.7. The results revealed that the velocity is reduced during the event of the injection, however after the end of the injection the velocity is similar to the motoring case. For DVA, during compression and more specifically at ignition timing the difference is 7%. Due to the momentum introduced by the spray, the in-cylinder velocity is maintained higher than the motoring case (4.93m/s against 4.58m/s). The reduction during the injection comes from the fact that the spray direction is opposite to the flow which affects the average velocity. Similarly for the SVA, the in-cylinder velocity is 0.2% higher with the fuel injection than the motoring case. The difference is much lower due to the high flow velocity established by the single valve which is barely affected by the injection.

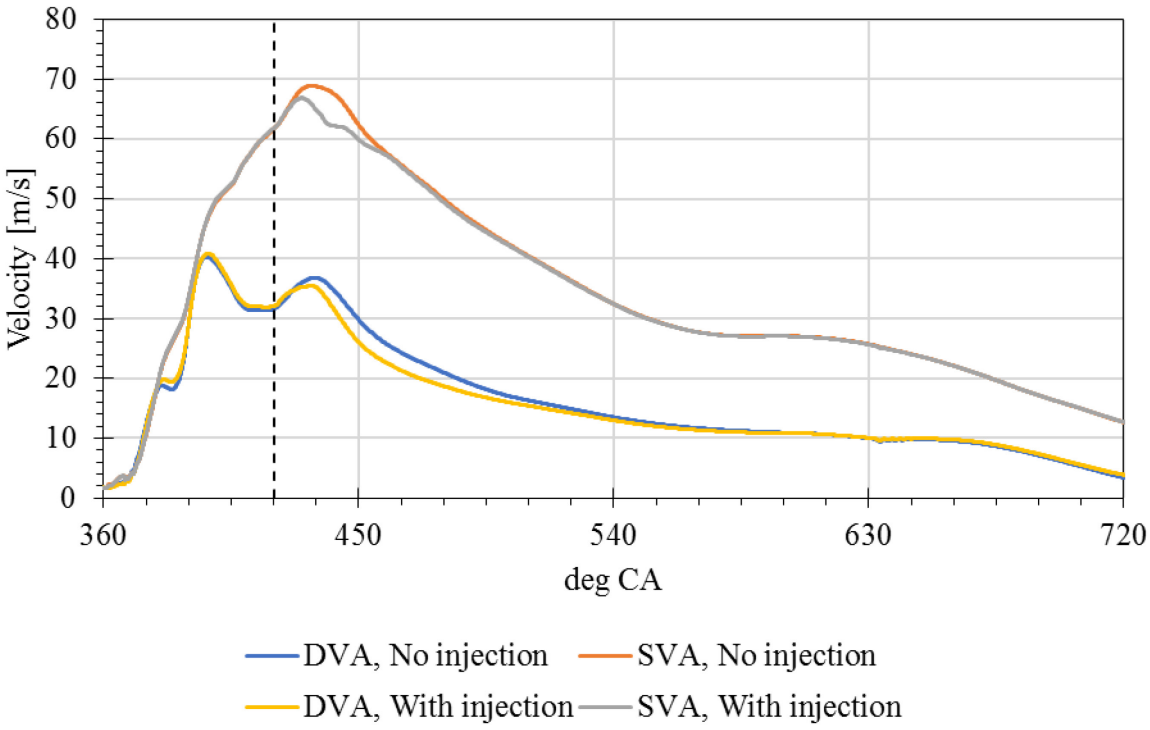


Figure 5.7 In-cylinder velocity magnitude for DVA and SVA, with and without injection. 7.9 bar GMEP, 1500 RPM

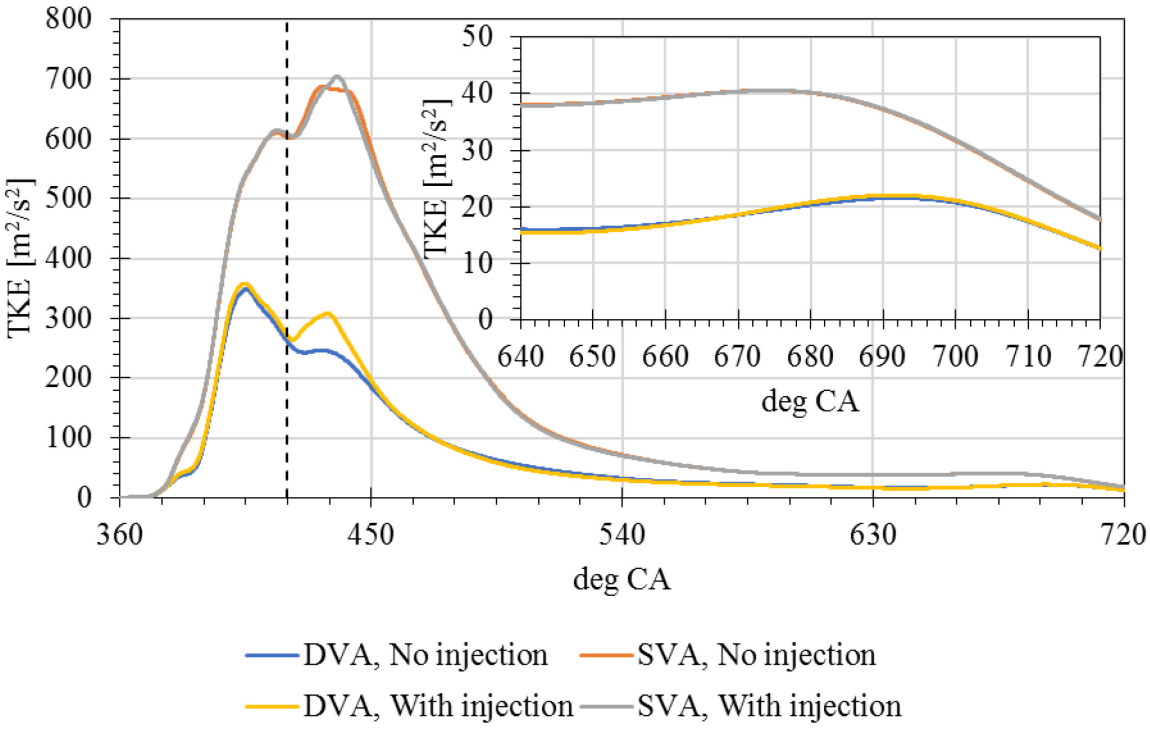


Figure 5.8 In-cylinder TKE magnitude for DVA and SVA, with and without injection. 7.9 bar GMEP, 1500 RPM

The turbulent kinetic energy was also compared for the cases without and with fuel injection (Figure 5.8). The TKE was increased during injection for both DVA and SVA cases. At the end of the compression stroke and at ignition, the TKE was increased due to the fuel injection. The increase for the DVA was 1% and for SVA was 0.6% near ignition. Again, due to the dominant strong in-cylinder flow with the SVA, the increase was smaller than the DVA.

The big differences of the in-cylinder quantities between the motoring case and the case with the fuel injection were seen for the temperature. As it was expected and described in the literature, the direct injection reduces the in-cylinder temperature. As the amount of the injected fuel for DVA and SVA was similar, the reduction in temperature was also similar. The reduction in temperature was about 80° for both cases meaning that a difference of 21° between the temperature of DVA and SVA was maintained. With the reduced in-cylinder temperature and the in-cylinder velocity maintained at the same level as the motoring case, it was expected a reduction in heat transfer from the gas to the walls. This was true as it can be seen from Figure 5.9 which shows the total heat transfer from the gas to the walls for DVA and SVA for the cases with and without the fuel injection. While the heat transfer is lower with the fuel injection due to lower in-cylinder temperatures, the increase from DVA to SVA is the same and about 50% compared to the case without fuel.

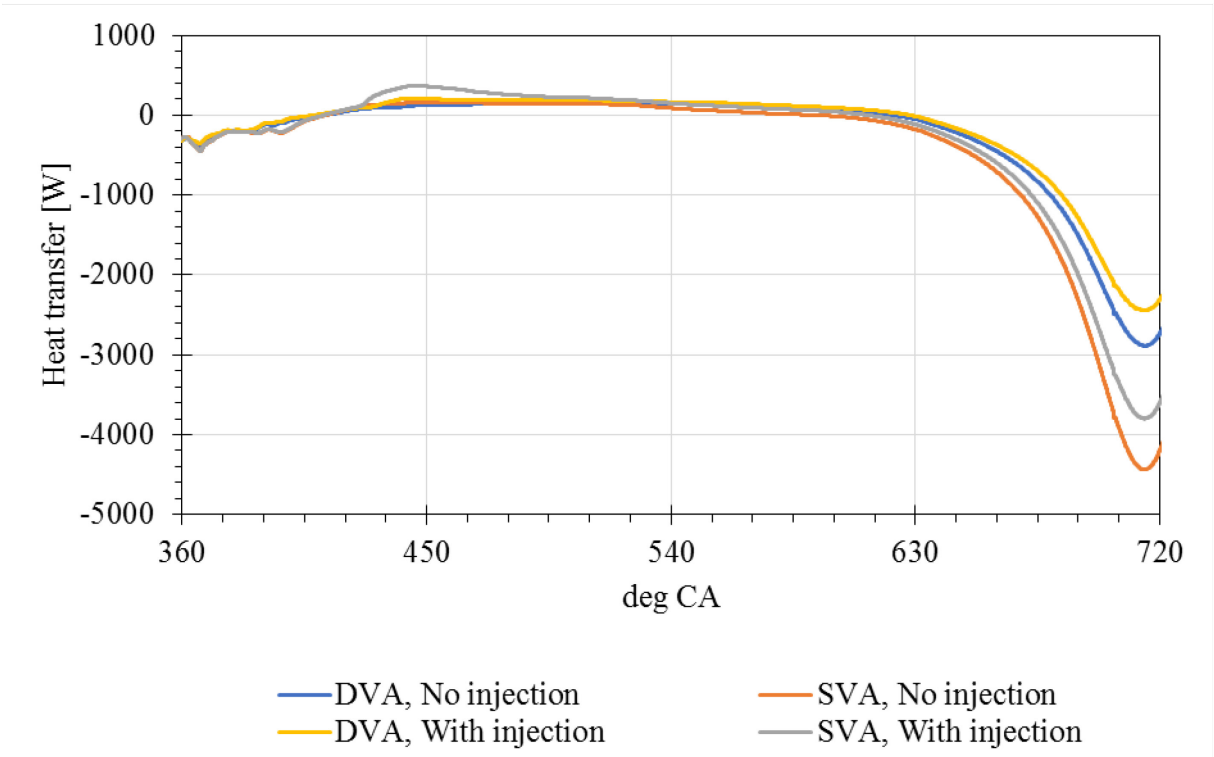


Figure 5.9 Total heat transfer for DVA and SVA, with and without injection. 7.9 bar GMEP, 1500 RPM

5.2.2. Mixture preparation

First of all, the air-fuel mixture for the λ=1.0 case was investigated for the two valve strategies (DVA and SVA). The progress of the Lambda contours for four different crank angles in the compression stroke and near ignition are displayed in Figure 5.10 for DVA and Figure 5.11 for SVA. From the Lambda contours it can be seen that in the case of the Dual Valve Actuation, while the global Lambda within the cylinder is λ=1.0 and also the mixture close to the centre of the cylinder is at λ=1.0, stratified areas of either lean or rich mixture exist. Especially at the edges of the cylinder, the lean area at the intake side is maintained during the compression, while the rich area is at the exhaust side. For DVA, at ignition, a lean area exists on the right side of the spark plug which is reduced as the cycle progresses. It can also be said that the mixture becomes more homogenous as the cycle progresses.

For the SVA, the Lambda contours are completely different to that of DVA. An axial stratification (piston movement direction) can be observed from the tumble plane of Figure 5.11 with a leaner mixture near the spark plug and the engine head. As the distance from the head is increased axially, the mixture becomes richer. Radially however, at a specific z location, the mixture is fairly homogenous which can be observed at the swirl plane of Figure 5.11 in which z=+5 mm. In addition, when the mixture formation of the DVA and SVA are compared qualitatively, it is clear that the mixture of the SVA is more homogenous than the DVA mixture formation.

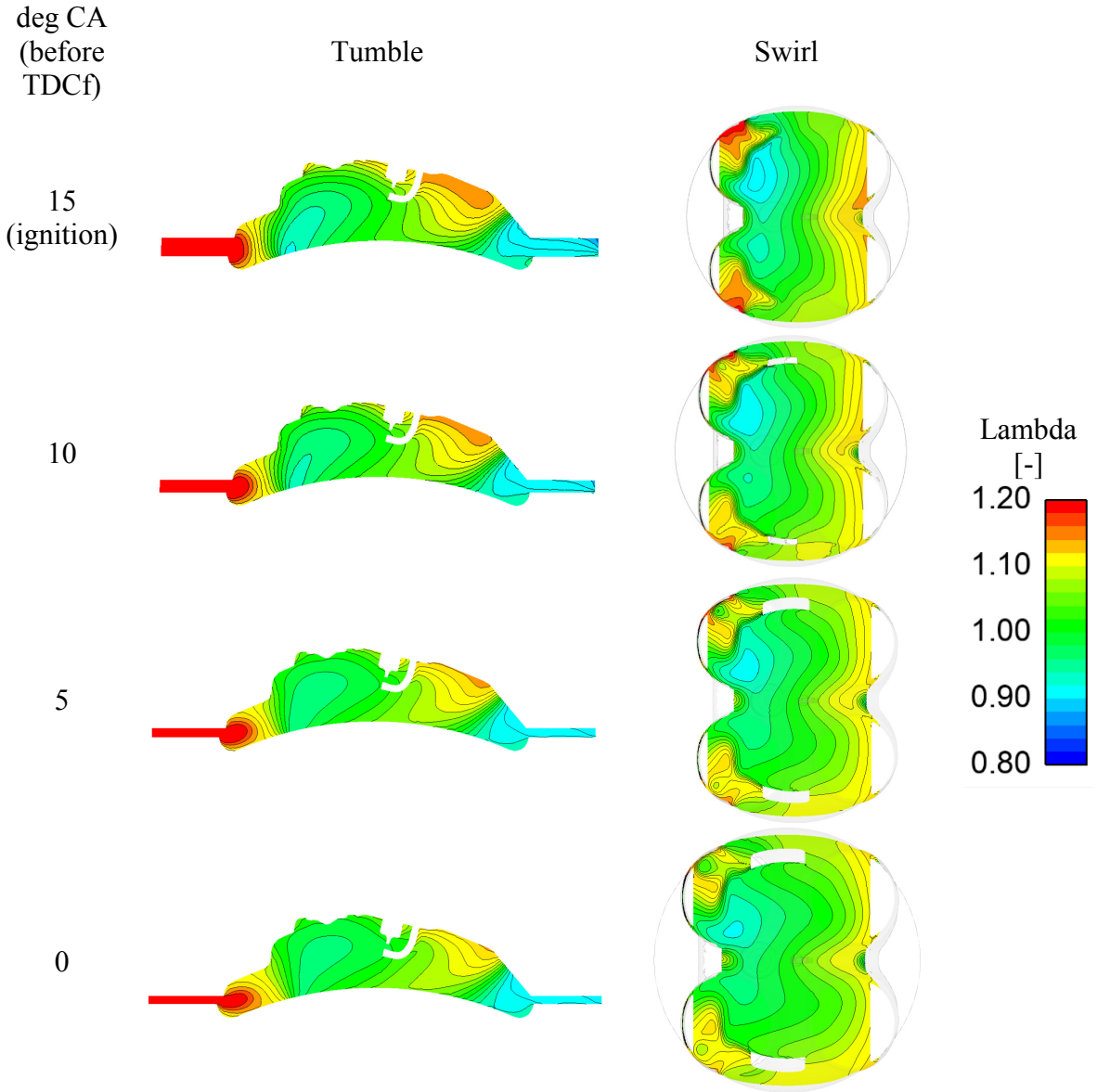


Figure 5.10 Spatial distribution of Lambda for DVA at various crank angles during compression, λ=1.0, 7.9 bar GMEP 1500 RPM

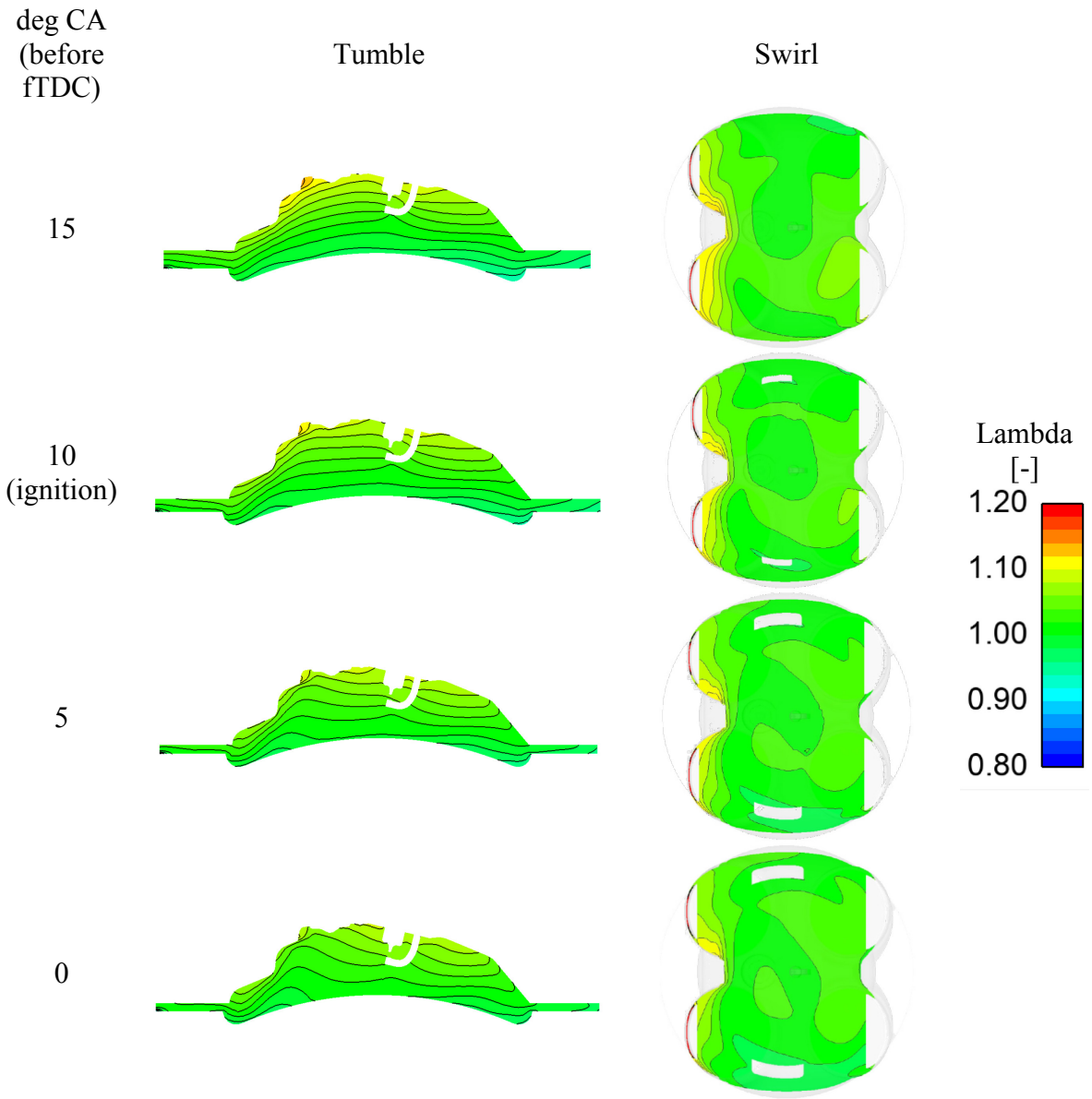


Figure 5.11 Spatial distribution of Lambda for SVA at various crank angles during compression, λ=1.0, 7.9 bar GMEP 1500 RPM

In order to quantify the homogeneity of the two cases and allow a better comparison, a Homogeneity Index was introduced. In the literature, various correlations exist (Munnannur *et al.* 2011; Lee, *et al.* 2000 and Weltens *et al.* 1993). In this study, a simpler term was used which is given by:

$$HI = 1 - CoV = 1 - \frac{Standard\ Deviation}{Mean} \tag{5.1}$$

This correlation also amplifies the differences between the two cases which makes the comparisons more profound. Both volume averaged and mass averaged cell calculations were tested for the HI but this did not have any effect on the HI trends and calculated values. The correlation has an upper limit of one which shows a completely homogenous mixture. The progress of the Homogeneity Index through the compression stroke and until 20 degrees after firing TDC is shown in Figure 5.12. From this graph, as the cycle progresses, the homogeneity of both DVA and SVA is improved. However, it is clear that the in-cylinder homogeneity is better for the SVA than DVA, something that confirms the observations from the Lambda contours. Due to the enhanced in-cylinder flow motion created by the SVA, the quality of air-fuel mixture was improved.

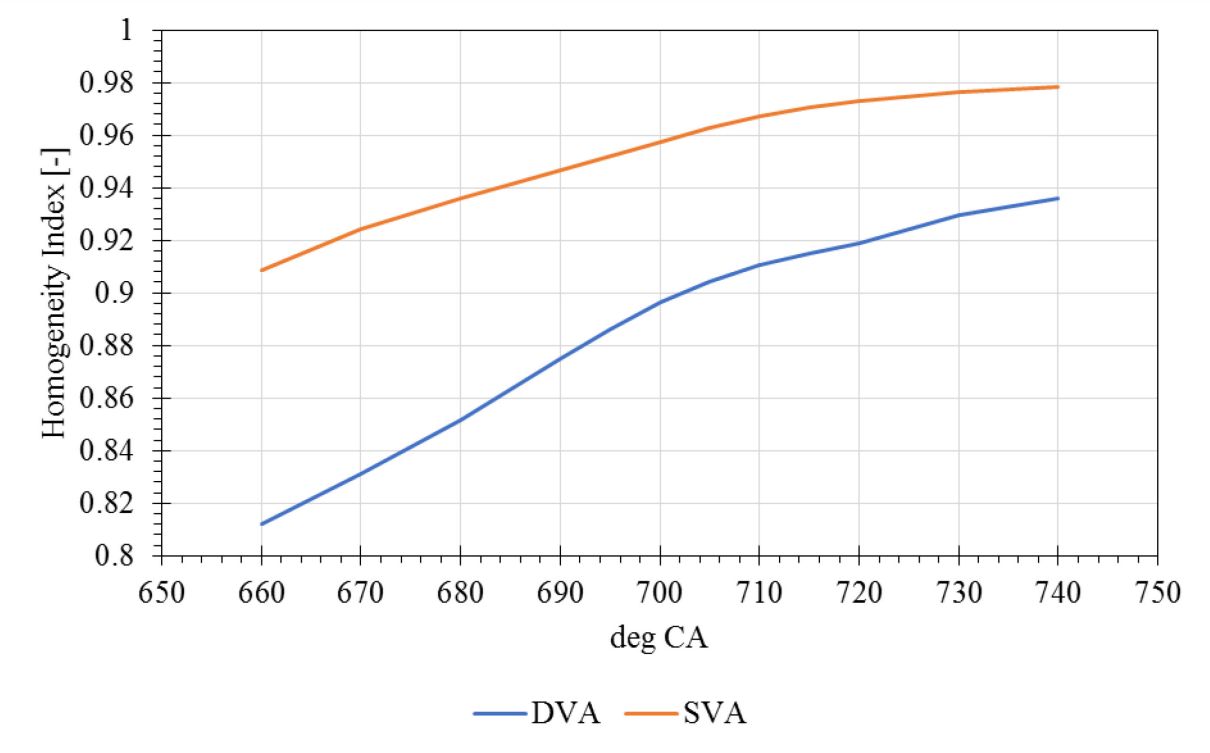


Figure 5.12 Homogeneity Index for DVA and SVA at 7.9 bar GMEP, 1500 RPM, λ=1.0

For completeness the air-fuel equivalence ratio contour plots for λ=1.5 at 10 degrees before TDC are shown in Figure 5.13. It is evident that qualitatively the patterns between λ=1.0 and λ=1.5 for a specific valvetrain strategy are similar. However, there are differences in the contour plots because the boundary conditions are different for different dilution. The intake pressure increases with higher Lambda to increase the trapped air, while the injected amount of the fuel remains at similar levels for all Lambda cases as the load of the engine is constant. The increase of the intake pressure affects the in-cylinder flow and the injection duration is

also slightly different for the different Lambda cases as already explained. In addition, the increase of the in-cylinder pressure due to increased intake pressure affects the spray penetration and evaporation.

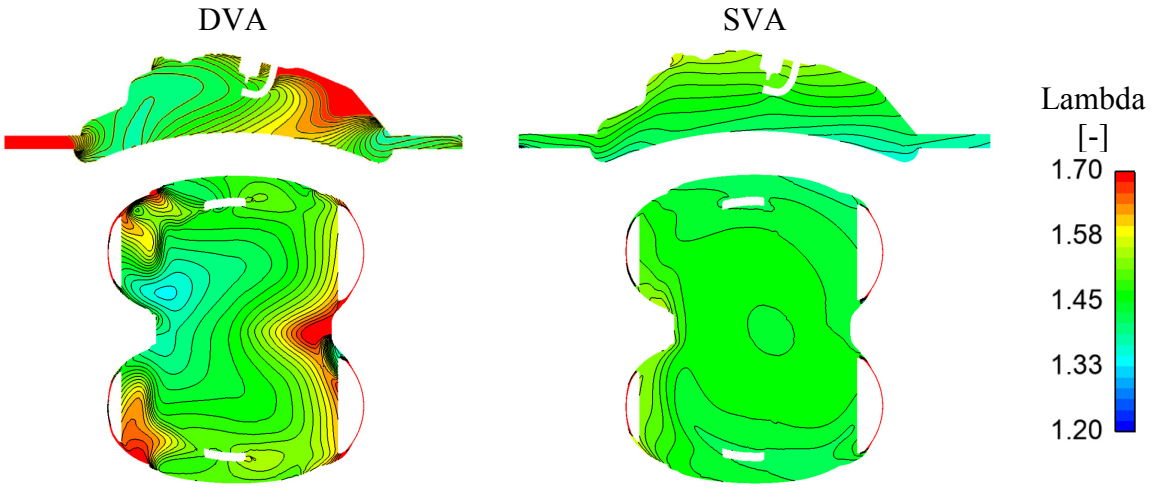


Figure 5.13 Spatial distribution of Lambda for DVA and SVA 10 degrees CA before TDC, λ=1.5, 7.9 bar GMEP 1500 RPM

In the previous chapter, an estimation of the laminar burning velocity was attempted using the properties of the flow (pressure, temperature, residuals) while assuming a completely homogenous mixture, thus the equivalence ratio was kept constant in the cylinder. Now, in a more detailed analysis the flow properties will be used as well as the equivalence ratio predicted by the air-fuel mixture. Figure 5.14 shows the laminar burning velocity taking account the air-fuel mixture for DVA and SVA, 10 degrees CA before firing TDC. The main difference in the calculations of laminar burning velocity with and without the spray (which was seen in both DVA and SVA) was the reduction of the burning velocity when the fuel injection was modelled. The reason for this reduction was the reduction of the in-cylinder temperature due to charge cooling. As it was discussed, especially with low residuals concentration, the temperature is a very important factor for the laminar burning velocity and a reduction of 80K can reduce the velocity from ~75 cm/s to ~60 cm/s. However, the same trends appear for the laminar burning velocity when DVA and SVA cases are compared. The higher temperature of the SVA, was the main contributor to the increased burning velocity. In addition, for DVA, in the areas where the Lambda is close to 1, the trend is the same as the case without the injection. This is because the temperature distribution is mostly affected by the flow motion which is very similar for the case with and for the case without injection. In areas where the Lambda values were deviating from the global Lambda, then differences in laminar burning velocities

appeared. This is more profound near the liner where very lean mixture exists at the intake side and a rich mixture exists at the exhaust side. Because of the much better homogeneity of the SVA case, qualitatively the cases with and without fuel injection are very similar. The main difference in the contour plots (except from the magnitude) is near the cylinder head where the mixture is leaner. Generally, the lean mixture is reducing the burning velocity while a richer mixture does not have a significant effect.

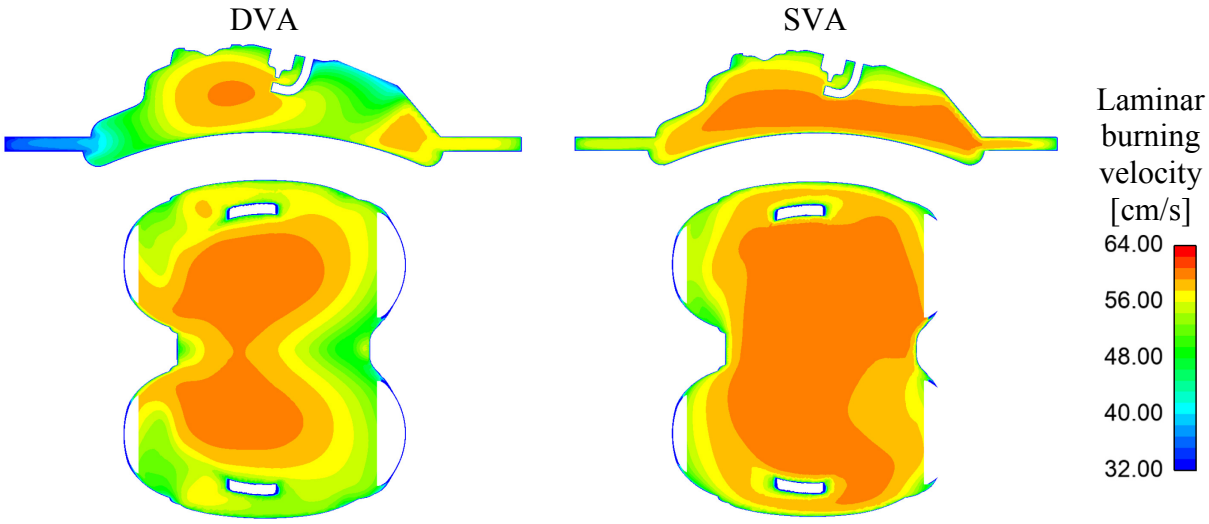


Figure 5.14 Spatial distribution of laminar burning velocity for DVA and SVA 10 degrees CA before TDC, λ=1.0, 7.9 bar GMEP 1500 RPM

The injector pattern was initially designed to target towards the piston crown in order to avoid the wetting of the liner and mixture of the liquid fuel with the oil film. It is evident from Figure 5.15 for DVA that the film mass is accumulated on the piston crown, while on the liner is two orders of magnitude less. 25 degrees after start of injection, the maximum accumulated mass is seen on the piston. After that, there is a decrease of liquid fuel mass which disappears before BDC. This is because of the evaporation of the fuel as well as the stripping of fuel from the film and re-entrainment in the cylinder. When the single valve was adopted, the maximum liquid film was reduced almost by half and the reduction after the peak was faster. This was expected as the enhanced in-cylinder flow motion can increase the evaporation rate as well as increase the striping process. However, this behaviour of the reduction of the liquid film mass may be overestimated because all the walls of the engine were initially dry with no oil film simulated. The blend of an already existing oil film with a fuel impinging on the surface has an effect on the evaporation of the fuel as shown by Zhang *et al.* (2018) and it was also shown the importance of the lighter and heavier components of gasoline on evaporation. Beavis *et al.* (2017b) also showed the differences in liquid film when simulating single and multi-

component fuels. In this study, the simulated fuel is single-component, represented by *iso*-Octane. Despite these assumptions, the predictions are important because they show that the enhanced flow motion is breaking the spray, deposits less fuel and assists on the faster reduction of the film. This can be beneficial is terms of emissions and especially reduction of soot. The liquid film on the piston at 20 degrees after start of injection, close to the peak of both cases is shown in Figure 5.16. For DVA, due to the symmetry of the injector and the symmetry of the flow, the liquid film pattern is also symmetric. However, for SVA, the film patterns do not have any symmetry. More liquid is formed at the +y side of the piston and under the closed valve and at the centre of the piston because the strong flow transports the spray downwards and towards the closed valve due to the swirl motion. In addition, the plumes under the closed valve are less affected by the in-cylinder flow.

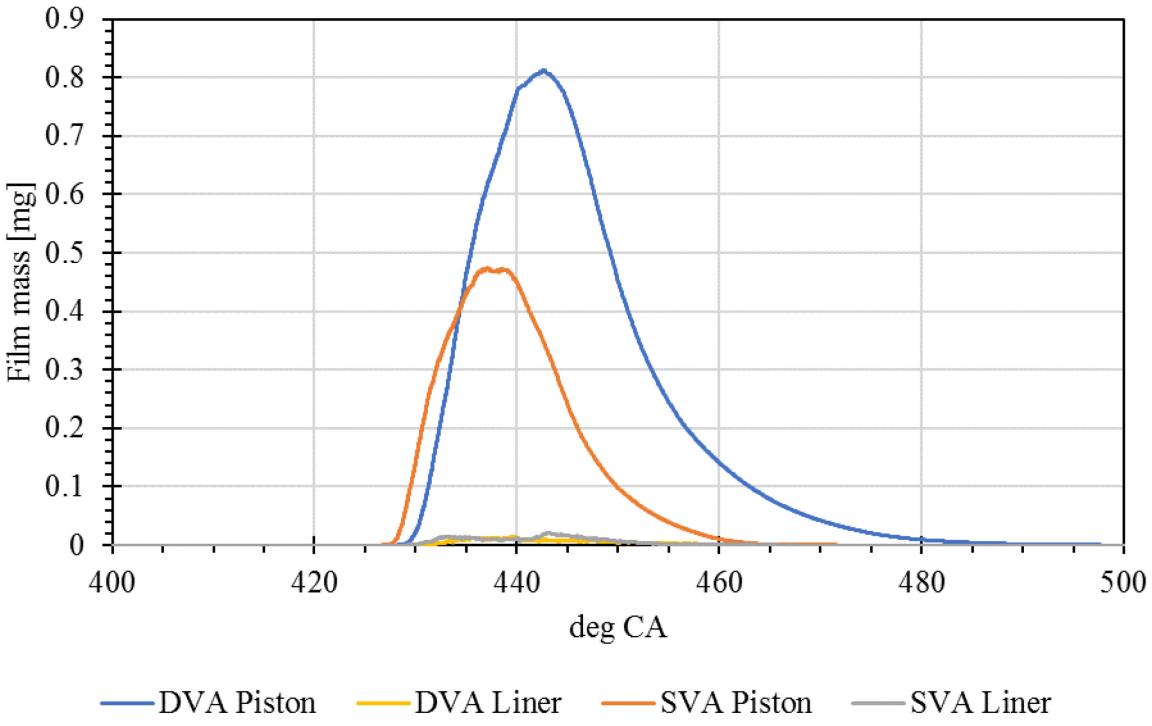


Figure 5.15 Accumulated liquid film mass at the piston and liner for DVA and SVA versus time. λ=1.0. 7.9 bar GMEP, 1500 RPM

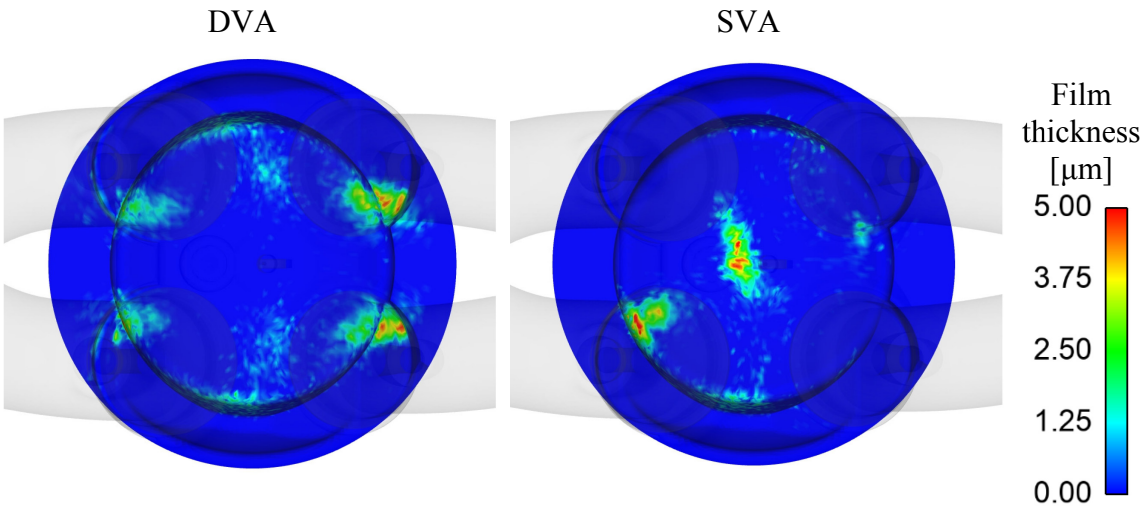


Figure 5.16 Liquid film thickness at the piston for DVA and SVA at 20 degrees after SOI. λ=1.0. 7.9 bar GMEP, 1500 RPM

5.2.3. Emissions

In any research and development study for improved fuel consumption, it is important to comply to emissions regulations and understand the reasons behind the numbers and the trends. The experimental data (Figure 5.17) revealed that for a given EGR (here EGR0%), NO_x emissions are greater for SVA compared to DVA for up to about lambda 1.2. As lambda increases further, the SVA to DVA difference in NO_x production decreases and from about λ=1.4 the NO_x levels for both valve strategies are very similar. In addition to this, the highest amount of NO_x is observed when the engine was running with global Lambda of 1.1 followed by the global Lambda of 1.2. These results agree with the literature (Heywood 1988, Lumley 1999) stating that the one of the most important factor affecting NO_x emissions is the air-fuel equivalence ratio (λ) with the highest production rate to be when λ~1.1. In addition to the NO_x production, the total hydrocarbons (THC) and the CO emissions were also studied. The trends of these two pollutants versus Lambda are in accordance to the literature as well, for both DVA and SVA (Figure 5.17). Nevertheless, there are quantitative differences between the two valve strategies. The unburnt hydrocarbons are always 30%-40% higher for the dual valve than the single valve. For the CO production, the values are very similar for both valve strategies for Lambdas greater than 1.1. For the stoichiometric case however, the CO emissions is greater for DVA by 40%. In this section, the differences in the emissions between the two valve strategies will be studied and linked to the mixture preparation. The air-fuel equivalence ratio was studied for the whole cylinder and for five spherical volumes which had the centre at the spark plug gap and their diameters were 10 mm, 20 mm, 30 mm, 40 mm, 60 mm. The size of these spheres

in respect to the engine geometry is shown in Figure 5.18. It has to be noted that only the cylinder domain that is included in the sphere is taken into account and not the total volume of the sphere.

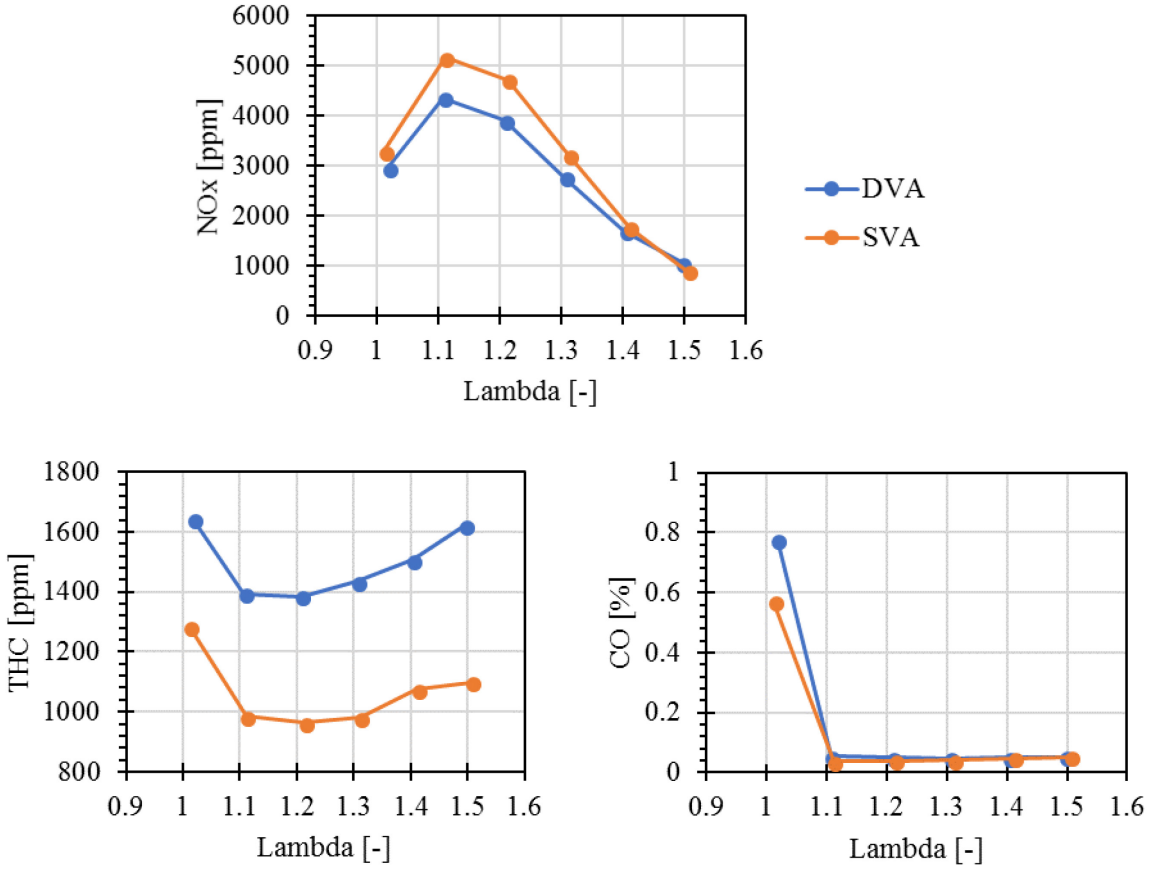


Figure 5.17 Experimental emissions of NO_x, THC and CO. 7.9 bar GMEP, 1500 RPM

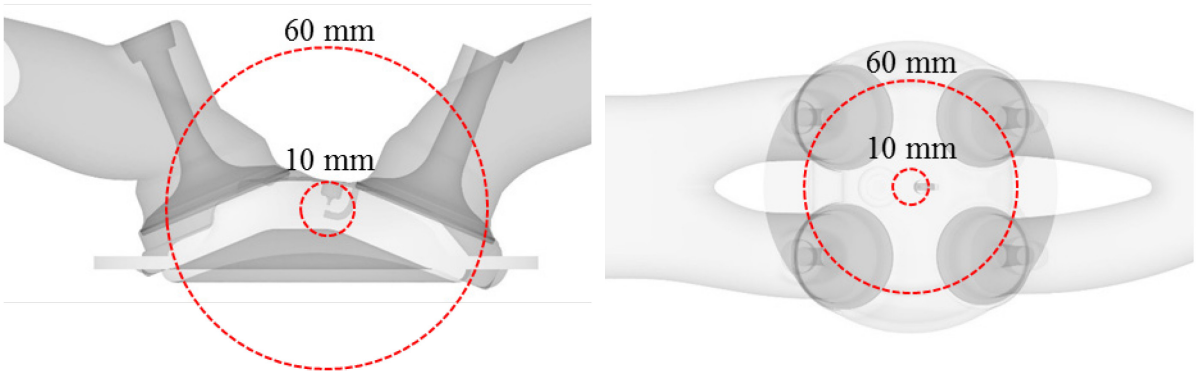


Figure 5.18 The size of the smallest and biggest spheres relative to the cylinder. Tumble and swirl views.

The behaviour of the CO and the unburnt hydrocarbons can be linked to the air-fuel equivalence ratio. For rich mixtures the levels of carbon monoxide are high because the complete oxidation of fuel to CO2 is not possible due to the insufficient oxygen. In the above section, the contour plots of Lambda for λ=1.0, showed that due to the inhomogeneity of the mixture, both DVA and SVA had areas that were richer than the stoichiometric. An analysis of the rich areas (λ<1) within the cylinder was carried out for λ=1.0 and λ=1.1. For higher dilution levels, the experimental results showed very small differences between the two valve strategies. The differences between the mixture formation of DVA and SVA were investigated. The Figures 5.19 and 5.20 show the percentage of the volume of rich mixture compared to the total volume of the investigated volume which was either the whole cylinder, or the volume of the respective sphere versus degrees CA at λ=1.0 for DVA and SVA.

It is evident that for the dual valve, there is a greater volume within the cylinder with rich mixture, especially after ignition. Generally, the size of the rich region is greater for DVA than SVA for all crank angles after the ignition. The ignition timing for DVA was 15 degrees CA before TDC (705 deg CA in the Figure 5.19) and for SVA it was 10 degrees CA before TDC (710 deg CA in the Figure 5.20). In addition, at ignition the mixture around the spark plug (10 mm sphere) has a greater amount of rich zone (25% of the volume of the sphere) for DVA than the SVA which is lean. As the combustion progresses, the flame front propagates in greater size of rich region for DVA. This can be seen from the bigger spheres at later crank angles. For all spheres at TDC, 60% of their volume is occupied by a rich mixture. The cylinder has constantly 50% of its volume covered by a rich mixture. In addition, the average Lambda of the rich mixture was studied for the DVA and SVA and is shown in Figures 5.21 and 5.22. The lowest average Lambda value after ignition is 0.98 for SVA, meaning that the mixture is very close to the stoichiometry. After the ignition of DVA, the average Lambda of the rich mixture is in the range of 0.96-0.97.The flame propagated in richer zone and in greater size when DVA was used. The combination of richer mixtures and greater volumes contributed to the production of CO which was higher for DVA.

The unburnt hydrocarbons can have various sources during the engine cycle. In this study, the quality of the air-fuel mixture was studied to explain the experimental results. The hydrocarbons increase when the mixture becomes richer than the stoichiometric combustion as not all the fuel is oxidised. In addition, the THC also increase at very lean mixtures due to the incomplete combustion or misfire. Here, the difference in THC between DVA and SVA at λ=1.0 and λ=1.1 will be investigated. For the leaner mixtures where the THC is fairly constant,

the difference between DVA and SVA is mostly due to the slower combustion of DVA and other sources of HC (quenching of the flame on the walls, outflow of HC from the crevices). Previously, it was shown that the volume of the rich region is higher for the DVA than SVA. For the amount of the unburnt hydrocarbons, not only the rich areas are important, but also how rich these areas are because more fuel will not be oxidised. The analysis for the whole cylinder and the five spherical volumes revealed that the for DVA, the rich area around the spark plug at ignition (710 deg CA) was rich (λ=0.99) but for greater spherical regions the lambda is lower, and the value is λ=0.97 for the sphere of 20 mm diameter and λ=0.96 for the sphere of 30 mm. As the cycle and the combustion progresses, the rich regions for greater spherical regions converges to a value of about λ=0.97. When SVA was adopted, the rich regions have an average lambda very close to stoichiometric. For bigger spherical volumes, the average lambda is again close to stoichiometric (λ=0.99). However, because the rich regions are close to the piston, the flame quenching at the rich region can result in unburnt hydrocarbons. However, as these regions are close to λ=1.0 and the volume was smaller, this reflected to the big differences of THC in the experiments.

For the leaner case where the global lambda is λ=1.1, the size of rich zones was reduced drastically for both valve strategies. This was also seen for the experimental measurements of CO and THC emissions. Nevertheless, the DVA showed again zones of rich mixture that were greater than the SVA. The DVA case showed rich regions within the cylinder and for spherical volumes greater than 30 mm in diameter. These rich regions had an average lambda in the region of [0.97,0.99]. For SVA, there was almost no rich mixture for λ=1.1. The rich regions for the SVA at λ=1.1 were seen only when the whole cylinder was investigated, and it was at the edges of the chamber. For this reason, even when the reduction of CO was severe, the differences between DVA and SVA were 40%. From this it can be concluded that for SVA the increased homogeneity of the mixture is beneficial for the reduction of the CO and THC production. The air-fuel equivalence ratio deviates less from the mean (global) Lambda value which leads to smaller number of rich regions in the cylinder. For the DVA however, the volume of the rich regions is greater, meaning more volume of the combustion at rich mixture. It is known that even at lean combustion CO and THC are formed because of the efficiency of the combustion but the above approach showed that the in-cylinder mixture played an important role to the emissions.

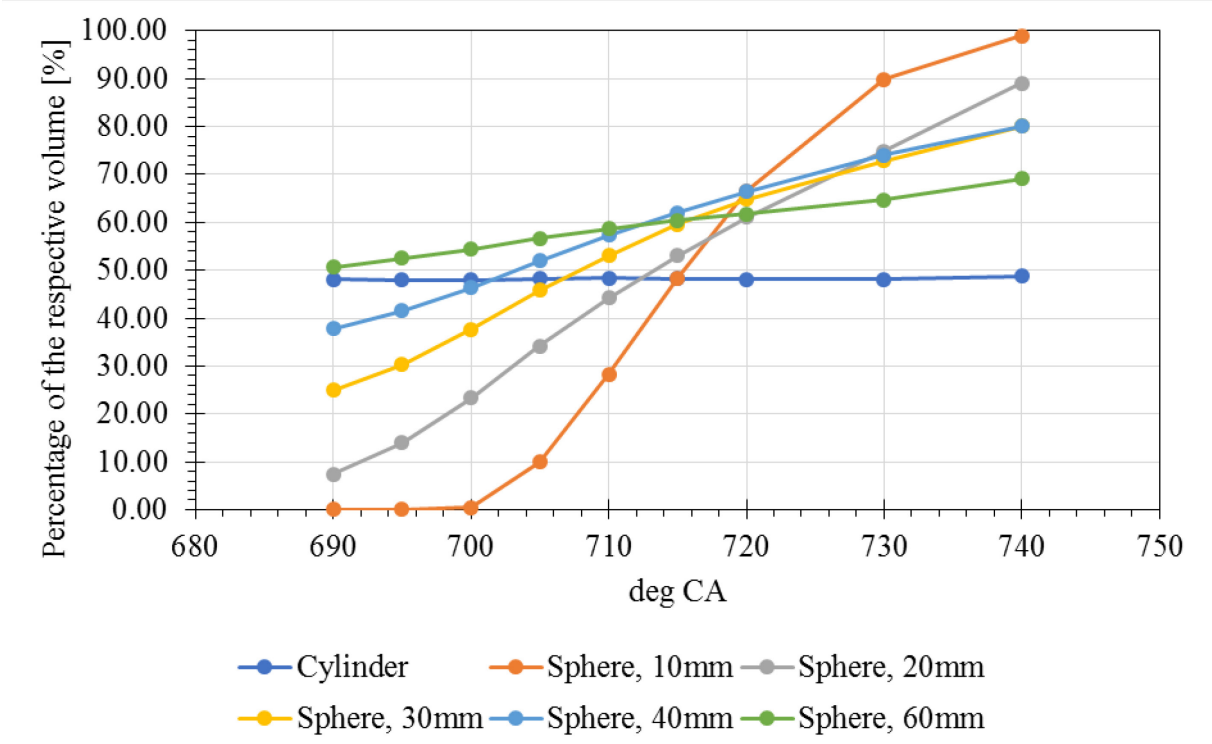


Figure 5.19 Percentage of the respective spherical volumes occupied with a rich mixture (λ<1.0) for DVA. Global λ=1.0. 7.9 bar GMEP, 1500RPM

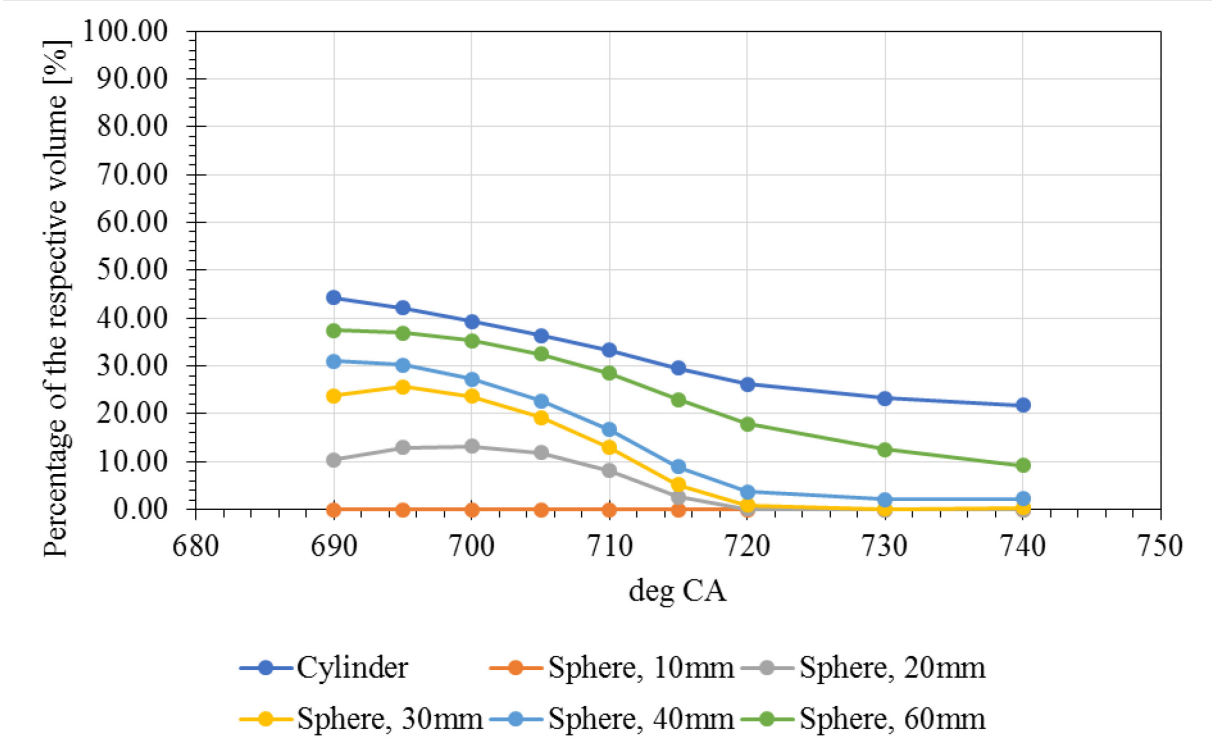


Figure 5.20 Percentage of the respective spherical volumes occupied with a rich mixture (λ<1.0) for SVA. Global λ=1.0. 7.9 bar GMEP, 1500RPM

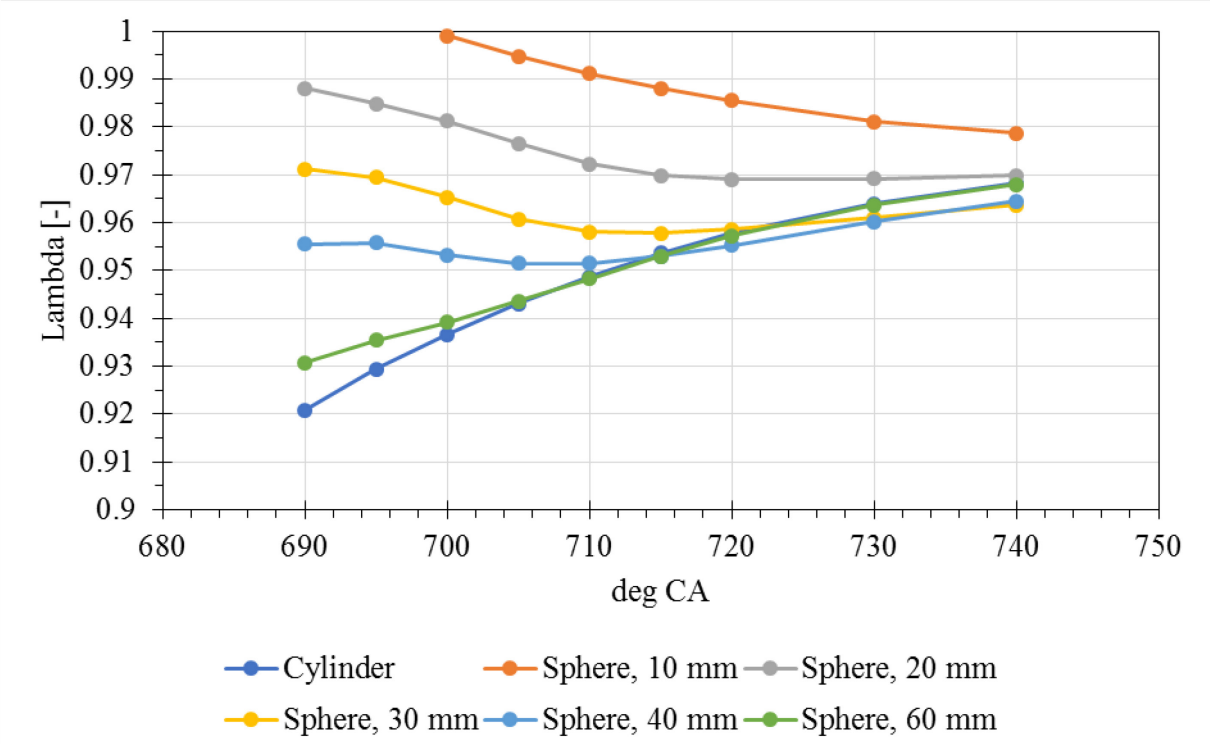


Figure 5.21 Average lambda of the rich mixture within each spherical volume for DVA. Global λ=1.0. 7.9 bar GMEP, 1500RPM

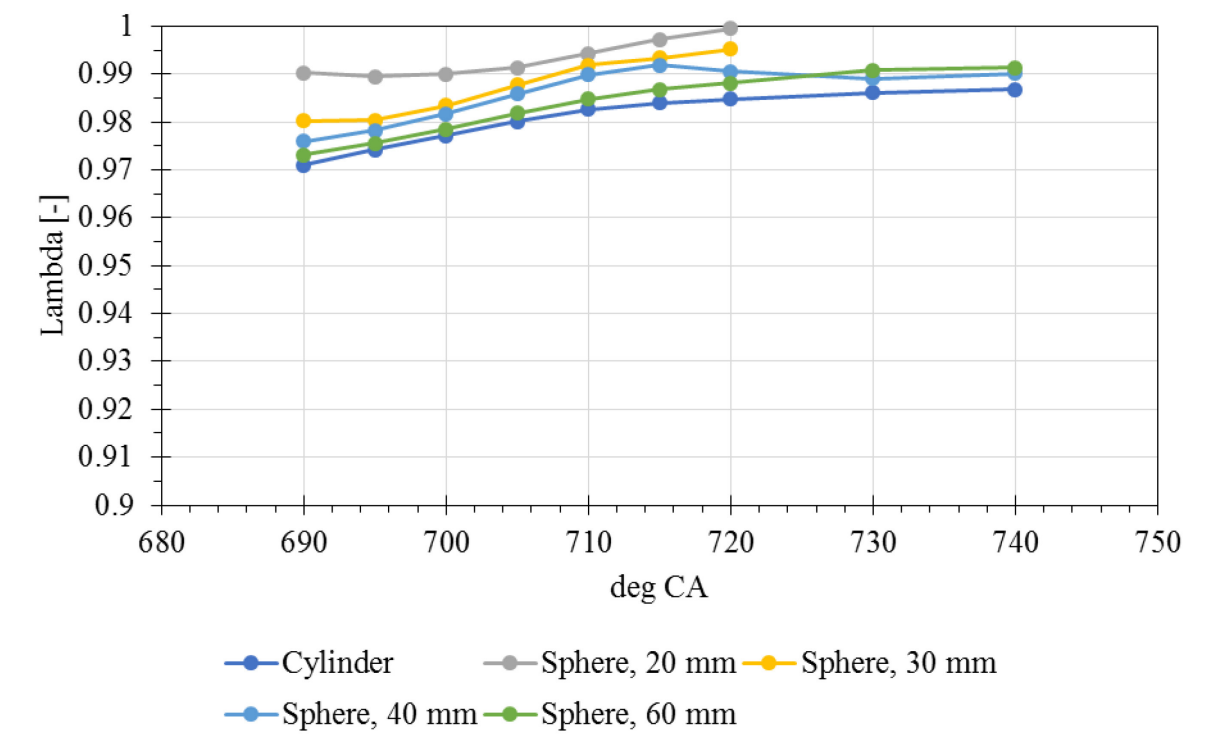


Figure 5.22 Average lambda of the rich mixture within each spherical volume for SVA. Global λ=1.0. 7.9 bar GMEP, 1500RPM

The differences between DVA and SVA for the NO_x emissions was more complicated as the air-fuel equivalence ratio, the temperature and the availability in oxygen and nitrogen is equally important in the NO_x production. Generally, and according to the experimental results of this study and the literature, the highest NO_x production appears in the region of λ=1.1. For the NO_x study, the same spherical regions as before were considered as well as the whole cylinder. A region of lambda [1.05,1.15] was considered as the worst-case scenario for NO_x production and it was chosen according to the existing data of NO_x versus lambda. It is acknowledged that this might be somehow an artificial range and possibly this can be tuned to match a set experimental data. However, this was used to investigate if this approach can be used as a generalised idea and guidance for predicting trends of NO_x production. Three different dilution cases were studied with global Lambdas: λ=1.0, λ=1.1 and λ=1.2. As the NO_x is mostly formed in the post-flame gases, the analysis is more important after ignition.

Figures 5.23 to 5.28 display the percentage of the respective volume of the sphere or the whole cylinder which is occupied by a mixture which is within the region of [1.05,1.15] and it progresses over time for DVA and SVA at the three dilution cases. For DVA and λ=1.0 at ignition (Figure 5.23), 28 % of the 10 mm sphere is occupied by a mixture in the region considered as the worst for NO_x production. For the SVA (Figure 5.24) at ignition, 45% of the 10 mm sphere is in that region. As the volume of the spheres increases, the percentage of the volume that is within the prescribed range reduces due to the increase of the homogeneity which brings the mixture closer to λ=1.0. However, for all spheres, the percentage of the volume within [1.05,1.15] is greater for SVA than DVA. Only the total volume of the cylinder for DVA has greater amount of mixture within that range when compared against the cylinder of the SVA. This is because the lean areas near the liner are also included in the calculation.

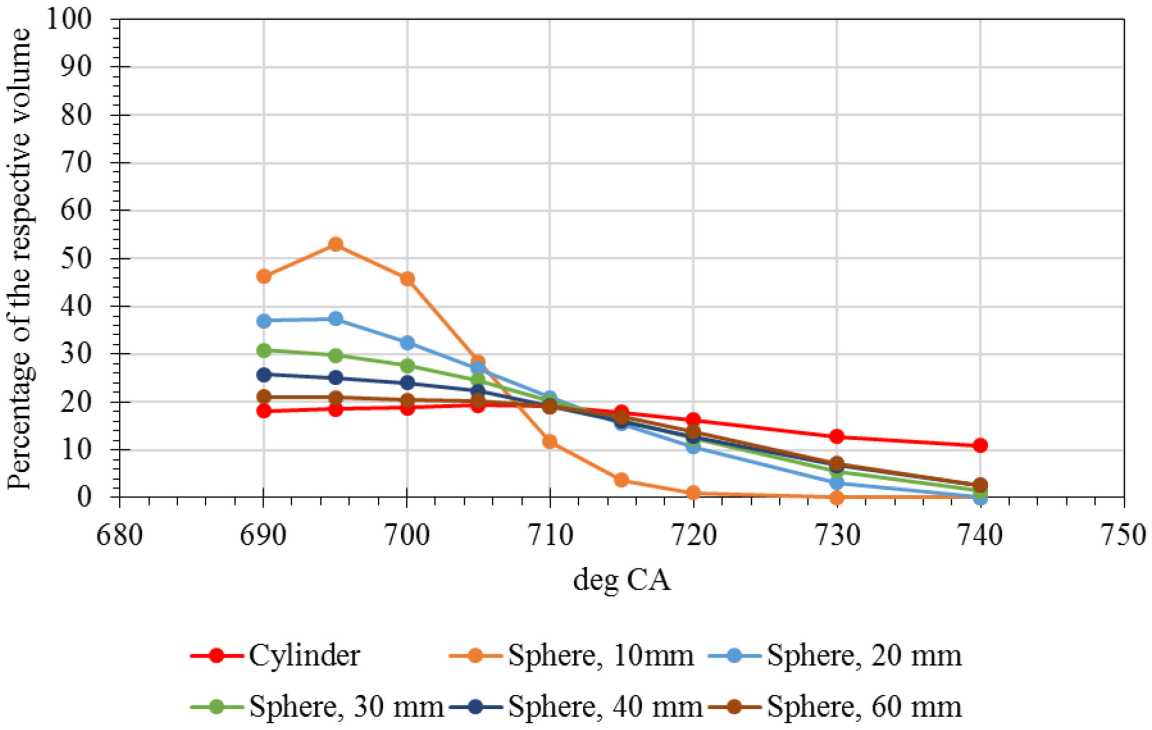


Figure 5.23 Percentage of the respective spherical volumes occupied with a lean mixture in the range λ[1.05,1.15] for DVA. Global λ=1.0. 7.9 bar GMEP, 1500RPM

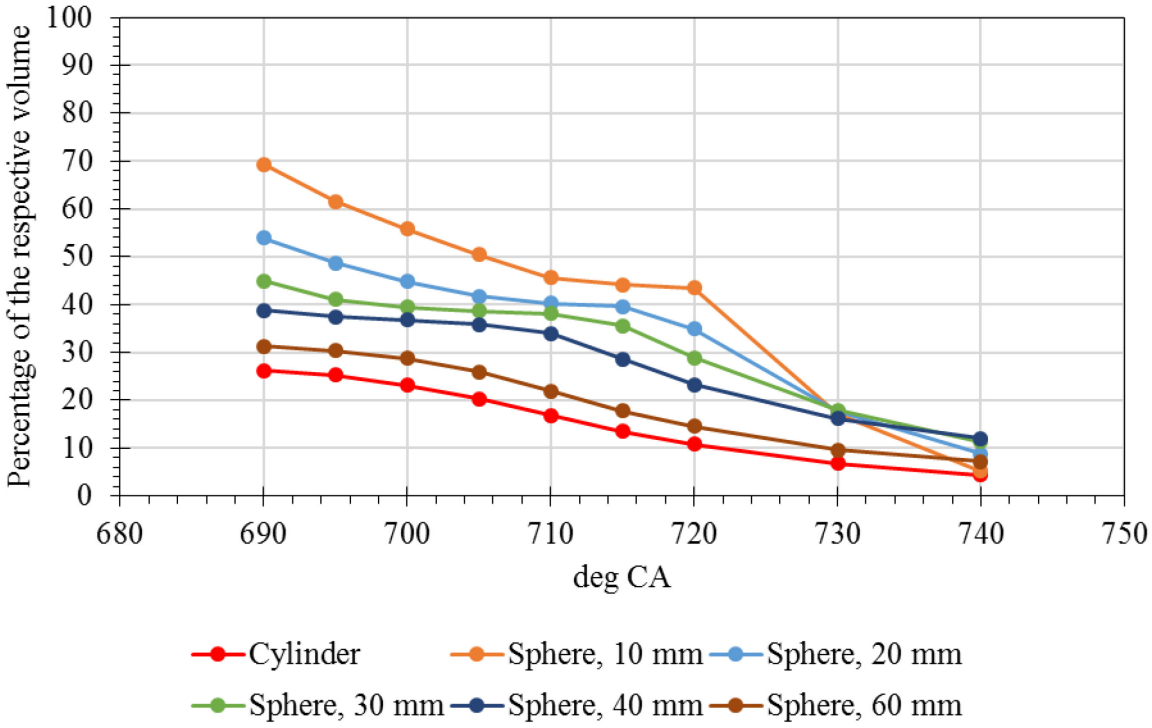


Figure 5.24 Percentage of the respective spherical volumes occupied with a lean mixture in the range λ[1.05,1.15] for SVA. Global λ=1.0. 7.9 bar GMEP, 1500RPM

When the global Lambda was increased to λ=1.1, the percentages of the spheres and total cylinder that were occupied by a mixture in the range of [1.05,1.15], were increased for both valve strategies. For DVA (Figure 5.25) and at ignition, 60% of the 10 mm sphere is within the range of Lambdas and 97% for SVA (Figure 5.26). By increasing the radius of the sphere, the percentage was reduced for both DVA and SVA with SVA maintaining higher values. In addition, for both cases, as the time progressed, for a specific sphere, the percentage was increasing again due to the improved homogeneity. During combustion, all spheres and the cylinder for SVA were constantly occupied by a much greater volume when compared to DVA. For SVA and after ignition, the volume of all spheres and the cylinder were at least 90% in the range of Lambdas [1.05,1.15]. For the DVA, the percentages that were calculated were in the range of 40%-90%. However, the 90% is seen only for the 20 mm diameter and at 20 degrees after TDC.

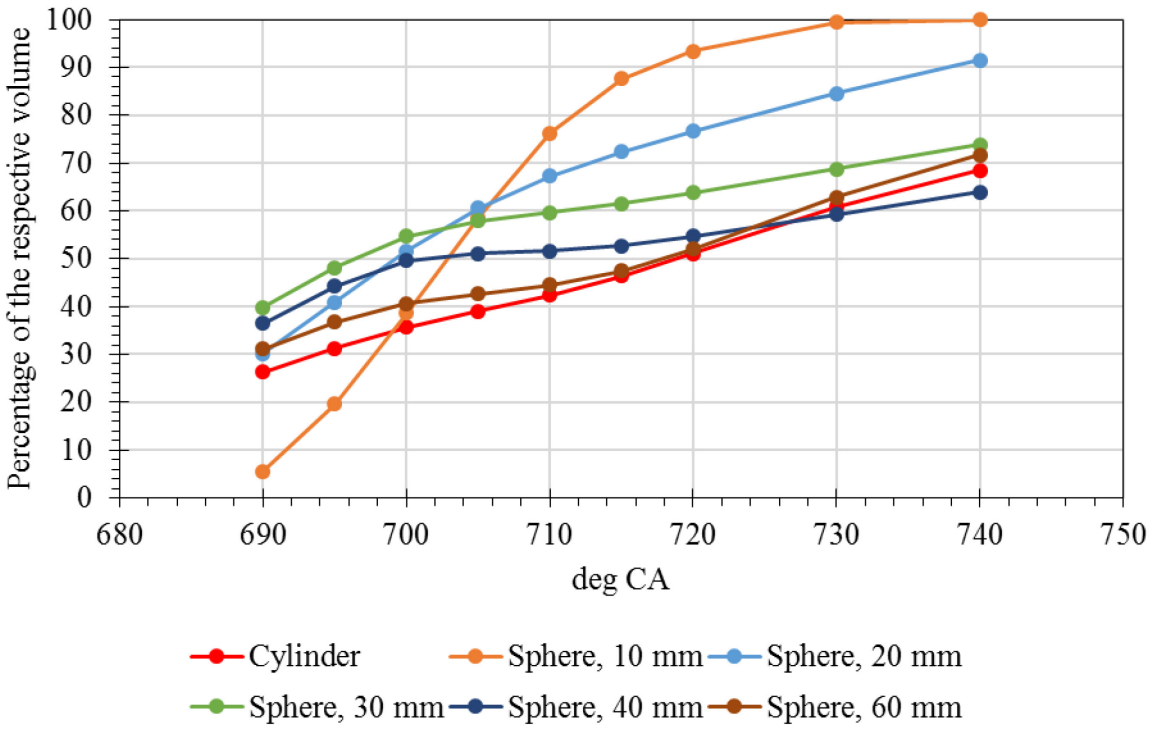


Figure 5.25 Percentage of the respective spherical volumes occupied with a lean mixture in the range λ[1.05,1.15] for DVA. Global λ=1.1. 7.9 bar GMEP, 1500RPM

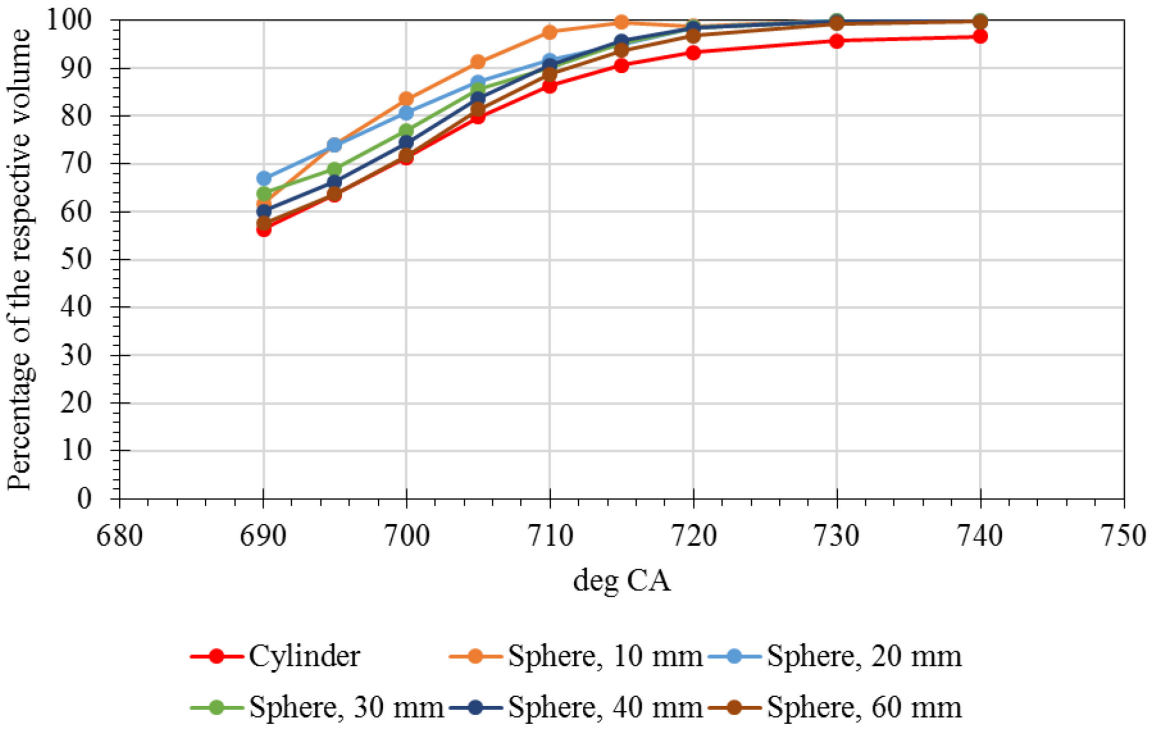


Figure 5.26 Percentage of the respective spherical volumes occupied with a lean mixture in the range λ[1.05,1.15] for SVA. Global λ=1.1. 7.9 bar GMEP, 1500RPM

Finally, when the mixture was further diluted, and the global Lambda was λ=1.2, due to the axial stratification of the SVA, the mixture near the head of the engine is leaner than λ=1.15 and thus, the sphere of 10 mm does not include mixture at the range of [1.05,1.15]. When the size of the sphere was increased and also up to the size of the cylinder, more mixture was in the specified range due to the axial stratification and thus the percentage was increased. The 60 mm sphere was 30%-15% occupied with mixture in the lambda range after ignition an the whole cylinder was 38%-28% occupied by this mixture. The above can be seen in Figure 5.28. For DVA at ignition (Figure 5.27), the sphere of 10 mm did not include the specific lean mixture, but later in the cycle, some percentage (~7%) was in that range. By increasing the diameter of the sphere, the percentage of the volume in the range for a specific sphere was increased for up to 40 mm sphere for the DVA. The percentage of the volume was 30% of the 40 mm sphere. Increasing further the diameter of the sphere, the percentage dropped to 26% (10 degrees after TDC). When the whole cylinder was considered, the percentage was further decreased to less than 20%. Comparing the DVA and SVA at this dilution level, the percentages in the range for spheres up to 40 mm are always lower for SVA. For the sphere of 60 mm, the volume occupied by the mixture of the range [1.05,1.15] was 35% around ignition and it was

reduced to up to 10%. When the whole cylinder was studied, the volume in the cylinder for SVA is greater than DVA.

Looking at the trends of the volumes mostly for spheres 40 mm and above, a conclusion that can be drawn is that there is a drastic increase in volumes within the range of [1.05,1.15] from λ=1.0 to λ=1.1. From λ=1.1 to λ=1.2 the volumes decrease but are higher than the λ=1.0 case. This trend is also seen in the experimental results of the NO_x emissions where the highest NO_x is at λ=1.1, followed by λ=1.2 and then by λ=1.0 (λ=1.1>λ=1.2>λ=1.0). In addition, when DVA and SVA were compared, bigger differences in the calculations were seen for λ=1.1 and then followed by the λ=1.2. There is a change is the trends between the spheres and the whole cylinder when DVA and SVA were compared for λ=1.0 and λ=1.2. At λ=1.0 the percentage of the whole cylinder in the specified range is greater for DVA that SVA. However, each specific sphere has greater percentage for SVA than DVA. At λ=1.2 on the other hand, the whole cylinder has greater percentage in the range of Lambdas when SVA was adopted but the spheres of DVA were occupied by a greater volume of mixture in the range of [1.05,1.15].

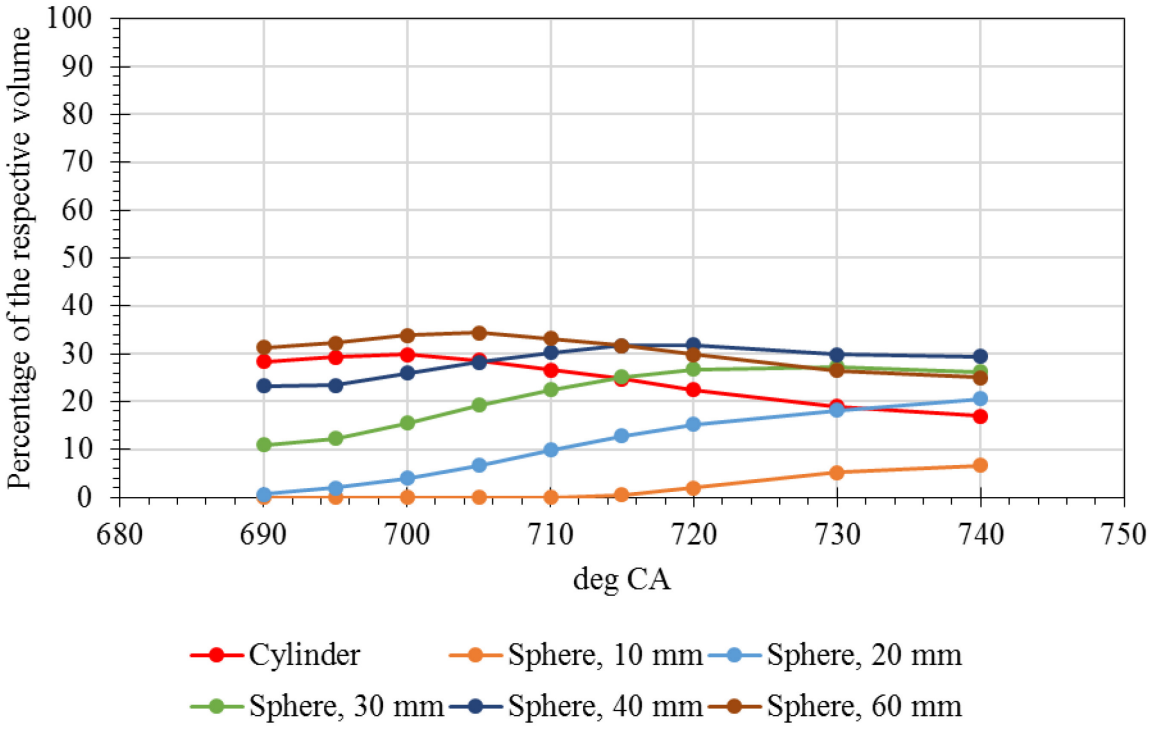


Figure 5.27 Percentage of the respective spherical volumes occupied with a lean mixture in the range λ[1.05,1.15] for DVA. Global λ=1.2. 7.9 bar GMEP, 1500RPM

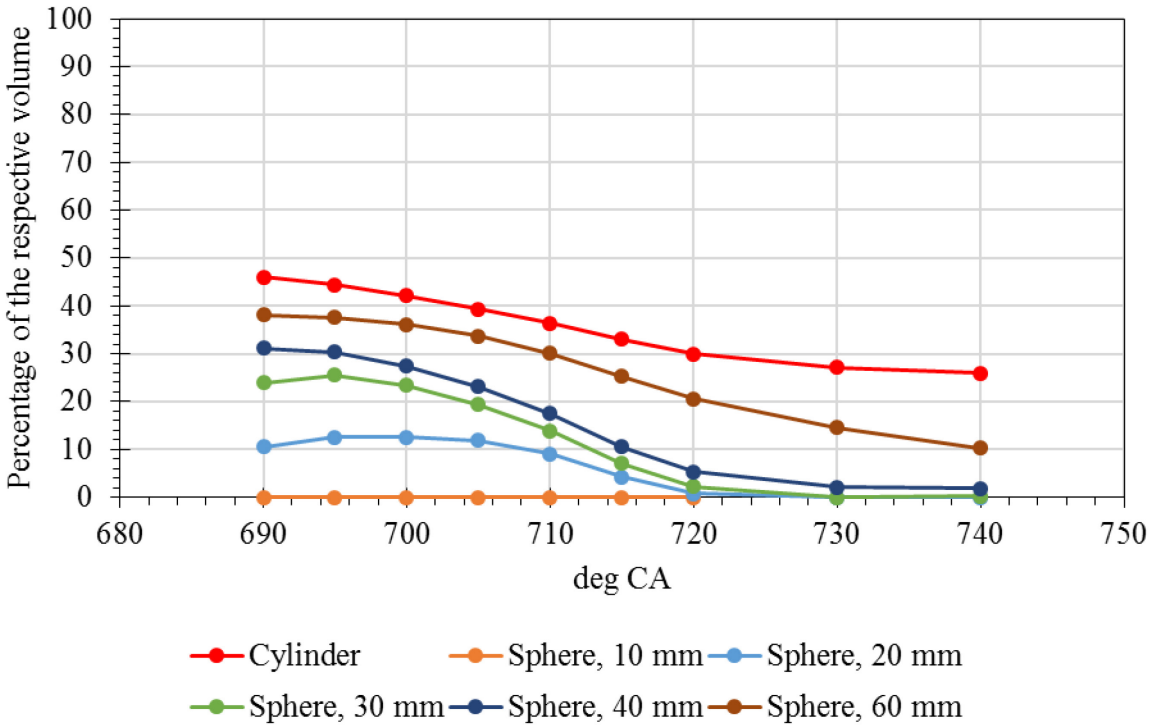


Figure 5.28 Percentage of the respective spherical volumes occupied with a lean mixture in the range λ[1.05,1.15] for SVA. Global λ=1.2. 7.9 bar GMEP, 1500RPM

Because of these differences between λ=1.0 and λ=1.2 of the calculated volumes of the mixture and because until now the temperature of combustion was not considered, the in-cylinder temperature was extracted from the pressure trace of DVA and SVA for the three Lambda cases described above as well as λ=1.5 for comparison, using the ideal gas law. The trapped mass was taken from the CFD results and the molecular weight of the exhaust gases was used.

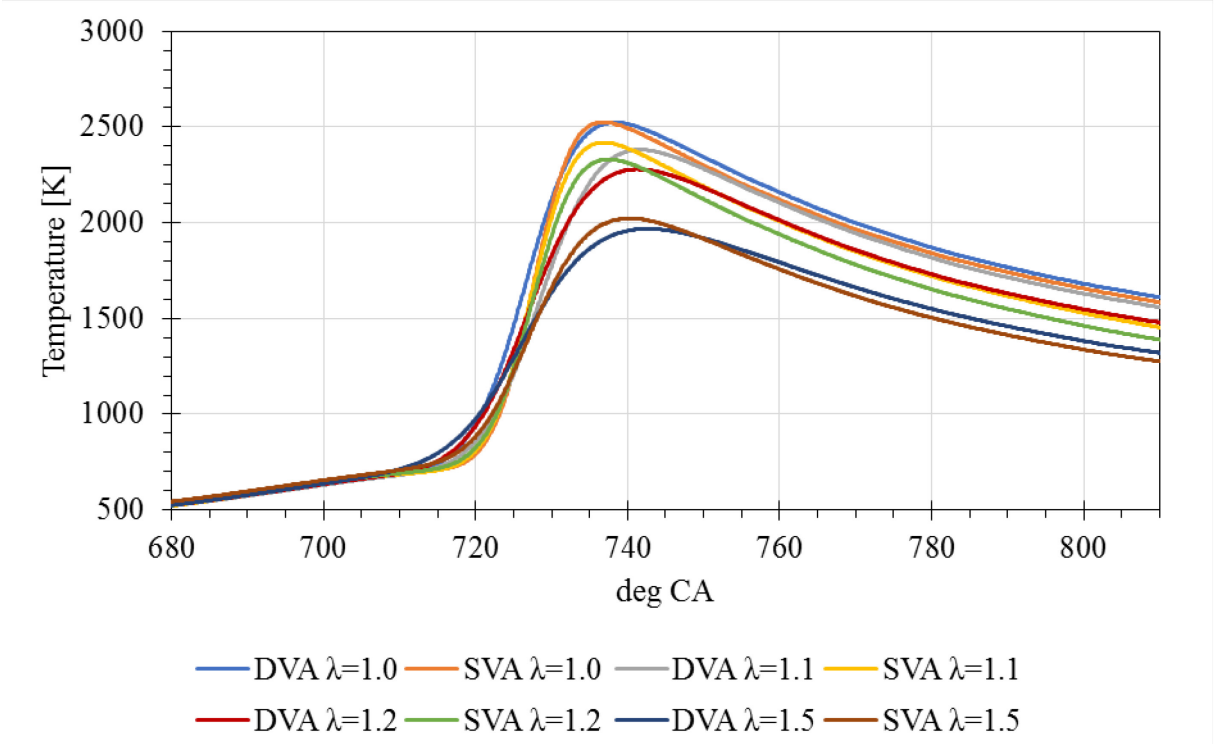


Figure 5.29 Experimental in-cylinder temperature derived from the experimental in-cylinder pressure for DVA and SVA and for four different dilution cases

This temperature was then introduced in the NO formation rate taken from Heywood and it is given by:

$$\frac{d[NO]}{dt} = \frac{6 \cdot 10^{16}}{T^{0.5}} \exp\left(\frac{-69090}{T}\right) [O_2]_e^{0.5} [N_2]_e \tag{5.2}$$

The equation shows that high temperatures and high oxygen concentrations give high NO production rate and it is based on the Zeldovich mechanism. The term in the above equation which takes account the temperature is displayed in Figure 5.30. It is evident from the graph that the effect of the temperature exponential. From λ=1.0 to λ=1.1, the decrease of the peak temperature by 100K dropped the contribution in the NO production rate by 80% (1535 units to 306 units for DVA). Another 100K decrease from λ=1.1 to λ=1.2 decreased the contribution to NO production rate for another 70%. For the lean cases (λ=1.1 and λ=1.2) the effect of the temperature for DVA and SVA is evident. For the λ=1.5 case, the peak value of the contribution of temperature in the NO production is two orders of magnitude smaller that the peak of the λ=1.2 and for this reason it is not plotted in the graph. The temperature of the SVA cases is higher and therefore, the effect on the NO production is increased for SVA which is in line

with the experiments. For the λ=1.0 case, the greater availability of oxygen in the SVA strategy has to be the reason of the increase of the NO_x production as seen from the experiments. This is linked to the lean mixture of SVA which is bigger than DVA in a 60 mm sphere region.

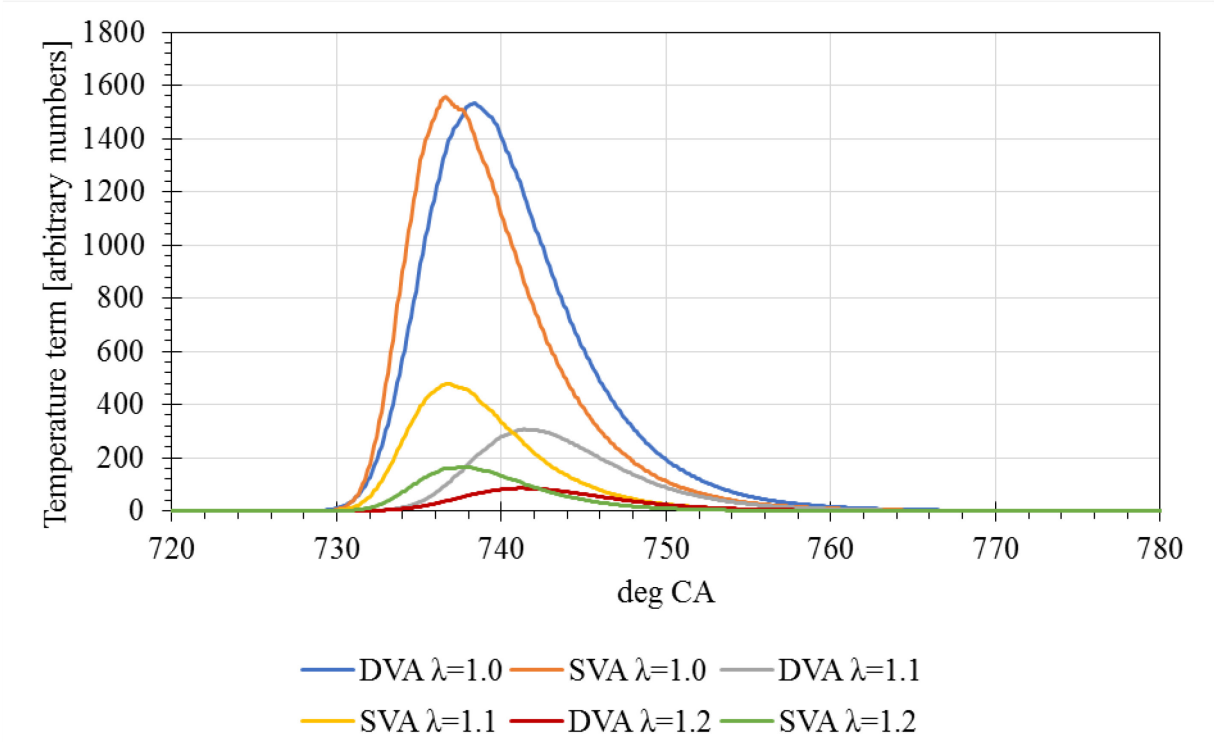


Figure 5.30 Temperature term angle of eq. 5.2 versus crank for three dilution cases. 7.9 bar GMEP, 1500RPM

In this study it was accepted that in reality other phenomena such as incomplete combustion even at lean mixtures may occur, which is why the CO emissions do not drop to zero at lean conditions when the experimental data are examined. However, the focus for the CO production was the rich mixtures, excluding regions above λ=1.0. In addition, for the unburnt hydrocarbons, sources from quenching of the flame on the walls and outflow of HC from the crevices also exist. Furthermore, the selection of the worst lambda region for NO_x production is an artificial range that can be modified. However, the air-fuel equivalence ratio and the mixture formation play an important role on the production of all these pollutants. Thus, a study of the mixture preparation can reveal benefits and shortfalls of an adopted strategy which in this case is the valve deactivation. Other, strategies could be variable valve lift strategies, injection timing and multiple injections for improved homogeneity.

5.2.4. Combustion

For completeness and in order to get an insight of the emissions production as a spatial distribution within the cylinder as well as to confirm the approach described above about the pollutants formation and their correlation to the quality of the mixture, a simulation of the λ=1.0 case for both DVA and SVA was run including combustion. This meant that 4 complete cycles had to be rerun because all the scalars and tracers within the model had to be initialised from scratch and tracked throughout the 4 cycles. The ECFM-3Z combustion model was used and all the constants were kept to their default values (Alpha=1.6 and Beta=1.0). However, the default value of Lower Heating Value of the fuel in the model (*iso*-Octane) was changed and the actual value of the experimental fuel (E10 gasoline) was used which was LHV_{exp}=41.5 MJ/kg. The emissions modelling was also kept with the default models as described it the mathematical formulation chapter. Moreover, the spark timing as it is shown in the experimental data was used without any adjustments.

First of all, the experimental in-cylinder pressure traces for both DVA and SVA were compared against the CFD predictions. The results are displayed in Figure 5.31. It is evident that the numerical predictions overpredict the peak pressure for both valve strategies however, for the SVA the predictions are in a better agreement with the experiment (5% difference for SVA and 12% for DVA). To understand the differences in the peak pressure, the accumulated heat release rate of the experiment for both DVA and SVA were compared against the numerical predictions. This revealed that for the DVA, the heat release in the simulation was faster during the whole phase of the combustion, while for the SVA, the heat release was slower but closer to the experiment. Because of the faster heat release of the DVA, the peak pressure was increased more than the SVA. Ways to adjust the heat release rate is to tune the Alpha and Beta coefficients. Other solution is to adjust the size of the initial flame kernel within the model. However, for the scope of this study, the predictions were satisfactory, and no further tuning was conducted. Other reasons for the over-prediction can be the mis-prediction of the heat transfer modelling at these high pressure and temperature conditions and the blow-by effect.

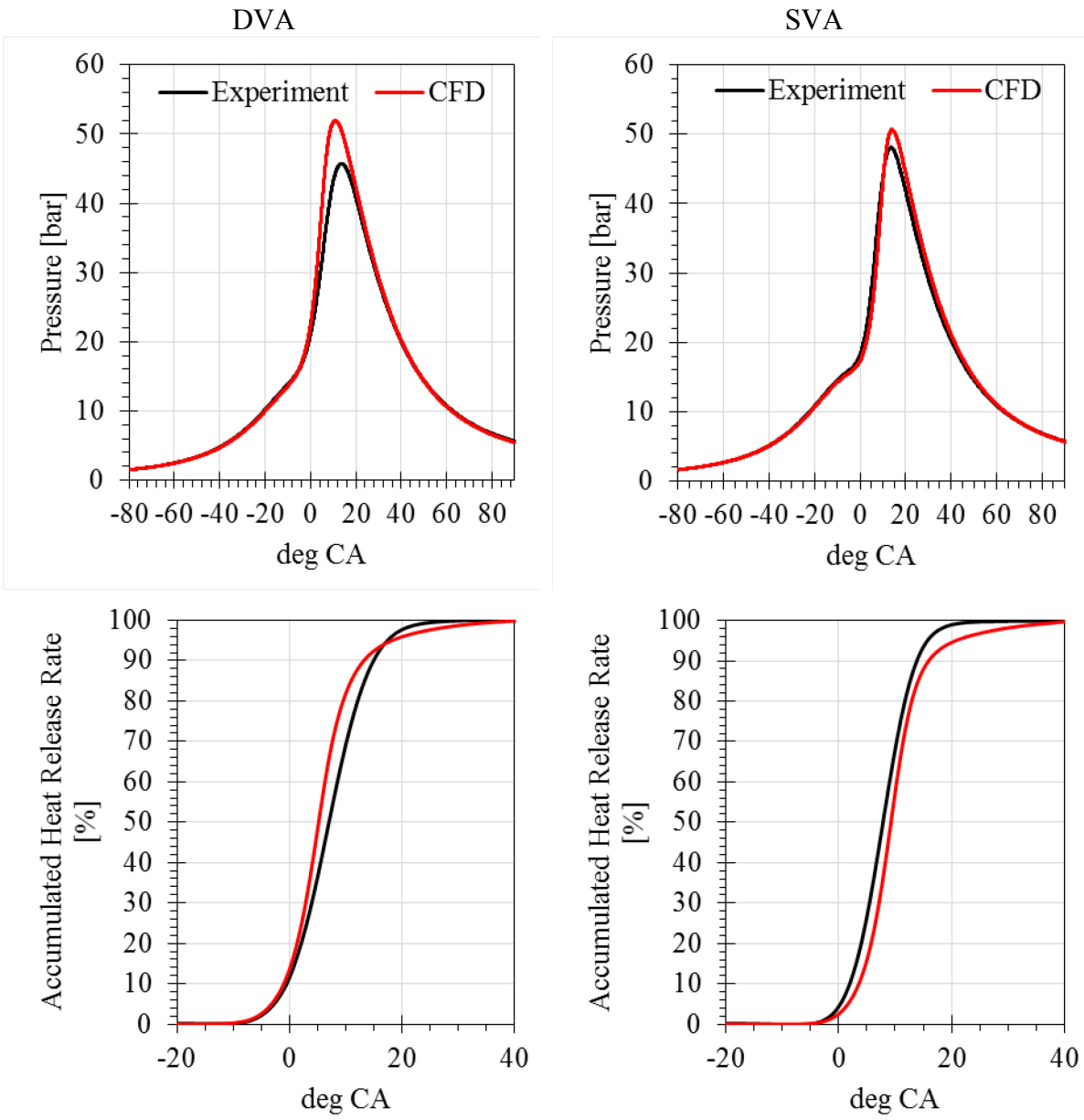


Figure 5.31 Validation of the in-cylinder pressure trace and accumulated heat release rate for DVA and SVA. Global λ=1.0. 7.9 bar GMEP, 1500RPM

After the validation, the predicted trends of the emissions between the DVA and SVA were compared against the trends of the experimental results. Figure 5.32 shows the total mass of the CO and NO in the cylinder. For the CO, the production with DVA starts earlier and it is faster which lead to higher peak and higher equilibrium during the expansion stroke compared to SVA. The same trend of higher CO concentration when DVA was used, was seen in the experiments. The NO production starts earlier with the DVA; however, the rate of production is greater with SVA which lead to higher peak and higher equilibrium at the expansion stroke. The ppm that correspond to the mass values of NO for DVA and SVA are: 1180ppm at the

peak and 1051ppm at the expansion and 1344 ppm at the peak and 1264ppm at the expansion. It is acknowledged that these predictions are ~50% below the experimental values (2966 ppm for DVA and 3290 ppm for SVA) however, the trend of higher NO with SVA is preserved. Within the code, more NO models exist based on NO_x libraries and more detailed reaction chemistry which may improve the predictions. It has to be re-iterated that the goal of this study was to investigate the main sources of NO based on the mixture preparation and understand the differences between DVA and SVA.

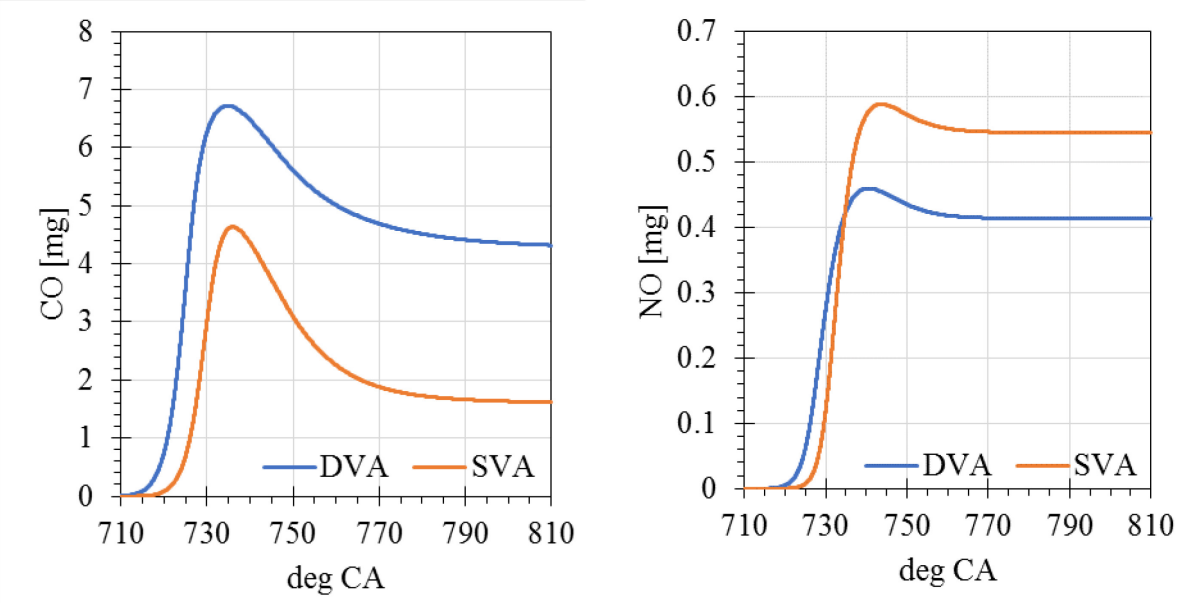


Figure 5.32 Numerical predictions of CO and NO_x for DVA and SVA. Global λ=1.0. 7.9 bar GMEP, 1500RPM

To investigate the locations where the highest CO and NO production rate took place, the spatial distribution of these two substances within the cylinder at the crank angle of the highest concentration was studied. For the CO, 16 degrees after firing TDC was chosen and for the NO 20 degrees after TDC was chosen for the DVA case and 23 degrees aTDCf for the SVA case. The same tumble and swirl planes were used, and the results are shown in Figure 5.33 for CO and Figure 5.34 for NO. When looking at the tumble plane of the CO production for the DVA case is evident that an area on the exhaust side was producing more CO than the rest of the tumble plane. This contour plot can be compared against the contour plot of Lambda distribution of Figure 5.10 which shows a region of rich region (λ<1) at that location. For the swirl plane of DVA, the -Y sector showed more CO than the +Y sector. Again this is linked to the Lambda contour plots which showed a richer mixture at the -Y sector. For the SVA case, at the tumble view, there is no area of concentrated CO due to the better homogeneity of the

mixture. However, it can be seen that the higher concentration of CO is near the piston because of the axial stratification of the SVA mixture which produced richer mixtures near the piston and leaner mixture at the head of the cylinder. The swirl plane also did not show any extremely localised CO formation. There is an area under the intake valve in the +Y direction because the mixture there was slightly richer.

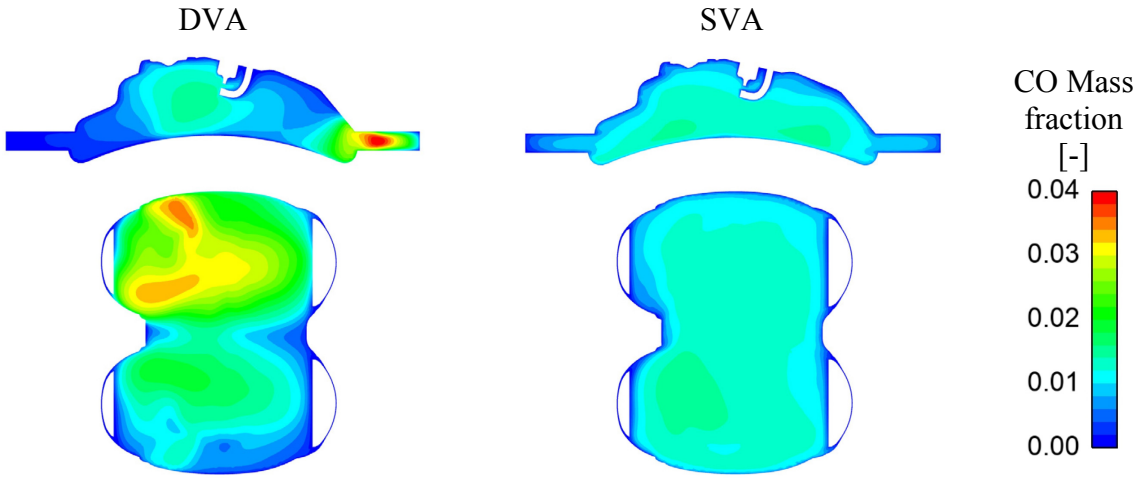


Figure 5.33 Spatial distribution of CO at the peak production (15 degrees after TDC) for DVA and SVA. Global λ=1.0. 7.9 bar GMEP, 1500RPM

The NO mass fraction in the cylinder at the time of the peak NO is shown in Figure 5.34. At the tumble view of the DVA case, two different areas were identified with higher NO concentration. The first one is under the injector, at the intake side and the second, which has higher concentration than the first location, is on the exhaust side. This is in line with the two lean areas as seen in the Lambda contour plots of Figure 5.10. Furthermore, the area of the exhaust side was leaner and closer to λ=1.1 than the area at the intake side. The swirl view of the DVA showed that the NO concentration is higher at the +Y sector of the cylinder. This sector also showed leaner mixture than the -Y sector. For the tumble view of the SVA, the higher concentration of NO was seen near the spark plug and the head of the cylinder. This was the location of leaner mixture as seen in Figure 5.11. Due to the axial stratification, the mixture near the piston is richer than regions near the head. Also it was seen, that at specific locations of the z-axis, axially the Lambda value was fairly stable and for this reason, the tumble view of the SVA has also smaller discrepancies of NO concentration.

In order to understand the contribution of temperature to the NO production, the contour plots of the temperature are shown in Figure 5.35. Firstly, it is clear that the DVA case has higher temperatures than SVA however, this is also due to the higher in-cylinder pressure. Despite the

fact of the higher temperatures of the DVA, the SVA gave higher NO mass. Moreover, there is a correlation between high NO concentration and high temperatures between the contour plots, these two factors are not totally linked. Especially for DVA, the temperature of the area of high NO at the intake side, is cooler than other areas of same NO concentration in both DVA and SVA. Furthermore, the hot area below the spark plug in the DVA case has low NO concentration.

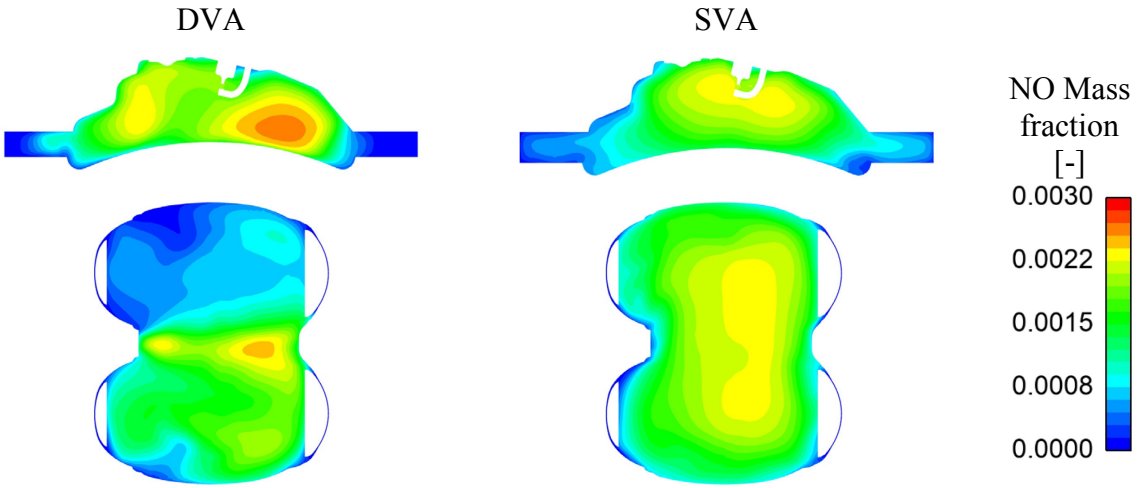


Figure 5.34 Spatial distribution of NO_x at the peak production (20 degrees after TDC) for DVA and SVA. Global λ=1.0. 7.9 bar GMEP, 1500RPM

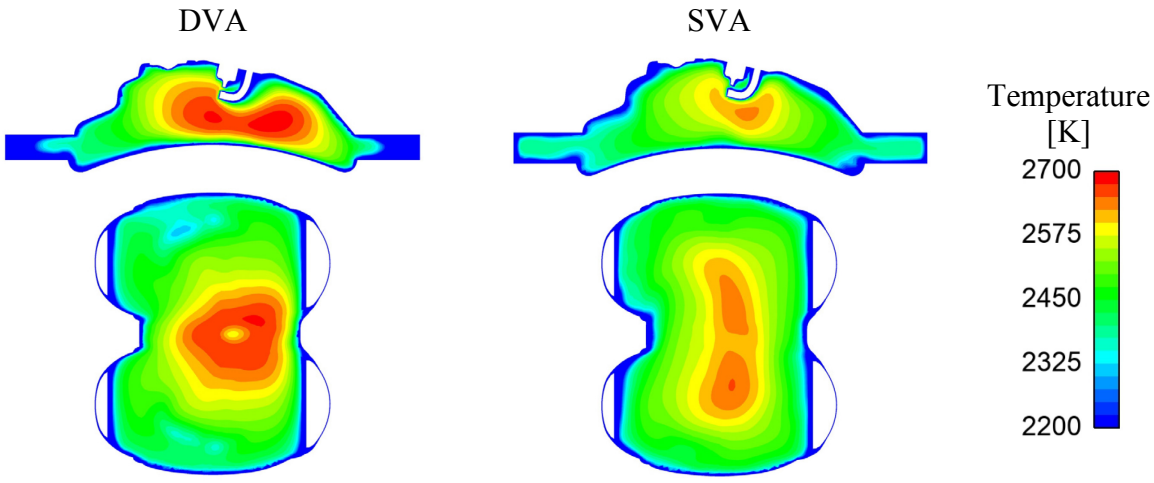


Figure 5.35 Spatial distribution of temperature at the peak NO_x production (20 degrees after TDC) for DVA and SVA. Global λ=1.0. 7.9 bar GMEP, 1500RPM

Lastly, the soot formation was investigated only with the use of the combustion CFD with the built-in model of Das *et al.* (1999) due to the absence of experimental data. The simulations showed (Figure 5.36) that the soot production started earlier with the dual valve activation

strategy and the rate of production was also higher than the single valve. Consequently, the total mass of soot was almost an order of magnitude greater with the DVA. This is a result that can be expected because the model is consuming fuel for the soot production and due to the greater volume of rich mixture, the soot was increased. In Figure 5.37, an iso-volume of the soot formation for DVA and SVA is shown at 90 degrees after firing TDC, which is near the EVO. To be able to visualise the SVA case, the legend had to be reduced, thus the values are not the same for the same colours. The DVA case produced soot at the exhaust side of the cylinder, where the richest mixture was seen earlier in the cycle. The SVA case produced soot near to the piston, and again, the richest mixture was seen near the piston but in smaller volumes.

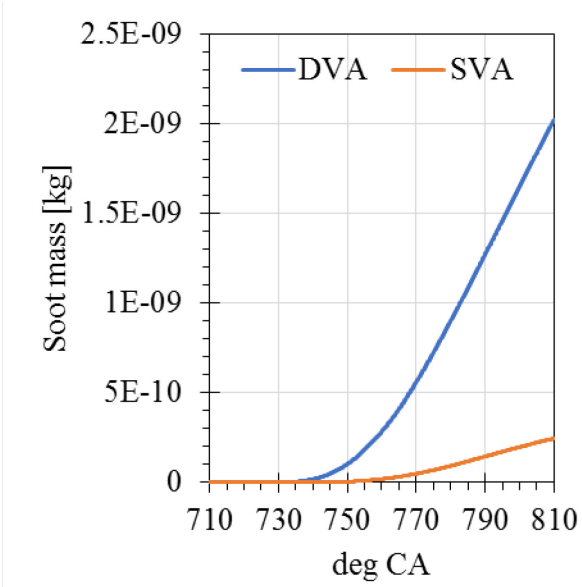


Figure 5.36 Numerical predictions of soot for DVA and SVA. Global λ=1.0. 7.9 bar GMEP, 1500RPM

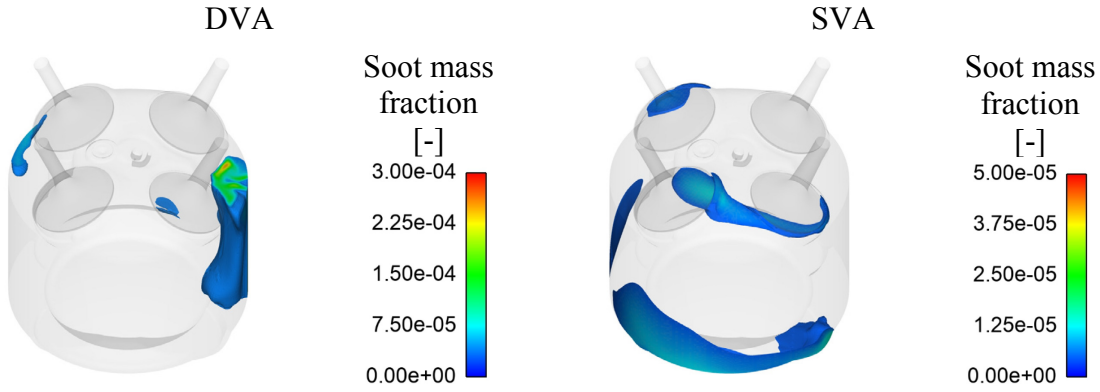


Figure 5.37 Spatial distribution (3D) of soot at EVO for DVA and SVA. Global λ=1.0. 7.9 bar GMEP, 1500RPM

From the combustion results it can be said that the approach which was used to identify the regions of rich mixture without the use of combustion modelling to qualitatively explain the experimental results was valid. Greater amount of CO was produced with the combustion modelling from the regions that were identified earlier as potential regions of CO production which was higher for DVA than SVA. Thus, the approach shows that important conclusions for CO can be drawn based on non-combustion CFD and on quantifying regions within the cylinder which can potentially increase the emissions. In addition, for cases with Late Intake Valve Closure where multi-cycle simulations are needed for converged Lambda can be avoided with the use of the normalisation, something that is not applicable in combustion simulations. Similar conclusions can be drawn from the NO calculations of the non-combustion CFD. The combustion showed that the NO is formed in the regions where the air-fuel equivalence ratio of the mixture is close to λ=1.1 and it is more important that the temperature as seen from the combustion. The choice of a Lambda region may be challenging, and it is acknowledged that a definite answer cannot be given, the range [1.05,1.15] however, can give an insight of the mixture formation and the locations in which NO production is most probable to occur. Again, it can be said that the non-combustion CFD can be used for comparison purposes and basic investigations and with the use of the normalisation, the process can be accelerated.

5.3. Engine load: 3.6 bar GMEP, 1500 RPM

At this low load, the in-cylinder pressure during injection is about 0.5 bar absolute and in combination with the increased fuel temperature which can be assumed to be at the head coolant temperature (~90°C) the gasoline will flash boil. When SVA was adopted, at the low load, the pressure at injection dropped at around 0.3 bar. The validated model of the flash boiling has been implemented at this load and the spray pattern has already been presented at the beginning of this chapter. The air-fuel equivalence ratio for the λ=1.0 case at this low load was investigated for the two valve strategies (DVA and SVA). Because of the flash boiling modelling of the injected fuel, differences between the two loads were expected and investigated.

5.3.1. In-cylinder flow properties

The same procedure as for the higher load was followed, by comparing the in-cylinder flow properties with the fuel injection against the same cases without the spray. The trends seen for the higher load for all the in-cylinder quantities were repeated for the low load. The in-cylinder average velocity was reduced during the injection for both DVA and SVA. However, due to the momentum given to the flow from the spray, the velocity was higher during compression again for both DVA and SVA. The increase was maintained through the whole compression and at ignition (20 deg CA before TDCf) the increase for DVA was 3.5% and for SVA 2%. Similarly to the higher load, the TKE was increased during the injection for DVA and it was maintained up to firing TDC and at ignition the increase was 7.5%. For the SVA, there was an initial reduction of the TKE during the spray event compared to the non-spray case however, at ignition there was an increase of about 2.5%. The higher increase of TKE at the low load is because of the weaker flow compared to the high load as well as the flash boiling mechanism which affected a wider volume due to the increased cone angle of the plumes. Furthermore, due to the evaporation of the fuel, the in-cylinder temperature was reduced and during compression and around ignition the reduction was in the range of 45K-55K for DVA and SVA respectively. Thus, the difference in temperature between DVA and SVA with the fuel injection was ~20K. Because of this reduction in temperature the heat transfer from the gas to the walls was also reduced for both valve strategies. The increase of heat transfer from DVA to SVA though was preserved at 23%, similar to the cases without the fuel injection.

5.3.2. Mixture preparation

The progress of the Lambda contours for four different crank angles in the compression stroke and near ignition are displayed in Figure 5.38 for DVA and Figure 5.39 for SVA. The same tumble and swirl planes as before have been chosen. Moreover, the minimum and maximum values of the legend have been kept the same as the higher load. A comparison of the DVA and SVA contour plots at the 3.6 bar GMEP load revealed that the again the SVA case appeared more homogeneous than the DVA case. In addition, the SVA contour of the low load was very similar to the higher load with the same axial stratification being visible. For the DVA strategy, some patterns that appeared on the higher load were as well visible for this load. These patterns were: the lean region on the right side of the spark plug close to the head and the lean region near the liner, at the intake side. The major difference in the DVA case between the two loads

was the relatively rich region under the injector and spark plug at the intake side of the low load which did not clearly appear at the higher load. This behaviour can be linked to the collapsing spray with the lower penetration which lead a greater fuel vapour near the engine's head.

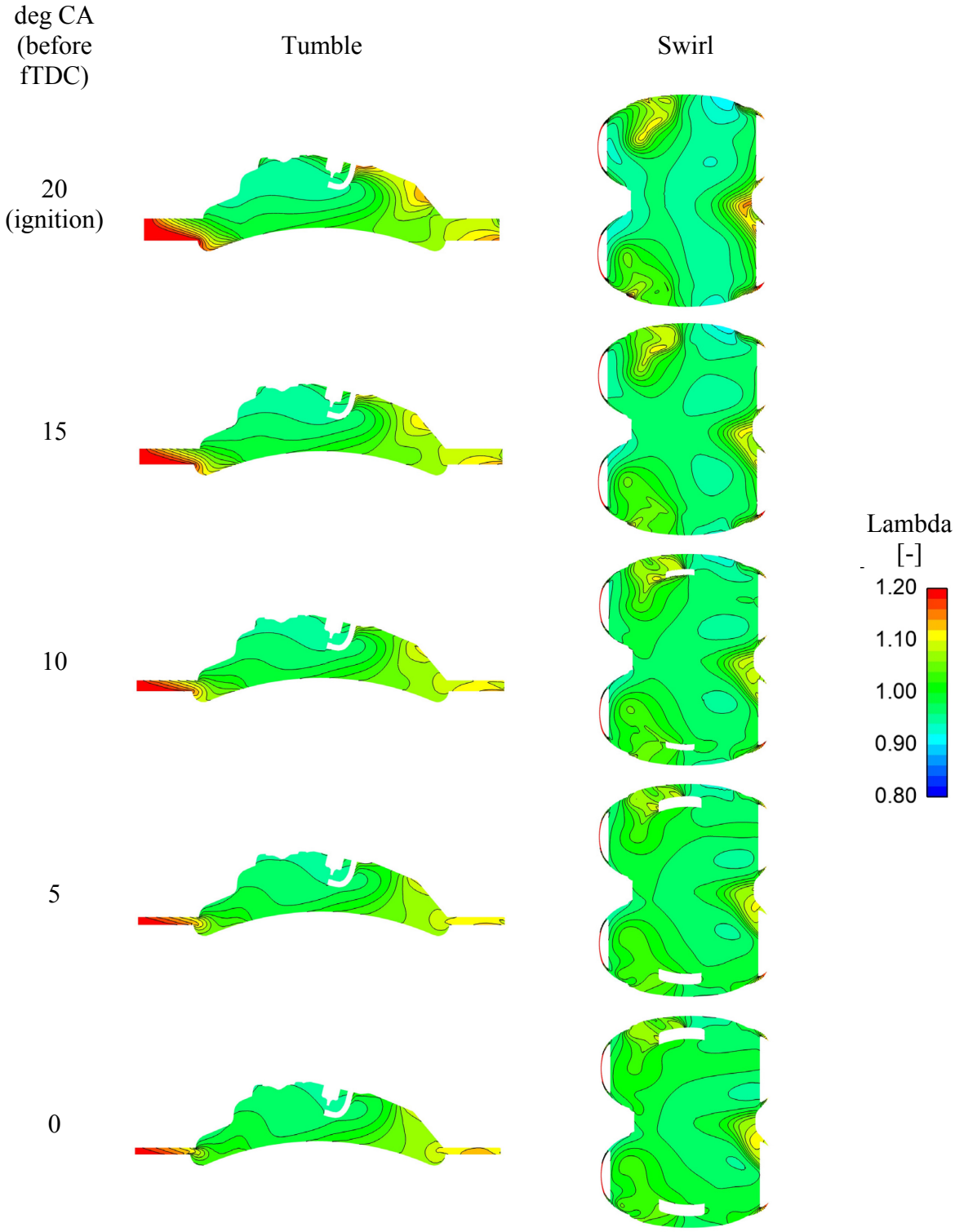


Figure 5.38 Spatial distribution of Lambda for DVA at various crank angles during compression, λ=1.0, 3.6 bar GMEP, 1500 RPM

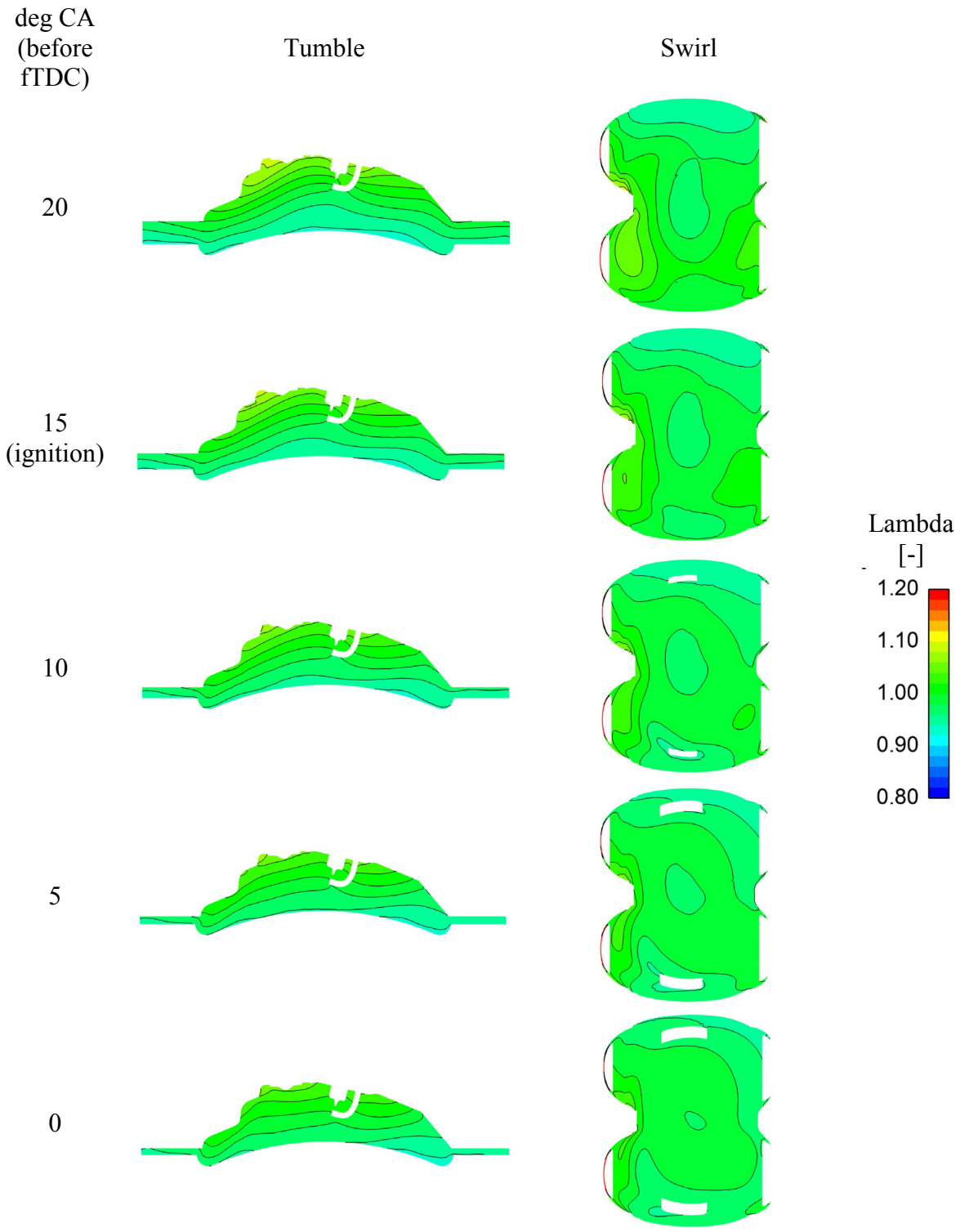


Figure 5.39 Spatial distribution of Lambda for SVA at various crank angles during compression, λ=1.0, 3.6 bar GMEP, 1500 RPM

When comparing the DVA contour plots of the two loads, a better homogeneity was probable. For this reason, the evolution of the homogeneity index was plotted for the lower load for DVA and SVA. This can be seen in Figure 5.40. The graph of the homogeneity index showed the

improvement of the homogeneity of the mixture for both strategies, however for the DVA is more significant. Improvement of the homogeneity due to flash boiling is reported in Baumgarten (2006).

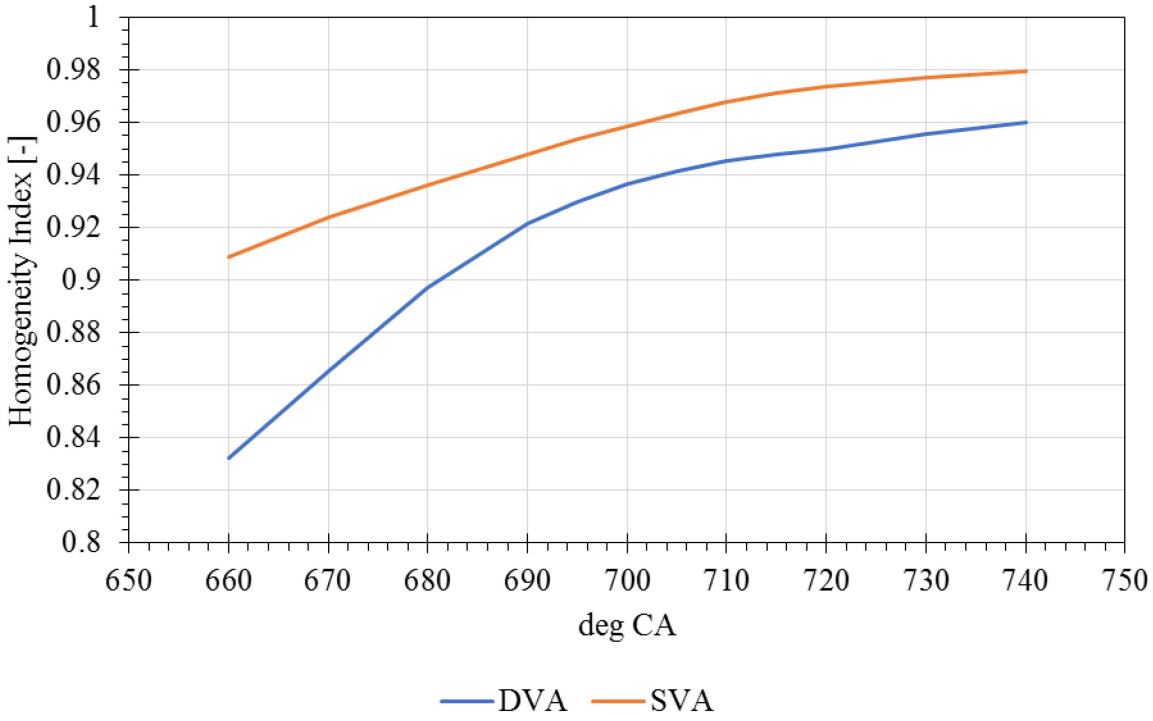


Figure 5.40 Homogeneity Index for DVA and SVA at 3.6 bar GMEP, 1500 RPM, λ=1.0

The laminar burning velocity for the lowest load was compared against the calculations of the same load without taking account the air-fuel mixture. Figure 5.41 shows the laminar burning velocity taking account the air-fuel mixture for DVA and SVA, 10 degrees CA before firing TDC. Similar to the higher load, the main difference in the calculations of laminar burning velocity with and without the spray (which was seen in both DVA and SVA) was the reduction of the burning velocity when the fuel injection was included. The reason for this reduction was again the reduction of the in-cylinder temperature due to charge cooling. A reduction of 65K can reduce the velocity from ~80 cm/s to ~65 cm/s. However, the same trends as the cases without injection appear for the laminar burning velocity when DVA and SVA are compared. The higher temperature of the SVA, was the main contributor to the increased burning velocity. In addition, for both valve strategies, qualitatively the contour plots are very similar to the cases without the injection. This is because of the increased homogeneity of the mixture for the low load. Furthermore, and as described for the higher load, the temperature distribution is mostly affected by the flow motion which is very similar for the case with and for the case without

injection. When the laminar burning velocities for the two loads were compared, the values for the lower load where higher than the high load due to the decreased in-cylinder pressure which was the half of the high load.

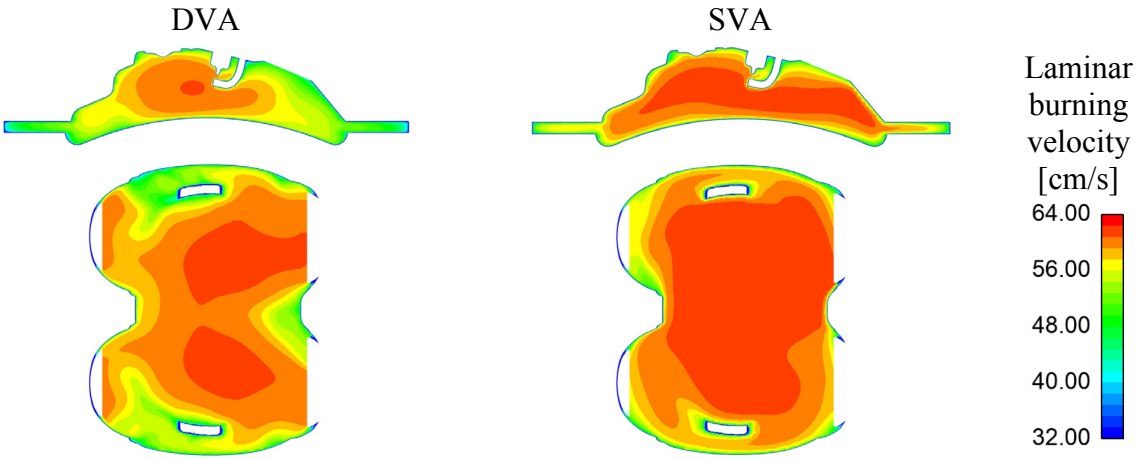


Figure 5.41 Spatial distribution of laminar burning velocity for DVA and SVA 10 degrees CA before TDC, λ=1.0, 3.6 bar GMEP 1500 RPM

During flash boiling, the penetration is generally decreased, but at very high superheat degrees (as it is expected with SVA), the penetration increases again. Because of this reduction of penetration for DVA, the liquid film formation was decreased when compared to the 7.9 bar GMEP load. However, with the use of SVA, the liquid was not reduced further, but it was the same level as the DVA case of the high load. Again, most of the fuel was accumulated on the piston crown. This can be seen from Figure 5.42. Due to the lower in-cylinder pressure and the enhanced flow motion which transported the spray at the SVA case, the film formation starts earlier than the DVA. After the peak film mass, the reduction is very similar for both cases. The liquid film on the piston at 14 degrees after start of injection, around the peak of both cases is shown in Figure 5.43. The film is again symmetric for the DVA, however, due to the collapsing mechanism of the spray, the pattern is different from the high load (Figure 5.16). The liquid film when SVA was adopted had a similar pattern to the higher load at the centre of the piston crown. This behaviour comes from the helical flow pattern which directed the spray towards the piston. Because of the faster evaporation and the collapsed spray, the thickness is reduced when compared to the higher load.

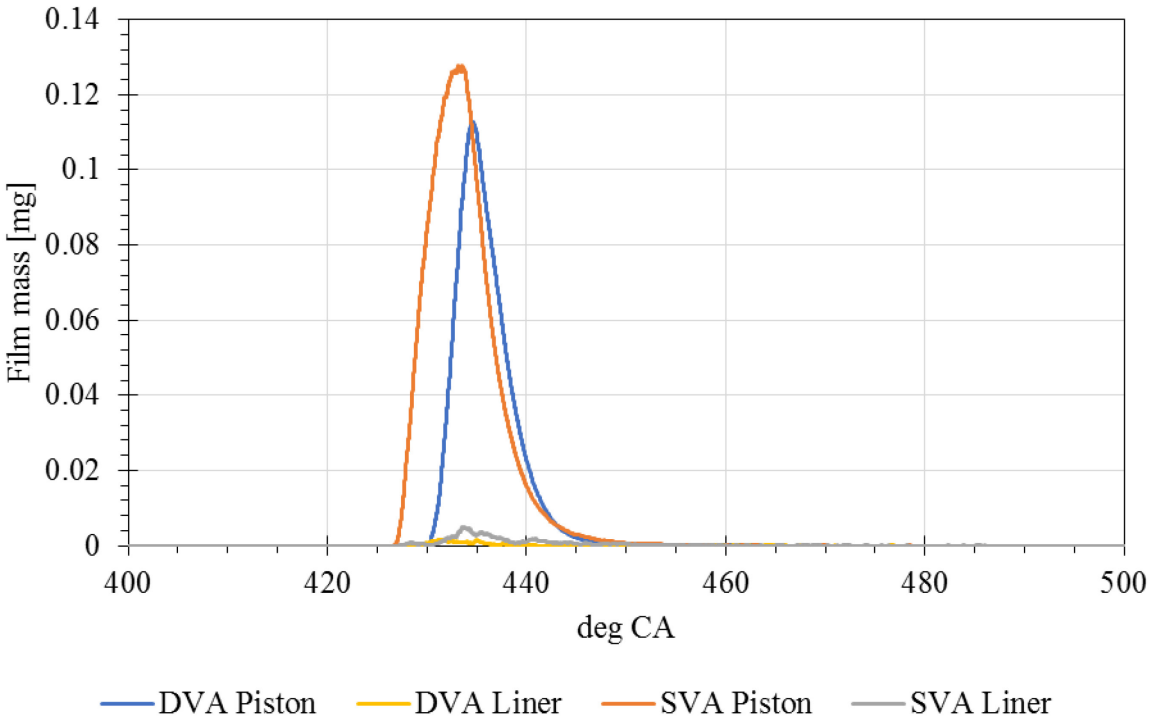


Figure 5.42 Accumulated liquid film mass at the piston and liner for DVA and SVA versus time. λ=1.0. 3.6 bar GMEP, 1500 RPM

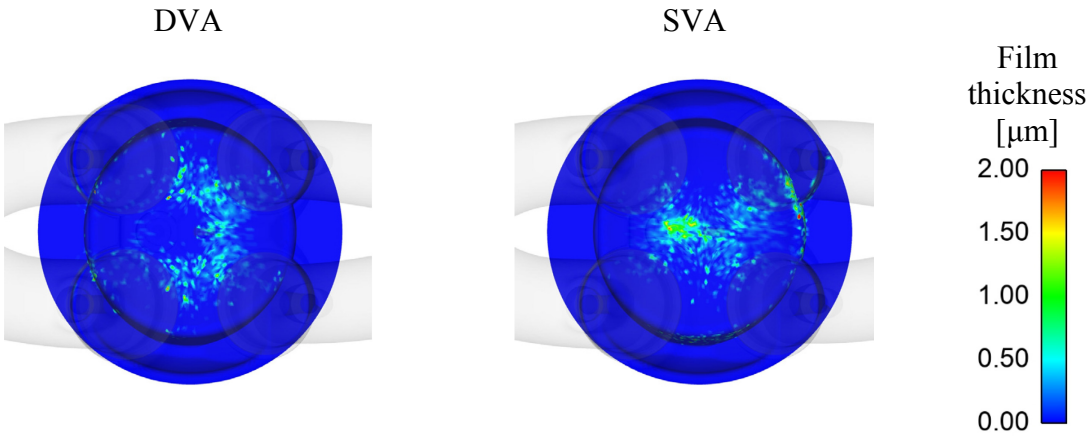


Figure 5.43 Liquid film thickness at the piston for DVA and SVA at 20 degrees after SOI. λ=1.0. 3.6 bar GMEP, 1500 RPM

5.3.3. Emissions

The emission of CO, NO_x and unburnt hydrocarbons was investigated for the low load condition and some general comparison against the higher load was carried out. The experimental data (Figure 5.44) revealed that for a given EGR (here EGR 0%), NO_x emissions are greater for SVA compared to DVA for up to about lambda 1.2. Above that lambda, the NO_x levels for both valve strategies are very similar. In addition to this, the highest amount of NO_x is observed when the engine was running with global Lambda of 1.1 followed by the global Lambda of 1.0. This is the first difference between the two loads. For the higher load, the NO_x emissions at λ=1.2 was greater than λ=1.0. For both loads, the highest production rate was when λ~1.1. The differences between DVA and SVA for Lambdas 1.0 to 1.2 are about 15%. Another major difference between the two loads was the emissions of the unburnt hydrocarbons. At λ=1.0, the difference between DVA and SVA was reduced to 10% compared to 40% difference at the higher load. In addition, at λ=1.0 the THC emissions of the SVA were higher than the DVA which was the opposite at higher load. The differences at λ=1.1 and λ=1.2 were minor (3%) between the two valve strategies at the 3.6 bar GMEP load, while at the higher load the differences were 40%. Above λ=1.2 the THC increase for both DVA and SVA but with higher rate for DVA. This has to do with the deterioration of the combustion at higher dilutions. For the CO production the trends are the same for both loads. The values are very similar for both valve strategies for Lambdas greater than 1.1. For the stoichiometric case, the CO emissions is greater for DVA by 20% while at the higher load the difference was 40%.

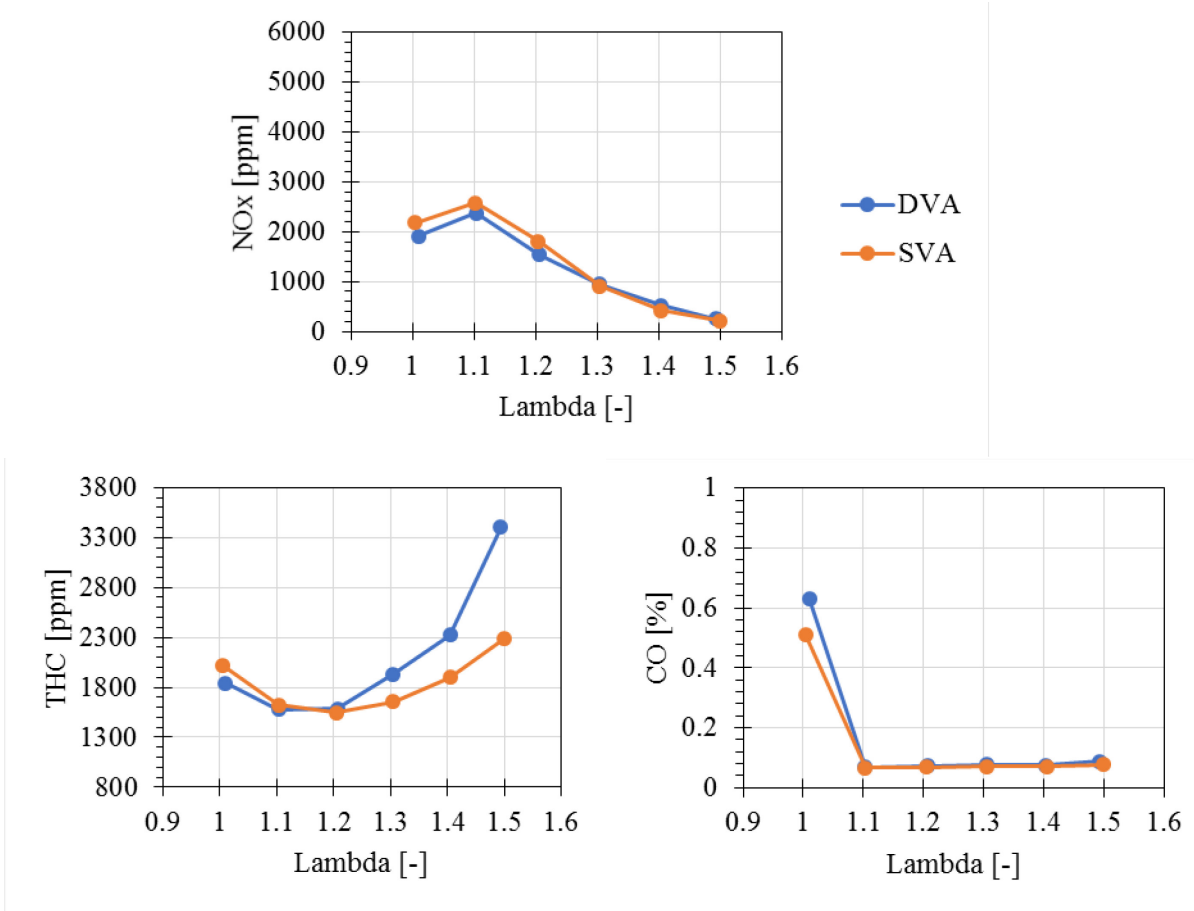


Figure 5.44 Experimental emissions of NO_x, THC and CO. 3.6 bar GMEP, 1500 RPM

The reduction of the differences in emissions between DVA and SVA can be linked to the better homogeneity of the mixture, which was due to the flash-boiling mechanism of the fuel that was implemented to the model. The same approach as at the higher load was followed. The air-fuel equivalence ratio was studied for the whole cylinder and for five spherical volumes which had the centre at the spark plug gap and their diameters were 10 mm, 20 mm, 30 mm, 40 mm, 60 mm.

For the unburnt hydrocarbons and the CO the rich mixture ($\lambda<1.0$) was studied as well as the average Lambda of the rich mixture. The ignition of the DVA occurred at 20 degrees before firing TDC (700 deg CA in the graph of Figure 5.45) and for the SVA at 15 degrees before firing TDC (705 deg CA in the graph of Figure 5.46). At ignition and up to the half of the cylinder diameter (10mm to 40mm spheres), the respective volumes are more than 80% with a rich mixture. With the adoption of SVA, the same spherical volumes were occupied by a rich mixture in the range of 40% to 60%. For greater spherical volumes (60 mm sphere or the whole cylinder) the results were reverted. The DVA strategy, showed reduced volume occupied by

the rich mixture because a lean mixture was present at the edges of the cylinder. Opposite to the DVA, the axial stratification of SVA lead to richer mixtures near the piston and thus, the percentage of the respective spherical volume with rich mixture was increased as the diameter of the sphere was increased. In addition, from the average lambda of the rich zones (Figure 5.47 for DVA and Figure 5.48 for SVA) is evident that near ignition and up to the half of the cylinder diameter (40 mm) the average lambda is richer for the DVA than the SVA. For greater spherical volumes the rich mixture is richer for the SVA (average lambda λ=0.97) than the DVA (average lambda λ=0.98). From these graphs it can be concluded that at the beginning of the combustion, when the flame propagates through a rich mixture, more CO is produced with the DVA than SVA. In addition, the mixture is richer thus, the incomplete combustion is more severe. As the flame arrives at the edges of the cylinder and quenches, the mixture is leaner which did not contribute to the unburnt hydrocarbons. For the SVA the flame initially would propagate to a rich region smaller in size than that of the DVA and also closer to stoichiometric mixture which produces less CO. However, the flame quenches on a rich region which can leave unburnt hydrocarbons. The numerical results of the average lambda showed that the rich regions are closer to the stoichiometric air-fuel ration due to the improved homogeneity. Generally, the differences in the simulations are smaller between DVA and SVA which is also reflected in the smaller differences of the experiments.

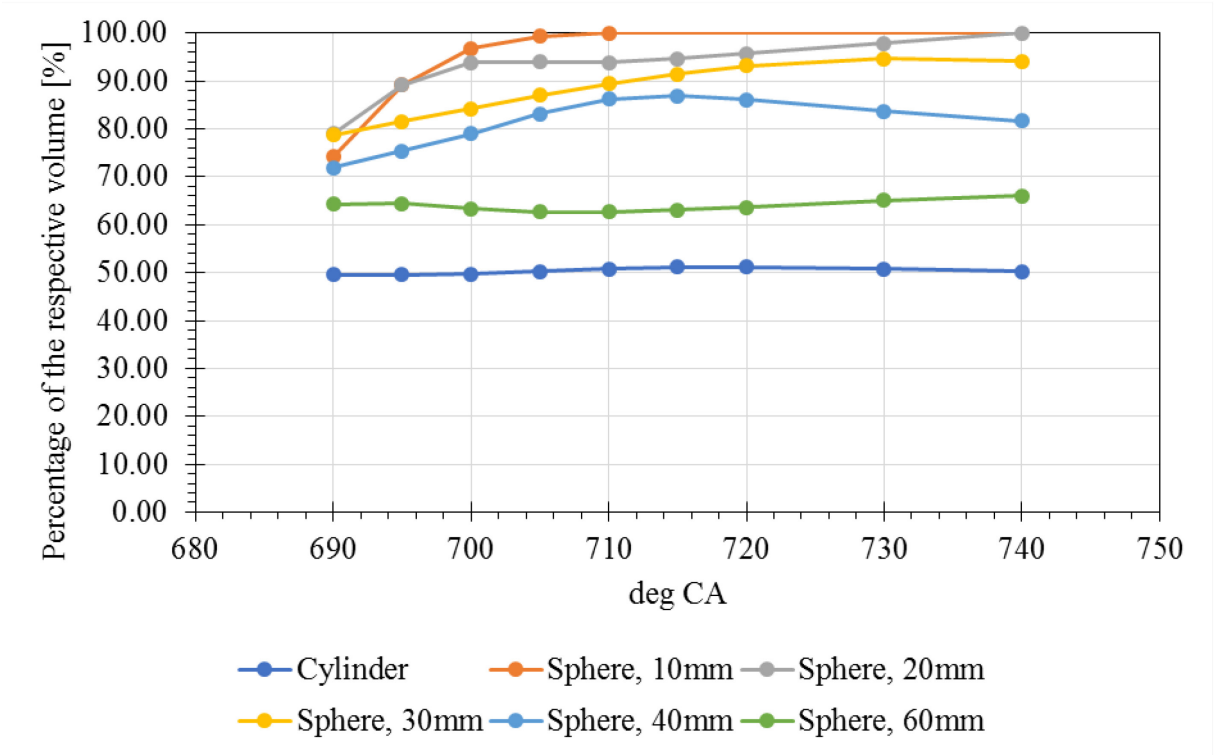


Figure 5.45 Percentage of the respective spherical volumes occupied with a rich mixture (λ<1.0) for DVA. Global λ=1.0. 3.6 bar GMEP, 1500RPM

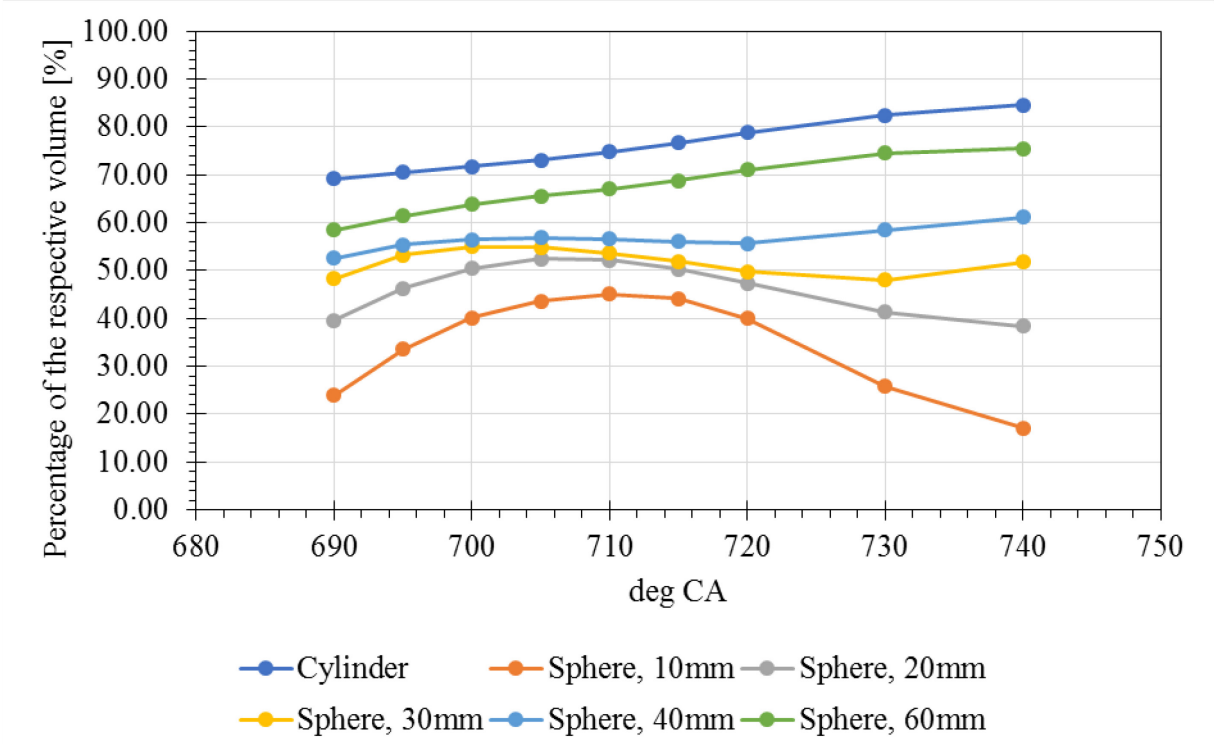


Figure 5.46 Percentage of the respective spherical volumes occupied with a rich mixture (λ<1.0) for SVA. Global λ=1.0. 3.6 bar GMEP, 1500RPM

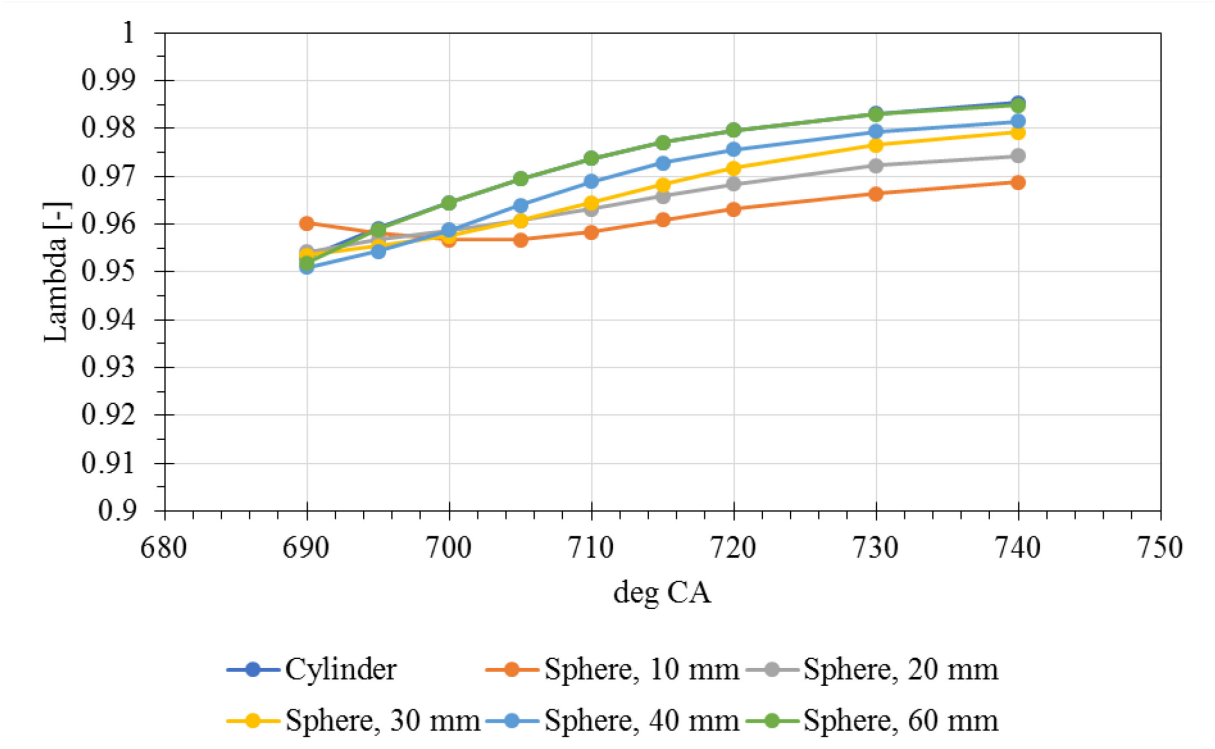


Figure 5.47 Average lambda of the rich mixture within each spherical volume for DVA. Global λ=1.0. 3.6 bar GMEP, 1500RPM

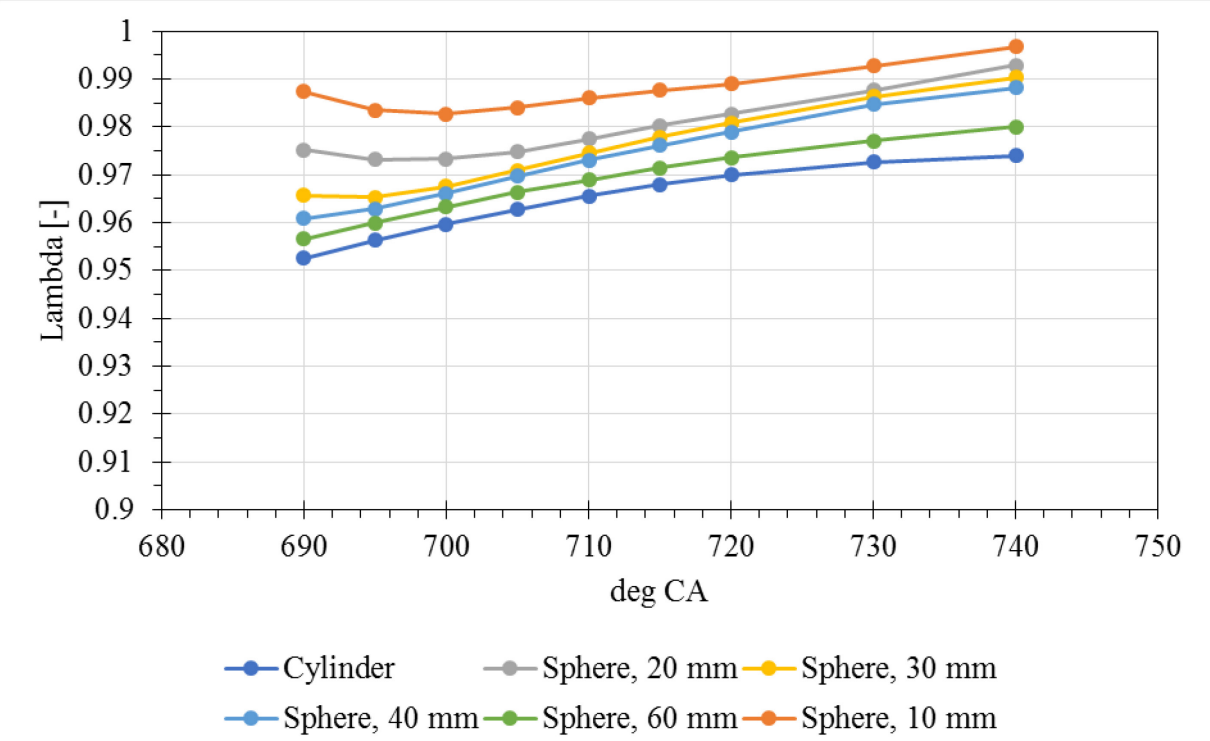


Figure 5.48 Average lambda of the rich mixture within each spherical volume for SVA. Global λ=1.0. 3.6 bar GMEP, 1500RPM

Lastly, the NO_x production was investigated for the lower load. Again, the same region of the worst lambda was assumed [1.05,1.15]. The volume of the five different spheres and the whole cylinder that are occupied by a mixture in the lambda region is plotted in Figure 5.49 for DVA and Figure 5.50 for SVA. The first interesting aspect of these plots is the reduced volume that is occupied by the mixture in the range of λ[1.05,1.15] for both DVA and SVA. The maximum value after ignition is 20% of the volume and correspond to the total cylinder volume for the DVA strategy. The maximum volume for the SVA after ignition is 12% and corresponds to the 40 mm diameter of the sphere. Generally, for the DVA and up to 40 mm sphere, the percentage of the volume of a specific sphere is less than 6% throughout the cycle after ignition. For the same spheres with SVA, the percentage between 6% and 12% at ignition and this percentage is reduced after ignition. From these results a definite answer cannot be given for the greater NO_x with SVA. However, it can be said that the differences between the two valve strategies in the simulations are smaller than the higher load which is a trend also seen in the experiments. In addition, the increased homogeneity should appear at higher dilution which means that at λ=1.1 the values for both valve strategies will be close to the global lambda with smaller deviation. Thus, the differences in the experiment between DVA and SVA are smaller in the lower load than the higher load.

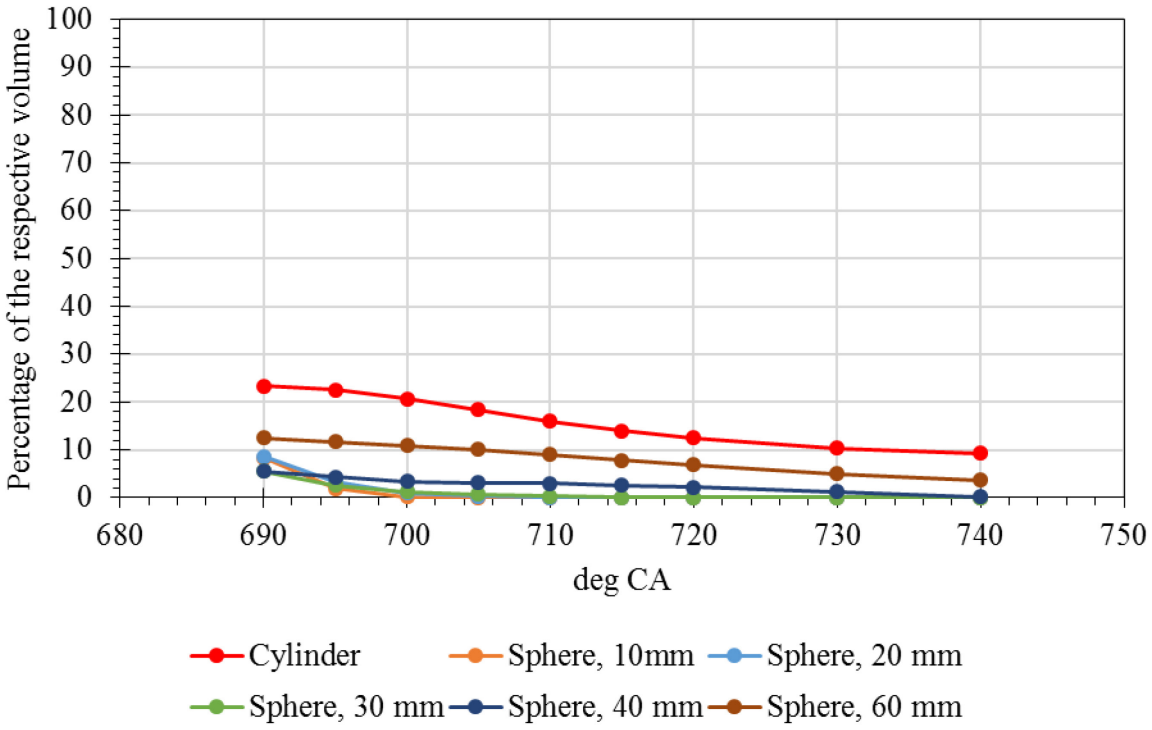


Figure 5.49 Percentage of the respective spherical volumes occupied with a lean mixture in the range λ[1.05,1.15] for DVA. Global λ=1.0. 3.6 bar GMEP, 1500RPM

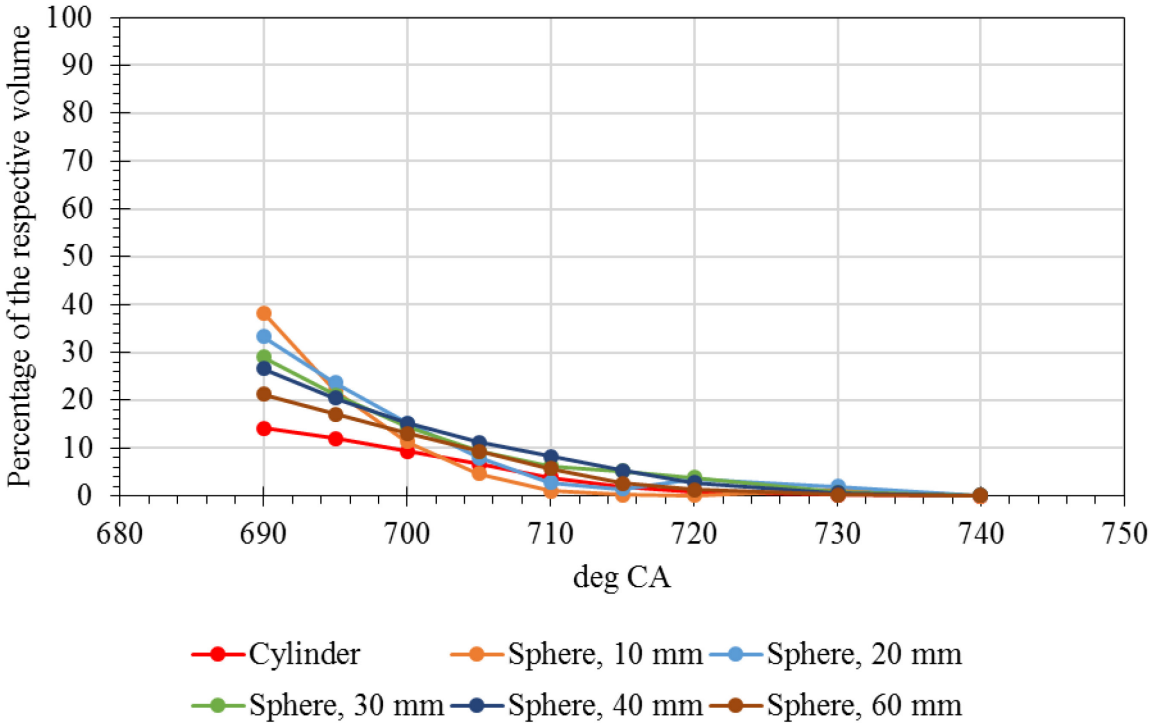


Figure 5.50 Percentage of the respective spherical volumes occupied with a lean mixture in the range λ[1.05,1.15] for SVA. Global λ=1.0. 3.6 bar GMEP, 1500RPM

Possible explanation of the uncertainties of the results at this load is the limitations of the flash boiling model especially in very high superheat degrees such as that of the SVA (very low ambient pressure ang high fuel temperature). More experimental measurements need to be taken in running engines at high superheat and compared against the numerical results. Another explanation is the strict limits that were chosen to represent the worst-case region of Lambdas for NO_x production. It was already said that these limits are chosen as a guidance for basic comparisons and do not represent exact values.

5.4. Closure

In this chapter, a spray modelling was included in the simulations to investigate the mixture preparation and the emissions formation of the Dual and Single valve actuation at two different engine loads. Especially for the low engine load, a newly developed in-house flash-boiling model was implemented to study the effects of a flashing spray on the air-fuel mixing. In addition, comparisons against the approach without the fuel injection was made for the in-cylinder flow properties.

The results irrespective of the engine load showed that:

- Because of the Late Intake Valve Closure, a portion of fuel vapour escaped into the intake port during compression and thus, a multi-cycle approach was needed in order to achieve a converged global in-cylinder Lambda. Generally, 4 to 5 cycles were needed depending on the DVA or SVA strategy. Due to the decreased loss of fuel vapour to the intake port with SVA, the cycles needed for this valve strategy were decreased.
- Due to the Reynolds-Averaged method, a normalisation approach can be utilised in order to acquire data for the converged values from the second cycle. The global Lambda of the second cycle can be normalised to the global Lambda that is desired This method showed to have a maximum error of 0.7% and an average error of 0.1%.
- With the use of the fuel injection, due to the presence of the fuel vapour, the compression polytropic index was improved when compared to the cases without the fuel and it was in a very good agreement with the experiments.
- The fuel injection at the high load increased the in-cylinder average velocity by 7% at ignition timing for DVA when compared against the motoring case without fuel injection. Due to the strong in-cylinder flow with the use of SVA, the effect of the injection was minor but increased the velocity by 0.2%.

- Similarly, at the high load the fuel injection increased the in-cylinder TKE during the event of the fuel injection, however it was dissipated during the intake and compression stroke which resulted in 1% increase for the DVA and 0.6% for the SVA at ignition.
- Due to direct-injection and consequently the evaporation of the liquid fuel, the temperature of the trapped mass dropped by about 80K when compared to the same case without the injection. The decrease of the in-cylinder temperature decreased the heat transfer for both DVA and SVA. However, the increase of the heat transfer from DVA to SVA remained at the same level as with the cases without the fuel injection.

Depending on the engine operating condition it was concluded that:

- At 7.9 bar GMEP, the Lambda contour plots revealed a better air-fuel mixing when SVA was adopted. The SVA showed an axial stratification where a leaner mixture was present near the head and a richer mixture near the piston. Radially the mixture was homogeneous. For the DVA cases however, areas of either very lean or rich mixture was seen in the cylinder. To quantify the differences a homogeneity index was used which showed that the SVA was better homogenised (HI=0.96) than the DVA (HI=0.9) at ignition. For the lower load (3.6 bar GMEP) because of the flash boiling mechanism with the smaller droplets and the faster evaporation the homogeneity was improved for both DVA and SVA but for the DVA the improvement was greater. Similar patterns between the two loads of a specific valve strategy were seen. At ignition for DVA the index was HI=0.94 and for SVA HI=0.97.
- The laminar burning velocity was also affected by the fuel injection. However, this was mostly due to the decrease of the in-cylinder temperature which also decreased the burning velocity for both loads. The maximum value dropped from ~75cm/s to ~60cm/s for both DVA and SVA at 7.9 bar GMEP and from ~80cm/s to ~65cm/s at the lower load. The differences between the two loads was because of the increased in-cylinder pressure at the higher load which was the double of the lower load. At 7.9 bar GMEP, the contour plots of the laminar burning velocity were similar to the cases without the fuel injection especially for the SVA which had increased homogeneity of the mixture. For the DVA, due to the areas of very lean or rich mixture, the contour plots at these locations deviated from the cases without the fuel. For the lower load, due to the increased homogeneity, the contour plots of the burning velocity were very close to those without the fuel injection cases.

- Due to the orientation and pattern of the injector, liquid film was formed at the piston crown. At the high load, the use of SVA reduced the liquid film almost by half (0.8 mg for DVA and 0.46 mg for SVA) because of the strong in-cylinder flow which was disintegrating the spray plumes. The reduction rate was faster for the SVA because of the enhanced flow which increased the evaporation rate and the stripping of the liquid film from the piston. At the low load, the liquid film on the piston crown was reduced (~0.12 mg). This was a result of the decreased spray penetration and faster evaporation with the flash boiling model. The film reduction rate was similar for both valve strategies but for the SVA was again faster. The engine walls were assumed to be dry before the spray impact which may affect the film formation and evaporation. However, the amount of predicted liquid film is important for improving the injector targeting and the valve strategies.
- When the emissions of the CO were investigated for λ=1.0 at 7.9 bar GMEP, it was found that greater percentage of various spherical volumes were occupied by a mixture that was richer than the stoichiometric. For the DVA case, the percentage of rich mixture during combustion was higher for DVA than SVA. In addition, the rich zones were richer for DVA (λ~0.96) than SVA (λ~0.99). Because of these reasons the production of CO is greater for DVA than SVA as seen in the experiments. In addition, due to the greater size of the rich zones and the enrichment, the unburnt hydrocarbons were increased when DVA was used. For the low load, more than the 80% of the spheres with up to 40 mm diameter, were in rich mixture when DVA was adopted and also the average lambda of these regions was λ=0.97. For SVA, for up to 40 mm spheres, the volume occupied by rich mixture was less than 60% and the average lambda was around λ=0.98. For bigger spherical volumes the percentage of the rich mixture decreased for DVA (50%-60%) and the average lambda increased (λ=0.98) and was closer to the stoichiometric. For SVA and bigger spheres than 40 mm diameter, their percentage in rich mixture increased to 70-85% with the average lambda in the range [0.97,0.98]. This increased rich mixture for the biggest volumes should contribute to the increased unburnt hydrocarbons of the experiments. However, the small differences between DVA and SVA in the simulations were also reflected in small differences in the experiments. Nonetheless, other factors such as the speed and the quality of the combustion play an important role which were not take account here.

- For the leaner cases of the higher load, the size of rich zones was reduced drastically for both valve strategies but for the DVA were greater than SVA which was again reflected to higher CO and THC in the experiments.
- To study the NO_x formation of the point of view of mixture preparation, a range of lambda which was considered as the worst case for NO_x production was assumed. This range was [1.05,1.15] considering that the highest NO_x production is seen for λ=1.1. for the high load and for λ=1.0, the percentage of the cylinder in that range is similar for both valve strategies but higher for DVA. For smaller volumes (up to 40 mm spheres) the percentage of was higher for SVA than DVA. As the NO_x is formed in the post flame gases, it is more probable to be formed within the 60mm to 80 mm (cylinder) spherical volumes. By diluting the mixture (global λ=1.1) and due to the high homogeneity of the SVA, 80% or more of all considered spheres were within the chosen range of lambdas. There was a great increase in NO_x from λ=1.0 to λ=1.1 and the increase was greater for SVA. Further dilution showed that the total cylinder has a greater volume of lean mixture in the chosen lambda range for SVA than DVA. However, for smaller volumes the DVA case has increased percentage of mixture in the lambda range. smaller volumes, the DVA case has increased percentage of mixture in the lambda range. For the lower load, the differences in the amount of mixture within the NO_x range was smaller and also the amount itself was smaller, which was inline with the experimental results.
- As temperature plays an important role in the NO_x production, it was calculated from the experimental in-cylinder pressure and then it was used in the Zeldovivh mechanism. It was found that for λ=1.0, the effect of temperature is very similar for both DVA and SVA. However, for the diluted cases, the increased temperature of the SVA was also attributing to the NO_x production.
- From the analysis of the mixture at various volumes within the cylinder, some basic conclusions can be drawn which showed that the mixture homogeneity is important for the emissions. Rich regions can produce high numbers of CO and THC. Lean mixtures at specific lambdas can increase the NO_x formation and can have a negative impact if the engine is running at lambdas near λ=1.1 and the homogeneity of the mixture is high.
- The above hypothesis was tested with a combustion simulation at λ=1.0 for DVA and SVA. There were some differences in the pressure traces between CFD and experiments, but the results were satisfactory without further tuning of the combustion

model. The faster heat release rate was a reason of the higher peak pressure of the DVA. The combustion showed increased CO production for DVA as seen in the experiments and the CO was produced at the locations of the rich mixture. The NO production was higher for the SVA even though the temperature was lower. The production was at the regions where λ was near 1.1.

Chapter 6

Differential Intake Valve Lift Studies

6.1. Introduction

In Chapter 4, it was showed that by deactivating one of the intake valves, the in-cylinder flow field and TKE were enhanced and as a result, the combustion duration was reduced, it allowed the engine to be run with high dilution and ultimately the thermal efficiency of the cycle was increased, and the fuel consumption was reduced. The enhanced in-cylinder flow however was associated with the increase in heat transfer from the trapped gas to the engine walls, especially at higher loads, which was limiting the aforementioned benefits. From these findings, it was concluded that an optimal level of charge motion exists where faster combustion will ultimately result in reduced fuel consumption without detrimental increases in heat transfer attributed to significant enhancements in charge motion or trapped residuals. The goal of this chapter is to investigate further the capabilities of the CVVL system with staggered intake valve lift in order to achieve the optimal level of charge motion for reduced fuel consumption and heat transfer. The study was focused on the 7.9 bar GMEP load at 1500 RPM as this was the operating point at which the use of SVA for equivalent levels of dilution did not give any benefit on fuel consumption. The same methodology as with the single valve actuation was followed, meaning that the valve lift profile of the one valve was kept the same for all the cases and it was the full lift, while the other valve was operated in either Early Intake Valve Closure (EIVC) or Late

Intake Valve Opening (LIVO) mode with various maximum lifts. More specifically, the maximum lift was from 1 mm up to 5 mm with 1 mm increment for both modes. The valve lifts as applied to the CFD model are shown in Figure 6.1 for the LIVO mode and Figure 6.2 for the EIVC mode. The simulation setup was the same as in Chapter 4 and 5 when fuel injection was included. The boundary and initial conditions were taken from the respective experiments. Due to the engine maintenance, the engine had to be rebuilt which resulted in slightly lower compression ratio (10.86:1) than that of the Chapters 4 and 5 (11:1). A DVA and an SVA case were rerun at the lower compression ratio for direct comparison with the EIVC and LIVO cases. The lower compression ratio resulted in slightly different boundary conditions, experimental and CFD results, however the trends and the conclusions are the same as in Chapters 4 and 5. Because the aforementioned benefits were significantly affected by the increase of the load, a detailed analysis was focused on the higher load of 7.9 bar GMEP, 1500 RPM.

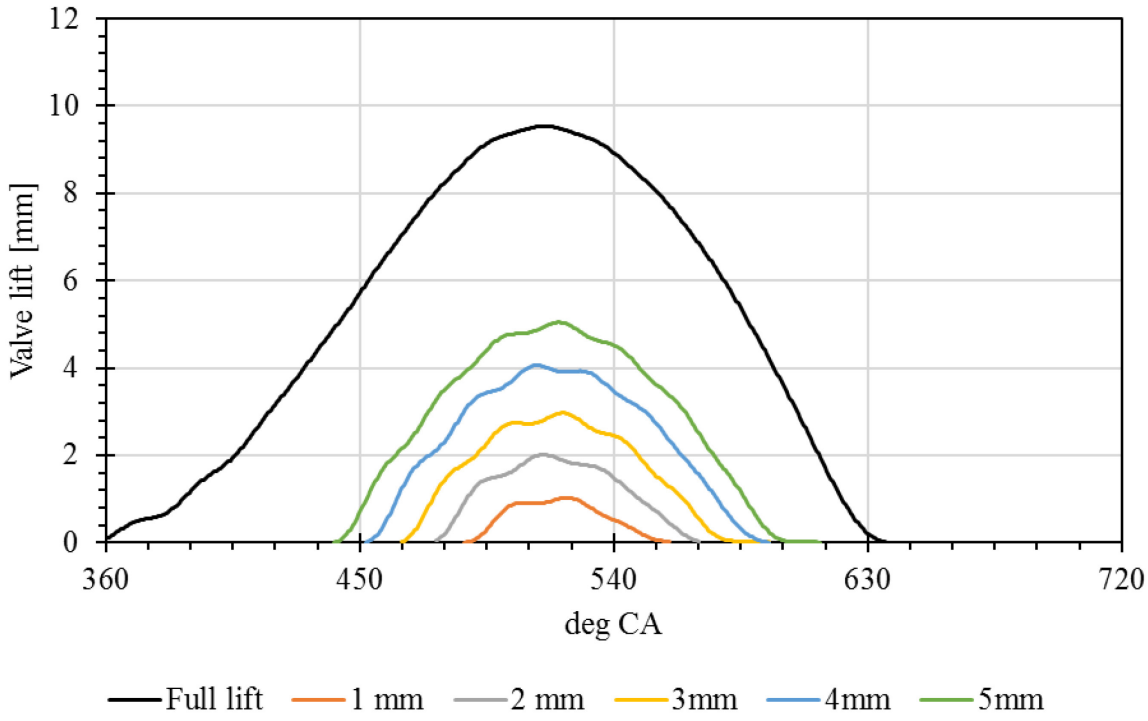


Figure 6.1 The five different LIVO valve lifts and the full lift as applied in the model

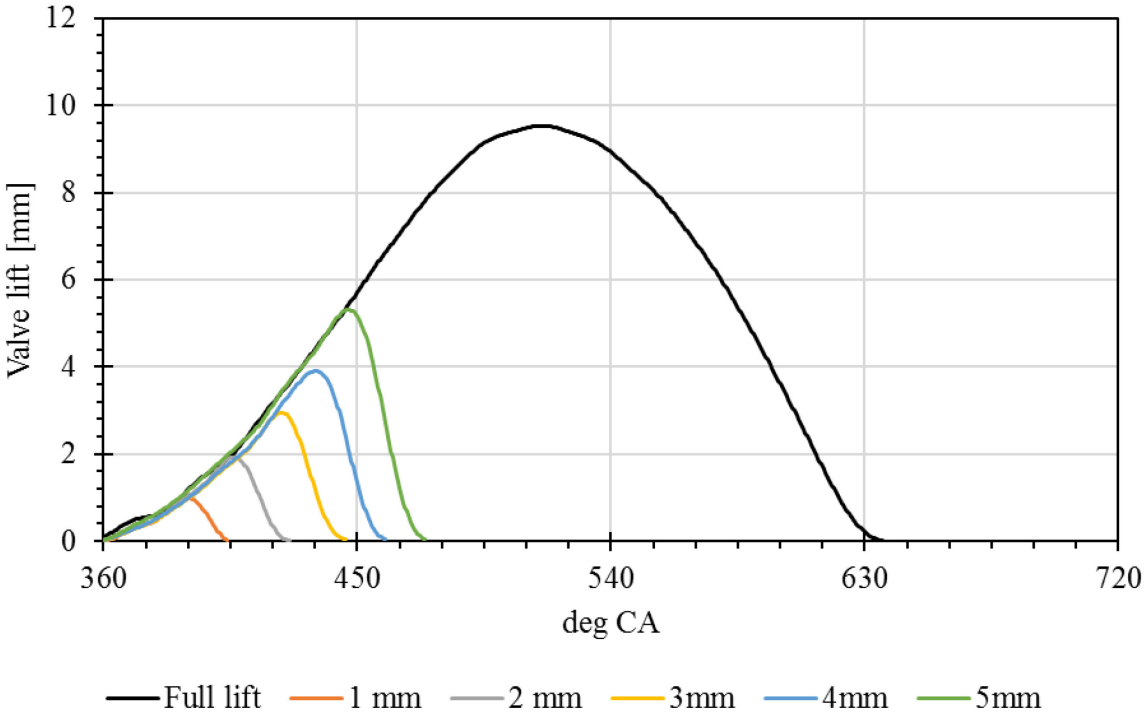


Figure 6.2 The five different EIVC valve lifts and the full lift as applied in the model

6.2. Experimental results

The experimental measurements of the combustion duration and more specifically, ignition to 10% MFB and 10-90% MFB are displayed in Figure 6.3 and 6.4 respectively. The Figure includes the DVA and SVA along with the durations of the five different lifts from LIVO and EIVC modes. It can be seen that when LIVO mode was adopted, the ignition to 10% MFB and the 10%-90% MFB were very similar for the SVA and for the staggered lift with up to 4 mm and much faster than the DVA. This was seen for all levels of dilution. When the LIVO mode with 5 mm maximum lift was adopted, the combustion was slower than the aforementioned cases but again much faster that the DVA case. When EIVC was adopted, the first two lift cases had similar combustion duration to the SVA case. When the maximum lift of EIVC was increased to 3 mm, the combustion duration was increased and it was between the DVA and SVA cases. Further increase of the maximum EIVC lift increased further the combustion duration and from 4 mm and above, the duration reached that of the DVA case or worse.

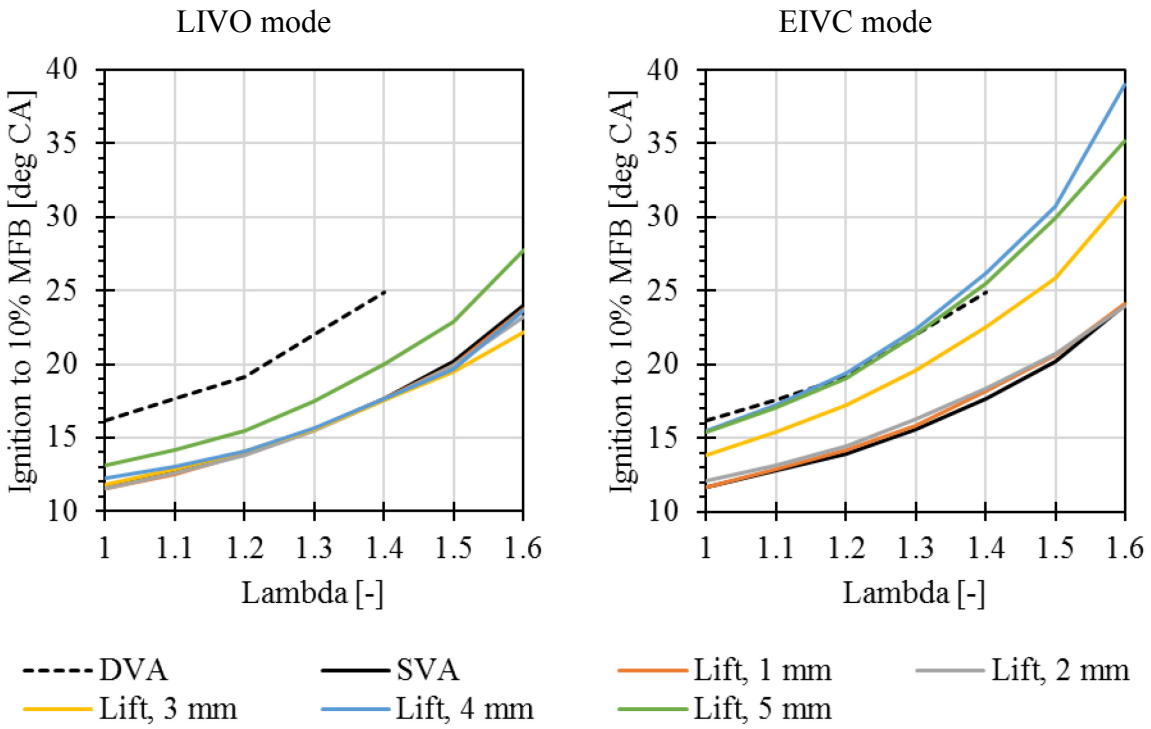


Figure 6.3 Comparison of the experimental ignition to 10% MFB duration between LIVO and EIVC mode. DVA and SVA are included

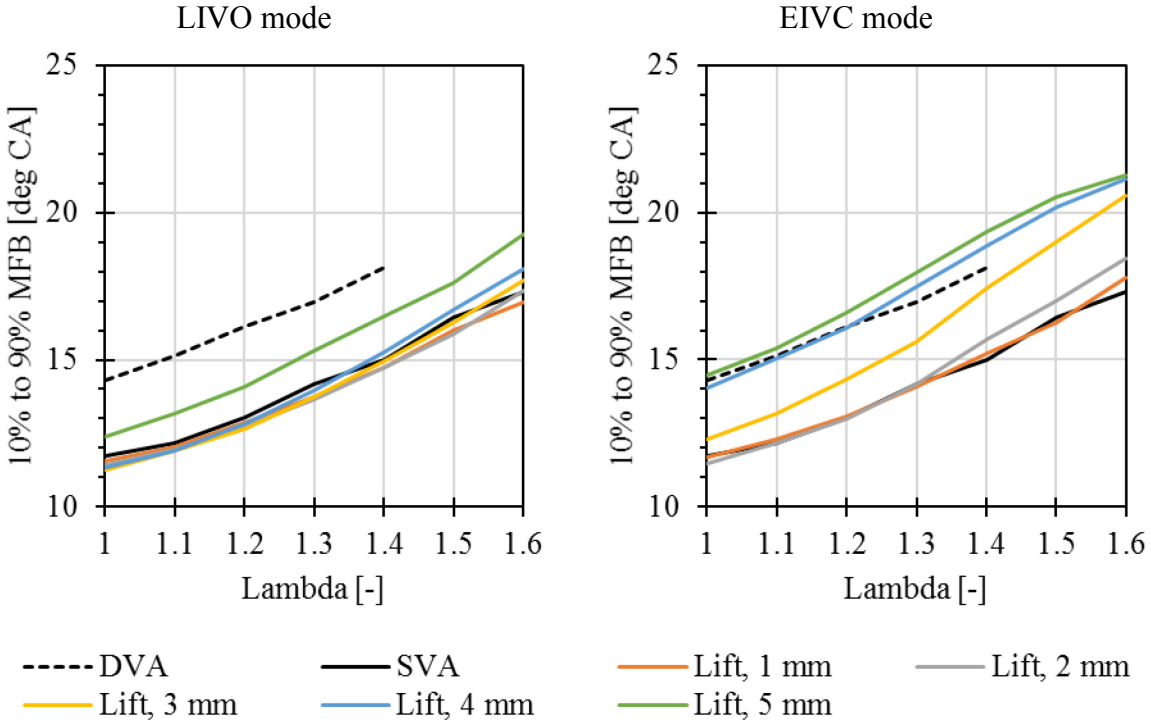


Figure 6.4 Comparison of the experimental 10% to 90% MFB duration between LIVO and EIVC mode. DVA and SVA are included

6.3. Late Intake Valve Opening (LIVO)

From the experimental measurements, it was seen that the combustion duration was very similar for the five cases which operated with LIVO mode. The in-cylinder pressure traces during combustion are very similar for the first four valve lifts, while for the highest valve lift case the speed of the combustion is lower than the other for cases which also resulted in reduced peak pressure (Figure 6.5). Furthermore, the reduced speed of the combustion was seen from the ignition timing which was retarded for lower valve lifts in order to achieve 50% mass fraction burnt at 8 degrees after TDC. For the 1 mm maximum lift the ignition was 9.24 degrees CA before TDC and for the 5 mm lift the ignition was 11.61 degrees CA before TDC.

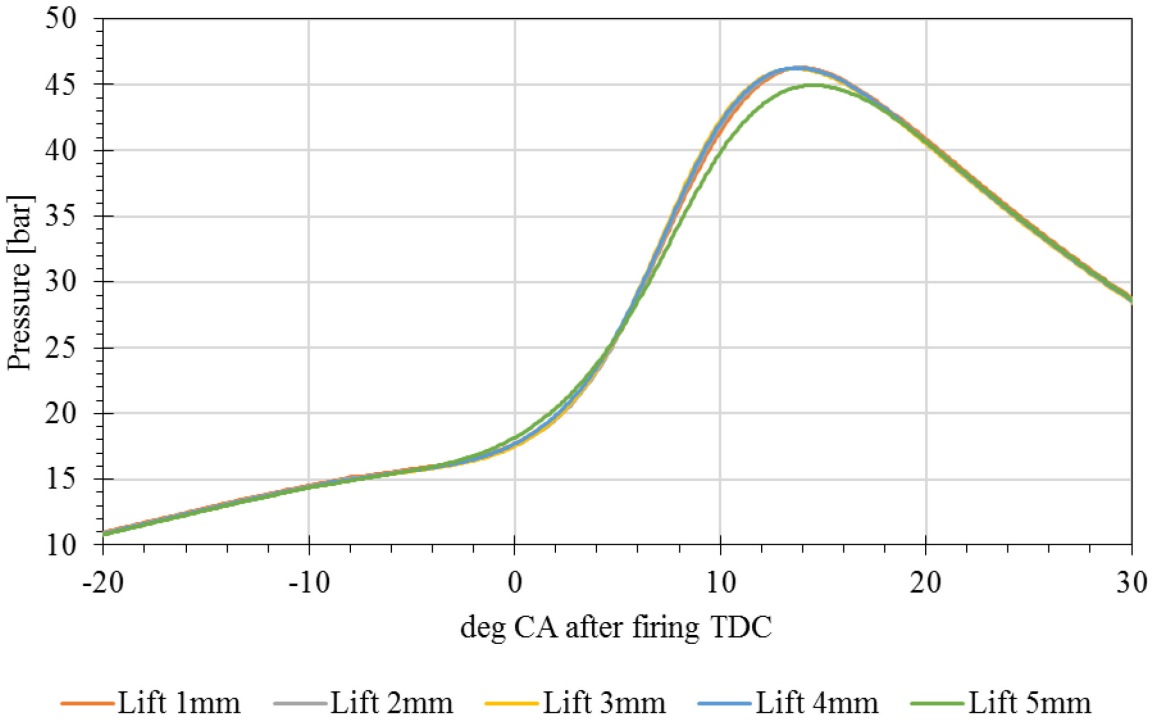


Figure 6.5 Experimental in-cylinder pressure trace during combustion for the five different LIVO cases

6.3.1. In-cylinder flow properties

Firstly, the simulations were run without fuel injections to investigate the heat transfer, the flow field and residuals concentration during the cycle and at ignition timing without the effect of spray. The in-cylinder flow quantities of velocity, tumble, swirl and turbulent kinetic energy were studied for the five lifts and compared against the dual and single valve actuation. Again, the analysis was focused from the IVO until firing TDC. From Figure 6.6 it is clear that for the intake stroke and up to 90 degrees after gas exchange TDC (450 deg CA in the figure), the in-

cylinder average velocity for all LIVO lifts was the same as the SVA. This behaviour was expected as the second valve opens at mid-intake stroke for the 5 mm lift or later in the cycle for lower maximum lifts. Generally, the in-cylinder velocity of the LIVO mode is the same as the SVA until the second intake valve opening. After the opening of the second valve, the in-cylinder average velocity diverges from the SVA behaviour and it is reduced, however the decreasing trend up to TDC is the same. The decrease of the in-cylinder velocity comes from the weakening of the valve jet during the time at which both valves are open and resulted in the increased intake throat area. As the maximum LIVO lift increased, the throat area was also increased resulting in further decrease of the in-cylinder velocity. Table 6.1 shows the velocity reduction of the five different lifts from the SVA and the ratio LIVO / DVA velocity, around ignition (10 degrees before firing TDC). The maximum reduction is 24% for the 5mm LIVO mode while from SVA to DVA the reduction is 67.5%.

Lift	Reduction from SVA	LIVO / DVA
SVA	-	3.1
1 mm	2.1 %	3
2 mm	3.8 %	2.96
3 mm	10.3 %	2.75
4 mm	16.1 %	2.58
5 mm	24.0 %	2.34
DVA	67.5 %	1

Table 6.1 Velocity reduction of the five different lifts from the SVA and the ratio LIVO / DVA velocity at ignition

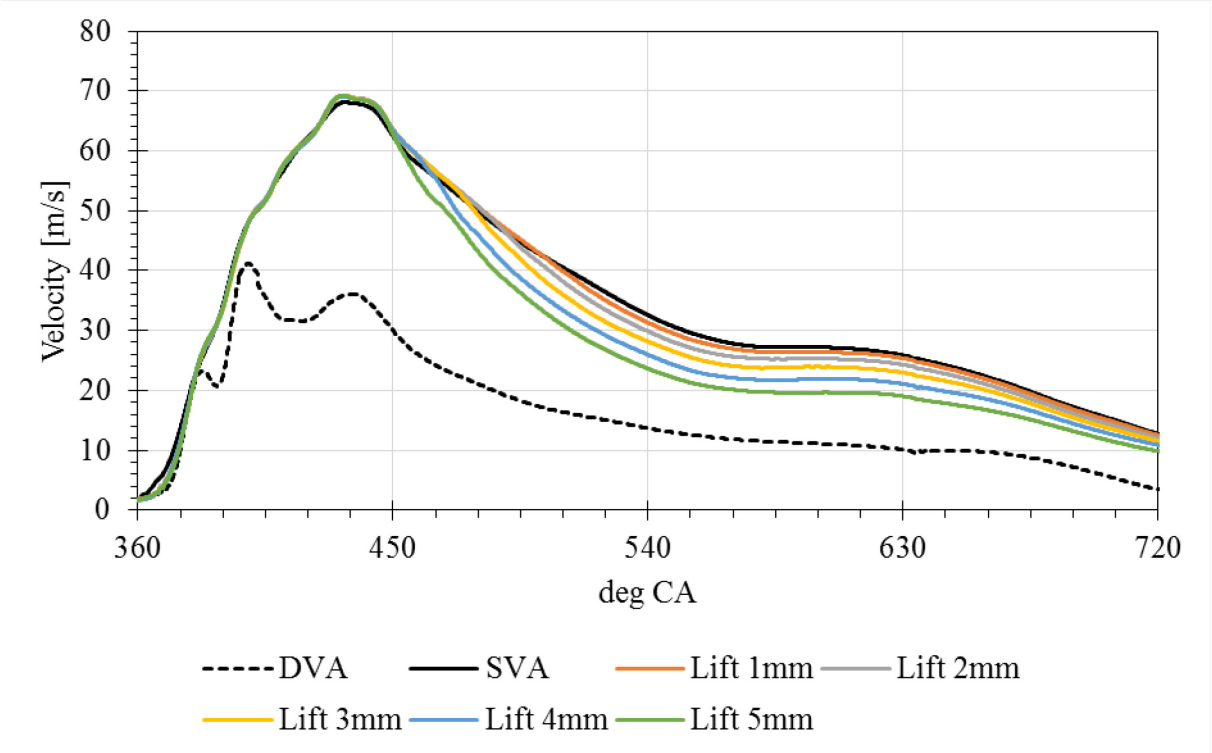


Figure 6.6 In-cylinder velocity magnitude for DVA, SVA and the five different LIVO lift cases

Due to the opening of only one valve at the beginning of the intake stroke for the LIVO mode, swirl motion was developed in the cylinder (Figure 6.7), the same as it was observed during the single valve actuation. The magnitude of the swirl is maintained the same as the SVA mode until the opening of the second valve. After that, the magnitude drops as the in-cylinder velocity decreases and with higher lifts, the swirl is reduced. At the end of the cycle however, a strong swirl motion was still preserved even for the highest LIVO lift. The percentage reduction of the swirl motion from the SVA around ignition (~10 degrees CA before firing TDC) is shown in Table 6.2. The maximum reduction was 23.3% and was observed with the 5 mm maximum lift.

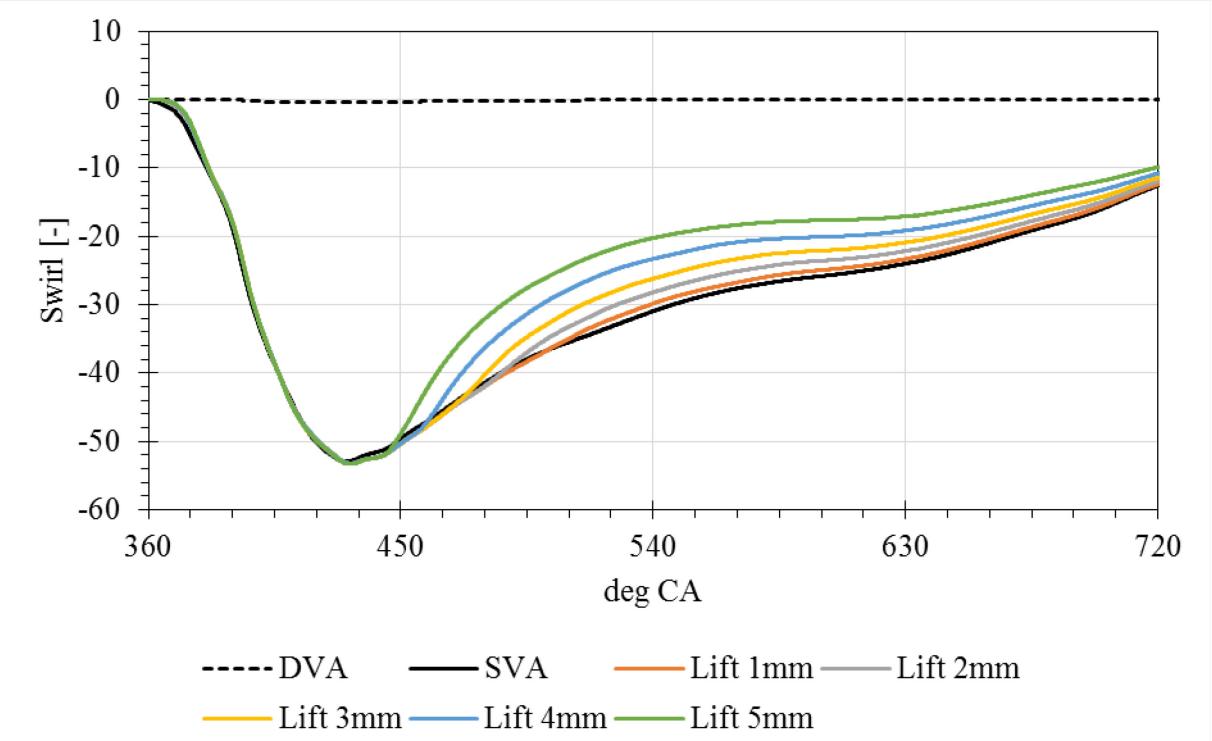


Figure 6.7 Swirl ratio for DVA, SVA and the five different LIVO lift cases

	1mm	2mm	3mm	4mm	5mm
Reduction from SVA	2.0%	5.6%	9.7%	15.3%	23.3%

Table 6.2 Percentage reduction of the swirl ratio from SVA at ignition for the LIVO mode

The tumble motion (Figure 6.8) was also preserved during the operation of the one valve with LIVO mode due to the geometry of the intake ports which promoted this flow as it was explained in a previous chapter. Until the opening of the second valve, the tumble followed the behaviour of the single valve as expected. While the second valve should promote the tumble motion, the weakening of the valve jet and consequently the in-cylinder velocity, the tumble motion was also weakened especially during the compression stroke. As the maximum lift of the second valve was increased, the magnitude of the tumble motion was reduced. The general behaviour however, was closer to the SVA due to the strong swirl motion which was established from the beginning to the intake stroke.

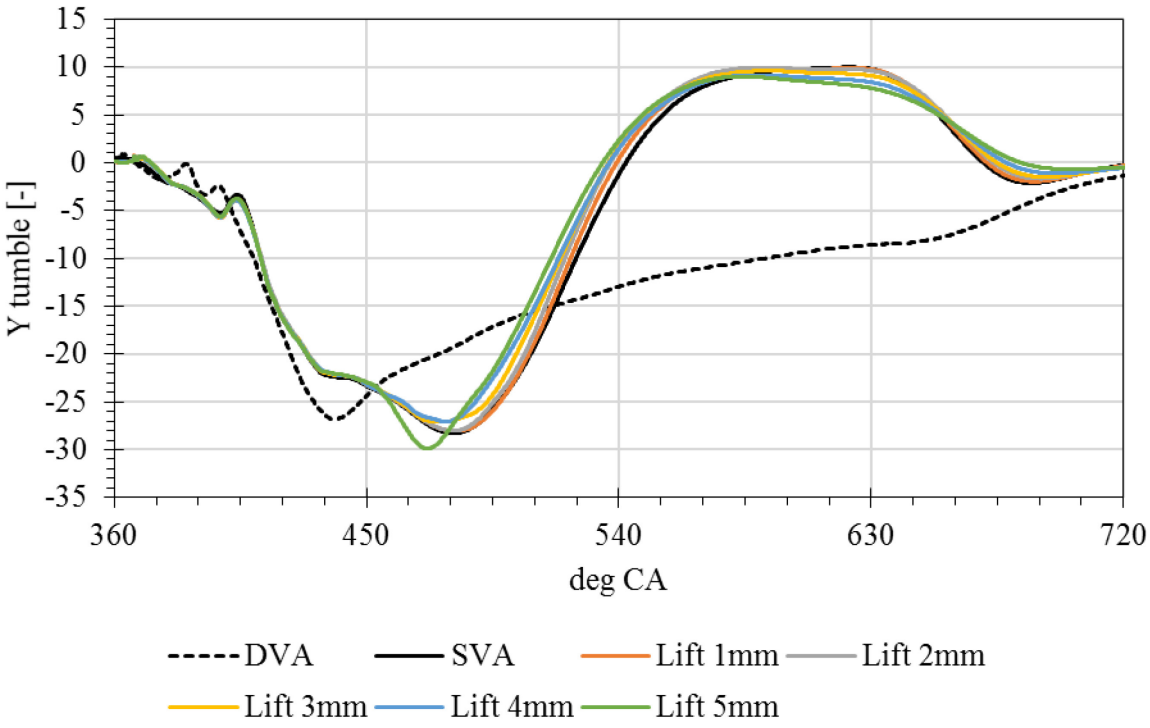


Figure 6.8 Tumble ratio for DVA, SVA and the five different LIVO lift cases

As it was discussed in Chapter 4, one of the important aspects of the SVA was the increase of the in-cylinder turbulent kinetic energy which resulted in faster combustion and the increased dilution tolerance of the engine. When the second valve was operated at LIVO mode, the same behaviour as the velocity was observed for the in-cylinder average turbulent kinetic energy and it can be seen in Figure 6.9. For all LIVO lifts, the in-cylinder average TKE was the same as the SVA until the opening of the second intake valve. After that, the TKE for the LIVO lifts was lower than the SVA but always higher that the DVA. Table 6.3 shows the reduction of the average TKE from the SVA case to the LIVO or DVA case and the ratio LIVO / DVA at ignition. It is clear that while there is as significant reduction of TKE as the maximum lift increases, for the 5mm lift case, a ~10% more TKE can be achieved.

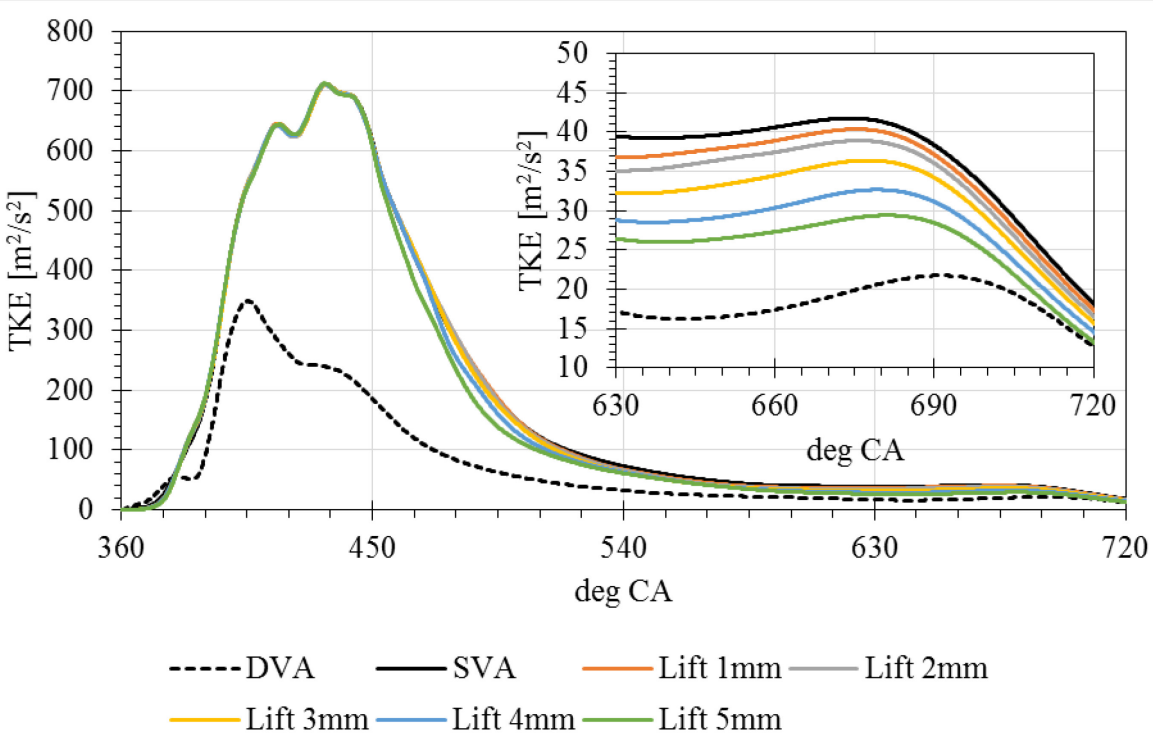


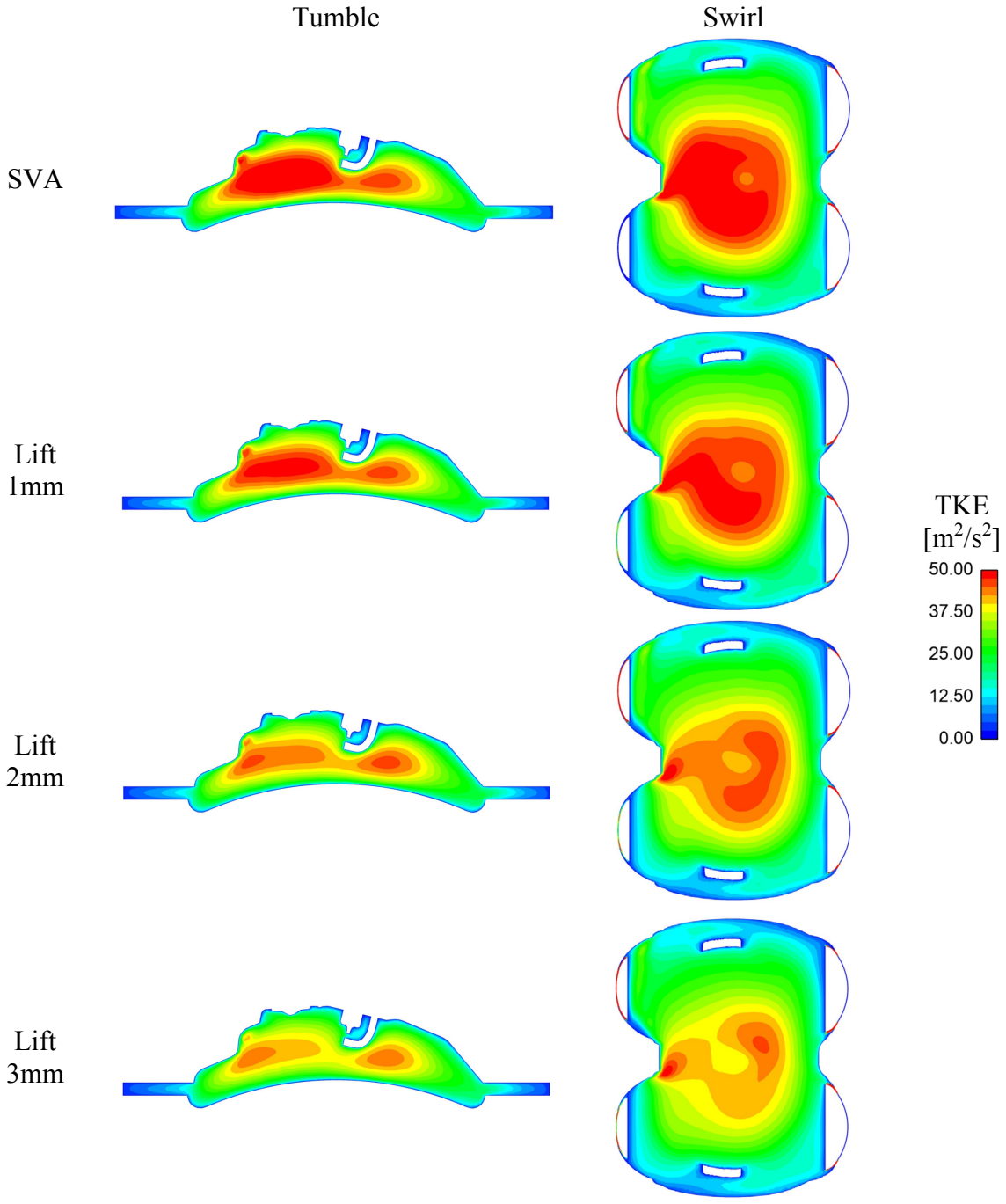
Figure 6.9 Turbulent kinetic energy for DVA, SVA and the five different LIVO lift cases with a zoom on the compression stroke after IVC

Lift	Reduction from SVA	LIVO / DVA
SVA	-	1.47
1 mm	6.1%	1.38
2 mm	7.3%	1.37
3 mm	14.0%	1.26
4 mm	20.6%	1.17
5 mm	26.7%	1.08
DVA	32.1%	1

Table 6.3 TKE reduction of the five different lifts from the SVA and the ratio LIVO / DVA velocity at ignition

While the in-cylinder averaged TKE is increased, the location and the volume of the high intensity TKE around ignition (10 degrees CA before TDCf) is also important for the combustion metrics. For this reason, the contour plots of TKE for the five staggered lifts in the tumble and swirl planes was studied and are presented in Figure 6.10. There is a significantly larger and more intense area of TKE under all LIVO cases compared to DVA that assists flame

propagation. While with the increase of the maximum valve lift, there is a reduction of TKE, the intense area is comparable to that of the SVA case which is spread radially and axially in the cylinder in a greater extent to that of the DVA. In addition, the location of the intense TKE is more favourable for all LIVO cases as it is enclosing the spark plug contrary to the DVA, in which the region of highest TKE is situated below the spark plug and slightly away from it, which will have a detrimental effect on flame propagation. The experiments also showed that for lifts up to 4 mm the combustion duration was very similar to that of the SVA and only the 5 mm lift case was slightly slower but again close to the SVA.



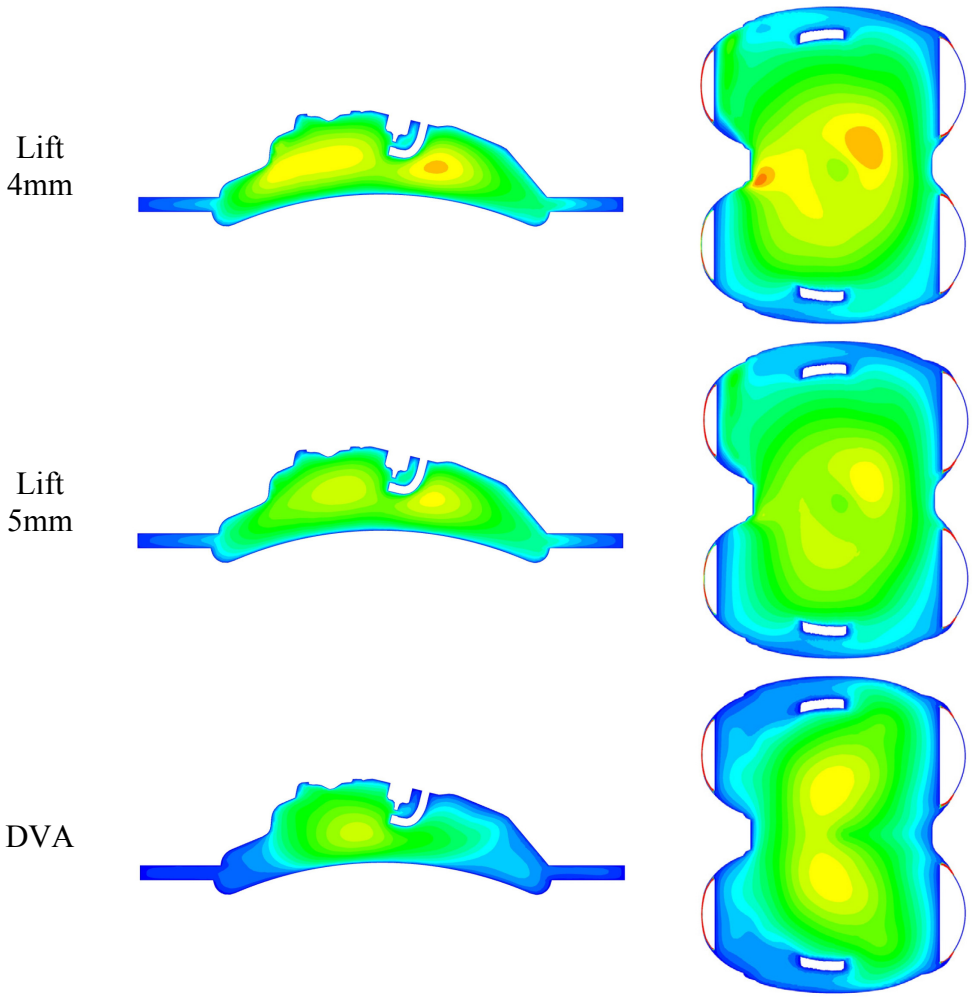


Figure 6.10 Spatial distribution of TKE for DVA, SVA and the five different LIVO lift cases for the tumble and swirl planes at ignition (10 degrees CA before TDCf)

It was observed that during the single valve actuation the average in-cylinder temperature during compression was increased about 25°C when compared with the dual valve actuation. This was one of the two main reason of the increased heat transfer when SVA was adopted. When the one valve was operated with the LIVO mode, the average in-cylinder temperature was following that of the SVA case irrespective of the maximum lift of the LIVO. The differences between LIVO cases and SVA are about 1°C. This behaviour can be explained with the amount of trapped mass during the intake and compression strokes. Similar to the SVA, for the LIVO cases a lower amount of fresh air is induced to the cylinder and thus, a higher amount of hot residuals is retained in the cylinder which increase the temperature. While there is a fraction of increase of the induced fresh air with the higher LIVO lifts, this is not enough to cool the mixture. At IVC, all the cases have the same trapped mass (there is 3.4% difference between the highest and lowest values which are for SVA and the 5mm lift respectively). From

these results it can be seen that the applied mechanism of the staggered lift with the LIVO mode cannot reduce the in-cylinder temperature.

The other important aspect which was discussed in the previous chapter was the increase of the heat transfer due to the enhanced charge motion and increased in-cylinder temperature when adopting single valve actuation. It has been seen that the adoption of the LIVO mode resulted in a reduction of the in-cylinder flow magnitude which should have an effect on the reduction of the heat transfer (Figure 6.11). It was also seen that for all the LIVO cases, the in-cylinder average temperature is at the same level as the SVA meaning that this factor for the increased heat transfer could not be affected by the LIVO mode for the cases investigated here (maximum lifts up to 5mm). It is important to investigate the heat transfer change when adopting the LIVO mode for one of the intake valves. The results showed that for all LIVO cases and the SVA the heat transfer from the gas to the engine walls starts 120 degrees CA before firing TDC while for the DVA, the heat transfer starts at around 100 degrees CA before firing TDC. This is due to the fact of the lower gas temperature with DVA. From about 90-80 degrees CA before firing TDC, the heat transfer of the LIVO cases started to deviate from the heat transfer of the SVA. There is a reduction of heat transfer as the maximum lift of the LIVO mode increases. For the lifts investigated here, at 5 degrees CA before firing TDC, where the maximum heat transfer occurred, the heat transfer reduction from SVA up to the 5mm lift case, the reduction is relatively linear. This trend follows the trend of the velocity reduction. With the 5mm case, the reduction in heat transfer is 15% in terms of absolute numbers. However, if this reduction is calculated in relative terms meaning that from the worst case of SVA (-4642 W) and the best case of DVA (-3012 W), the heat transfer with the 5 mm max lift is (-3944 W), the reduction is 43%. The relative term is calculated by (SVA-LIVO)/(SVA-DVA). The rest of the differences can be seen in Table 6.4

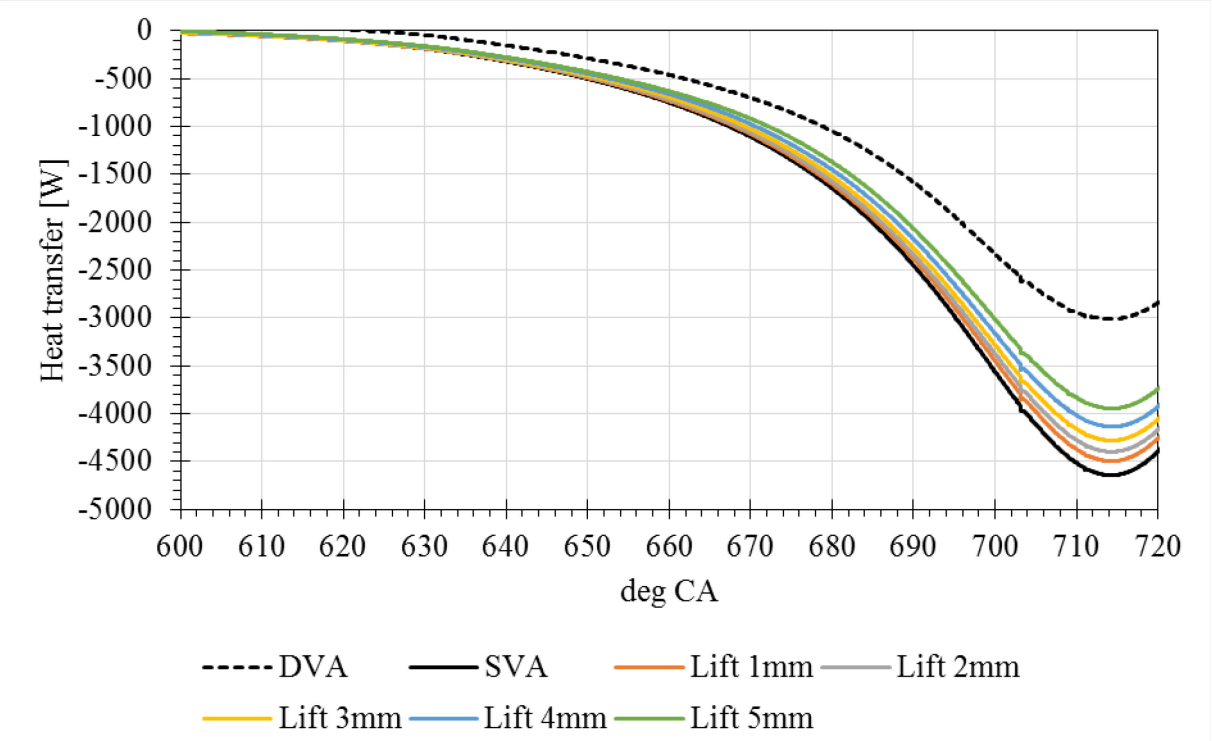


Figure 6.11 Heat transfer from the gas to the walls for DVA, SVA and the five different LIVO lift cases

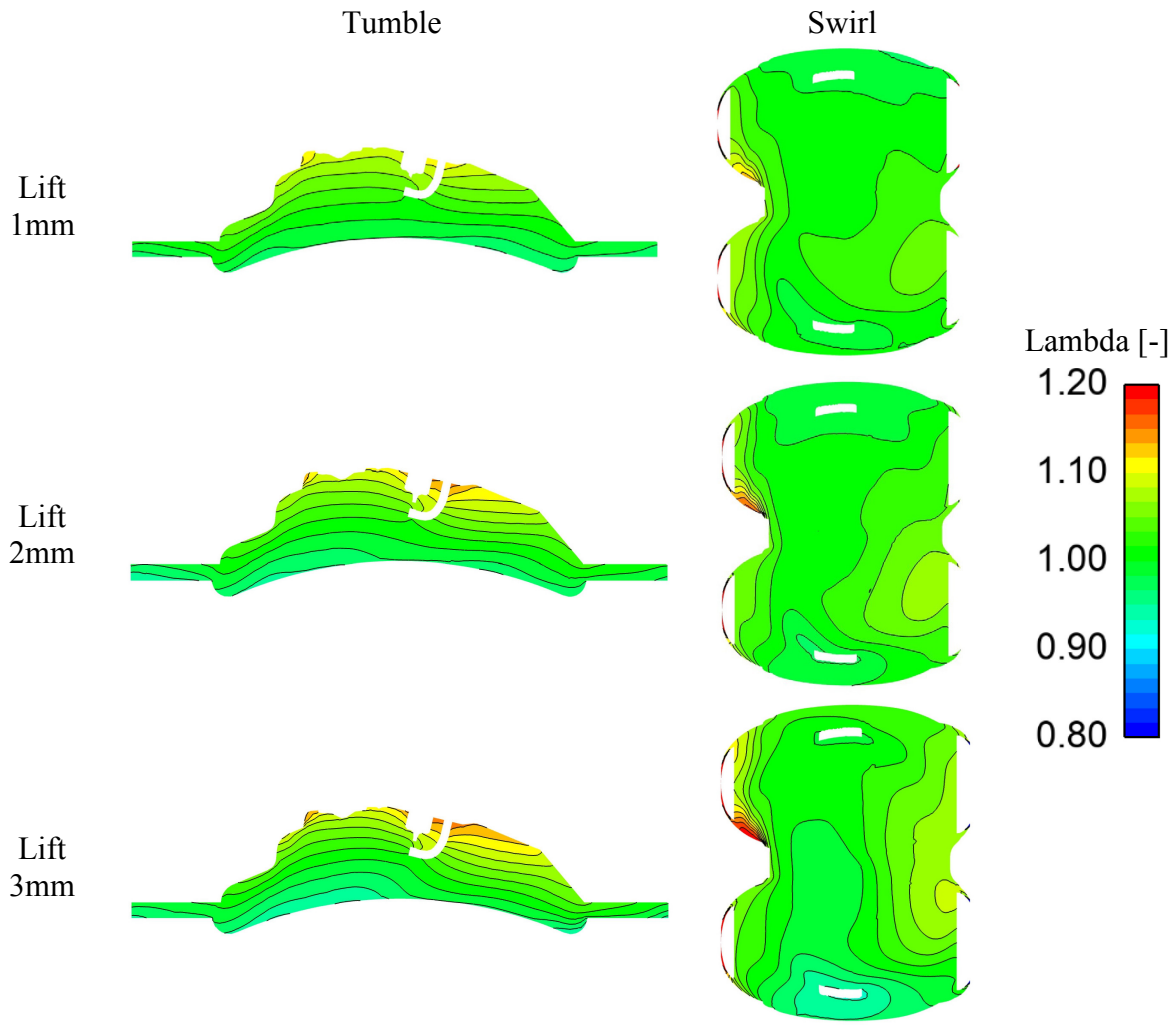
Lift	Reduction from SVA	Relative reduction
SVA	-	0
1 mm	3.2%	9.1%
2 mm	5.3%	15.1%
3 mm	7.8%	22.3%
4 mm	10.9%	31.1%
5 mm	15.0%	42.8%
DVA	35.1%	100%

Table 6.4 Heat transfer reduction of the five different LIVO lifts from the SVA and the relative reduction with respect to DVA and SVA

6.3.2. Mixture Preparation

After the investigation of the in-cylinder properties for the five different differential valve lifts, the air-fuel equivalence ration was studied. The Lambda contour for the five different LIVO cases near ignition (10 degrees CA before TDCf) at the tumble and swirl views are displayed in Figure 6.12. Firstly, when the tumble plane was studied, it was clear that the axial stratification, as seen for the SVA, was maintained however, by increasing the maximum lift

of the staggered valve, the homogeneity was reduced and leaner mixture was produced near the head and richer mixture near the piston. Moreover, it was evident that by increasing the maximum lift of the staggered valve, the homogeneity started to be reduced and a rich region was formed at the +Y sector of the cylinder when the swirl plane was observed. Moreover, this region was also changing location slightly and it was moving anticlockwise when the maximum lift was increased. This is more evident for the 3mm to 5mm lifts. Generally, the very high swirl motion which was maintained through all the investigated lifts, dictated the mixture formation which was always similar to the SVA pattern.



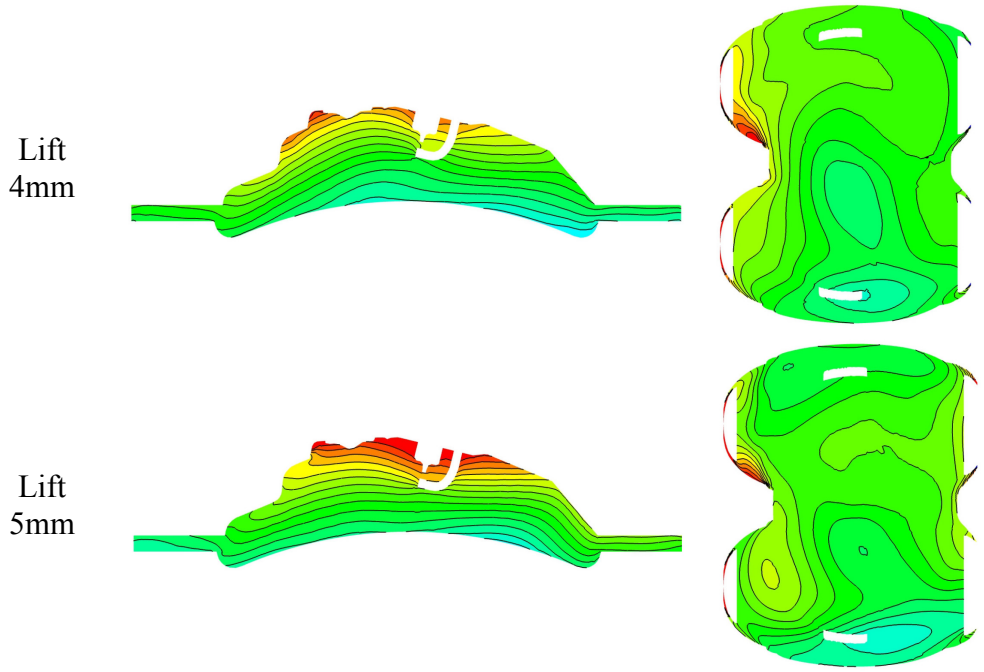


Figure 6.12 Spatial distribution of Lambda for DVA, SVA and the five different LIVO lift cases for the tumble and swirl planes at ignition

To quantify the change in the homogeneity, the Homogeneity Index for the five lifts was calculated and it is shown in Figure 6.13. In the same figure the HI for DVA and SVA were also included. During compression, by increasing the maximum lift the homogeneity was reduced and it was below the SVA case but always above DVA. For the 1mm lift however, the homogeneity was very similar to the SVA near ignition (10 degrees before TDC and later). The HI for the 5mm lift at ignition was the lowest and it was 0.93 which is improved by 2.5% compared to the DVA.

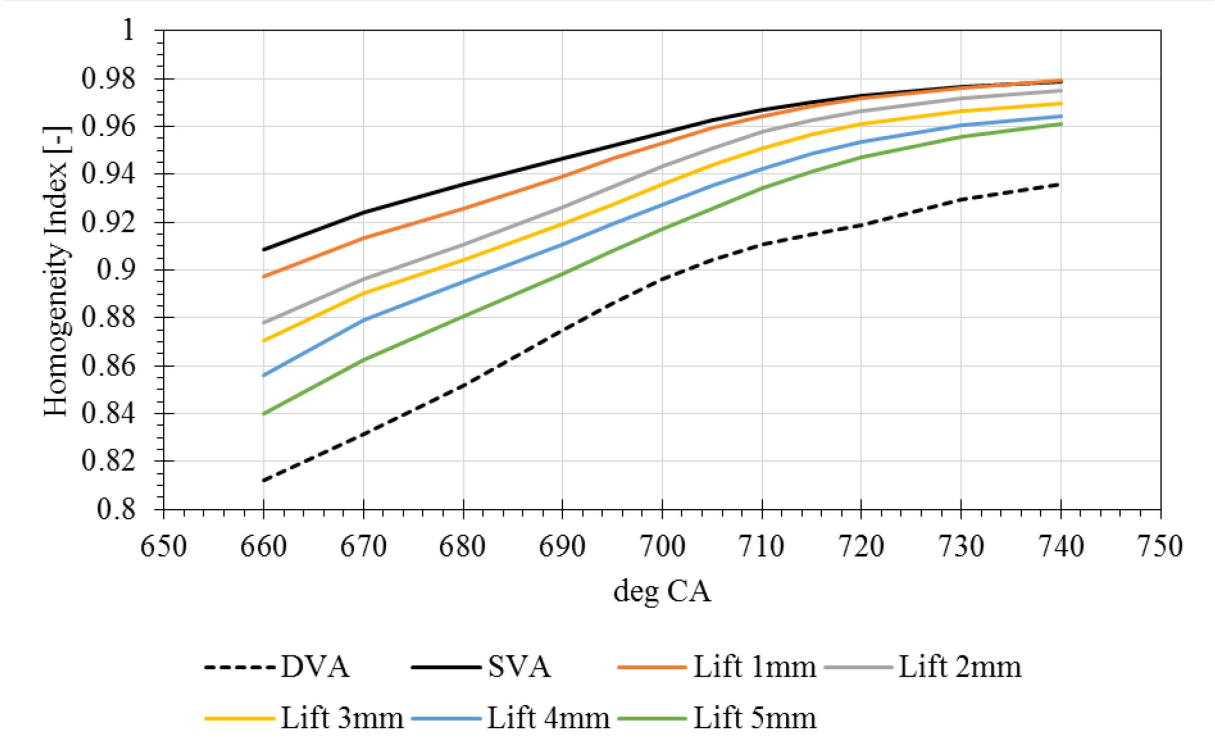


Figure 6.13 Homogeneity Index for DVA, SVA and the five different LIVO lift cases

The liquid film was studied for the five different LIVO lifts. The simulations showed that there was no significant difference on the accumulated mass on the piston for the five lifts (Figure 6.14). In addition, the peak film mass is comparable to the SVA peak film mass (~0.48 mg). There is a difference on the maximum liquid mass between the first three lifts (1mm-3mm) and the last two lifts (4mm and 5mm) which is 5%. The event of the fuel injection occurred during the single valve opening when the maximum lift was up to 3 mm and thus the spray was impinging on the piston while having the same in-cylinder flow. For the other two lifts, the end of the injection occurred at the time near the opening of the staggered valve which resulted in that slight difference of the film mass due to the reduction of the swirl motion. However, even with this small difference, as most of the fuel injection event was under the same or very similar in-cylinder flow, the liquid film pattern was also very similar in all five cases and they were also very similar to the SVA liquid film. The difference between the liquid film patterns 20 degrees after SOI for the 1 mm and 5 mm lift cases can be seen in Figure 6.15.

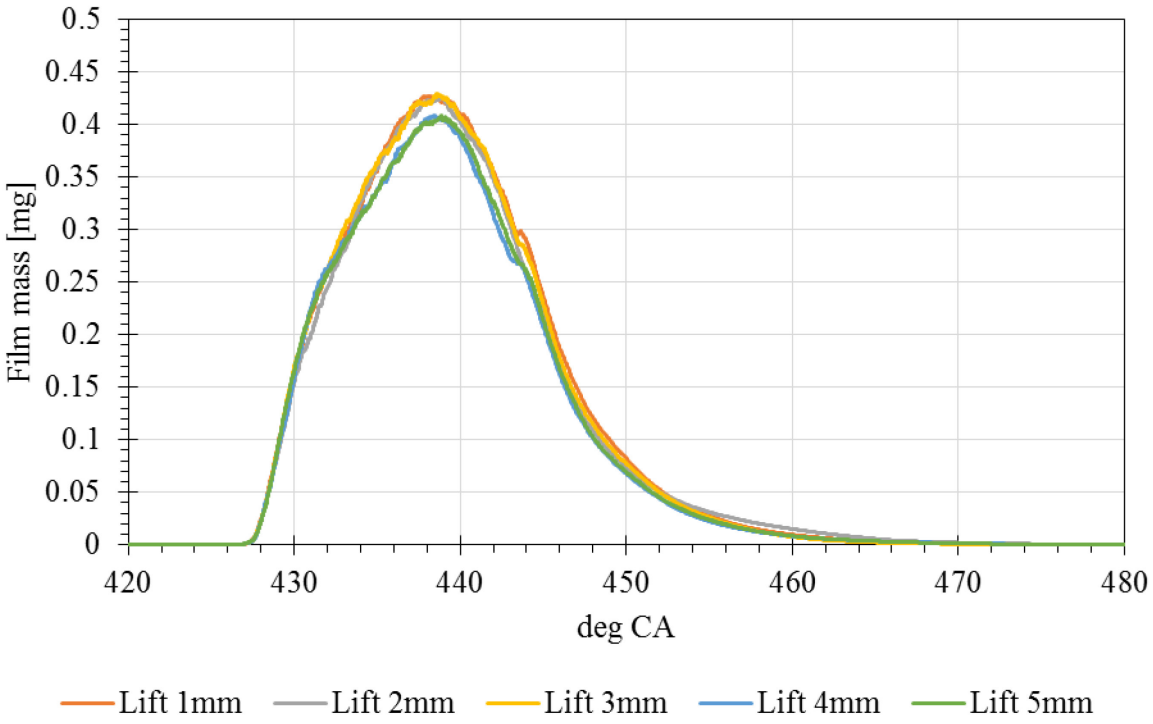


Figure 6.14 Total film mass on the piston versus crank angle for DVA, SVA and the five different LIVO lift cases

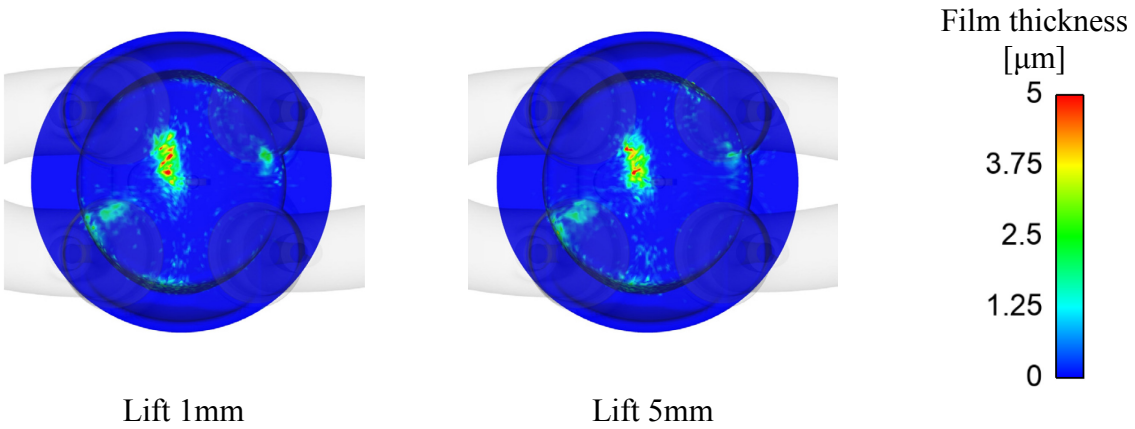


Figure 6.15 Film thickness on the piston at maximum accumulated film mass for 1 mm and 5 mm lift LIVO cases

6.3.3. Emissions

Lastly, the emissions of CO, NO_x and unburnt hydrocarbons were investigated for this load and for the five different valve lifts. The experimental emissions of CO revealed that at λ=1.0 there is an increase of CO production from SVA which has the lowest CO through the increase of the maximum lift of the staggered valve and up to DVA. For higher Lambdas the differences between the different maximum valve lifts was minor. Similarly, there was an increase of the

unburnt hydrocarbons with the lowest values being produced by SVA and the highest with DVA and the increase of the THC was following the increase of the maximum valve lift. Lastly, for the NO_x at λ=1.0 the differences between the various staggered lifts was minor but the trend (if any) throughout the lambda range was a reduction with increased valve lift. The experimental results can be seen in Figure 6.16.

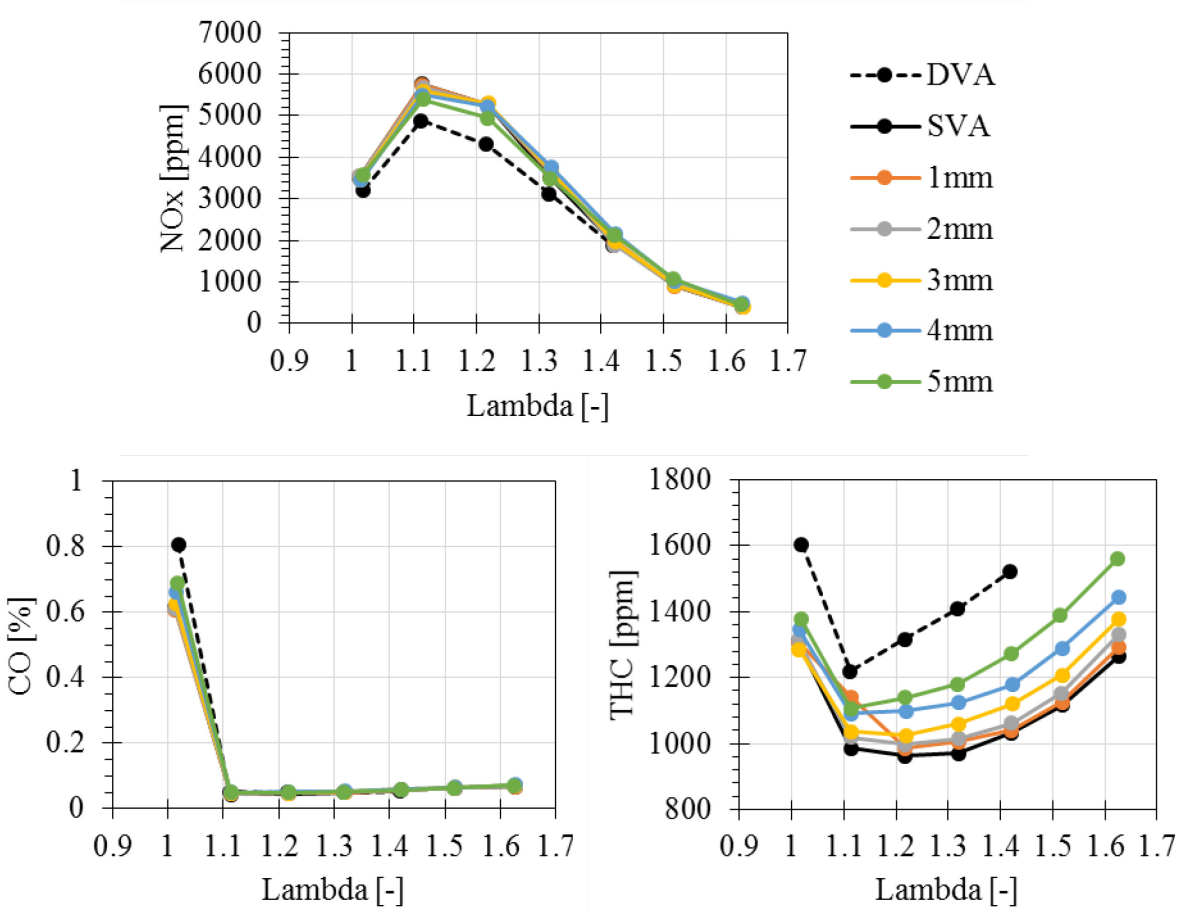


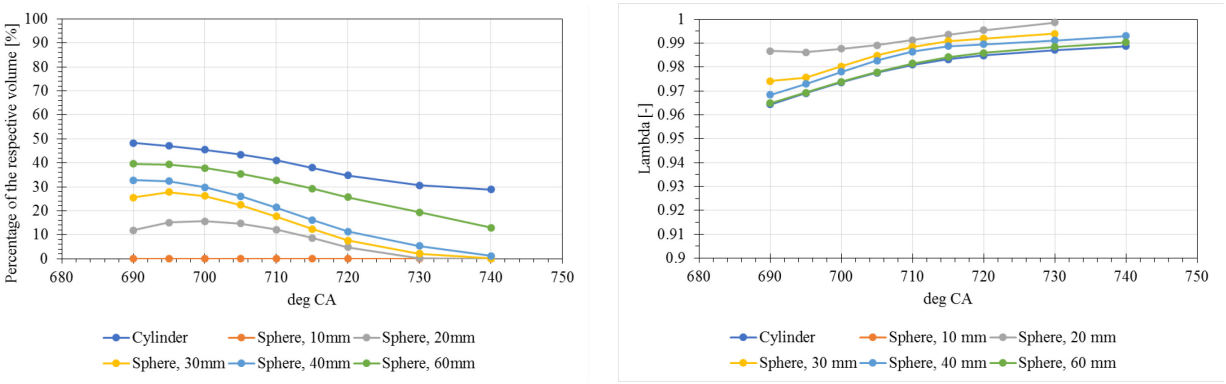
Figure 6.16 Experimental data of NO_x, CO and THC for DVA, SVA and the five different LIVO lift cases with various dilution

The same approach as in the previous chapter was applied for all three emissions. The air-fuel equivalence ratio within the cylinder and five different sizes of spheres was studied. For the CO and THC, the rich regions (λ<1) and their average lambda were identified and the trends from the five cases were studied (Figure 6.17). It was found that when the maximum valve lift of the staggered valve was increased, the amount of the rich region was increased in the whole cylinder. For the 1mm lift, the percentage of the cylinder with rich mixture after ignition (10 degrees CA before TDC) was 30%-40% depending on the crank angle. For the 5mm lift case, the cylinder was 35%-45% filled with rich mixture. The average lambda of the rich mixture for the 1mm lift was about 0.98-0.99 while for the 5 mm lift was 0.96-0.97. Because the rich

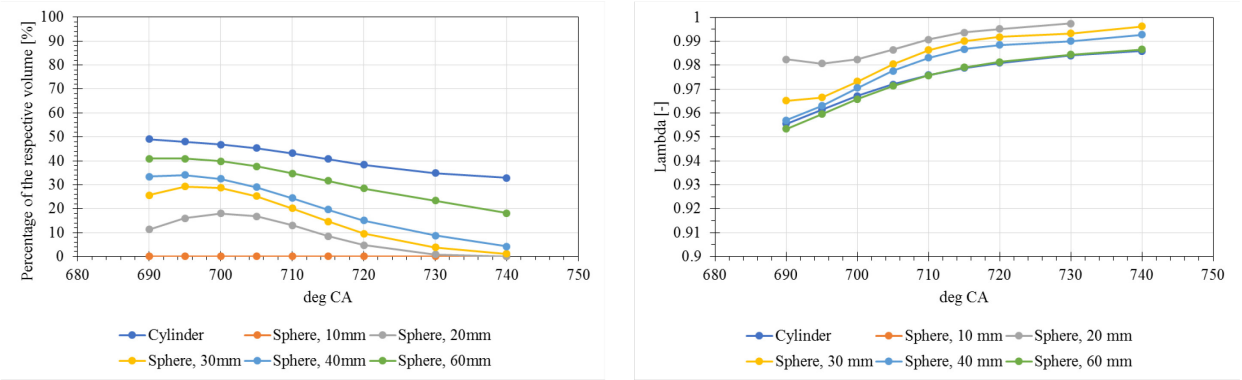
mixture was located near the piston, for the 10 mm sphere, no rich mixture was detected for the cases with better homogeneity. For bigger spheres however, there was an increase with increased valve lift. In addition, in each respective control volume (sphere), there was a reduction of the mean lambda of the rich mixture. From the above results it can be said, that the increase of the rich zones and also the reduction of the average lambda of these zones with the increase of the valve lift, contributed to the increase of the CO and THC.

Percentage of the interrogating spherical volumes occupied by a mixture with λ<1.0

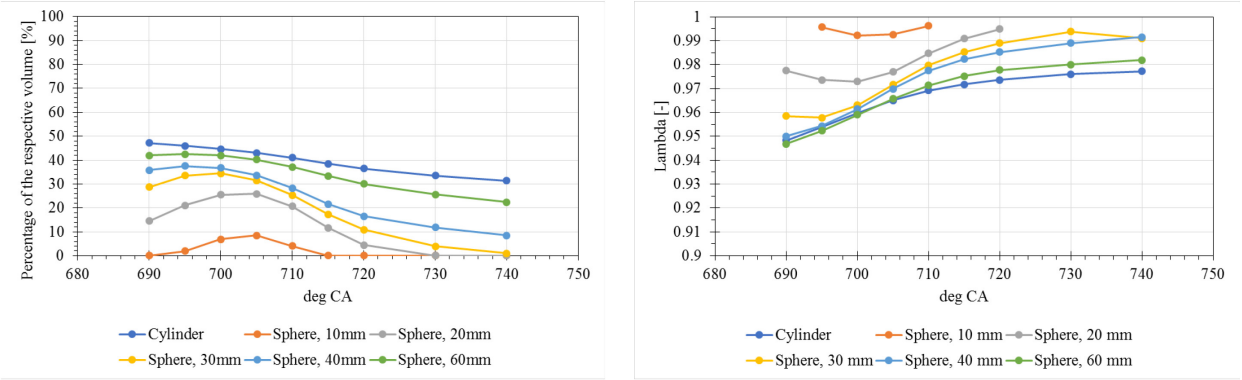
Average Lambda of the lambda zones below λ=1.0 for various interrogating spherical volumes



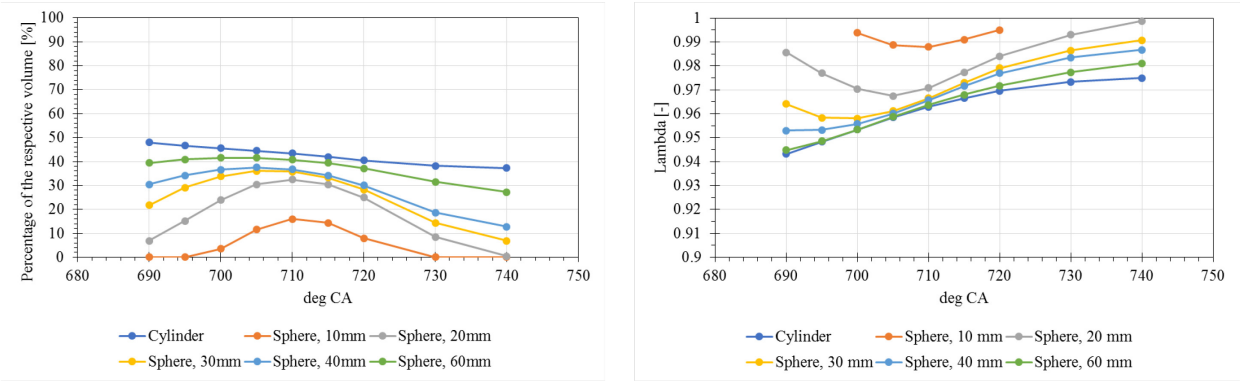
Lift 1mm



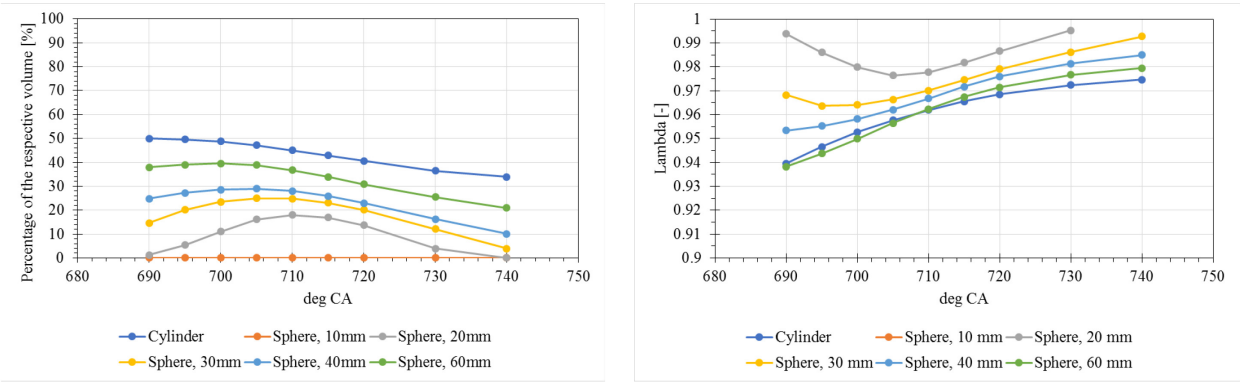
Lift 2mm



Lift 3mm



Lift 4mm



Lift 5mm

Figure 6.17 Percentage of the interrogating spherical volumes occupied by a mixture with λ<1.0 and Average Lambda of the lambda zones below λ=1.0 for various interrogating spherical volumes for the five different LIVO lift cases

When the range of lambda [1.05,1.15] was investigated for the NO_x formation (Figure 6.18), the whole cylinder for the 1mm lift at ignition was filled by about 20%-30% of mixture within the aforementioned range and the higher percentages were seen for higher lifts. The same trend of increased percentage when the maximum lift was increased, was seen for the 60 mm sphere. For the 20 mm and up to 40 mm spheres, the percentage within the lambda range was within 40% and 50% for the lifts 1mm to 4 mm. For the 5 mm lift case, the percentage of these spheres increased to up to 65% for the 20 mm sphere and ~55% for the 40mm sphere 15 degrees after TDC. From these data, it can be said that because the percentages varied around the 50%, the differences in NO_x are small as the experiments revealed. It has to be reiterated here that the no other parameters were studied with this approach, such as the temperature distribution, the flame development etc. and only the perspective of mixture formation was investigated. In addition, the assumption of the range of lambda [1.05,1.15] can introduce errors but it was chosen for a generalised approach of all cases.

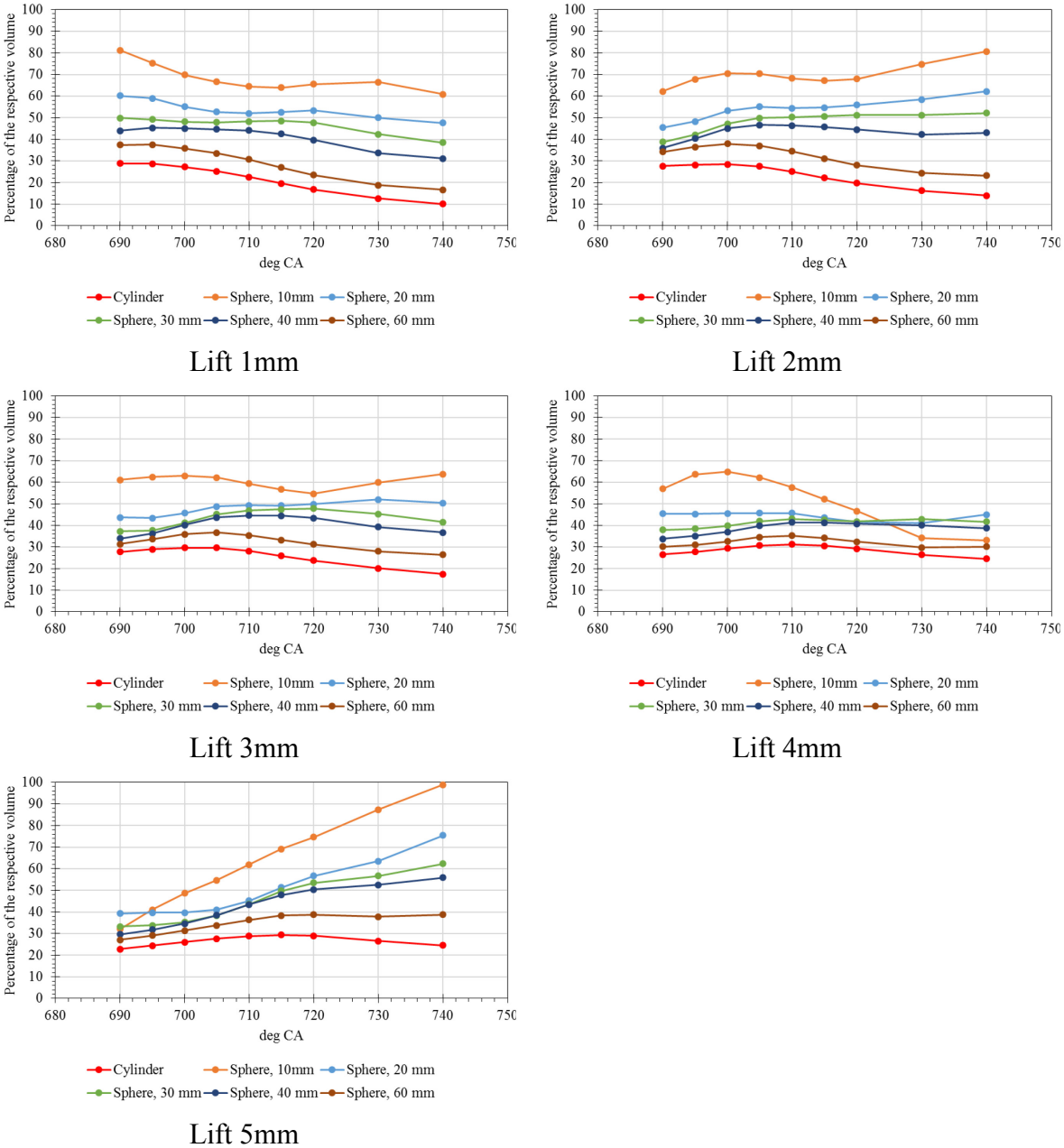


Figure 6.18 Percentage of different interrogating spherical volumes occupied by a mixture with λ in the region [1.05,1.15] for the five different LIVO lift cases

6.4. Early Intake Valve Closure (EIVC)

The experimental in-cylinder pressure trace during the compression and expansion, which is focused on the combustion event is shown in Figure 6.19. From that graph, it is evident that the increase of the in-cylinder pressure is very similar for the first three EIVC lifts and also the 4mm and 5mm are also similar to each other. Moreover, it can be seen that the increase of the pressure is more rapid for the first three cases that the last two. This denoted that for the lifts 1mm-3mm the combustion event is faster than the other two higher lifts. The faster combustion

was also evident from the retard of the ignition with the lower valve lifts which was from 9.46 degrees CA before TDC for the 1mm lift, up to 14.54 degrees CA before TDC for the 5mm lift. This range is greater that the range when LIVO was adopted with the same maximum valve lifts. Furthermore, for up to 5mm maximum lift, the lambda was increased up to λ=1.6 without exceeding the stability limit of 3% CoV of NMEP.

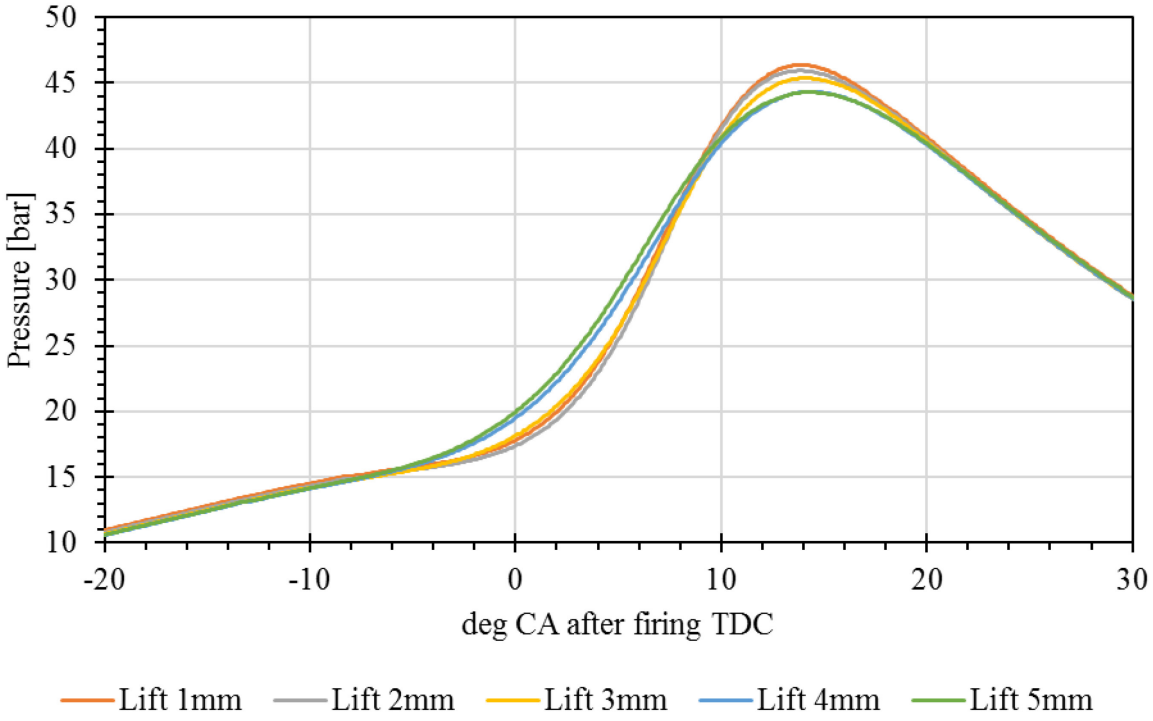


Figure 6.19 Experimental in-cylinder pressure trace during combustion for the five different EIVC cases

6.4.1. In-cylinder flow properties

The same approach as for the LIVO study was followed for the in-cylinder flow quantities of velocity, tumble, swirl and turbulent kinetic energy which were studied for the five lifts and compared against the dual and single valve actuation. Again, the analysis was focused from the IVO until firing TDC. During the initial phase of the intake stroke and up to ~45 degrees after TDC, the in-cylinder average velocity of all the EIVC cases is the same as the DVA case as both intake valves are opening at the same time with the same lift profile (Figure 6.20). As soon as the valve operating with the EIVC mode closes then the in-cylinder velocity increases due to the restriction of the intake throat. However, with the increase of the maximum valve lift to the EIVC mode, the increase of the velocity is less than the lower lifts. In all EIVC cases though, the average in-cylinder velocity is above the DVA line. Table 6.5 shows the velocity

reduction of the five different lifts from the SVA and the ratio EIVC / DVA velocity, around ignition (~10 degrees before firing TDC). As it can be seen, there is a significant reduction on the velocity which is not the case for the LIVO cases as described before. With the 5mm EIVC case, the in-cylinder velocity is very similar to that of the DVA. Due to the reduction of the in-cylinder velocity, the heat transfer from the gas to the walls should also be reduced. This will be investigated later on.

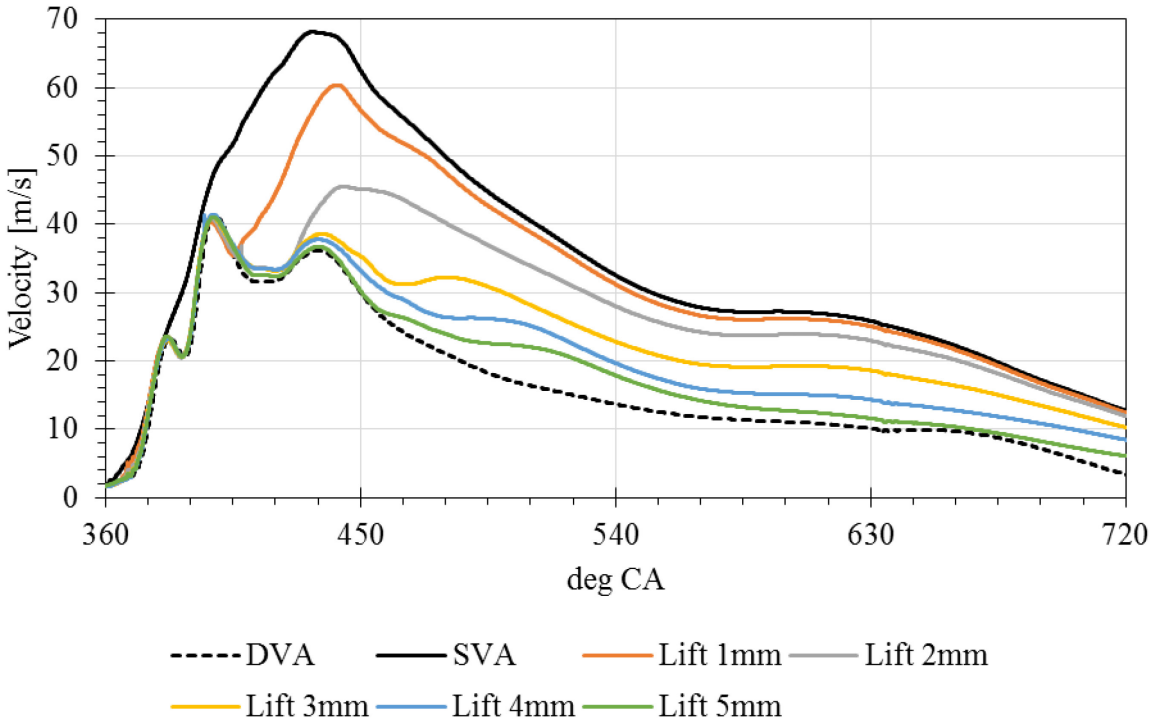


Figure 6.20 In-cylinder velocity magnitude for DVA, SVA and the five different EIVC lift cases

Lift	Reduction from SVA	EIVC / DVA
SVA	-	3.07
1 mm	2.24%	3.00
2 mm	6.53%	2.87
3 mm	20.23%	2.45
4 mm	34.74%	2.00
5 mm	52.58%	1.46
DVA	67.47%	1

Table 6.5 Velocity reduction of the five different lifts from the SVA and the ratio EIVC / DVA velocity at ignition

During the time frame in which both intake valves were opening simultaneously, the in-cylinder flow is symmetric without any production of swirl motion (Figure 6.21). There are some small deviations from 0 swirl because the intake valve lift profiles were taken from the experimental measurements and some deviations were found between each EIVC case and the full lift profile. When the valve with the EIVC mode started to close, an asymmetric flow at the beginning was created and after the valve closure, flow from the single valve lead to swirl motion. As the EIVC maximum lift was increased, the swirl motion started to appear later in the cycle and weaker due to the reduced in-cylinder velocity. The reduction from the SVA case of the swirl motion around ignition (~10 degrees CA before firing TDC) can be seen in Table 6.6. With the use of the EIVC mode and the highest max lift, the reduction of the swirl motion was more than 54% as it is displayed in Table 6.6.

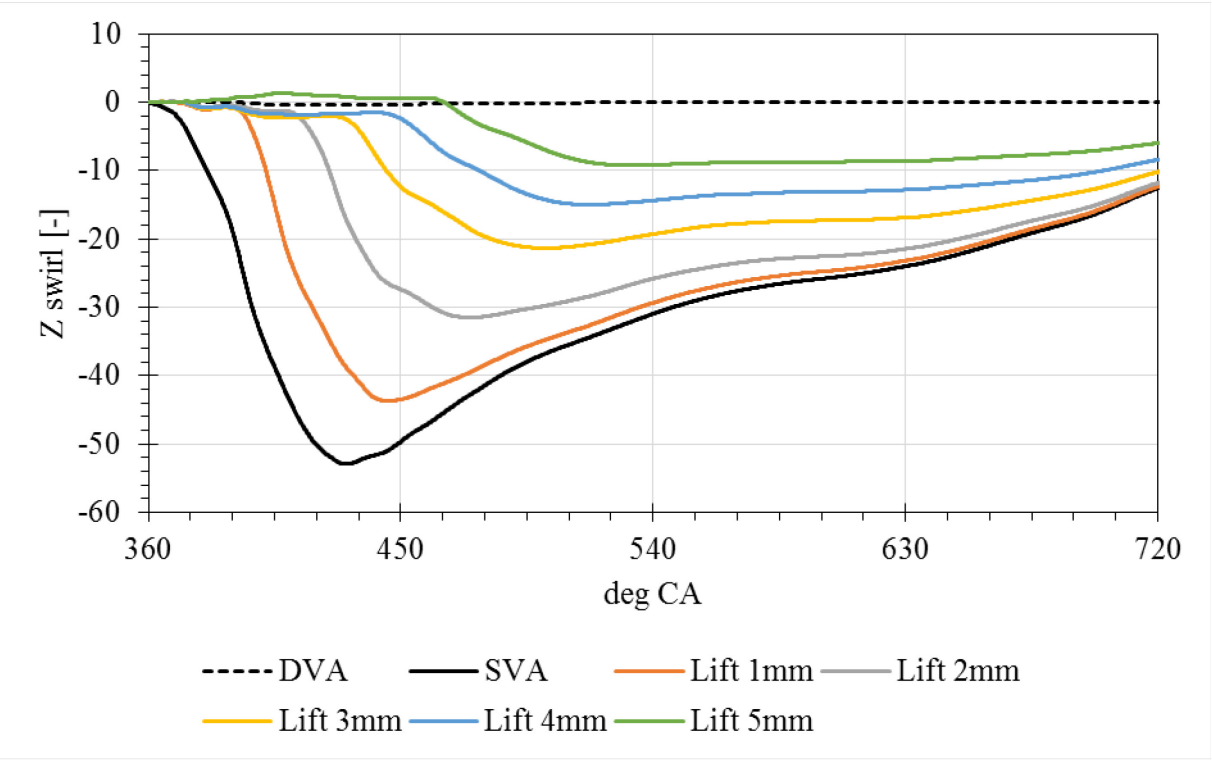


Figure 6.21 Swirl ratio for DVA, SVA and the five different EIVC lift cases

	1mm	2mm	3mm	4mm	5mm
Reduction from SVA	2.3%	6.8%	20.3%	35.1%	54.2%

Table 6.6 Percentage reduction of the swirl ratio from SVA at ignition for the EIVC mode

The tumble motion with EIVC mode was following the trend of the tumble with the DVA during the period in which both intake valves were opening simultaneously (Figure 6.22). From the maximum lift of the EIVC and later in the cycle, the behaviour of the tumble approached that of the SVA with the mechanism of the reverse tumble to appear. However, as the maximum EIVC lift was increased this mechanism was weakened and especially for the 4mm and 5mm max lifts, the tumble motion was significantly reduced from 120 degrees before firing TDC and up to TDC. This was due to the weak swirl motion which reduced the effect of the reserve tumble mechanism as explained in Chapter 4 (Figure 4.8). Especially for the 5mm case, there was no reverse of the tumble. Generally, from 50 degrees before firing TDC, the tumble motion was weakened with the use of SVA and it was further reduced with the use of the EIVC mode.

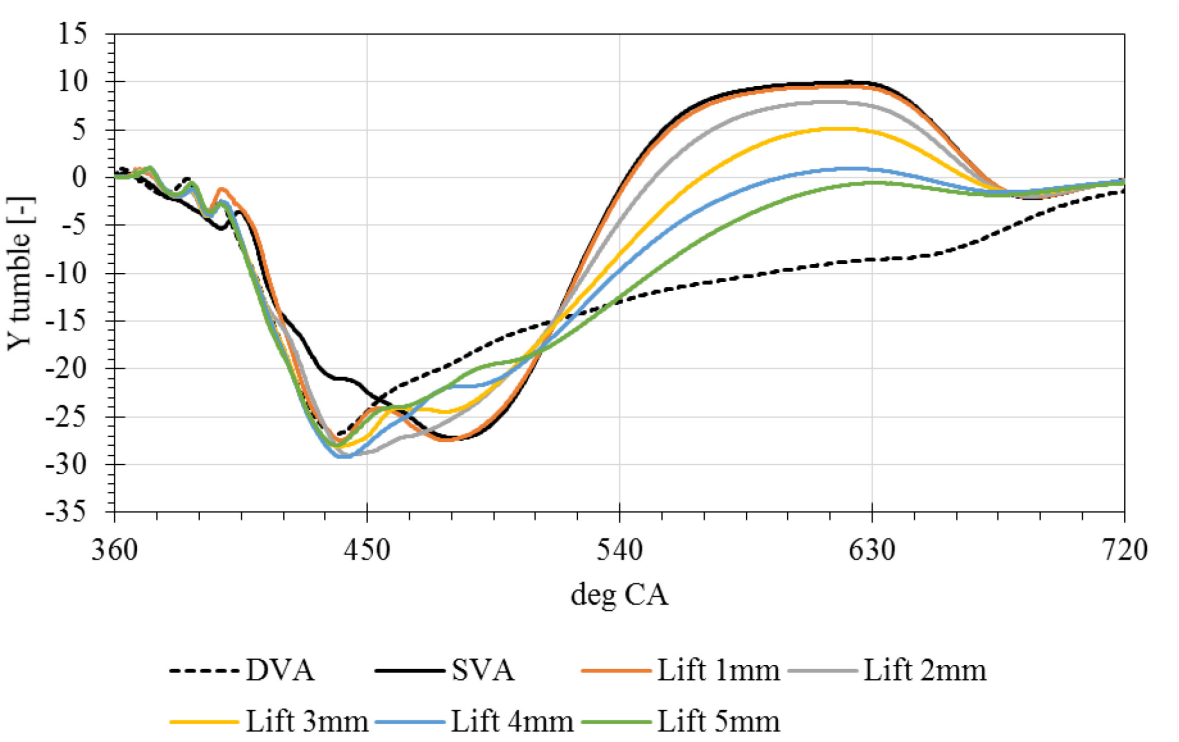


Figure 6.22 Tumble ratio for DVA, SVA and the five different EIVC lift cases

From the above data it can be seen that the increase of the maximum lift of EIVC mode has a major effect on the enhancement of the flow field which should also have an impact on the in-cylinder turbulent kinetic energy. All EIVC modes followed the DVA behaviour during the valve opening and there was an increase during intake, after the maximum lift. When the maximum lift was increased, the increase of the TKE during intake was reduced and was affected throughout the cycle (Figure 6.23). Especially for maximum lifts greater than 3mm, the in-cylinder TKE was dropped below the benchmark of the DVA. This is also evident in

Table 6.7 which shows the reduction of the average TKE from the SVA case to the EIVC and DVA case and the ratio EIVC / DVA at ignition (~10 degrees CA before firing TDC).

Lift	Reduction from SVA	EIVC / DVA
SVA	-	1.42
1 mm	2.91%	1.38
2 mm	11.34%	1.26
3 mm	29.03%	1.01
4 mm	41.87%	0.82
5 mm	43.26%	0.80
DVA	29.47%	1

Table 6.7 TKE reduction of the five different lifts from the SVA and the ratio EIVC / DVA velocity at ignition

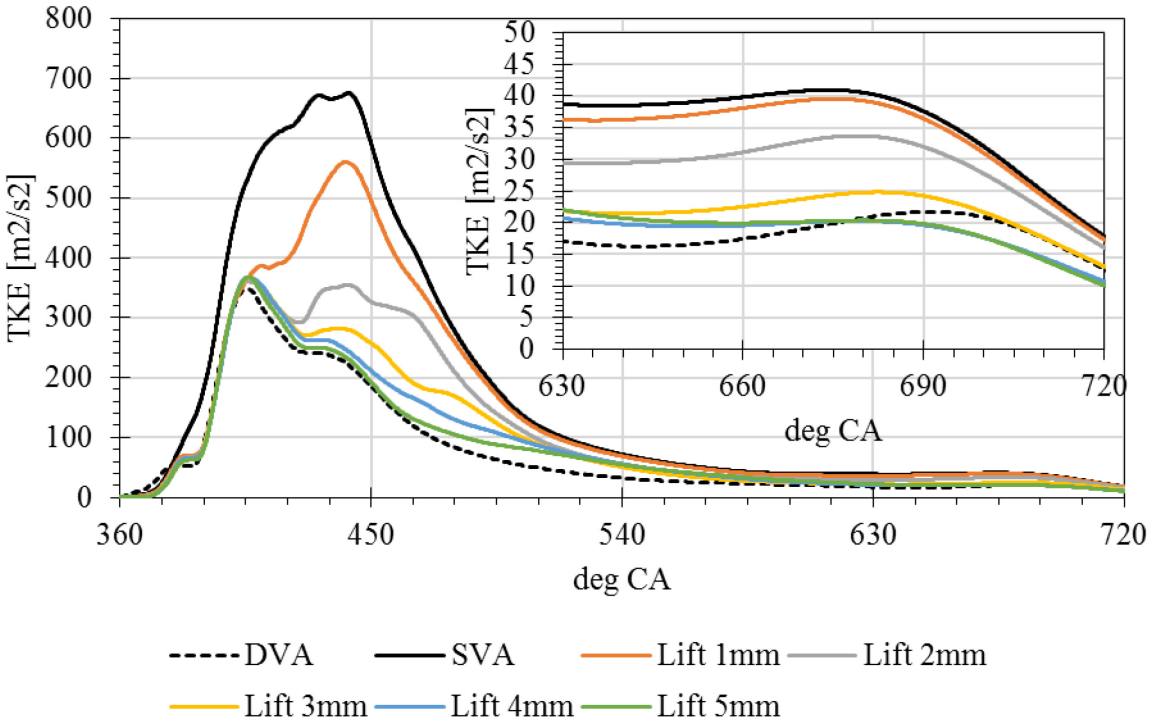
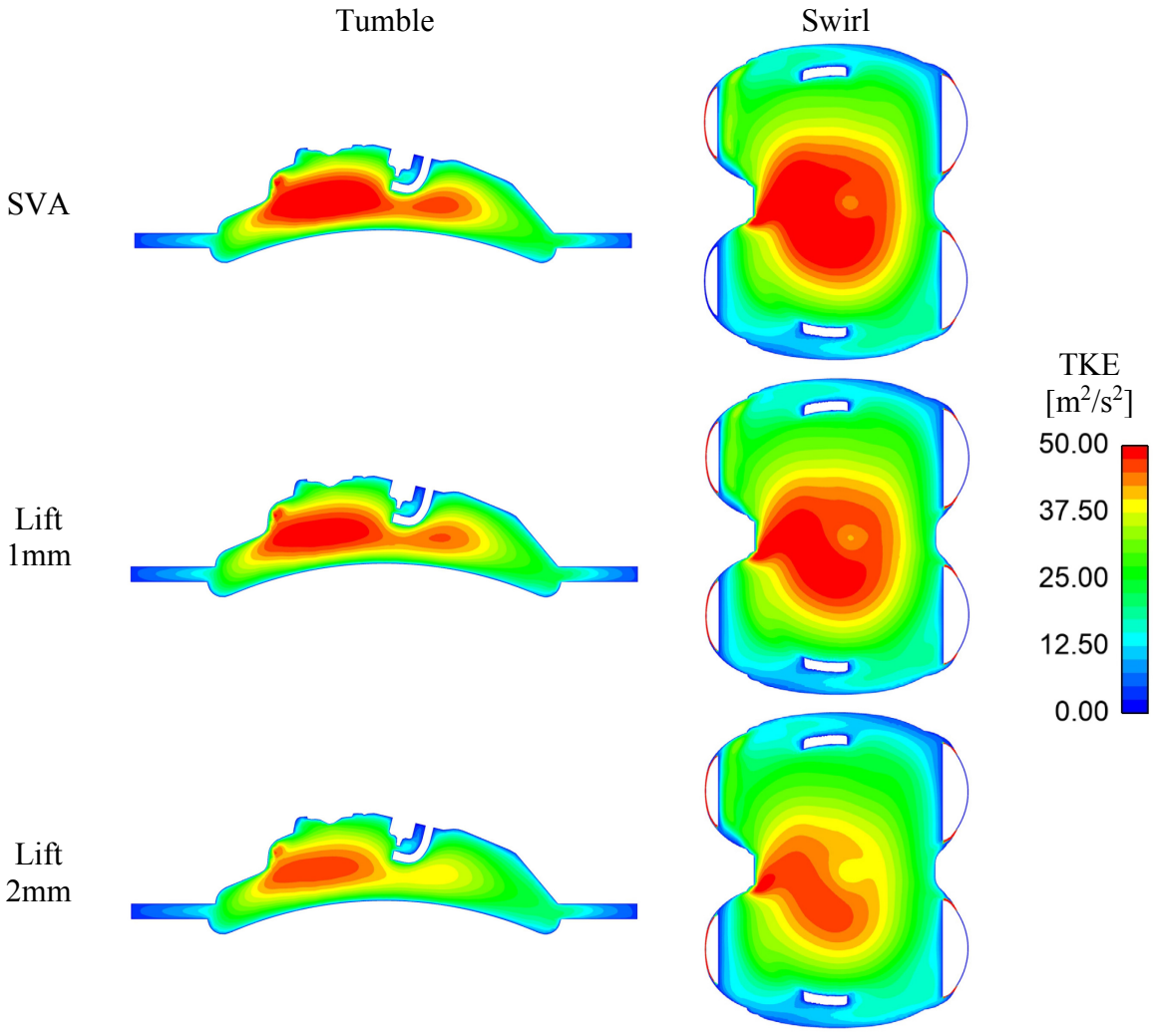


Figure 6.23 Turbulent kinetic energy for DVA, SVA and the five different EIVC lift cases with a zoom on the compression stroke after IVC

The contour plots of Figure 6.24 show the distribution of the TKE on the tumble and swirl planes. The contour of the TKE with the 1mm and 2 mm is very similar to the SVA case but with lower magnitude. The TKE is spread radially in the cylinder with values higher than the

DVA, which leads to faster combustion. While there is only 1% difference between DVA and the 3mm case, the in-cylinder location of the TKE is more favourable with the EIVC mode. The TKE is spread radially and surrounds the spark plug with the EIVC which can accelerate the flame propagation. For the DVA however, The higher magnitude of the TKE is more concentrated in the area below and away from the spark plug. These plots show the improvement of the in-cylinder TKE in both magnitude and location when the EIVC mode is used with up to 3 mm maximum lift. It has to be noted that for lifts above 3 mm with the EIVC mode, the weakening of the in-cylinder flow can result in levels of TKE even lower than the DVA. This behaviour was also recorder in the experiments where the combustion duration for lifts above 3 mm was similar to that of the DVA.



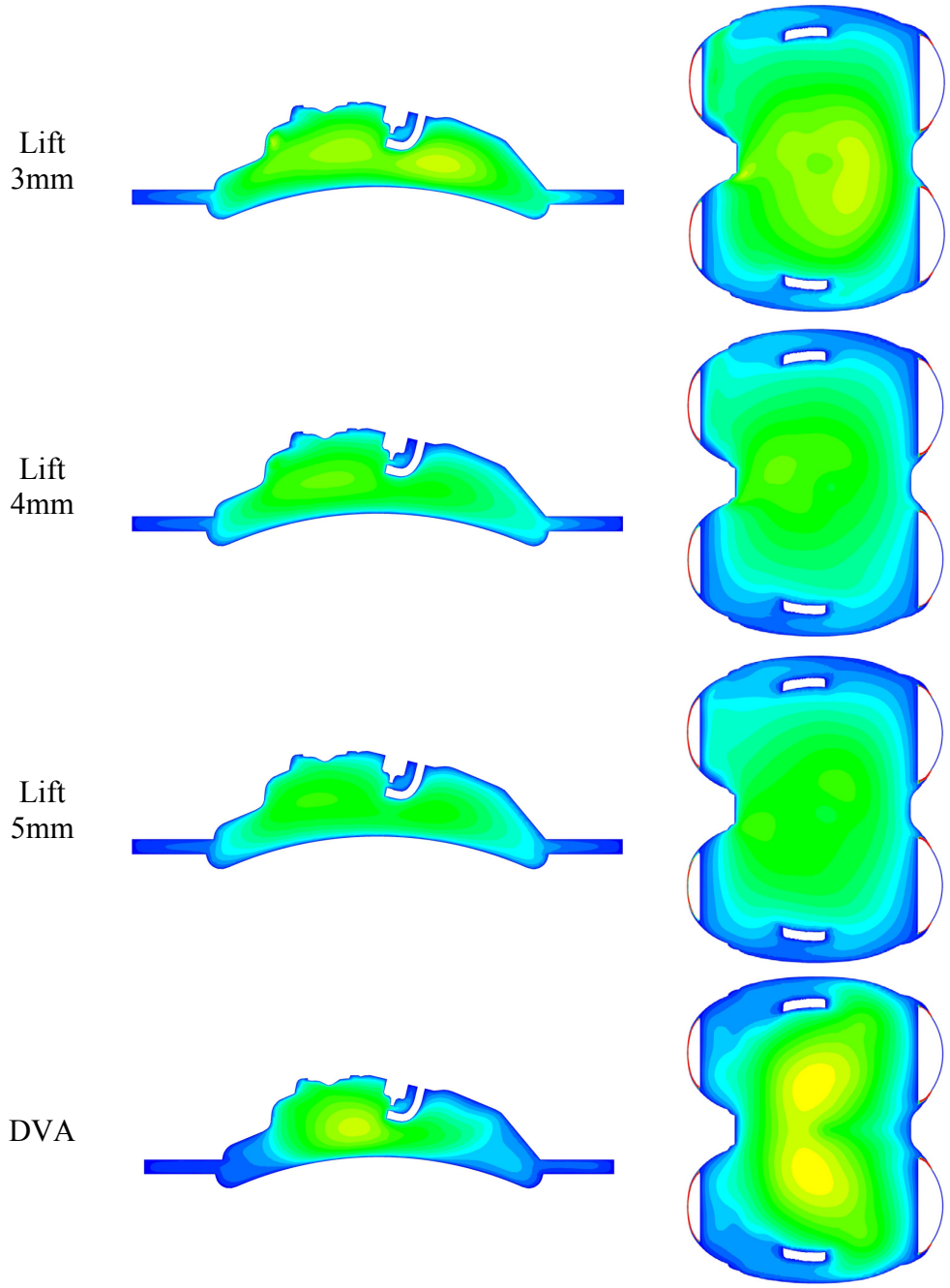


Figure 6.24 Spatial distribution of TKE for DVA, SVA and the five different EIVC lift cases for the tumble and swirl planes at ignition

The in-cylinder temperature was also investigated for the cases with the EIVC mode. The differences between DVA and SVA was about 25°C at ignition timing (15-5 degrees before firing TDC). When EIVC mode was adopted, a decrease on the in-cylinder temperature was observed. More specifically, with 1mm maximum lift, the temperature was decreased from the SVA temperature by 4°C. Further increase of the maximum lift resulted in a reduction of 6°C to 8°C in the temperature. This again can be explained with the evolution of the in-cylinder

mass. During the initial stage of the intake, in which both the valves are open, a greater amount of fresh air is induced to the cylinder when it is compared to the SVA case. After the closure of the EIVC valve, the trapped mass followed the curve of the SVA however, the extra amount of fresh air is able to reduce the in-cylinder temperature. With this mode it can be seen that the first factor of the heat transfer could be affected and reduced in order to reduce the heat transfer from the gas to the walls.

Lastly, the effect of the EIVC mode on the heat transfer was studied and presented in Figure 6.25. For these cases the combined effect of the reduction of the in-cylinder flow intensity and temperature resulted in a significant reduction of the heat transfer. From about 90-80 degrees CA before firing TDC, the heat transfer of the EIVC cases started to deviate from the heat transfer of the SVA. Table 6.8 shows the reduction of heat transfer from the SVA case and the relative reduction assuming that the maximum heat transfer is obtained with SVA and the minimum with DVA.

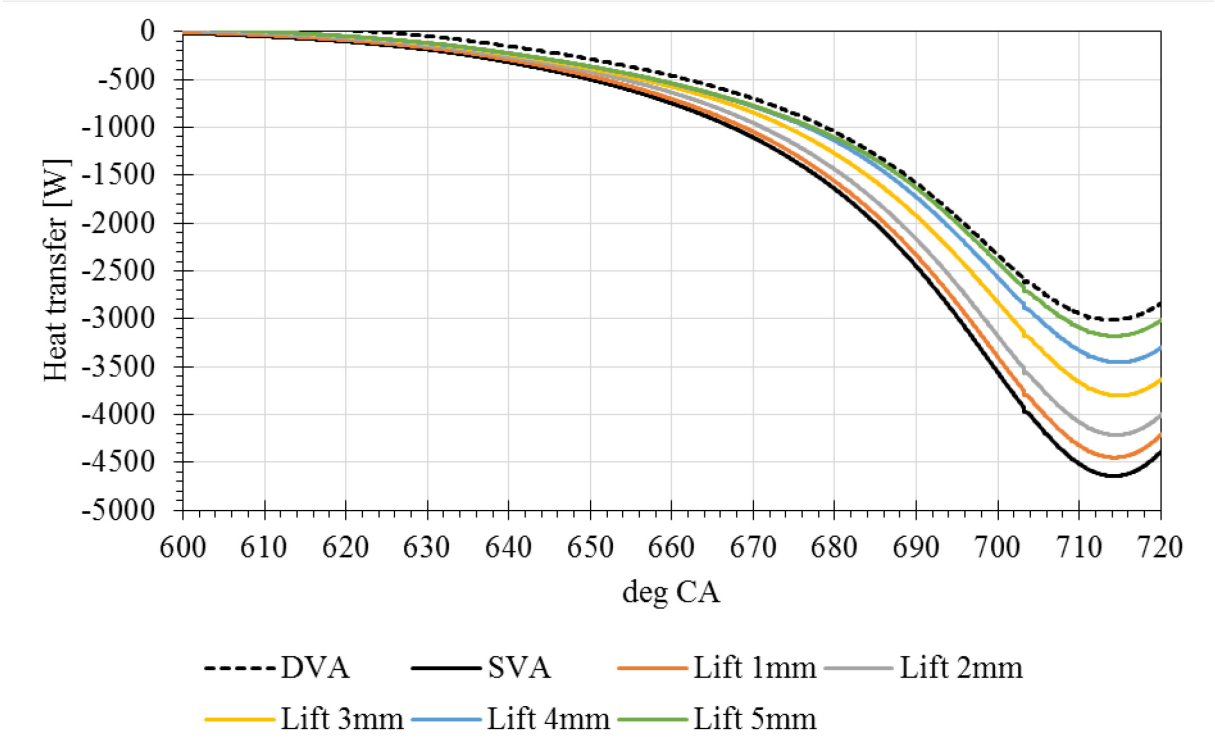


Figure 6.25 Heat transfer from the gas to the walls for DVA, SVA and the five different EIVC lift cases

Lift	Reduction from SVA	Relative reduction
SVA	-	0%
1 mm	4.2%	11.9%
2 mm	9.2%	26.3%
3 mm	18.1%	51.5%
4 mm	25.6%	72.8%
5 mm	31.5%	89.7%
DVA	35.1%	100%

Table 6.8 Heat transfer reduction of the five different EIVC lifts from the SVA and the relative reduction with respect to DVA and SVA

6.4.2. Mixture preparation

The mixture preparation and the homogeneity of the mixture during compression was studied for the five EIVC cases. The Lambda contour for the five different LIVO cases near ignition (10 degrees CA before TDCf) at the tumble and swirl views are displayed in Figure 6.26. In order to have the same reference with the rest of the contour plots, the same range of lambda for the legend was used and it was [0.8,1.2] for global lambda λ=1.0. From the lambda contour plots it can be seen that there was no distinct pattern as the maximum valve lift was increased. For the 1mm lift case, the contour plot is very similar to the Single Valve Actuation for both tumble and swirl planes. For the tumble plane specifically, the axial stratification existed and the lean region was located near the head while near the piston the mixture was rich. By increasing the valve lift the pattern in the tumble plane changed with a radial stratification which is more evident in the swirl plane. By increasing the maximum valve lift further (4mm and 5mm), the axial stratification appeared again however, the rich mixture was located near the head and the lean regions close to the piston. The weakening of both swirl and tumble flows affected the in-cylinder flow in an indistinct way.

Because of the differences in the contour plots for the five lifts of the EIVC mode, the Homogeneity Index of the five cases was plotted in Figure 6.27. From the HI, it is again clear that an ambiguous pattern is followed by increasing the maximum lift. All the cases started with an Index which was very close to the SVA Index however, the rate of increase was smaller than that of the SVA. For the 1 mm lift case, it was expected that the HI would be close to the SVA as the very small duration of the EIVC valve had a minor effect on the in-cylinder flow when compared to that of SVA. In addition, as the valve lift was increased, the homogeneity

was reduced and for the 5 mm maximum lift case, the homogeneity was the closest to the DVA case. However, the 4 mm lift case did not follow the trend of the reduction and it was higher than the 1 mm lift case.

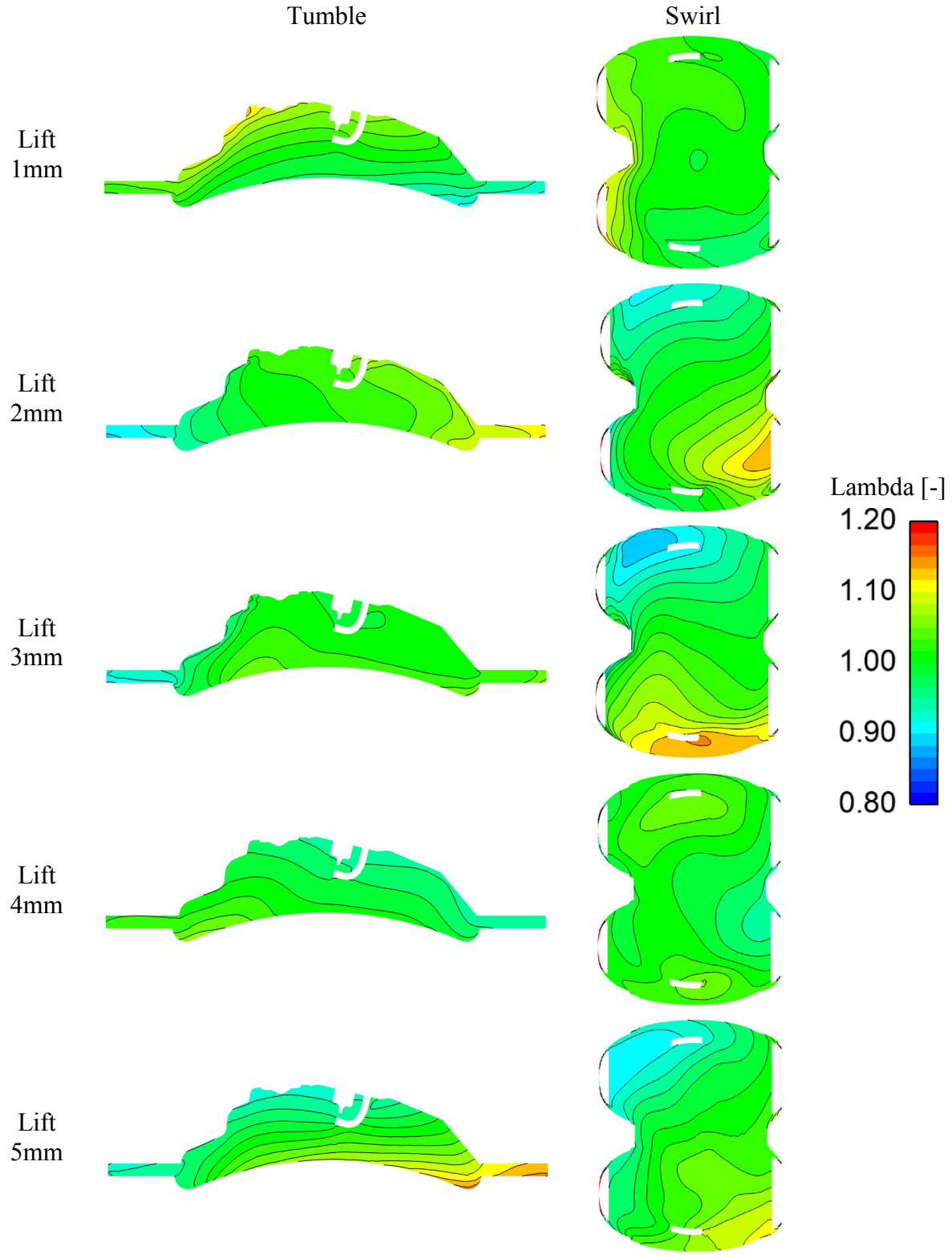


Figure 6.26 Spatial distribution of Lambda for DVA, SVA and the five different EIVC lift cases for the tumble and swirl planes at ignition

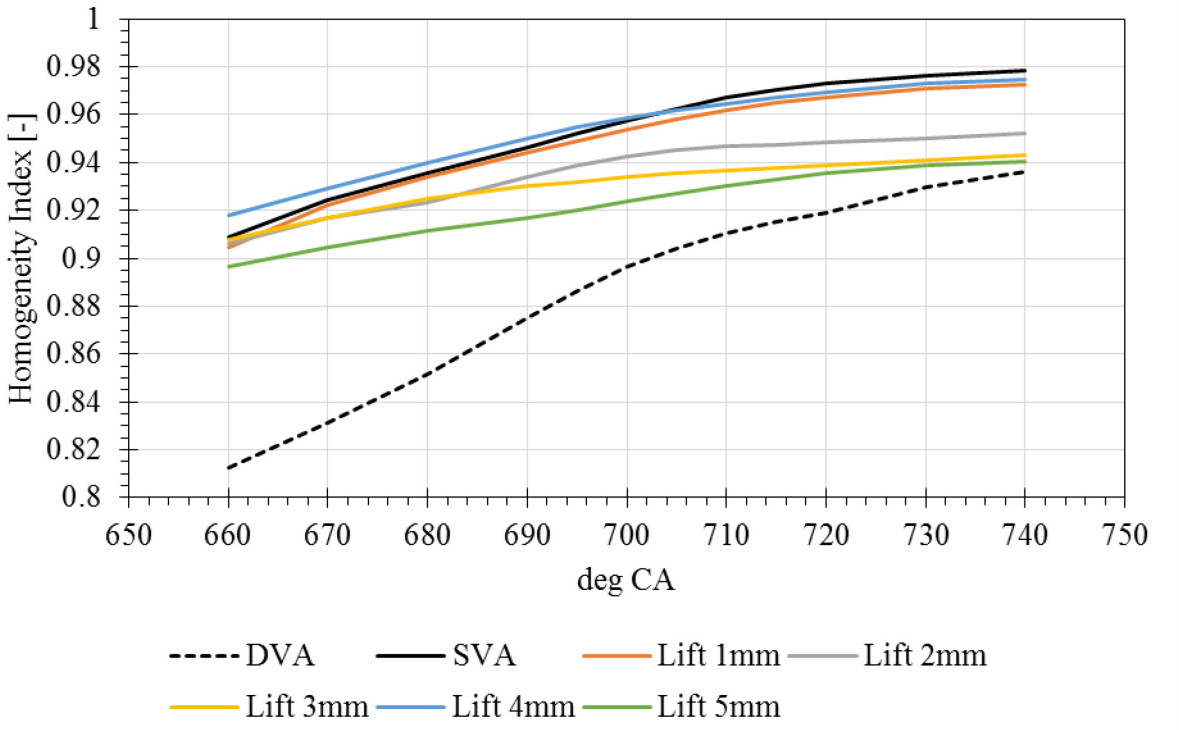


Figure 6.27 Homogeneity Index for DVA, SVA and the five different EIVC lift cases

When the liquid film mass was investigated for the five EIVC cases, a pattern could be identified. Except from the 1 mm lift, the rest of the cases had an increasing accumulated film mass as the valve lift was increased. Due to the different swirl flows during the injection and the change of the valve jet, the spray of each case was affected differently. The higher accumulated mass along with the weakening of the in-cylinder flow, reduced the evaporation rate from the piston as the valve lift was increased. This can be seen in Figure 6.28. For the 1 mm lift case, the jet of the full lift valve which was established earlier in the cycle, was directing the two plumes which were close to the intake port and in the +Y sector, directly to the piston crown. Due to the different flows affecting the spray during injection, the liquid film footprint was also different for each case as it can be seen in Figure 6.29. For the 1 mm case, because of the helical intake flow, the plume closest to the open intake valve produced the high thickness film because the valve jet changed the direction of the plume and it was vertically directed towards the piston. The second plume on the +Y sector produced the elongated footprint as the swirl motion was established. By increasing the maximum lift, the liquid film pattern was closer to the DVA pattern however, the effect of the swirl motion was still visible on the liquid film. This increase of the liquid film mass as well as the increase of the time at

which the film remains on the piston can have a negative impact on the pollutant formation, especially particulates, due to so called pool fire.

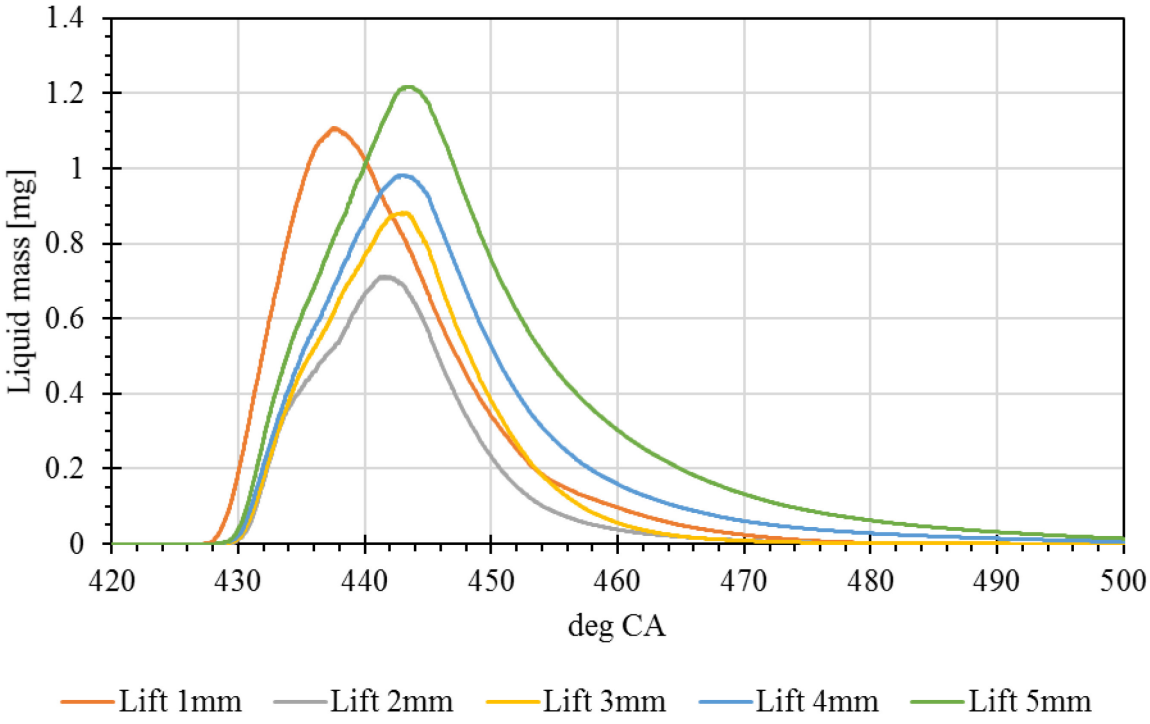


Figure 6.28 Total film mass on the piston versus crank angle for DVA, SVA and the five different EIVC lift cases

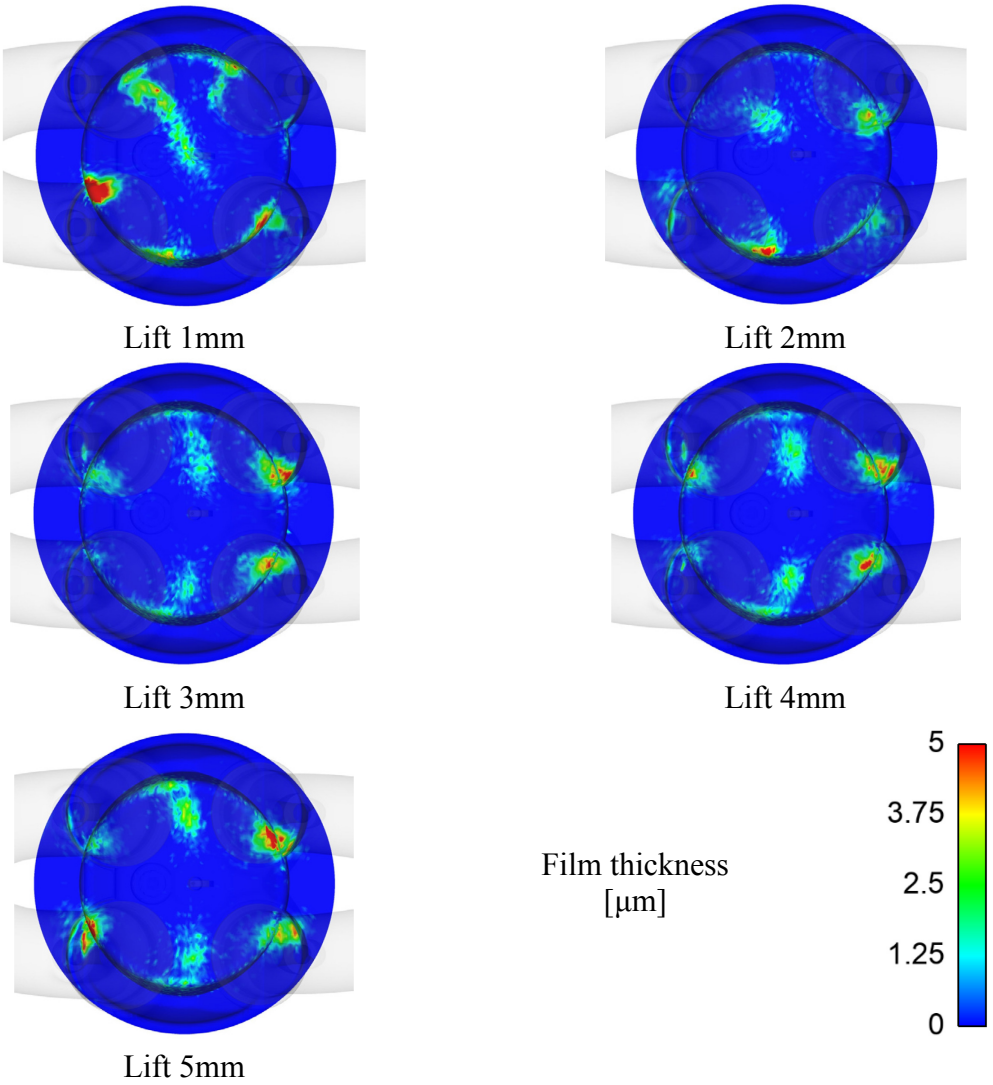


Figure 6.29 Film thickness on the piston at 20 degrees after SOI for the five different EIVC lift cases

6.4.3. Emissions

The emissions of CO, NO_x and unburnt hydrocarbons was investigated for the five different valve lifts when EIVC was adopted and the experimental results are shown in Figure 6.30. The experimental emissions of CO were very similar to the trends with the LIVO mode. At λ=1.0 there is an increase of CO production from SVA which has the lowest CO through the increase of the maximum lift of the staggered valve and up to DVA. For higher Lambdas the differences between the different maximum valve lifts was minor. Similarly, there was an increase of the unburnt hydrocarbons with the lowest values being produced by SVA and the highest with DVA and the increase of the THC was following the increase of the maximum valve lift. With the EIVC mode however, the increase of the THC with the increase of the maximum lift was more rapid than the increase when LIVO was used. From Figure 6.30 this high increase is clear,

and it can also be seen that with the 5mm EIVC lift, the unburnt hydrocarbons were higher than those of the DVA. Lastly, for the NO_x at λ=1.0 the differences between the various staggered lifts was minor (5% maximum difference) but the trend that appears throughout the lambda range was a reduction with increased valve lift which collapsed to a single value above λ=1.5.

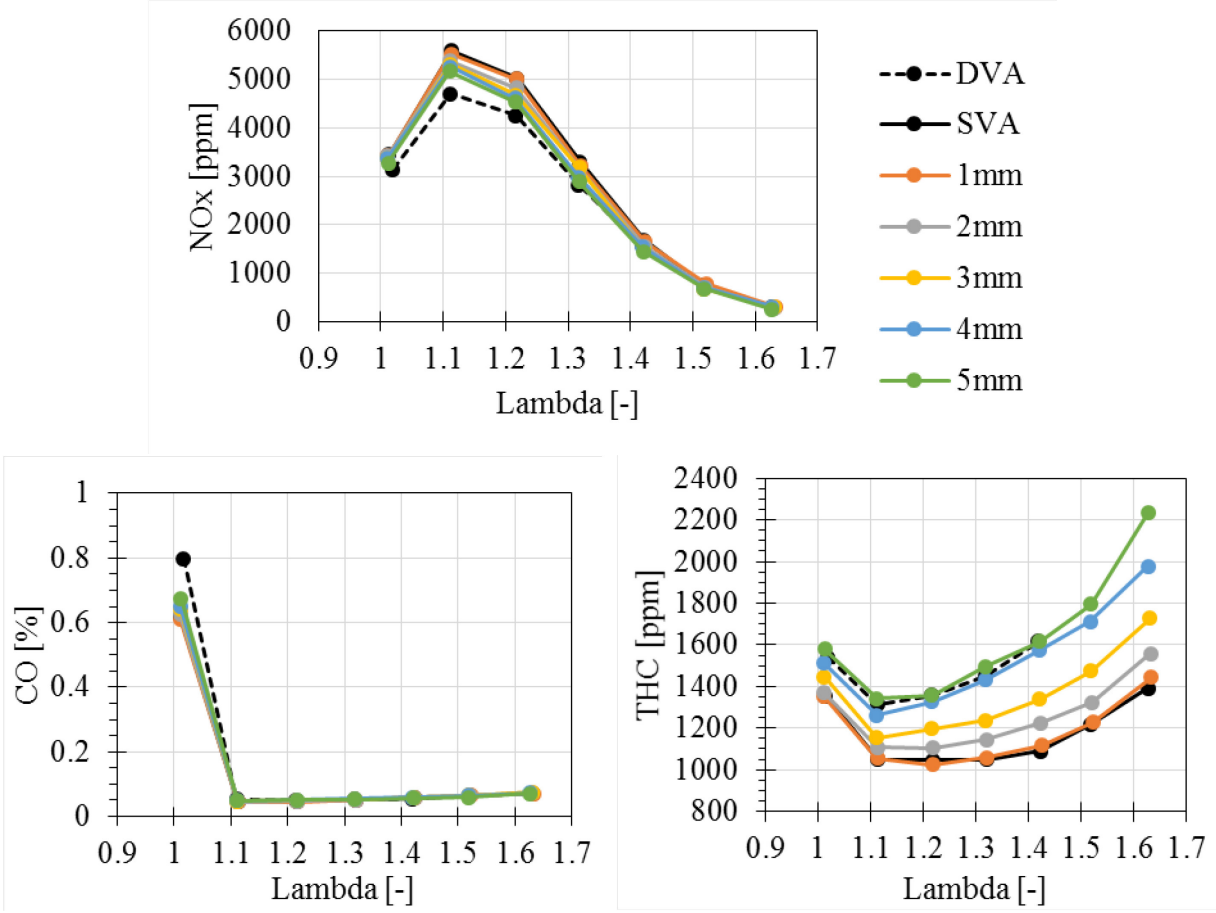
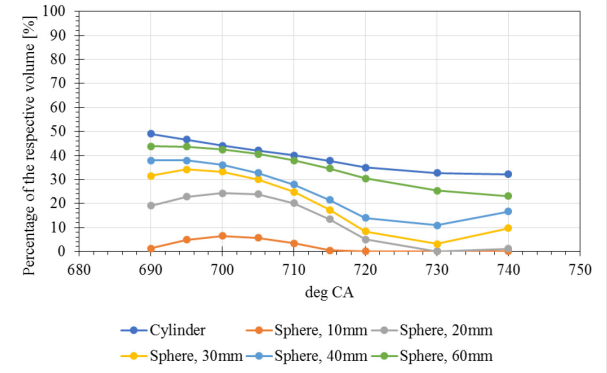


Figure 6.30 Experimental data of NO_x, CO and THC for DVA, SVA and the five different EIVC lift cases with various dilution

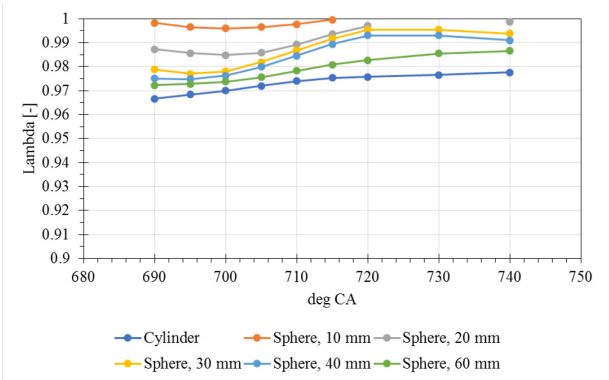
For the investigation of the causes behind the increase of CO and unburnt hydrocarbons, the rich regions of the air-fuel mixture within the cylinder were studied (Figure 6.31). From the analysis, it was showed that there was an increase of rich mixture at ignition and later within the cylinder when the valve lift was increased from 1mm (30% - 40% of the cylinder) to 5mm (45% - 50%). The same trend can be seen for the 60 mm and 40 mm spheres. The volumes with the smaller diameter were more sensitive to the local air-fuel mixture and because the lambda contours are different for the five different lifts this is reflected on the graphs. For example, for the 1mm lift, when the axial stratification has the lean mixture near the spark plug, the percentage of the rich mixture for the 10 mm sphere is either below 10% or zero. For the 5

mm lift, there was again axial stratification, but the lean mixture was near the piston, more than 80% of the occupied volume of the 10 mm sphere is rich mixture. The average lambda of the rich mixture for the cylinder and for all the spheres was reduced when the maximum valve lift was increased. This showed that not only the amount of rich mixture was increased but also that the mixture was further enriched. The behaviour of the 4mm lift case was similar to the 5 mm lift case with axial stratification which had the rich zone near the head and the lean zone near the piston. For the 4 mm case, the spheres with up to 40 mm diameter, were covered by a rich mixture which was more than 60% of the respective volume while for the 5mm case, and the same spheres, the range was 50%-80%. Due to the homogeneity of the 4 mm case the average lambda was between 0.97 and 0.98. For the 5 mm EIVC case, the average lambda was above 0.95 for the cylinder and above 0.96 but below 0.98 for the spheres. The combined effect of the rich zones and the level of the rich mixture is the reason that the 4mm and 5mm cases produced the highest CO and THC emissions.

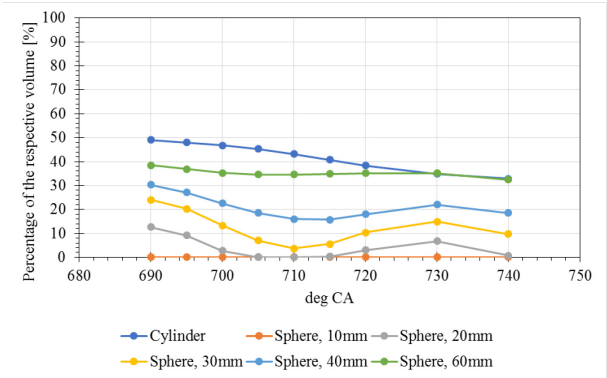
Percentage of the interrogating spherical volumes occupied by a mixture with λ<1.0

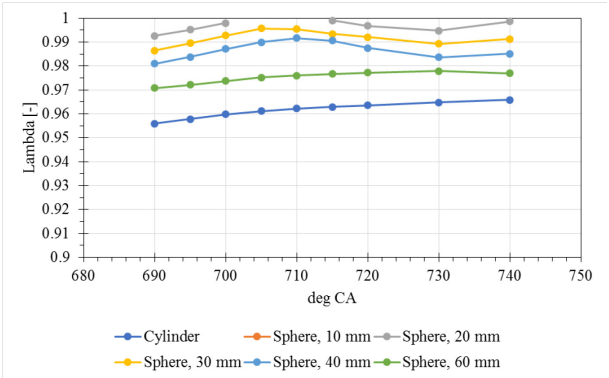


Average Lambda of the lambda zones below λ=1.0 for various interrogating spherical volumes



Lift 1mm





Lift 2mm

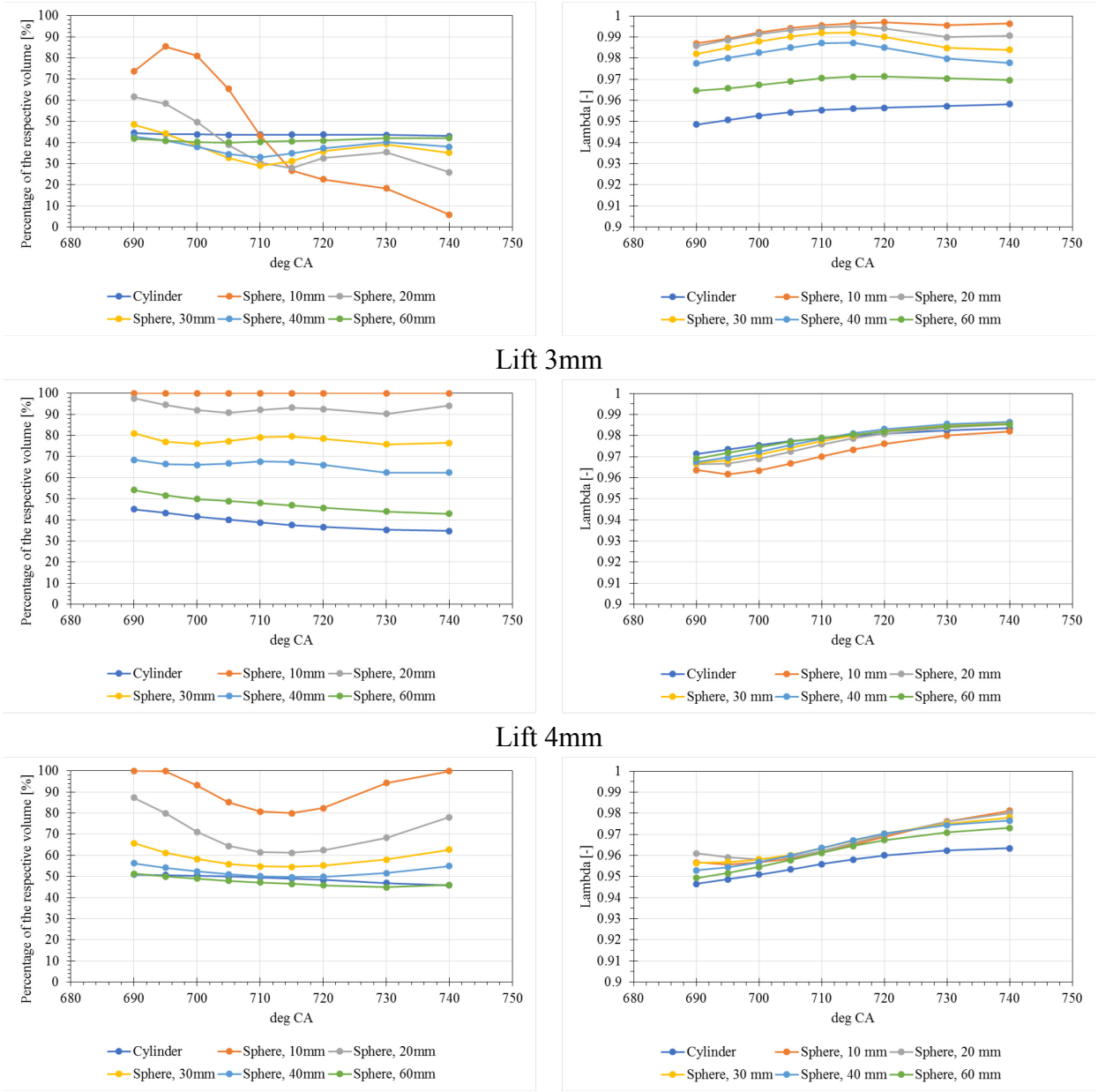


Figure 6.31 Percentage of the interrogating spherical volumes occupied by a mixture with λ<1.0 and Average Lambda of the lambda zones below λ=1.0 for various interrogating spherical volumes for the five different EIVC lift cases

The air-fuel equivalence ratio within the range of lambda [1.05,1.15] was studied for the five EIVC cases (Figure 6.32). Due to the differences in the mixture formation as seen in the lambda contour plots of Figure 6.26, the graphs of the percentage occupied by the mixture for the different spherical volumes did not follow an apparent trend. However, some conclusions can be drawn. From the combustion modelling it was seen that the peak NO production occurred in mixture of lambda within the range [1.05,1.15] but it was not produced in the total volume of cylinder and it was more concentrated in a volume of 30mm-40mm. For these sizes of

spheres and for lifts of 1mm and 2 mm the percentage of these volumes with the critical lambda are between 10% and 30%. When the lift was increased further, the percentage of these spheres was reduced and for the 4 mm lift the percentage fell to 0%. For the 5 mm lift, the percentage of these spheres was increased again to up to 20%. Due to the differences on the in-cylinder pressure traces with the highest peak to occur for the lowest lift, the temperature of the post flame gases may also contribute to the NO_x production nevertheless, it was not possible to identify it with this approach. In addition, for the highest lifts where the stratification is reversed, and the combustion of the lean mixture is at the end of the combustion event, may have an effect on the NO_x production.

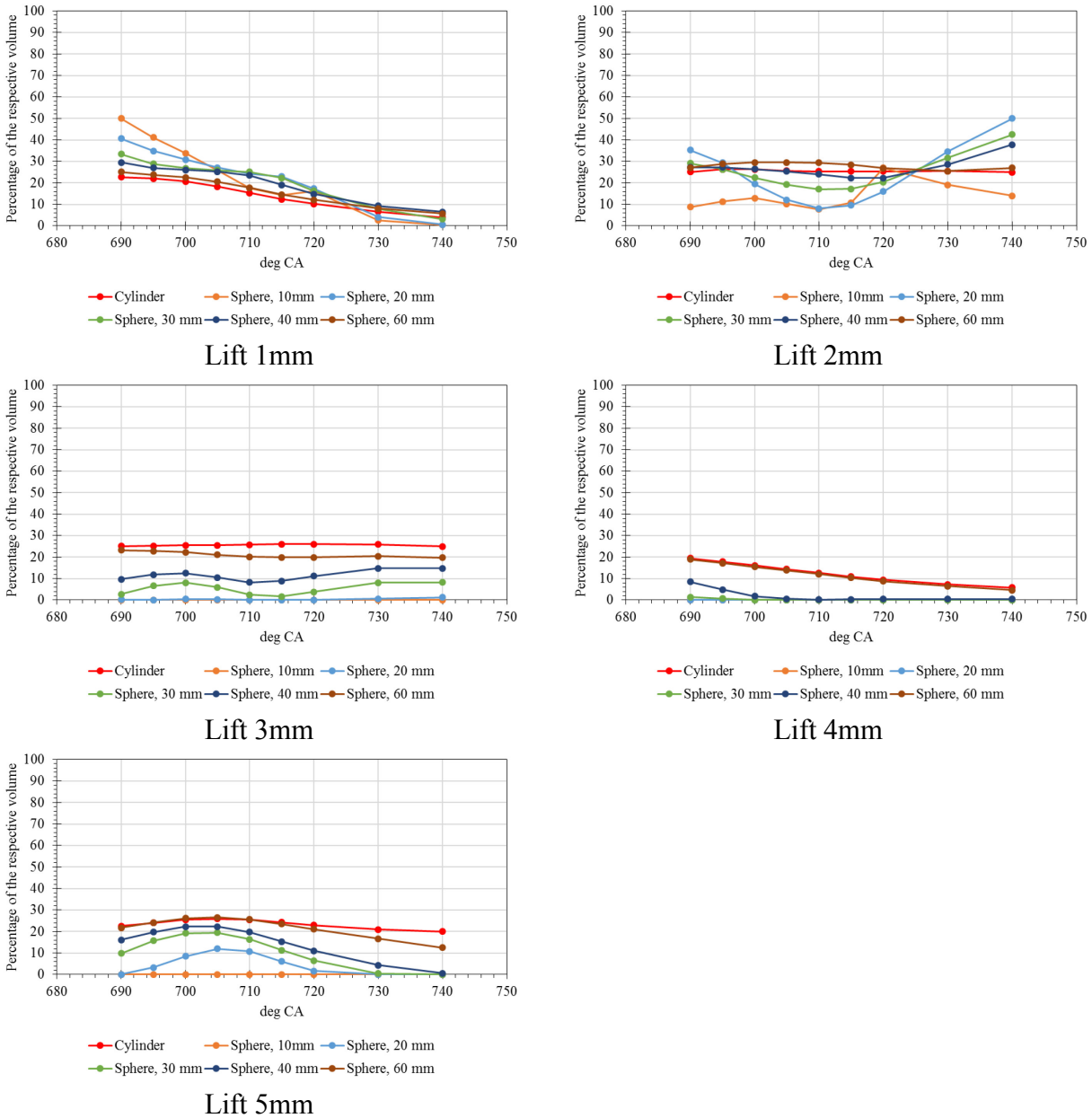


Figure 6.32 Percentage of different interrogating spherical volumes occupied by a mixture with λ in the region [1.05,1.15] for the five different EIVC lift cases

6.5. Closure

Two different approaches for differential intake valve lift were simulated in order to give an insight of the experimental measurements and understand the main beneficial factors attributing to the improved combustion metrics. The two approaches were either the Late Intake Valve Opening or the Early Intake Valve Closure and the maximum valve lift was increased from 1mm up to 5 mm with 1mm increment.

From the cases investigated with the LIVO mode it can be concluded that the optimum maximum valve lift for the LIVO mode concerning the in-cylinder quantities of heat transfer and enhanced charge motion is the 5mm. With the 5 mm a ~10% more TKE than the DVA can be achieved which is also in a more favourable location and a significant reduction of 43% on heat transfer could be achieved when compared to the ideal case of heat transfer which was the DVA. This also agreed with the experimental results. The use of the EIVC mode has a strong effect on the in-cylinder flow and the in-cylinder quantities of temperature, TKE and heat transfer. For the EIVC mode, the 3mm maximum lift is a good compromise between the reduced heat transfer (51% relative to the ideal DVA heat transfer) and the marginally increase but more favourably located TKE.

A comparison of the ideal cases of LIVO and EIVC showed that the in-cylinder velocity with the LIVO mode is much greater that the EIVC mode during the intake stroke. However, after the peak of the velocity with the LIVO mode, which occurred at around 80 degrees after gas exchange TDC, the velocity dropped and from BDC the average in-cylinder velocities were almost the same, with only minor differences of about 3%. Very similar behaviour was seen for the swirl motion which is stronger for the LIVO mode due to the initial single valve actuation. After the peak, the swirl motion of the LIVO mode was reduced and after BDC, the strength of the swirl is very similar for both cases with a maximum difference of about 4.5%. The behaviour of the tumble motion is similar for both modes at the beginning of the intake stroke due to the promotion of tumble from the geometry of the ports. Because of the stronger swirl, and due to the mechanism described in a previous chapter about the reverse tumble, the tumble turns from negative to positive faster, but the higher in-cylinder velocity maintained the tumble at high levels after BDC for the LIVO mode. For the EIVC mode, the reverse tumble is slower and also is weaker after it is reversed. Only at the end of compression stroke (20 degrees before firing TDC) the tumble of both modes come at the same levels. From the analysis of the flow data, the enhanced flow field during the intake provided by the LIVO mode can contribute to better air-fuel mixing process and it will be studied later in the chapter. The

key factor of the faster combustion when adopted the SVA was the increased TKE. When the two optimum cases of the staggered lifts were compared, it was found that with the LIVO mode, the TKE was also greater than that of the EIVC mode. 30 degrees before firing TDC, the difference was about 15% and it was reduced to 5% difference 5 degrees before firing TDC. In addition, the comparison of the contour plots, showed that the LIVO mode had better distribution of the TKE in the cylinder. All these, point to the direction of the better combustion metrics with the use of the optimum LIVO mode. Last but not least, the heat transfer differences from the two optimum cases were compared. The heat transfer for both cases is at similar levels but always higher for the LIVO mode. At the peak heat transfer, the difference is about 3.6%. This can be contributed by the small differences in the velocity and flow field but also by the difference in the gas temperature during compression which is 8°C higher for the LIVO mode.

From all the above, it can be concluded that:

- The generation of swirl motion played a very important role on the production and maintenance of the TKE at high levels, an important factor for improved combustion metrics such as the faster combustion. As both optimum cases revealed, the swirl has to be conserved at levels of about 20-10 units during compression in order to keep high levels of TKE.
- The tumble motion was of a secondary importance because the EIVC mode had significantly weaker tumble but the TKE was maintained at high levels due to the swirl motion.
- It was seen that not only the increase of TKE is important but also the location and the distribution within the cylinder is important. Especially for EIVC mode, the increase was marginal, but the location was improved compared to DVA which gave a benefit by the faster combustion.
- The heat transfer can be reduced by ~50% without compromising the TKE by reducing the strong in-cylinder flow motion by either LIVO or EIVC staggered lifts.
- When the LIVO mode was adopted, the air-fuel mixture at ignition was very similar to the SVA axial stratification. By increasing the maximum valve lift the homogeneity was decreased but the axial stratification was maintained. The mixture formation at ignition varied with the EIVC mode. In the small lifts the mixture formation was also similar to SVA. With increased valve lift, air-fuel mixture differed from both DVA and SVA patters. For lifts of 4mm-5mm, a reverse axial stratification was apparent.

- The liquid film formation was reduced with the use of the LIVO mode and both the film mass and the pattern were similar to the SVA. When EIVC was adopted, the liquid film mass was increased due to the flow interacting with the spray plumes, directing them towards the piston. In addition, the rate at which the film mass was reduced, increased with the increase of the valve lift.
- The emissions of CO and THC were increased with increased valve lift for both modes. This was the result of the combination of greater volumes of rich mixtures in the different interrogating volumes and the reduction of the lambda value of the rich regions when the valve lift was increased.
- Lastly the NO_x production for the LIVO mode was reduced with the increased valve lift but the decrease was minor. This is believed to be due to the small differences seen for the mixture in the region of [1.05,1.15] in the spheres 20mm-40mm (around 40%-50%) of the volumes for the 1mm up to 4mm cases. For the EIVC mode, there is no apparent trend of the regions with the mixture at the specified lambda range for the spheres 20mm-40mm, but a reduction can be observed. The temperature reduction suggested by the experiments (peak pressure reduction) has an effect which was not taken into account with this approach.

Chapter 7

Effects of Valve Deactivation on Cyclic Variations

7.1. Introduction

Comparison of the in-cylinder pressure measurements for a number of cycles from a spark-ignition engine shows significant variations of the pressure during the combustion event on a cycle-by-cycle basis. Minimising the cycle-to-cycle variations (CCV) is important otherwise they can lead to unstable engine operation which is related to vehicle driveability. In addition, as the ignition is set to the average cycle, faster burning cycles may be susceptible to knock and slower burning cycles are likely to burn incompletely with increase of pollutant formation and loss of power. The causes of the combustion variations are the cycle-to-cycle discrepancies in the in-cylinder flow motion, the air-fuel mixture and the mixture of the fresh air with the residual gases especially at the time of the ignition and at the vicinity of the spark plug. The variabilities introduced by these factors result on different flame kernel development and thus variations in the heat release and in-cylinder pressure.

Experimentally, to study the CCV of the in-cylinder flow field, PIV measurements are the most common method. In the work of Justham, *et al.* (2006) and Jarvis *et al.* (2006) the in-cylinder variability was linked to the intake port flow variability with the use of PIV in both cylinder

and intake runner. Fischer *et al.* (2004) investigated the CCV with the use of PIV in an optical engine with variable tumble mechanism. They found that with the use of a tumble flap, the flow variability could be decreased which in turn reduced the variability of the air-fuel mixture at the spark plug. Zeng *et al.* (2015) examined the cycle-to-cycle variations of the swirl plane for cases with and without the intake generated swirl. The results showed that the increase of the swirl motion increased the flow stability. The increased flow stability was correlated with higher combustion stability. For improved accuracy of the PIV, high-speed PIV has been used for the in-cylinder flow studies by Müller *et al.* (2010) and Towers and Towers (2004). An improvement of the PIV measurements is the tomographic PIV (TPIV) which measures the 3D flow field and it was applied in a motored DISI optical engine by Baum *et al.* (2013).

With the increase of the computational power and the high parallelism of the CFD codes, LES can be used to perform multi-cycle engine simulations and statistical analysis to investigate the CCV. Numerous studies have been carried in motoring and combustion engine simulations with the use of LES to validate the CFD code, identify the number of cycles required for statistically converged mean and RMS flow field, speed-up the simulations and identify reasons of the cycle-to-cycle variations. According to Ameen *et al.* (2017a), 20 cycles are adequate to obtain statistically converged mean velocity field while Enaux *et al.* (2011) suggested 25 cycles. Simple validation studies used experimental in-cylinder pressure trace Schmitt *et al.* (2015), Enaux *et al.* (2011), Vermorel *et al.* (2007). However, more detailed validation requires in-cylinder flow data such as PIV which were used in the work of Baumann *et al.* (2014), Ameen *et al.* (2017a) and Beavis *et al.* (2016). In order to minimise the time in which a sufficient number of engine cycles is collected for statistically converged data, Ameen *et al.* (2017b proposed to perform several parallel simulations by perturbing the initial and boundary conditions of each of these simulations. This approach showed a good agreement with experimental optical data. The same approach has been used by Van Dam *et al.* (2017) again with good agreement with experiments. The reviews of Haworth (1999), Celik *et al.* (2001) and Rutland (2011) summarise the development and the achievements of the work that has been done with the use of LES in the in-cylinder flow.

In this chapter, the investigation on the CCV of the two different valvetrain strategies namely Dual Valve Actuation and Single Valve Actuation will be presented. From the experimental measurements presented in chapter 4 (Figure 4.2), it can be seen that at the lowest load of 3.6 bar GMEP and for the dilution case of λ=1.0 and 20% EGR, there is a significant difference in the CoV of NMEP between the DVA (3.6%) and SVA (1.4%). The differences between these

two cases at their respective ignition timing (30 deg CA bTDC for DVA and 25 deg CA bTDC for SVA) were studied with the use of LES in a motoring case without fuel injection. However, the cycle started before EVO, with the initial conditions of a combustion case, the same approach as in the previous chapters. The approach of Ameen *et al.* of the parallel simulations was adopted and 25 cycles for each valve strategy were obtained. At the beginning, four RANS simulations were run with the approach of chapter five, meaning that at the end of each cycle (after 720 degrees), the initial conditions of the pressure and temperature and gas composition were applied to the existing solution for the exhaust and cylinder domain, while keeping intact the intake domain. This was done in order to trap an amount of residual gases in the intake port due to the LIVC and to do it accurately, the model with the elongated intake runner was used. In addition, while the 2D template of the mesh was kept the same, more collapsing layers were added which means that more cell layers were added during the expansion, in order to increase the resolution of the grid. With this, the total number of cells at BDC was increased to 3.5 million.

The boundary conditions for the RANS simulations were the experimental average time dependent pressure traces of the intake and exhaust ports and experimental constant temperatures. After the four RANS cycles, two consecutive LES cycles were run, again with the same approach of initialising the exhaust and cylinder domain after a complete cycle. The solution at the end of the second LES cycle was acquired, initialised according to the aforementioned procedure and it was used as the initial conditions for the parallel simulations. The perturbation was introduced by using 25 different experimental pressure traces from individual cycles for both intake and exhaust boundaries. The temperature at the pressure boundaries was kept constant, according to the experimental measurements and the wall temperature was 90°C.

From the validation of the RANS flow field of Chapter 3 in the AJ133 optical engine, it was showed that the results from the study were in an agreement with the work of Beavis *et al.* (2015) who did the RANS validation in the same engine. The same authors validated their LES model against the experimental data of the same engine (Beavis *et al.* 2016) and for this reason, their LES approach was used is this study. The Smagorinsky turbulence model was used with the default constants.

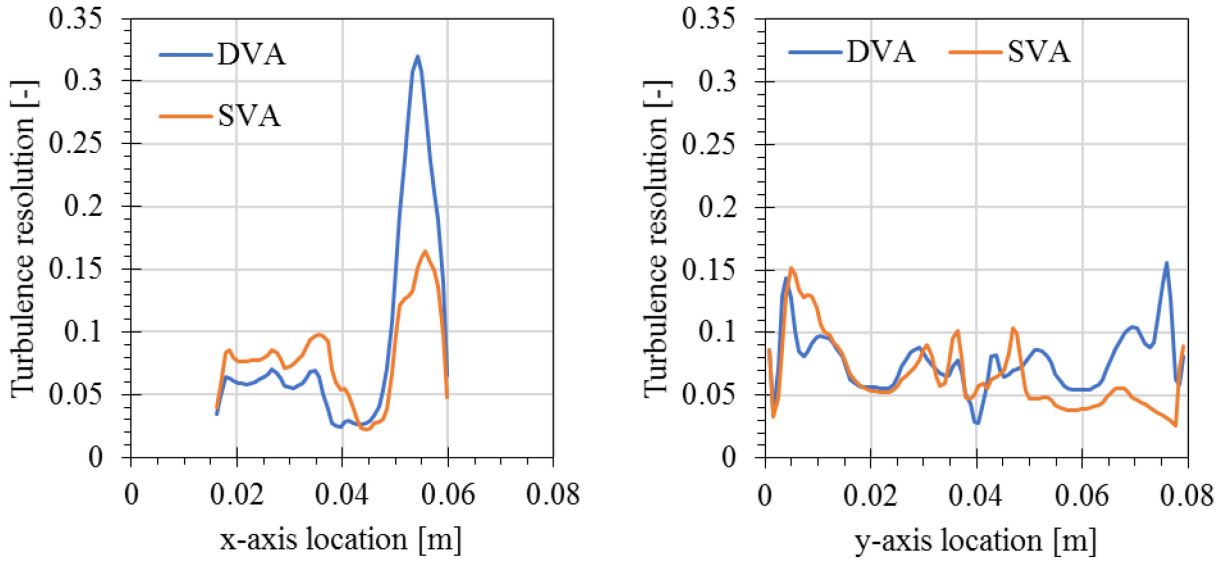
7.2. Model validation

Firstly, the turbulence resolution parameter was calculated to assess that the mesh resolution is satisfactory for the LES study. This parameter was proposed by Pope (2004) and it is given by:

$$M = \frac{k_r}{K + k_r} \tag{7.1}$$

Where K is the turbulence kinetic energy of the resolved motions and k_r the modelled SGS TKE. The value of M is in the range [0,1] and M=0 corresponds to DNS and M=1 corresponds to RANS. For an LES simulation it is recommended that $M \leq 0.2$. A general approach for the LES is to evaluate the parameter M and for the locations where $M > 0.2$ the mesh will be refined, while for very small values of M, the mesh can be coarsened.

This test was carried out for both DVA and SVA simulations and the results at ignition along the x-axis and y-axis at z=+5 mm are showed in Figure 7.1. The results showed that most locations within the cylinder, the turbulence resolution is below the 0.2 criterion except from the DVA, near sharp edges of the cylinder head where the parameter reached M=0.32. However, no further refinement was done in order to keep the computational time in reasonable level of ~48 hours per cycle.



Along x-axis (y=0mm) Along y-axis (x=0mm)

Figure 7.1 Turbulence resolution parameter for DVA and SVA at 30 and 25 degrees before TDC respectively. Cutting line at z=+5mm, x=0mm and y=0mm.

After the check of the mesh suitability, a validation of the LES average in-cylinder pressure trace for both DVA and SVA was carried out and compared against the experimental measurements (Figure 7.2 for DVA and Figure 7.3 for SVA). As it can be seen, the average LES is in a good agreement with the experiment throughout the expansion, intake and compression strokes for both valve strategies. The differences remain at gas exchange TDC where the recompression is not captured which showed that the change of the turbulence modelling did not improve the predictions which were coming from the discharge coefficient of the valves in order to capture the increase of pressure. Moreover, there is a small difference of the polytropic index due to the absence of the fuel vapour as it has already been discussed in chapter 5.

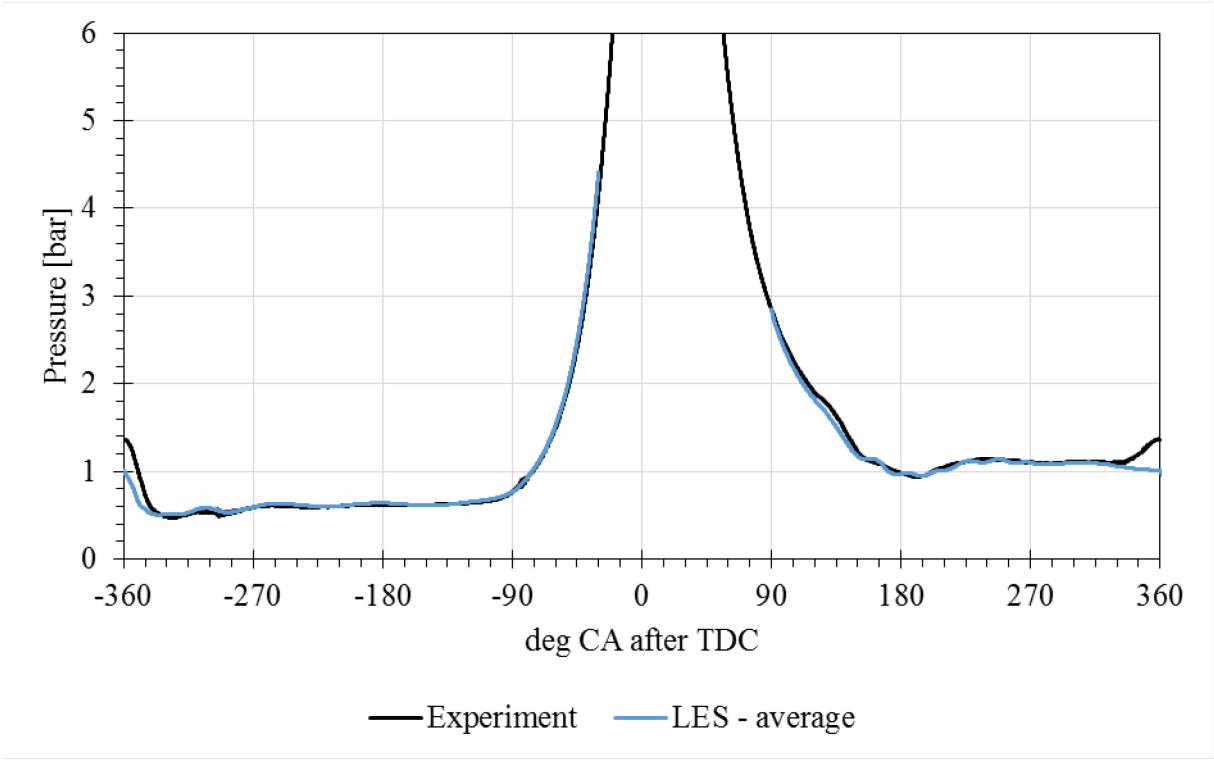


Figure 7.2 Experimental and average over 25 cycles LES in-cylinder pressure trace for DVA

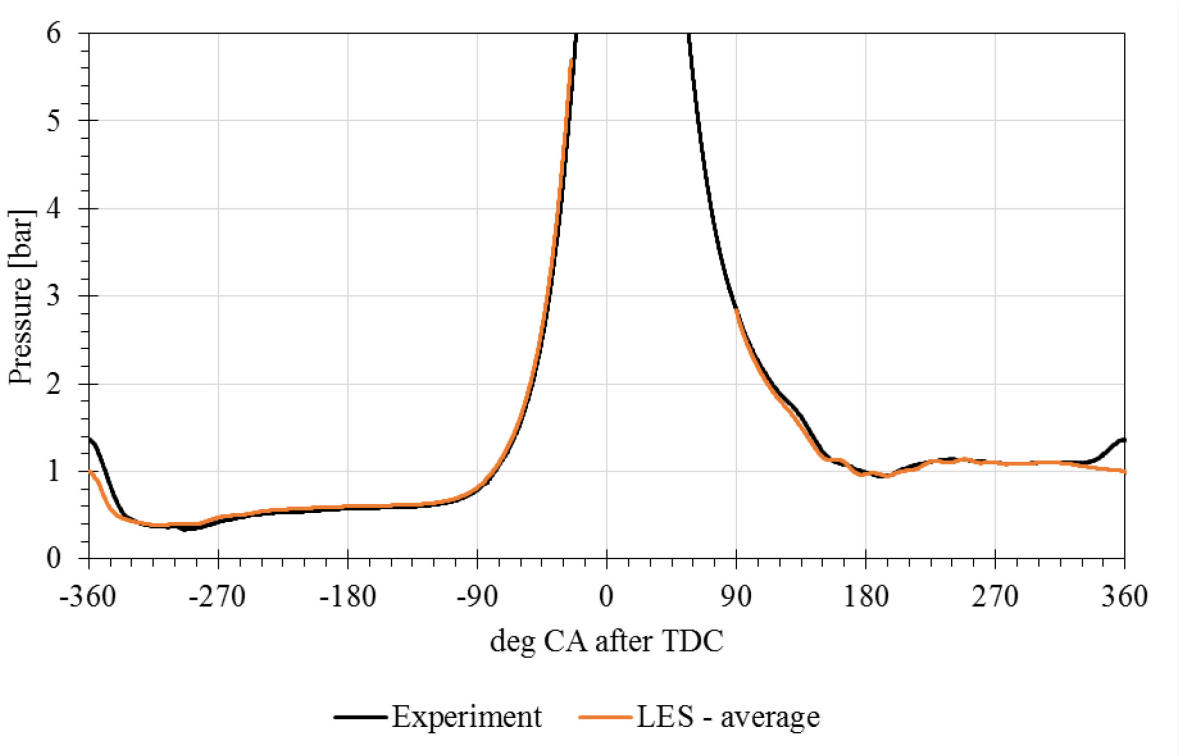


Figure 7.3 Experimental and average over 25 cycles LES in-cylinder pressure trace for SVA

7.3. Averaged in-cylinder flow properties

To investigate the variability of the LES simulations for the DVA and SVA cases, firstly the average in-cylinder quantities of pressure, temperature and velocity were analysed, and the study was focused at ignition of DVA and SVA respectively. In the analysis, the mean (μ) and standard deviation (σ) of the average in-cylinder quantities was calculated. In addition, the coefficient of variation (CoV) was also calculated. This was principally useful for comparing the degree of variation from the two valve strategies especially at ignition, where the means of the quantities were different from one another. The coefficient of variation is defined as:

$$CoV = \frac{\sigma}{\mu} * 100\ \% \tag{7.2}$$

The statistical convergence of the in-cylinder average velocity, standard deviation and CoV at ignition was studied and displayed in Table 7.1. It shows the mean, standard deviation and CoV of 5 and up to 25 LES cycles with an increment of 5 cycles for both DVA and SVA. It can be seen that for DVA, a minimum number of 20 cycles is necessary for statistical convergence of all three quantities. The in-cylinder velocity difference between the 20 and 25 cycles is 0.07% and the biggest difference is 2.5% which is between the mean of 10 and 15 cycles. For SVA,

the maximum difference between the five means was seen for the averages of 5 and 10 cycles and it was 0.4%. It was seen that the mean velocity converged faster and the difference between the means of 20 and 25 cycles was 0.07%. However, the standard deviation and the CoV needed 25 cycles to converge. It is possible that more than 25 cycles were needed for better estimate the convergence of standard deviation and COV for the SVA.

	DVA			**SVA**		
# of Cycles	**Mean [m/s]**	**Standard Deviation [m/s]**	**CoV [%]**	**Mean [m/s]**	**Standard Deviation [m/s]**	**CoV [%]**
5	9.12	0.32	3.47	19.13	0.26	1.36
10	9.02	0.42	4.66	19.21	0.24	1.25
15	9.12	0.40	4.36	19.20	0.24	1.25
20	9.237	0.442	4.785	19.178	0.225	1.17
25	9.243	0.443	4.793	19.191	0.212	1.10

Table 7.1 Statistical convergence of the mean, standard deviation and CoV average in-cylinder velocity for DVA and SVA

After confirming that the in-cylinder velocity was statistically converged, the in-cylinder pressure, temperature and velocity were studied at the respective DVA and SVA ignition timings. The LES average in-cylinder pressure over 25 cycles for DVA and SVA is shown in Table 7.2. It can be said that the standard deviation (SD) and the CoV are very low and no substantial differences in the pressure traces for both valve strategies were observed. The standard deviation for the SVA is 800Pa which is well within the atmospheric pressure changes due to weather conditions, meaning that these changes are not significant. The higher pressure variation of the SVA comes from the higher variation in trapped mass (0.1% CoV of trapped mass for DVA and 0.12% for SVA).

	DVA	**SVA**
Mean (25 cycles) [bar]	4.43	5.69
Standard deviation (25 cycles) [bar]	0.0036	0.008
Coefficient of variation (25 cycles) [-]	0.08%	0.14%

Table 7.2 Mean, standard deviation and CoV of in-cylinder pressure over 25 cycles

Similarly, small variations were also observed for the bulk in-cylinder temperature as it can be seen from Table 7.3. The standard deviation for both cases is very similar (0.54K) as well as the coefficient of variation (0.09%-0.08%).

	DVA	**SVA**
Mean (25 cycles) [K]	611.4	669.7
Standard deviation (25 cycles) [K]	0.54	0.54
Coefficient of variation (25 cycles) [-]	0.09%	0.08%

Table 7.3 Mean, standard deviation and CoV of in-cylinder temperature over 25 cycles

The maximum variations were observed for the in-cylinder velocity magnitude and the DVA produced significant higher coefficient of variation comparing to the SVA. The in-cylinder velocity magnitude of the 25 individual cycles and their mean for DVA and SVA are displayed in Figure 7.4. In the same graph, the in-cylinder velocity of the RANS simulation is also plotted. It can be seen that for a great period and especially during compression and near ignition, the RANS velocity is below the average LES. Similar differences between RANS and LES in the tumble and swirl ratios (which are directly linked to the in-cylinder velocity) were also seen by Bottone *et al.* (2012). However, the relative difference between SVA/DVA velocity at ignition is the very similar for both RANS and LES (2.06 and 2.08 respectively). Because of the differences between RANS and LES and not to overpopulate the graphs, the study was focused only on the LES results.

For the LES runs, it is evident that for DVA, the deviation is greater than the SVA case, especially during the compression stroke. To quantify these differences, the standard deviation (Figure 7.5) and the coefficient of variation (Figure 7.6) were also plotted for the intake and compression stroke. The standard deviation of the in-cylinder velocity magnitude is very similar for both valve strategies especially until mid-intake stroke. After that, for the DVA the standard deviation is around 0.3 m/s while for the SVA was 0.3 m/s. From IVC up to TDC the standard deviation is reduced for SVA and it dropped to 0.2 m/s while for the DVA it was increased to ~0.5 m/s. Because of the small standard deviation for both DVA and SVA and the very different mean velocity, the CoV was used to quantify the differences of the variations. It is clear that from the mid-intake stroke, the CoV of the DVA in-cylinder velocity magnitude was constantly increased and at ignition it reached the value of 4.8%. For the SVA however, the CoV did not vary and it was around 1.5% and at ignition it was 1.17%. Similar variations

between the DVA and SVA were seen for the combustion stability (CoV of NMEP) of the experimental data (3.6% for DVA and 1.4% for SVA). The data at ignition for DVA and SVA have been already displayed in Table 7.1.

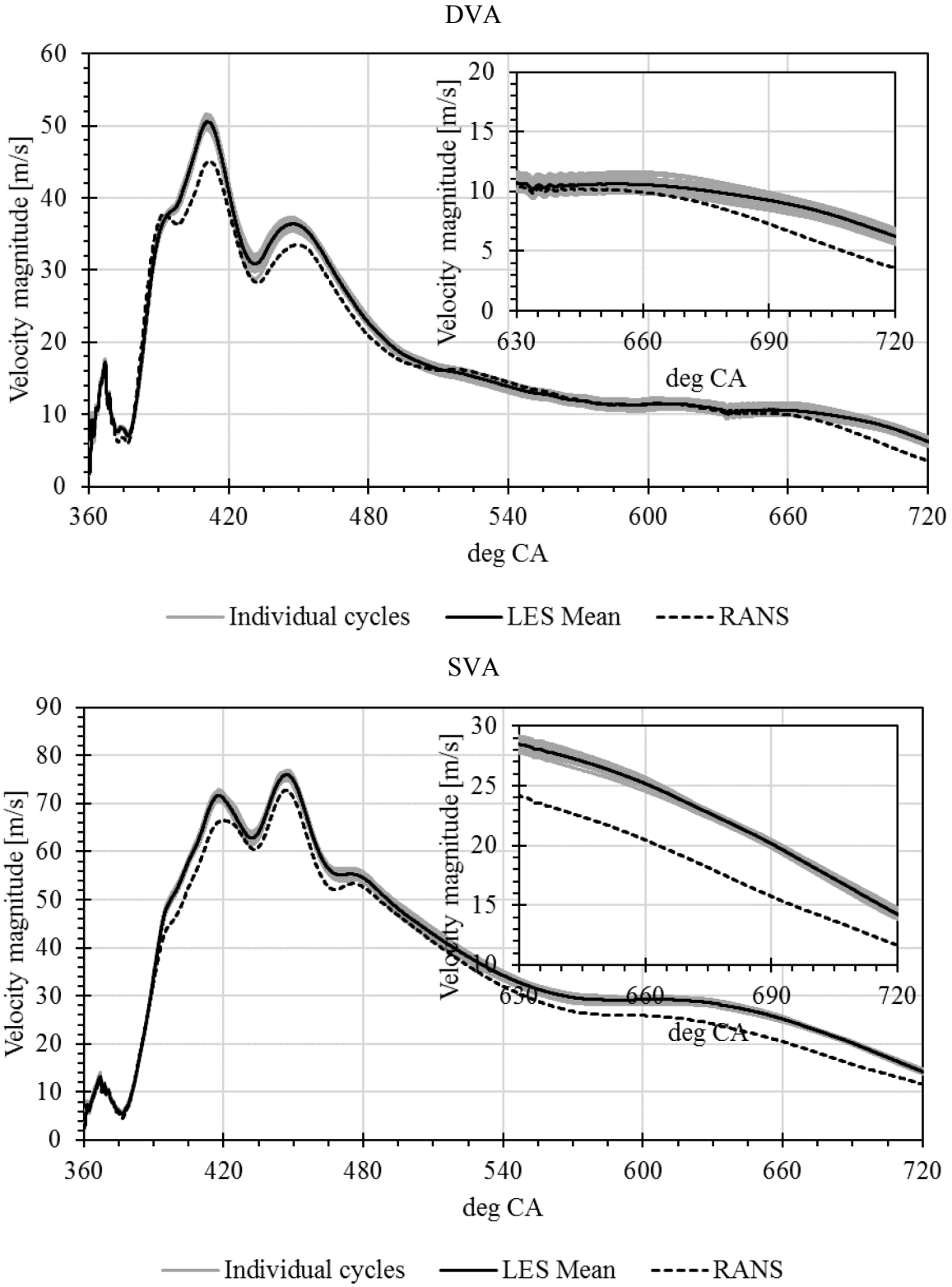


Figure 7.4 in-cylinder velocity magnitude of the 25 individual cycles and their mean for DVA and SVA

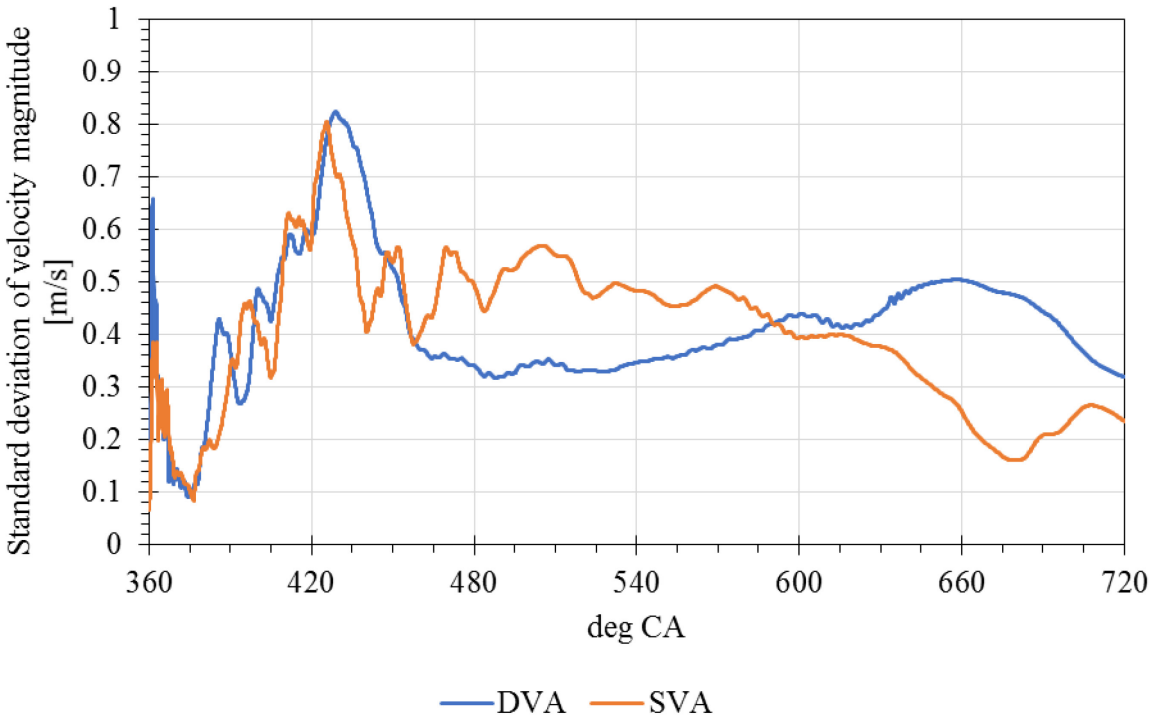


Figure 7.5 Standard deviation of average in-cylinder velocity for 25 cycles during intake and compression strokes for DVA and SVA

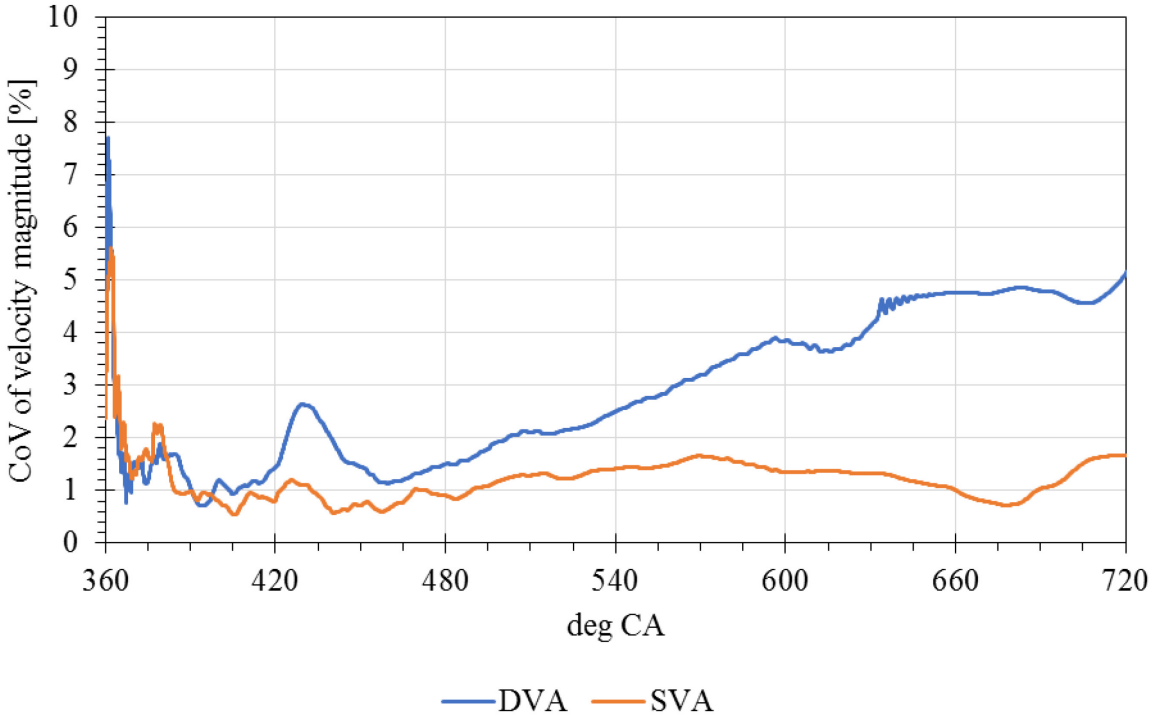
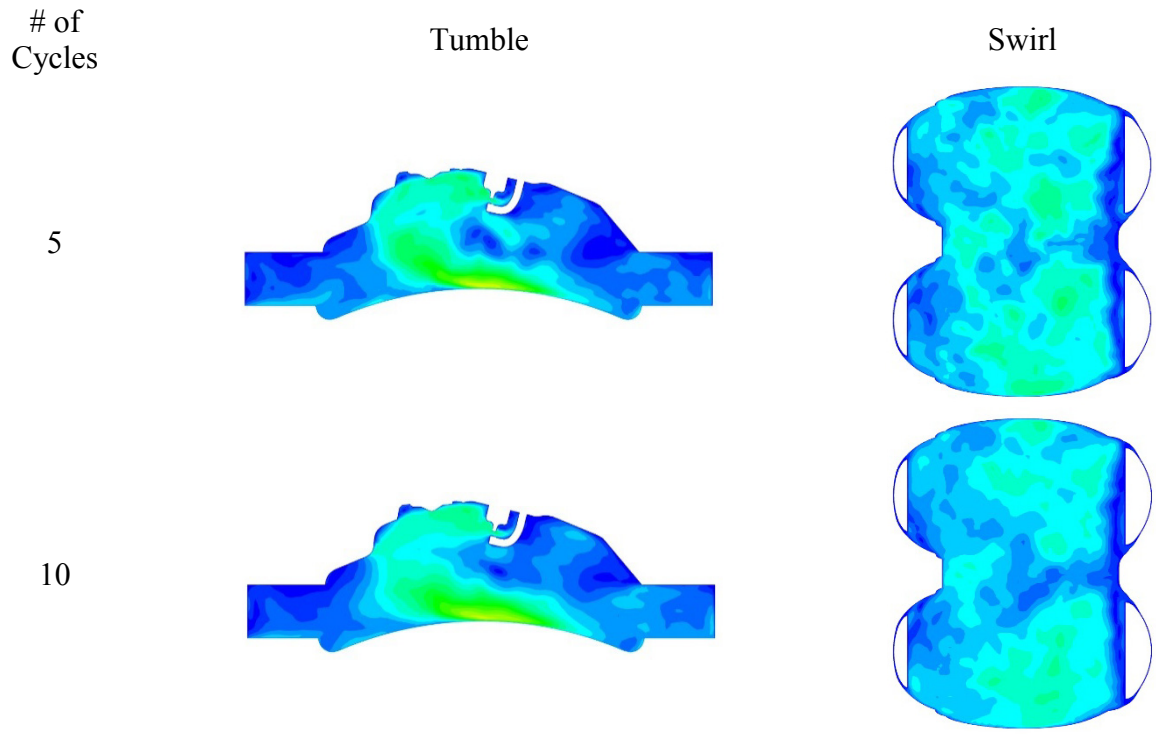


Figure 7.6 CoV of average in-cylinder velocity for 25 cycles during intake and compression strokes for DVA and SVA

7.4. Spatial distribution of in-cylinder flow properties

Firstly, the statistical convergence of the velocity magnitude was studied spatially within the cylinder at ignition for both valve strategies. The ensemble-average velocity magnitude of the velocity magnitude were plotted in Figure 7.7 for the first 5, 10, 15, 20 and 25 cycles in the tumble and swirl planes for DVA. From the contour plots of velocity, it was evident that the differences between the average of 20 and 25 cycles are minor. To quantify the differences, the mean velocity magnitude along the x-axis of the tumble plane at z=+5 mm and along the y-axis of the swirl plane at x=0 mm was plotted for the five different averaging groups and displayed in Figure 7.8. Both graphs showed the convergence even after 15 cycles, which agrees with studies showing that after 10 cycles there is a reasonable statistical convergence of the velocity field Vermorel *et al.* (2009), Enaux *et al.* (2011) and Hasse *et al.* (2010). Moreover, the spatial distribution of the standard deviation of the velocity magnitude was also plotted for the five averaging groups (Figure 7.9) as well as the graphs along the x- and y-axis (Figure 7.10). Again, with 15 cycles and above there was a statistical convergence.



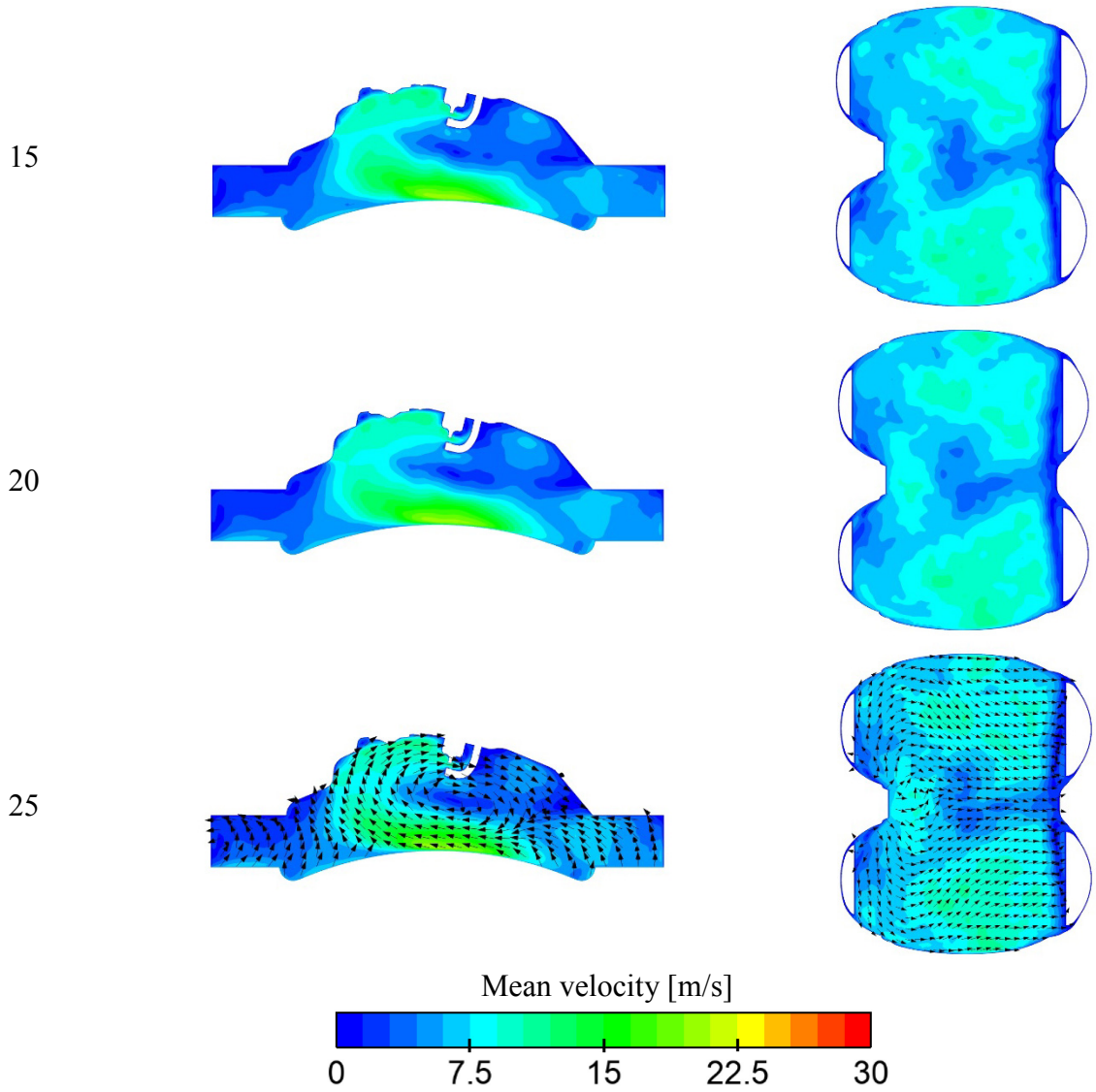


Figure 7.7 Statistical convergence of the velocity magnitude for the first 5, 10, 15, 20 and 25 cycles in the tumble and swirl planes for DVA

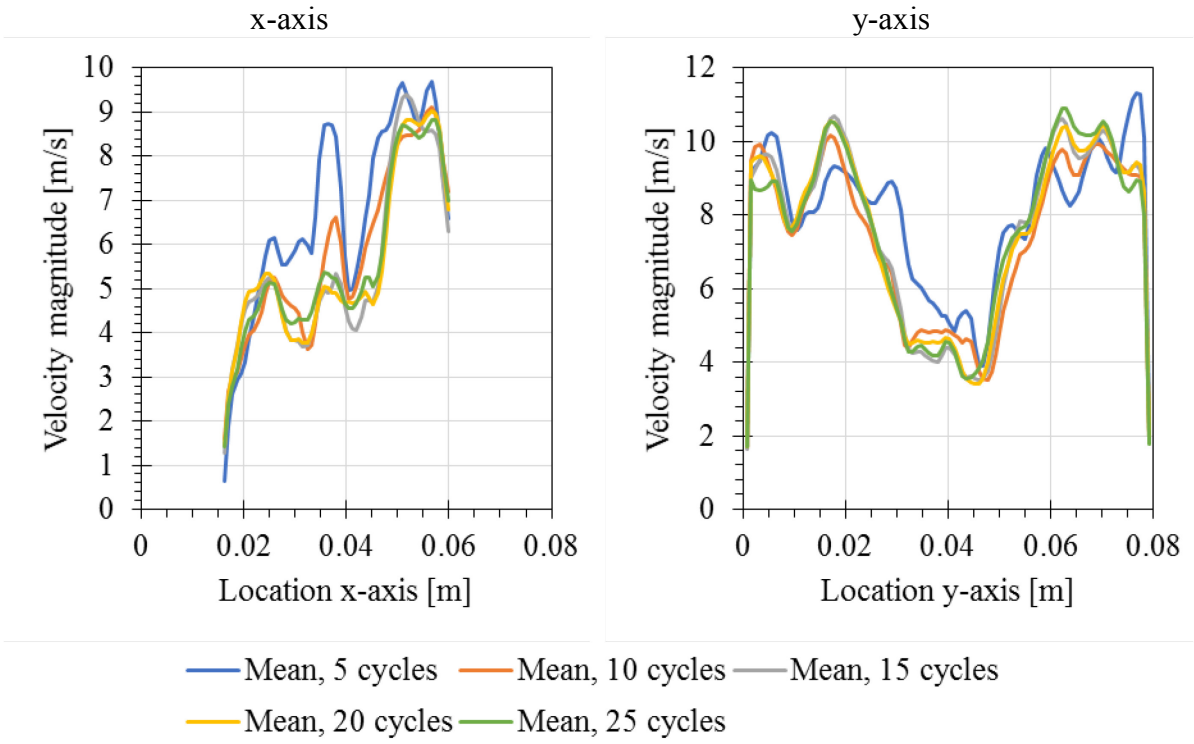
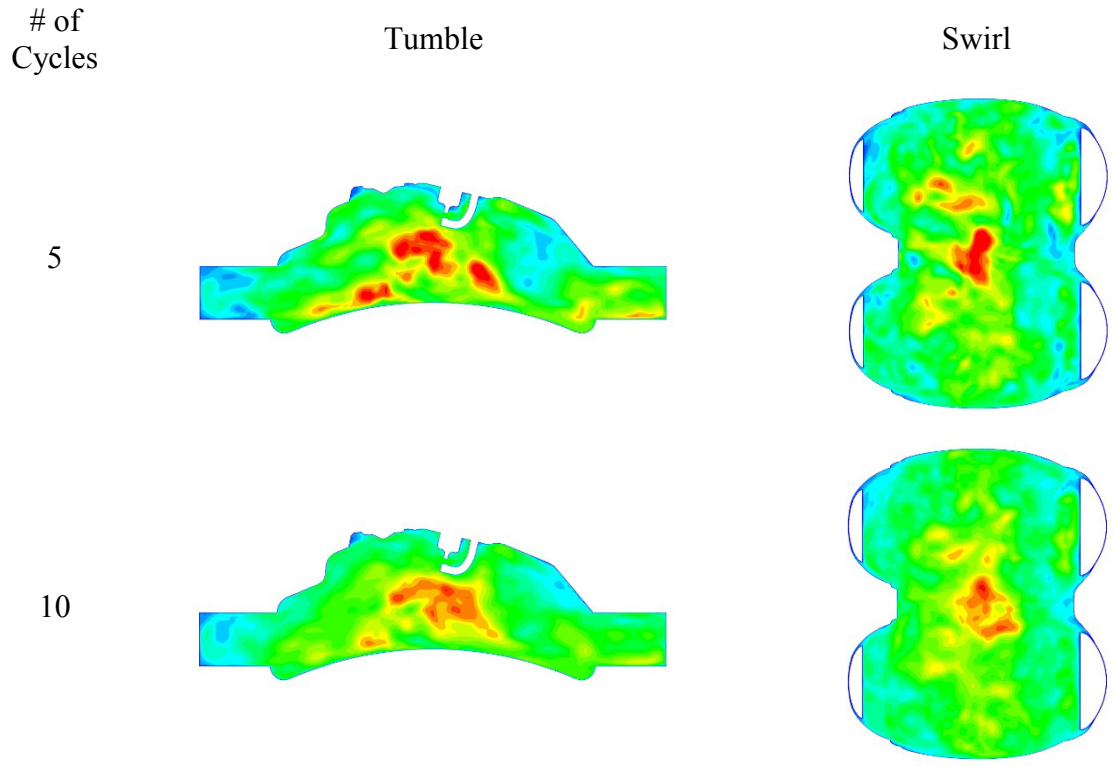


Figure 7.8 Mean velocity magnitude along the x- and y-axis at z=+5 mm for the five different averaging groups. DVA



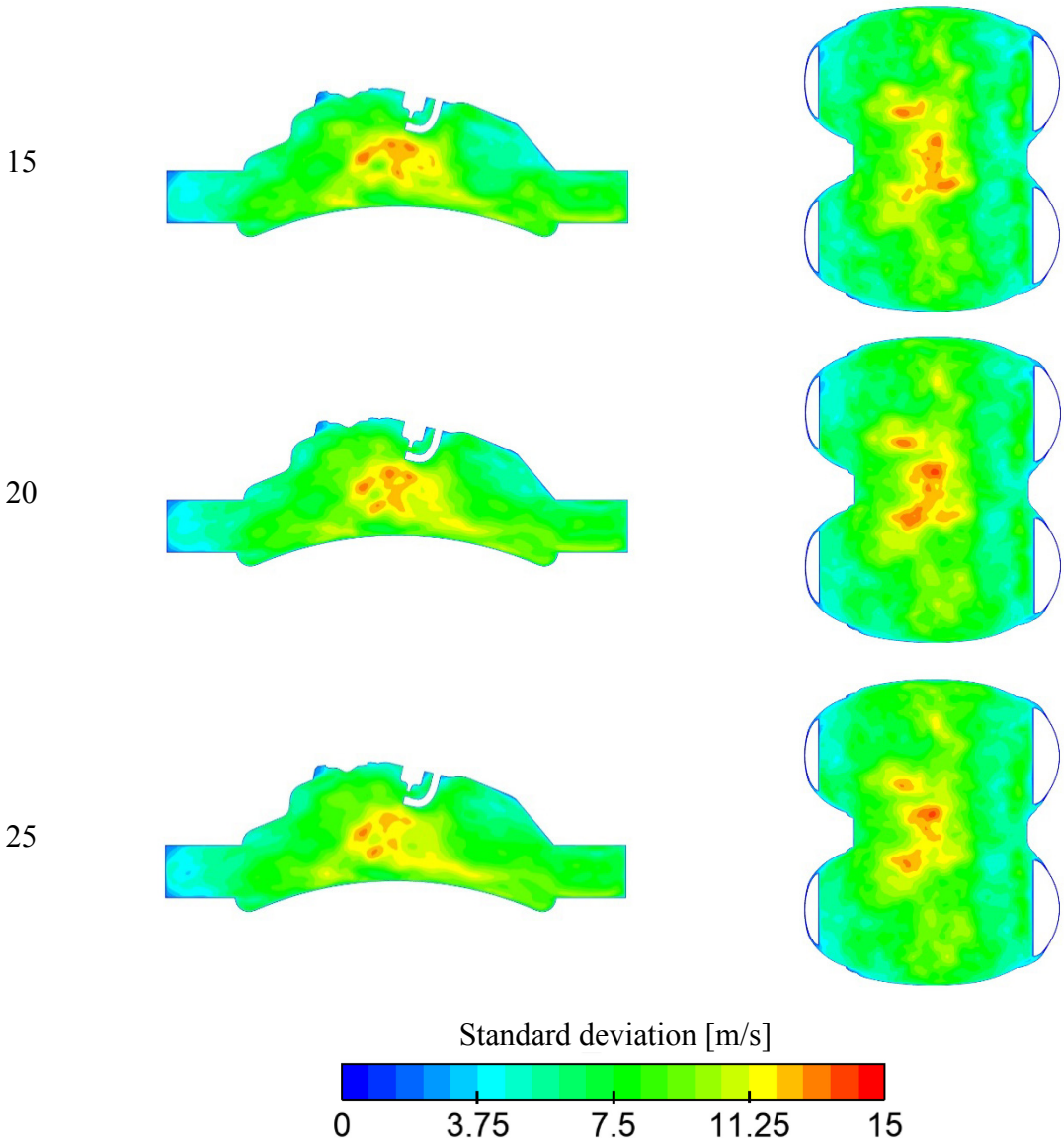


Figure 7.9 Statistical convergence of the standard deviation of the velocity magnitude for the first 5, 10, 15, 20 and 25 cycles in the tumble and swirl planes for DVA

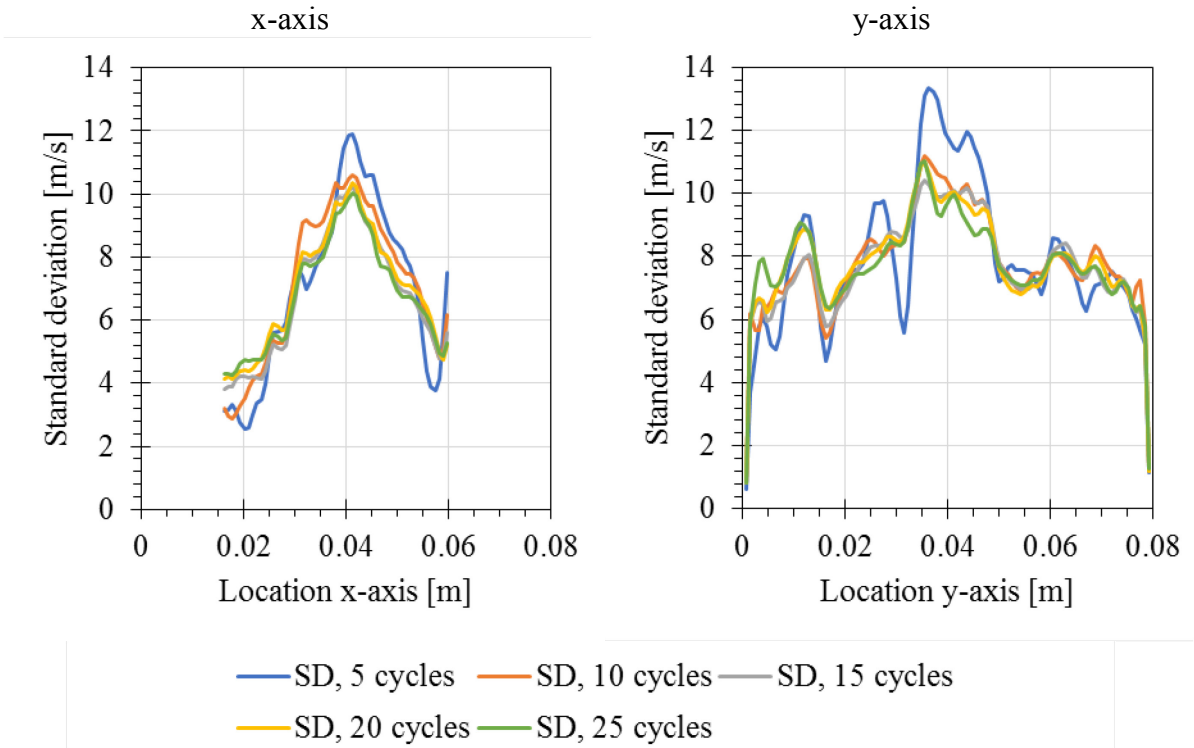


Figure 7.10 Standard deviation of velocity magnitude along the x- and y-axis at z=+5 mm for the five different averaging groups. DVA

The spatial distribution of ensemble-average velocity magnitude in Figure 7.11 and the standard deviation of the velocity magnitude in Figure 7.13 were plotted for SVA for the first 5, 10, 15, 20 and 25 cycles in the tumble and swirl planes. From the contour plots of velocity, it can be seen that the differences between the average of 20 and 25 cycles are minor. Again, to quantify the differences, the mean velocity magnitude along the x-axis of the tumble plane at z=+5 mm and along the y-axis of the swirl plane at x=0 mm was plotted in Figure 7.12. Both graphs showed the convergence even after 15 cycles. The same behaviour was seen for the standard deviation of the velocity magnitude which started to converge after 20 cycles. This is evident from the graphs of standard deviation along the x- and y-axis shown in Figure 7.14. It has to be mentioned that the limits of the SD legend are different for DVA and SVA due to the higher standard deviation of SVA. However, this was expected as the standard deviation of the velocity or otherwise, the velocity RMS is linked to the turbulent kinetic energy with higher RMS showing higher TKE, which is the case of SVA over DVA.

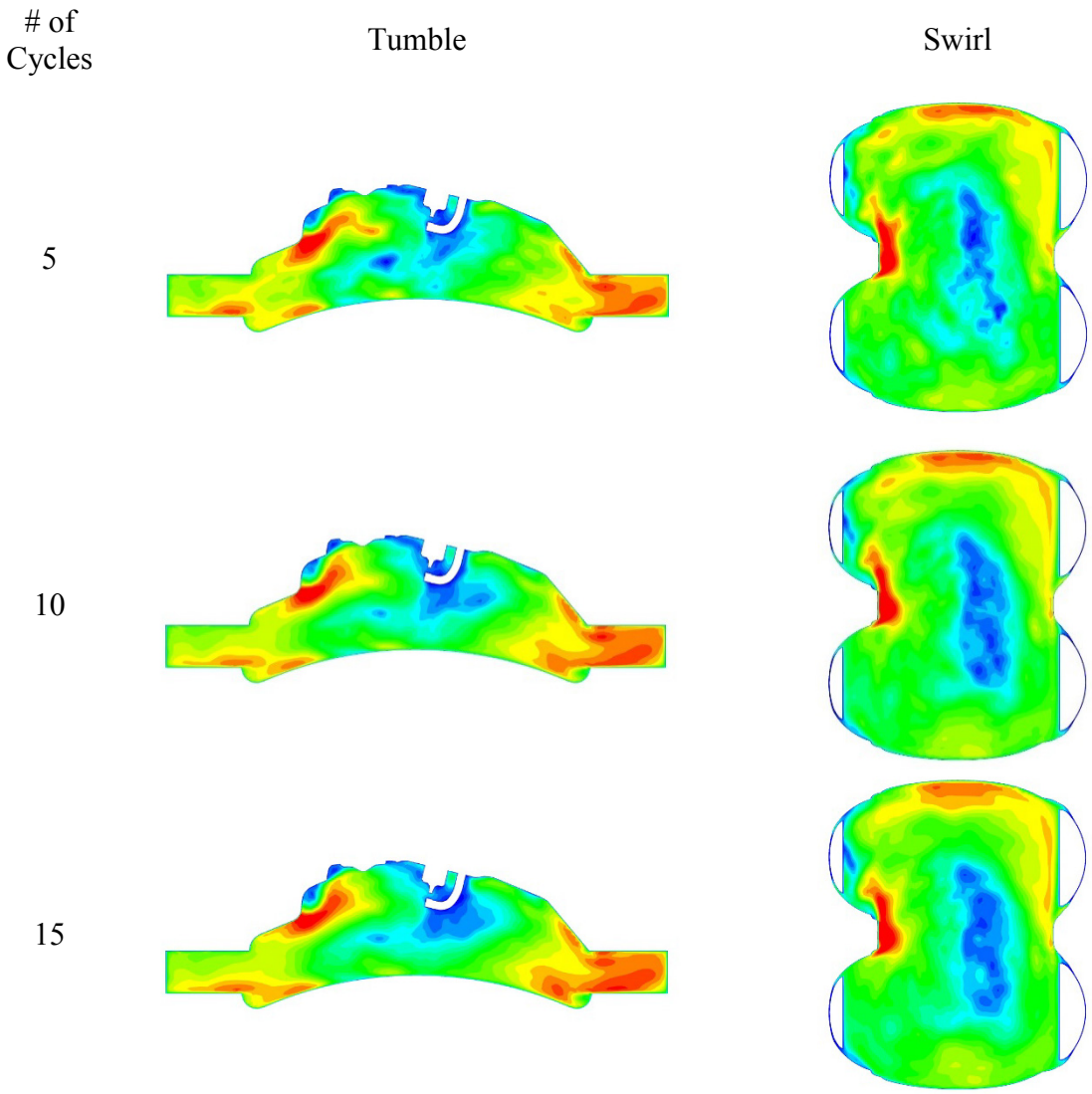


Figure 7.11 Statistical convergence of the velocity magnitude for the first 5, 10, 15, 20 and 25 cycles in the tumble and swirl planes for SVA

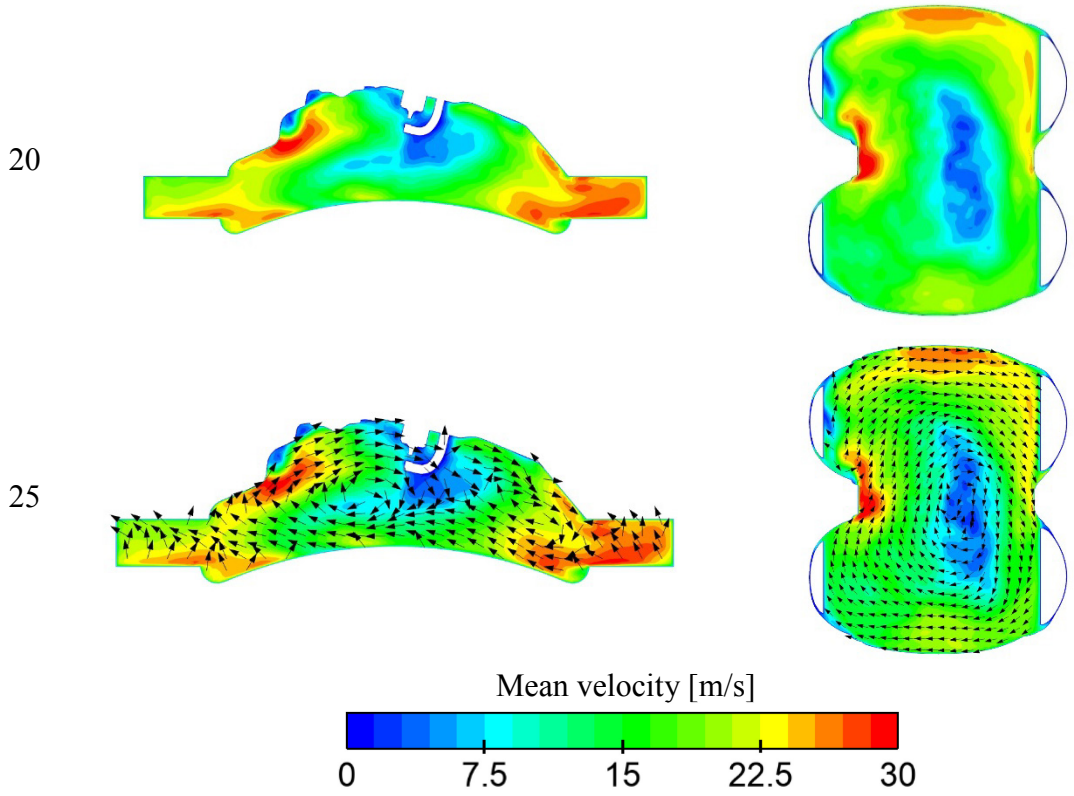


Figure 7.11cont. Statistical convergence of the velocity magnitude for the first 5, 10, 15, 20 and 25 cycles in the tumble and swirl planes for SVA

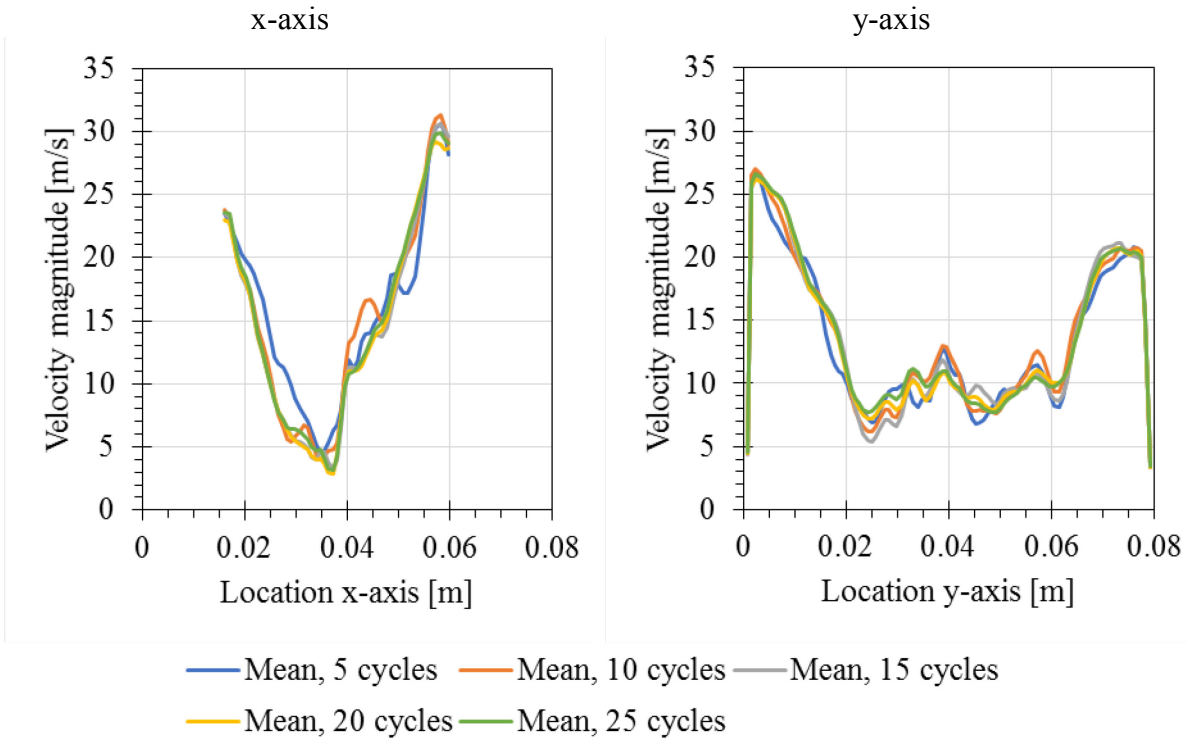


Figure 7.12 Mean velocity magnitude along the x- and y-axis at z=+5 mm for the five different averaging groups. SVA

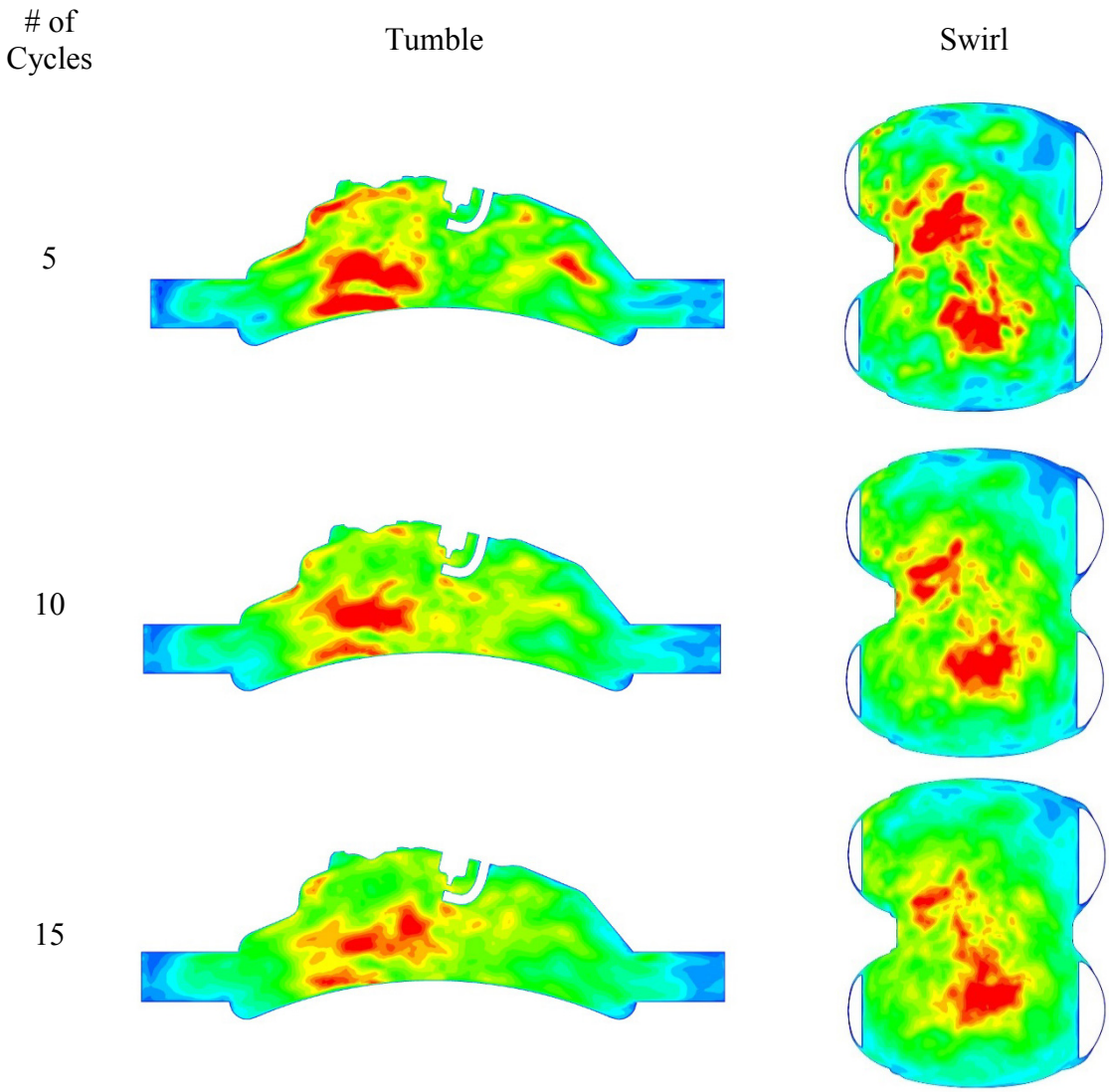


Figure 7.13 Statistical convergence of the standard deviation of the velocity magnitude for the first 5, 10, 15, 20 and 25 cycles in the tumble and swirl planes for SVA

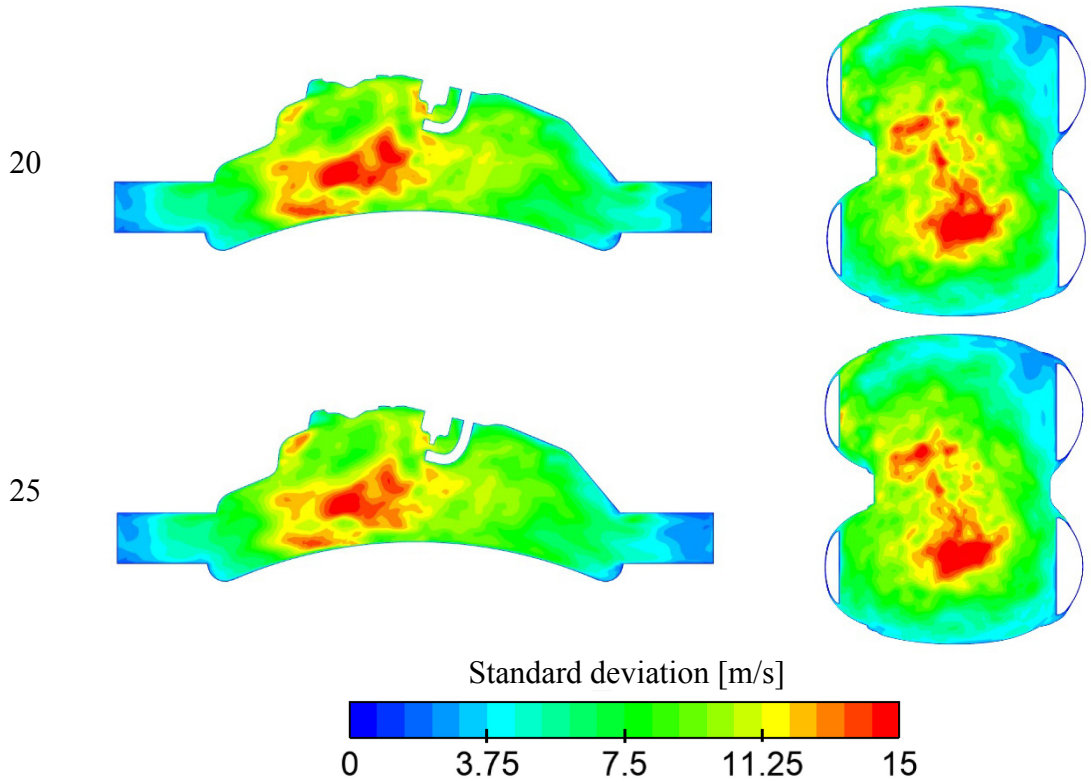


Figure 7.13cont. Statistical convergence of the standard deviation of the velocity magnitude for the first 5, 10, 15, 20 and 25 cycles in the tumble and swirl planes for SVA

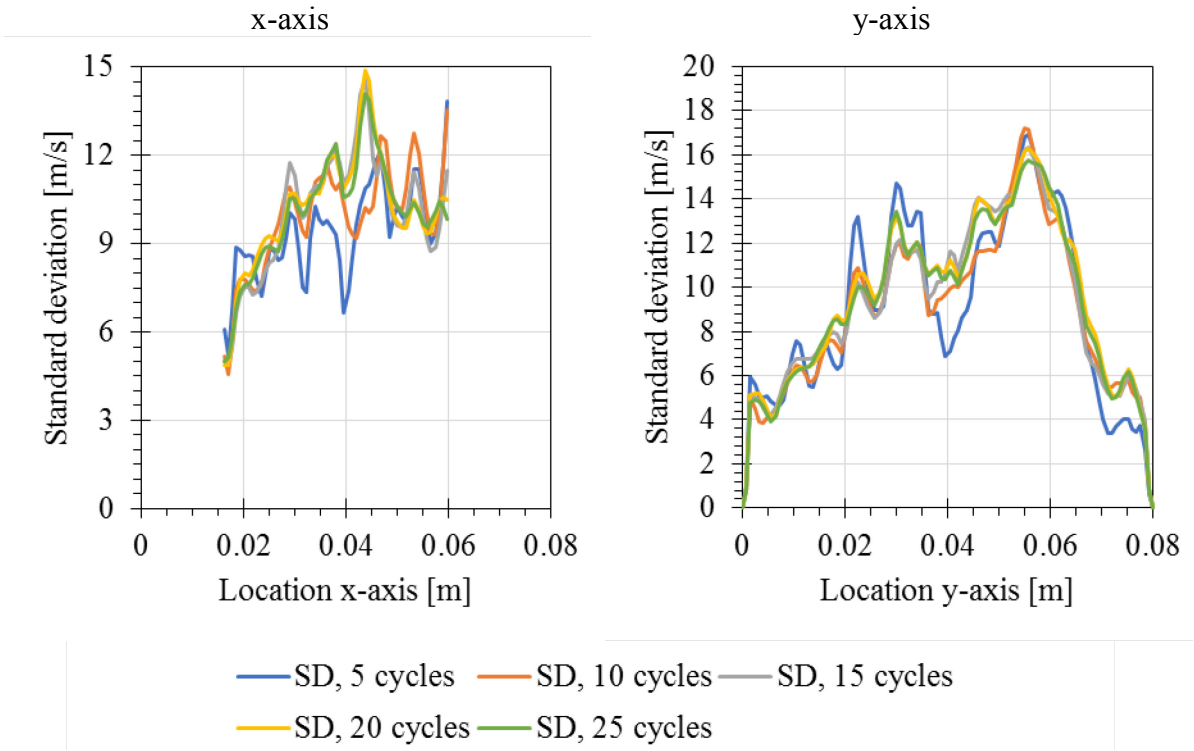
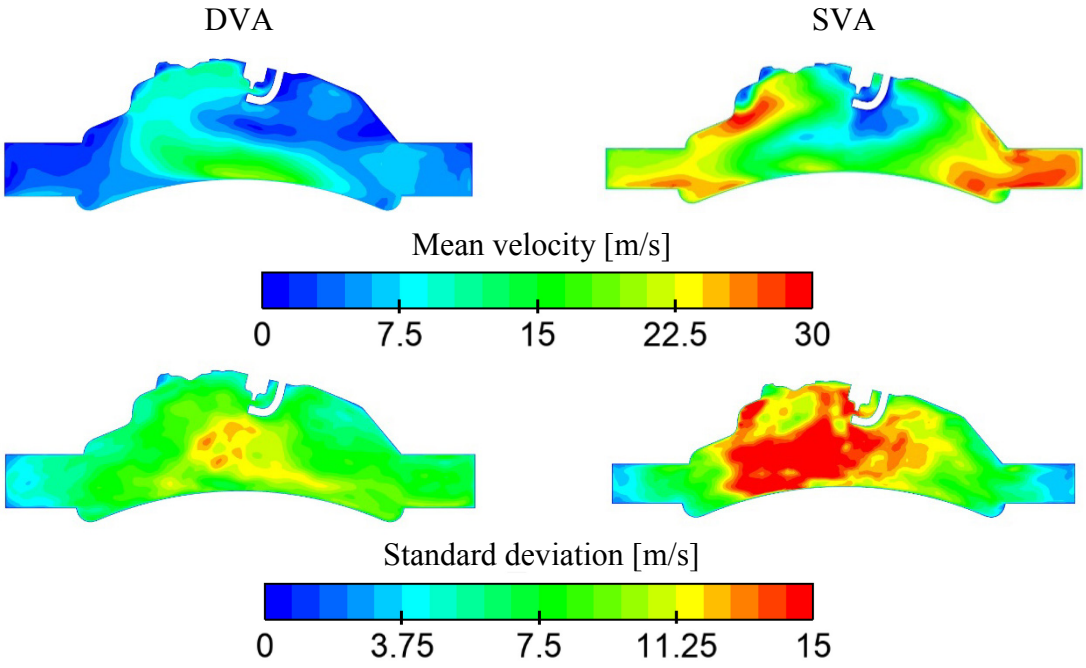


Figure 7.14 Standard deviation of velocity magnitude along the x- and y-axis at z=+5 mm for the five different averaging groups. SVA

To further investigate the CCV of the DVA and SVA strategies, the spatial distribution of the mean, standard deviation and the variability of the velocity magnitude, temperature, residual gases and laminar burning velocity were investigated at the same swirl and tumble planes as before. All the analysis was based on the sample of 25 cycles. Firstly, the spatial distribution of the velocity variations were examined. Figure 7.15 compares the mean, standard deviation and coefficient of variation of DVA and SVA in the tumble plane and Figure 7.16 in the swirl plane. For the SD, the same limits have been used in the legend for direct comparison. For another representation of the SD with different limits on the legend for SVA the reader can refer to Figure 7.13. As it was already said, the SD of the velocity (Velocity RMS) is greater for SVA than DVA which denoted higher turbulent kinetic energy and was also better located for SVA. A comparison of the coefficient of variation between the two valve strategies showed that in the vicinity of the spark plug, both DVA and SVA showed high coefficient of variation due to the very low mean velocity. Similarly for the swirl plane, the CoV is high in the areas where the mean velocity of the flow is close to zero. In addition, it was observed that for both DVA and SVA, the fluctuations in the dominant stream (tumble flow for DVA and swirl plane for SVA and are represented by the highest velocity magnitude) were reduced, but for DVA they were higher than SVA. These can be seen at the contour plots with low CoV values.



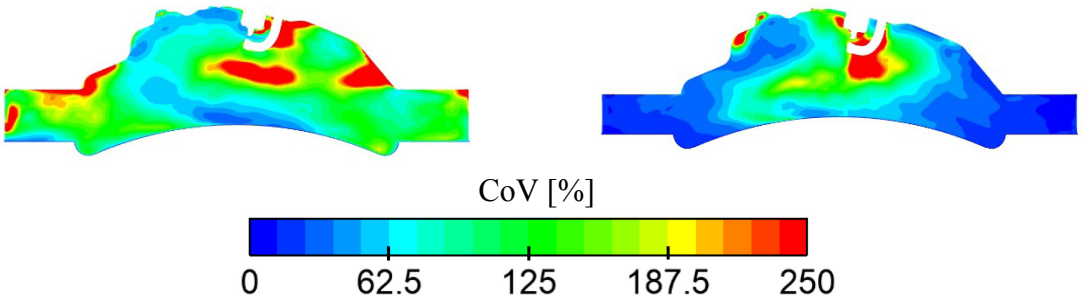
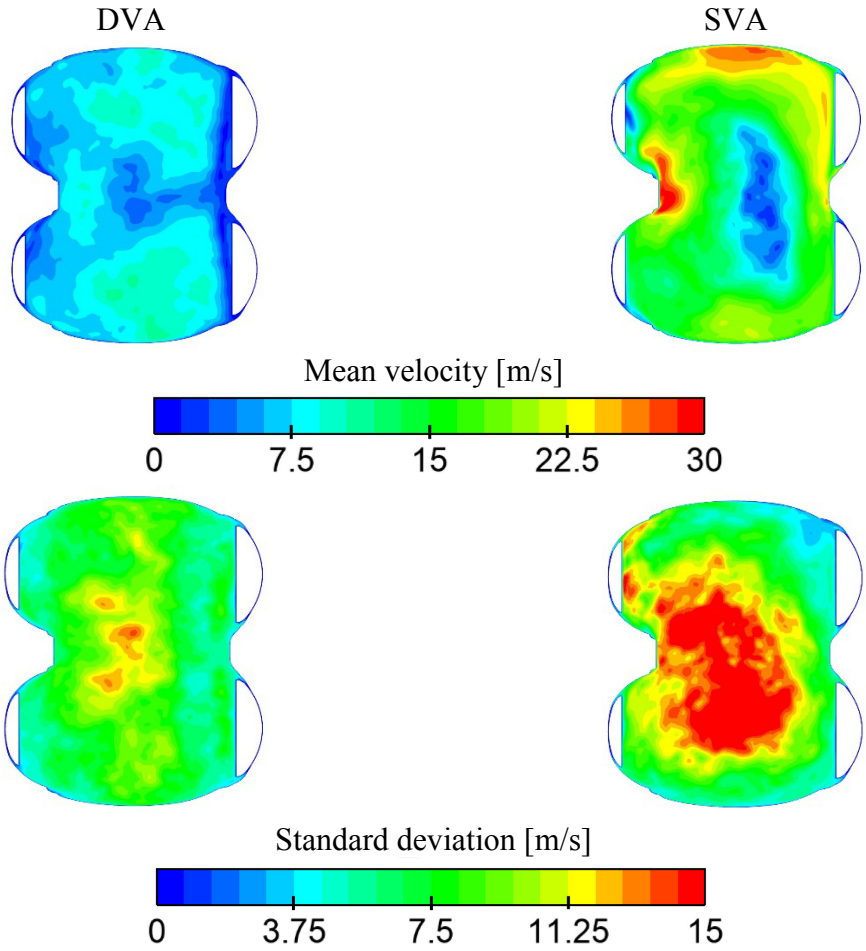


Figure 7.15 Spatial distribution of mean, standard deviation and coefficient of variation of DVA and SVA over 25 cycles. Tumble plane



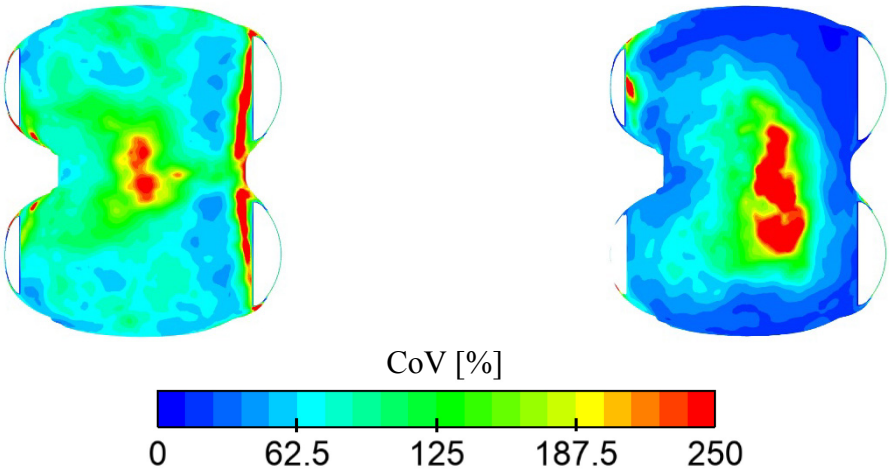


Figure 7.16 Spatial distribution of mean, standard deviation and CoV of DVA and SVA over 25 cycles. Swirl plane

The mean, the standard deviation and the coefficient of variation of the laminar burning velocity was studied spatially within the cylinder. The variations of the laminar burning velocity are important as they affect the combustion behaviour. In addition, due to the increased dilution with EGR, the laminar burning velocity is expected to decrease which makes its impact more severe. An inspection of the mean laminar burning velocity in the tumble and swirl planes for DVA and SVA showed that at ignition, the S_L is around 29 cm/s and 34 cm/s respectively. This was expected as the gas temperature was much higher for SVA. In addition, the standard deviation of the laminar burning velocity in the cylinder was similar for the two valve strategies but lower for the SVA. This was also reflected on the CoV which was lower for SVA. This showed that for DVA with lower burning velocities and higher variations, this can lead to very low burning velocities in some cycles which will in turn affect the combustion event as seen in the variations of the experiments. The variations were quantified in the x-axis and y-axis, 5mm above the fire face of the head and are showed in Figure 7.19. It is evident that the Single Valve Actuation exhibited lower variations of the laminar burning velocity with the maximum value of 3.2% and 3.8 % when Dual Valve was adopted (The values near the walls were excluded). Within the cylinder, the SVA variations are in the order of 1.5% and for the DVA 2%-3%.

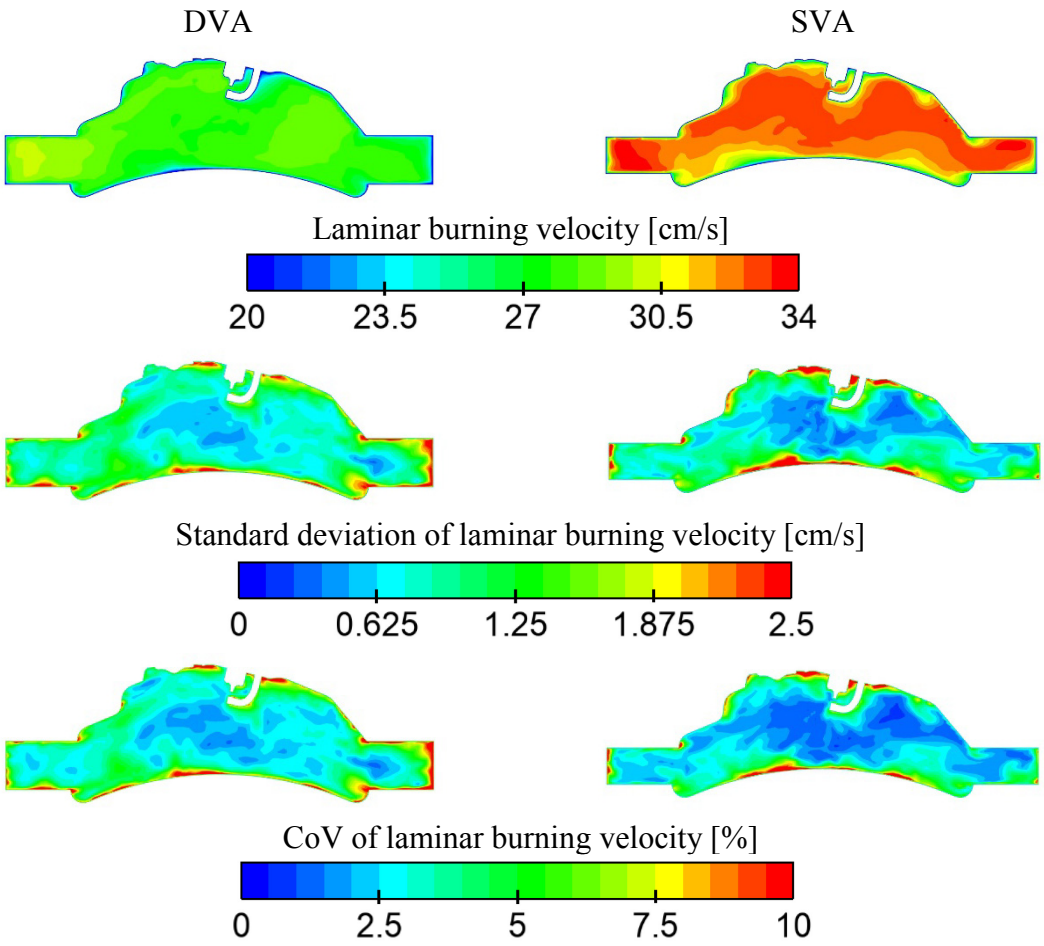
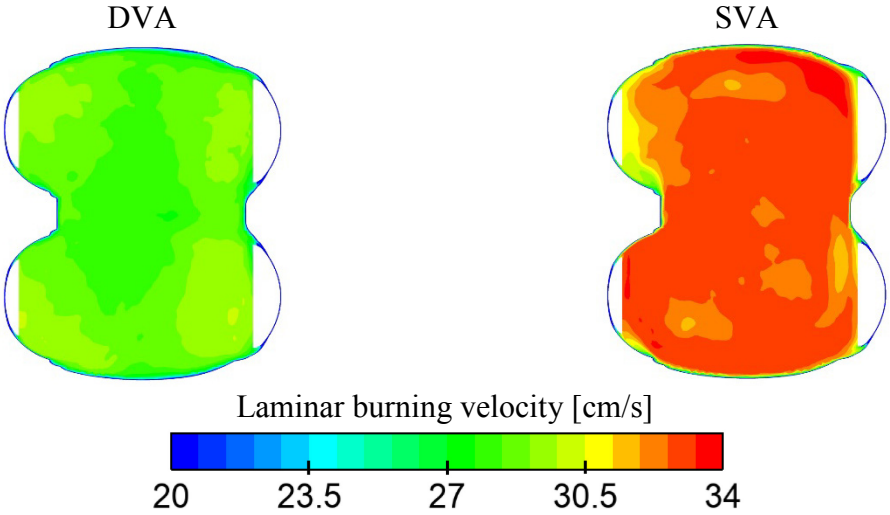


Figure 7.17 Spatial distribution of mean, standard deviation and CoV of laminar burning velocity of DVA and SVA over 25 cycles. Tumble plane



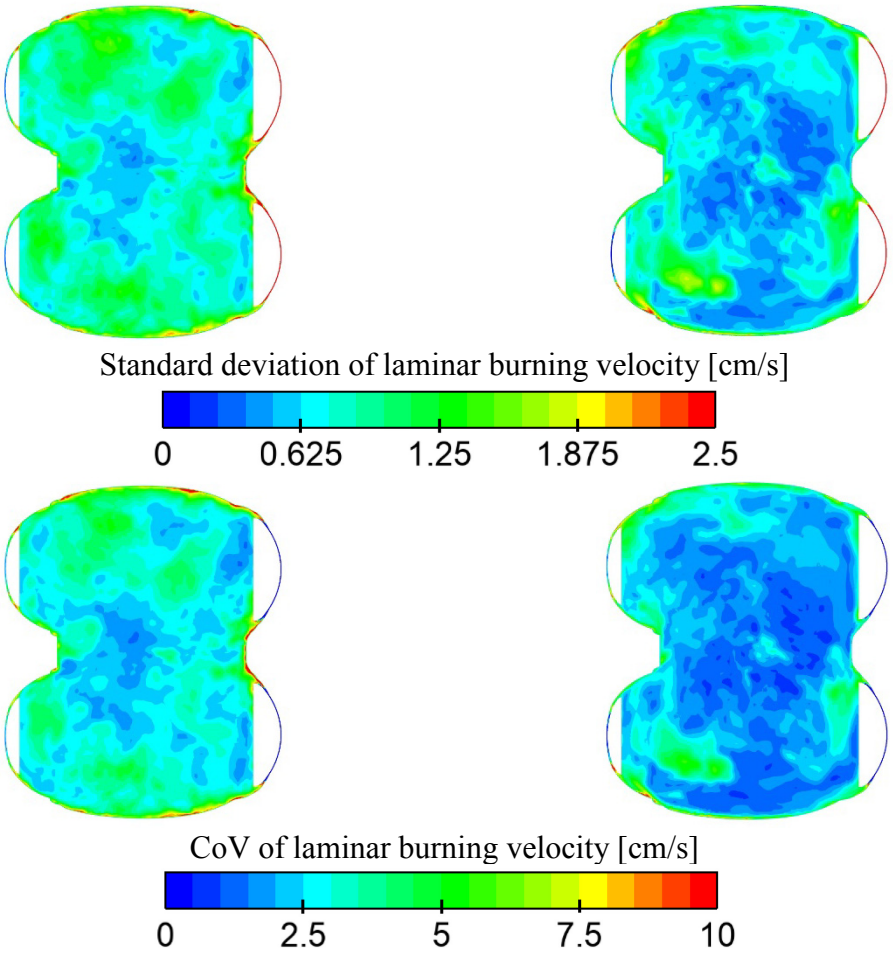


Figure 7.18 Spatial distribution of mean, standard deviation and CoV of laminar burning velocity of DVA and SVA over 25 cycles. Swirl plane

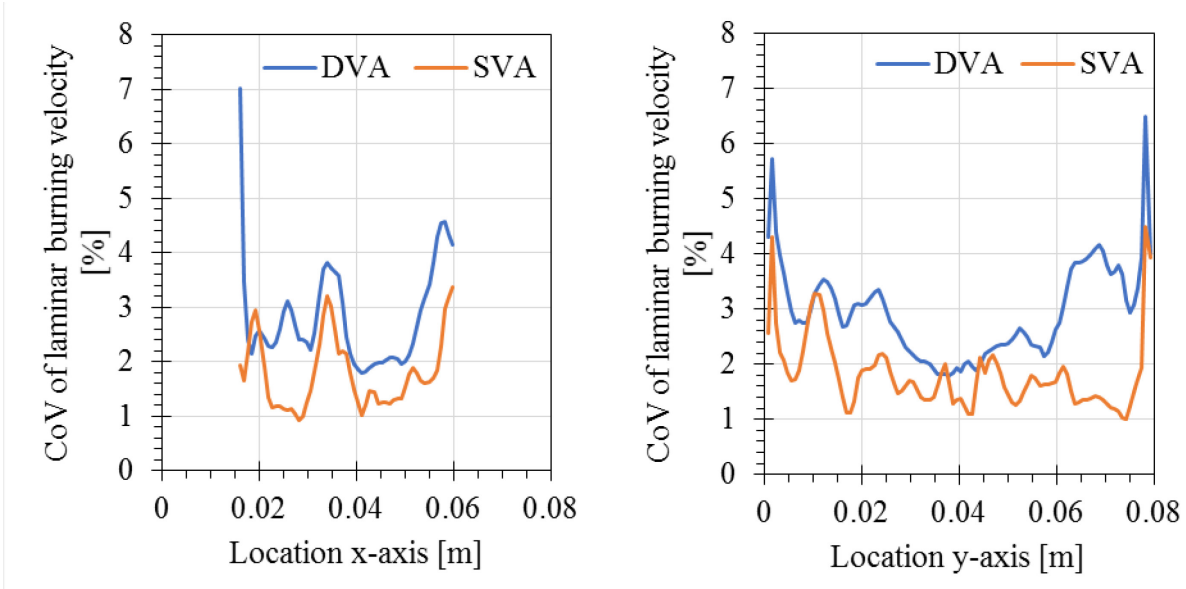
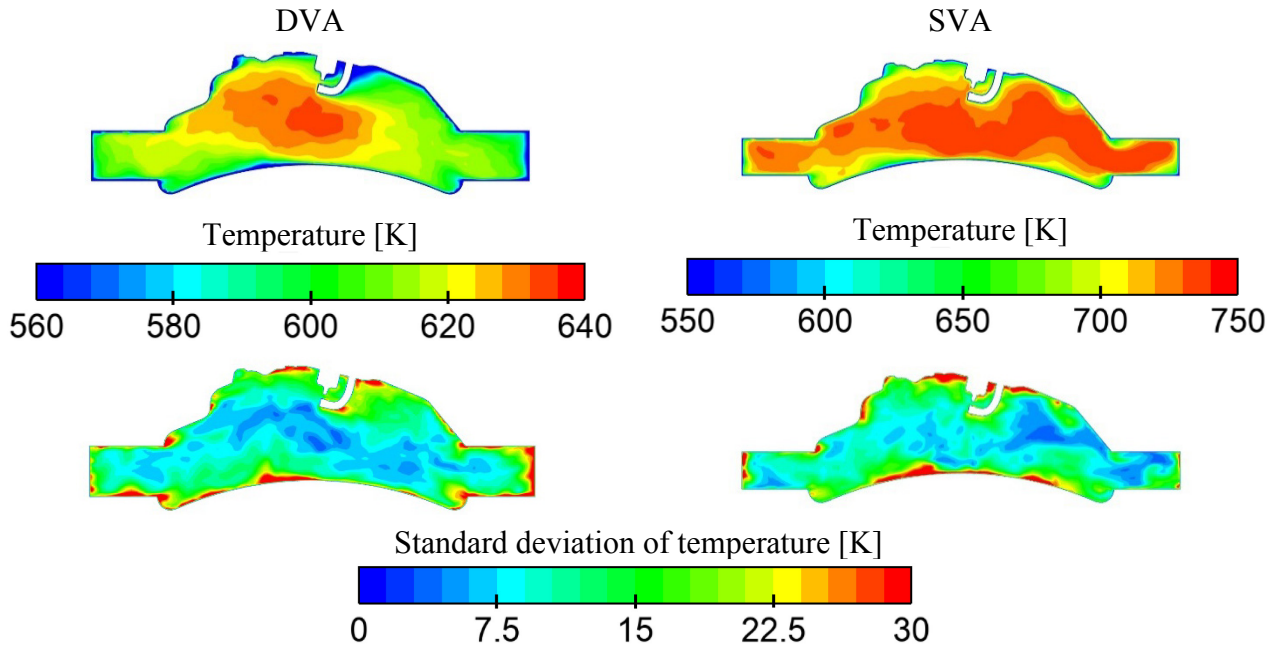


Figure 7.19 CoV of laminar burning velocity for DVA and SVA along the x- and y-axis at z=+5mm

The two main contributors for the laminar burning velocity variations were the temperature and the residuals concentration. The pressure variations within the cylinder were that small that the effect on the burning velocity was insignificant and the equivalence ratio was assumed as the global ratio which in this case was 1. The mean temperature field over 25 cycles, the standard deviation and the coefficient of variation for DVA and SVA at the tumble and swirl planes are showed in Figures 7.20 and 7.21. For the mean temperature field, different limits have been applied on the legends of the two strategies because of the ~60K difference in the in-cylinder average temperatures. For the SD and CoV, the same limits have been applied. Firstly, the mean temperature contour plots showed that the DVA has a more concentrated higher temperature field at the center of the tumble vortex, which agrees with the observations of Chapter 4. The temperature for the SVA is more homogeneous and again agreed with the results of Chapter 4. An observation of the spatial distribution of the SD and CoV showed that within the cylinder, both the deviation and the variation are very similar. More specifically, the deviation is in the range of 7K-20K for both DVA and SVA but the spatial distribution is different due to the different flow which mixed the residual gases with the fresh mixture of air and EGR. When the CoV was plotted for the x- and y-axis 5mm above the fire face of the dome (Figure 7.22) the variations of temperature for both valve strategies were very similar and around 1%-2%. In the x-axis the variations of temperature for SVA are higher for the half of the domain and the trend reversed for the other half of the domain. In the y-axis the centre of the cylinder exhibited higher temperature variations with SVA and the trend was reversed for the regions near to the liner.



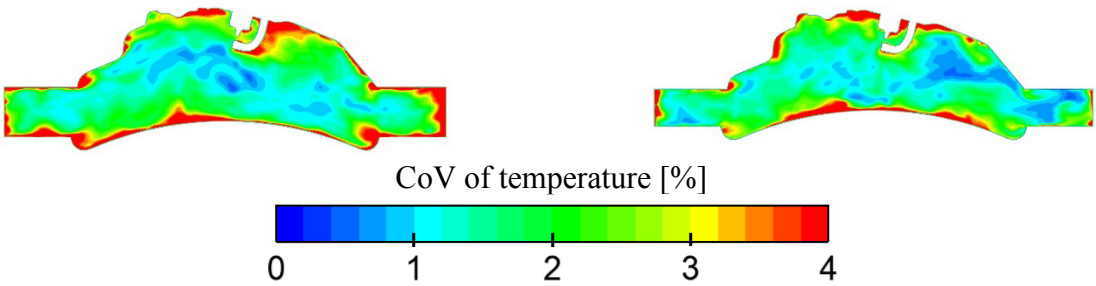
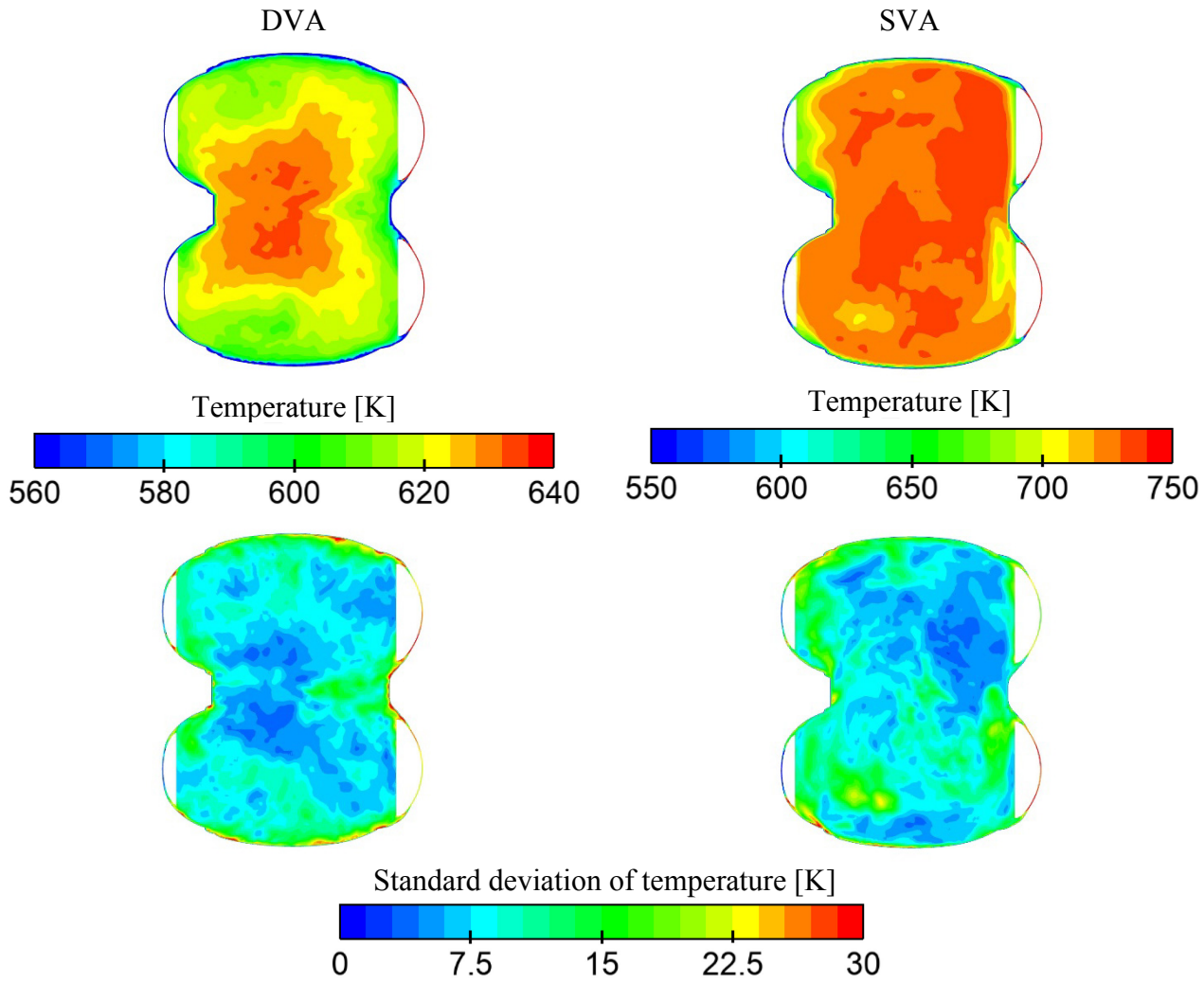


Figure 7.20 Spatial distribution of mean, standard deviation and CoV of temperature for DVA and SVA over 25 cycles. Tumble plane



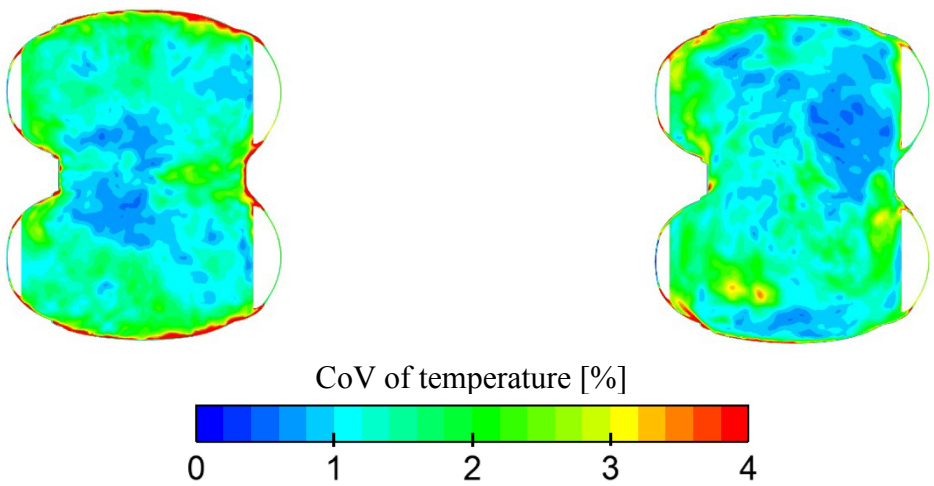


Figure 7.21 Spatial distribution of mean, standard deviation and CoV of temperature for DVA and SVA over 25 cycles. Swirl plane

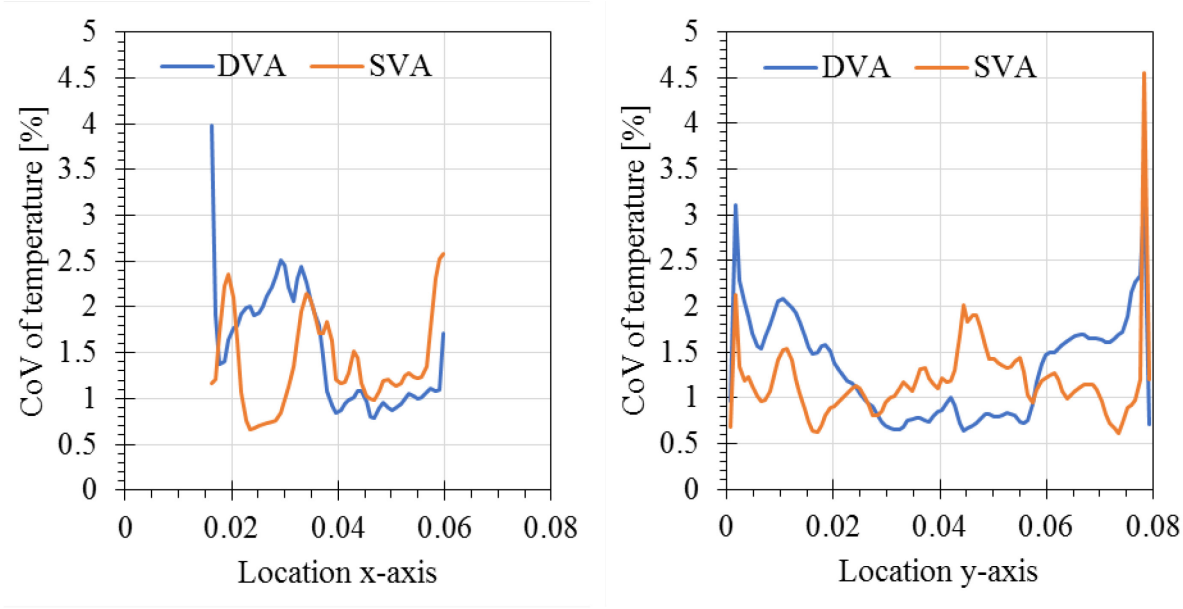
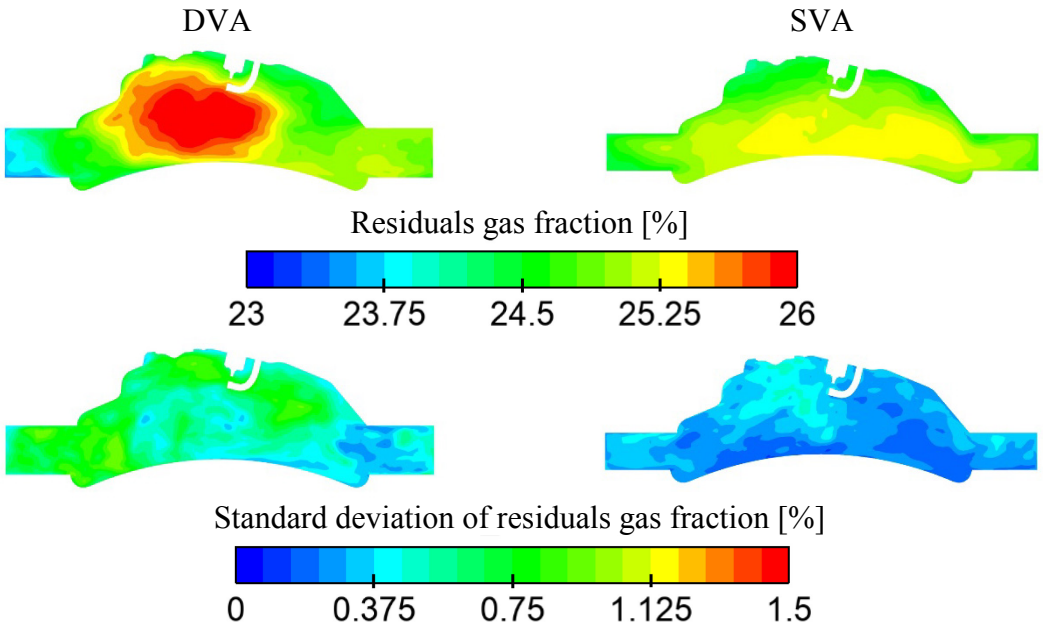


Figure 7.22 CoV of temperature for DVA and SVA along the x- and y-axis at z=+5mm

The temperature variations for the two valvetrain strategies were very similar and a concrete conclusion could not be drawn as within the cylinder, the spatial distribution of the CoV showed that some regions exhibit higher variations with DVA and some others had higher variations with SVA, but in all the cases the variations were in the order of 1%-2%. Thus, the second contributor for the variations of the laminar burning velocity, the residuals gas fraction, was studied. In this case, the total RGF was considered which means the internal residuals from the combustion of the previous cycle, the residuals trapped due to the LIVC of the full lift and the external exhaust gas recirculation (EGR). Plots of the mean RGF, the standard deviation

and the coefficient of variation at the tumble and swirl planes for DVA and SVA have been displayed in Figures 7.23 and 7.24. For both cases, the mean trapped residuals gas fraction is around 25%. For DVA, a higher concentration was seen in the tumble core, where the higher temperatures were also seen while for the SVA is better homogenised. By looking at the standard deviation contour plots it is clear that the deviation from the mean is smaller for the SVA than that of the DVA in both planes. Because the distribution of the RGF concentrations was different for the two strategies, the CoV of the RGF was compared for DVA and SVA. Once more, it was evident that the variations were lower for SVA than DVA. The maximum variations for SVA were 2% while in some regions with the DVA the variations reached 4%. This is also showed in the graphs of Figure 7.25 which show the CoV in the x- and y-axis. The variations for SVA are always below 2% and below the variations of DVA. The combination of residuals and temperature variations resulted in the lower variability of laminar burning velocity when SVA was adopted. Because of the high residual fractions (25%) the effect of temperature on the burning velocity is highly suppressed as it has been showed in Chapter 4. Thus, the variability of the residual gas concentration is the dominant factor of the variabilities in the laminar burning velocity. A study of Pera *et al.* (2014) concluded that the residual gas heterogeneity in lean combustion can lead to an additional cyclic variation in flame development. Due to the higher variability of RGF for DVA, the heterogeneity could be deteriorated.



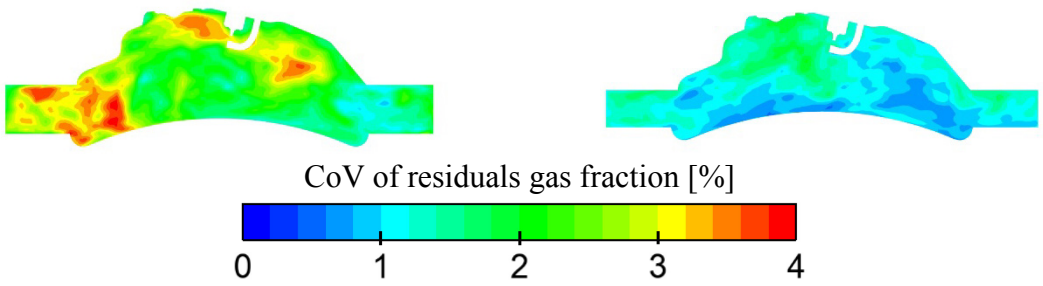
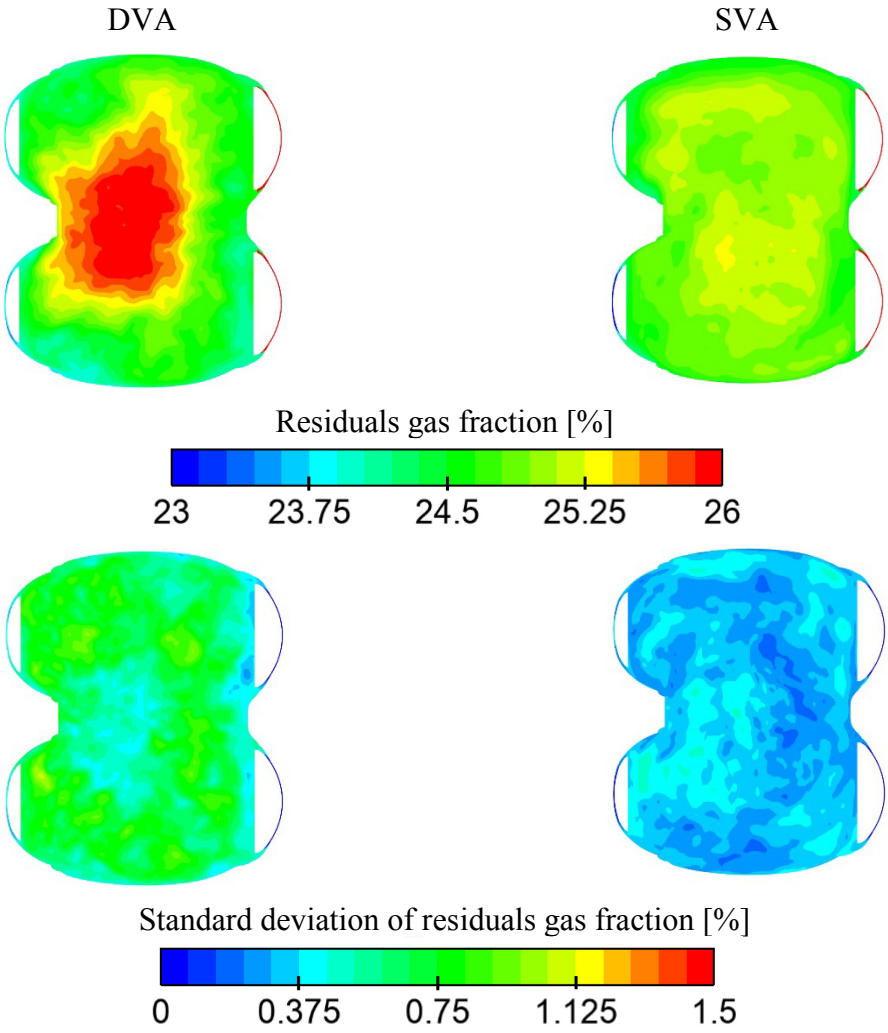


Figure 7.23 Spatial distribution of mean, standard deviation and CoV of residuals for DVA and SVA over 25 cycles. Tumble plane



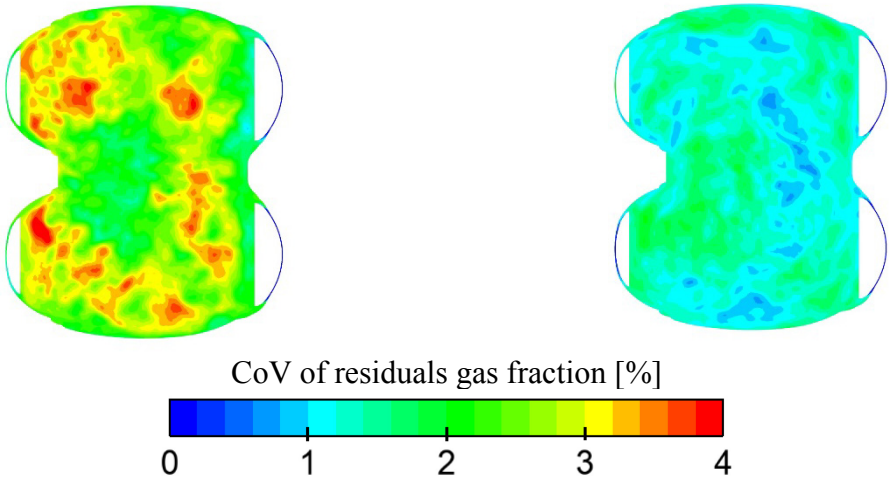


Figure 7.24 Spatial distribution of mean, standard deviation and CoV of residuals for DVA and SVA over 25 cycles. Swirl plane

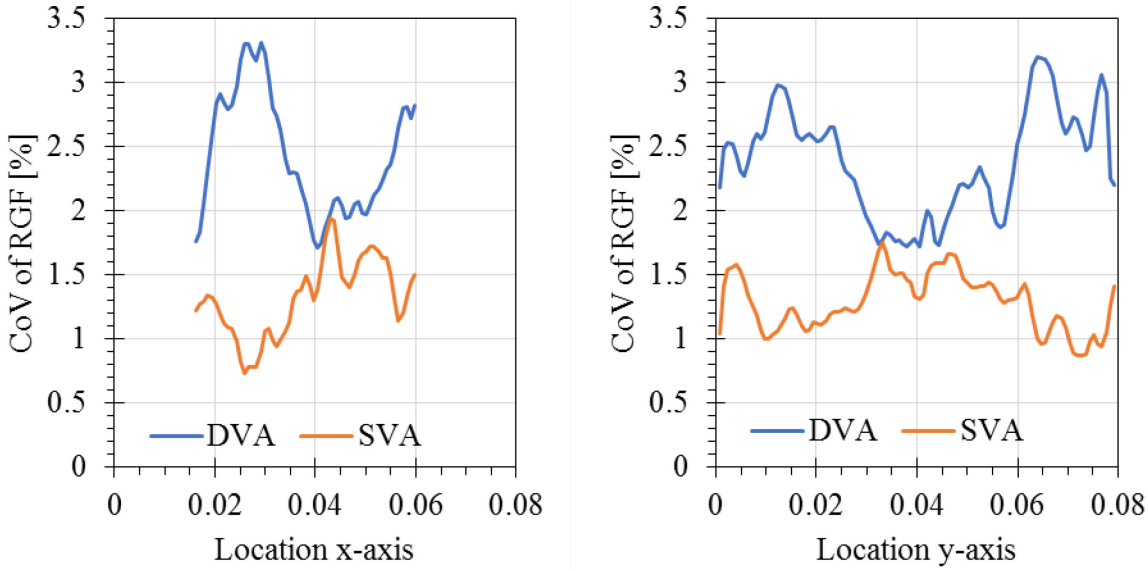


Figure 7.25 CoV of residuals for DVA and SVA along the x- and y-axis at z=+5mm

7.5. Closure

From an experimental point of view, it was seen that the cycle-to-cycle variability was decreased when Single Valve Actuation was adopted. This was manifested at high levels of dilution at which the DVA was above the stability limit of 3% CoV of NMEP while with SVA was below that limit. The differences of variability between DVA and SVA at 3.6 bar GMEP, 1500 RPM and 20%EGR and λ=1 was studied with the use of LES. The conclusions of this study were:

- The mesh resolution was sufficient for LES simulations as the turbulence resolution was below the threshold of 0.2 in most of the cylinder domain and in locations near sharp edges of the walls it was around 0.32.
- The validation showed a good agreement between the average LES and experimental pressure trace for both DVA and SVA.
- A study on the statistical convergence of the in-cylinder average velocity was carried out according to the literature. The results showed that after 20 cycles, the mean in-cylinder velocity and the standard deviation was converged with a difference of 0.07% between the average of 20 and 25 cycles. Similarly, the study of the convergence of the spatial distribution of the mean velocity and standard deviation showed that after 20 cycle the convergence was sufficient.
- The data were compared at the ignition of each valve strategy and because of the different mean values, the coefficient of variation was used to compare the two cases. In terms of in-cylinder average pressure and temperature, the variations over 25 cycles were minor. For the pressure, the variations were 0.08% with DVA and 0.14% with SVA. For the temperature the variations were 0.09% and 0.08% with DVA and SVA respectively.
- The first indication of higher variability when DVA was operated was the coefficient of variation of the in-cylinder velocity. At ignition, the CoV for DVA was 4.8% and for SVA 1.1%, which agreed with the experimental trends of variability.
- When the spatial distribution of the mean velocity and standard deviation (or velocity RMS) for DVA and SVA, the tumble flow and the swirl flow of DVA and SVA respectively was predicted. In addition, the higher deviation with the SVA is linked to the higher TKE which has already been seen. The variations in the flow field were more difficult to be evaluated because of areas with mean velocities close to zero which increased the CoV. However, in the core of the flow (tumble for DVA and swirl for SVA), the variations were greater for DVA.
- The variations of the laminar burning velocity were greater for DVA (2%-3%) than SVA(1%) and this, in combination with the lower mean burning velocity at ignition for DVA, can reduce the values further which in turn can have a detrimental effect on the combustion event.
- The effect of temperature and residuals gas fraction on the laminar burning velocity were investigated as they were the two main factors affecting the variations of the

laminar burning velocity. The temperature variations were very similar for DVA and SVA (1%-2%) and mostly the distribution was different. The residual gas variations though showed a clear difference between DVA and SVA. The variation of SVA were always lower than those of DVA with the values of up to 2% (average was 1%-1.5%) for SVA and up to 4% in some regions with an average of 2.5%. The higher variations of residuals gases can play an important role in flame propagation and cycle-to-cycle variability as it has been shown in other studies (Pera *et al.* 2014).

- Thus, the mixing process of the intake charge with the internal residuals exhibited greater variations when DVA was adopted over SVA, which can also have an effect of the air-fuel mixture which was not studied in this work.

Chapter 8

Conclusions and Future Work

8.1. Summary and conclusions

The present work documented the numerical investigations of airflow, mixture preparation and heat transfer in a direct-injection spark-ignition engine with advanced valvetrain system with aim to increase the dilution tolerance for reduced fuel consumption and emissions at various engine loads. For this work, the commercial code STAR-CD was used with all associated sub-models to simulate the airflow, mixture preparation and heat transfer of a DISI engine. Firstly, a validation of the code was carried out along with all the necessary sub-models such as heat transfer, fuel injection, droplet wall-interaction etc. All these were combined to form a complete working model to represent the exhaust, intake and compression strokes and it would be valid for various engine loads. For this reason, a generalised methodology was developed for sub-cooled and for a newly developed flash-boiling model spray which would have the least possible differences in terms of implementation to engine modelling. After that, the validated model was used to provide interpretation about the benefits and drawbacks of the valve deactivation of a single cylinder thermal engine running at different loads and speeds. Furthermore, the mixture preparation and the pollutant formation were studied for the dual and single valve actuation for two different loads. Here, the flash-boiling model was necessary for the low engine load because of the low ambient pressure and high fuel temperature. Moreover,

two differential valve lift strategies were investigated in order to minimise the drawbacks while maintain the benefits of the single valve actuation. Lastly, the differences in the cyclic variations of the DVA and SVA at high dilution levels were investigated with the use of LES. The main findings of the current work are presented in the following sections:

Model validation

The conclusions of the preliminary studies and the model validation were:

- From a grid independent study, it was concluded that a model consisted of 2.2 million cells at BDC with cell size ranging from 0.5 mm to 0.8mm was adequate for mesh independent in-cylinder average and spatial distribution of velocity.
- The initialisation study showed that starting the simulation before EVO could minimise the effect of initial conditions from the first cycle and the conditions could be easier predicted and applied.
- From the validation of the pressure trace it was showed that wall heat fluxes have to be modelled for accurate in-cylinder pressure predictions. The importance of time dependent pressure and averaged temperature boundaries from the engine was demonstrated. The need of accurate valve lift curves was also showed.
- A comparison of the predicted flow field with PIV data of the AJ133 optical engine revealed some differences on the velocity magnitude at the beginning of the intake stroke which were damped out during compression stroke. The main characteristics of the flow were well predicted by the CFD and were in an agreement with other researchers who worked on the same engine.

The differences of the velocity magnitude between CFD and PIV were examined by investigating the flow coefficient of the intake manifold of the optical engine with different turbulence models.

- At low and medium valve lifts the flow coefficient was over-predicted by k-ε RNG while the other models gave better predictions. At higher lifts, k-ε RNG well predicted the flow coefficient but the other models under-predicted it. These results were acquired with refined regions around the valves.
- The same turbulence models were tested on the dynamic model with no effect on the in-cylinder quantities such as pressure and trapped mass. The comparison of the

predicted flow with different turbulence models revealed that the k-ε RNG was closer to the PIV data followed by the standard k-ε.

The heat fluxes from the gas to the walls of the AJ133 motoring engine were also validated on two engine loads:

- The numerical heat fluxes were in a good agreement with the experimental data for both investigated cases. Specific behaviour, especially during the expansion which was unique for each case was also predicted.

The conclusions of the fuel injection validation were:

- In a quiescent chamber, two different methods to initialise the droplets were tested (Blob method and Rosin-Rammler) and tuned to match the experimental data of spray structure, plume penetration, plume velocity and droplet diameter. More realistic behaviour and results closer to the experimental data were achieved with the Rosin-Rammler distribution.
- The spray structure and the behaviour of the sub-cooled spray in the engine simulation was in a good agreement with the experimental data of the motoring engine during different instants of the injection
- A newly developed flash-boiling spray model was implemented into the motoring AJ133 optical engine. Two different single component fuels were tested (n-pentane and iso-hexane) for their suitability to replicate gasoline flashing sprays. The n-pentane was found to be more suitable due to the better tuning process. The prediction of the flash-boiling spray structure in a motoring engine was in a good agreement with the experimental data.
- The flash-boiling model was further improved by introducing a generalised approach for implementing it in quiescent chambers and dynamic models without the effects of the grid dependence seen in the original model. The sub-cooled and flash-boiling models had the least possible differences for easier implementation.
- Two droplet-wall interaction models were tested (Bai-ONERA and Senda). A droplet to film transition model and a 1D conjugate heat transfer model were also considered. The droplet to film transition model showed a high grid dependence and it was not considered. The 1D conjugate heat transfer model did not improve the results and thus was not used. Overall, Senda model produced results closer to all the experimental data

of heat flux and liquid film footprint and it was chosen as the most suitable for the rest of the work.

Effects of valve deactivation on in-cylinder flow

Firstly, the differences between the Dual and Single Valve Actuation on the in-cylinder flow and various in-cylinder quantities were investigated without the effect of fuel injection for three different engine loads and two engine speeds. It was found that irrespective of engine load:

- There was an increased in-cylinder flow activity by adopting SVA due to higher valve jet which increases the in-cylinder flow velocity.
- Due to the asymmetry created by SVA, a strong swirl motion is generated while maintaining the magnitude of the Y-tumble at the same level as with the DVA due to the geometry of the port.
- With the use of SVA, the turbulent kinetic energy was increased at spark timing when compared to DVA. Also, the area of high TKE within the cylinder was increased by adopting SVA and also the location is more favourable for the combustion as it encloses the spark plug. This is a factor that denotes faster combustion as seen in the experiments.
- With SVA, the trapped residuals were increased which in turn, increased the in-cylinder temperature.
- Due to the increased in-cylinder temperature, the laminar burning velocity was also increased. This is another factor for the faster combustion with SVA. With the level of residuals trapped in these cases, the dominant factor for the laminar burning velocity behaviour was the temperature.
- When the stoichiometric and lean cases were compared, there was a small increase on the in-cylinder flow quantities (Velocity, tumble and swirl, TKE). This increase was due to the increased intake pressure of the lean cases. As a consequence of the increased TKE, the engine could tolerate more dilution without detrimental increases in the ignition to 10% MFB and 10-90% MFB durations. As a result of the extension of dilution, a fuel consumption reduction of up to 3.8% (at 3.6 bar GMEP, 1500RPM) could be achieved, as seen in the experiments.
- The increased activity with the SVA and the higher in-cylinder temperature have a result of increased heat transfer from the gas to the engine walls. This explains the reduction of the polytropic index with SVA for both experiments and numerical

predictions. For all test points, this increased heat transfer resulted in fractional improvements in fuel consumption for equivalent levels of dilution.

Depending on the engine load and speed it was found that:

- With the increase in engine load, the heat transfer from the gas to the walls was increased mainly because of the increase of the density of the working fluid for both DVA and SVA. Moreover, the maximum heat transfer difference between DVA and SVA was increased at higher loads. The significant increase of heat transfer with SVA at higher loads, offset the favourably shorter burn durations resulting in a negligible benefit in fuel consumption for equivalent dilution, but some benefit could be gained through the extension of dilution (3.1% at 7.9 bar GMEP, 1500RPM and 1.3% at 9.8 bar GMEP, 2000RPM).
- The two main contributors for the increased heat transfer when adopting SVA is the enhanced flow motion and the increased in-cylinder temperature for equivalent dilutions. Due to the same trapped mass, the density for DVA and SVA was the same and the difference in Cp due to the different residuals was insignificant (less than 1%).
- At low loads (1500RPM, 3.6 bar GMEP), the dominant factor for the additional heat transfer for SVA is the increase in in-cylinder temperature which increased the heat transfer by 12.5%. The enhanced charge motion increased the heat transfer by 10.5%.
- At higher loads, (1500RPM, 7.9 bar GMEP and 2000RPM, 9.8 bar GMEP) the dominant factor is the increased flow velocity close to the walls. The increase of heat transfer due to the higher temperature was 13.5% at 7.9 bar GMEP and 16% ta 9.8 bar GMEP. Due to the enhanced charge motion the increase was 34% and 36% respectively.
- It appears that an optimum level of enhanced in-cylinder charge motion attributed to SVA exists whereby the benefits of reduced burn duration and increased dilution tolerance can be realised without the shortfalls of invoking significantly increased heat transfer

Effects of valve deactivation on mixture preparation and emissions

A spray modelling was included in the simulations to investigate the mixture preparation and the emissions formation of the Dual and Single valve actuation at two different engine loads. The flash boiling model was used for the low load and sub-cooled spray for the higher load.

The results irrespective of the engine load showed that:

- Because of the Late Intake Valve Closure, a portion of fuel vapour escaped into the intake port during compression and thus, a multi-cycle approach was needed in order to achieve a converged global in-cylinder Lambda. Generally, 4 to 5 cycles were needed depending on the DVA or SVA strategy.
- Due to the Reynolds-Averaged method, a normalisation approach can be utilised in order to acquire data for the converged values from the second cycle. The global Lambda of the second cycle can be normalised to the global Lambda that is desired This method showed to have a maximum error of 0.7% and an average error of 0.1%.
- With the use of fuel injection, the in-cylinder velocity and TKE were increased at the time of ignition. Due to the strong in-cylinder flow with the use of SVA, the effect of the injection on the two aforementioned quantities was minor.
- Due to direct-injection, the temperature of the trapped mass dropped by about 80K when compared to the same case without the injection. The decrease of the in-cylinder temperature decreased the heat transfer for both DVA and SVA. However, the increase of the heat transfer from DVA to SVA (50%) remained at the same level as with the cases without the fuel injection.

Depending on the engine operating condition it was concluded that:

- At 7.9 bar GMEP, the Lambda contour plots revealed a better air-fuel mixing when SVA was adopted. The SVA showed an axial stratification where a leaner mixture was present near the head and a richer mixture near the piston. Radially the mixture was homogeneous. For the DVA cases, areas of either very lean or rich mixture were seen in the cylinder. The homogeneity index showed that the SVA was better homogenised than DVA at ignition. For the lower load (3.6 bar GMEP) because of the flash boiling mechanism with the smaller droplets and the faster evaporation the homogeneity was improved for both DVA and SVA but for the DVA the improvement was greater.

- The laminar burning velocity was reduced when fuel injection was introduced. This was mostly due to the decrease of the in-cylinder temperature. At 7.9 bar GMEP, the contour plots of the laminar burning velocity were similar to the cases without the fuel injection especially for the SVA which had increased homogeneity of the mixture. For the DVA, due to the areas of very lean or rich mixture, the contour plots at these locations deviated from the cases without the fuel. For the lower load, due to the increased homogeneity, the contour plots of the burning velocity were very close to those without the fuel injection cases.
- Due to the orientation and pattern of the injector, liquid film was formed at the piston crown. At the high load, the use of SVA reduced the liquid film almost by half because of the strong in-cylinder flow which was disintegrating the spray plumes. The reduction rate was faster for the SVA because of the enhanced flow which increased the evaporation rate and the stripping of the liquid film from the piston. At the low load, the liquid film on the piston crown was further reduced. This was a result of the decreased spray penetration and faster evaporation with the flash boiling model.
- When the emissions of the CO and unburnt hydrocarbons were investigated for λ=1.0 at 7.9 bar GMEP, it was found that for the DVA case, the percentage of rich mixture during combustion was higher for DVA than SVA. In addition, the rich zones were richer for DVA than SVA. Because of these reasons the production of CO and THC is greater for DVA than SVA as seen in the experiments.
- For the low load with DVA, a big region of rich mixture was found near and around the spark plug at ignition. For SVA, near the spark plug, the volume occupied by rich mixture was smaller and the average lambda was closer to stoichiometric which contributed less to the CO and THC emissions. Near the edges of the chamber, the rich mixture was increased with the SVA compared to the DVA which should contribute to the increased unburnt hydrocarbons of the experiments with SVA. However, the small differences between DVA and SVA in the rich regions of the simulations were also reflected in small differences in the experiments.
- For the leaner cases of the higher load, the size of rich zones was reduced drastically for both valve strategies but for the DVA were greater than SVA which was again reflected to higher CO and THC in the experiments.
- To study the NOx formation of the point of view of mixture preparation, a range of lambda which was considered as the worst case for NOx production was assumed. This

range was [1.05,1.15] considering that the highest NOx production is seen for λ=1.1. For the high load and for λ=1.0, for volumes up to 60 mm spheres the percentage of lean mixture was higher for SVA than DVA. As the NOx is formed in the post flame gases, it is more probable to be formed within the 60mm spherical volumes.

- By diluting the mixture (global λ=1.1) and due to the high homogeneity of the SVA, 80% or more of all considered spheres were within the chosen range of lambdas. For DVA this percentage was lower. Thus, there was a great increase in experimental NOx emissions from λ=1.0 to λ=1.1 and the increase was greater for SVA. Further dilution showed that the total cylinder has a greater volume of lean mixture in the chosen lambda range for SVA than DVA.
- For the lower load, the differences in the amount of mixture within the NOx range were smaller and also the amount itself was smaller, which was inline with the experimental results of lower NOx emissions and smaller differences between DVA and SVA.
- As temperature plays an important role in the NOx production, it was calculated from the experimental in-cylinder pressure and then it was used in the Zeldovivh mechanism. It was found that for λ=1.0, the effect of temperature is very similar for both DVA and SVA. However, for the diluted cases, the increased temperature of the SVA was also a factor attributing to the NOx production.
- From the analysis of the mixture at various volumes within the cylinder, some basic conclusions can be drawn which showed that the mixture homogeneity is important for the emissions. Rich regions can produce high numbers of CO and THC. Lean mixtures at specific lambdas can increase the NOx formation and can have a negative impact if the engine is running at lambdas near λ=1.1 and the homogeneity of the mixture is high.
- The above hypotheses were tested with a combustion simulation at λ=1.0 for DVA and SVA. There were some differences in the pressure traces between CFD and experiments, but the results were satisfactory without further tuning of the combustion model. The faster heat release rate was a reason of the higher peak pressure of the DVA. The combustion showed increased CO production for DVA as seen in the experiments and the CO was produced at the locations of the rich mixture. The NO production was higher for the SVA as seen in the experiments even though the temperature was lower. The production was at the regions where λ was near 1.1.

Differential Intake Valve Lift Studies

Two different approaches for differential intake valve lift were simulated in order to give an insight of the experimental measurements and understand the main beneficial factors attributing to the improved combustion metrics. It was concluded that:

- The generation of swirl motion played a very important role on the production and maintenance of the TKE at high levels, an important factor for improved combustion metrics such as the faster combustion.
- The tumble motion was of a secondary importance because the EIVC mode had significantly weaker tumble but the TKE was maintained at high levels due to the swirl motion
- Not only the increase of TKE is important but also the location and the distribution within the cylinder is important. Especially for EIVC mode, the increase was marginal, but the location was improved compared to DVA which gave a benefit by the faster combustion
- The heat transfer can be reduced by ~50% without compromising the TKE by reducing the strong in-cylinder flow motion by either LIVO or EIVC staggered lifts.
- An optimum case for each differential valve lift mode could be selected based on the in-cylinder TKE and heat transfer. These were the 5mm lift of LIVO mode and the 3 mm lift of the EIVC mode. Both cases had very similar heat transfer, TKE and swirl ratios. As both optimum cases revealed, the swirl has to be conserved at levels of about 20-10 units during compression in order to maintain high levels of TKE. These optimum cases for the CFD also agreed with the optimum cases from the experimental work.
- When the LIVO mode was adopted, the air-fuel mixture at ignition was very similar to the SVA axial stratification. By increasing the maximum valve lift the homogeneity was decreased but the axial stratification was maintained. The mixture formation at ignition varied with the EIVC mode. In the small lifts the mixture formation was also similar to SVA. With increased valve lift, air-fuel mixture differed from both DVA and SVA patters. For lifts of 4mm-5mm, a reverse axial stratification was apparent.
- The liquid film formation was reduced with the use of the LIVO mode and both the film mass and the pattern were similar to the SVA. When EIVC was adopted, the liquid film mass was increased due to the flow interacting with the spray plumes, directing

them towards the piston. In addition, the rate at which the film mass was reduced, increased with the increase of the valve lift.

- The emissions of CO and THC were increased with increased valve lift for both modes. This was the result of the combination of greater volumes of rich mixtures in the different interrogating volumes and the reduction of the lambda value of the rich regions when the valve lift was increased.
- Lastly the NOx production for the LIVO mode was reduced with the increased valve lift but the decrease was minor. This is believed to be due to the small differences seen for the mixture in the region of [1.05,1.15] in the spheres 20mm-40mm (around 40%-50%) of the volumes for the 1mm up to 4mm cases. For the EIVC mode, there is no apparent trend of the regions with the mixture at the specified lambda range for the spheres 20mm-40mm, but a reduction can be observed. The temperature reduction suggested by the experiments (peak pressure reduction) has an effect which was not taken into account with this approach.

Effects of valve deactivation on cyclic variations

The differences of variability between DVA and SVA at 3.6 bar GMEP, 1500 RPM and 20%EGR and λ=1 was studied with the use of parallel multi-cycle LES. The conclusions of this study were:

- The mesh resolution was sufficient for LES simulations as the turbulence resolution was below the threshold of 0.2 in most of the cylinder domain and in locations near sharp edges of the walls it was around 0.32.
- The validation showed a good agreement between the average LES and experimental pressure trace for both DVA and SVA.
- A study on the statistical convergence of the in-cylinder average velocity was carried out according to the literature. The results showed that after 20 cycles, the mean in-cylinder velocity and the standard deviation was converged with a difference of 0.07% between the average of 20 and 25 cycles. Similarly, the study of the convergence of the spatial distribution of the mean velocity and standard deviation showed that after 20 cycle the convergence was sufficient.

- The data were compared at the ignition of each valve strategy and because of the different mean values, the coefficient of variation was used to compare the two cases. In terms of in-cylinder average pressure and temperature, the variations over 25 cycles were minor.
- The first indication of higher variability when DVA was operated was the coefficient of variation of the in-cylinder velocity. At ignition, the CoV for DVA was 4.8% and for SVA 1.1%, which agreed with the experimental trends of variability.
- When the spatial distribution of the mean velocity and standard deviation (or velocity RMS) for DVA and SVA, the tumble flow and the swirl flow of DVA and SVA respectively was predicted. In addition, the higher deviation with the SVA is linked to the higher TKE which had already been seen. The variations in the flow field were more difficult to be evaluated because of areas with mean velocities close to zero which increased the CoV. However, in the core of the flow (tumble for DVA and swirl for SVA), the variations were greater for DVA.
- The variations of the laminar burning velocity were greater for DVA (2%-3%) than SVA(1%) and this, in combination with the lower mean burning velocity at ignition for DVA, can reduce the values further which in turn can have a detrimental effect on the combustion event.
- The effect of temperature and residuals gas fraction on the laminar burning velocity were investigated as they were the two main factors affecting the variations of the laminar burning velocity. The temperature variations were very similar for DVA and SVA and mostly the distribution was different. The residual gas variations though showed a clear difference between DVA and SVA. The variation of SVA were always lower than those of DVA. The higher variations of residuals gases can play an important role in flame propagation and cycle-to-cycle variability as it has been shown in other studies (Pera *et al*. 2014).
- The mixing process of the intake charge with the internal residuals exhibited greater variations when DVA was adopted over SVA, which can also have an effect of the air-fuel mixture which was not studied in this work.

8.2. Future work

Future studies based on the findings of the current work are summarised in this chapter. These further steps that can improve the accuracy of the results and increase the understanding of the physical phenomena studied in this thesis.

- Further investigation is needed on the incapability of the code to capture the recompression seen in both thermal and optical engine around gas exchange TDC. Different RANS turbulence models and LES studies did not predict the pressure at that time. Grid refinement, turbulence modelling can be studied. In addition, the actual exhaust valve lift has to be measured in the same way as the intake valve lift was measured and applied in this work.
- Additional studies could be carried out for the steady state port flow simulations to determine the resolution of the grid around the valves to capture more accurately the flow coefficient and compressibility effects at all lift ranges. This could then be transferred to a dynamic engine model, identify the limitations of refinement there and categorise the deviation between experiments, port flow simulations and engine simulations.
- Flash-boiling modelling is still in early stages of development. Further investigations are needed to improve the accuracy of the sprays, for various types of injectors and from low to high superheat sprays. This must be linked with in-nozzle flow simulations and experiments to understand the complex physical mechanisms of flash boiling in and out of the nozzle and how these can be applied in the Lagrangian multi-phase context.
- In this work, single-component fuels were used to replicate gasoline injection. A step further would be the use of multi-component fuels for both sub-cooled and flash boiling sprays. This can be extended to the multi-component liquid films.
- The collision model was found to produce unrealistic results especially for flash-boiling sprays. In addition, it was sensitive to the mesh resolution and the relative position of the injector in respect to the mesh. Solutions have been proposed but a unified method and modelling of collisions focused on fuel injection is necessary for accurate predictions.
- For cases with Late Intake Valve Closure where multiple cycles are needed for converged global in-cylinder Lambda, an approach similar to the normalisation

suggested in this work has to be implemented for combustion simulations. Normalisation of each scalar used in the combustion model is needed and test against the multi-cycle approach are necessary. This however, can significantly reduce the running time of this kind of simulations in the future.

- With the use of combustion simulations and experimental data, the approach suggested here for NOx predictions with the use of the range of lambdas in the cylinder can be refined and improved. In addition, the use of combustion modelling can improve the understanding of pollutant formation with various valve strategies and different air-fuel mixtures. The latter may also need to focus on soot/nanoparticulate modelling in terms of both mass and number, as nanoparticulate tailpipe emissions from direct injection spark ignition engines are to be regulated and their in-cylinder formation is still not well understood.
- Within the LES framework, the parallel multi-cycle approach has to be further investigated. More cycles have to be run for better statistical convergence and these need to be compared against consecutive LES cycles. In addition, for better understanding the cyclic variations, fuel injection is necessary. An indication of lower mixing variability with SVA has been shown here but this needs to be confirmed with the air-fuel mixture. Ultimately, LES combustion can complete the studies of the cycle-to-cycle variations. In this context, understanding the cyclic behaviour of flow and mixing variability in terms of energy contained in the larger scales and the smaller scales from cycle to cycle, and in the process identifying what may be termed ‘turbulence’ and what is ‘variability’ over a range of frequencies, is of paramount importance and still a topic of fundamental research in conjunction with experiments in optical engines.

References

Aamir, M.A. and Watkins, A.P., 1999, July. Dense propane spray analysis with a modified collision model. In ILASS-Europe 99 Congress (pp. 5-7).

Adachi, M., Tanaka, D., Hojyo, Y., Al-Roub, M., Senda, J. and Fujimoto, H., 1996. Measurement of fuel vapor concentration in flash boiling spray by infrared extinction/scattering technique. JSAE review, 17(3), pp.231-237.

AIAA Standards Committee, 1998. AIAA Guide for the Verification and Validation of Computational Fluid Dynamics Simuations (G-077-1998).

Aleiferis, P.G. and Van Romunde, Z.R., 2013. An analysis of spray development with iso-octane, n-pentane, gasoline, ethanol and n-butanol from a multi-hole injector under hot fuel conditions. Fuel, 105, pp.143-168.

Alger, T., Gingrich, J., Mangold, B. and Roberts, C., 2011. A continuous discharge ignition system for EGR limit extension in SI engines. SAE International Journal of Engines, 4(1), pp.677-692.

Alger, T., Gingrich, J., Roberts, C., Mangold, B. and Sellnau, M., 2013. A high-energy continuous discharge ignition system for dilute engine applications (No. 2013-01-1628). SAE Technical Paper.

Algieri, A., Bova, S., De Bartolo, C. and Nigro, A., 2007. Numerical and experimental analysis of the intake flow in a high performance four-stroke motorcycle engine: influence of the two-equation turbulence models. Journal of Engineering for Gas Turbines and Power, 129(4), pp.1095-1105.

Alkidas, A.C. and El Tahry, S.H., 2003. Contributors to the Fuel Economy Advantage of DISI Engines Over PFI Engines (No. 2003-01–3101). SAE Technical Paper.

Ameen, M.M., Yang, X., Kuo, T.W. and Som, S., 2017a, October. Using LES to simulate cycle-to-cycle variability during the gas exchange process. In: ASME 2017 Internal Combustion Engine Division Fall Technical Conference (pp. V002T06A015-V002T06A015). American Society of Mechanical Engineers

Ameen, M.M., Yang, X., Kuo, T.W. and Som, S., 2017b. Parallel methodology to capture cyclic variability in motored engines. International Journal of Engine Research, 18(4), pp.366-377

Aneja, R. and Abraham, J., 1998. How far does the liquid penetrate in a diesel engine: Computed results vs. measurements?. Combustion Science and Technology, 138(1-6), pp.233-255.

Angelberger, C., Poinsot, T. and Delhay, B., 1997. Improving near-wall combustion and wall heat transfer modeling in SI engine computations (No. 972881). SAE Technical Paper.

Arcoumanis, C., Gavaises, M. and French, B., 1997. Effect of fuel injection processes on the structure of diesel sprays (No. 970799). SAE Technical Paper.

Arcoumanis, C., Flora, H., Gavaises, M. and Badami, M., 2000. Cavitation in real-size multi-hole diesel injector nozzles (No. 2000-01-1249). SAE Technical Paper

Ashida, K., Takahashe, T., Tanaka, T., Yeom, J., Senda, J. and Fujimoto, H. 2000. 'Spray-wall interaction model considering superheating degree of the wall surface', ICLASS

Bai, C. and Gosman, A.D., 1995. Development of methodology for spray impingement simulation (No. 950283). SAE Technical Paper.

Bai, C. and Gosman, A.D., 1996. Mathematical modelling of wall films formed by impinging sprays (No. 960626). SAE Technical Paper.

Banaeizadeh, A., Afshari, A., Schock, H. and Jaberi, F., 2013. Large-eddy simulations of turbulent flows in internal combustion engines. International Journal of Heat and Mass Transfer, 60, pp.781-796.

Baum, E., Peterson, B., Surmann, C., Michaelis, D., Böhm, B. and Dreizler, A., 2013. Investigation of the 3D flow field in an IC engine using tomographic PIV. Proceedings of the Combustion Institute, 34(2), pp.2903-2910

Baumann, M., Di Mare, F. and Janicka, J., 2014. On the validation of large eddy simulation applied to internal combustion engine flows part II: numerical analysis. Flow, turbulence and combustion, 92(1-2), pp.299-317.

Baumgarten, C., 2006. Mixture formation in internal combustion engines. Springer Science & Business Media.

Beavis, N.J., Ibrahim, S.S., Manickam, P. and Malalasekera, W., 2015. Characteristics of GDI engine flow structures. IN: Leipertz, A. (ed.) Engine Combustion Processes, ESYTEC GmbH, Erlangen, pp.385-396

Beavis, N., Ibrahim, S., and Malalasekera, W., Numerical Simulations of a GDI Engine Flow Using LES and POD (No. 2016-01-0598). SAE Technical Paper

Beavis, N.J., Ibrahim, S.S. and Malalasekera, W., 2017a. Numerical evaluation of combustion regimes in a GDI engine. Flow, Turbulence and Combustion, pp.1-23.

Beavis, N.J., Ibrahim, S.S. and Malalasekera, W., 2017b. Impingement characteristics of an early injection gasoline direct injection engine: A numerical study. International Journal of Engine Research, 18(4), pp.378-393.

Beavis, N.J., 2017. Numerical studies of gasoline direct injection engine processes. PhD thesis. Loughborough University.

Benz, A., Rieβ, M., Sens, M., Wöbke, M. 2013. Valve Train Variabilities on Gasoline Engines between Dethrottling and Turbulence Generation. In: SIA International Powertrain Conference The Spark Ignition Engine of the Future, Strasbourg.

Binjuwair, S. and Ibrahim, S., 2013. Numerical Analysis of Flow Structure inside a Single Cylinder of a 4 Valve Head under Steady-State Condition (No. 2013-24-0186). SAE Technical Paper.

Bird, R.B., Stewart, E.W., Lightfoot, E.N. 1966. Transport phenomena. New York, John Wiley & Sons.

Blazek, J., 2015. Computational fluid dynamics: principles and applications. Butterworth-Heinemann.

Bonatesta, F., La Rocca, S., Hopkins, E. and Bell, D., 2014. Application of Computational Fluid Dynamics to Explore the Sources of Soot Formation in a Gasoline Direct Injection Engine (No. 2014-01-2569). SAE Technical Paper.

Borman, G.L. and Johnson, J.H., 1962. Unsteady vaporization histories and trajectories of fuel drops injected into swirling air (No. 620271). SAE Technical Paper.

Bottone, F., Kronenburg, A., Gosman, D. and Marquis, A., 2012. Large eddy simulation of diesel engine in-cylinder flow. Flow, turbulence and combustion, 88(1-2), pp.233-253.

Breda, S., D'Adamo, A., Fontanesi, S., Giovannoni, N., Testa, F., Irimescu, A., Merola, S., Tornatore, C. and Valentino, G., 2016. CFD analysis of combustion and knock in an optically accessible GDI engine. SAE International Journal of Engines, 9(2016-01-0601), pp.641-656.

Brenn, G., (2011) Droplet Collision. In: Ashgriz, Nasser, ed. Handbook of atomization and sprays: theory and applications. Springer Science & Business Media, pp. 157-181

Butcher, A.J., Aleiferis, P.G. and Richardson, D., 2015. Characterisation of Spray Development from Spark-Eroded and Laser-Drilled Multi-Hole Injectors in an Optical DISI Engine and in a Quiescent Injection Chamber (No. 2015-01-1903). SAE Technical Paper.

Caton, J.A., 2013. A Comparison of Lean Operation and Exhaust Gas Recirculation: Thermodynamic Reasons for the Increases of Efficiency (No. 2013-01-0266). SAE Technical Paper.

Celik, I., Yavuz, I. and Smirnov, A., 2001. Large eddy simulations of in-cylinder turbulence for internal combustion engines: a review. International Journal of Engine Research, 2(2), pp.119-148.

Cengel, Y.A., Ghajar, A.J. and Kanoglu, M., 2011. Heat and mass transfer: fundamentals & applications (Vol. 4). New York: McGraw-Hill

Çengel, Y. A. and Boles, M. A. 2015. Thermodynamics: an engineering approach. McGraw-Hill Education

Chryssakis, C.A., Assanis, D.N., Lee, J.K. and Nishida, K., 2003. Fuel spray simulation of high-pressure swirl-injector for DISI engines and comparison with laser diagnostic measurements (No. 2003-01-0007). SAE Technical Paper.

Clenci, A.C., Iorga-Simăn, V., Deligant, M., Podevin, P., Descombes, G. and Niculescu, R., 2014. A CFD (computational fluid dynamics) study on the effects of operating an engine with low intake valve lift at idle corresponding speed. Energy, 71, pp.202-217.

Colin, O., Benkenida, A. and Angelberger, C., 2003. 3D modeling of mixing, ignition and combustion phenomena in highly stratified gasoline engines. Oil & gas science and technology, 58(1), pp.47-62.

Colin, O. and Benkenida, A., 2004. The 3-zones extended coherent flame model (ECFM3Z) for computing premixed/diffusion combustion. Oil & Gas Science and Technology, 59(6), pp.593-609.

Copeland, C.D., Gao, X., Freeland, P.A., Neumeister, J. and Mitcalf, J., 2013. Simulation of exhaust gas residuals in a turbocharged, spark ignition engine (No. 2013-01-2705). SAE Technical Paper.

Costa, M., Iorio, B., Sorge, U. and Alfuso, S., 2009. Assessment of a numerical model for multi-hole gasoline sprays to be employed in the simulation of spark ignition GDI engines with a jet-guided combustion mode (No. 2009-01-1915). SAE Technical Paper.

Costa, M., Marchitto, L., Merola, S.S. and Sorge, U., 2014. Study of mixture formation and early flame development in a research GDI (gasoline direct injection) engine through numerical simulation and UV-digital imaging. Energy, 77, pp.88-96.

Dahms, R., Fansler, T.D., Drake, M.C., Kuo, T.W., Lippert, A.M. and Peters, N., 2009. Modeling ignition phenomena in spray-guided spark-ignited engines. Proceedings of the Combustion Institute, 32(2), pp.2743-2750.

Das, S., Houtz, P.J. and Reitz, R.D., 1999. Effect of injection spray angle and combustion chamber geometry on engine performance and emission characteristics of a large bore diesel engine. Proceedings of 1999 Spring Technical Conference of ASME Internal Combustion Engine, 32, pp.1-12.

De Bellis, V., Severi, E., Fontanesi, S. and Bozza, F., 2014a. Hierarchical 1D/3D approach for the development of a turbulent combustion model applied to a VVA turbocharged engine. Part I: Turbulence model. Energy Procedia, 45, pp.829-838.

De Bellis, V., Severi, E., Fontanesi, S. and Bozza, F., 2014b. Hierarchical 1D/3D approach for the development of a turbulent combustion model applied to a VVA turbocharged engine. Part II: Combustion model. Energy Procedia, 45, pp.1027-1036.

Devassy, B.M., Bakshi, S. and Ramesh, A., 2014. A new injector concept for multimode operation in gasoline direct injection engines. International Journal of Engine Research, 15(5), pp.626-638.

Diana, S., Iorio, B., Giglio, V. and Police, G., 2001. The effect of valve lift shape and timing on air motion and mixture formation of DISI engines adopting different VVA actuators (No. 2001-01-3553). SAE Technical Paper.

Dong, M., Chen, G., Xu, M. and Daniels, C., 2002. A preliminary CFD investigation of in-cylinder stratified EGR for spark ignition engines (No. 2002-01-1734). SAE Technical Paper.

Drake, M.C., Fansler, T.D., Solomon, A.S. and Szekely, G.A., 2003. Piston fuel films as a source of smoke and hydrocarbon emissions from a wall-controlled spark-ignited direct-injection engine (No. 2003-01-0547). SAE Technical Paper.

Dukowicz, J.K., 1979. Quasi-Steady Droplet Change in the Presence of Convection, Informal Report Los Alamos Scientific Laboratory, Los Alamos. N. Mex., USA, LA7997-MS. http://dx.doi.org/10.2172/6012968

Eichlseder, H., Baumann, E., Muller, P. and Neugebauer, S., 2000. Potential and risks of gasoline direct injection engines for passenger cardrivelines. MTZ worldwide, 61(3), pp.2-5.

El Wakil, M.M., Uyehara, O.A. and Myers, P.S., 1954. A theoretical investigation of the heating-up period of injected fuel droplets vaporizing in air.

Enaux, B., Granet, V., Vermorel, O., Lacour, C., Thobois, L., Dugué, V. and Poinsot, T., 2011. Large eddy simulation of a motored single-cylinder piston engine: numerical strategies and validation. Flow, turbulence and combustion, 86(2), pp.153-177

Ferrey, P., Miehe, Y., Constensou, C. and Collee, V. 2014. Potential of a Variable Compression Ratio Gasoline SI Engine with Very High Expansion Ratio and Variable Valve Actuation. SAE International Journal of Engines, 7(1), pp.468-487.

Ferziger, J.H. and Peric, M., 2012. Computational methods for fluid dynamics. Springer Science & Business Media.

Fischer, J., Velji, A. and Spicher, U., 2004. Investigation of cycle-to-cycle variations of in-cylinder processes in gasoline direct injection engines operating with variable tumble systems (No. 2004-01-0044). SAE Technical Paper

Fontana, G. and Galloni, E., 2009. Variable valve timing for fuel economy improvement in a small spark-ignition engine. Applied Energy, 86(1), pp.96-105.

Fontanesi, S., Gagliardi, V., Malaguti, S. and Valentino, G., 2006. Detailed Experimental and Numerical Investigation of the Spray Structure in a GDI High-Pressure Swirling Injector. In 10th International Congress on liquid atomization and spray systems iclass-2006 (pp. 1-8). International Institute for Liquid Atomization and Spray Systems.

Fontanesi, S., Cicalese, G., d'Adamo, A. and Cantore, G., 2014. A methodology to improve knock tendency prediction in high performance engines. Energy Procedia, 45, pp.769-778.

Forte, C., Bianchi, G.M., Corti, E., Fantoni, S. and Costa, M., 2014a. Cfd methodology for the evaluation of knock of a pfi twin spark engine. Energy Procedia, 45, pp.859-868.

Forte, C., Bianchi, G.M., Corti, E., Michele, B. and Stefano, F., 2014b. Evaluation of the mixture formation process of high performance engine with a combined experimental and numerical methodology. Energy Procedia, 45, pp.869-878.

Foucart, H., 1998. Modélisation tridimensionnelle des films liquides pariétaux dans les moteurs à combustion interne. PhD thesis. Faculté des sciences de l'Université de Rouen, France

Friedrich, M.A., Lan, H., Wegener, J.L., Drallmeier, J.A. and Armaly, B.F., 2008. A separation criterion with experimental validation for shear-driven films in separated flows. Journal of Fluids Engineering, 130(5), p.051301.

Frottier, C., Sens, M., Rieß, M., Wigger, M., Benz, A., Maekawa, N., Onishi, K., Oryoji, K. and Machida, K., 2014. Achieving Very Low PN Emissions with an Advanced Multi-Hole Injector Functionality and Adapted Spray Targeting Under High Fuel Pressure Conditions. SAE International Journal of Engines, 7(2014-01-2605), pp.1744-1751.

Fujimoto, H., Nakagawa, T., Kudo, H., Wakisaka, T. and Shimamoto, Y., 1995. A study on the formation of vertical vortex in the cylinder of an IC engine using CFD: Effect of intake valve closing timing. JSAE review, 16(4), pp.349-355.

Galloni, E., Fontana, G. and Palmaccio, R., 2012. Numerical analyses of EGR techniques in a turbocharged spark-ignition engine. Applied Thermal Engineering, 39, pp.95-104.

Gandhi, A.H. and Meinhart, M., 2009. Fuel Injector Flow Rate Analysis for the Duratec 35 EcoBoost Engine (No. 2009-01-1505). SAE Technical Paper.

Gilles-Birth, I., Bernhardt, S., Spicher, U. and Rechs, M., 2005. A study of the in-nozzle flow characteristic of valve covered orifice nozzles for gasoline direct injection (No. 2005-01-3684). SAE Technical Paper.

Godrie, P. and Zellat, M., 1994. Simulation of flow field generated by intake port-valve-cylinder configurations-comparison with measurements and applications (No. 940521). SAE Technical Paper.

Gülder, Ö.L., 1991, January. Turbulent premixed flame propagation models for different combustion regimes. In Symposium (International) on Combustion (Vol. 23, No. 1, pp. 743-750). Elsevier.

Habchi, C., Foucart, H. and Baritaud, T., 1999. Influence of the wall temperature on the mixture preparation in DI gasoline engines. Oil & Gas Science and Technology, 54(2), pp.211-222.

Habchi, C., 2010. A comprehensive model for liquid film boiling in internal combustion engines. Oil & Gas Science and Technology–Revue de l'Institut Français du Pétrole, 65(2), pp.331-343.

Harshavardhan, B. and Mallikarjuna, J.M., 2015. Effect of piston shape on in-cylinder flows and air–fuel interaction in a direct injection spark ignition engine–A CFD analysis. Energy, 81, pp.361-372.

Hasse, C., Sohm, V. and Durst, B., 2010. Numerical investigation of cyclic variations in gasoline engines using a hybrid URANS/LES modeling approach. Computers & Fluids, 39(1), pp.25-48.

Haworth, D.C., 1999. Large-eddy simulation of in-cylinder flows. Oil & Gas Science and Technology, 54(2), pp.175-185.

Heisler, H., 1999. Vehicle and engine technology. 2nd ed. London: Arnold

Heywood, J.B., 1988. Internal combustion engine fundamentals (Vol. 930). New York: Mcgraw-hill.

Horie, K., Nishizawa, K., Ogawa, T., Akazaki, S. and Miura, K., 1992. The development of a high fuel economy and high performance four-valve lean burn engine (No. 920455). SAE Technical Paper.

Hosaka, T., Sugii, T., Ishii, E., Oryoji, K. and Sukegawa, Y., 2016. Numerical Study of Internal Combustion Engine using OpenFOAM® (No. 2016-01-1346). SAE Technical Paper.

Hou, S. and Schmidt, D.P., 2006. Adaptive collision meshing and satellite droplet formation in spray simulations. International Journal of Multiphase Flow, 32(8), pp.935-956.

Hsiang, L.P. and Faeth, G.M., 1992. Near-limit drop deformation and secondary breakup. International Journal of Multiphase Flow, 18(5), pp. 635–652.

Huang, C. and Lipatnikov, A., 2011. Modelling of gasoline and ethanol hollow-cone sprays using OpenFOAM (No. 2011-01-1896). SAE Technical Paper.

Huang, Y., Hong, G. and Huang, R., 2014. Numerical Investigation to the Effect of Ethanol/Gasoline Ratio on Charge Cooling in an EDI+ GPI Engine (No. 2014-01-2612). SAE Technical Paper.

Huang, Y., Hong, G. and Huang, R., 2016. Effect of injection timing on mixture formation and combustion in an ethanol direct injection plus gasoline port injection (EDI+ GPI) engine. Energy, 111, pp.92-103.

Huang, Y., Hong, G. and Zhou, J., 2017. Numerical Modelling of Ethanol Direct Injection (EDI) Sprays of a Multi-Hole Injector under Non-Evaporating, Transition and Flash-Boiling Conditions (No. 2017-01-2316). SAE Technical Paper.

Huh, K.Y. and Gosman, A.D. 1991. 'A phenomenological model of Diesel spray atomisation', Proc. Int. Conf. on Multiphase Flows (ICMF '91), Tsukuba, 24-27 September.

Hwang, S.S., Liu, Z. and Reitz, R.D., 1996. Breakup mechanisms and drag coefficients of high-speed vaporizing liquid drops. Atomization and Sprays, 6(3).

Janet, J.P., Liao, Y. and Lucas, D., 2015. Heterogeneous nucleation in CFD simulation of flashing flows in converging–diverging nozzles. International Journal of Multiphase Flow, 74, pp.106-117.

Jarvis, S., Justham, T., Clarke, A., Garner, C.P., Hargrave, G.K. and Richardson, D., 2006. Motored SI IC engine in-cylinder flow field measurement using time resolved digital PIV for characterisation of cyclic variation (No. 2006-01-1044). SAE Technical Paper

Jones, W.P. and Launder, B., 1972. The prediction of laminarization with a two-equation model of turbulence. International journal of heat and mass transfer, 15(2), pp.301-314.

Jovanovic, Z.S., Basara, B.S., Tomić, M.V. and Petrović, V.S., 2011. Some subtleties concerning fluid flow and turbulence modeling in 4.-valve engines. Thermal science, 15(4), pp.1065-1079.

Justham, T., Jarvis, S., Garner, C.P., Hargrave, G.K., Clarke, A. and Richardson, D., 2006. Single cylinder motored SI IC engine intake runner flow measurement using time resolved digital particle image velocimetry (No. 2006-01-1043). SAE Technical Paper.

Justham, T., 2010. Cyclic variation in the flow field behaviour within a direct injection spark ignition engine: a high speed digital particle image velocimetry study. PhD thesis. Loughborough University.

Kampa, M. and Castanas, E., 2008. Human health effects of air pollution. Environmental pollution, 151(2), pp.362-367.

Keller, P., Knorsch, T., Wensing, M. and Hasse, C., 2015. Experimental and numerical analysis of iso-octane/ethanol sprays under gasoline engine conditions. International Journal of Heat and Mass Transfer, 84, pp.497-510.

Kim, J.N., Kim, H.Y., Yoon, S.S. and Sa, S.D., 2008. Effect of intake valve swirl on fuel-gas mixing and subsequent combustion in a CAI engine. International journal of automotive technology, 9(6), pp.649-657.

Kim, T. and Park, S., 2018. Modeling flash boiling breakup phenomena of fuel spray from multi-hole type direct-injection spark-ignition injector for various fuel components. Energy Conversion and Management, 160, pp.165-175.

Köpple, F., Jochmann, P., Hettinger, A., Kufferath, A. and Bargende, M., 2015. A novel CFD approach for an improved prediction of particulate emissions in GDI engines by considering the spray-cooling on the piston (No. 2015-01-0385). SAE Technical Paper.

Kountouriotis, A., Aleiferis, P.G. and Charalambides, A.G., 2014. Numerical investigation of VOC levels in the area of petrol stations. Science of The Total Environment, 470, pp.1205-1224.

Kreuter, P., Heuser, P. and Schebitz, M., 1992. Strategies to improve SI-engine performance by means of variable intake lift, timing and duration (No. 920449). SAE Technical Paper.

Krzeczkowski, S.A., 1980. Measurement of liquid droplet disintegration mechanisms. International Journal of Multiphase Flow, 6(3), pp.227-239.

Kurniawan, W.H., Abdullah, S. and Shamsudeen, A., 2007. A computational fluid dynamics study of cold-flow analysis for mixture preparation in a motored four-stroke direct injection engine. Journal of Applied Sciences, 7(19), pp.2710-2724.

Launder, B.E. and Spalding, D.B., 1974. The numerical computation of turbulent flows. Computer methods in applied mechanics and engineering, 3(2), pp.269-289.

Lavoie, G.A., Heywood, J.B. and Keck, J.C., 1970. Experimental and theoretical study of nitric oxide formation in internal combustion engines. Combustion science and technology, 1(4), pp.313-326.

Lee, J.H., Goto, S., Tsurushima, T., Miyamoto, T. and Wakisaka, T., 2000. Effects of injection conditions on mixture formation process in a premixed compression ignition engine (No. 2000-01-1831). SAE Technical Paper.

Lee, K. and Abraham, J., 2011. Spray Applications in Internal Combustion Engines, Ashgriz, N. ed., Handbook of Atomization and Sprays. Boston, MA: Springer US.

Lefebvre, A.H. and McDonell, V.G., 2017. Atomization and sprays. CRC press.

Levy, N., Amara, S. and Champoussin, J.C., 1998. Simulation of a diesel jet assumed fully atomized at the nozzle exit (No. 981067). SAE Technical Paper.

Li, Q., Cai, T.M., He, G.Q. and Hu, C.B., 2006. Droplet collision and coalescence model. Applied Mathematics and Mechanics, 27(1), pp.67-73.

Li, Z.H., He, B.Q. and Zhao, H., 2014. Application of a hybrid breakup model for the spray simulation of a multi-hole injector used for a DISI gasoline engine. Applied Thermal Engineering, 65(1-2), pp.282-292.

Liu AB, Mather D, Reitz RD (1993) Modelling the Effects of Drop Drag and Breakup on Fuel Sprays (No. 930072). SAE Technical Paper.

Lucchini, T., D'Errico, G., Onorati, A., Bonandrini, G., Venturoli, L. and Di Gioia, R., 2012. Development of a CFD approach to model fuel-air mixing in gasoline direct-injection engines (No. 2012-01-0146). SAE Technical Paper.

Lucchini, T., Fiocco, M., Onorati, A., Montanaro, A., Allocca, L., Sementa, P., Vaglieco, B.M. and Catapano, F., 2013. Full-cycle CFD modeling of air/fuel mixing process in an optically accessible GDI engine. SAE International Journal of Engines, 6(2013-24-0024), pp.1610-1625.

Lucchini, T., D'Errico, G., Onorati, A., Bonandrini, G., Venturoli, L. and Di Gioia, R., 2014. Development and application of a computational fluid dynamics methodology to predict fuel–air mixing and sources of soot formation in gasoline direct injection engines. International Journal of Engine Research, 15(5), pp.581-596.

Lumley, J.L., 1999. Engines: an introduction. Cambridge University Press.

Mahrous, A.F.M., Wyszynski, M.L., Xu, H., Tsolakis, A. and Qiao, J., 2007. A CFD Investigation Into the Effects of Intake Valves Events on Airflow Characteristics in a Motored 4-Valve Engine Cylinder With Negative Valve Overlapping (No. 2007-24-0032). SAE Technical Paper.

Mahrous, A.F.M., Wyszynski, M.L., Xu, H., Tsolakis, A. and Qiao, J., 2008. Effect of intake valves timings on in-cylinder charge characteristics in a DI engine cylinder with negative valve overlapping (No. 2008-01-1347). SAE Technical Paper.

Malaguti, S., Fontanesi, S., Vaglieco, B.M., Sementa, P. and Catapano, F., 2011. Experimental and numerical investigation of the idle operating engine condition for a GDI engine (No. 2011-24-0031). SAE Technical Paper.

Malaguti, S., Fontanesi, S., Cantore, G., Montanaro, A. and Allocca, L., 2013. Modelling of primary breakup process of a gasoline direct engine multi-hole spray. Atomization and Sprays, 23(10).

Malcolm, J., Behringer, M., Aleiferis, P., Mitcalf, J. and OudeNijeweme, D., 2011. Characterisation of flow structures in a direct-injection spark-ignition engine using PIV, LDV and CFD (No. 2011-01-1290). SAE Technical Paper.

Mardi, M.K., Khalilarya, S. and Nemati, A., 2014. A numerical investigation on the influence of EGR in a supercharged SI engine fueled with gasoline and alternative fuels. Energy Conversion and Management, 83, pp.260-269.

Maroteaux, F., Llory, D., Le Coz, J.F. and Habchi, C., 2002. Liquid film atomization on wall edges—separation criterion and droplets formation model. Journal of fluids engineering, 124(3), pp.565-575.

Martinelli, L., Bracco, F.V. and Reitz, R.D., 1985. Comparisons of computed and measured dense spray jets (No. CONF-830704-10). Princeton Univ., NJ (USA); General Motors Technical Center, Warren, MI (USA).

Masi, M., Artico, L. and Gobbato, P., 2015. Measurements of the Intake and In-Cylinder Flow Field to Investigate the Reliability of CFD Steady-State Simulations for Actual Engines (No. 2015-24-2404). SAE Technical Paper.

Matsuda, T. and Senda, J., 2003. Modeling on spray wall interaction for direct gasoline injection engines. Nippon Kikai Gakkai Ronbunshu B Hen(Transactions of the Japan Society of Mechanical Engineers Part B)(Japan), 15(12), pp.2698-2705.

Matsumoto, A., Zheng, Y., Xie, X., Lai, M.C. and Moore, W., 2011. Interactions of Multi-hole DI Sprays with Charge Motion and their Implications to Flexible Valve-trained Engine Performance (No. 2011-01-1883). SAE Technical Paper.

Menter, F.R., 1993. Zonal two equation k-turbulence models for aerodynamic flows. AIAA paper, 2906, p.1993.

Mito, Y., Tanzawa, K., Watanabe, M. and Eiyama, Y., 2012. Advanced Combustion Performance for High Efficiency in New I3 1.2 L Supercharged Gasoline Engine by Effective Use of 3D Engine Simulation (No. 2012-01-0422). SAE Technical Paper.

Montanaro, A., Allocca, L., Ettorre, D., Lucchini, T., Brusiani, F. and Cazzoli, G., 2011. Experimental characterization of high-pressure impinging sprays for CFD modeling of GDI engines. SAE International Journal of Engines, 4(2011-01-0685), pp.747-763.

Moon, S., Bae, C., Choi, J. and Abo-Serie, E., 2007. The influence of airflow on fuel spray characteristics from a slit injector. Fuel, 86(3), pp.400-409.

Moore, W., Foster, M., Lai, M.C., Xie, X.B., Zheng, Y. and Matsumoto, A., 2011. Charge motion benefits of valve deactivation to reduce fuel consumption and emissions in a gdi, vva engine (No. 2011-01-1221). SAE Technical Paper.

Moreira, A.L., Moita, A.S. and Chandra, S. (2011). Droplet impact on a solid surface. In: Ashgriz, N. (ed.) Handbook of Atomization and Sprays. Springer US. (pp. 183-211)

Müller, S.H.R., Böhm, B., Gleißner, M., Grzeszik, R., Arndt, S. and Dreizler, A., 2010. Flow field measurements in an optically accessible, direct-injection spray-guided internal combustion engine using high-speed PIV. Experiments in fluids, 48(2), pp.281-290

Munnannur, A., Cremeens, C.M. and Liu, Z.G., 2011. Development of Flow Uniformity Indices for Performance Evaluation of Aftertreatment Systems. SAE International Journal of Engines, 4(1), pp.1545-1555

Naber, J.D. and Reitz, R.D., 1988. Modeling engine spray/wall impingement (No. 880107). SAE Technical Paper.

Nakata, K., Nogawa, S., Takahashi, D., Yoshihara, Y., Kumagai, A. and Suzuki, T., 2016. Engine technologies for achieving 45% thermal efficiency of SI engine. SAE International Journal of Engines, 9(1), pp.179-192.

Nakayama, Y., Maruya, T., Oikawa, T., Fujiwara, M. and Kawamata, M., 1994. Reduction of Emission from VTEC Engine During Cold-Start Condition (No. 940481). SAE Technical Paper.

Negro, S., Brusiani, F. and Bianchi, G.M., 2011. A numerical model for flash boiling of gasoline-ethanol blends in fuel injector nozzles. SAE International Journal of Fuels and Lubricants, 4(2011-24-0003), pp.237-256.

Nordin, P.A., 2001. Complex chemistry modeling of diesel spray combustion. PhD thesis. Chalmers University of Technology.

Nukiyama, S., 1939. An experiment on the atomization of liquid. Trans. Soc. Mech. Engrs. Japan, 5, pp.1-4.

Okroj, P., 2018. Thesis in preparation. PhD thesis, Imperial College London

O'Rourke, P.J., 1981. Collective drop effects on vaporizing liquid sprays (No. LA-9069-T). Los Alamos National Lab., NM (USA).

O'Rourke PJ, Amsden AA (1987) The TAB Method for Numerical Calculation of Spray Droplet Breakup (No. 872089). SAE Technical Paper.

O'Rourke, P.J. and Amsden, A.A., 2000. A spray/wall interaction submodel for the KIVA-3 wall film model (No. 2000-01-0271). SAE Technical Paper.

Otto, F. and Kruger, C. (2011) Simulation of Injection Processes. In: Merker, G.P., Schwarz, C. and Teichmann, R. eds., Combustion engines development: mixture formation, combustion, emissions and simulation. Springer Science & Business Media.

Pan, M., Shu, G., Wei, H., Zhu, T., Liang, Y. and Liu, C. 2014. Effects of EGR, compression ratio and boost pressure on cyclic variation of PFI gasoline engine at WOT operation. Applied Thermal Engineering, 64(1), pp.491-498.

Patterson, M.A. and Reitz, R.D. 1998. Modeling the Effects of Fuel Spray Characteristics on Diesel Engine Combustion and Emission (No. 980131). SAE Technical Paper.

Pei, Y.Q., Qin, J. and Pan, S.Z., 2014. Experimental study on the particulate matter emission characteristics for a direct-injection gasoline engine. Proceedings of the Institution of Mechanical Engineers, Part D: Journal of Automobile Engineering, 228(6), pp.604-616.

Pera, C., Knop, V., Chevillard, S. and Reveillon, J., 2014. Effects of residual burnt gas heterogeneity on cyclic variability in lean-burn SI engines. Flow, Turbulence and Combustion, 92(4), pp.837-863.

Piazzullo, D., Costa, M., Allocca, L., Montanaro, A. and Rocco, V., 2017. A 3D CFD Simulation of GDI Sprays Accounting for Heat Transfer Effects on Wallfilm Formation. SAE International Journal of Engines, 10(2017-24-0041), pp.2166-2175.

Pilch, M. and Erdman, C.A., 1987. Use of breakup time data and velocity history data to predict the maximum size of stable fragments for acceleration-induced breakup of a liquid drop. International journal of multiphase flow, 13(6), pp.741-757.

Polat, S., Uyumaz, A., Solmaz, H., Yilmaz, E., Topgül, T. and Yücesu, H.S., 2016. A numerical study on the effects of EGR and spark timing to combustion characteristics and NO x emission of a GDI engine. International Journal of Green Energy, 13(1), pp.63-70.

Pomraning, E., Richards, K. and Senecal, P.K., 2014. Modeling turbulent combustion using a RANS model, detailed chemistry, and adaptive mesh refinement (No. 2014-01-1116). SAE Technical Paper.

Pope, S.B., 2004. Ten questions concerning the large-eddy simulation of turbulent flows. New journal of Physics, 6(1), p.35.

Postrioti, L., Bosi, M., Cavicchi, A., AbuZahra, F., Di Gioia, R. and Bonandrini, G., 2015. Momentum Flux Measurement on Single-Hole GDI Injector under Flash-Boiling Condition (No. 2015-24-2480). SAE Technical Paper.

Price, C., Hamzehloo, A., Aleiferis, P. and Richardson, D., 2015. Aspects of Numerical Modelling of Flash-Boiling Fuel Sprays (No. 2015-24-2463). SAE Technical Paper.

Price, C., Hamzehloo, A., Aleiferis, P. and Richardson, D., 2016. An approach to modeling flash-boiling fuel sprays for direct-injection spark-ignition engines. Atomization and Sprays, 26(12).

Ramajo, D.E. and Nigro, N.M., 2010. In-cylinder flow computational fluid dynamics analysis of a four-valve spark ignition engine: comparison between steady and dynamic tests. Journal of Engineering for Gas Turbines and Power, 132(5), p.052804.

Ramasamy, D., Zainal, Z.A., Kadirgama, K. and Briggs, H.W.G., 2016. Effect of dissimilar valve lift on a bi-fuel CNG engine operation. Energy, 112, pp.509-519.

Ranz, W.E. and Marshall, W.R., 1952. Evaporation from drops. Chem. Eng. Prog, 48(3), pp.141-146.

Raza, M., Chen, L., Leach, F. and Ding, S., 2018. A review of particulate number (PN) emissions from gasoline direct injection (GDI) engines and their control techniques. Energies, 11(6), p.1417.

Reitz, R.D., Bracco, F.V., (1982), Mechanisms of Atomisation of a Liquid Jet, Physics of Fluids, Vol. 25, pp. 1730–42

Reitz, R.D. and Diwakar, R., 1986. Effect of drop breakup on fuel sprays (No. 860469). SAE Technical Paper.

Reitz, R.D. and Diwakar, R., 1987. Structure of high-pressure fuel sprays (No. 870598). SAE Technical Paper.

Riznic, J.R. and Ishii, M., 1989. Bubble number density and vapor generation in flashing flow. International Journal of Heat and Mass Transfer, 32(10), pp.1821-1833.

Roberts, P., Kountouriotis, A., Okroj, P., Aleiferis, P. and Cooper, B., 2018 Effects of Valve Deactivation on Thermal Efficiency in a Direct Injection Spark Ignition Engine under Dilute Conditions, (No. 2018-01-0892). SAE Technical Paper

Rodi, W., 1979. Influence of buoyancy and rotation on equations for the turbulent length scale. In 2nd symposium on turbulent shear flows (Vol. 1, p. 10).

Rosa, N.G., Villedieu, P., Dewitte, J. and Lavergne, G., 2006, August. A new droplet-wall interaction model. In: Proceedings of the 10th International Conference on Liquid Atomization and Spray Systems, Tokyo, Japan (Vol. 27, pp. 29-32).

Rutland, C.J., 2011. Large-eddy simulations for internal combustion engines–a review. International Journal of Engine Research, 12(5), pp.421-451

Sarikoc, F., Kettner, M., Velji, A., Spicher, U., Krause, A. and Elsaesser, A., 2006. Potential of reducing the NOx emissions in a spray guided DI gasoline engine by stratified exhaust gas recirculation (EGR) (No. 2006-01-1261). SAE Technical Paper.

Scarcelli, R., Matthias, N.S. and Wallner, T., 2014, October. Numerical and Experimental Analysis of Ignition and Combustion Stability in EGR Dilute GDI Operation. In: ASME 2014 Internal Combustion Engine Division Fall Technical Conference (pp. V001T03A015-V001T03A015). American Society of Mechanical Engineers.

Scarcelli, R., Sevik, J., Wallner, T., Richards, K., Pomraning, E. and Senecal, P.K., 2015, November. Capturing Cyclic Variability in EGR Dilute SI Combustion Using Multi-Cycle RANS. In: ASME 2015 Internal Combustion Engine Division Fall Technical Conference (pp. V002T06A010-V002T06A010). American Society of Mechanical Engineers.

Schernus, C., Ewald, J., DI Matteo, F., Morcinkowski, B. 2013. Methods to Reduce End Gas Temperature for Lower Knocking Sensitivity - A simulation Study. In: SIA International Powertrain Conference The Spark Ignition Engine of the Future, Strasbourg.

Schmidt, D.P. and Rutland, C.J., 2000. A new droplet collision algorithm. Journal of Computational Physics, 164(1), pp.62-80.

Schmitt, M., Hu, R., Wright, Y.M., Soltic, P. and Boulouchos, K., 2015. Multiple cycle LES simulations of a direct injection natural gas engine. Flow, Turbulence and Combustion, 95(4), pp.645-668.

Schulz, F., Schmidt, J., Kufferath, A. and Samenfink, W., 2014. Gasoline wall films and spray/wall interaction analyzed by infrared thermography. SAE International Journal of Engines, 7(3), pp.1165-1177.

Schulz, F., Schmidt, J. and Beyrau, F., 2015. Development of a sensitive experimental set-up for LIF fuel wall film measurements in a pressure vessel. Experiments in Fluids, 56(5), p.98.

Schulz, F., Samenfink, W., Schmidt, J. and Beyrau, F., 2016. Systematic LIF fuel wall film investigation. Fuel, 172, pp.284-292.

Senda, J., Hojyo, Y. and Fujimoto, H., 1994. Modelling of atomization process in flash boiling spray (No. 941925). SAE Technical Paper.

Senda, J., Kobayashi, M., Iwashita, S. and Fujimoto, H., 1996. Modeling of diesel spray impinging on flat wall. JSME International Journal Series B Fluids and Thermal Engineering, 39(4), pp.859-866.

Senda, J., Kanda, T., Al-Roub, M., Farrell, P.V., Fukami, T. and Fujimoto, H., 1997. Modeling spray impingement considering fuel film formation on the wall (No. 970047). SAE Technical Paper.

Senda, J. and Fujimoto, H.G., 1999. Multidimensional modeling of impinging sprays on the wall in diesel engines. Applied Mechanics Reviews, 52(4), pp.119-138.

Serras-Pereira, J., Aleiferis, P.G., Richardson, D. and Wallace, S., 2007. Mixture preparation and combustion variability in a spray-guided DISI engine (No. 2007-01-4033). SAE Technical Paper.

Serras-Pereira, J., Aleiferis, P.G., Richardson, D. and Wallace, S., 2008. Characteristics of Ethanol, Butanol, Iso-Octane and Gasoline Sprays and Combustion from a Multi-Hole Injector in a DISI Engine. SAE International Journal of Fuels and Lubricants, 1(2008-01-1591), pp.893-909.

Serras-Pereira, J., 2010. Spray formation and combustion of alcohols and gasoline in a direct-injection spark-ignition engine (Doctoral dissertation, PhD Thesis, University of London).

Serras-Pereira, J., Van Romunde, Z., Aleiferis, P.G., Richardson, D., Wallace, S. and Cracknell, R.F., 2010. Cavitation, primary break-up and flash boiling of gasoline, iso-octane and n-pentane with a real-size optical direct-injection nozzle. Fuel, 89(9), pp.2592-2607.

Serras-Pereira, J., Aleiferis, P.G. and Richardson, D., 2012. Imaging and heat flux measurements of wall impinging sprays of hydrocarbons and alcohols in a direct-injection spark-ignition engine. Fuel, 91(1), pp.264-297.

Serras-Pereira, J., Aleiferis, P.G., Walmsley, H.L., Davies, T.J. and Cracknell, R.F., 2013. Heat flux characteristics of spray wall impingement with ethanol, butanol, iso-octane, gasoline and E10 fuels. International Journal of Heat and Fluid Flow, 44, pp.662-683.

Sirignano, W.A. & Mehring, C., 2000. Review of theory of distortion and disintegration of liquid streams. Progress in Energy and Combustion Science, 26(4), pp.609–655.

Smagorinsky, J., 1963. General circulation experiments with the primitive equations: I. The basic experiment. Monthly weather review, 91(3), pp.99-164.

Solsjo, R., ICE Application Support Engineer (Personal communication, 17th May 2017)

Spiegler, P., Hopenfeld, J., Silberberg, M., Bumpus Jr, C.F. and Norman, A., 1963. Onset of stable film boiling and the foam limit. International Journal of Heat and Mass Transfer, 6(11), pp.987-989.

Stanton, D.W. and Rutland, C.J., 1996. Modeling Fuel Film Formation and Wall Interaction in Diesel Engines (No. 960628). SAE Technical Paper.

Sukegawa, Y., Kumano, K. and Ogata, K., 2014. Estimation of Particulate Matter in Direct Injection Gasoline Engines by Non-Combustion CFD (No. 2014-01-1142). SAE Technical Paper.

Sureshkumar, J., Ganesan, V., Mallikarjuna, J.M. and Govindarajan, S., 2013. Effect of Piston Crown Shape on In-Cylinder Flow Characteristics in a Direct Injection Engine-A CFD Study (No. 2013-01-2797). SAE Technical Paper.

Torres, D.J., O'rourke, P.J. and Amsden, A.A., 2003. Efficient multicomponent fuel algorithm. Combustion Theory and Modelling, 7(1), pp.67-86.

Towers, D.P. and Towers, C.E., 2004. Cyclic variability measurements of in-cylinder engine flows using high-speed particle image velocimetry. Measurement Science and Technology, 15(9), p.1917.

Van Dam, N., Zeng, W., Sjöberg, M. and Som, S., 2017, October. Parallel Multi-Cycle LES of an Optical Pent-Roof DISI Engine Under Motored Operating Conditions. In: ASME 2017 Internal Combustion Engine Division Fall Technical Conference (pp. V002T06A019-V002T06A019). American Society of Mechanical Engineers.

Van Romunde, Z., Aleiferis, P.G., Cracknell, R.F. and Walmsley, H.L., 2007. Effect of fuel properties on spray development from a multi-hole DISI engine injector (No. 2007-01-4032). SAE Technical Paper.

Van Romunde, Z. and Aleiferis, P., 2009. Effect of operating conditions and fuel volatility on development and variability of sprays from gasoline direct-injection multihole injectors. Atomization and Sprays, 19(3).

Verma, I., Bish, E., Kuntz, M., Meeks, E., Puduppakkam, K., Naik, C. and Liang, L., 2016. CFD Modeling of Spark Ignited Gasoline Engines-Part 2: Modeling the Engine in Direct Injection Mode along with Spray Validation (No. 2016-01-0579). SAE Technical Paper.

Vermorel, O., Richard, S., Colin, O., Angelberger, C., Benkenida, A. and Veynante, D., 2007. Multi-cycle LES simulations of flow and combustion in a PFI SI 4-valve production engine (No. 2007-01-0151). SAE Technical Paper.

Vermorel, O., Richard, S., Colin, O., Angelberger, C., Benkenida, A. and Veynante, D., 2009. Towards the understanding of cyclic variability in a spark ignited engine using multi-cycle LES. Combustion and Flame, 156(8), pp.1525-1541

Versteeg, H.K. and Malalasekera, W., 2007. An introduction to computational fluid dynamics: the finite volume method. Pearson Education.

von Kuensberg Sarre, C., Kong, S.C. and Reitz, R.D., 1999. Modeling the effects of injector nozzle geometry on diesel sprays (No. 1999-01-0912). SAE Technical Paper.

Wang, X., Zhao, H., Xie, H. and He, B.Q., 2014. Numerical study of the effect of piston shapes and fuel injection strategies on in-cylinder conditions in a PFI/GDI gasoline engine. SAE International Journal of Engines, 7(4), pp.1888-1899.

Wang, X., Zhao, H. and Xie, H., 2015. Effect of piston shapes and fuel injection strategies on stoichiometric stratified flame ignition (SFI) hybrid combustion in a PFI/DI gasoline engine by numerical simulations. Energy Conversion and Management, 98, pp.387-400.

Wei, H., Zhu, T., Shu, G., Tan, L. and Wang, Y., 2012. Gasoline engine exhaust gas recirculation - A review. Applied energy, 99, pp.534-544.

Weltens, H., Bressler, H., Terres, F., Neumaier, H. and Rammoser, D., 1993. Optimisation of catalytic converter gas flow distribution by CFD prediction (No. 930780). SAE Technical Paper.

White, F. M., 1988. Heat and Mass Transfer. Reading, MA: Addison-Wesley.

Wierzba, A., 1990. Deformation and breakup of liquid drops in a gas stream at nearly critical Weber numbers. Experiments in Fluids, 9(1), pp.59-64.

Wilcox, D.C., 1998. Turbulence modeling for CFD (Vol. 2, pp. 103-217). La Canada, CA: DCW industries.

Williams, B., Ewart, P., Wang, X., Stone, R., Ma, H., Walmsley, H., Cracknell, R., Stevens, R., Richardson, D., Fu, H. and Wallace, S., 2010. Quantitative planar laser-induced fluorescence imaging of multi-component fuel/air mixing in a firing gasoline-direct-injection engine: effects of residual exhaust gas on quantitative PLIF. Combustion and Flame, 157(10), pp.1866-1878.

Wilson, N.D., Watkins, A.J. and Dopson, C., 1993. Asymmetric valve strategies and their effect on combustion (No. 930821). SAE Technical Paper.

Xu, M., Chen, G., Daniels, C. and Dong, M., 2000. Numerical study on swirl-type high-dilution stratified EGR combustion system (No. 2000-01-1949). SAE Technical Paper.

Yakhot, V. and Orszag, S.A., 1986. Renormalization group analysis of turbulence. I. Basic theory. Journal of scientific computing, 1(1), pp.3-51.

Yakhot, V., Orszag, S.A., Thangam, S., Gatski, T.B. and Speziale, C.G., 1992. Development of turbulence models for shear flows by a double expansion technique. Physics of Fluids A: Fluid Dynamics (1989-1993), 4(7), pp.1510-1520.

Yamakawa, M., Youso, T., Fujikawa, T., Nishimoto, T., Wada, Y., Sato, K. and Yokohata, H. 2012. Combustion technology development for a high compression ratio SI engine. SAE International Journal of Fuels and Lubricants, 5(1), pp.98-105.

Yang, S., Song, Z., Wang, T. and Yao, Z., 2013. An experiment study on phenomenon and mechanism of flash boiling spray from a multi-hole gasoline direct injector. Atomization and Sprays, 23(5).

Yaws, C.L. and Gabbula, C., 2003. Yaws" Handbook of Thermodynamic and Physical Properties of Chemical Compounds. Knovel.

Zeldovich, Y.A., Frank-Kamenetskii, D. and Sadovnikov, P., 1947. Oxidation of nitrogen in combustion. Publishing House of the Acad of Sciences of USSR.

Zeng, Y. and Lee, C.F.F., 2001. An atomization model for flash boiling sprays. Combustion Science and Technology, 169(1), pp.45-67.

Zeng, W., Sjöberg, M. and Reuss, D.L., 2015. PIV examination of spray-enhanced swirl flow for combustion stabilization in a spray-guided stratified-charge direct-injection spark-ignition engine. International Journal of Engine Research, 16(3), pp.306-322

Zhang, Q., Kalva, V.T. and Tian, T., 2018. Modeling the Evolution of Fuel and Lubricant Interactions on the Liner in Internal Combustion Engines (No. 2018-01-0279). SAE Technical Paper.

Zhao, H., 2010. Advanced direct injection combustion engine technologies and development Volume 2: Diesel engines, Boca Raton : Oxford: CRC Press ; Woodhead Pub.

Zheng, Z., Liu, C., Tian, X. and Zhang, X., 2015. Numerical study of the effect of piston top contour on GDI engine performance under catalyst heating mode. Fuel, 157, pp.64-72.

Zhou, F., Fu, J., Ke, W., Liu, J., Yuan, Z. and Luo, B., 2017. Effects of lean combustion coupling with intake tumble on economy and emission performance of gasoline engine. Energy, 133, pp.366-379.

Zuo, B., Gomes, A.M. and Rutland, C.J., 2000. Modelling superheated fuel sprays and vaproization. International Journal of Engine Research, 1(4), pp.321-336.